

Robert Barthorpe *Editor*

Model Validation and Uncertainty Quantification, Volume 3

Proceedings of the 36th IMAC, A Conference and Exposition
on Structural Dynamics 2018



Conference Proceedings of the Society for Experimental Mechanics Series

Series Editor

Kristin B. Zimmerman, Ph.D.
Society for Experimental Mechanics, Inc.,
Bethel, CT, USA

More information about this series at <http://www.springer.com/series/8922>

Robert Barthelemy
Editor

Model Validation and Uncertainty Quantification, Volume 3

Proceedings of the 36th IMAC, A Conference and Exposition
on Structural Dynamics 2018

Editor

Robert Barthorpe
Department of Mechanical Engineering
University of Sheffield
Sheffield, UK

ISSN 2191-5644 ISSN 2191-5652 (electronic)
Conference Proceedings of the Society for Experimental Mechanics Series
ISBN 978-3-319-74792-7 ISBN 978-3-319-74793-4 (eBook)
<https://doi.org/10.1007/978-3-319-74793-4>

Library of Congress Control Number: 2018947382

© The Society for Experimental Mechanics, Inc. 2019

This work is subject to copyright. All rights are reserved by the Publisher, whether the whole or part of the material is concerned, specifically the rights of translation, reprinting, reuse of illustrations, recitation, broadcasting, reproduction on microfilms or in any other physical way, and transmission or information storage and retrieval, electronic adaptation, computer software, or by similar or dissimilar methodology now known or hereafter developed.

The use of general descriptive names, registered names, trademarks, service marks, etc. in this publication does not imply, even in the absence of a specific statement, that such names are exempt from the relevant protective laws and regulations and therefore free for general use.

The publisher, the authors and the editors are safe to assume that the advice and information in this book are believed to be true and accurate at the date of publication. Neither the publisher nor the authors or the editors give a warranty, express or implied, with respect to the material contained herein or for any errors or omissions that may have been made. The publisher remains neutral with regard to jurisdictional claims in published maps and institutional affiliations.

Printed on acid-free paper

This Springer imprint is published by the registered company Springer Nature Switzerland AG.
The registered company address is: Gewerbestrasse 11, 6330 Cham, Switzerland

Preface

Model Validation and Uncertainty Quantification represents one of nine volumes of technical papers presented at the 36th IMAC, A Conference and Exposition on Structural Dynamics, organized by the Society for Experimental Mechanics, and held in Orlando, Florida, February 12–15, 2018. The full proceedings also include volumes on Nonlinear Dynamics; Dynamics of Civil Structures; Dynamics of Coupled Structures; Special Topics in Structural Dynamics; Structural Health Monitoring, Photogrammetry and DIC; Rotating Machinery, Vibro-Acoustics and Laser Vibrometry; Sensors and Instrumentation, Aircraft/Aerospace and Energy Harvesting; and Topics in Modal Analysis and Testing.

Each collection presents early findings from experimental and computational investigations on an important area within structural dynamics. Model validation and uncertainty quantification (MVUQ) is one of these areas.

Modeling and simulation are routinely implemented to predict the behavior of complex dynamical systems. These tools powerfully unite theoretical foundations, numerical models, and experimental data which include associated uncertainties and errors. The field of MVUQ research entails the development of methods and metrics to test model prediction accuracy and robustness while considering all relevant sources of uncertainties and errors through systematic comparisons against experimental observations.

The organizers would like to thank the authors, presenters, session organizers, and session chairs for their participation in this track.

Sheffield, UK

Robert Barthorpe

Contents

1	Sparse Deconvolution for the Inverse Problem of Multiple-Impact Force Identification	1
	Baijie Qiao, Zhu Mao, Jinxin Liu, and Xuefeng Chen	
2	Validation of Container System Component Models for Drops	11
	Thomas M. Hall, Philip R. Ind, and Thomas J. Anthistle	
3	Validation of Container System Finite Element Models for IAEA Compliance	17
	Philip R. Ind, Thomas M. Hall, Thomas J. Anthistle, and Steve Nicholls	
4	Nonlinear Squeezing Wavelet Transform for Rotor Rub-Impact Fault Detection	21
	Chaowei Tong, Xuefeng Chen, and Shibin Wang	
5	Experimental Credibility and Its Role in Model Validation and Decision Making	31
	Sarah L. Kieweg and Walt R. Witkowski	
6	An Experimental Case Study for Nonlinear Model Validation: Effect of Nonlinearities in an Aero-Engine Structure	37
	Samson B. Cooper, Dario DiMaio, Ibrahim A. Sever, and Sophoclis Patsias	
7	Finite Element Model Updating of a Connecting Structure Based on Strain	49
	Ming Zhan, Qintao Guo, Lin Yue, and Baoqiang Zhang	
8	Nonlinearities of an Aircraft Piccolo Tube: Identification and Modeling	57
	T. Dossogne, P. Trillet, M. Schoukens, B. Bernay, J. P. Noël, and G. Kerschen	
9	Reliability Analysis of Existing Bridge Foundations for Reuse	61
	Nathan Davis and Masoud Sanayei	
10	Recent Developments in Hardware-in-the-Loop Testing	65
	Jonathan Millitzer, Dirk Mayer, Christian Henke, Torben Jersch, Christoph Tamm, Jan Michael, and Christopher Ranisch	
11	Assessing Structural Reliability at the Component Test Stage Using Real-Time Hybrid Substructuring	75
	Connor Ligeikis, Alex Freeman, and Richard Christenson	
12	Modal Identification Using a Roving Actuator and a Fixed Sensor	79
	Rajdip Nayek, Suparno Mukhopadhyay, and Sriram Narasimhan	
13	Validation of Lightweight Antenna Reflector Model for Environmental Acoustic Testing Operating Conditions	87
	M. Alvarez Blanco, R. Hallez, A. Carrella, K. Janssens, and B. Peeters	
14	Confidence in the Prediction of Unmeasured System Output Using Roll-Up Methodology	105
	Kyle Neal, Chenzhao Li, Zhen Hu, Sankaran Mahadevan, Joshua Mullins, Benjamin Schroeder, and Abhinav Subramanian	

15	Application of the Transfer Matrix Method for the Analysis of Lateral Vibrations of Drillstrings with Parameter Uncertainties	109
	Ilja Gorelik, Mats Wiese, Lukas Bürger, Sebastian Tatzko, Hanno Reckmann, Andreas Hohl, and Jörg Wallaschek	
16	Consolidation of Weakly Coupled Experimental System Modes	119
	Robert N. Coppelino	
17	Fatigue Monitoring and Remaining Lifetime Prognosis Using Operational Vibration Measurements	133
	Costas Papadimitriou, Eleni N. Chatzi, Saeed Eftekhar Azam, and Vasilis K. Dertimanis	
18	Feasibility of Applying Phase-Based Video Processing for Modal Identification of Concrete Gravity Dams .	137
	Qi Li, Gaohui Wang, Aral Sarrafi, Zhu Mao, and Wenbo Lu	
19	Using 2D Phase-Based Motion Estimation and Video Magnification for Binary Damage Identification on a Wind Turbine Blade	145
	Aral Sarrafi and Zhu Mao	
20	Hierarchical Bayesian Calibration and Response Prediction of a 10-Story Building Model	153
	Mingming Song, Iman Behmanesh, Babak Moaveni, and Costas Papadimitriou	
21	Scaling and Structural Similarity Under Uncertainty	167
	Mo E. Asl, Christopher Niezrecki, James Sherwood, and Peter Avitabile	
22	Bayesian History Matching for Forward Model-Driven Structural Health Monitoring	175
	P. Gardner, C. Lord, and R. J. Barthorpe	
23	Augmented Reality for Next Generation Infrastructure Inspections	185
	JoAnn P. Ballor, Oscar L. McClain, Miranda A. Mellor, Alessandro Cattaneo, Troy A. Harden, Philo Shelton, Eric Martinez, Ben Narushof, Fernando Moreu, and David D. L. Mascareñas	
24	A Distribution-Based Damping Estimation Method for Random Vibration Response and Its Applications .	193
	Ibrahim A. Sever	
25	A Case Study for Integrating Comp/Sim Credibility and Convolved UQ and Evidence Theory Results to Support Risk Informed Decision Making	203
	G. Orient, V. Babuska, D. Lo, J. Mersch, and W. Wapman	
26	Material Parameter Identification and Response Prediction of Shearing Process for Flying Shear Machine Based on Model Validation	209
	Hongbo Huang, Qintao Guo, Mingli Yu, Yanhe Tao, Yelan Wang, and Ming Zhan	
27	Probabilistic Maintenance-Free Operating Period via Bayesian Filter with Markov Chain Monte Carlo (MCMC) Simulations and Subset Simulation	225
	Michael Shiao, Tzi-Kang Chen, and Zhu Mao	
28	Bayesian Model Updating of a Damaged School Building in Sankhu, Nepal	235
	Mehdi M. Akhlaghi, Supratik Bose, Babak Moaveni, and Andreas Stavridis	
29	Interpreting the Eigenbasis of Principal Component Analysis to Identify Design Space Regions of Interest	245
	B. Daughton, P. Alexeenko, D. Alexander IV, G. N. Stevens, and E. M. Casleton	
30	Uncertainty Quantification in Nanoscale Impact Experiment in Energetic Materials	257
	Chandra Prakash, I. Emre Gunduz, and Vikas Tomar	
31	Analysis of Contact Dynamics Using Controlled Impact Excitations	265
	Shivang Shekhar, Sudhanshu Nahata, and O. Burak Ozdoganlar	
32	Extraction of Coupling Stiffness of Specimens Printed with Selective Laser Melting Using Modal Analysis	275
	Brian West, Nicholas E. Capps, James S. Urban, Troy Hartwig, Ben Brown, Douglas A. Bristow, Robert G. Landers, and Edward C. Kinzel	

33 Quantification of Dynamic Model Validation Metrics Using Uncertainty Propagation from Requirements	283
Andrew M. Brown, Jeffrey A. Peck, and Eric C. Stewart	
34 Natural Frequency Testing and Model Correlation of Rocket Engine Structures in Liquid Hydrogen: Phase I, Cantilever Beam	291
Andrew M. Brown, Jennifer L. DeLessio, and Preston W. Jacobs	
35 Optimal Maintenance of Naval Vessels Considering Service Life Uncertainty	301
Yan Liu and Dan M. Frangopol	
36 On the Monitoring-Driven Assessment of Engineered Systems	309
Eleni N. Chatzi and Vasilis K. Dertimanis	



Chapter 1

Sparse Deconvolution for the Inverse Problem of Multiple-Impact Force Identification

Baijie Qiao, Zhu Mao, Jinxin Liu, and Xuefeng Chen

Abstract The traditional regularization methods for impact force identification such as Tikhonov regularization and truncated singular value decomposition are to minimize the l_2 -norm of the desired force, commonly leading to a low accurate solution. In this paper, considering the inherent sparse nature of multiple impact forces, the idea of sparse deconvolution in signal/image processing is introduced to solve the ill-posed inverse problem of impact force identification. The primal-dual interior point method is applied to solve the convex optimization problem of the impact force deconvolution, where minimizing the l_2 -norm is replaced by minimizing the l_1 -norm. Experiments of two-input-two-output system is conducted on a shell structure to illustrate the advantage of the sparse deconvolution method. Due to the sparse regularization term, the elements of the sparse solution are nearly zeros in the unloading stage of impact force, where the small noise from the observed response is greatly inhibited. Compared with the traditional Tikhonov regularization method, the proposed sparse deconvolution method greatly improves the identification accuracy of the multiple-impact force.

Keywords Sparse deconvolution · Impact force identification · l_1 -norm regularization · Inverse problem

1.1 Introduction

The information of the impact force acting on mechanical structures is essential in a large number of industrial applications [1–4]. For instance, in structural health monitoring of the wind turbine blade, it is highly desirable to quantify the impact force induced by ice, bird or debris before additional damage accumulates [1]. The fan blades of aero-engine are frequently attacked by bird or other debris, leading to the terrible foreign object damage [4]. However, it is difficult and perhaps impossible to directly measure the force using the sensor, because either the excitation location is not accessible or potentially changes the dynamic characteristics of structures. The indirect determination of unknown forces from the measured responses (typically such as acceleration and strain) is regarded as force identification. However, force identification remains a challenging inverse problem, since it is highly sensitive to noise. To overcome the ill-posedness of inverse problem, various regularization methods have been developed for impact force identification.

In general, the regularization techniques applied in the inverse problem of force identification can be divided into two major categories, i.e., the frequency-domain method and the time-domain method. The traditional frequency-domain method based on Fourier transformation has been widely used for stationary or pseudo-stationary conditions [5]. Actually, the time history of force is of great interest to engineers in many cases such as transient or impulsive phenomena. In recent years, more and more scholars have switched their attentions to the time-domain methods and thus amounts of both theories and algorithms have been developed. For instance, Doyle proposed a wavelet deconvolution method for impact force identification, which produced a more accurate solution than the frequency-domain approach [6]. Jacquelin et al. applied singular value decomposition, Tikhonov regularization and truncated singular value decomposition (TSVD) for impact force deconvolution [7]. Qiao et al. applied cubic B-spline scaling functions based on wavelet multi-resolution analysis to reconstruct impact and sinusoidal forces, where the number of basis function is quantitatively determined by the condition number of coefficient matrix [8]. Qiao et al. proposed a cubic B-spline collocation method for impact force identification, where the optimum number of basis functions is indirectly determined by a modified generalized cross validation criterion

B. Qiao (✉) · J. Liu · X. Chen
School of Mechanical Engineering, Xi'an Jiaotong University, Xi'an, PR China
e-mail: qiao1224@xjtu.edu.cn

Z. Mao
Structural Dynamics and Acoustic Systems Laboratory, Department of Mechanical Engineering, University of Massachusetts Lowell, Lowell, MA, USA

[9]. In [10], three basis function expansion methods including the TSVD-based, Chebyshev-based, discrete cosine transform-based methods were considered in impact force identification. These previous methods are effective when a single impact force is reconstructed in a small-scale or medium-scale frame.

In practice, the multiple-impact force identification is a more interesting topic and is even more challenging due to the involvement of the large-scale matrix inversion. One fact is that the impact force is sufficiently sparse relative to its dimension in the total measurement time. In recent years, sparsity constraints for inverse problem have emerged as a fundamental type of regularizer by l_1 penalty instead of l_2 penalty [11]. Particularly, the concept of sparse deconvolution has received a lot of interest in signal/image processing. Different from the traditional regularization methods such as Tikhonov regularization using l_2 penalty, the sparse regularization methods using l_1 penalty require that the solution should have minimum nonzero values. Recently, motivated by the recent signal/image sparse representation, Qiao et al. have developed a comprehensive sparse regularization framework for force identification [12–14]. In [14], Qiao et al. proposed the sparse deconvolution method for the single-impact force identification. In this paper, we will develop the sparse deconvolution method for the multiple-impact force identification following the previous work.

1.2 Problem Statement

1.2.1 Single Impact Force Identification

For a linear time-invariant system with initial conditions $y(0) = 0$ and $\dot{y}(0) = 0$, a convolution relationship between force and response is described as

$$y(t) = h(t) \otimes f(t) = \int_0^t h(t - \tau) f(\tau) d\tau \quad (1.1)$$

where $h(t)$ presents the impulse response function, $f(t)$ presents the excitation force, the symbol \otimes denotes the convolution product and τ is the time delayed operation satisfying $t \geq \tau$. Equation 1.1 describes a forward problem, in which given $h(t)$ and $f(t)$, the forced response $y(t)$ is calculated. Conversely, given $y(t)$ and $h(t)$, solving $f(t)$ is an inverse problem.

The forward model of Eq. 1.1 as a continuous problem should be discretized in applications. Thereby, it leads to a set of algebraic equations

$$\begin{bmatrix} y(\Delta t) \\ y(2\Delta t) \\ \vdots \\ y((n-1)\Delta t) \\ y(n\Delta t) \end{bmatrix} = \Delta t \begin{bmatrix} h(\Delta t) & 0 & \dots & 0 & 0 \\ h(2\Delta t) & h(\Delta t) & \dots & 0 & 0 \\ \vdots & \vdots & \dots & \vdots & \vdots \\ h((n-1)\Delta t) & h((n-2)\Delta t) & \dots & h(\Delta t) & 0 \\ h(n\Delta t) & h((n-1)\Delta t) & \dots & h(2\Delta t) & h(\Delta t) \end{bmatrix} \begin{bmatrix} f(\Delta t) \\ f(2\Delta t) \\ \vdots \\ f((n-1)\Delta t) \\ f(n\Delta t) \end{bmatrix} \quad (1.2)$$

where Δt is the time interval and n is the sampled length. Furthermore, such a convolution model can be rewritten in a compact matrix-vector form

$$\mathbf{y} = \mathbf{H}\mathbf{f} \quad (1.3)$$

where the transfer matrix $\mathbf{H} \in \mathbf{R}^{n \times n}$ is a lower triangular matrix. Therefore, given the transfer matrix \mathbf{H} and the observed response vector \mathbf{y} , solving Eq. 1.3 for the unknown force vector \mathbf{f} is also called force deconvolution. The force identification problems discussed in this work have the condition number ranging from $1.0\text{E} + 17$ to $1.0\text{E} + 19$, which presents severely ill-posed and even rank-deficient ones. It means that the desired solution \mathbf{f} is highly sensitive to the small noise in response \mathbf{y} . Then, in order to stabilize the inverse problem, special regularization methods must be developed for force identification.

1.2.2 Multiple Impact Force Identification

For the inverse problem of the multi-source impact-force reconstruction, several unknown forces acting on different points over a structure and several responses at different points should be synchronously recorded over a small time period. Here, the governing equation of such a multiple-input multiple-output system can be derived as

$$\begin{bmatrix} \mathbf{y}_1 \\ \mathbf{y}_2 \\ \vdots \\ \mathbf{y}_M \end{bmatrix} = \begin{bmatrix} \mathbf{H}_{11} & \mathbf{H}_{12} & \cdots & \mathbf{H}_{1N} \\ \mathbf{H}_{21} & \mathbf{H}_{22} & \cdots & \mathbf{H}_{2N} \\ \vdots & \vdots & \ddots & \vdots \\ \mathbf{H}_{M1} & \mathbf{H}_{M1} & \cdots & \mathbf{H}_{MN} \end{bmatrix} \begin{bmatrix} \mathbf{f}_1 \\ \mathbf{f}_2 \\ \vdots \\ \mathbf{f}_N \end{bmatrix} \quad (1.4)$$

where the real numbers M and N denote the number of the measurement sensors and the excitation sources, respectively. Submatrix \mathbf{H}_{ij} is the transfer matrix between the response point i and the excitation point j . In this context, each response vector \mathbf{y}_i in the left-hand side corresponds to a measurement sensor and each exciting force vector \mathbf{f}_j corresponds to an excitation source. As mentioned in Sect. 1.2.1, \mathbf{H}_{ij} is very poorly conditioned and then finding a stable solution is not guaranteed.

Similarly, for the sake of simplicity, the input-output relation in Eq. 1.4 can be expressed as a matrix-vector form

$$\mathbf{y} = \mathbf{H}\mathbf{f} \quad (1.5)$$

where the rewritten transfer matrix $\mathbf{H} \in \mathbf{R}^{nM \times nN}$ is a Toeplitz block matrix and also named the measurement matrix. In this case, the unknown excitation field \mathbf{f} can be regarded as a multi-channel vector consisting of N forces, and the vibration response filed \mathbf{y} is also a multi-channel vector consisting of M measurements that might be noisy. Note that each of measurements has an n -dimensional signal $\mathbf{y}_i \in \mathbf{R}^n$, $n = 1, \dots, M$. In order to overcome the ill-conditioned nature of force identification and then improve the reconstruction accuracy of the unknown forces, the number of measurement sensors M is required to be no less than the number of excitation sources N .

In practice, a noiseless measurement model rarely occurs. A force identification inverse problem with noise takes the following form

$$\mathbf{y} = \mathbf{H}\mathbf{f} + \mathbf{w} \quad (1.6)$$

where the vector \mathbf{w} denotes the inevitable measurement error that corrupts the real response \mathbf{y} .

1.3 Regularization Methods

Regularization methods based on the l_2 norm minimization have been widely developed, such as Tikhonov regularization, truncated singular value decomposition and the function expansion method [12–14]. More recently, sparse deconvolution based on the l_1 norm minimization has emerged in the field of signal/image processing. Moreover, if the unknown forces themselves are sufficiently sparse, the force can be accurately reconstructed by means of the idea of sparse deconvolution.

1.3.1 Tikhonov Regularization

Tikhonov regularization as an effective method for solving linear inverse problems, plays a central role in regularization theory. The purpose of Tikhonov regularization is to find a stability solution by minimizing the weighted combination of the residual norm and the solution norm.

$$\underset{\mathbf{f}}{\text{minimize}} \quad \|\mathbf{H}\mathbf{f} - \mathbf{y}\|_2^2 + \lambda \|\mathbf{f}\|_2^2 \quad (1.7)$$

where $\|\cdot\|_2$ denotes the l_2 norm and λ is the regularization parameter that establishes a fair balance between minimizing $\|\mathbf{H}\mathbf{f} - \mathbf{y}\|_2$ and $\|\mathbf{f}\|_2$.

For any fixed λ , Tikhonov regularization always has an explicit and unique solution to Eq. 1.7

$$\mathbf{f} = (\mathbf{H}^T\mathbf{H} + \lambda\mathbf{I})^{-1}\mathbf{H}^T\mathbf{y} \quad (1.8)$$

where \mathbf{I} is an identity matrix. We notice that as $\lambda \rightarrow 0$, the Tikhonov solution \mathbf{f} converges to the LS solution $\mathbf{H}^+\mathbf{y}$, where $\mathbf{H}^+ = (\mathbf{H}^T\mathbf{H})^{-1}\mathbf{H}^T$ is the Moore-Penrose pseudo inverse; as $\lambda \rightarrow \infty$, the Tikhonov solution \mathbf{f} tends to be zero. The regularization parameter λ specifies the amount of regularization but an optimum value is unknown in advance. To select an optimum one, the L-curve criterion as a convenient graphical tool is commonly employed. For most inverse problems, the L-curve plot displays an L-shaped appearance with a distinct corner separating the vertical part $\|\mathbf{f}\|_2$ and the horizontal part $\|\mathbf{H}\mathbf{f} - \mathbf{y}\|_2$ on a log-log scale [15]. The corner of L-curve corresponds to the optimum regularization parameter of Tikhonov regularization. As for the computation complexity, Tikhonov regularization requires $O(n^3)$ flops [11].

1.3.2 Sparse Deconvolution

Due to the prior information of impact events acting on mechanical structures, one can assume that the impact force vector \mathbf{f} is sufficiently sparse, relative to its dimension. In order to obtain a sparse solution, it is very intuitive to reconstruct the impact force vector \mathbf{f} from the measurement response vector \mathbf{y} by solving the following l_0 -norm regularization

$$\underset{\mathbf{f}}{\text{minimize}} \quad \|\mathbf{f}\|_0; \quad \text{subject to} \quad \mathbf{y} = \mathbf{H}\mathbf{f} \quad (1.9)$$

where $\|\mathbf{f}\|_0$ denotes the l_0 -norm of the impact force vector \mathbf{f} , i.e., the number of nonzero elements in \mathbf{f} . However, the algorithm for solving the l_0 -norm regularization problem is NP-hard. To surmount this obstacle, Chen et al. [16] replaced the l_0 -norm with the l_1 -norm for a convex optimization problem. Therefore, we use the l_1 -norm regularization, which still promotes sparse solutions (e.g. sparser than l_2 -norm regularization), rather than the l_0 -norm regularization. This leads to the following well-known l_1 -norm regularization

$$\underset{\mathbf{f}}{\text{minimize}} \quad \|\mathbf{f}\|_1; \quad \text{subject to} \quad \mathbf{y} = \mathbf{H}\mathbf{f} \quad (1.10)$$

where $\|\mathbf{f}\|_1 = \sum_{i=1}^n |f_i|$ denotes the l_1 -norm of the identified impact force vector. Different from the l_2 -norm regularization, the l_1 -norm regularization prevents diffusing the energy of \mathbf{f} over a lot of entries in the desired solution and keeps the sparse property of the original signal.

However, the measured responses are commonly contaminated by noise, and thus the equality condition in Eq. 1.10 needs to be transformed to the inequality one

$$\underset{\mathbf{f}}{\text{minimize}} \quad \|\mathbf{f}\|_1; \quad \text{subject to} \quad \|\mathbf{y} - \mathbf{H}\mathbf{f}\|_2^2 \leq \delta \quad (1.11)$$

where the tolerance δ denotes the noise level. For the l_1 -norm regularization, a convex unconstrained optimization version is equivalent to Eq. 1.11, which is given by the following sparsity model

$$\underset{\mathbf{f}}{\text{minimize}} \quad \|\mathbf{H}\mathbf{f} - \mathbf{y}\|_2^2 + \lambda\|\mathbf{f}\|_1 \quad (1.12)$$

where λ is the regularization parameter of the l_1 -norm regularization. The presence of the l_1 -norm term encourages small components of the impact force vector \mathbf{f} to become zeros, and thus it will promote sparse solutions. Unlike the l_2 -norm regularization, there exists no analytic expression for the optimal solution to Eq. 1.12. The l_1 -norm regularization problem of Eq. 1.12 is convex and can be solved by many classical optimization algorithms [11]. Here, the primal-dual interior point method is applied to solve the convex optimization problem of the impact force deconvolution.

In order to further understand how minimizing the l_1 -norm promote sparsity, a comparison between the l_1 -norm regularization and l_2 -norm regularization in a two-dimensional model is implemented in Fig. 1.1. The circle shaded area

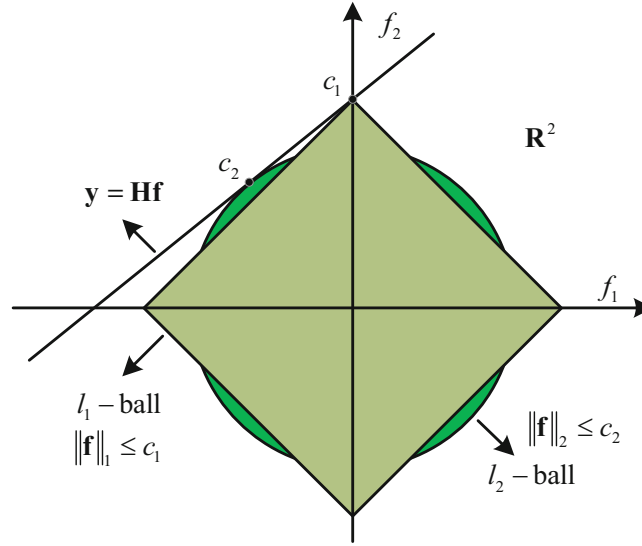


Fig. 1.1 The comparison of the l_1 -norm regularization and the l_2 -norm regularization in a two-dimensional model

in Fig. 1.1 shows the region $\|\mathbf{f}\|_2 \leq c_2$, while the square shows the region $\|\mathbf{f}\|_1 \leq c_1$. An arbitrary constraint equation in \mathbf{R}^2 , $(\mathbf{y})_i = (\mathbf{H}\mathbf{f})_i$ defines a line. It can be seen from Fig. 1.1 that the l_1 -norm regularization indeed yields the sparse solution $\mathbf{f}_{l1} = [0, c_1]^T$ due to the presence of the corners in the l_1 -ball; conversely, the l_2 -norm regularization cannot obtain the zero solution. The tendency for the l_1 -norm regularization to be sparse becomes even more prominent as the size of the model increases.

1.4 Experimental Verification

In authors' previous work, the sparse deconvolution method has been successfully used for identifying the single impact force with high accuracy [14]. Here, we will further verify the advantage of the sparse deconvolution method over the traditional Tikhonov regularization method on the multiple-impact force identification. Experiments with two sequential impact forces are conducted on a shell structure to illustrate the performance of the sparse deconvolution by comparing with Tikhonov regularization. Speaking of impact force identification accuracy, the peak of impact force is a vitally important indicator particularly in structural health monitoring. Here, the peak relative error is defined as

$$\text{Peak relative error} = \frac{|\max(\mathbf{f}_{\text{exact}}) - \max(\mathbf{f}_{\text{identified}})|}{\max(\mathbf{f}_{\text{exact}})} \times 100\% \quad (1.13)$$

where $\mathbf{f}_{\text{exact}}$ denotes the vector of the measured force from the force transducer that can be regarded as the exact force; and $\mathbf{f}_{\text{identified}}$ is the identified force by regularization methods.

1.4.1 Problem Description

To validate the sparse deconvolution method, a clamped-free shell structure (similar to the one in [12, 13]) is impacted by an impulse hammer at different points, as shown in Fig. 1.2. The shell structure made of structural steel can be thought as a quarter of a whole cylinder with radius $r = 200$ mm, length 500 mm and thickness 5 mm. The root of the shell structure that has an 80 mm length is clamped by five bolts. A regular gird with 15 nodes is drawn on the shell structure and two accelerometers are installed on the 2nd and 4th points to record the impact response. The impact force is assumed to impact two of the 15 candidate nodes. The PCB model 086C01 impact hammer is used to impose impact on the surface of the shell structure. A force transducer is inserted on the tip of the hammer. In this experiment, the exciting location labeled as F in Fig. 1.2 are impacted successively many times, and simultaneously the responses of two locations labeled as R1

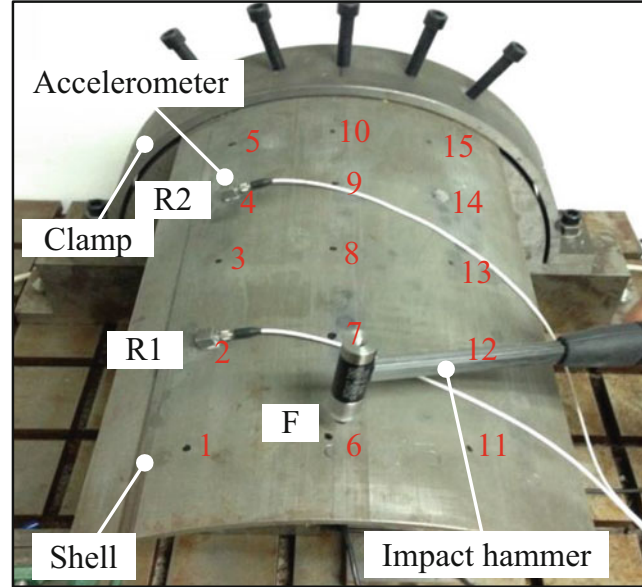


Fig. 1.2 The clamped-free shell structure applied for sparse deconvolution of multiple impact forces

and R2 in Fig. 1.2 are also recorded. LMS SCADASIII data acquisition is used to record synchronously the force and acceleration signals with sampling frequency 2048 Hz. For the measurement of frequency response functions, the measured signals containing force and acceleration are synchronously recorded by LMS SCADASIII data acquisition with sampling frequency 2048 Hz and spectral lines 2050. The total measurement time is 2 s.

1.4.2 Results and Discussions

In the measurement time [0 2] s, two adjacent impact-forces from the same hammer acting on the 3rd and 8th points successively occur. According to Eq. 1.4, the number of the responses should not be less than that of the excitations. Considering multiple-input and multiple-output case, both two acceleration responses are simultaneously applied to identify the two impact forces acting on different points. In this case, the dimension of the response vector \mathbf{y} composed of two acceleration vectors $\mathbf{y}_j \in \mathbb{R}^{4099 \times 1}$ ($j = 1, 2$) is 8198×1 ; the dimension of the unknown force vector \mathbf{f} composed of two impact-force vectors $\mathbf{f}_j \in \mathbb{R}^{4099 \times 1}$ ($j = 1, 2$) is also 8198×1 ; the dimension of the measurement matrix \mathbf{H} composed of four transfer matrices $\mathbf{H} \in \mathbb{R}^{4099 \times 4099}$ is 8198×8198 . Figure 1.3 illustrates that the acceleration responses at R1 and R2 subjected to the impact forces acting on the 3rd and 8th points. From the acceleration time history, one can find that each impact response displays an attenuation phenomenon and the adjacent impact events exist a strong overlap.

Figure 1.4 demonstrates the identification results of the multiple-impact force acting on the 3rd and 8th points of the shell structure using the sparse deconvolution method and the Tikhonov regularization method. For Tikhonov regularization, the L-curve criterion is used to select the optimal regularization parameter from 200 candidates [15]. In order to make comparison, the measured multiply impact forces by the same force sensor is plotted as the first subplot (Location = 0) of the waterfall plot. Note that in Fig. 1.4 the two pulses from the same hammer correspond to the impact forces acting on the 3rd and 8th points, respectively. Clearly, the measured impact forces in the time domain are sufficiently sparse. Comparing Fig. 1.4a with b, we can see that the sparse deconvolution solution has a good match with the measured force and is sufficiently sparse in the time interval [0 2]s; conversely, the Tikhonov solution deviates from the measured one and has many small peaks on the unloading stage of impact force. In detail, the measured peak forces acting on the 3rd and 8th points are 38.90 N and 60.32 N, respectively; the identified peak forces using the sparse deconvolution method are 36.78 N and 60.50 N, corresponding to the relative error 5.45% and 0.30%; the identified peak forces using the traditional Tikhonov method are 29.05 N and 34.41 N, corresponding to the relative error 25.32% and 42.95%. Additionally, the computing time of the sparse deconvolution method is 103.83 s. The Tikhonov regularization method consumes 357.43 s for solving the inverse problem of two-input and two-output system.

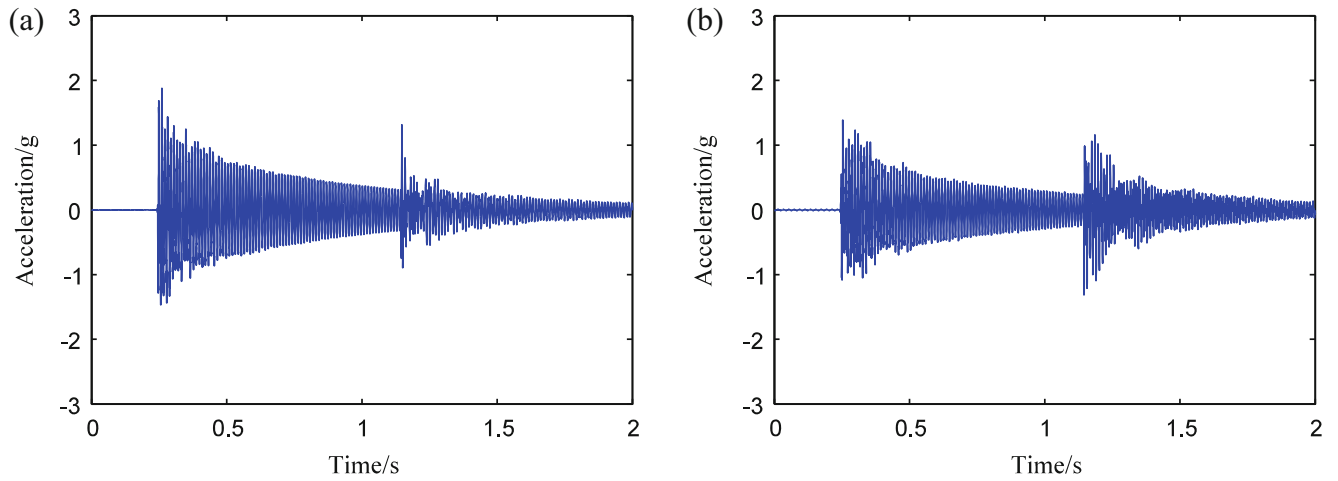


Fig. 1.3 The measured data of the shell structure by two accelerometers subjected to the impact force acting on the 3rd and 8th points: (a) the acceleration response at R1; and (b) the acceleration response at R2

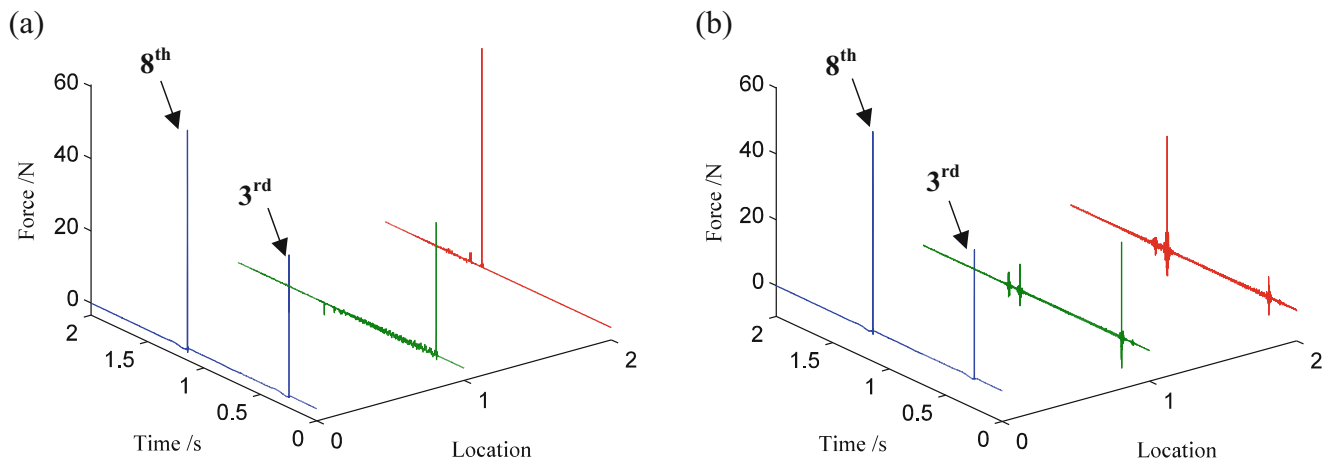


Fig. 1.4 The identification results of the multiple-impact force acting on the 3rd and 8th points of the shell structure: (a) the sparse deconvolution solution; and (b) the Tikhonov solution

In order to verify the superior ability of the proposed method, we make the hammer continuously act on the 8th and 13th points. Two consecutive impact responses are truncated from sequential impact events as shown in Fig. 1.5. We can clearly see that there also exist a strong overlap between the impact responses of the 8th and 13th points. Meanwhile, both the acceleration signals are corrupted by the previous impact event. Such influence is namely colored noise [12]. In this case, the initial condition of the vibration system belongs to the state of the free vibration. That's to say, it does not satisfy the zero initial condition. Nevertheless, comparing Fig. 1.6a with b, one can see that the sparse deconvolution method still has a highly accurate solution but the Tikhonov regularization method has a bad result. In detail, the measured peak forces acting on the 8th and 13th points are 80.46 N and 77.94 N, respectively; the identified peak forces using the sparse deconvolution method are 82.08 N and 76.26 N, corresponding to the relative error 2.01% and 2.16%; the identified peak forces using the traditional Tikhonov method are 37.68 and 45.53 N, corresponding to the relative error 53.17% and 41.58%.

One can conclude from the two cases with/without colored noise that the sparse deconvolution method is less sensitive to the colored noise, i.e., the initial condition of the vibration system, but the Tikhonov regularization method is more sensitive to the colored noise.

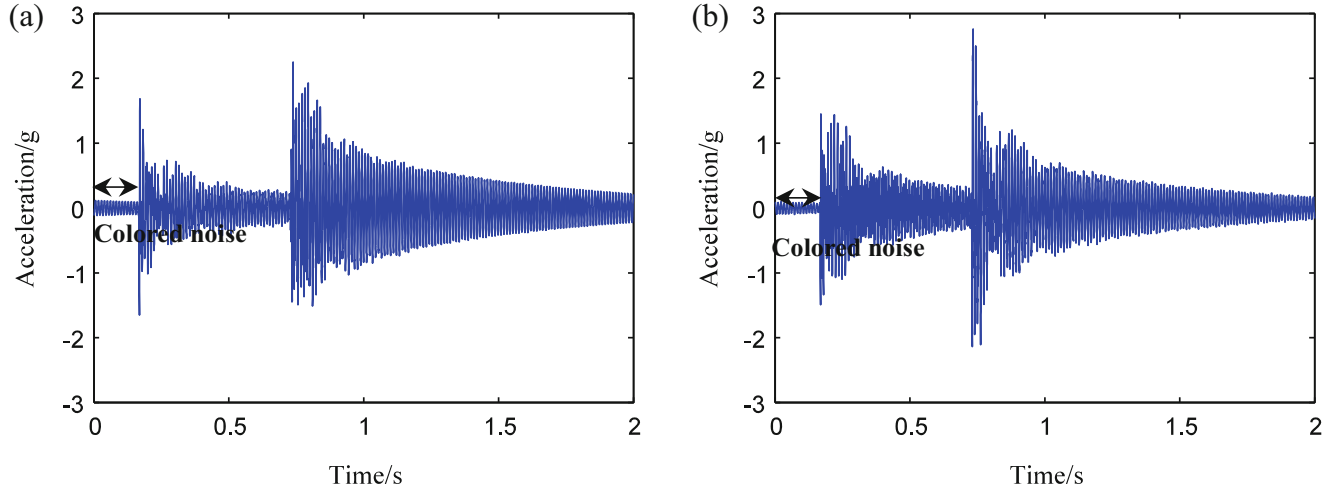


Fig. 1.5 The measured data of the shell structure by two accelerometers subjected to the impact forces acting on the 8th and 13th points with pink noise: (a) the acceleration response at R1; and (b) the acceleration response at R2

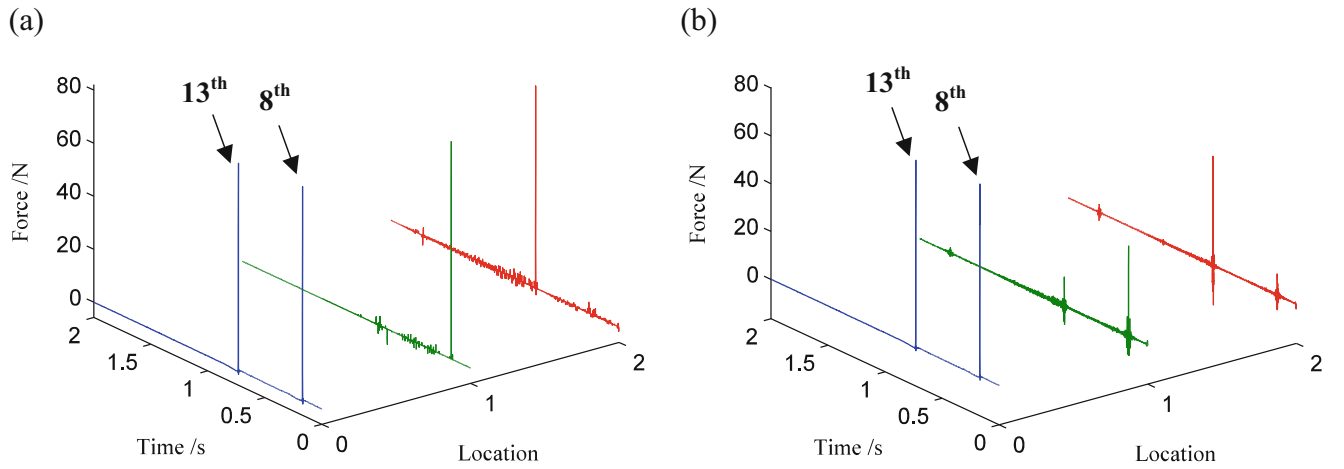


Fig. 1.6 The identification results of the multiple-impact force acting on the 8th and 13th points of the shell structure: (a) the sparse deconvolution solution; and (b) the Tikhonov solution

1.5 Conclusions

Considering the sparse characteristic of impact-force in the time domain, the sparse deconvolution method is developed to identify the multiply impact forces, where the regularization term, minimizing l_2 norm, is replaced by minimizing l_1 norm. The primal-dual interior point method is applied to solve the convex optimization problem of the impact force sparse deconvolution. The sparse deconvolution method is examined and compared with the traditional Tikhonov regularization method based on l_2 norm. The experiment demonstrates that the sparse deconvolution solution is sufficiently sparse in the measured time interval, and nearly zeros in the unloading stage of impact force; the sparse deconvolution method can identify the multiply impact forces with high accuracy, and the peak relative error is less than 6%; comparing with the Tikhonov regularization method, the sparse deconvolution method has higher accuracy, is less sensitive to the colored noise and consumes less computing time.

Acknowledgements This work was supported by the National Natural Science Foundation of China (No. 51705397 and 51705396), China Postdoctoral Science Foundation (No. 2017M610636) and the National Key Basic Research Program of China (No. 2015CB057400).

References

1. Niezrecki, C., Poozesh, P., Aizawa, K., et al.: Wind turbine blade health monitoring using acoustic beamforming techniques. *J. Acoust. Soc. Am.* **135**(4), 2392–2393 (2014)
2. Chen, Y., Zhang, B., Zhang, N., et al.: A condensation method for the dynamic analysis of vertical vehicle–track interaction considering vehicle flexibility. *J. Vib. Acoust.* **137**(4), 041010 (2015)
3. Qiao, B., Zhao, T., Chen, X., et al.: The assessment of active vibration isolation performance of rotating machinery using power flow and vibrational energy: experimental investigation. *Proc. IME C J. Mech. Eng. Sci.* **230**(2), 159–173 (2016)
4. Lin, J., Hu, Z., Chen, Z., et al.: Sparse reconstruction of blade tip-timing signals for multi-mode blade vibration monitoring. *Mech. Syst. Signal Process.* **81**, 250–258 (2016)
5. Thite, A.N., Thompson, D.J.: The quantification of structure-borne transmission paths by inverse methods. Part 2: use of regularization techniques. *J. Sound Vib.* **264**(8), 433–451 (2003)
6. Doyle, J.F.: A wavelet deconvolution method for impact force identification. *Exp. Mech.* **37**(4), 403–408 (1997)
7. Jacquelin, E., Bennani, A., Hamelin, P.: Force reconstruction: analysis and regularization of a deconvolution problem. *J. Sound Vib.* **265**(1), 81–107 (2003)
8. Qiao, B., Zhang, X., Luo, X., et al.: A force identification method using cubic B-spline scaling functions. *J. Sound Vib.* **337**, 28–44 (2015)
9. Qiao, B., Chen, X., Xue, X., et al.: The application of cubic B-spline collocation method in impact force identification. *Mech. Syst. Signal Process.* **64–65**, 413–427 (2015)
10. Qiao, B., Chen, X., Luo, X., et al.: A novel method for force identification based on the discrete cosine transform. *Trans. ASME J. Vib. Acoust.* **137**(5), 051012 (2015)
11. Kim, S.J., Koh, K., Lustig, M., et al.: An interior-point method for large-scale l_1 -regularized least squares. *IEEE J. Sel. Top. Sign. Proces.* **1**(4), 606–617 (2007)
12. Qiao, B., Zhang, X., Wang, C., et al.: Sparse regularization for force identification using dictionaries. *J. Sound Vib.* **368**, 71–86 (2016)
13. Qiao, B., Zhang, X., Gao, J., et al.: Impact-force sparse reconstruction from highly incomplete and inaccurate measurements. *J. Sound Vib.* **376**, 72–94 (2016)
14. Qiao, B., Zhang, X., Gao, J., Liu, N., et al.: Sparse deconvolution for the large-scale ill-posed inverse problem of impact force reconstruction. *Mech. Syst. Signal Process.* **83**, 93–115 (2017)
15. Hansen, P.C.: Regularization tools version 4.1 for Matlab 7.3. *Numer. Algorithms.* **46**, 189–194 (2007)
16. Chen, S.S., Donoho, D.L., Saunders, M.A.: Atomic decomposition by basis pursuit. *SIAM J. Sci. Comput.* **20**(1), 33–61 (1998)

Chapter 2

Validation of Container System Component Models for Drops



Thomas M. Hall, Philip R. Ind, and Thomas J. Anthistle

Abstract The validation of computational models that are used for simulating drops, shocks and other severely nonlinear environments has very different challenges to the validation of lower level vibration models. This paper details the tactics used for validating computational models for drop environments as applied to components of a container system, including the use of multi-code approaches and the use of testing and the techniques used to compare the data from the various sources, giving examples.

When validating a model for a highly nonlinear environment, such as a drop, it is important to consider the question that the model is to answer. If the question is about the damage that occurs in terms of plastic deformation or fracture, a qualitative approach will be taken to validation, whereas if the question is about something measurable, such as acceleration or strain, the approach to validation will be quantitative.

Keywords Model validation · Nonlinear environments · Finite element modelling · Industry practice · Nonlinear mechanics

2.1 Introduction

Computational modelling is used in engineering for several reasons, including where experiments are hindered due to time, money, or safety. One example of a typical use of computational models is in the product development cycle, where it is not necessarily cost effective to create hardware to be tested at each iteration of the development cycle. Computational models have become widely used to investigate the effects of various environments on a design, from low level, linear environments such as the vibration from transport, through to high level, highly nonlinear environments such as large drops or spigot intrusions.

It is important to note that these computational models are built using assumptions and simplifications, as it would be impossible to computationally simulate all the physics present in the problem. In order to gain confidence in the ability of the model to predict the environment there is a need to validate the model, proving that the assumptions are valid and that the simplifications do not affect the outcome of the simulations significantly. However, while the method to validate models in vibration at low levels is well established and rigorous, there is no established method for validating models of highly nonlinear environments.

Typically computational model validation is carried out against physical test data, as this allows the assessment of the assumptions and simplifications against the real world. There are other ways to validate computational models such as the “two-model” or “dual-code” approach. This involves using two models, typically made in different codes by different modellers, and these models validate each other. This is because the assumptions and simplifications that are made in the making of each model are different, or if they are the same then two modellers have made the same assumption. If the assumptions and simplifications are different and the models agree, the confidence in the models increases, and if the assumptions or simplifications are the same, the confidence in that assumption or simplification increases as two independent modellers have made the same assumption or simplification, giving it credibility. The issue with this method comes when the two models differ, as it is unclear which model, if any, is accurate. Much of the validation that will be discussed in this paper will be against physical test data, however the component models are part of an assembly model that is in a two-model validation, using many of the techniques that will be discussed below.

T. M. Hall (✉) · P. R. Ind · T. J. Anthistle
AWE Plc, Berkshire, UK
e-mail: tom.hall@awe.co.uk

2.2 Highly Nonlinear Validation Example 1: Object Impacting Multiple Plate Layers

When looking to validate a low level, linear model, it is desirable to use quantitative methods, as this provides the strongest evidence towards increasing the confidence in the model. At low level vibration environments the path to model validation is well defined, using modal analysis to compare the natural frequencies and mode shapes in a quantitative way. These methods can be a good starting point for the validation of a highly nonlinear model, as having an accurate linear model is important in most nonlinear models. However it is not sufficient to only use low-level techniques for nonlinear model validation.

It is important to note one of the problems with nonlinear model validation is that when the model is validated it is only validated at similar levels to the validation data. Due to this, when designing validation tests it is important to know the approximate levels of the environment that the model will simulate and design the tests accordingly. As with all models, when validating highly nonlinear models it is important to consider the important results of the model, which are typically the failure criteria of the design. In many designs the failure criteria are related to damage, however in some cases the failure criteria may be an acceleration or stress on part of the design. Due to the chaotic nature of the highly nonlinear environments, exact prediction of an environment may be unfeasible. This means that the aiming point for a highly nonlinear simulation is typically similar final outcomes or maximum levels, rather than a perfectly matching time history. This is not to say that time histories are not useful in model validation, and particularly in model updating.

Figure 2.1 shows the acceleration, velocity and position time histories of a drop environment from test data and from a Finite Element (FE) model, and Fig. 2.2 shows a simplified version of the environment.

The velocity time history is derived by integrating the acceleration time history. The acceleration time history does not compare well in this case, as it is significantly lower in general indicating the overall stiffness of the plates are too low. Some useful information can also be taken from the velocity time history. For instance, the velocity time history shows that the FE model's velocity initially rises quicker than the test data, but then remains at a steady rate of energy loss lower than the test data achieves, indicating that whatever is slowing the item down too stiff initially in the FE model, likely in the linear regime, but is not stiff enough later in the time history, possibly indicating there is not enough work hardening in the plastic regime.

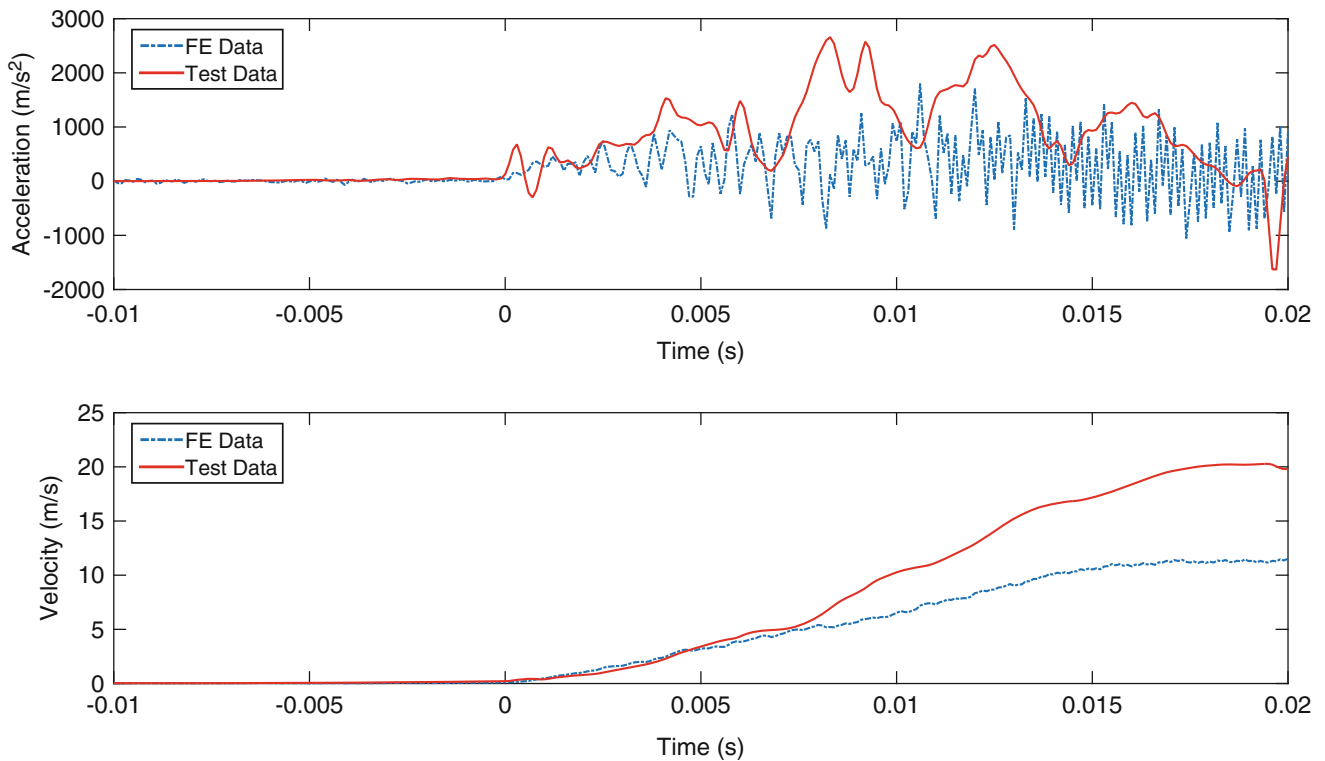


Fig. 2.1 Acceleration and Velocity time histories

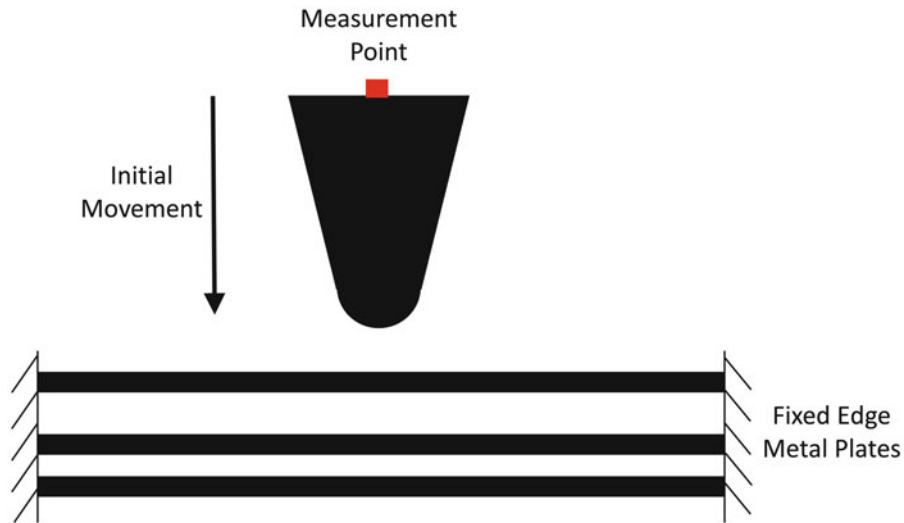


Fig. 2.2 Simplified representation of the environment

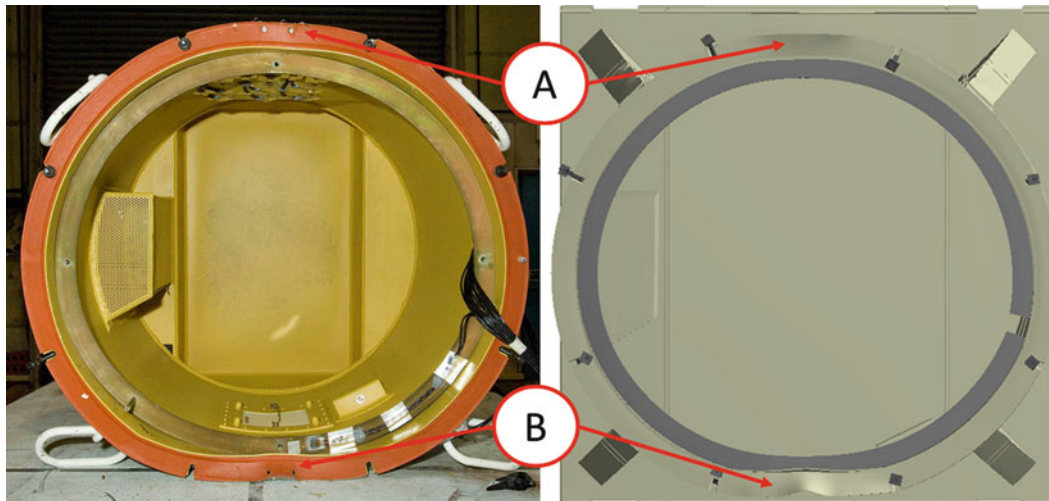


Fig. 2.3 Final state of container component from 700 kg mass drop onto side, test to FE comparison

2.3 Highly Nonlinear Validation Example 2: 700 kg Mass Drop onto Container Side

While time histories can give useful validation data, they can rarely on their own indicate whether damage has happened, and if it has, where and to what extent. As the damage to the item is often a large part of the failure criteria of the design, it is important to be able to validate a model for damage. This is often done in a qualitative way, by listing any damage that occurs in both the model to be validated and the data it is being validated against. Figures 2.3 and 2.4 show examples of comparisons between test and FE when looking at damage, specifically permanent plastic deformation.

Figure 2.3 shows the outcome of dropping a 700 kg mass on a container assembly component. It can be seen that the FE model predicts the damage at A and B well, with the shape and extent of the deformation accurately predicted. Also the slight oval shape of the opening can be seen in both the test photos and the FE model.

Figure 2.4 shows another angle of the same environment. The impact damage at A and B are shown to be well predicted, however the damage at C is not predicted in the same place by the FE model. Upon inspection of the time history of the FE model, the damage at A is from a second impact after the mass bounces. The exact timing of the damage is hard to discern from the slow-motion video of the test, but the mass moves in a similar way initially and it can be assumed that the damage at both A and C occur during the second impact. In the FE model, the mass bounces and rotates slightly, explaining the damage at C being predicted in a different place to the test.

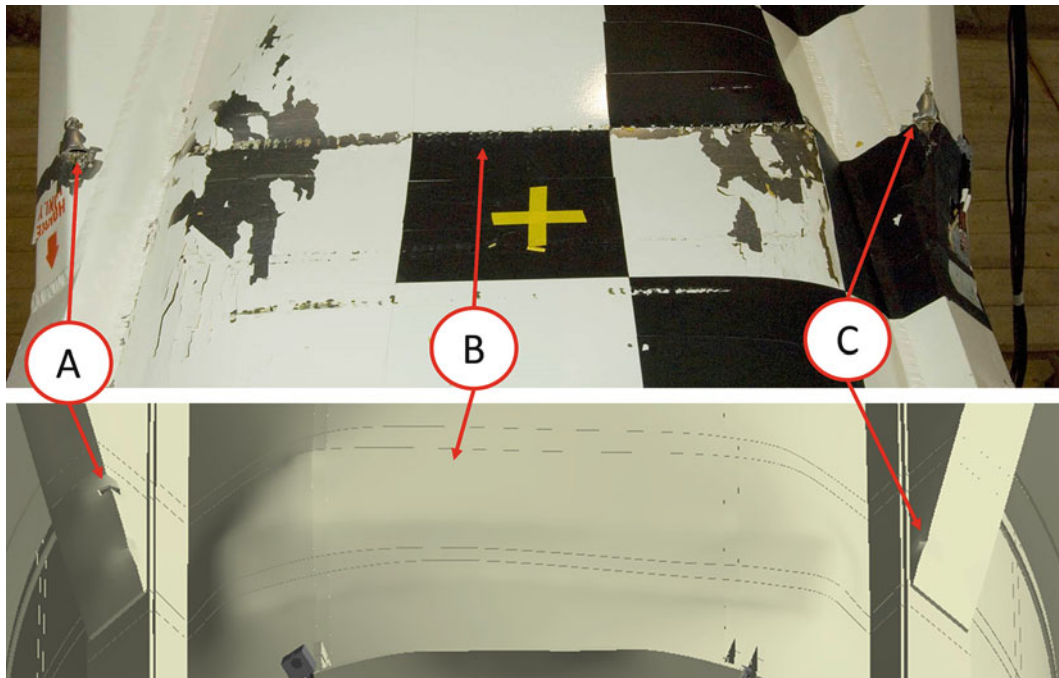


Fig. 2.4 Impact damage from 700 kg mass drop onto container component onto side, test to FE comparison

Due to the high level of similarity in many of the results and the explanations given for the differences, there would be high confidence in the model for this and similar environments.

2.4 Highly Nonlinear Validation Example 3: 1100 kg Mass Drop onto Container Top

Figures 2.5 and 2.6 show the test and simulation results of dropping a 1100 kg mass onto a container component. This environment drives damage in the item, both as permanent plastic deformation and as fracture.

Figure 2.5 shows the damage to the top of the container component in this environment. The deformation predicted by the FE model is more symmetrical than the test results. At A the test item is significantly more damaged than at B, with a sharp edged deformation and fracture of the welds holding the top plate to the sides at B, whereas in the FE simulation there is similar damage at both A and B, and the damage is not at the welds, it is on the side panel. There is asymmetry in the design of the component, but it is also possible that the asymmetry of the results in the test come from the test mass landing slightly off centre and/or not landing perfectly horizontal, this would require investigation in the FE model to determine the effects of these factors.

Figure 2.6 shows the fracture of welds between the top plate and a supporting beam. In the test the first three welds fractured, in the FE model only the first weld fractured. This result and the difference in fracture location in Fig. 2.5 indicate that the failure model for the welds in the FE model is incorrect. Further action to take on the FE model would be to alter this failure model for the welds and re-run the environment, and then repeat the comparison between the test and FE data.

2.5 Concluding Remarks

When validating a model it is important to consider the question being asked and how to improve the confidence in the answer a model gives. This will help to design validation tests and define the validation criteria. In highly nonlinear environments, the question being asked is usually around failure criteria, in particular damage. If validation tests are designed they need to be designed to create a similar environment on the test item in order to provide good validation evidence for the model.

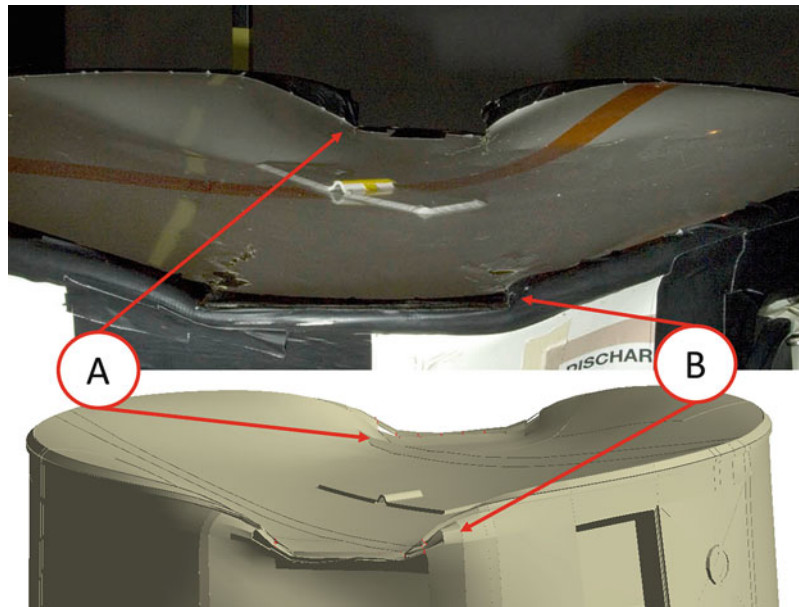


Fig. 2.5 Damage to top of container component after 1100 kg mass drop, test and FE comparison

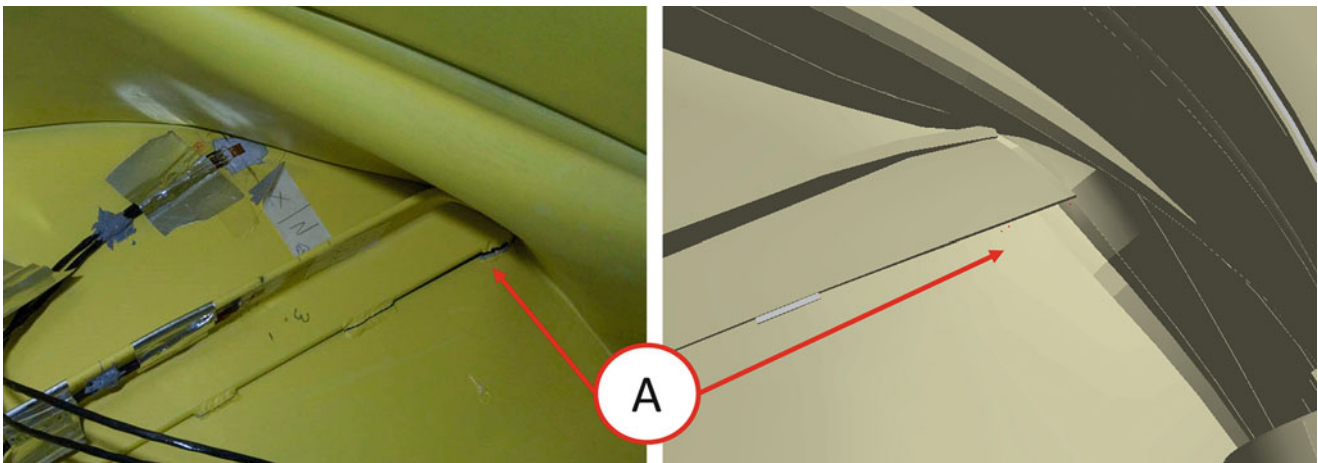


Fig. 2.6 Damage to weld between top plate and supporting beams, test and FE comparison

When validating on damage, typically qualitative validation is used to compare the extent and location of damage between the test and FE model. The models discussed in this paper use qualitative validation to investigate the damage caused by the environments. There are also failure criteria that may be best validated using quantitative methods, such as acceleration or strain peak levels and time histories in a component.

Chapter 3

Validation of Container System Finite Element Models for IAEA Compliance



Philip R. Ind, Thomas M. Hall, Thomas J. Anthistle, and Steve Nicholls

Abstract The International Atomic Energy Agency (IAEA) place requirements on container systems used to transport nuclear materials. To demonstrate compliance with these requirements it is necessary to use validated models alongside full system qualification tests. This paper discusses the approach currently being taken to demonstrate regulatory compliance for a container system. In this example the container must be subjected to worst case combination of a 9 m drop, 1 m spigot intrusion test and a 30 min Liquid Fuel Fire (LFF). To aid in the verification and validation of the Finite Element Models two independent teams are conducting the modelling in two separate FE codes in addition to using modal, sub-system and full system destructive tests. Ultimately it is intended that a capability will exist to allow the full sequence (including the LFF) to be modelled and simulated, this will allow for multiple different scenarios and damage levels to be considered.

Keywords Model validation · Non-linear models · Container systems · Drop and spigot testing · Liquid fuel fires

3.1 Introduction

This paper gives a top level overview of the combined use of modelling and testing in the qualification of container systems for the transportation of nuclear materials. The International Atomic Energy Agency (IAEA) place requirements on the design of containers systems and how they are to be qualified. Three environments are specified; a 9 m drop (representative of a fall from a motorway bridge), a spigot intrusion test (representative of impact with bridge bollards) and a 30 min. Liquid Fuel Fire with unassisted cooling (representative of a fire caused by an aircraft impact or collision with a fuel tanker). The 9 m drop and spigot intrusion test must be conducted in worst case orientations and in a worst case order before the fire, which must be fully engulfing and a minimum of 800 degrees C for 30 min. The container system must not be changed or opened between test phases, this makes instrumentation design and implementation more challenging than would otherwise be the case. Container systems are often multi-layered such that they provide layers of thermal and mechanical protections to protect the contents in the event of an accident. Figure 3.1 shows a full container system immediately before a 9 m drop.

3.2 What Is Worst Case?

The worst case aspects of the test must be decided upon by the container system owner and demonstrated to the regulator as a credible worst case. This is often a challenging part in the design of a qualification test and has formed a considerable portion of the work required for the regulator to-date. Determining a credible worst case through testing alone is not viable economically and so upfront modelling is essential. Relatively simple models are generated which will run quickly and can be used in parametric studies – an example is given in Fig. 3.2. The use of parametric models enables worst case drop attitudes and spigot dimensions to be determined and demonstrated to regulatory bodies.

Significant complexity can arise when two cases lead to differing but credible worst case scenarios. For an example one orientation leads to a significant shock to the internal store while another leads to significant damage to the outer container allowing the ingress of flames and higher internal temperatures. A combination of modelling and testing is often used when two possible worst cases arise allowing the product owner and regulatory bodies to agree which is more significant.

P. R. Ind · T. M. Hall (✉) · T. J. Anthistle · S. Nicholls
AWE Plc, Berkshire, UK
e-mail: tom.hall@awe.co.uk

Fig. 3.1 Preparation for a 9 m container drop

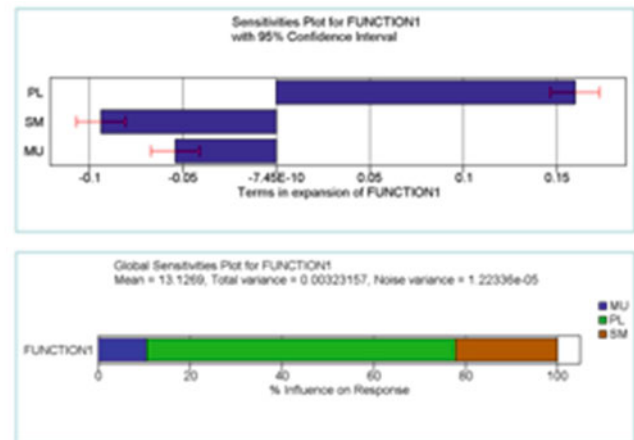
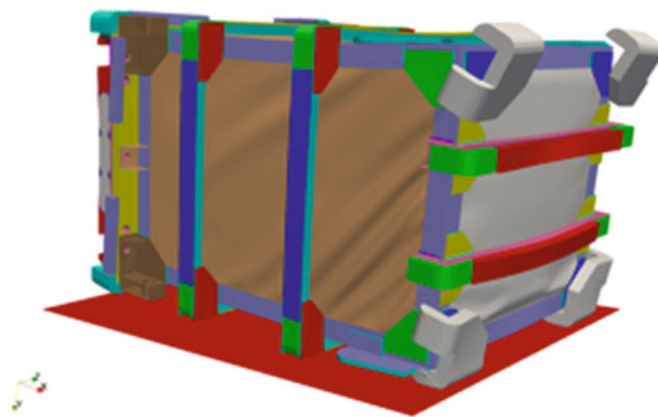


Fig. 3.2 Fast running model used for sensitivity analysis

3.3 Detailed Modelling

The development of more detailed container models which will ultimately form part of the evidence which underwrites the container system are developed more slowly using a hierarchical approach to their validation (Fig. 3.3).

The vast majority of tests and trials in this first phase of validation relate to gathering of material data including both elastic and plastic responses at appropriate strain rates. Failure models and all necessary thermal properties are also gathered at this stage. At the component level of the triangle, modal testing and correlation are used to build confidence in the underlying linear models and ensure that the underlying mass and stiffness distributions of the model are accurate. Destructive tests may also be conducted at sub-system level, often these are designed to drive the material models into specific regimes and to assess the performance of areas such as welds and joints. Figure 3.4 show the results of a 1.2 tonne impact from 3 m against the results of an analytical model. This test was designed to exercise the failure model of the material (6061 Aluminium) used for this component. Sub-System modal tests are used to ensure a good linear model is maintained through the model assembly process. Sub-System destructive tests are relatively few but are conducted to assess the full sub-system response

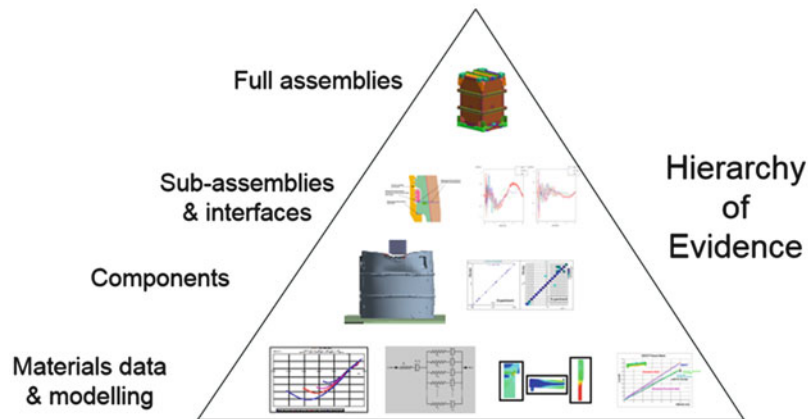


Fig. 3.3 Illustration of the model validation triangle



Fig. 3.4 Comparison of validation drop results

in nonlinear environments. Fewest of all are full systems tests although these are often still necessary. Such full system tests not only provide valuable validation of the model but also allow test engineers to develop instrumentations systems that are robust enough to survive the full suite of IAEA tests. The combination of full system tests and a validate suite of models are ultimately used to demonstrate compliance to regulatory bodies.

At all stages in the validation process FE modelling is used to aid test planning activities, such as ensuring accelerometers are well placed for modal testing or determining where strain is to be measured. Parametric studies may also be used to derive the masses and drop heights required to drive material models into regions of interest.

Alongside the mechanical response, thermal aspects must also be considered these include not only material response but also the simulation of the LFF as shown in Fig. 3.5. Data from empty hearth fires is essential to underwriting these models. From a design point of view fire modelling is extremely useful since computational fires are repeatable when experimental ones are not. The repeatability of a computational fire allows different designs to be assessed against identical thermal inputs since changes in performance can be attributed solely to design changes.

3.4 Dual Model/Dual Code Approach

In order to provide higher confidence and better verification of the model AWE have adopted a dual model, dual code approach to the mechanical aspects of the model. The main model has been constructed in Sandia's Massively Parallel Processing (MPP) nonlinear dynamics code Presto with the second model using Ansys' Explicit STR. The use of Presto for the main model allows rapid solves for sensitivity and parametric solves.

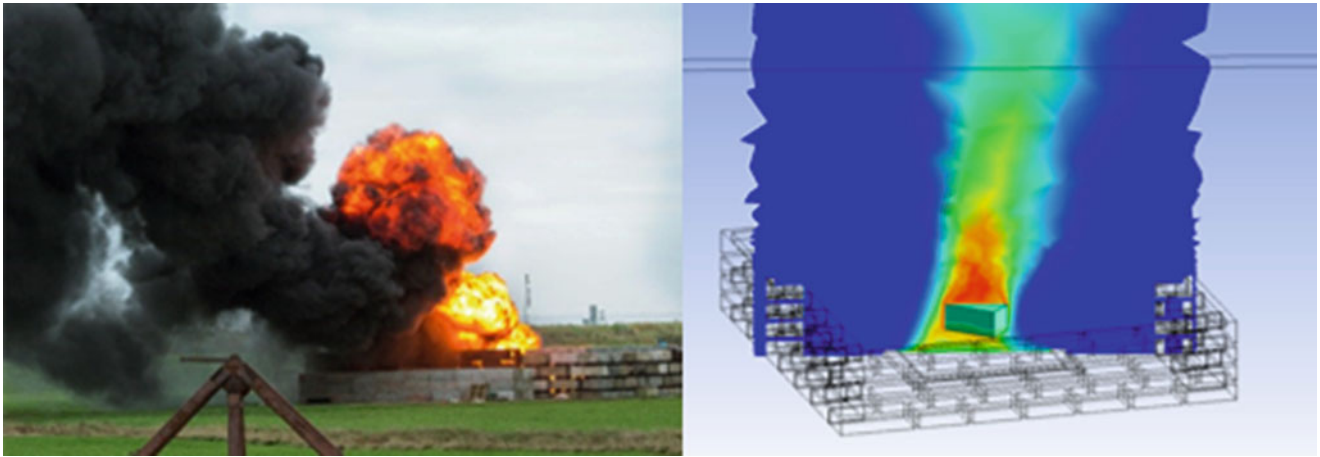


Fig. 3.5 Liquid fuel fire test and simulation

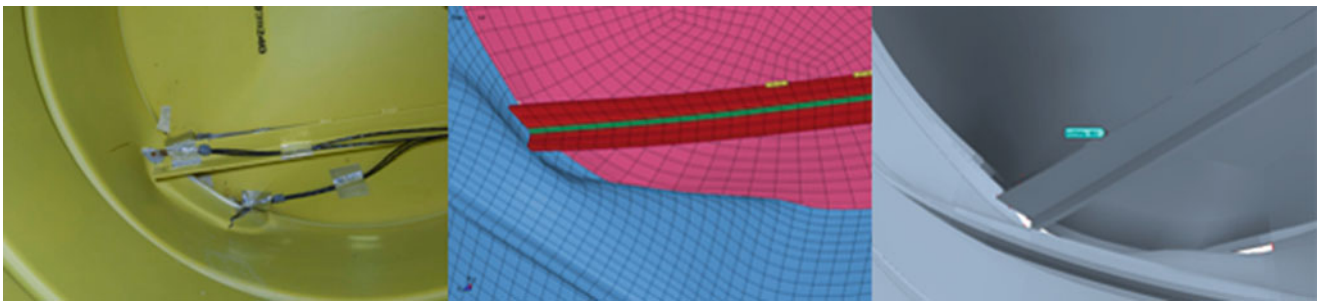


Fig. 3.6 Comparison of models generated by different teams using different codes

The two models are produced by separate teams who have no input into each other's models but who do come together to review results and compare answers. In the early phases of modelling the model reviews compare high level results and check against basic physical responses for example, was damage/failure seen at a particular component? Does the damage look representative? These high level comparisons allow the underlying assumptions made by the analyst and the code to be compared and where significant differences are found these can be investigated. Example results for a component level test are shown in Fig. 3.6.

3.5 Integrating Multiple Analyses

Ultimately AWE are working to develop a capability in which the results of a previous analysis can be moved to the next event, up to and including the LFF. In general, transition from explicit drop to spigot is fairly easy to accomplish but the generation of the thermal model based on the mechanically damaged model is more challenging. It is likely that the thermal portion of the model will be based on geometry refitted to the structural geometry nodes. The results of early investigations into this area have been encouraging although where significant damage has led to holes and tears, this complicate the surface fitting process.

3.6 Concluding Remarks

The environments required by IAEA testing are severe and it is only through the combined use of analysis and test that container systems can be designed and qualified against them. Increases in computing power are enabling the consideration of simulating the full sequence of tests, propagating the damage from the previous analysis into the next.

Chapter 4

Nonlinear Squeezing Wavelet Transform for Rotor Rub-Impact Fault Detection



Chaowei Tong, Xuefeng Chen, and Shibin Wang

Abstract Classical time-frequency analysis methods can depict time-frequency structure of non-stationary signals. However, they may have a shortage in extracting the weak components with small amplitude hidden in complex signals, because their time-frequency representation coefficients are proportional to the amplitude or energy of a signal. In this paper, we present a new data analysis method, called nonlinear squeezing wavelet transform, to extract the weak feature of highly oscillating frequency modulation for rotor rub-impact fault. The time-frequency representation of the proposed method is independent of the signal amplitude and only relevant to the signal phase, thus it can be used to characterize the time-frequency pattern of non-stationary multi-component signals, especially for weak components detection. The experiments on simulated signals verify the effectiveness of the proposed method in weak signal detection. Finally, the validity of this method is demonstrated to extracting the feature on a real rotor system with weak rub-impact fault.

Keywords Time-frequency analysis · Nonlinear squeezing wavelet transform · Rub-impact · Weak signal detection

4.1 Introduction

Rub-impact is one of the most common malfunctions in rotating machines, which may cause a serious hazard to equipment [1, 2]. Therefore, it is significant to study effective signal processing methods to timely detect the feature of rub-impact fault. Cheng found that the vibration signal will present nonlinear frequency modulation (FM) feature, especially at an initial stage of the rub-impact fault [3]. That means the signal has a nonlinear time-varying instantaneous frequency (IF). Naturally, IF becomes a direct concept to describe this feature.

Time-frequency representation (TFR) provides a powerful tool to show IFs of signals. The most classic methods are short time Fourier transform (STFT) and wavelet transform (WT), which can depict the time-frequency distribution of signals. However, both of them will get low resolution results limited by the Heisenberg uncertainty principle. In addition, there are all kinds of bilinear TFR methods, e.g. Wigner Ville Distribution (WVD), which possesses the best time-frequency resolution. But cross-term restricts its application. Although a variety of improved approaches for bilinear TFR were put forward by many researchers, the price of these methods is decreasing the resolution simultaneously [4].

Recent years, a series of new methods, such as empirical mode decomposition (EMD) [5], parametric TFR [6, 7], reassignment method (RM) [8], have been proposed to reach the core of concentrating the energy of a signal around the IF in the TF plane. As a data driven method, EMD gets rid of the constraint of constructing suitable basic functions, while it could not guarantee the result a real physical meaning. On the contrary, considering the TF structure of a signal, parametric TF transforms need to construct more complex and matched TF atoms to obtain satisfactory energy concentration. However, the excessive computational cost caused by the complex parameters limits its application. RM, a kind of post-processing method, transfers the value at any point to the gravity center of the signal's energy distribution, and greatly increases the energy concentration [9]. With the purpose of reconstructing a signal, Synchrosqueezing transform (SST) were developed and ensured the energy concentration in the meanwhile [10].

Nonetheless, all these methods may have a shortage in extracting the weak components of signals, especially the signals with weak rotor rub-impact fault, as a result of their TFR coefficients being proportional to the amplitude or energy of a signal.

In this paper, we introduce a new method called nonlinear squeezing wavelet transform (NSWT) to characterize the TF pattern of weak components whose amplitudes are far less than the principal components. The experiments on simulated

C. Tong · X. Chen (✉) · S. Wang
School of Mechanical Engineering, Xi'an Jiaotong University, Xi'an, PR China
e-mail: chenxf@xjtu.edu.cn

signals verify the effectiveness of the proposed method in weak signal detection. Finally, the validity of this method is demonstrated to extracting the feature on a real rotor system with weak rub-impact fault.

The rest of this paper is organized as follows. In Sect. 4.2, the rationale of the NSWT algorithm is described. Then, the simulation experiment is presented in Sect. 4.3. In Sect. 4.4, the application to weak feature extraction of a rotor rub-impact fault is given. The conclusions are drawn in Sect. 4.5.

4.2 Nonlinear Squeezing Wavelet Transform

For a given signal $x(t) \in L^2(R)$, continuous wavelet transform (CWT) at time u and scale s ends up with a representation of the form:

$$W_x(u, s) = \int_{-\infty}^{+\infty} x(t) \frac{1}{\sqrt{s}} \overline{\psi\left(\frac{t-u}{s}\right)} dt \quad (4.1)$$

where $\psi(t)$ is an appropriately chosen wavelet function which can be constructed with a frequency modulation of a real and symmetric window $g(t)$ while it is analytic, i.e.

$$\psi(t) = g(t)e^{i\eta t} \quad (4.2)$$

where η is the center frequency of wavelet $\psi(t)$.

Thus, an analytic wavelet transform is calculated as following:

$$W_x(u, s) = \int_{-\infty}^{+\infty} x(t) \frac{1}{\sqrt{s}} g\left(\frac{t-u}{s}\right) e^{-i\eta \frac{t-u}{s}} dt \quad (4.3)$$

and it is easy to obtain the time-shift derivative of $W_x(u, s)$,

$$\partial_u W_x(u, s) = i \frac{\eta}{s} \int_{-\infty}^{+\infty} x(t) \frac{1}{\sqrt{s}} g\left(\frac{t-u}{s}\right) e^{-i\eta \frac{t-u}{s}} dt - \frac{1}{s} \int_{-\infty}^{+\infty} x(t) \frac{1}{\sqrt{s}} g'\left(\frac{t-u}{s}\right) e^{-i\eta \frac{t-u}{s}} dt = i \frac{\eta}{s} W_x(u, s) - \frac{1}{s} W_x^{g'}(u, s), \quad (4.4)$$

where $W_x^{g'}(u, s)$ denotes the CWT of $x(t)$ obtained by using the window $g'(t)$ which is the time derivative of the original window $g(t)$.

To motivate the idea, a purely harmonic signal $x(t) = Ae^{i2\pi f_0 t}$ is considered, and we have the Fourier transform

$$\widehat{x}(\omega) = 2\pi A \delta(\omega - 2\pi f_0), \quad (4.5)$$

by Plancherel's theorem, we can rewrite $W_x(u, s)$,

$$W_x(u, s) = \frac{1}{2\pi} \int_{-\infty}^{+\infty} \widehat{x}(\omega) \sqrt{se^{-i\omega u}} \overline{\widehat{\psi}(\omega s)} d\omega = A \sqrt{se^{i2\pi f_0 u}} \widehat{g}(2\pi f_0 s - \eta), \quad (4.6)$$

similarly,

$$\partial_u W_x(u, s) = i2\pi f_0 W_x(u, s) = i \frac{\eta}{s} W_x(u, s) - \frac{1}{s} W_x^{g'}(u, s), \quad (4.7)$$

i.e.

$$\frac{W_x(u, s)}{W_x^{g'}(u, s)} = \frac{1}{i(\eta - 2\pi f_0 s)} = \frac{1}{is(\eta/s - 2\pi f_0)}. \quad (4.8)$$

where η/s denotes the frequency ξ .

It can be seen that the value of the module $\left|W_x(u, s) / W_x^{g'}(u, s)\right|$ will increase quickly when η/s is close to $2\pi f_0$ (the IF of the signal $x(t)$). In the meanwhile, it is independent of the amplitude A of the signal $x(t)$ so that it will be useful to detect the weak signal buried in noise. Naturally, we define $P_x(u, s)$ as the ratio of the two TF representations $W_x(u, s)$ and $W_x^{g'}(u, s)$, i.e.

$$P_x(u, s) = \frac{W_x(u, s)}{W_x^{g'}(u, s)} \quad (4.9)$$

Because of the nonlinear effect of the CWT $W_x^{g'}(u, s)$, the representation $P_x(u, s)$ is named as nonlinear squeezing wavelet transform (NSWT).

More generally, considering the signal $x(t) = A(t)e^{i\phi(t)}$, we have the following proposition.

Proposition Let $x(t) = A(t)e^{i\phi(t)}$, and the symmetric window $g(t)$ has a support equal to $[-1/2, 1/2]$. If $s > 0$, the NSWT representation is

$$P_x(u, s) = \frac{1 + \frac{\varepsilon(u, s)}{\widehat{g(\eta - \phi'(u)s)}}}{i[\eta - s\phi'(u)] + \frac{\varepsilon^{g'}(u, s)}{\widehat{g(\eta - \phi'(u)s)}}}, \quad (4.10)$$

The corrective term satisfies

$$|\varepsilon(u, s)| \leq \varepsilon_{a,1} + \varepsilon_{a,2} + \varepsilon_{\phi,2}, \quad \left|\varepsilon^{g'}(u, s)\right| \leq \varepsilon_{a,1}^{g'} + \varepsilon_{a,2}^{g'} + \varepsilon_{\phi,2}^{g'} \quad (4.11)$$

with,

$$\varepsilon_{a,1} \leq \frac{s|A'(u)|}{|A(u)|}, \quad \varepsilon_{a,2} \leq \sup_{|t-u| \leq s/2} \frac{s^2|A''(t)|}{2|A(u)|}, \quad \varepsilon_{\phi,2} \leq \sup_{|t-u| \leq s/2} \frac{s^2|\phi''(t)|}{2} \left(1 + \frac{s|A'(u)|}{|A(u)|}\right) \quad (4.12)$$

$$\begin{aligned} \varepsilon_{a,1}^{g'} &\leq \frac{A'(u)[|(\eta - s\phi'(u))| + 1]}{|A(u)|}, \quad \varepsilon_{a,2}^{g'} \leq \sup_{|t-u| \leq s/2} \frac{s|A''(t)|}{2|A(u)|} (2 + |(\eta - s\phi'(u))|), \\ \varepsilon_{\phi,2}^{g'} &\leq \sup_{|t-u| \leq s/2} \frac{s|\phi''(t)|}{2} \left(2 + |(\eta - s\phi'(u))| + \frac{3s|A'(u)|}{|A(u)|} + \frac{s^2|A''(t)|}{|A(u)|}\right) \end{aligned} \quad (4.13)$$

Remark The six corrective terms are enough small to be negligible if $A(t)$ and $\phi'(t)$ have small relative variations over the support of window $g(t)$, especially when the scale s is small. Then, the NSWT $P_x(u, s)$ can be approximated as

$$P_x(u, s) \approx \frac{1}{i[\eta - s\phi'(u)]} = \frac{1}{is[\eta/s - \phi'(u)]} \quad (4.14)$$

This indicates that the NSWT $P_x(u, s)$ will increase quickly when η/s is close to $\phi'(u)$ (the IF of the signal $x(t)$). In the meanwhile, it is independent of the amplitude $A(t)$ of the general signal $x(t)$ so that it will be useful to detect the weak signal buried in noise. It should be noticed that the main energy of window $g(t)$ is supported in the interval $[-1/2, 1/2]$, the performance for weak signal detection can be maintained. In this study, Morlet wavelet function which contains Gaussian window is adopted, because Gaussian window has the minimal area of the Heisenberg box for better time-frequency energy concentration.

4.3 Simulation

In order to test the performance of the proposed method NSWT, we consider a three-component simulation signal, given by

$$x(t) = \sum_{i=1}^3 s_i(t) \quad (4.15)$$

Table 4.1 Amplitudes of the three components in three cases

Cases	Amplitudes		
	A_1	A_2	A_3
Case1	0.01	1	1
Case2	1	0.01	1
Case3	1	1	0.01

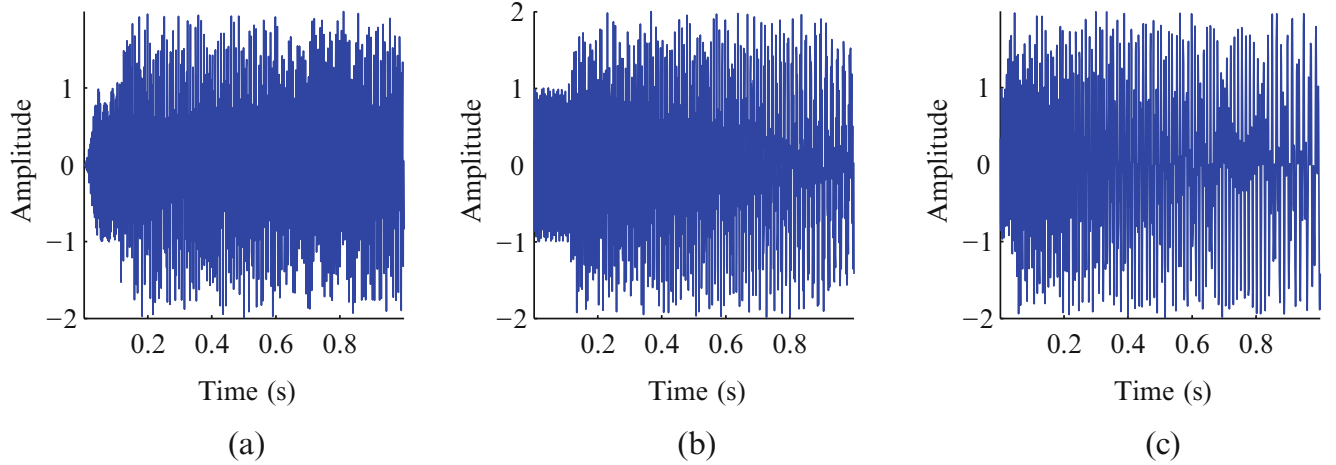


Fig. 4.1 The waveform in three cases: (a) case 1; (b) case 2; (c) case3

where the components $s_i(t)$ are frequency modulated signals which can be expressed as follow:

$$s_1(t) = A_1 \cos 2\pi (200t - 77.5t^2), \quad (4.16)$$

$$s_2(t) = A_2 \cos 2\pi (280t - 77.5t^2 - 2/(t + 0.1)), \quad (4.17)$$

$$s_3(t) = A_3 \cos 2\pi (320t - 5/(t + 0.068)), \quad (4.18)$$

where the amplitudes of the three components in three cases are listed in Table 4.1. The IFs of the three components are

$$IF_1(t) = 200 - 155t, \quad (4.19)$$

$$IF_2(t) = 280 - 155t + 2/(t + 0.1)^2, \quad (4.20)$$

$$IF_3(t) = 320 + 5/(t + 0.068)^2. \quad (4.21)$$

The sampling frequency is 1024 Hz and the number of samples is 1024. The waveforms in three cases are shown in Fig. 4.1a–c and the corresponding IFs in these three cases are identical, which is shown in Fig. 4.2. Figure 4.3a–f provide the TFR results of an advanced method SST and the proposed method NSWT respectively. It is obviously that SST could hardly extract the weak component whose amplitude is only 0.01 in the three cases, while the result of NSWT can be more effective in representing the TF structures of the simulation signals, even for the weak component. Moreover, the representations of NSWT, as shown in Fig. 4.3b, d, f, illustrate that these three simulation signals always have approximated TFR results, which verifies that the NSWT is independent of the signal amplitude and only relevant to the signal phase. This comparison study shows the advantages of the proposed NSWT method in weak signal detection.

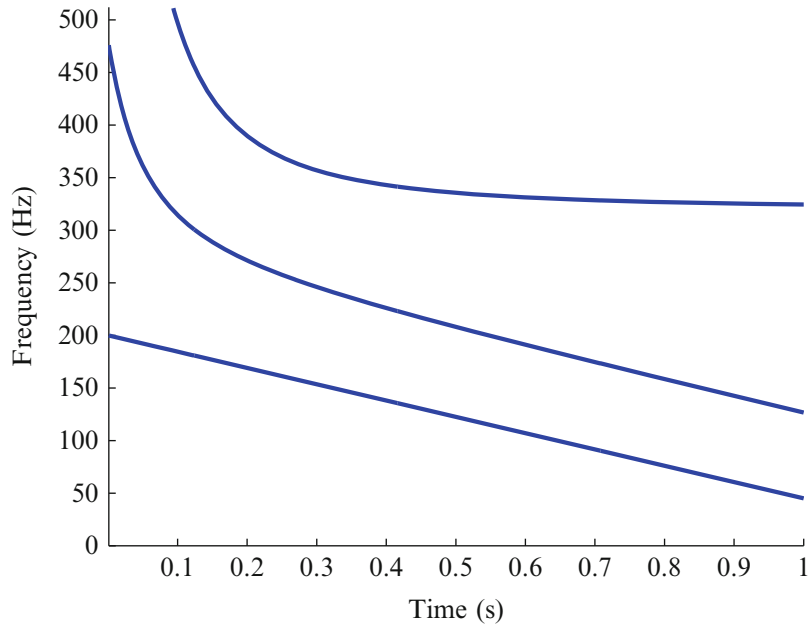


Fig. 4.2 The IFs of the three components

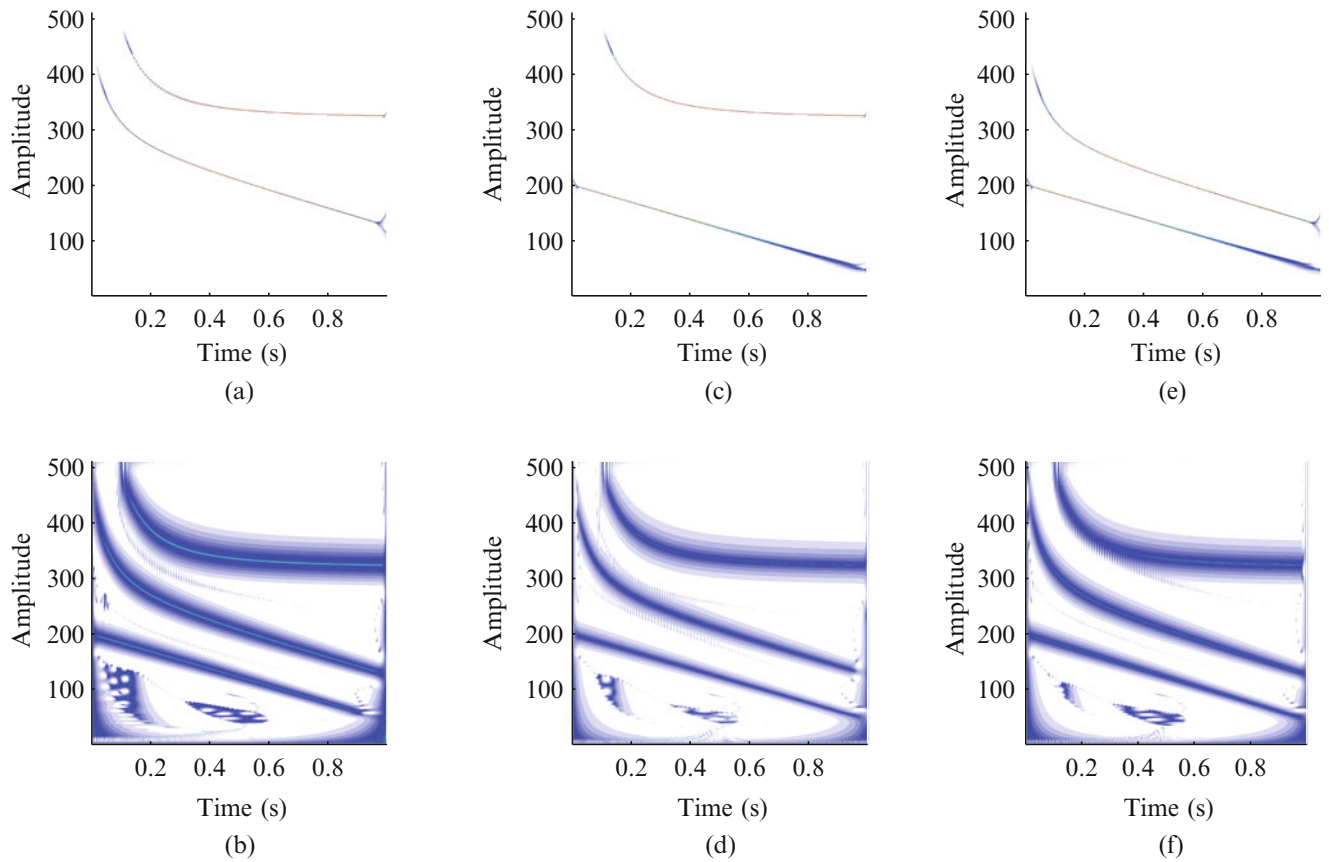


Fig. 4.3 The comparison study of three cases: (a, b) the TF representations obtained by SST and NSWT for Case 1; (c, d) the TF representations obtained by SST and NSWT for Case 2; (e, f) the TF representations obtained by SST and NSWT for Case 3

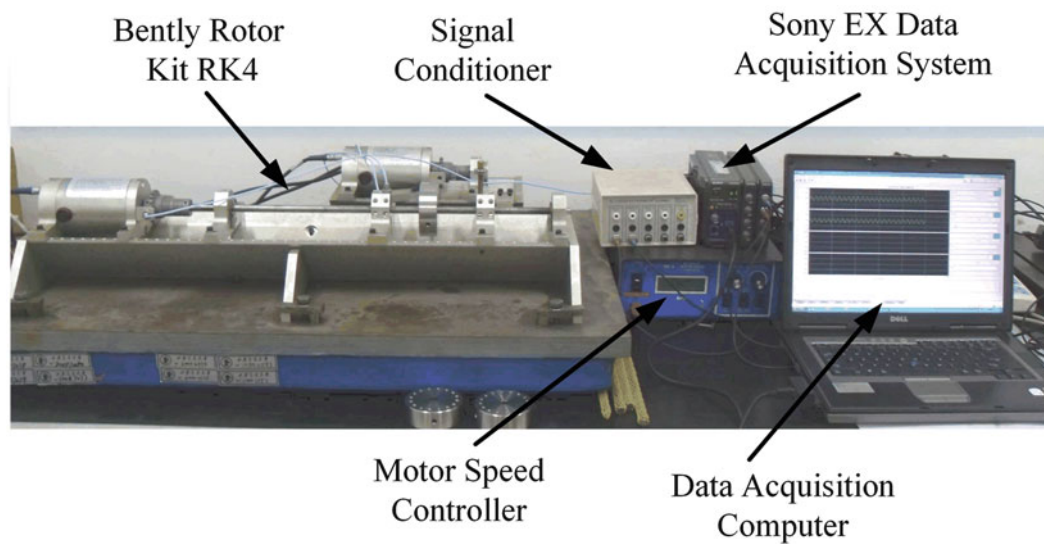


Fig. 4.4 The experimental system

4.4 Application to Feature Extraction

Rub-impact is a common nonlinear fault in rotating machines, which may cause a disastrous failure to equipment. Therefore, it is important to monitoring the condition of the rotor system. When the rub-impact phenomenon occurs, the vibration signal will present nonlinear frequency modulation (FM) feature. Generally, the IF of the signal will oscillate periodically with a frequency equivalent to the rotating frequency of the rotor with rub-impact fault.

In this section, the NSWT method will be applied in the feature extraction of vibration signal collected from a rotor test rig of Bently RK4 rotor kit with a rub-impact fault. Figure 4.4 shows the overall view of the experiment system including the Bently rotor kit, rotor speed controller, signal conditioner, data acquisition system and computer.

In this experiment, the rub-impact fault is slight, so the feature component is weak. The rotor displacement signals in the horizontal and the vertical directions are collected by eddy current sensors mounted on the probe base. The operation speed of the rotor kit is 2000 rpm, thus the rotating frequency of the rotor is $f = 33.33$ Hz. The sampling frequency is 2000 Hz and the sampling points are 1024.

The measured vibration signal and its Fourier spectrum are shown in Fig. 4.5. Due to the slight rub-impact fault, only the basic harmonic and its second harmonic can be observed in the frequency spectrum.

The NSWT algorithm is used to analyze this measured vibration signal. The TFR result obtained by NSWT is displayed in Fig. 4.6. It can be noted that the extracted IF based on NSWT representation fluctuates periodically approximately equal to 33.33 Hz when the rotor rub-impact fault occurs, and the oscillation frequency is near to 33.33 Hz as well, which is equal to the rotating frequency of the rotor with rub-impact fault. It is apparent that the experimental results agree well with the feature of rub-impact fault, thus the effectiveness of the application of NSWT method to extract the highly oscillated IF for the rotor system with rub-impact fault is verified qualitatively.

For the purpose of comparison, the vibration signal is analyzed by the advanced TFR methods Hilbert-Huang transform (HHT) and SST. The TFRs obtained by HHT and SST is presented in Figs. 4.7 and 4.8 respectively. The HHT spectrum and SST result both have shortages in characterizing the entire oscillation feature of the vibration signal in this case. Compared with these representations, the NSWT algorithm provides TFR with satisfying energy concentration to represent the nonlinear FM feature and reveal the feature of the rub-impact fault.

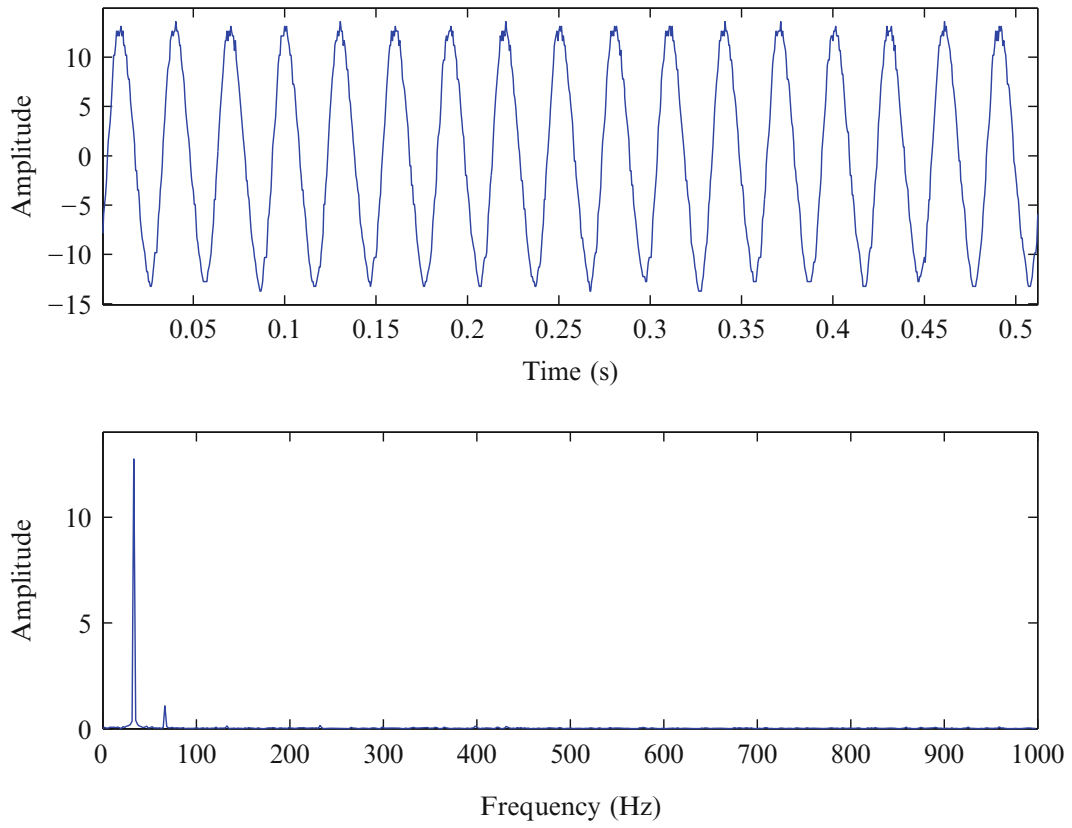


Fig. 4.5 The vibration signal and its Fourier spectrum

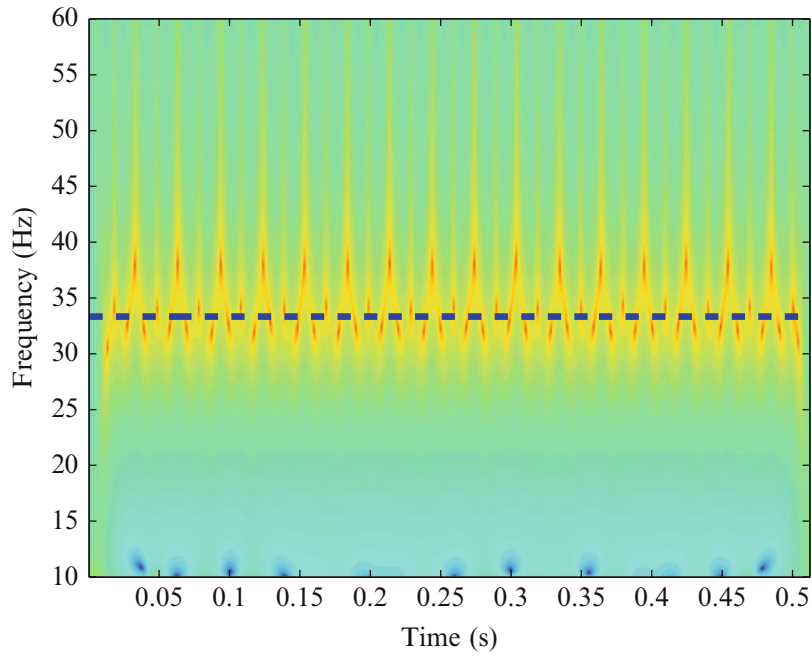


Fig. 4.6 The TFR result obtained by NSWT

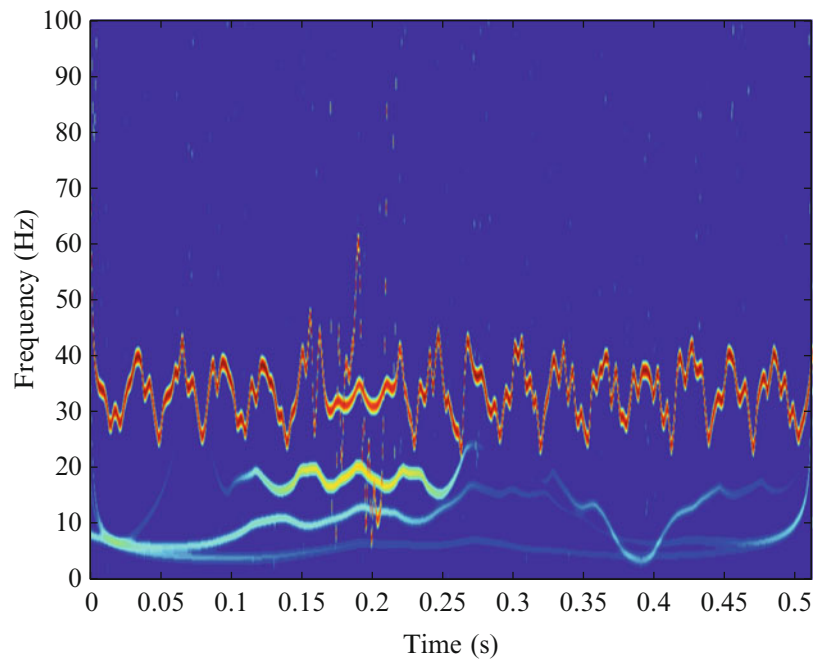


Fig. 4.7 The TFR result obtained by HHT

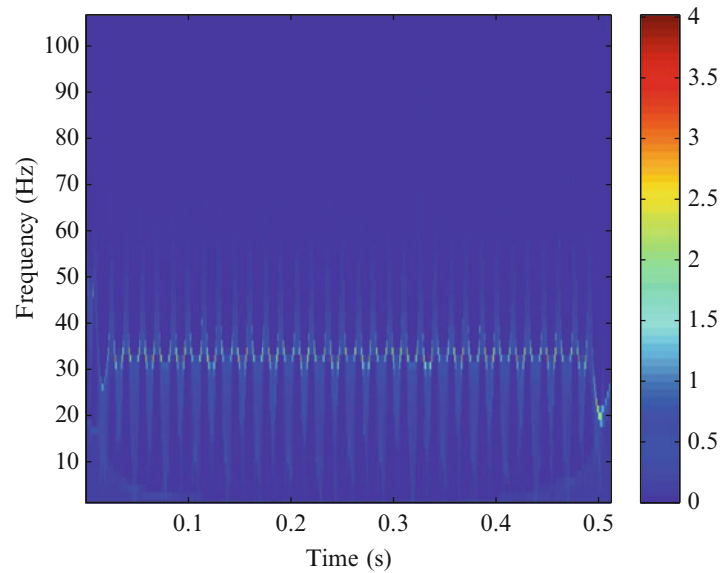


Fig. 4.8 The TFR result obtained by SST

4.5 Conclusions

A new approach called nonlinear squeezing wavelet transform has been proposed to detect the weak components of non-stationary signals. Simulation result demonstrates that the proposed method is effective in extracting the interested component, especially the weak segment from the multi-component signal. And the experiment result is shown to demonstrate the effectiveness of this method in the weak feature extraction of rotor rub-impact fault.

Acknowledgements This work was supported in part by the National Key Basic Research Program of China (No. 2015CB057400), the National Natural Science Foundation of China (No. 51605366) and the China Postdoctoral Science Foundation (No. 2016 M590937).

References

1. Peng, Z., He, Y., Lu, Q., Chu, F.: Feature extraction of the rub-impact rotor system by means of wavelet analysis. *J. Sound. Vib.* **259**, 1000–1010 (2003)
2. Wang, S., Chen, X., Li, G., Li, X., He, Z.: Matching demodulation transform with application to feature extraction of rotor rub-impact fault. *IEEE Trans. Instrum. Meas.* **63**, 1372–1383 (2014)
3. Cheng, J., Yu, D., Tang, J., Yang, Y.: Local rub-impact fault diagnosis of the rotor systems based on EMD. *Mech. Mach. Theory.* **44**, 784–791 (2009)
4. Cohen, L.: *Time-Frequency Analysis* Vol. 299. Prentice Hall, Englewood Cliffs (1995)
5. Huang, N.E., Liu, H.H., et al.: The empirical mode decomposition and the Hilbert spectrum for nonlinear and non-stationary time series analysis, *Proc. R. Soc. Lond. A Math. Phys. Eng. Sci.*, vol. 454, pp. 903–995 1998
6. Mann, S., Haykin, S.: The chirplet transform: physical considerations. *IEEE Trans. Signal Process.* **43**, 2745–2761 (1995)
7. Yang, Y., Peng, Z., Dong, X., Zhang, W., Meng, G.: Application of parameterized time-frequency analysis on multicomponent frequency modulated signals. *IEEE Trans. Instrum. Meas.* **63**, 3169–3180 (2014)
8. Auger, F., Flandrin, P.: Improving the readability of time-frequency and time-scale representations by the reassignment method. *IEEE Trans. Signal Process.* **43**, 1068–1089 (1995)
9. Meignen, S., Oberlin, T., Wu, H.-T.: *Time-Frequency Reassignment and Synchrosqueezing* (2013)
10. Daubechies, I., Lu, J., Wu, H.-T.: Synchrosqueezed wavelet transforms: an empirical mode decomposition-like tool. *Appl. Comput. Harmon. Anal.* **30**, 243–261 (2011)



Chapter 5

Experimental Credibility and Its Role in Model Validation and Decision Making

Sarah L. Kieweg and Walt R. Witkowski

Abstract Experiments are a critical part of the model validation process, and the credibility of the resulting simulations are themselves dependent on the credibility of the experiments. The impact of experimental credibility on model validation occurs at several points through the model validation and uncertainty quantification (MVUQ) process. Many aspects of experiments involved in the development and verification and validation (V&V) of computational simulations will impact the overall simulation credibility. In this document, we define experimental credibility in the context of model validation and decision making. We summarize possible elements for evaluating experimental credibility, sometimes drawing from existing and preliminary frameworks developed for evaluation of computational simulation credibility. The proposed framework is an expert elicitation tool for planning, assessing, and communicating the completeness and correctness of an experiment (“test”) in the context of its intended use—validation. The goals of the assessment are (1) to encourage early communication and planning between the experimentalist, computational analyst, and customer, and (2) the communication of experimental credibility. This assessment tool could also be used to decide between potential existing data sets to be used for validation. The evidence and story of experimental credibility will support the communication of overall simulation credibility.

Keywords Credibility · Experimental credibility · Data quality · Model validation · Decision making

5.1 Introduction

Experiments are a critical part of the model validation process, and the credibility of the resulting simulations are themselves dependent on the credibility of the experiments. A model calibration activity or a validation assessment is only as good as the experimental data. In particular, experimental uncertainty plays a key role in a validation assessment and the determination of model form uncertainty. The American Society of Mechanical Engineers (ASME) V&V guidelines [1, 2], standards [3], and the Coleman and Steele textbook [4] provide excellent resources for how to characterize experimental uncertainty and include it in the validation assessment activities.

The term credibility in the context of model validation and decision-making is not a universally-defined or accepted term. Credibility may encompass the trust a user or decision-maker has in the computational simulation outcomes. It may include an assessment of the correctness or completeness of the MVUQ process, such as the assessment made in a Predictive Capability Maturity Model (PCMM) [5, 6]. A statement of credibility may include both the outcomes as well as the uncertainty in predictions from a computational simulation. Credibility ideally includes evidence that is communicated in a convincing manner.

The impact of experimental credibility on model validation occurs at several points through the MVUQ process: calibration and uncertainty of model parameters in independent tests (e.g. material properties), measurement and uncertainty of experimental conditions (and thus initial/boundary conditions of a simulation), and measurement and uncertainty of experimental outcomes (used in metrics for comparison with simulation). These last two can apply to both calibration tests (of either unit, subassembly, or full system) and validation tests. In some cases, experiments also play a role in the specification of environmental conditions or the design of the experiments.

In this document, we present attributes of experimental credibility and the scope of experimental credibility in the context of *model validation* and decision making. The focus here is on a class of tests involving large systems or components for validation assessments. Similar frameworks may be proposed in the future for other classes of tests, such as separate effects tests with greater replication or material property tests for calibration. Likewise, tests with a sole use in certification

S. L. Kieweg (✉) · W. R. Witkowski
Verification & Validation, UQ, and Credibility Processes, Sandia National Laboratories, Albuquerque, NM, USA
e-mail: skieweg@sandia.gov

without use in computational simulation are not in the scope of this document and framework. We summarize possible elements for evaluating experimental credibility, drawing from existing and preliminary frameworks developed for evaluation of computational simulation credibility. Finally, we prioritize and categorize the possible credibility elements into a proposed assessment tool.

5.2 Approach

5.2.1 What Is Experimental Credibility and Why Is It Important?

For computational simulation credibility, Sandia uses a Predictive Capability Maturity Model (PCMM) [5, 6] to assess the completeness and rigor of the modeling and simulation approaches. An analogous widely accepted model/framework does not exist for validation experiments either at Sandia or in published literature. Previous efforts by others at Sandia and outside Sandia have proposed versions of such assessment frameworks. The previous frameworks differ significantly in possible elements to consider in the assessment and in their context of use. This project seeks to examine previously-proposed and other possible frameworks, evaluate their applicability, and propose an experimental assessment framework with appropriate elements.

Many aspects of experiments (e.g. the planning, UQ, analysis, and documentation) used in the development and V&V of computational simulations will impact the overall simulation credibility. These aspects fall into categories of: experimental planning, experimental UQ, processing of test data, use of data for model calibration/validation, documentation, and archiving. In this document, this collection of experimental aspects will be labeled “experimental credibility for computational simulations.” *Experimental credibility is the assessment of both the correctness and completeness of these experimental aspects and the process as a whole, and an assessment of the experiment’s use with its stated purpose – in this case, model validation. The assessment focuses on the correctness, completeness, and applicability of these experimental aspects and use.* Because experiments are used throughout the development and MVUQ of computational simulations, the experimental credibility has a strong impact on the overall simulation credibility. In particular, the completeness of the quantification and documentation of experimental uncertainty will impact the quality and use of the validation metric. In addition, an incomplete understanding and documentation of the uncertainty in the experimental conditions will impact the comparison to the simulation.

The overall goal is to provide a framework that is a structured method for assessing the level of correctness, completeness, and applicability of the experimental conditions and measurements that are intended to contribute to model validation. A similar framework (the PCMM) exists for assessing the level of maturity of computational simulation elements [5, 6].

Often, institutions may have existing requirements for testing used to qualify or evaluate a material, component, or system. However, one common misconception is that a test that meets a test plan’s specification by the customer is adequate for MVUQ purposes. This may not always be true, and in fact, without direct involvement of the analyst in the specification and planning of a test, often tests are not designed and specified for validation purposes alone. Thus, it is imperative to create a tool that helps in the planning and assessment of experiments that are intended to contribute to MVUQ processes.

5.2.2 PCMM and Other PCMM-Like Frameworks

In 2002, Trucano *et al.* published a report [7] which provided many best practices and general concepts for experimental validation of ASCI code applications. Much of these general concepts eventually made it into the PCMM in 2007. In 2007, a report documented the PCMM – the Predictive Capability Maturity Model – for computational simulation [6]. It was based on a maturity model framework concept previously used to evaluate the maturity or quality of a technological process. The report provides a historical summary of these frameworks and the many reasons they are useful. The original PCMM had six elements of computational simulations: (1) representation and geometric fidelity, (2) physics and material model fidelity, (3) code verification, (4) solution verification, (5) model validation, and (6) uncertainty quantification and sensitivity analysis. In 2013, a 4th generation PCMM was proposed [8]. The six original elements were expanded into nine, each with included sub-elements. In particular, the revised PCMM included two elements which explicitly evaluate the experimental data for both constitutive model calibration and overall model validation. Since then, others at Sandia have discussed other possible frameworks focused solely on assessing the experimental data itself, for use in validation.

In 2014, Oberkampf and Smith developed assessment criteria for evaluating CFD validation benchmark experiments [9]. Each element included descriptors for completeness level, in the spirit of the PCMM. While intended for CFD experiments, the elements have some broader applicability. Lance and Smith used that assessment to guide the development and documentation of benchmark experiments [10, 11]. Elele *et al.* developed a risk assessment matrix for tests and facilities based on an assessment for modeling and simulation [12]. Each element was assessed for risk, instead of level of maturity. The elements were divided into categories of capability, accuracy, and usability. Notably, that assessment included elements of intended use and usability.

5.2.3 Summary of Potential Assessment Elements

The following list of possible attributes, or elements, for assessment of experimental credibility captures most of the elements that appeared in the summarized frameworks in the previous section. It also reflects some of the best practices for validation tests [6, 7]. These elements will be prioritized and categorized in the final proposed assessment tool in the section below. It is possible to group these with different affinities – the proposed element affinity is just one possible framework. In future work, this proposed framework will be demonstrated and evaluated with a set of experimental-computational partners to evaluate its efficacy for improving planning and communication.

- Planning
- Hardware/material fidelity
- Experimental/environmental fidelity
- Experimental verification: Control code
- Experimental verification: Data analysis code
- Experimental verification: Test facility
- Experimental verification: Evidence test performed correctly
- Experimental validation: Confirmation of measurements
- Intended use: Test conditions
 - Rigor and completeness of characterizing test conditions for use as a validation test.
- Intended use: Test Output
 - Applicability and completeness of measured test outputs for purposes of validation assessments.
- Uncertainty Quantification (UQ)
 - Elements of this will be detailed in a sub-assessment tool described in a later section.
 - Applicable to both test conditions and output measurements.
- Peer review of all the above elements
- Documentation

5.2.4 Lessons Learned from the PCMM and PCMM-Like Frameworks

The 4th-generation PCMM development project [8] emphasized some key lessons learned that should be applied to a framework for assessing experimental uncertainty and credibility:

- The purpose of the tool should be clear.
- The purpose of the tool is not to “grade” or “score” the work, but rather to provide a tool that facilitates planning and communication. A summary score should not be used – a quantitative score is artificial and misleading.
- The assessment should involve an inclusive team-based SME elicitation process.
- The requirements of the customer should be documented in the evaluation process, and be specific about how the tool and the work will be used to communicate credibility to the customer.

These lessons are applied to the following two proposed frameworks for (1) assessing the correctness, completeness, and applicability of a validation experiment, and (2) assessing experimental uncertainty. The goal is to provide tools that

encourage early planning and continual communication. Unlike previous frameworks like the PCMM, this proposed structure does not include any “scoring” activities. Instead, these frameworks include open-ended questions that should encourage discussion of advantages and limitations of each element, and communication of credibility evidence.

5.3 Proposed Framework to Assess Validation Experiments

The two primary goals of the proposed assessment tools are to encourage early planning and facilitate communication of credibility of final products. Thus, the format of the assessment has been altered from the format seen in the PCMM in order to promote communication and avoid the graded levels. Rather than use graded maturity levels in these assessment frameworks as was done in the PCMM, descriptors for each element are casted as open-ended questions. Thus, instead of prescriptive levels that dictate what should be done at each level, the frameworks proposed below provide prompts and open-ended questions to facilitate planning and communication.

Rather than simply indicating the maturity level for each element, users are expected to respond with a description addressing the prompts and open-ended questions. The users are asked to consider the strengths and weaknesses of the experiment using each element to guide their assessment. The written responses allow users to differentiate how individual aspects of that element are assessed. The user’s descriptive discussion of evidence for each element can contribute to a written credibility story for the simulation as a whole (i.e. augment the PCMM analysis of the simulation), and aid communication to the customer.

Two frameworks are proposed. First, is an “Assess Validation Experiment” tool (see Fig. 5.1) for assessing the correctness, completeness, and applicability of a validation experiment. The second is an “Assess Experimental Uncertainty” tool (see Fig. 5.2). The second tool is used to address the Uncertainty Quantification element of the first tool. The second tool also

Assess Validation Experiment	Read these prompts, discuss with team, and write a response for each element. Use this when assessing and communicating credibility evidence for computational simulation (i.e. CompSim) that uses this experiment for validation. Complete during pre-test planning and again during post-test analysis.	How did these elements impact the strength and weakness of this test for the purpose of CompSim validation?
Element	Prompts to Consider	Assessment Commentary
Planning	<ul style="list-style-type: none"> Was/is the purpose of the test known to the experimentalist and end-user (e.g. CompSim analyst)? Was the test originally intended for validation purposes? How much communication was there between the experimentalist, customer, and end-use analyst during both the planning and post-test stages? Did this create any strengths or weaknesses to the outcomes? Was CompSim involved in the planning of this experiment, and in what way? 	
Sample / Geometric / Material Fidelity	<ul style="list-style-type: none"> Was the sample, geometry, and/or material relevant to the specified requirement and/or intended application? Is the proximity sufficient for this type of test and validation assessment? Do you know the pedigree? Was there any pre-processing of the sample/material that could impact applicability? 	
Experimental / Environmental Fidelity	<ul style="list-style-type: none"> How relevant is the environment and test conditions to the requirement and/or application? Is the proximity sufficient for this type of test and validation assessment? What could have been changed to improve the applicability? 	
Experimental Verification	<ul style="list-style-type: none"> Was the code that controls the testing apparatus verified? Was the code that post-processes the raw data verified? Are the test facility and equipment documented well and calibrated? How do you know you measured what you think you measured? Do you have any confirmation of the measurements? What is the evidence that the test performed correctly? 	
Intended Use / Validation	<ul style="list-style-type: none"> Were the test conditions characterized well enough for the intended validation assessment? Where any conditions missing, not well-characterized, or suspicious? Were the output measurements characterized well enough for the intended use as a validation test? Were enough quantities of interests measured, and were the right ones measured? Where the validation metrics and criteria specified before the testing, or after? 	
Uncertainty Quantification	<ul style="list-style-type: none"> This includes uncertainty on both test conditions and outputs - did the test provide the uncertainty on both needed for making the validation assessment? To assess the uncertainty quantification, use the elements of the "Assess Experimental Uncertainty" framework. 	
Peer Review and Documentation	<ul style="list-style-type: none"> Which of the above elements of the test were reviewed by subject matter experts? Which elements were not, and of those, which may need further review and why? Are the above elements of the test all documented? Does the documentation serve the need for making the validation assessment, and helping write the credibility evidence for the CompSim? Or is there anything missing that would have improved the validation process? 	

Fig. 5.1 “Assess Validation Experiment” Tool. (CompSim = Computational Simulation)

Assess Experimental Uncertainty	Read these prompts, discuss with team, and write a response assessment for each element. Use this when assessing the Uncertainty Quantification element of the Assess Validation Experiment tool.		Assess the pros and cons of this experiment in terms of its quantified uncertainty
Element	Prompts to Consider	Best Practices	Assessment Commentary
Pre-test planning:	<ul style="list-style-type: none"> Was there pre-test planning between experimentalist and end-user? Was there discussion on use of data and documentation needs? 	<ul style="list-style-type: none"> Discussion initiated pre-test Decide who will do which parts of data analysis and UQ Agree upon level of documentation on data pedigree and UQ Clearly define end use of experiment 	
Pre-test: Define measurand(s) needed to obtain QOI(s)	<ul style="list-style-type: none"> Are the Quantities of Interest (QOIs) defined and specified how will be measured and/or quantified? How do measurands relate to QOIs? Require post-processing? 	<ul style="list-style-type: none"> Discussion/activity initiated pre-test Plan to measure range of local and globally integrated quantities Specify and document functional relationship between measurand(s) and final QOI(s), and how data processed and/or reduced. Document other unmeasured quantities used to calculate QOI. 	
Pre-test: Measurement process and management of uncertainties	<ul style="list-style-type: none"> Is the measurement and calibration process well described? Where expected uncertainties considered in experimental design? 	<ul style="list-style-type: none"> Define test objectives Map measurement parameters and nominal level to what calibrations and instruments will determine each. Identify correlated errors (e.g. measurements that come from same calibration/instrument) Specify required uncertainty for each measurand so that final result has required uncertainty 	
Pre-test/Post-test: Expected and Estimated Uncertainties	<ul style="list-style-type: none"> Is there an uncertainty inventory for all conditions and measurements? What is missing or a limitation for use of test (e.g. UQ and validation)? 	<ul style="list-style-type: none"> Should be done both pre-test (expected) and post-test For each measurand in test, complete spreadsheet of (expected) uncertainties Consider all possible sources of uncertainty Consider documentation, calibration histories, previous tests with similar instruments, previous uncertainty analyses, expert judgement 	
Pre-test/Post-test: Uncertainty Propagation and Sensitivity Analysis	<ul style="list-style-type: none"> What uncertainty sources are small compared to others? Which uncertainties are not well characterized and can something be done to improve that? What could be done now or in future to reduce predicted or measured uncertainties? 	<ul style="list-style-type: none"> Propagate estimated/measured measurement uncertainties into the expected/measured range of results for the QOI(s). Pre-test analysis: just based on precision limits; Post-test analysis: both precision and bias. Identify which measurand(s) have greatest impact on uncertainty of result Identify if there is a better measurement technique to use. Communicate between experimentalist and analyst on whether expected result uncertainty will be adequate for intended use. If have multiple tests, repeat calculation of results and then find uncertainty of the result directly, and compare to propagated uncertainties from each measurement; extract info about zeroth and first order replication level analysis (e.g. infer sample-to-sample variability with multiple tests). 	

Fig. 5.2 “Assess Experimental Uncertainty” Tool. This framework includes a list of best practices for quantifying experimental uncertainty, most of which were summarized from published pre-test and post-test uncertainty analysis guidelines [3, 4]

includes a list of best practices for quantifying experimental uncertainty, most of which were summarized from published pre-test and post-test uncertainty analysis guidelines [3, 4]. For example, best practices include the identification of all sources of uncertainty, e.g. measurement, data analysis, repeatability, and unsteadiness. Guidelines, standards, and textbooks provide methods for characterizing types of uncertainty, quantifying uncertainty, and using experimental uncertainty in the validation assessment [1–4].

5.4 Conclusions

The proposed frameworks are expert elicitation tools for planning, assessing, and communicating the completeness, correctness, and applicability of an experiment (“test”) and its uncertainty in the context of its intended use. The goals of the assessment are (1) to encourage early communication and planning between the experimentalist, computational analyst, and customer, and (2) the communication of experimental credibility. The evidence and story of experimental credibility will support the communication of overall simulation credibility to the customer. The primary application of this tool is for tests used for validation of simulations. Ideally, such tests are designed specifically for validation, but in practical conditions, often existing tests developed for another purpose will need to be used for validation purposes. Thus, these tools can also be used to evaluate existing data sets for potential use in validation. In future work, this proposed framework will be demonstrated and evaluated with a set of experimental-computational partners to evaluate its efficacy for improving planning and communication.

Acknowledgements The authors thank Martin Pilch, PhD, and Angel Urbina, PhD, for valuable conversations and feedback. This project was funded by the Advance Simulation and Computing (ASC) Program of the Department of Energy's National Nuclear Security Administration and the Weapons Systems Engineering Assessment Technology (WSEAT) Program at Sandia National Laboratories.

Sandia National Laboratories is a multimission laboratory managed and operated by National Technology and Engineering Solutions of Sandia LLC, a wholly owned subsidiary of Honeywell International Inc. for the U.S. Department of Energy's National Nuclear Security Administration under contract DE-NA0003525. SAND2017-11505 C.

References

1. ASME V&V 10-2006: Guide for Verification and Validation in Computational Solid Mechanics. ASME, New York (2006)
2. ASME V&V 20-2009: Standard for Verification and Validation in Computational Fluid Dynamics and Heat Transfer. ASME, New York (2009)
3. ASME Performance Test Codes Supervisory Committee: *ASME PTC 19.1-2013: Test Uncertainty*. ASME, New York (2013)
4. Coleman, H.W., Steele, W.G.: *Experimentation, Validation, and Uncertainty Analysis for Engineers*, 3rd edn. Wiley, New York (2009)
5. What is Predictive Capability Maturity Model (PCMM) SAND2016-7399TR (UUR). Sandia National Laboratories, Livermore (2016)
6. Oberkampf, W.L., Pilch, M., Trucano, T.G.: Predictive Capability Maturity Model for Computational Modeling and Simulations. SAND2007-5948 (UUR). Sandia National Laboratories, Livermore (2007)
7. Trucano, T.G., Pilch, M., Oberkampf, W.L.: General Concepts for Experimental Validation of ASCI Code Applications. SAND2002-0341 (UUR). Sandia National Laboratories, Livermore (2002)
8. Hills, R.G., et al.: Development of a Fourth Generation Predictive Capability Maturity Model. SAND2013-8051 (UUR). Sandia National Laboratories, Livermore (2013)
9. Oberkampf, W.L., Smith, B.L.: Assessment Criteria for Computational Fluid Dynamics Validation Benchmark Experiments. in 52nd Aerospace Sciences Meeting. National Harbor, Maryland (2014)
10. Lance, B.W., Harris, J.R., Smith, B.L.: Experimental validation benchmark data for computational fluid dynamics of mixed convection on a vertical flat plat. *ASME J. Verification Validation Uncertainty Propagation*. **1**(September 2016), 021005 (2016)
11. Lance, B.W., Smith, B.L.: Experimental validation benchmark data for computational fluid dynamics of transient convection from forced to natural with flow reversal on a vertical flat plat. *ASME J. Verification Validation Uncertainty Propagation*. **1**(September 2016), 031005 (2016)
12. Elele, J., et al.: Applying Modeling and Simulation Verification, validation and Accreditation (VV&A) Techniques to Test and Laboratory Facilities, in ASME V&V Conference (2012)



Chapter 6

An Experimental Case Study for Nonlinear Model Validation: Effect of Nonlinearities in an Aero-Engine Structure

Samson B. Cooper, Dario DiMaio, Ibrahim A. Sever, and Sophoclis Patsias

Abstract Linear FE-models are commonly validated with measured data obtained from experimental test conducted under similar FE-simulated boundary conditions. However, measured data at higher or operational amplitudes of vibration often exhibit evidence of nonlinear characteristics. Research has proven that majority of the causes and sources of these nonlinearities are frequently local in nature while a large proportion of the structure can be represented using linear theory. This paper presents the experimental investigations conducted on an aircraft structure ranging from linear to nonlinear regime, the aim of the investigation was to understand the influence of connecting accessories or components to the proposed aircraft structure. Broadband, sine-sweeps and stepped-sine excitations were used to detect and characterise the nature of the nonlinear behaviour in the assembly.

Keywords Experimental Test · Operating Condition · Nonlinear Characterisation and Aircraft Structure

6.1 Introduction

In most cases, aircraft structures are generally modelled using linear identification theory. However, the increasing level in the complexity of designing lighter and more flexible structures can require the implementation of different design procedures and options. These procedures in some cases may lead to design of aircraft structures which are inevitably prone to severe nonlinear vibration problems. Several researches reporting the evidence of existing nonlinearities in aerospace structures can be found in the literature [1–3]. However, understanding the effects of these nonlinearities most importantly at flight operational conditions remains an area of major challenge to current engineers in the field of structural dynamics and aircraft design. Hence researchers are beginning to receive a growing demand from aerospace industries that would normally not account for nonlinearities in their design process [4]. To be precise, these industries are seeking for viable techniques and methodologies that can be used to detect and understand the behaviours of these nonlinearities whilst sustaining the appropriate industrial approved design and certification procedures.

Research on the successful identification of nonlinearities from measured data have also received a growing level of improvements, where major research outputs have led to the development of several nonlinear identification techniques such as the frequency domain nonlinear subspace identification (FNLSI) [5], the reverse path method [6, 7], the restoring force surface (RFS) [8, 9], Hilbert transform (HT) [10, 11] and black-box methods [12]. Further case studies where these identification techniques have been applied to real aerospace structures are present in the literature. For example, the wavelet and RFS identification techniques were used gain more insight into the nonlinear behaviour observed during the Ground Vibration Test (GVT) of the F-16 fighter aircraft [13]. Still, one specific challenge currently experienced by some aerospace engineers is understanding the nonlinear behaviours observed during the experimental testing of final assembled aerospace component most especially for operational conditions. Gaining insight and modelling the nonlinearities observed at mounting interfaces between aero-structure subcomponents is increasingly becoming a major challenge that can no longer be ignored or modelled using linear tools. Research on bolted joints and other types of nonlinear features have been found to introduce large uncertainties in the stiffness and damping properties of a structure which can often render the behaviour of the structure nonlinear [14].

S. B. Cooper (✉) · D. DiMaio
University of Bristol, Department of Mechanical Engineering, Bristol, UK
e-mail: sc14784@bristol.ac.uk; dario.dimaio@bristol.ac.uk

I. A. Sever · S. Patsias
Rolls Royce plc, Westhampnett, Derbyshire, UK



Fig. 6.1 Photograph of the Aero-engine casing

In this context, the objective of this present paper is to highlight the nonlinearities observed during the vibration test of an assembled aero-engine casing. Most importantly at high amplitudes of vibrations where nonlinearities and complex dynamic mechanics are triggered at the bolted connections and interfaces. Nonlinear detection is performed by comparing frequency response functions obtained at low and high excitation levels, followed by a finite element model of the casing with major attentions to modes that could trigger nonlinear behaviours. Finally, stepped sine test at low and high excitation levels is specifically conducted to visualise the nonlinear trend in the stiffness and damping characteristics of the assembly.

6.2 Description of the Aero-Engine Casing

The test structure represented in Fig. 6.1 is the casing of an aircraft engine used for powering a typical commercial aircraft. The structural configuration considered in this paper is a three-layer architecture of the aircraft engine casing without any internally attached accessories. The entire casing has structural features that are typical of a full-size assembled system e.g. multiple body sections and bolted joints, the total mass of the casing assembly is 461 kg.

6.3 Experimental Setup and Linear Modal Analysis

The casing was suspended horizontally from a blue test frame using four elastic chords to support the suspension as shown in Fig. 6.2a. The test frame used in this research is classified as a Technology Research Level (TRL6) structure developed under the HITEA project while the elastic chords are used to represent a free-free boundary test condition. The experimental set-up was designed to replicate the traditional horizontal configuration of such component when attached to an aircraft. A total of 32 accelerometers was employed to instrument the structure, all of which are single-axial sensors. For this investigation, only the first subassembly section of the engine casing illustrated in Fig. 6.2b was fully instrumented, a large shaker visible in Fig. 6.2a was used to apply excitation inputs to the casing in a vertical direction.

The experimental investigation was conducted in two stages, the first stage of the experimental investigation involved conducting a set of traditional modal test on the aero-engine casing to obtain the natural frequencies and damping ratios at low amplitude of vibration. In addition, stepped-sine test at high excitation levels was carried out on the casing to check for symptoms of nonlinearity that may be present in the instrumented section of the casing. The second stage of the experimental investigation involved the execution of another set of modal tests on the engine casing with a potential nonlinear device attached to the first subassembly of the engine casing. The aim of the second stage was to access the influence and nonlinear effects of attaching accessories on the engine casing assembly. In this stage, specific tests were performed on the engine casing assembly using different types of excitation inputs with the intentions of gaining valuable insights into the nonlinear behaviour introduced by the attached device.

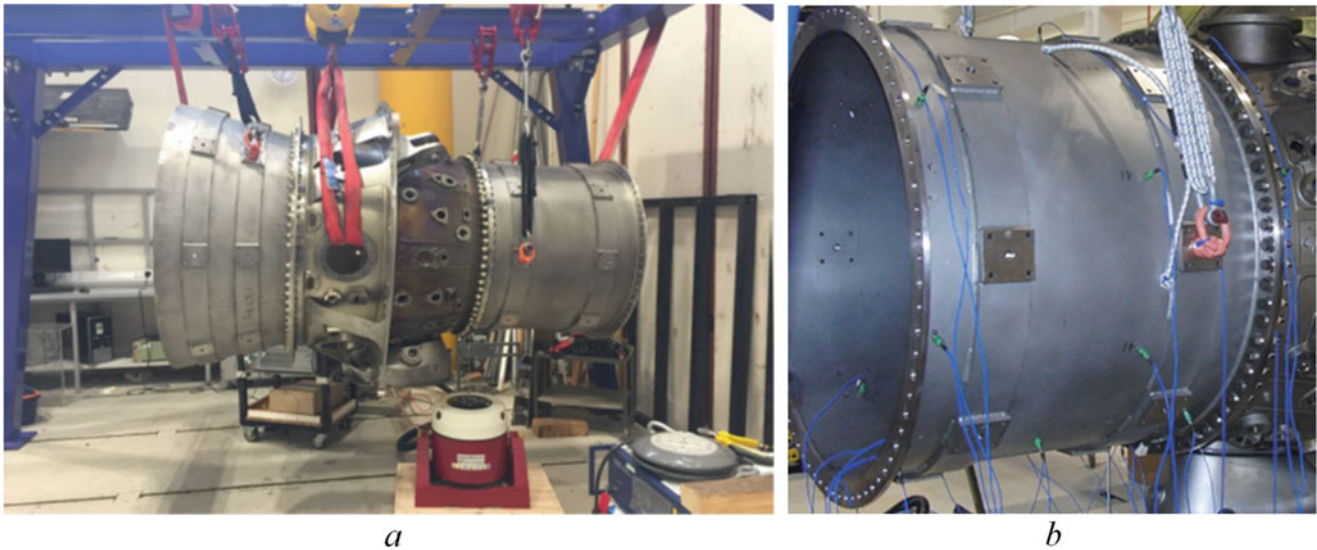


Fig. 6.2 Experimental set-up of the engine casing suspended on a TRL-6 frame. (a) Test Set-up, (b) Instrumented section of the casing

6.4 Low Level Modal Testing and Analysis

The first measurements obtained from the experimental test comprised of several low random data which were acquired based on broadband excitation, the choice of broadband excitation was made based on its conventional use in modal testing. Broadband excitation also provides some early information on the behaviour of the structure and experimental configuration, the low level random test was performed using the Spectral Test module in LMS Test Lab. The test structure was excited near the flange connecting the inter-case (middle case) with the first case as shown in Fig. 6.2a. The structure was excited using burst random excitation ranging between 30 and 500 Hz. The Frequency Response Function (FRFs) obtained from the test were exploited to identify the linear modal parameters of the engine casing. Figure 6.3 shows a selection of the FRFs obtained from the low-level test.

Before getting an insight of the nonlinear behaviour of the casing, a linear modal analysis based on the FRF's obtained from low-level random test was conducted using the PolyMAX method [15]. The applied random excitation has an RMS value of 45 N, the first two modal shapes of the casing are illustrated in Fig. 6.4. The natural frequencies and damping ratios are listed in Table 6.1.

6.5 Linear Finite Element Model

A Finite Element (FE) model of the casing was built using SIMULIA Abaqus software to perform the linear FE analysis. The model consists of three different parts namely the CCOC, INTERCASE, and IPCC. The CCOC represents the first instrumented cylinder shown in Fig. 6.2b, the INTERCASE represents the central part of the casing while the IPCC is the last section of the casing. Different physical parameters were set such that the FE model represents the real casing, the three parts were assembled together using the tie constraint function in Abaqus. The FE model was calibrated to reproduce the first two modes of the casing as they indicate the most instrumented section of the casing and are also expected to show some form of nonlinear behaviour when different devices are attached to the casing (Fig. 6.5) shows the results obtained from the linear FE analysis.

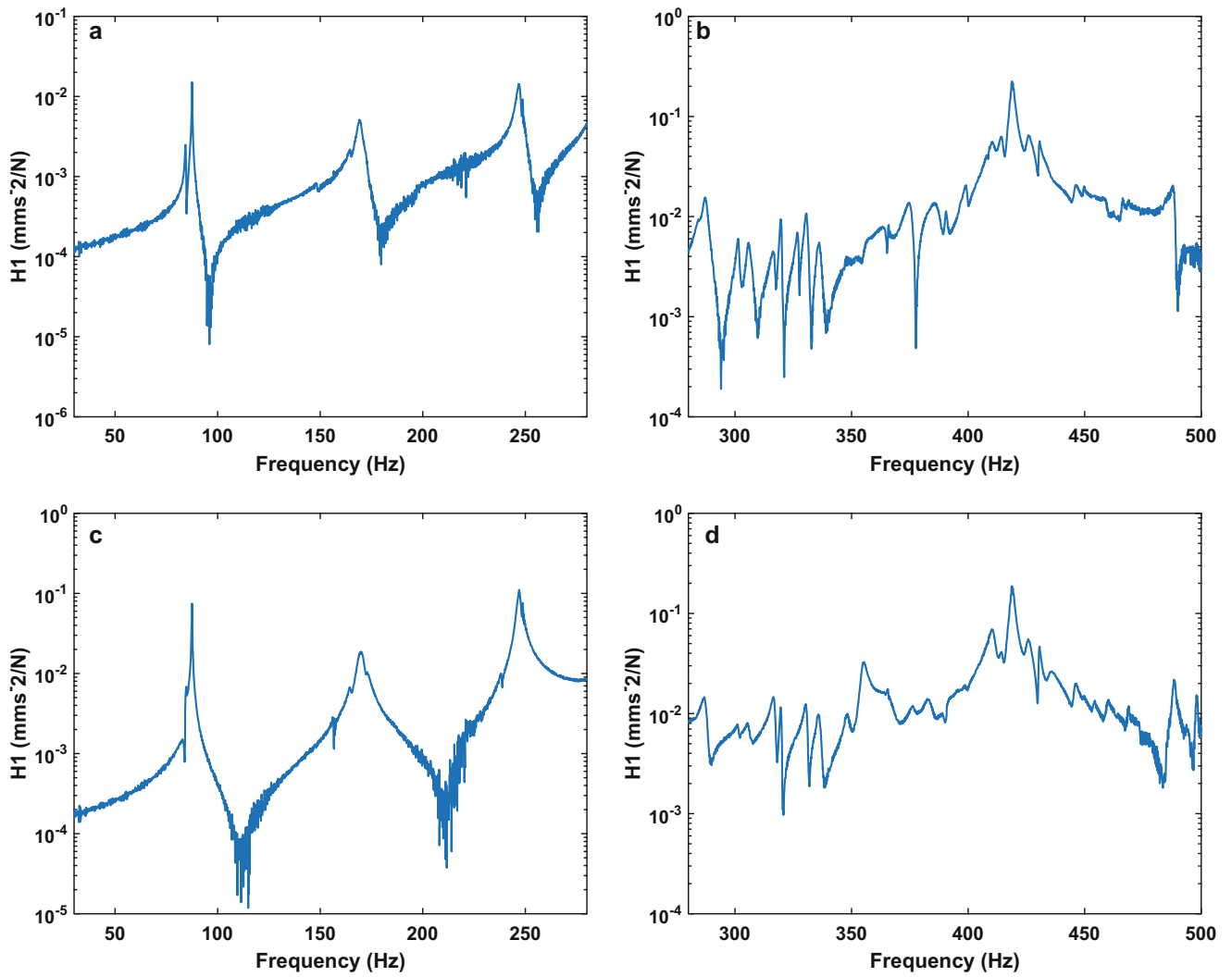


Fig. 6.3 Linear acceleration response function measured at low-level excitation for the Engine Casing. (a, b) (Bottom centre of the first cylinder) (c, d) (Drive point)

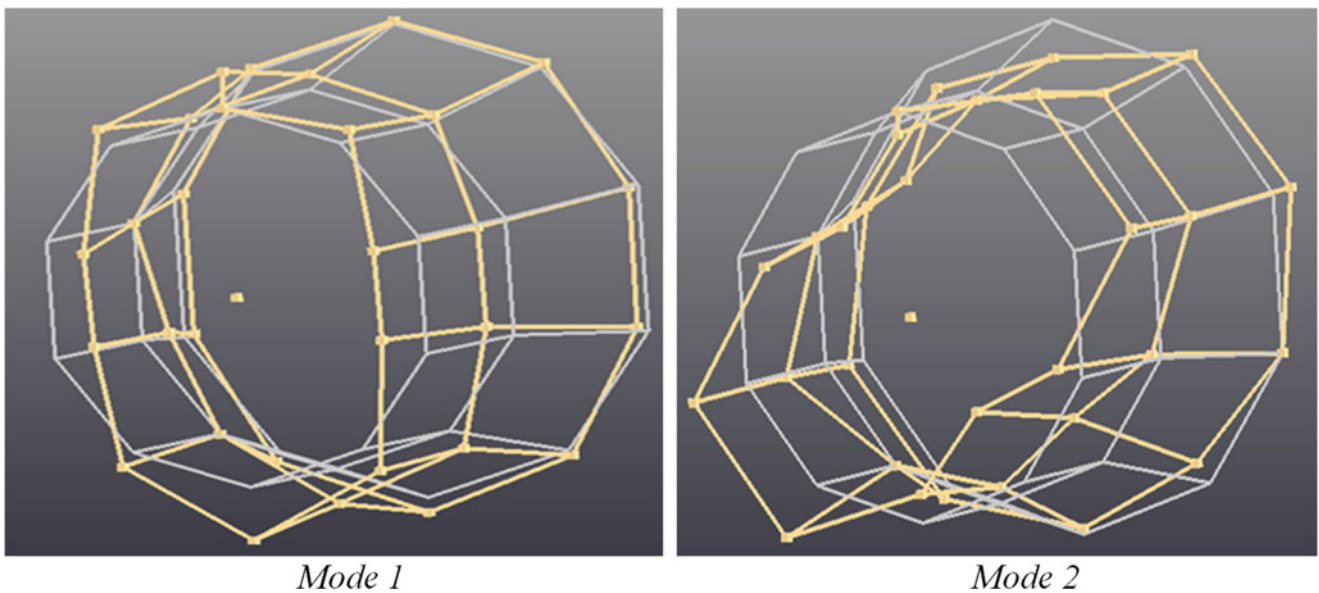
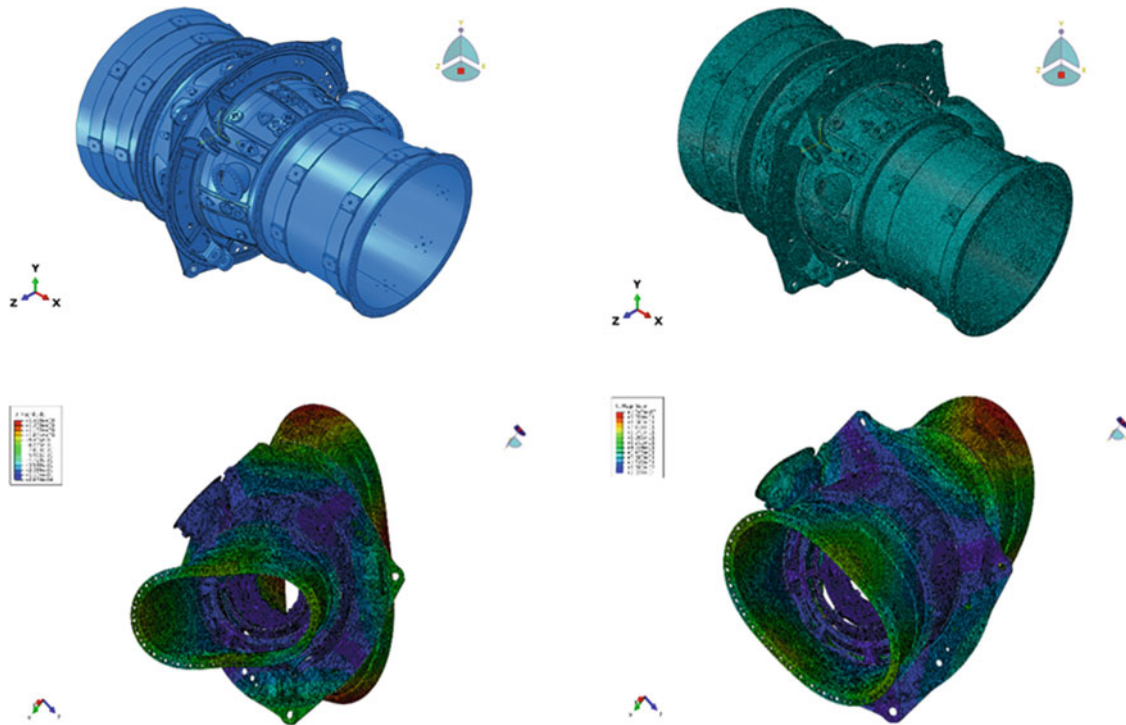


Fig. 6.4 Deformed and un-deformed mode shapes of the casing estimated using POLYMAX method

Table 6.1 Estimated linear natural frequencies and damping ratios based on low-level random data

Mode number	Natural frequency (Hz)	Damping ratio (%)	Mode number	Natural frequency (Hz)	Damping ratio (%)
1	84.39	0.19	7	238.33	0.10
2	87.40	0.10	8	246.85	0.39
3	156.26	0.07	9	248.27	0.05
4	164.61	0.33	10	285.07	0.37
5	170.07	0.43	11	287.45	0.36
6	178.54	0.47	12	316.92	0.26

**Fig. 6.5** Finite element model and mode shapes of the engine casing (a) (model Assembly) (b) (FE Mesh) (c) (FE Mode 1) (d) (FE Mode 2)

To check for symptoms of nonlinear behaviour, a stepped sine test was conducted on the casing. The casing was excited at several excitation levels covering a frequency bandwidth of 80–90 Hz. The test was conducted to observe and detect any frequency or damping shifts from the response of the structure resulting from this specific test. A selection of the FRFs and phase plots obtained from low to high level excitation test are presented in Fig. 6.6.

Results obtained from the stepped sine test indicates that the casing can be regarded to behave linearly within the excited range. The FRFs for the presented in Fig. 6.6 shows minimal shift in the frequency and damping values over a range of forcing levels, most especially for the response obtained at the drive point where there are on change observed in the frequency and amplitude values for the first mode around 84 Hz.

6.6 Modal Testing of the Plate-Casing Assembly

This section addresses the experimental investigation conducted when a potential nonlinear component is attached to the casing. The component used in this demonstration is a flat aluminium plate bolted on four stiffness shaped steel blocks, Fig. 6.7a shows an illustration of the plate assembly. The plate is then bolted on the first cylinder of the casing very close to the excitation position as shown in Fig. 6.7b. The test set-up and boundary conditions remained the same as previously shown in Fig. 6.2a, the bolted connections between the plate and the casing were instrumented appropriately to gain more insight into any nonlinear phenomena.

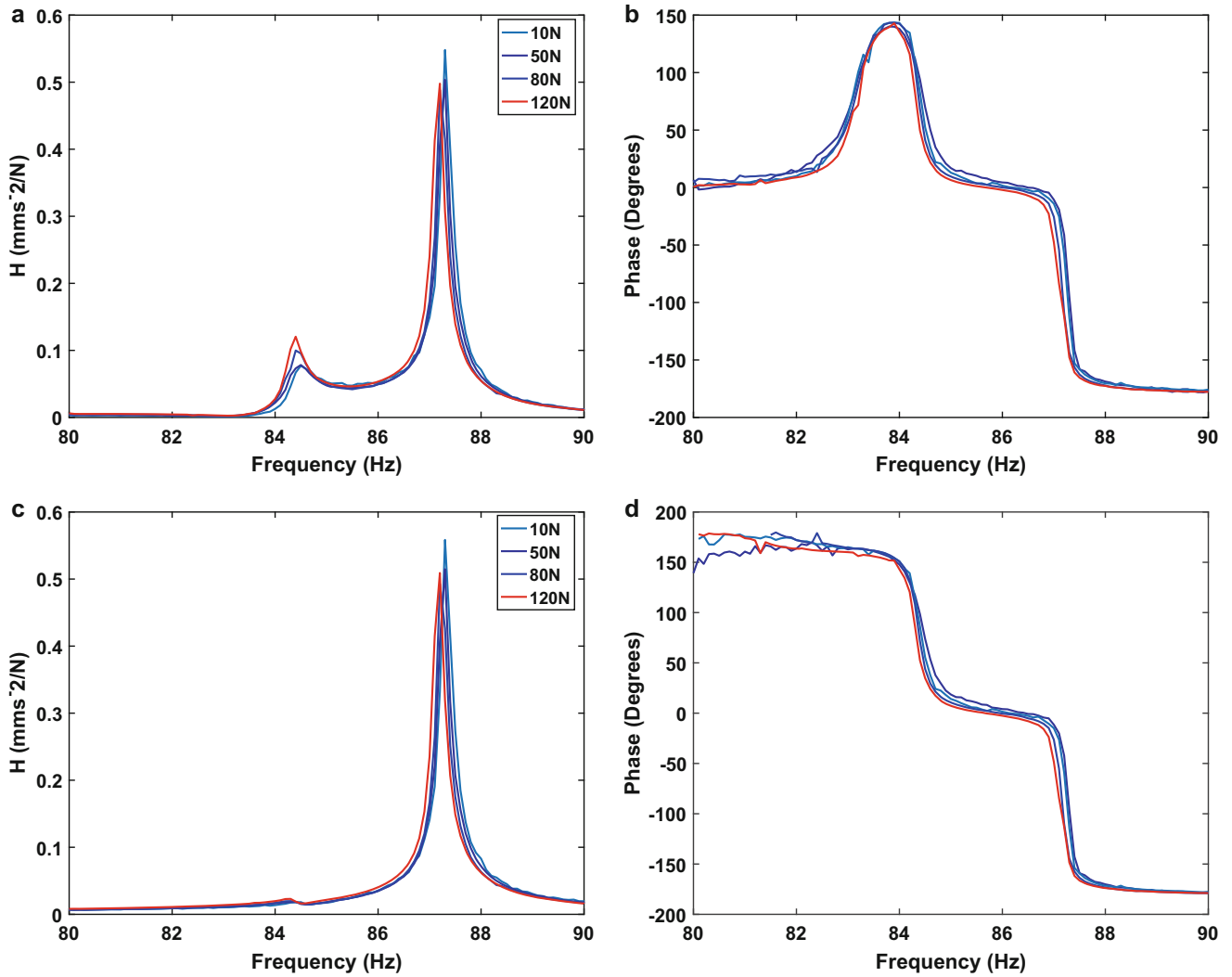


Fig. 6.6 Comparison of stepped sine FRFs measured at several excitation levels obtained from a stepped sine test on the casing. (a, b) (FRF and phase at the bottom centre of the first cylinder), (c, d) (FRF and Phase of the Drive Point)

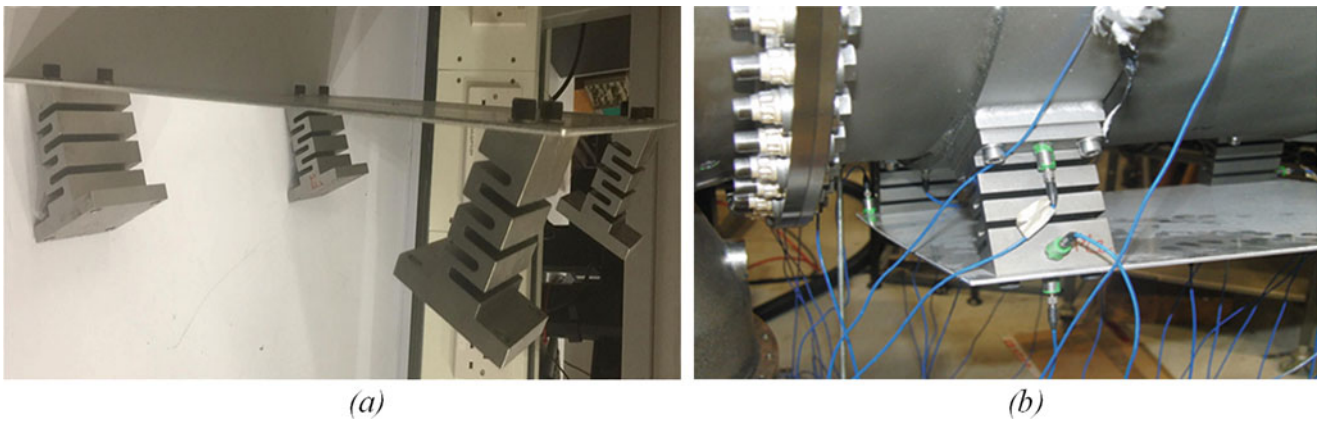


Fig. 6.7 Assembly of the casing with an aluminium plate for nonlinear investigation. (a) (Aluminium plate), (b) (casing and plate assembly)

Similarly, low-level test was conducted on the new casing assembly using random excitation covering a frequency bandwidth of 10-500 Hz to obtain FRFs which were used for modal analysis. Linear modal analysis was conducted to extract the natural frequencies and damping ratios based on the FRFs obtained from the new test. Figure 6.8 shows a selection of the FRFs obtained from the low-level test and Table 6.2 presents the corresponding natural frequencies and damping ratios of the casing with the plate bolted to the first cylinder.

Comparing a selected linear FRF plot from the casing with the same point FRF when the plate is attached to the casing as shown in Fig. 6.9, it is obvious that the addition of the plate to the casing introduces new dynamics into the system where the new assembly can be regarded as a new structure. Also in Table 6.2 more natural frequencies and modal damping ratios are identified and compared with those identified from the casing alone.

6.7 Linear Finite Element of the Plate Assembly

The calibrated FE model of the casing was amended by adding the geometry design of the plate. The plate was modelled with the exact dimensions. The bolted joint between each corner step of the plate and the casing was modelled using the tie constraint in ABAQUS. For this FE model, standard material properties of aluminium were also used to model the plate and the material properties of the other components in the assembly were left unchanged since they were already updated. Similarly, a linear frequency analysis was conducted on this version of the FE model to obtain the natural frequencies and mode shapes. Figure 6.10 illustrates the first two mode shapes obtained from the analysis.

Based on the deformation of the plate and their corresponding connection, it is possible to have gain an insight into the potential regions of the assembly that are prone to exhibit some form of complex nonlinear phenomena. This is most evident in Fig. 6.10c, d where a large deformation is observed at the centre of the plate for both modes 1 and 2, it is also obvious that each mode has a greater influence on different bolted connections between the plate and the casing.

6.8 Nonlinear Detection

Equally, to check for symptoms of nonlinear behaviour in the plate and casing assembly, a stepped sine test was conducted on the casing. The new assembly was also excited at several excitation levels covering a frequency bandwidth of 80–90 Hz. Figure 6.11 shows a selection of the FRFs and phase results obtained from the stepped sine test. In Fig. 6.11 stepped-sine FRFs and phase are presented for plate casing assembly, the test was concentrated around the first three modes of the assembly ranging from the lowest (10 N) to a highest (120 N) input levels of excitation. These stepped-sine FRFs only consider the first harmonic and neglects all other higher-order harmonic components in both input and output. In Fig. 6.11a, a clear symptom of nonlinearity is observed based on the shift in frequency and maximum amplitude, most especially for the first mode around 82 Hz. The corresponding phase plot in Fig. 6.11b also show the presence of nonlinear behaviour through the reduction observed in the phase plot as the excitation increases. Based on Fig. 6.11, one can conclude that the addition of the plate to the casing has certainly changed the dynamics of the structure and mostly importantly the degree of nonlinear behaviour observed from the FRFs and phase plots are more noticeable compared to the results obtained from the test on the casing alone.

6.9 Conclusion

This paper shows how broadband and stepped sine measurements from a vibration test campaign can provide insightful information about the nonlinear behaviour of a large-scale aircraft structure when connected to simple plate structure. Nonlinear detection on plate and casing assembly was performed by comparing stepped sine FRFs at several excitation levels. The mode shapes and deformation plots obtained from the finite element model of the assembly was also used to gain some useful insights to the areas of the assembly that could potentially exhibit nonlinear behaviours. A better understanding of the complex nonlinear behaviour observed most especially on the first and second mode could be investigated by using simple theoretical but powerful tools, such as the acceleration surface method and the wavelet transform-based time frequency analysis.

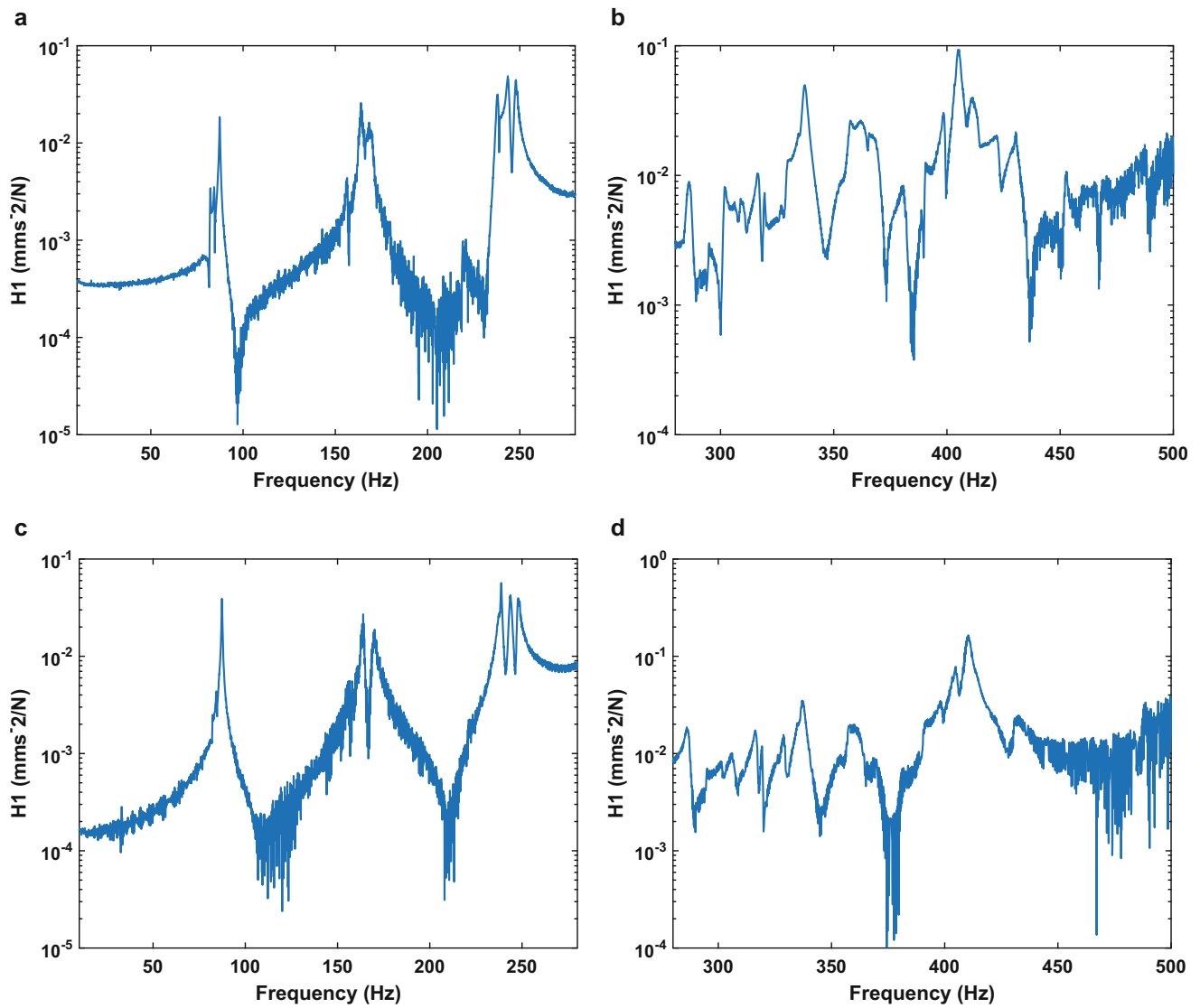


Fig. 6.8 Acceleration response function obtained from low-level broadband excitation performed on the nonlinear assembly. (a, b) (Bottom centre of the first cylinder) (c, d) (Drive point)

Table 6.2 Estimated linear resonance frequencies and damping ratios based on low-level random data

Mode number	Natural frequency (Hz)	Damping ratio (%)	Mode number	Natural frequency (Hz)	Damping ratio (%)
1	82.17	0.29	7	169.98	0.46
2	84.34	0.19	8	172.05	0.46
3	87.17	0.09	9	179.68	0.19
4	158.42	0.13	10	237.51	0.34
5	163.41	0.39	11	238.68	0.12
6	167.29	0.57	12	243.45	0.28

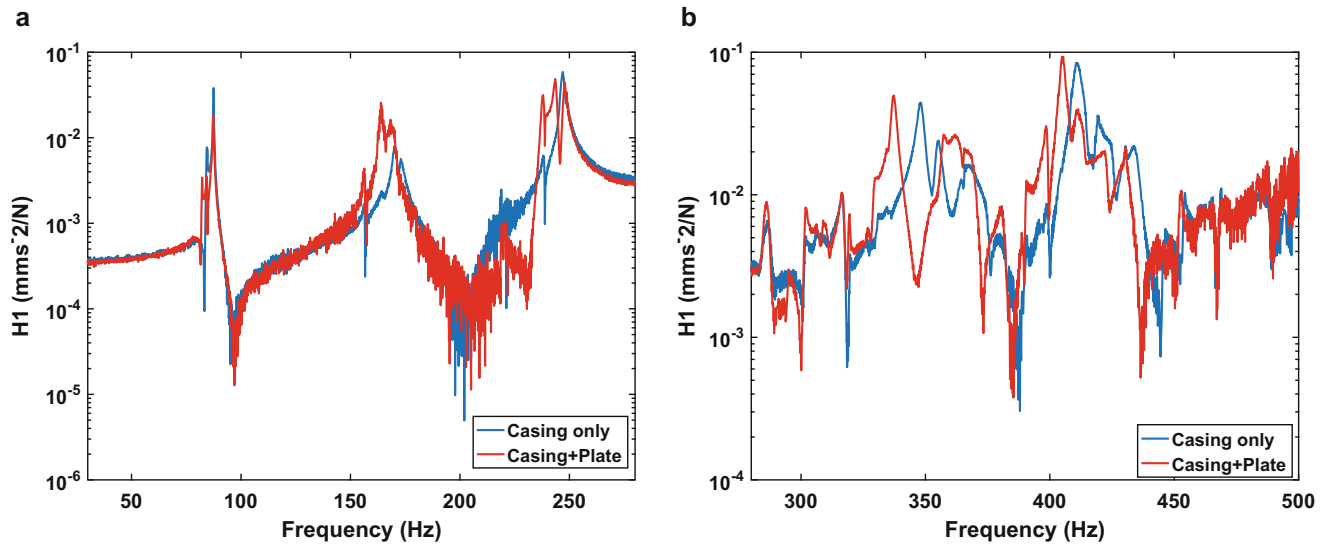


Fig. 6.9 Comparison of low-level acceleration response function of the casing and the plate casing assembly (a) (Drive point 30-280Hz) (b) (Drive point 280-500 Hz)

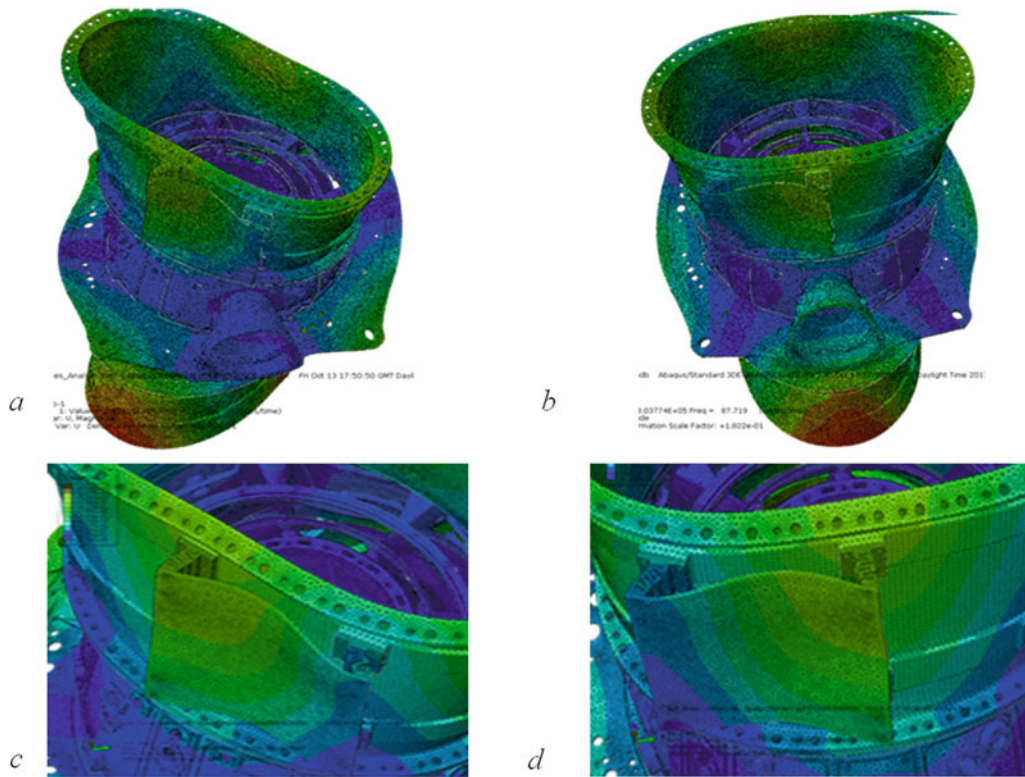


Fig. 6.10 Finite Element mode shapes of the casing and plate assembly. (a) (Mode 1), (b) (Mode 2), (c, d) (closer view of the plate connections for modes 1 and 2)

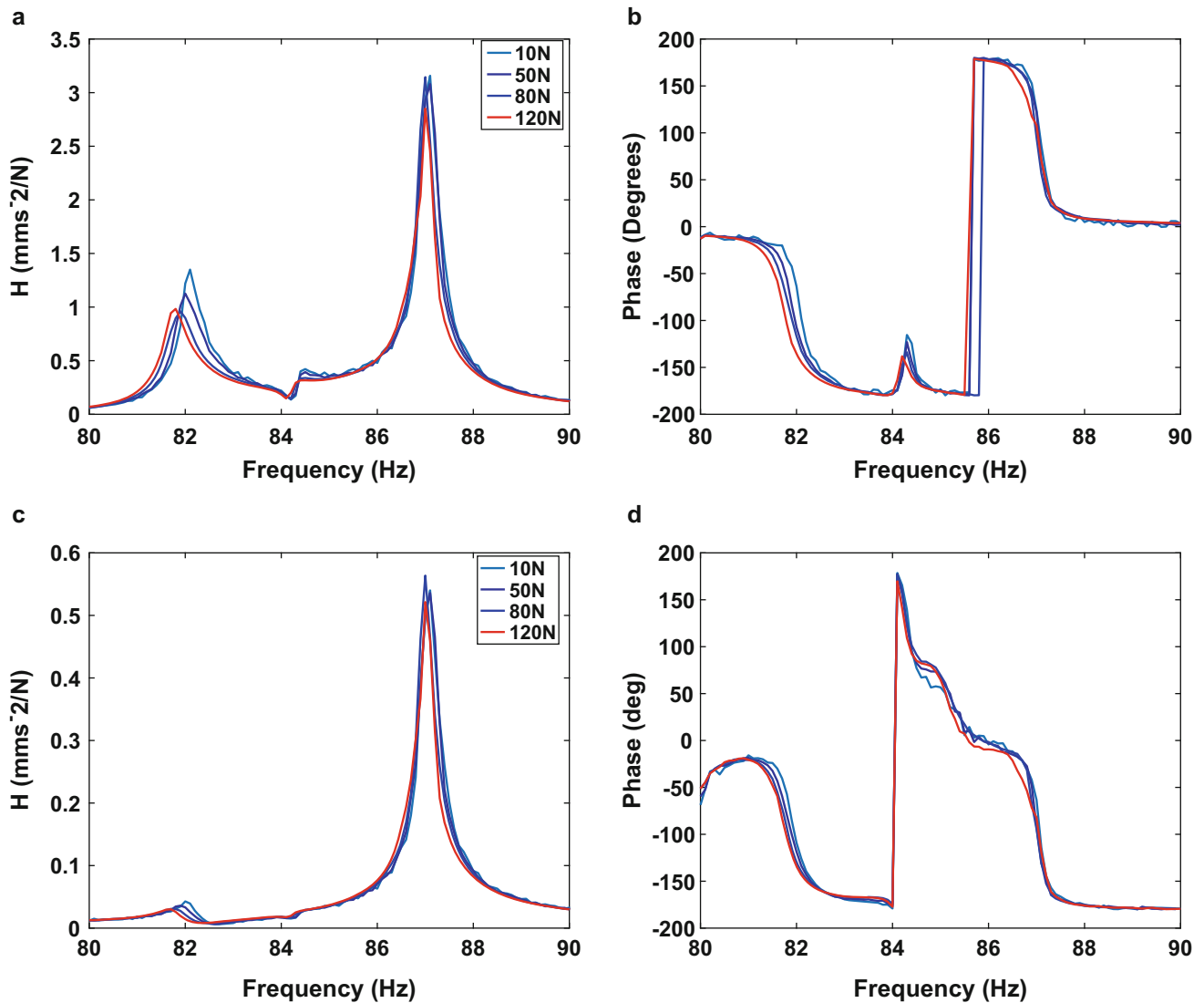


Fig. 6.11 Comparison of stepped sine FRFs measured at several excitation levels obtained from a Stepped Sine Test on the casing. (a, b) (FRF and phase at the first connection as shown in Fig. 6.10c), (c, d) (FRF and Phase of the Drive Point)

References

1. Goege, D.: Fast identification and characterization of nonlinearities in experimental modal analysis of large aircraft. *J. Aircr.* **44**(2), 399–409 (2007)
2. Noel, J.P., et al.: Nonlinear dynamic analysis of an F-16 aircraft using GVT data. In: *Proceedings of the International Forum on Aeroelasticity and Structural Dynamics (IFASD)*, Bristol (2013)
3. Kerschen, G., Golinval, J.C.: Generation of accurate finite element models of nonlinear systems – application to an aeroplane-like structure. *Nonlinear Dyn.* **39**, 129–142 (2005)
4. Ahlquist, J.R., et al.: Assessment of nonlinear structural response in A400M GVT. In: *Proceedings of the 28th International Modal Analysis Conference (IMAC)*, Springer, Jacksonville, Florida (2010)
5. Noel, J.P.: A Frequency-domain Approach to Subspace Identification of Nonlinear Systems, in *Aerospace and Mechanical Engineering*, p. 160. University of Liege, Liege (2014)
6. Richards, C.M., Singh, R.: Identification of multi-degree of freedom non-linear systems under random excitation by the reverse path spectral method. *J. Sound Vib.* **213**(4), 673–708 (1998)
7. Kerschen, G., Lenaerts, V., Golinval, J.C.: Identification of a continuous structure with a geometrical non-linearity. Part I: Conditioned reverse path method. *J. Sound Vib.* **262**(4), 889–906 (2003)
8. Masri, S.F., et al.: Identification of the state equation in complex non-linear systems. *Int. J. Non Linear Mech.* **39**(7), 1111–1127 (2004)
9. Masri, S.F., Miller, R.K., Saud, A.F.: Identification of nonlinear vibrating structures. *J. Appl. Mech.* **109**, 918–922 (1987)
10. Feldman, M.: Hilbert transform in vibration analysis. *Mech. Syst. Signal Process.* **25**(3), 735–802 (2011)

11. Ondra, V., Sever, I.A., Schwingshackl, C.W.: A method for detection and characterisation of structural non-linearities using the Hilbert transform and neural networks. *Mech. Syst. Signal Process.* **83**, 210–227 (2017)
12. Worden, K., et al.: Identification of pre-sliding and sliding friction dynamics: grey box and black-box models. *Mech. Syst. Signal Process.* **21**(1), 514–534 (2007)
13. Dossogne, T., et al.: Nonlinear Ground Vibration Identification of an F-16 Aircraft - Part II Understanding Nonlinear Behaviour in Aerospace Structures Using Sine-sweep Testing. In: *International Forum on Aeroelasticity and Structural Dynamics*, Bristol (2015)
14. Cooper, S.B., DiMaio, D., Ewins, D.J.: Integration of system identification and finite element modelling of nonlinear vibrating structures. *J. Mech. Syst. Sig. Process.* **102**, 401–430 (2017)
15. Peeters, B., et al.: The PolyMAX frequency-domain method: a new standard for modal parameter estimation. *Shock. Vib.* **11**(3–4), 395–409 (2004)

Chapter 7

Finite Element Model Updating of a Connecting Structure Based on Strain



Ming Zhan, Qintao Guo, Lin Yue, and Baoqiang Zhang

Abstract In terms of the fact that model simplification and equivalence is inevitable during the modeling process. In this paper, model updating of a connecting structure in the static condition was conducted. The process to obtain theoretical static responses was briefly introduced, and the correlation of static response was defined. And then, the fundamental of model updating and thin-layer elements were described. In order to verify the effectiveness of the method, taking a connecting structure as the object, a series of activities including structure modeling, model updating and response prediction were conducted. The connecting structure was divided into several substructures, each of them were meshed with solid elements. The interfaces between substructures were represented by thin-layer elements. And the boundary conditions were represented by bush elements. After sensitivity analysis, parameters to be calibrated were selected. Based on the experimental tests of multi load cases, the model updating of the connecting structure was accomplished. The result shows that, the model after updating can reproduce responses that used in the process of model updating. In addition, the responses that are not used in model updating are predicted precisely.

Keywords Connecting structure · Strain · Finite element model updating · Response prediction

In recent years, in the engineering fields of aeronautics and astronautics, military hardware, civil and bridge engineering etc., modeling and simulation analysis already become powerful means which can calculate structural characteristics and responses in the process of structural design, use, maintenance and so on [1, 2]. Therefore, establishing accurate and reasonable finite element models are particularly important for model-based calculation and analysis. For complex engineering structures, there exists a variety of mechanical joints in everywhere of the structure such as bolted connections, riveted joints, welded joints, etc. When building the finite element model of such structures, simplification of geometric characteristics, equivalence of connection forms and determination of model parameters could cause errors between the finite element model and the real world structure. According to the degree of cognition to the structure and experience of the modeler, the errors between the finite element model and the actual structure present as different levels, but these errors don't disappear. The finite element model updating is the process to calibrate the parameters of the model, and even the structural form of the model based on the measured structural response information. The aim of finite element model updating is to narrow the gap between the simulation analysis and the real structure responses, and it has been an important part of model based engineering.

Based on requirement of accurate model in engineering practice, a large number of scholars have carried out relative research on the finite element model updating. Friswell and Mottershead [3] classified the finite element model updating methods and showed that the parametric method has the superiority of clear physical meaning and strong maneuverability through the research. Xiong et al. [4] compared different finite element model updating strategies and elaborated the validity of model updating to improve the prediction ability of model. In the aspect of parameter selection and optimization algorithm of finite element updating, Zang et al. [5] used the equivalent element modal strain energy and the equivalent element modal kinetic energy to select the sensitive parameters in model updating. Zhang and Chen [6] proposed a finite model updating strategy based on the hybrid artificial fish swarm algorithm and verified it utilizing the example of GARTEUR model. The choice of the response that to be revised is another key problem of the finite element model updating. The accuracy and usage of the updated model are greatly dependent on the responses used in the finite element model updating. Pascual et

M. Zhan · Q. Guo (✉) · L. Yue

College of Mechanical and Electrical Engineering, Nanjing University of Aeronautics and Astronautics, Nanjing, China
e-mail: zhanming@nuaa.edu.cn; guo_qintao@nuaa.edu.cn

B. Zhang

School of Aerospace Engineering, Xiamen University, Xiamen, China

al. [7] updated the finite element model of a truss structure by employing operation modes as the target response. Ribeiro et al. [8] calibrated the 3D finite element model of Alfa Pendular railway locomotive according to the modal test results. Jaishi and Ren [9] constructed the objective function by using eigenvalues and strain energy residuals, and implemented the finite element model updating based on the multi-objective optimization technique. Ghrib et al. [10] identified the damage in the beam structure based on the finite element model updating method. Xiao et al. [11] expounded the relationship between the influence line and the mode shape, and updated the finite element of a bridge model by using modal frequencies and multi-scale static influence lines. Fei et al. [12] considered the different modeling errors, modified the GARTEUR model by using the frequency response function of the structure under the basic excitation. Esfandiari [13] derived the sensitivity of the strain transfer function and the finite element model updating of the frame structure is realized based on the least square method. Zhang et al. [14] constructed the objective function by using the residual of modal frequency and effective modal mass, and updated the finite element model of a beam structure based on genetic algorithm. Oh et al. [15] used the modal participation factor to calibrate the finite element model of the beam structure, and verified the accuracy of the updated model by the strain response. Okasha et al. [16] proposed a novel updating strategy and updated the finite element model of the bridge structure according to the strain data. In addition, for the sake of reducing the computational cost and improving the computational efficiency of finite element model updating for complex structures, Bao et al. [17] updated the GARTEUR model by combining response surface methodology with optimization techniques. Ren et al. [18] established the response surface between the updating parameters and the static strain instead of the finite element model, and calibrated the finite element model of the bridge. Weng et al. [19] proposed a finite element model updating method based on substructure and validated the method by using a certain bridge structure.

As is shown in the literatures published by now, finite element model updating were conducted by using structural dynamics characteristics, such as modal or derived indexes, and obtained better results. Meanwhile, the static response based correction method is mainly used in the damage identification of bridge structures, and is rarely used in other fields. For structure containing connection, the overall performance of the structure are greatly affected by characteristics of joints. Selecting responses that can represent the change of connecting state is of great significance to construct and update the finite element model of the connecting structure. In this paper, finite element modeling and simulation, as well as the model calibration based on global optimization algorithm of a connecting structure by using strain response are conducted.

7.1 Calculation of Structural Strain Response and Its Correlation

7.1.1 Strain Response Calculation

In the finite element analysis of the loaded structure, the relationship between displacement and force satisfies the following equilibrium equation:

$$\mathbf{p} = \mathbf{K}\mathbf{u} \quad (7.1)$$

where \mathbf{p} is nodal load vector; \mathbf{K} is stiffness matrix of element; \mathbf{u} is nodal displacement vector.

The relationship between displacement and strain is as follows:

$$\boldsymbol{\varepsilon} = \mathbf{B}\mathbf{u} = \mathbf{B}\mathbf{K}^{-1}\mathbf{p} \quad (7.2)$$

where $\boldsymbol{\varepsilon}$ is nodal strain vector; \mathbf{B} is geometric function matrix.

For test cases with multiple load cases, the external load can be expressed as $\mathbf{P} = [\mathbf{p}_1, \mathbf{p}_2, \dots, \mathbf{p}_n]^T$, n represents the number of working conditions. The strain matrix can be expressed as $\mathbf{E} = [\boldsymbol{\varepsilon}_1, \boldsymbol{\varepsilon}_2, \dots, \boldsymbol{\varepsilon}_n]^T$, and $\boldsymbol{\varepsilon}_i = [\varepsilon_{i1}, \varepsilon_{i2}, \dots, \varepsilon_{im}]$, ($i = 1, 2, \dots, n$), m represents the number of measuring points.

7.1.2 Correlation of Strain Response

In order to evaluate the consistency between the simulation and the test results, the correlation of strain obtained by the two methods can be calculated. Suppose that the strain obtained from the test under multiple working conditions is \mathbf{E}_T , and strain obtained by finite element simulation is \mathbf{E}_A , shape correlation coefficient (SC) and amplitude correlation system (MC) are defined as:

$$SC = \frac{\left| (\mathbf{E}_A(n, X))^H \mathbf{E}_T(n) \right|^2}{\left| (\mathbf{E}_A(n, X))^H \mathbf{E}_A(n, X) \right| \left| (\mathbf{E}_T(n))^H \mathbf{E}_T(n) \right|} \quad (7.3)$$

$$MC = \frac{2 \left| (\mathbf{E}_A(n, X))^H \mathbf{E}_T(n) \right|}{\left| (\mathbf{E}_A(n, X))^H \mathbf{E}_A(n, X) \right| + \left| (\mathbf{E}_T(n))^H \mathbf{E}_T(n) \right|} \quad (7.4)$$

where H is Transpose of a representation matrix, n represents the serial number of the loading conditions, X represents updating parameters in the model.

7.1.3 Sensitivity Analysis of Correlation Function

The parameters in the initial finite element model, such as material properties and joint stiffness, need to be given according to the nominal values or the experience of the modeler. The parameters of the model have different effects on the model characteristics and model responses. In the process of finite element model updating, if all the parameters are taken as the updating parameters, a large amount of computational calculation are usually inevitable and sometimes non convergence occurs which results in the updating process can't get the reasonable results. The sensitivity analysis is used to calculate the influence degree of responses with respect to each updating parameters, and the selection of sensitive parameters can not only ensure the convergence of the results, but also reduce the computational cost. The sensitivity of two strain correlation coefficients are presented as follows:

$$\frac{\partial SC}{\partial X} = \frac{2}{\left| (\mathbf{E}_A)^H \mathbf{E}_A \right|^2 \left| (\mathbf{E}_T)^H \mathbf{E}_T \right|} \left((\mathbf{E}_T)^H \frac{\partial \mathbf{E}_A}{\partial X} (\mathbf{E}_A)^H \mathbf{E}_T(n) \left| (\mathbf{E}_A)^H \mathbf{E}_A \right| - \frac{\partial (\mathbf{E}_A)^H}{\partial X} \mathbf{E}_A \left| (\mathbf{E}_A)^H \mathbf{E}_T \right|^2 \right) \quad (7.5)$$

$$\frac{\partial MC}{\partial X} = \frac{2}{\left(\left| (\mathbf{E}_A)^H \mathbf{E}_A \right| + \left| (\mathbf{E}_T)^H \mathbf{E}_T \right| \right)^2} \left(\frac{\partial (\mathbf{E}_A)^H}{\partial X} \mathbf{E}_T \left(\left| (\mathbf{E}_A)^H \mathbf{E}_A \right| + \left| (\mathbf{E}_T)^H \mathbf{E}_T \right| \right) - 2 \frac{\partial (\mathbf{E}_A)^H}{\partial X} \mathbf{E}_A \left| (\mathbf{E}_A)^H \mathbf{E}_T \right| \right) \quad (7.6)$$

In the above equations, for the simplicity of expression, $\mathbf{E}_A(n, X)$ is assigned as \mathbf{E}_A , and $\mathbf{E}_T(n)$ is assigned as \mathbf{E}_T .

7.2 Finite Element Model Updating Based on Optimization Algorithm

The parametric finite element model updating can be described as an optimization problem in the following form:

$$\begin{aligned} \min F(\theta) \quad & F(\theta) = R_A(\theta) - R_T \\ \text{s.t.} \quad & \theta_{lb} \leq \theta \leq \theta_{ub} \end{aligned} \quad (7.7)$$

where θ is the updating parameters, θ_{lb} and θ_{ub} are the lower and upper bounds of the updating parameters. $F(\theta)$ is objective function for model updating, $R_A(\theta)$ and R_T are the responses of the simulation analysis and the test, respectively.

In engineering practices, the traditional optimization algorithm and intelligent optimization algorithm are often used to optimize the objective model defined in the finite element model updating. After optimization, the combination of updating parameters in the simulation model with the least difference from experimental tests is obtained.

7.3 Finite Element Modeling Principle and Realization of Connection Structure

7.3.1 Basic Principle of Thin Layer Element

The idea of thin layer element was first put forward by Desai et al. [20], and successfully applied to modeling rock interface surface in geology field. The so-called thin layer element is an element whose thickness is much smaller than the sizes in other directions. The upper and lower interfaces of the thin layer elements coincide with meshes of the structures to be connected in the contact zone, and the connection stiffness is defined by the virtual material attribute of the thin layer element. According to some reasonable assumptions [21], the stress-strain relationship of the three dimensional anisotropic thin layer element can be given as:

$$\begin{Bmatrix} \sigma_{33} \\ \tau_{23} \\ \tau_{31} \end{Bmatrix} = \begin{bmatrix} K_{33} & & \\ & G_{23} & \\ & & G_{31} \end{bmatrix} \begin{Bmatrix} \varepsilon_{33} \\ \tau_{23} \\ \tau_{31} \end{Bmatrix} \quad (7.8)$$

where σ_{33} is normal stress, τ_{23} and τ_{31} are tangential stress. K_{33} is normal stiffness, G_{23} and G_{31} are tangential stiffness. ε_{33} is normal strain, τ_{23} and τ_{31} are tangential strain.

The thickness of the thin layer element is an important factor that affect the accuracy of the model, and is measured by the maximum aspect ratio:

$$R = \frac{\max(l, w)}{t} \quad (7.9)$$

where l and w are the length and width of the thin layer element, that is, the two transverse dimensions of the element, t is thickness of thin layer element.

Although thin layer elements have been widely applied in aerospace, mechanical engineering and other fields, there exists no standard about the maximum aspect ratio of thin layer element. Desai et al. [20] suggested that the maximum aspect ratio should be less than 100. Pande and Sharma [22] believed that the maximum aspect ratio greater than 1000 can effectively eliminate the numerical error. Therefore, in engineering practice, it is necessary to determine the maximum aspect ratio of the thin layer element according to the specific structure and the operating environment.

7.3.2 Finite Element Modeling of Connecting Structure

In this paper, taking a similar crane structure with single beam as the object of study, the length of beam is 1680 mm and the height of side column is 765 mm. The beam and side column are hollow structures, the thickness of wall thickness is 4 mm. The beam and side column are connected by rectangular flange and bolt. In the finite element modeling process, beam and the side columns are modeled with 3D solid elements. The interfaces between the beam and the side columns are described by the thin layer elements. The boundary of the bottom of the side columns are described by bush elements. The finite element model of the structure is shown in Fig. 7.1.

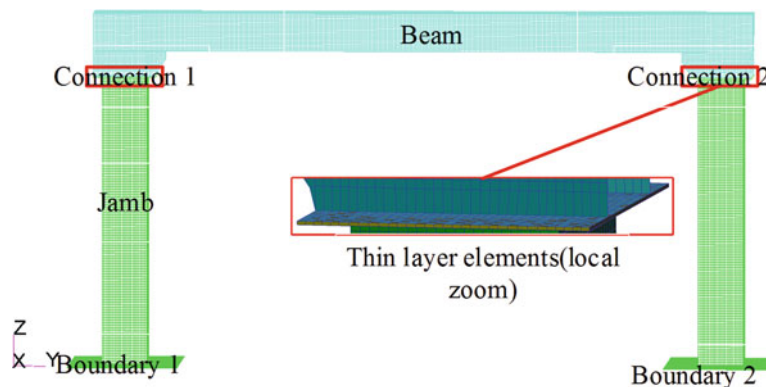


Fig. 7.1 Finite element model of connecting structure

7.4 Strain Test of Connection Structure

Engineering practice shows that strain can reflect local features of structure, and the strain under static load is utilized as the target response for finite element model updating in this paper. In order to provide enough response information for the finite element model updating and verify the accuracy of the calibrated model, the strain tests are carried out under five working conditions. The test scheme is shown in Fig. 7.2, C1–C5 are the loading point positions, the corresponding test sequence number are 1–5. The 1/4 Wheatstone bridge is employed in the test and the resistance of strain gauge is $120\ \Omega$. As shown in Fig. 7.2, the blue rectangle represents the position of strain gauges, the direction of the length of the rectangle is the deformation direction of the strain gauge. The method of hanging heavy objects was used to simulate load during the test, three tests were repeated under each working condition, and the average value of the three tests was obtained.

7.5 Model Updating of a Connecting Structure Based on Strain

7.5.1 Definition of Objective Function

When the finite element model of the connecting structure is constructed, the strain response under the three test conditions corresponding to C1, C3 and C4 are selected to update. According to the definition of the two kinds of correlation, the objective function is constructed by weighted form:

$$f_{\text{obj}} = \sum (\omega_S (1 - SC) + \omega_M (1 - MC)) \quad (7.10)$$

where ω_S and ω_M are the weights of error of shape correlation coefficient and amplitude correlation coefficient, respectively.

7.5.2 Sensitivity Analysis and Updating Parameter Selection

In the finite element modeling process, the connection between the interface between the beam and the side column and the boundary connection state of side column bottom surface are taken into account, and the connections at different positions are grouped and the parameters are set respectively. In order to select the reasonable parameters to be updated, 12 parameters

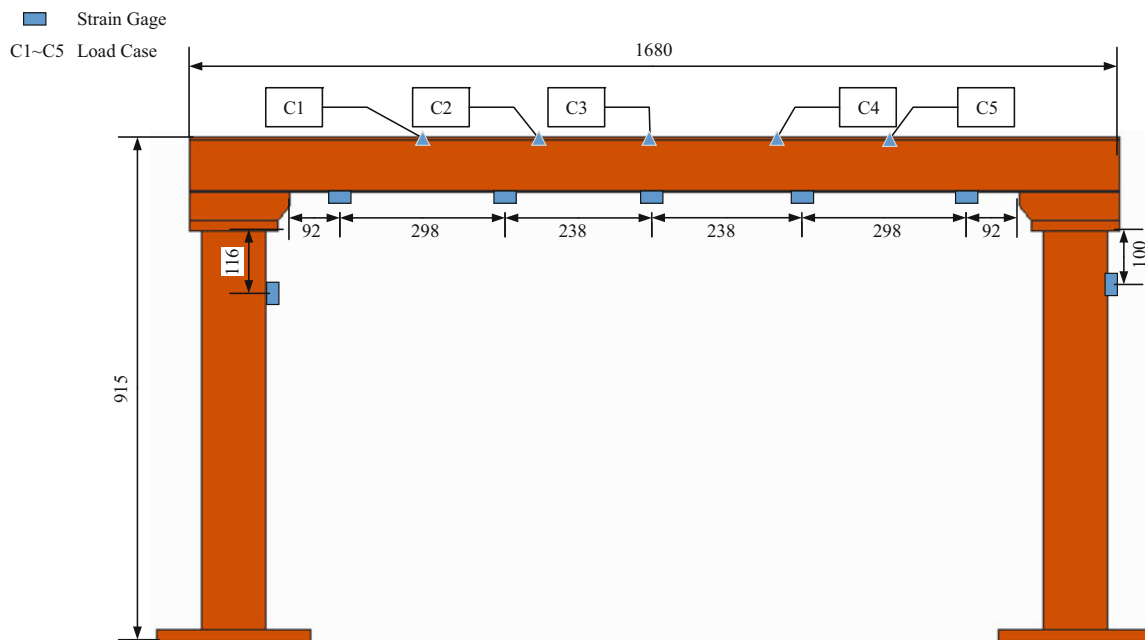


Fig. 7.2 Test scheme of connecting structure

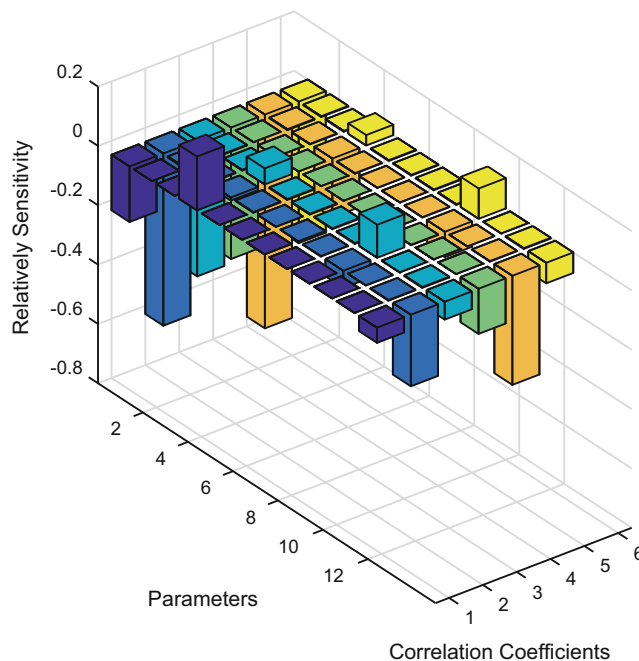


Fig. 7.3 Relative sensitivity analysis

Table 7.1 Correlation coefficient error of updating load case

Test condition	Before updating/%		After updating/%	
	1-SC	1-MC	1-SC	1-MC
1	5.27	6.06	7.88×10^{-2}	3.94×10^{-2}
3	6.46	5.33	7.23×10^{-2}	3.70×10^{-2}
4	6.32	5.53	4.81×10^{-2}	2.66×10^{-2}
Average	6.02	5.64	6.64×10^{-2}	3.43×10^{-2}

such as the virtual material attribute of thin layer element and the boundary stiffness of bottom surface of side column is taken to do some sensitivity analysis as the preselected parameter, and the relative sensitivity results are shown in Fig. 7.3.

In Fig. 7.3, selected parameters of 1–6 were virtual material properties of thin layer elements in the contact zone, 7–12 were the connection stiffness of the bottom boundary of the side columns, correlation coefficients of 1–3 and 4–6 are shape and amplitude correlation coefficients, respectively. From the sensitivity analysis, it can be seen that the virtual material properties that represent normal stiffness of thin layer elements and the boundary stiffness in the Z direction have great influence on the correlation coefficients, so the two sets of parameters above are defined as the updating parameters.

7.5.3 Finite Element Model Updating of Connection Structure Based on Multi Working Conditions

The purpose of finite element model updating is to reduce the difference between the simulation analysis and the experimental tests. The test results corresponding to 1, 3 and 4 of the test conditions are used as the updating targets. According to the objective function of defined as Eq. (7.10), the weight coefficient $\omega_S = \omega_M = 1$, The global search algorithm is performed in the feasible region of the updating parameters by using the Globalsearch in Matlab. The errors of two types of correlation coefficient in the corresponding operating conditions before and after the updating are shown in Table 7.1.

It can be seen from Table 7.1, after model updating, the maximum error of shape correlation coefficients used for constructing the objective function decreased from 6.46% to $4.81 \times 10^{-2}\%$ and the maximum error of amplitude correlation coefficient decreased from 6.06% to $2.66 \times 10^{-2}\%$. The results show that the errors of strain response between the experimental test and model simulation are greatly reduced, and the modified finite element model can effectively reproduce the test strain response.

Table 7.2 Correlation coefficient error of prediction load case

Test condition	Before updating/%		After updating/%	
	1-SC	1-MC	1-SC	1-MC
2	5.51	5.18	3.23×10^{-2}	1.63×10^{-2}
5	6.71	6.05	5.25×10^{-2}	3.32×10^{-2}
Average	6.11	5.62	4.24×10^{-2}	2.33×10^{-2}

The predictive ability of the finite element model is a key factor to evaluate the usage of the model. The experimental results of test conditions 7.2 and 7.5 are used to evaluate the prediction ability of the finite element model of the connection structure model. The errors of the two types of correlation coefficients before and after the correction are shown in Table 7.2.

It can be seen from Table 7.2 that, after the procedure of finite element model updating, the maximum error of shape correlation coefficient of two prediction cases reduced from 6.71% to $3.23 \times 10^{-2}\%$, and the maximum error of amplitude correlation coefficient reduced from 6.05% to $1.63 \times 10^{-2}\%$. The results show that the predicted strain response errors based on the updated finite element model have been greatly decreased. The finite element model updated can accurately predict the experimental strain responses that not used in the procedure of finite element model updating.

7.6 Conclusion

This paper takes a connecting structure as the research object. The modeling and finite element model updating are conducted. The strain of the structure under different working conditions is taken as the correction target response, and the finite element model updating of the structure is realized based on the global optimization algorithm. Through the case study, the following conclusions are obtained:

1. The strain is sensitive to the local connection state of the structure, and it can be used as the target response of the finite element model updating of the connecting structure, which can effectively reduce the error of the model response between simulation and experimental tests.
2. The updated finite element model can accurately reproduce the target responses, and also has good prediction ability for the conditions that not updated.

References

1. Zhang, L.: Computer simulation & model validation with application to strength and environment engineering [J]. *Struct. Environ. Eng.* **29**(2), 42–47 (2002)
2. Oberkampf, W.L., Roy, C.J.: *Verification and Validation in Scientific Computing* [M], pp. 1–20. Cambridge University Press, Cambridge (2010)
3. Friswell, M.I., Mottershead, J.E.: *Finite Element Model Updating in Structural Dynamics* [M]. Kluwer Academic Publisher, London (1995)
4. Xiong, Y., Chen, W., Tsui, K.L., et al.: A better understanding of model updating strategies in validating engineering models [J]. *Comput. Methods Appl. Mech. Eng.* **198**, 1327–1337 (2009)
5. Zang, C., Ma, S.C., Friswell, M.I.: Structural model updating with an improved parameter selection method [C]. In: *Proceeding of the 25th International Conference on Noise and Vibration Engineering*, Leuven (2012)
6. Zhang, A., Chen, G.: Structural finite element model updating based on hybrid artificial fish swarm algorithm [J]. *Acta Aeronautica et Astronautica Sinica.* **31**(5), 940–945 (2010)
7. Pascual, R., Golinval, J.C., Razeto, M.: Model updating using operating deflection shapes [J]. In: *Proceedings of the 16th International Modal Analysis Conference*, 1998, 3243
8. Ribeiro, D., Calçada, R., Delgado, R., et al.: Finite element model calibration of a railway vehicle based on experimental modal parameters [J]. *Veh. Syst. Dyn.* **51**(6), 821–856 (2013)
9. Jaishi, B., Ren, W.X.: Finite element model updating based on eigenvalue and strain energy residuals using multi objective optimization technique [J]. *Mech. Syst. Signal Process.* **21**, 2292–2317 (2007)
10. Ghrib, F., Li, L., Wilbur, P.: Damage identification of Euler Bernoulli beam using static responses [J]. *J. Eng. Mech.* **138**(5), 405–415 (2012)
11. Xiao, X., Xu, Y.L., Zhu, Q.: Multiscale modeling and model updating of a cable stayed bridge. II: model updating using modal frequencies and influence lines [J]. *J. Bridg. Eng.* **20**(10), 1–12 (2015)
12. Fei, Q.G., Jiang, D., Zhang, D.H., et al.: Finite element model updating using base excitation response function [J]. *J. Vibroeng.* **15**(1), 9–22 (2013)
13. Esfandiari, A.: Structural model updating using incomplete transfer function of strain data [J]. *J. Sound Vib.* **333**, 3657–3670 (2014)

14. Zhang, B., Chen, G., Guo, Q.: Finite element model updating using effective modal mass with genetic algorithm [J]. *J. Vib. Measure. Diagn.* **32**(4), 577–580 (2012)
15. Oh, B.K., Kim, M.S., Kim, Y., et al.: Model updating technique based on modal participation factors for beam structures [J]. *Comput. Aided Civ. Inf. Eng.* **30**, 733–747 (2015)
16. Okasha, N.M., Frangopol, D.M., Orcesi, A.D.: Automated finite element updating using strain data for the lifetime reliability assessment of bridges [J]. *Reliab. Eng. Syst. Saf.* **99**, 139–150 (2012)
17. Bao, N., Wang, C., Zhao, J., et al.: Model updating of structure dynamics based on response surface methodology [J]. *J. Vib. Shock.* **32**(16), 54–58 (2012)
18. Ren, W.X., Fang, S.E., Deng, M.Y.: Response surface based finite element model updating using structural static responses [J]. *J. Eng. Mech.* **137**(4), 248–257 (2011)
19. Weng, S., Zuo, Y., Zhu, H., et al.: Model updating based on a substructuring method [J]. *J. Vib. Shock.* **36**(4), 99–104 (2017.) 138
20. Desai, C.S., Zaman, M.M., Lightner, J.G., et al.: Thin-layer element for interfaces and joints [J]. *Int. J. Numer. Anal. Methods Geomech.* **8**, 19–43 (1984)
21. Jiang, D., Wu, S., Shi, Q., et al.: Parameter identification of bolted-joint based on the model with thin-layer elements with isotropic constitutive relationship [J]. *J. Vib. Shock.* **33**(22), 35–40 (2014)
22. Pande, G.N., Sharma, K.G.: On joint/interface elements and associated problems of ill-conditioning. *Int. J. Numer. Anal. Methods Geomech.* **3**, 293–300 (1979)



Chapter 8

Nonlinearities of an Aircraft Piccolo Tube: Identification and Modeling

T. Dossogne, P. Trillet, M. Schoukens, B. Bernay, J. P. Noël, and G. Kerschen

Abstract Piccolo tubes are parts of aircraft wings anti-icing system and consist of titanium pipes inserted into the internal structure of the slat. Due to differential thermal expansion, clearances between the tube and its support are unavoidable and cause the overall system to exhibit highly nonlinear behavior, resulting from impacts and friction. This paper addresses the identification and modeling of the nonlinearities present in the slat-Piccolo tube connection. The complete identification procedure, from nonlinearity detection and characterization to parameter estimation, is carried out based upon sine-sweep measurements. The use of several techniques, such as the acceleration surface method, enables to understand the complex dynamics of the Piccolo tube and build a reliable model of its nonlinearities. In particular, the parameters of nonsmooth nonlinear stiffness and damping mechanisms are estimated. The nonlinear model is finally validated on standard qualification tests for airborne equipments.

Keywords Nonlinear system identification · Finite element model updating · Finite element model upgrading · Aircraft anti-icing system · Piccolo tube · Acceleration surface method (ASM) · Vibroimpact · Contact force model

8.1 Introduction

Subsystems of commercial aircraft are submitted to rigorous qualification processes imposed by aeronautical norms. In this context, the need for trustworthy finite element (FE) models is crucial. However, the growing occurrence of nonlinear structural mechanisms makes the validation of numerical models more arduous, if not impossible, by using only linear analysis. Upgrading the model with nonlinear elements and performing a complete identification of their parameters is therefore required.

A typical case of such a subsystem is the Piccolo tube, which is part of the hot-air, anti-icing system. They are widely used in commercial aircraft as they represent a simple and efficient solution to address the accumulation of ice on the wings, which remains a critical issue for the aircraft safety and performance. They consist of titanium pipes inserted in the internal structure of the slat, that distribute some high-temperature air extracted from the engine compressor into the wing leading edge. During the flight, they are hence exposed to a wide range of temperatures, resulting in substantial changes in their dimensions due to thermal expansion. These variations create clearances between the tube and its support and cause the overall system to exhibit nonlinear behavior due to impacts and friction [1]. Linear FE models have proved to be insufficient to reproduce the experimentally observed dynamics of the tube.

The present paper addresses the identification and the validation of a Piccolo tube nonlinear model. Starting from an updated linear FE model, a complete identification methodology is achieved to characterize and estimate nonlinearities. They are modeled as nonlinear elements that reproduce contact forces including dissipation, at the impact location. Measurements from qualification tests are eventually used to validate the proposed nonlinear model.

T. Dossogne (✉) · P. Trillet · J. P. Noël · G. Kerschen
Space Structures and Systems Lab, Aerospace and Mechanical Engineering Department, University of Liège, Liège, Belgium
e-mail: tdossogne@uliege.be; jp.noel@uliege.be; g.kerschen@uliege.be

M. Schoukens
Control Systems Group, Department of Electrical Engineering, Eindhoven University of Technology, Eindhoven, The Netherlands
e-mail: m.schoukens@tue.nl

B. Bernay
SONACA SA, Gosselies, Belgium
e-mail: bruno.bernay@sonaca.com

8.2 Linear Finite Element Modeling and Updating

A finite element model made of linear shell elements is first built using the measured geometry and masses. It is then updated, based on linear modal parameters estimated from data collected during low-level sine-sweep tests. Such tests are assumed to take place in the linear regime as the amount of energy injected in the system is not sufficient to trigger the contact between the different components. Pictures of the experimental setup in clamped configuration (left) as well as a close-up on the nonlinear connection (right) are shown in Fig. 8.1a.

8.3 Nonlinearity Characterization Using the Acceleration Surface Method

The Acceleration Surface Method (ASM) is a qualitative variant of the well-known Restoring Force Surface method [2]. The ASM offers a fast visualization tool of nonlinear mechanisms. It relies on an approximation of the nonlinear restoring forces by the acceleration signal plotted with a minus sign over the phase plane [3]. The application of the ASM to high-level sine-sweep data enables unveiling the nonsmooth dynamics occurring at the connection between the tube and its support, as illustrated in Fig. 8.1b. A piecewise-linear stiffness is observed and an estimation of the physical clearances can be obtained through this plot. Additional nonlinear identification methods, such as the Best Linear Approximation [4], the wavelet transform analysis [5] or the homogeneity test, were successfully applied to quantify the amount of nonlinearity in the system and highlight the presence of dissipation during the impacts.

8.4 Estimation of the Nonlinear Contact Forces Using the EXTENDED Acceleration Surface Method

By means of Craig-Bampton reduction method, a superelement of the linear FE model is created, only retaining the excitation point and the nodes where nonlinear behavior was previously located. Nonlinear elements with functional forms determined from the characterization step are added between these degrees of freedom, namely a nonlinear spring with a piecewise-linear characteristic to reproduce contact, and a nonlinear damper to model dissipation [6] during the impacts.

An eXtended version of the Acceleration Surface Method (x-ASM) is used to estimate the parameters of the nonlinear contact force model. The x-ASM makes use of the FE model upgraded with nonlinear elements. Starting with initial guesses of the nonlinear parameters, it carries out numerical simulations using a Newmark scheme to reproduce the experimental tests. Similarly to the characterization step, the classical ASM is applied to the simulated data. The values of the nonlinear parameters are then updated, following an optimization algorithm that uses the difference between the numerical and the

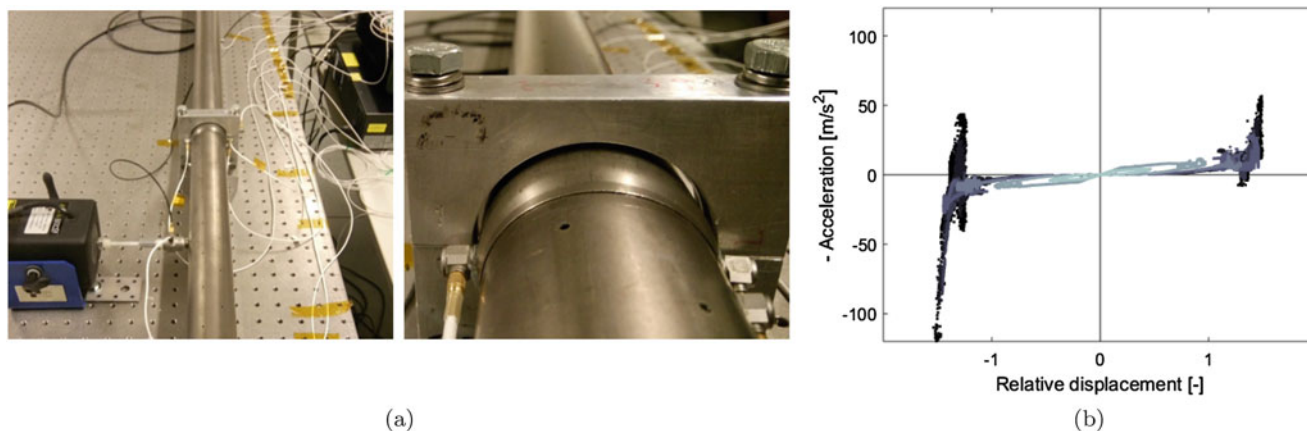


Fig. 8.1 (a) Experimental setup of the Piccolo tube, SONACA property. Left: setup in clamped configuration – right: zoom on the nonlinear connection. (b) Qualitative nonlinear stiffness curve of the connection between the Piccolo tube and its support using ASM

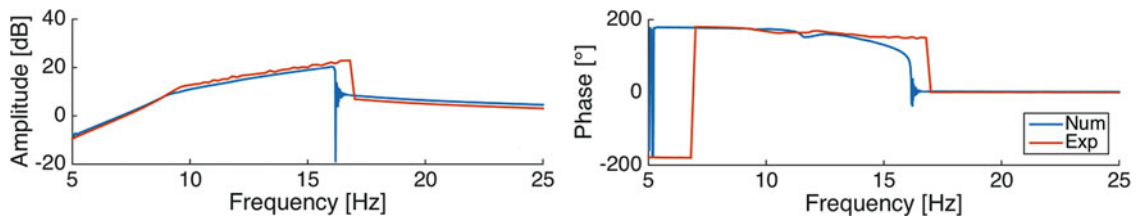


Fig. 8.2 Comparison of the frequency responses in both amplitude and phase between the numerical model (in blue) and the measurement (in orange) during fan blade-off tests, focusing on the first vibration mode

experimental ASM results as an objective function. Once the x -ASM is achieved, the contact stiffness parameter of the nonlinear spring and the coefficient of restitution of the nonlinear damper in the Piccolo tube are identified.

8.5 Validation of the Nonlinear Model

To validate the updated nonlinear FE model, standard qualification tests imposed by the aeronautical norm RTCA DO160 [7] are performed both on the numerical model and on the experimental setup. The case of fan blade-off, shown in Fig. 8.2, and of windmilling were successfully passed.

Acknowledgements The authors T. Dossogne and J.P. Noël are Research Fellow (FRIA fellowship) and Postdoctoral Researcher, respectively, of the *Fonds de la Recherche Scientifique – FNRS* which is gratefully acknowledged.

References

1. Van Der Vorst, R., Magerman, J., Bernay, B., Vandenberk, S., et al.: Vibration qualification test of an aircraft piccolo tube using multiple-input-multiple-output control technology. SAE technical paper, 2013-01-2315 (2013)
2. Masri, S.F., Caughey, T.K.: A nonparametric identification technique for nonlinear dynamic problems. *J. Appl. Mech.* **46**, 433–447 (1979)
3. Dossogne, T., et al.: Nonlinear ground vibration identification of an F-16 aircraft – part II understanding nonlinear behaviour in aerospace structures using sine-sweep testing. In: *Proceedings of the International Forum on Aeroelasticity and Structural Dynamics, St-Petersburg* (2015)
4. Pintelon, R., Schoukens, J.: *System Identification: A Frequency Domain Approach*. IEEE Press, Piscataway (2001)
5. Noël, J.-P., Renson, L., Kerschen, G.: Complex dynamics of a nonlinear aerospace structure: experimental identification and modal interactions. *J. Sound Vib.* **33**, 2588–2607 (2014)
6. Lankarani, H.M., Nikraves, P.E.: A contact force model with hysteresis damping for impact analysis of multibody systems. *J. Mech. Des.* **112**, 369–376 (1990)
7. RTCA SC-135: Environmental conditions and test procedures for airborne equipment. RTCA, Washington, DC (2010)

Chapter 9

Reliability Analysis of Existing Bridge Foundations for Reuse



Nathan Davis and Masoud Sanayei

Abstract Reuse of bridge foundations often requires determining the capacity of in-situ driven piles and drilled shafts. These piles have a proven history of load carrying capacity, but often lack test data from which the capacity can be obtained. It is possible to estimate the pile capacity with empirical calculations based on pile geometry and soil properties, but these produce highly uncertain results due to the variable nature of soil and impacts from the installation method. As a result, the LRFD code requires lower resistance factors be used for these calculations than would be required for piles with test data. Estimation of pile capacity using empirical calculations often produces over conservative results due to these low resistance factors. Since the piles have been in service for the lifespan of the original bridge, they have proven that as a system they have more capacity than the total dead and live loads previously applied. The amount of load applied to each pile, however, is uncertain due to variability of the loading and uncertainties of how the load is distributed to the individual piles. This research proposes reliability based methodology to determine the capacity of driven piles or drilled shafts accounting for these uncertainties.

Keywords Foundations · Reliability · Bayesian updating · Bridges · Testing · Design codes

Figure 9.1 shows an example probability density function (PDF) of the normalized ultimate capacity for an H-pile in clay with its capacity is predicted using the β -method. Similar distributions can be obtained for piles with capacity predicted through various methods, following the work of Paikowsky et al. [1]. This work performed a parametric study of pile capacity prediction techniques, finding that ultimate pile capacity can reasonably be modeled as following a lognormal distribution. This work also provides the parameters for these distributions. As can be seen from this PDF, the ultimate capacity of the pile can vary greatly from the predicted capacity, including the potential for the ultimate capacity being much lower than the predicted capacity. Distributions like the one in Fig. 9.1 were used by Paikowsky et al. [1] in reliability analyses to determine the required resistance factor for this prediction method. The resistance factor is largely driven by the left-hand tail of the distribution, which is where the ultimate capacity is significantly below the predicted.

For a pile being considered for reuse, there is a history of bridge in-service loading that can be used to update the distribution of ultimate pile capacity. Using this updated distribution in the reliability analysis for the pile allows for the determination of a new resistance factor that accounts for previous loading. Due to the ductility of pile systems, the knowledge gained from the previous loading is limited to understanding the minimum population mean. The capacity of any individual pile may be lower than the population mean. The distribution of the population mean is determined from the individual pile capacity PDF and assuming an in-population variance of pile capacity, following the methodology provided by Zhang and Tang [2]. Figure 9.2 shows the population mean PDF for piles following the distribution in Fig. 9.1 for 3 possible typical in-site variances.

Using a Bayesian sampling methodology, the population mean can be assumed to be conditional to the capacity of any individual pile. As such, a posterior population capacity distribution can be found for all possible capacities of any single pile, shown in Fig. 9.3 for two possible single pile capacities.

N. Davis (✉) · M. Sanayei
Department of Civil & Environmental Engineering, Tufts University, Medford, MA, USA
e-mail: nathan.davis@tufts.edu; masoud.sanayei@tufts.edu

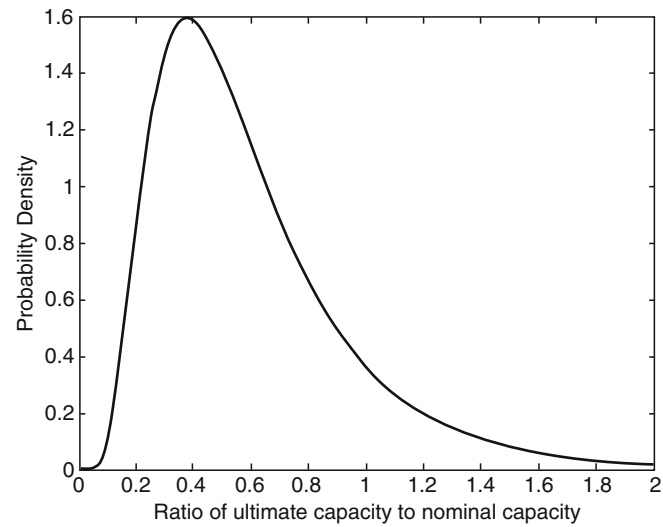


Fig. 9.1 Normalized PDF of pile capacity prediction using data from Paikowsky et al. [1]

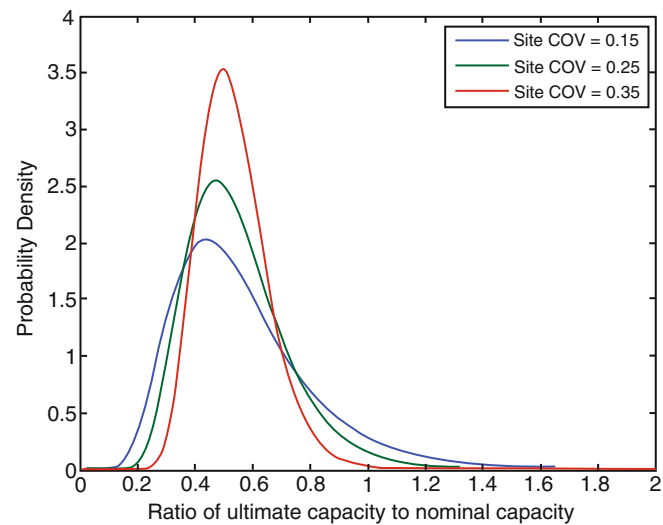


Fig. 9.2 PDF of population mean, normalized to pile capacity prediction

A likelihood function of a pile of that capacity existing given the previously observed loading can be taken from the likelihood of population mean being greater than the observed loading, for all possible pile capacities. Figure 9.4 shows two such likelihoods for the distributions shown in Fig. 9.3, with an observed loading of 20% of the nominal pile capacity.

By calculating the likelihood function for all possible pile capacities, a new distribution of pile capacity can be determined using Bayes' theorem, as described by Ang and Tang [3].

The updated pile PDF for the distribution shown in Fig. 9.1 when a previously applied proof loading of 20% of the nominal pile capacity is shown in Fig. 9.5. This updated distribution can be used to perform reliability analysis and determine new resistance factors for reuse of pile foundations.

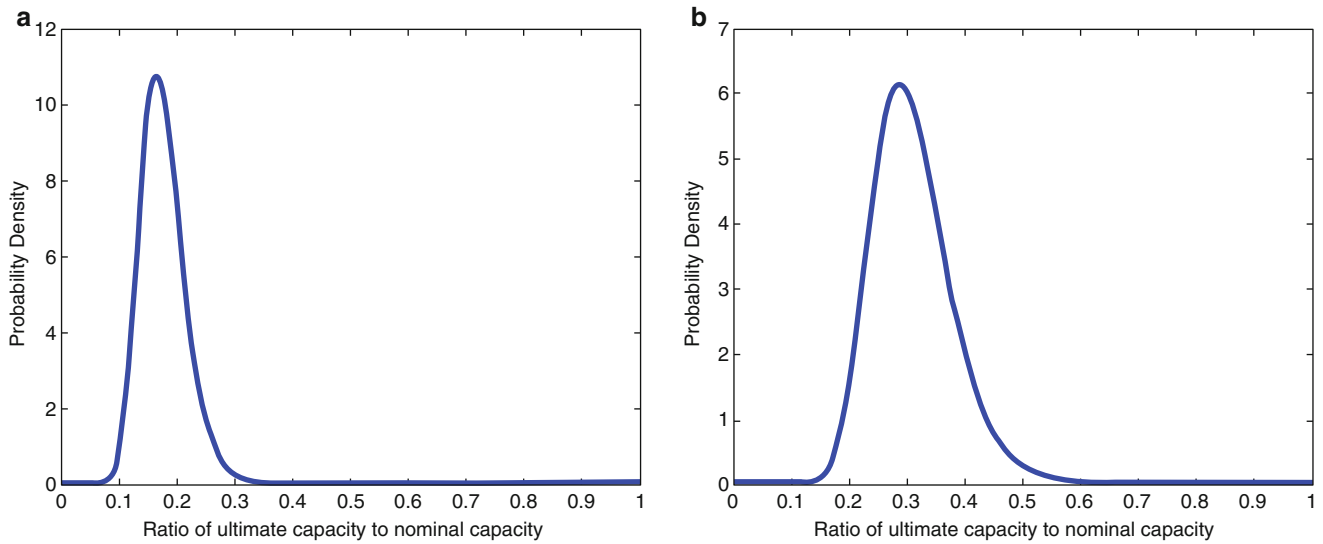


Fig. 9.3 Distribution of population mean given (a) a pile with capacity of 10% of nominal, and (b) a pile with capacity of 75% of nominal

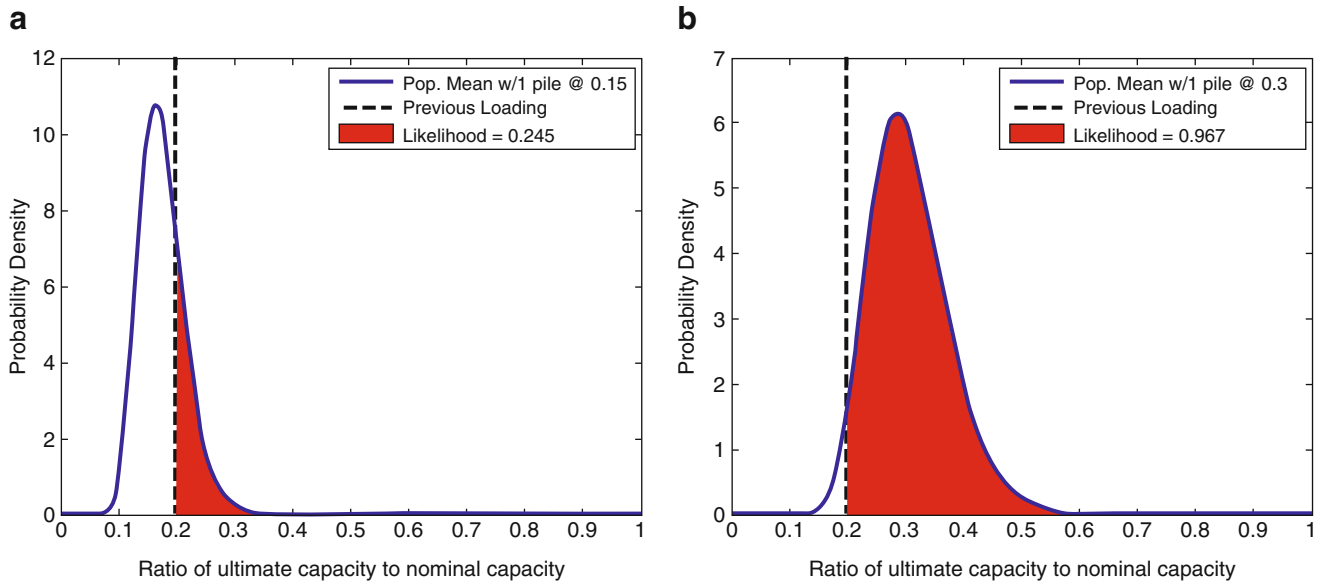


Fig. 9.4 Normalized capacity distributions with a past loading of 0.2 times the nominal capacity for cases in Fig. 9.3a, b

Using the updated PDF of pile capacity to perform a reliability analysis considering the past applied loading allows for selection of a new resistance factor. The reliability analysis is performed using the lognormally distributed loading considered by Nowak [4] and Paikowsky et al. [1]. The updated factor will be dependent on the magnitude of the past applied loading, as shown in Fig. 9.6.

In conclusion, this research demonstrates that upgraded resistance factors can be used for driven piles that have been in use and load tested. The use of upgraded resistance factors allows for additional capacity in reused piles than traditional static analyses would allow.

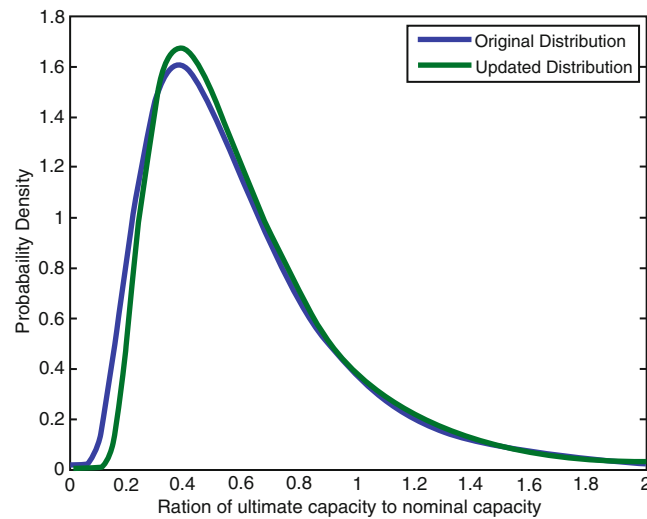


Fig. 9.5 Original and updated normalized capacity distributions for pile subjected to previous loading

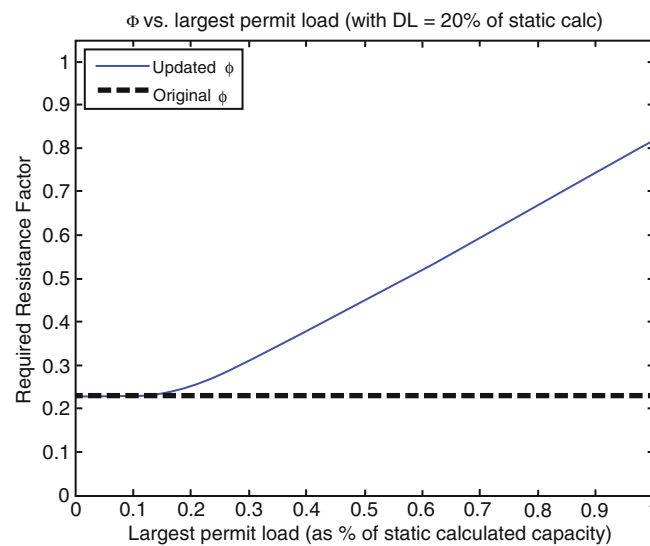


Fig. 9.6 Phi versus the largest load supported by pile group

References

1. Paikowsky, S., Birgisson, B., McVay, M., Nguyen, T., Kuo, C., Baecher, G., Ayyub, B., Stenersen, K., O'Malley, K., Chernauskas, L., O'Neill, M.: Design (LRFD) for Deep Foundations. NCHRP REPORT 507. Transportation Research Board, Washington, DC (2004.) 20001
2. Zhang, L., Tang, W.: Use of Load Tests for Reducing Pile Length, pp. 993–1005. Deep Foundations, ASCE, Reston (2002)
3. Ang, A.H.-S., Tang, W.H.: Probability Concepts in Engineering Planning and Design, Vol 1, Basic Principles. Wiley, New York (1974)
4. Nowak, A.: Calibration of LRFD Bridge Design Code., NCHRP 368. Transportation Research Board, Washington, DC (1999.) 20001

Chapter 10

Recent Developments in Hardware-in-the-Loop Testing



Jonathan Millitzer, Dirk Mayer, Christian Henke, Torben Jersch, Christoph Tamm, Jan Michael, and Christopher Ranisch

Abstract Future applications of mechatronic systems will be characterized by a high degree of digitization enabling the integration of numerous innovative functions. The validation and reliability analysis of such complex systems often requires the realization of cost intensive full system prototypes and the evaluation of field tests. Innovative technologies are therefore integrated slowly in industrial sectors that focus on system reliability. Hence, there is a strong interest in a reliability orientated development and test process for complex mechatronic systems.

The integration of real-time simulations in test environments allows efficient development and verification of the individual components of a mechatronic system in many cases. Currently, this especially applies for the test-driven development of embedded control units and their corresponding software. A reduced number of field tests, the automated run of test procedures and the application of error injection methods can be achieved by the widely used Hardware-in-the-Loop (HIL) technique. In signal level HIL tests, an existing control unit is connected to a virtual real-time simulation of the residual system. If however the device under test includes a mechanical or power electrical interface, the coupling of the test object to a virtual residual system requires the application of a mechanical or power electrical HIL interface. Current activities aim for this extension of In-the-Loop technologies for the validation of mechanical and power electronic subsystems.

This paper highlights the potential of combined signal level, mechanical level and power electrical HIL tests for the validation of complex mechatronic systems in an early phase of design. The paper also points out the key topics of test-driven development, real-time simulation and the realization of hybrid test environments by means of mechanical and power electrical HIL interfaces.

Keywords Hardware-in-the-loop · Hybrid testing · Real-time substructuring · Development of mechatronic systems · Early stage validation

10.1 Introduction and Motivation

While digitization has led to many innovations in the consumer goods sector, digital technologies are integrated much slower into specific products in sectors like machinery and plant engineering, energy technology, or the automotive industry. Usually in those sectors there are considerably higher demands on reliability, safety and machine availability compared to consumer goods. Furthermore, future applications of mechatronic systems will be characterized by a high degree of digitization enabling the integration of numerous innovative functions (e.g. an interaction between several mechatronic systems on different physical domains or cyber-physical systems). Often a model based development process is utilized due to the potentially high system complexity and the mutual interaction between different subsystems. The iterative increase of the simulation model's accuracy and the related early stage validation of numerical submodel by means of accompanying laboratory tests is one focal point within the model based design process.

The assessment of the function and system reliability of the drive train and generator of a wind turbine for example requires the close analysis of the interactions between the generator itself, the support structure, the power grid and the dynamic behavior of the rotor blades. Until today, an overall system validation requires a field test of the completely installed

J. Millitzer (✉) · D. Mayer · C. Tamm · C. Ranisch
Fraunhofer Institute for Structural Durability and System Reliability LBF, Darmstadt, Germany
e-mail: jonathan.millitzer@lbf.fraunhofer.de

C. Henke · J. Michael
Fraunhofer Institute for Mechatronic System Design IEM, Paderborn, Germany

T. Jersch
Fraunhofer Institute for Wind Energy and Energy System Technology IWES, Bremerhaven, Germany

wind turbine. According to manufacturer's information, a measurement campaign takes up to 12 months and leads to costs up to one million Euros. Many other sectors are facing similar challenges: The automotive industry usually realizes extended early stage test phases with over 100 pre-series vehicles. Also, in machinery and plant engineering there are extensive and challenging test and commissioning phases especially for control-oriented applications in the context of Internet of Things (IoT) and Industry 4.0 (e.g. intelligent picking systems or force controlled Machine to Machine interaction). In this context, changing environmental conditions, ad hoc networking, and reconfiguration are destined to create major challenges with regard to model uncertainty and not suitable laboratory tests during early stage design.

If the overall system's functionality and related models can only be sufficiently validated at the end of the development phase, the introduction of disruptive technologies is slowed down or even prevented. Test and validation methods for innovative functions or products based on digital technologies (e.g. complex, interconnecting systems in terms of smart home, smart city, smart grid, autonomous driving or smart structures) are often inadequate or non-existent. Therefore, incremental innovations are often preferred in developing reliable products. New technologies and processes for the systematic derivation of testing environments for development-accompanying tests which assist the model based development process are thus a key factor for sustainable innovativeness. An appropriate, early stage test and validation method for complex mechatronic systems can provide an additional economic value as the effort for extensive overall system tests or field tests can be reduced. Furthermore, early stage and sufficient validation increases the development speed without constraining reliability objectives. It is a mutually beneficial process as early stage numerical simulation and premature experimental validation are moving closer together. As soon as new numerical models are available, they serve the design of more accurate test environments which for their part help to identify more detailed numerical models of the device under test due to the enhanced boundary conditions throughout the experimental investigation. Even more relevant results can be gained by including critical test cases from requirements analyses in tailored test environments.

In summary, there is a strong need for a development process for complex mechatronic systems that integrates validation tests from an early stage concept phase until component test on system level. This allows for high model accuracy during every step of system development and for the detection of critical aspects during system design. Applying such a design process, a test environment is derived from the system's requirements prior to the development of the actual component. Currently, this approach of test-driven development is widely used in software development and it is characterized by short development cycles. Comparative studies showed that the error rate in the final product can be reduced up to 50% using test-driven development [1]. For complex real-time embedded systems, hardware-in-the-loop (HIL) simulations allow for an early stage model and functional validation without having the overall system available in physical hardware. A first HIL test environment was realized more than 50 years ago for a realistic validation of the Gemini mission's embedded control system because a field test (i.e. the rocket launch) would have been an unreasonable burden. Within this HIL environment the embedded control system was connected to a real-time simulation of the avionics, the sensors and flight dynamics [2]. The HIL test method has gained currency especially in automotive and aviation industries since then. However, it is mostly used for the validation of embedded control hardware and their respective software. These ideas and methods create the foundation for the proposed concept of a test-driven and model-based development process for complex mechatronic systems. The following sections give a brief introduction to model-based development and highlight current activities and research issues in HIL testing.

10.2 Model-Based Design and Virtual Testing

The realization of mechatronic systems often results in a large number of basic system considerations in early stage design, which especially applies for innovative solutions. For a given application, each of the possible approaches then again might be realized by means of different actuators as well as sensors and control principles, resulting in an even larger number of potential system setups. On the one hand, this is desired since the additional degrees of freedom during early stage design allow for resolving constraints and enhancing functionality. On the other hand, the resulting diversity has to be handled within the design process.

Another challenge can result from the fact that beside the intended interactions between the various subsystems within a mechatronic system also unwanted interdependencies might occur. In vibration engineering, the excitation of mode shapes at higher frequencies due to a nonlinear behavior of the actuator is a common example. For the development of an active vibration control system, the overall system comprising the excitation, the mechanical structures, the actuators, the sensors as well as digital signal processing has to be considered during early stage design. Hence, a model-based design process is applied more frequently. A suitable methodological approach for a model-based design process for active vibration control systems is presented in Ref. [3].

The key component of a model-based design process is an integrated system simulation which is continuously adapted regarding its level of detail and with respect to the current development phase. These phases are organized along the entire development process for complex mechatronic systems [4]. In a first step, the model describes the initial topology based on

elementary submodels. A basic structure can be initially derived from requirements engineering in early stage design. As the system progressively becomes more firmly established, the submodels are then successively replaced by more precise descriptions of the components. The iterative increase in model complexity thus supports the clarification of specific tasks as well as the assessment of basic system setups. At a later stage of development, an integrated system simulation supports the design and virtual test of specific components. However, the generation and validation of individual component models remains a challenge during the design of complex systems since the behavior of a component might strongly depend on its interaction within the overall system context. Summarizing, this leads to three crucial points for the model-based design and testing. Beside the design and validation of simulation models, which represents the physical behavior of the technical system, consistency throughout the entire process is mandatory and traceability of the defined requirements from the design phase till the integrity tests has to be ensured. A holistic model-based approach aggregates these three crucial points and reduces time-to-market and design costs while maximizing quality due to mature products, which meets the defined requirements.

10.3 Hardware-in-the-Loop Testing

Recent developments in hardware-in-the-loop (HIL) testing are focusing on combining the method of test-driven development and the model-based design methods for complex mechatronic systems. The key objective is an overall development method that allows the systematic derivation of HIL test environments based on system requirements. Within the HIL test environment, the device under test (DUT) interacts with a real-time simulation of the respective rest of the system (ROTS) which provides a high level of flexibility due to the rapid interchangeability of the underlying real-time simulation models. The integration of multiphysical HIL simulations allows the real-time emulation of mechanical, electrical or informational boundary conditions within the test environments and improves the early validation and iterative increase in model accuracy during system development. A distinction is made between signal-level, (electrical) power-level and mechanical-level HIL simulation depending on the interface between the physical and the simulated numerical subsystem [5, 6]. Figure 10.1 illustrates the above mentioned basic concepts based on an example of a controlled electromechanical system.

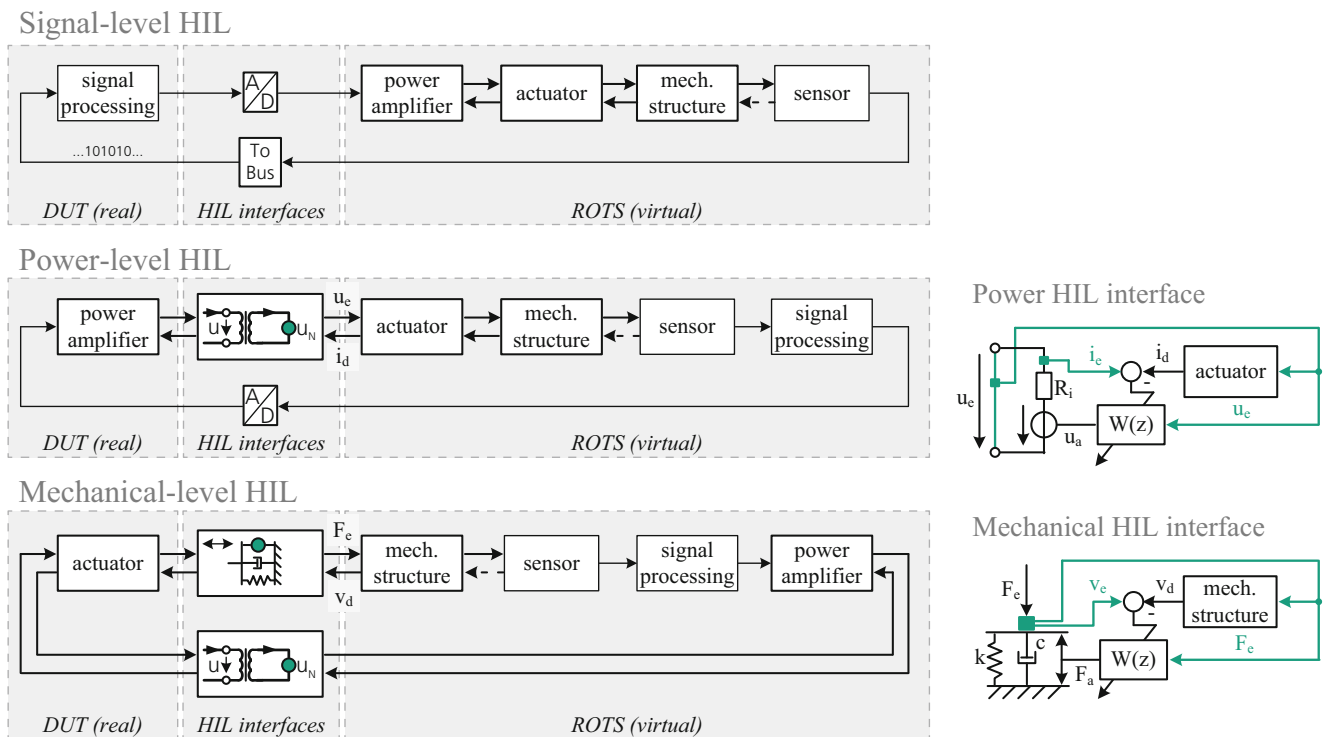


Fig. 10.1 Signal-level, power-level and mechanical-level hardware-in-the-loop test environment (left) and realization of electrical power-level and mechanical-level HIL interfaces (right)

A *signal-level HIL* simulation (sHIL) comprises an interconnection of a physical subsystem (i.e. signal processing) and a virtual residual system at signal level. Signal-level HIL simulation is an often applied method in automotive and aviation applications. The concept of (electrical) *power-level HIL* simulation (pHIL) summarizes HIL procedures which include a significant exchange of electrical power within the interface between the physical subsystem and the residual simulated system. Current activities also focus on power-level HIL tests for power electronic applications in the megawatt range. *Mechanical-level HIL* simulation (mHIL) enables the close analysis of the mechanical interaction between a yet unrealized mechanical structure and an existing mechanical substructure or actuator system in the HIL test environment. Apart from a few exceptions, primarily simplified mechanical load tests with mechanical shakers are used to qualify the mechanical strength not taking into account the interaction between the DUT and the ROTS.

10.4 Current Activities in Hardware-in-the-Loop Testing

There are special challenges related to the further establishment of the test-driven and model based development method for complex mechatronic systems, the real-time simulation of a heterogeneous, multiphysic ROTS and the realization of electrical and mechanical HIL interfaces of high bandwidth and power and signal HIL interfaces for highly interconnected systems. The following subsections will discuss the focal priorities in detail.

10.4.1 Integrating Test-Driven Development into a Model-Based Design Process

At present time digitization, rising complexity and strong multidisciplinary are growing challenges for the development of innovative technical products. This led to an increased perceptibility of systems engineering, especially Model-Based Systems Engineering (MBSE), in these areas. With this background, there took place a rapid development of methodologies and processes in order to develop complex products systematically. Estefan presents some Model-Based Systems Engineering methodologies [7].

MBSE activities aim on offering a guided process for a system to develop. Consistency from requirements to the actual system needs to be provided. The rising importance of modeling for systems engineering processes in this context is obtained by the MBSE initiative [8].

Starting with requirements, basically three development phases occur in this design process of intelligent systems. A system design phase in early stages is followed by a domain-specific design phase. After achieving a specific solution for each discipline concerning the specified requirements, the system integration phase completes the process. Particularly to support developers in the early conceptual phases, partial models are established [9]. According to SysML, a system model can contain different elements. In the CONSENS notation a set of eight coherent partial models is suggested. CONSENS represents a specification technique for mechatronic systems, which starts with focusing all the important stakeholder of a system to ensure that all the necessary requirements are captured. This is done by considering all the outside influences of the targeted system. To fulfil the requirements, which are included in the associated partial model, CONSENS defines functions, which are structured in form of a functional hierarchy. The structure of active principles shows an abstract solution to fulfil the defined functionality. Elements within their relations between each other and disturbances are implemented in the active structure. Furthermore, the behavior of the system is build up.

Beside the system model, which is the central model inside an MBSE approach, the model-based development can be conducted by the V-Model as a description of a model-based development process [4]. To develop the simulation models the first step is to regard the system architecture. This architecture is used, to define the architecture of the simulation model. This enables a clear and comprehensible development of simulation models and submodels, which could easily be allocated to the related components. The V-Model envisages a phased validation of the component to the system. The special challenge consists in the diversity of the components (electrical, mechanical, software) and the complexity of the systems. For such systems, there are no conventionally established schemes for the universal function and property modeling [10].

An approach for solving these challenges is a test-driven development, which is currently only established in the area of software development and enables high-quality, reliable and at the same time a short development time of innovative software products through systematic test definitions at partial and overall system levels [11]. Henke et al. presents a holistic approach for virtual commissioning of a turn-milling-center. The approach encompasses the MBSE activities beginning with a system model and covers requirements engineering in four level of detail. With a systematic generation of test cases by the House-of-Quality and the application of Model- and Hardware-in-the-Loop scenarios the test depth for programmable logic controllers and NC controllers can be enhanced significantly [12].

A transfer of the method of test-driven development to mechatronic systems that integrate energy interfaces is a subject of current research. The different methods of HIL testing allow for an early stage validation of the different components of mechatronic system within its system context and under more realistic conditions. In this context, also test cases for the overall system gained from requirements engineering or preliminary failure mode and effects analyses can be integrated into HIL test environments. Critical operating states can thus be reproducibly investigated prior to field tests of the actual system.

10.4.2 Simulation Tools and Model Generation

An efficient modeling strategy enables and enhances the development process of mechatronic systems and especially vibration control measures in an essential manner. Using a model-based system development, different specifications and measures can be compared with respect to their capability. Once a promising concept is defined, passive or active measures, control concepts or other components can be designed and proven virtually. Moreover, the integration of real-time simulations in test environments allows an efficient verification of the individual components of a mechatronic system. This especially applies for the test-driven development of embedded control units and their corresponding software. In signal-level HIL tests, an existing control unit is connected to a virtual real-time simulation of the residual system. Expanding these methods to devices under test that include a mechanical or power electrical interface, the coupling of the test object to a virtual residual system requires the application of a mechanical or power electrical HIL interface.

For holistic system simulations of mechanical structures, power electronics, and active components, i.e. actuators and sensors, the usage of an impedances-admittances layout of the system simulation model is highly recommended. The advantages are an easy exchangeability of single system components due to standardized interfaces and the possible combination of mechanical, electrical and hydraulic components [3, 13]. The components themselves are represented at different detailing levels, thus defining a certain detailing level of the holistic system. Complex multidisciplinary coupled dynamic systems can be consistently built up in system simulation in dependence of the particular stage of development [14, 15]. The independently modeled subsystems can be derived from various modelling approaches, e.g. electronic circuit, multi body and finite element simulation or can be determined by system identification methods based on experimental testing.

Starting from detailed and modular built up system models, real-time simulation models are generated. The ROTS models are created by extracting the subsystems and components under test, which can easily be done by an automated process due to predefined and standardized interfaces according to the modelling strategy. Consequently, the necessary system states for the coupling between virtual and real subsystems result directly from the ROTS model.

The generation of real-time models is a substantial part for HIL simulations, since a realistic testing of components and subsystems is highly dependent on the exact numerical emulation of the ROTS. Numerically efficient models with reduced number of states and degrees-of-freedom that simulate the dynamic behavior at the system boundaries are required. On the one hand they can be based on the physical properties of a system; on the other hand models with reduced complexity can be generated from existing models by means of mathematical methods [16]. For mechanical structures, simplified continuous models with sufficiently similar input and output behavior can be derived using model order reduction techniques [17]. The use of time-discrete, order reduced models offers the potential to eliminate existing limitations in the dynamic range of HIL applications. Recent research activities deal with the automated generation of high-frequency real-time simulation models for multiphysical coupled problems. As the simulation models are used in different applications along the design process, there are several models with different detail level. To design sustainable processes, the simulation models are created modularly, by using an object-oriented approach. This enables to work with basic model classes, which are extended for the special applications. Changes in these base-classes causes an automatically change in each specialized model, so that the effort for these changes is minimized. Furthermore, different levels of details can be handled easily and serve the dynamic adaptation of simulation model properties during run-time (model reconfiguration).

10.4.3 Realization of Hybrid Test Environments

The third focal point is the development and realization of HIL interfaces for the real-time emulation of informational, electrical and mechanical signals, loads and boundary conditions. Signal-level HIL (sHIL) and model-based testing are widely used in automotive and aviation industries for the test of embedded control units [18, 19]. Current activities are focusing in increasing the bandwidth of sHIL tests up to 1 kHz for the evaluation of controllers used in vibro-acoustic applications like active noise and vibration control. This is achieved by identifying parasitic characteristics (i.e. dead times

of analog-digital and digital-analog conversion, filters and signal processing) and either self-learning or static compensation measures [20]. Present work is also concerned with the model-based development in production and automation engineering [21] and addresses the automated generation of simulation models for the validation of control systems within a virtual commissioning environment (e.g. by physical three-dimensional virtualizations [22]). Consistent validation methods for communication in IoT or Industry 4.0 are increasingly demanded by users, expert committees and researchers [23]. An important issue concerning interconnected elements is a robust and flexible communication between all these system-elements. There are standards used to set up a communication between heterogeneous elements. In the context of machine engineering and in automotive applications field buses (e.g. CAN or Profibus) or Ethernet-based protocols (e.g. EtherCAT or OPC-UA) are applied typically for distributed control, data mining or simple information sharing. Concerning functionality tests of complex distributed systems the test of communications structures becomes an important discipline. Varying latencies jitter effects and communication breakdown have strong influences on the stability of closed-loop control and impairs the interaction of distributed systems. The functionality can be investigated by Hardware-in-the-Loop tests with fault injection for communication restrictions. Henke et al. describe a pattern-based approach for design and testing of distributed control systems for autonomously driven railway vehicles [24].

Besides power-level HIL (pHIL) tests also standardized validation procedures for power electric devices (e.g. electromagnetic interference, short circuit, reversed voltage, or discontinuities in supply voltage) exist (e.g. [25]). Power-level HIL test methods are especially getting important whenever the device under test shows a strong interaction with its electrical load or its power supply. Power-level HIL has thus been realized for the early stage validation of power electronics applications [26–30] also in the megawatt range. However, in many applications the bandwidth of the power-level HIL simulation is restricted due to the controller’s stability constraints. For the emulation of low bandwidth signals either open-loop [29] or closed-loop control is used [26, 27]. The emulation of mechanical boundary conditions is achieved by mechanical-level HIL (mHIL) simulations. Purely passive substructures for the emulation of the mechanical ROTS only provide a low degree of accuracy [31, 32]. Semi-active [33] and active mechanical HIL interfaces [34] offer a greater flexibility compared to passive substructures. Active mechanical HIL interfaces are used in the automotive sector or energy technology [5, 35–37], in mechanical engineering [38, 39] or in civil engineering. The dynamic and the bandwidth is often limited due to the actuator types being used or the applied control method (usually $D = 10\text{--}20\%$ and $f_{\max} = 30\text{ Hz}$). In order to allow for a flexible use of pHIL and mHIL simulations with active controlled HIL interfaces, current activities focus on the transfer of the model based development of smart structures for the development of active pHIL and mHIL interfaces [40, 41]. This also includes the derivation of design catalogs for adjustable mechanical elements [42], actuators, adaptive admittance control and power electronics. Due to the strong interaction of the desired numerical behavior of the ROTS and the dynamic properties of the device under test, adaptive feedforward control of pHIL and mHIL interfaces is an essential component for high bandwidth, high dynamic and robust pHIL and mHIL environments [34, 41, 43, 44].

10.5 Application Example: Early Stage Validation of an Active Vibration Control System

The potential of combined model based development and signal-level, power-level and mechanical-level HIL testing is investigated for an exemplary active vibration control (AVC) application. Figure 10.2 illustrates the basic HIL scenarios. A primary structure (m_1 , k_1 and c_1) is excited by an external force F . A linear chirp signal from $f = 20$ to 200 Hz within 20 s is chosen for exciting the primary structure. An inertial mass actuator (m_2 , k_2 , c_2 , Ψ and Z_e) serves the cancelation of the

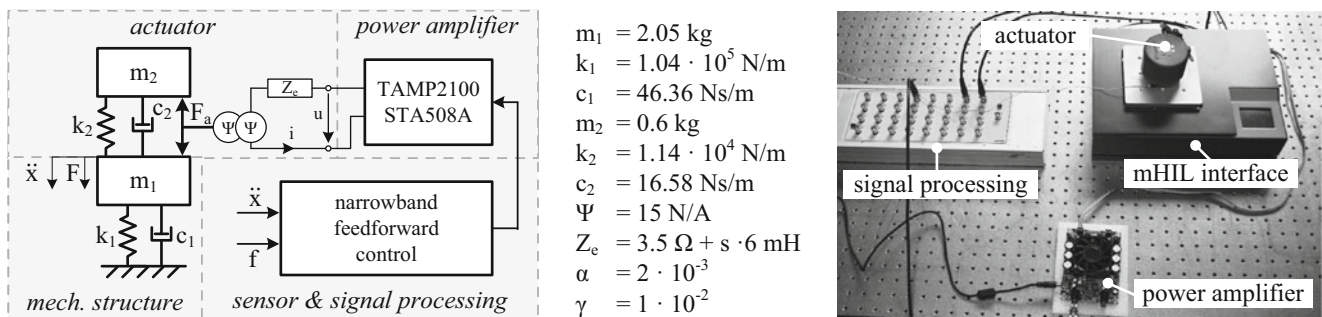


Fig. 10.2 Test set-up for the investigation of hybrid simulation environments (left) and realization of the test rig in the laboratory (right)

acceleration \ddot{x} . The actuator is driven by a low-cost amplifier namely the TAMP2100 from Sure Electronics. The actuator's control signal is computed by the narrowband feedforward FxLMS algorithm [45] whereas the normalized adaptation step size α and the leakage weighting factor γ serve the adjustment of the control performance. Digital signal processing is realized by means of a dSPACE DS1005 rapid control prototyping system with a sampling frequency of 10 kHz. Analogue eighth order Butterworth filters ($f_{3dB} = 4$ kHz) are used for anti-aliasing and reconstruction filters.

A key challenge during the design of an AVC system is the strong interaction (i.e. power exchange) between the components of the mechanical and electrical domain. Therefore, this interaction has to be considered at an early stage of development since the strong interaction and feedback between the components significantly influences the design of the actuator and the power amplifier. Furthermore, the adaptive narrowband feedforward controller implements a numerical model of the cumulated transfer function of the overall system. Hence, the controller's performance also strongly depends on the accuracy of the underlying model.

In order to investigate the overall system's performance and to evaluate the accuracy of the numerical models, an experimental setup, a signal-level (sHIL), an electrical power-level (pHIL) and a mechanical-level HIL (mHIL) test environment is realized. The structure of the respective HIL simulation is based on the topologies illustrated in Fig. 10.1. The results are then compared with the results obtained from a numerical investigation. The focus is not on optimal model accuracy at this stage but rather on the detection of stronger deviations between the respective HIL investigation and the numerical models derived from early stage model-based development. In order to increase model accuracy during different stages of system development, the numerical models can be detailed subsequent to the respective HIL investigation. The mechanical HIL interface [41] is realized by an in-parallel arrangement of a variable stiffness element (continuous adjustment between 12 and 840 N/mm) and a voice coil actuator with a peak force of 350 N. The power electrical HIL interface [40] comprises a pulse-width-modulated current controlled H-bridge amplifier ($I_{max} = \pm 2$ A, $U_{max} = \pm 30$ V) which is based on the BTN8982 evaluation board.

Figure 10.3 summarizes the results of the investigations by means of an order cut of the remaining acceleration at the primary structure and the apparent power at the output of the power amplifier. The results show a good accordance between the initial and not yet adapted numerical simulation, the different HIL setups and the experiment. However, there are some slight deviations between the numerical model and the respective validation setup. Regarding the remaining acceleration at the interface, there are some model deviations within the numerical model in the higher frequency range above 100 Hz compared to the signal-level HIL test. This can be caused by a not yet considered dead time within the digital signal processing unit. The deviations between the numerical model, the experimental setup and the mechanical-level HIL test are getting even more noticeable. Besides the overestimated damping within the numerical model of the primary structure (deviations at 40 Hz), there is a second resonance frequency between 20 and 40 Hz that has not been considered yet. One of the most significant deviations is the higher power demand of the power amplifier especially in the frequency range above 60 Hz which can be caused by a larger inductive load of the actuator. The deviations between the mechanical-level HIL test and the experiment in the frequency range between 80 and 160 Hz might be caused by a parasitic stick-slip effect within the mechanical HIL interface. This, however, requires a further investigation.

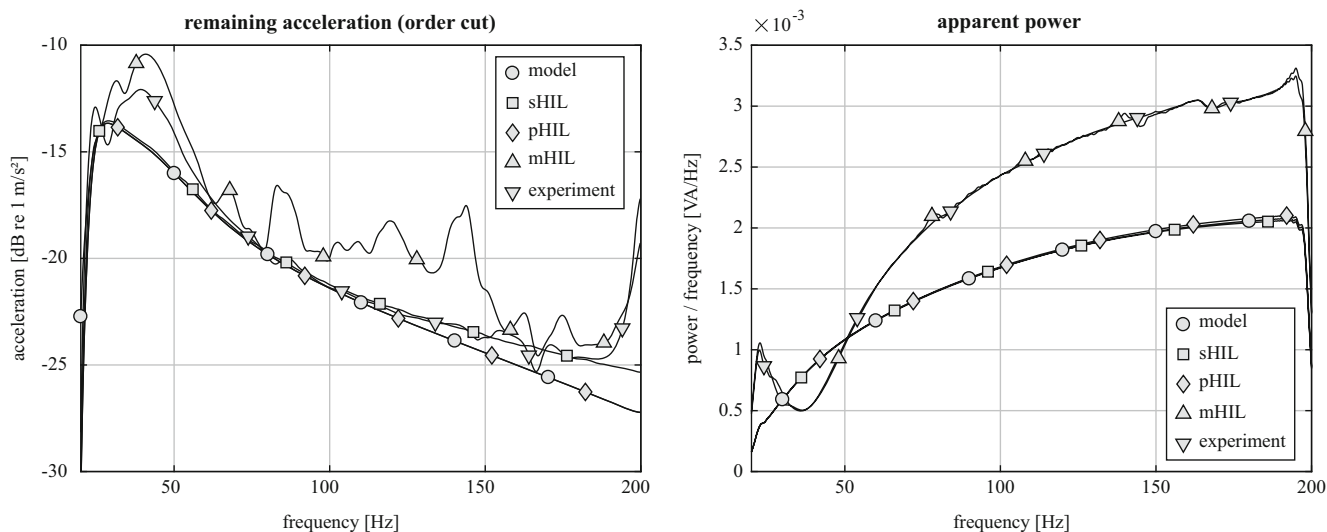


Fig. 10.3 Order cut of the remaining acceleration \ddot{x} of the primary structure (left) apparent power (one-sided cross spectral density) at the output of the power amplifier (right)

10.6 Conclusion

There are growing challenges for the development of innovative technical products such as digitization, rising complexity and strong multidisciplinary. In this context, multiphysical hardware-in-the-loop (HIL) testing is deemed to be an integral part of early stage validation and future methods of system development. Besides the further establishment of the test-driven and model-based development method for complex mechatronic systems, there are special challenges related to the real-time simulation of a heterogeneous, multiphysical systems and the realization of electrical and mechanical HIL interfaces of high bandwidth and power as well as signal HIL interfaces for highly interconnected systems.

The flexible combination of numerical, signal-level, mechanical-level and electrical power-level HIL simulations throughout the design and development of a mechatronic system allows the early stage validation of numerical models and already realized components.

References

1. Maximilien, E.M., Williams, L.: Assessing test-driven development at IBM. In: Proceedings 25th International Conference on Software Engineering, Portland, OR, pp. 564–569 (2003)
2. Gross, J.-L.: Real time hardware-in-the-loop simulation verifies performance of Gemini computer and operational program. *Simulation*. **9**(3), 141–148 (1967)
3. Herold, S., Jungblut, T., Kurch, M.: A systematic approach to simulate active mechanical structures. In: International Association for the Engineering Analysis Community, NAFEMS-Seminar: Multidisciplinary Simulations – The Future of Virtual Product Development, Wiesbaden, Germany (2009)
4. VDI Guideline, VDI2206: Design Methodology for Mechatronic Systems. VDI-Verlag, Düsseldorf (2004)
5. Bouscayrol, A.: Different types of hardware-in-the-loop simulation for electric drives. In: IEEE International Symposium on Industrial Electronics (ISIE 2008), Cambridge, UK (2008)
6. Lentijo, S., D’Arco, S., Monti, A.: Comparing the dynamic performances of power hardware-in-the-loop interfaces. *IEEE Trans. Ind. Electron.* **57**(4), 1195–1207 (April 2010)
7. Estefan, J.A.: Survey of model-based systems engineering (MBSE) methodologies. In: INCOSE MBSE Initiative (2008)
8. Friedenthal, S., Griego, R., Sampson, M.: INCOSE model based systems engineering (MBSE) initiative. In: INCOSE 2007, San Diego, CA, USA (2007)
9. Oestersötebier, F., Just, V., Trächtler, A., Bauer, F., Dziwok, S.: Model-based design of mechatronic systems by means of semantic web ontologies and reusable solution elements. In: Proceedings of the ASME 2012 11th Biennial Conference on Engineering Systems Design and Analysis ESDA2012, Nantes, France (2012)
10. Eisenbart, B., Blessing, L., Gericke, K.: Functional modeling perspectives across disciplines: a literature review. In: Proceedings of International Design Conference – DESIGN 2012, Dubrovnik, Croatia (2012)
11. Bhat, T., Nagappan, N.: Evaluating the efficacy of test-driven development: industrial case studies. In: Proceedings of the 2006 ACM/IEEE International Symposium on Empirical Software Engineering, ACM, pp. 356–363 (2006)
12. Henke, C., Michael, J., Lankeit, C., Trächtler, A.: A holistic approach for virtual commissioning of intelligent systems. In: 11th Annual IEEE Systems Conference, Montreal, Canada (April 2017)
13. Herold, S., Atzrodt, H., Mayer, D., Thomaier, M.: Modeling approaches for active systems. In: SPIE Proceedings Series 6173, Paper 61730N: Smart Structures and Materials 2006. Smart Structures and Integrated Systems, American Society of Mechanical Engineers – ASME (2006)
14. Bartel, T., Gaisbauer, S., Stöhr, P., Herold, S., Melz, T.: Development of functionally integrated mounts for three- and six-axial vibration isolation of sensitive equipment. In: ISMA – International Conference on Noise and Vibration Engineering, Leuven, Belgium (2014)
15. Tamm, C., Bartel, T., Dautfest, A., Debes, C., Herold, S., Heim, R.: Multi physical domain simulation of a NVH reduction system for a generator-electric vehicle. In: 45th International Congress and Exposition on Noise Control Engineering, INTER-NOISE 2016, Hamburg, Germany (2016)
16. Kurch, M.: Entwicklung einer Simulationsumgebung für die Auslegung piezoelektrischer Energy Harvester. Dissertation, TU Darmstadt, Germany (2014)
17. Antoulas, A.: Approximation of Large-Scale Dynamical Systems. Vol. 6: Advances in Design and Control. Society for Industrial & Applied Mathematics, Philadelphia, PA (2005)
18. Wagner, F., Frey, G.: Hardware-in-the-Loop-Simulationen bei kurzfristig zu langsamen Simulationsmodellen. In: VDI-Berichte Nr. 1980 (2007)
19. Barth, M., Fay, A.: Automated generation of simulation models for control code tests. *Control. Eng. Pract.* **21**(2), 218–230 (2013)
20. Potrafke, T.: Modeling of dynamic systems for signal level hardware-in-the-loop applications. Master Thesis, TU Darmstadt, Germany (2017)
21. Puntel-Schmidt, P., Fay, A., Riediger, W., Schulte, T., Köslin, F., Diehl, S.: Validierung von Steuerungscode mit Hilfe automatisch generierter Simulationsmodelle. at – Automatisierungstechnik, Methoden und Anwendungen der Steuerungs-, Regelungs- und Informationstechnik, Band 63, Heft 2 (2015)
22. Damrath, F., Strahilov, A., Bär, T., Vielhaber, M.: Method for energy-efficient assembly system design within physics-based virtual engineering in the automotive industry. *Procedia CIRP*. **41**, 307–312 (2016)
23. Kowalewski, S., Rumpe, B., Stollenwerk, A.: Cyber-physical systems – eine Herausforderung an die Automatisierungstechnik? In: Proceedings of Automation, VDI Berichte 2012, VDI-Verlag, pp. 113–116 (2012)

24. Henke, C., Tichy, M., Schneider, T., Böcker, J., Schäfer, W.: Organization and control of autonomous railway convoys. In: 9th International Symposium on Advanced Vehicle Control (AVEC 08), Kobe, Japan (2008)
25. ISO16750: Road vehicles – environmental conditions and electrical testing for electrical and electronic equipment (2006)
26. de Jong, E., de Graaf, R., Vaessen, P., Crolla, P., Roscoe, A., Lehfuß, F., Lauss, G., Kotsampopoulos, P., Gafaro, F.: European white book on real-time power-hardware-in-the-loop testing. DERlab Report No. R-005.0, KEMA Netherlands (2011)
27. Edrington, C.S., Vodyakho, O., Hacker, B., Azongha, S., Khaligh, A., Onar, O.: Virtual battery charging station utilizing power-hardware-in-the-loop: application to V2G impact analysis. In: Proceedings of the Vehicle Power and Propulsion Conference (VPPC), IEEE, Lille, France (2010)
28. Ren, W., Steurer, M., Woodruff, S.: Applying controller and power hardware-in-the-loop simulation in designing and prototyping apparatuses for future all electric ship. In: Proceeding of the Electric Ship Technologies Symposium, ESTS '07. IEEE, Arlington, VA (2007)
29. Steurer, M., Edrington, C.S., Sloderbeck, M., Ren, W., Langston, J.: A megawatt-scale power hardware-in-the-loop simulation setup for motor drives. *IEEE Trans. Ind. Electron.* **57**(4), 1254–1260 (2010)
30. Uhlenbrock, R., Schugt, M., Tyble, M.: Testlücke mit Power-HiL schließen. In: *Automobil Elektronik* 03/2013, pp. 48–50 (2013)
31. Kauba, M., Herold, S., Koch, T., Mayer, D., Melz, T.: Design and application of an active vibration control system for a marine engine mount. In: Proceedings of ISMA 2008, Leuven, Belgium (2008)
32. Kraus, R.: Auslegung und Umsetzung eines Labordemonstrators zur aktiven Lagerung im Fahrwerksbereich eines Kraftfahrzeugs. Diploma thesis, Fachhochschule Gießen-Friedberg, Germany (2010)
33. Jungblut, T., Alber, O., Wolter, S.: Semi-aktive Anbindungsimpedanzen: Ein Ansatz zur Nachbildung realistischer Randbedingungen in Versuchsaufbauten, Tagungsband 38. Deutsche Jahrestagung für Akustik (DAGA), Darmstadt, Germany, pp. 765–766 (2012)
34. Jungblut, T.: Ein Beitrag zur modellbasierten, hybriden Entwicklung elektromechanischer Systeme zur Schwingungsminderung. Dissertation, TU Darmstadt, Germany (2015)
35. Plummer, A.R.: Model-in-the-loop testing. *Proc. Inst. Mech. Eng. I, J. Syst. Control Eng.* **220**, 183–199 (2006)
36. Correa, B.A., Zhang, Y., Dougal, R.A., Chiocchio, T., Schoder, K.: Mechanical power-hardware-in-the-loop: emulation of an aeroderivative twin-shaft turbine engine. In: 2013 IEEE Electric Ship Technologies Symposium (ESTS), Arlington, VA, pp. 464–468 (2013)
37. Bartl, A., Karamooz Mahdiabadi, M., Rixen, D.J.: Conception of a noise and vibration hardware-in-the-loop test bed. In: 35th IMAC Annual Conference on Experimental and Applied Mechanics (2017)
38. Facchinetti, A., Bruni, S.: Hardware-in-the-loop hybrid simulation of pantograph–catenary interaction. *J. Sound Vib.* **331**(12), 2783–2797 (2012)
39. Karpenko, M., Sepehri, N.: Hardware-in-the-loop simulator for research on fault tolerant control of electrohydraulic flight control systems. In: 2006 American Control Conference, Minneapolis, MN (2006)
40. Millitzer, J., Ranisch, C., Kloepfer, J.: Electrical power-hardware-in-the-loop simulation for the early validation of power amplifiers used in active vibration control. In: Symposium für Smarte Strukturen und Systeme, 4SMARTS, Darmstadt, Germany (2016)
41. Millitzer, J., Ranisch, C., Tamm, C., Bartolozzi, R., Melz, T.: An approach for the design of a mechanical hardware-in-the-loop interface. In: Symposium für Smarte Strukturen und Systeme, 4SMARTS, Braunschweig, Germany (2017)
42. Hansmann, J., Kaal, W., Seipel, B., Melz, T.: Tuneable spring element for an adaptable vibration absorber. In: *ATZ Worldwide*. No. 03, pp. 36–39 (2012)
43. Bartl, A., Mayet, J., Rixen, D.J.: Adaptive feedforward compensation for realtime hybrid testing with harmonic excitation. In: 11th International Conference in Engineering Vibration, Ljubljana, Slovenia (2015)
44. Vrbata, J., Atzrodt, H., Kimpel, T., Koch, T., Mayer, D.: Development of a multiaxial test environment for highly dynamically loaded mechatronic components. In: Symposium on Structural Durability SoSDiD 2017, Darmstadt, Germany (2017)
45. Kuo, S.M., Morgan, D.R.: *Active Noise Control Systems – Algorithms and DSP Implementations*. Wiley, New York (1996)



Chapter 11

Assessing Structural Reliability at the Component Test Stage Using Real-Time Hybrid Substructuring

Connor Ligeikis, Alex Freeman, and Richard Christenson

Abstract The propagation of uncertainties through complex systems is a challenging endeavor. While numerical simulations can be used to accurately predict the dynamic performance of structural systems, there are some instances where the dynamics and uncertainties of specific components may be less understood or difficult to accurately model. This paper will implement a structural reliability assessment employing the cyber-physical real-time hybrid substructuring (RTHS) method to combine a numerical model of a larger structural system, incorporating uncertainty in specific parameters, with a physical test specimen of a component of the system while fully incorporating the system-level dynamic interactions and uncertainty propagation. This RTHS approach will allow for uncertainty and reliability to be addressed in the early stage of the design process as components become available and the remainder of the system remains numerically modeled. A small-scale RTHS experiment will be used to demonstrate the probability of failure of a spring-mass-damper system with a relatively small number of component tests by employing the previously proposed Adaptive Kriging-Hybrid Simulation (AK-HS) reliability method.

Keywords Real-time hybrid substructuring · Structural reliability · Metamodeling · Adaptive kriging · Vibration control

11.1 Introduction

The main objective of a structural reliability assessment is to determine the probability of failure of a system or a particular structural component within a system. This probability of failure is dependent on both some specified failure criteria and on the distributions of random input variables. The most common approach for determining probability of failure is the Monte Carlo simulation (MCS). In this method, a large number of numerical simulations are performed according to the distributions of the random input variables and the resulting distribution of the system's response is analyzed. However, solely using numerical simulations may not result in accurate results if the system's behavior is difficult to model. For example, there may exist a non-linear component within the system that cannot be adequately represented numerically. In cases such as this, it becomes necessary to conduct physical experiments. Real-time hybrid substructuring (RTHS) is a vibration testing methodology which combines numerical simulations with physical testing [1]. In RTHS, a system is partitioned into a numerical substructure and a physical substructure. The physical substructure is a physical specimen of the system component which is not well understood and the numerical substructure consists of a computational model of the remainder of the system. During an RTHS experiment, these substructures interact with each other in real time and the performance of the full system can be studied. However, RTHS alone is not conducive to performing structural reliability assessments. It is simply impractical to conduct the large number of tests required for a standard MCS. Abbiati et al. [2] proposed a method which combines an adaptive kriging algorithm with hybrid simulations to examine a two degree-of-freedom system connected with a nonlinear spring element. This Adaptive Kriging-Hybrid Simulation (AK-HS) method allows engineers to obtain a fairly accurate prediction of a system's probability of failure while requiring a relatively small number of experiments to be performed.

Kriging is a statistical interpolation method that originated in the field of geo-statistics. Recently, kriging has been used as a technique by engineers to create metamodels that can be used to represent complex numerical models that require extensive computation time to evaluate [3]. Kriging treats the deterministic model response as the realization of a Gaussian process [4]. Echard et al. [5] developed the Adaptive Kriging-Monte Carlo Simulation (AK-MCS) method which uses kriging combined with an iterative learning algorithm to obtain relatively fast and accurate probabilities of failure for complex deterministic

C. Ligeikis · A. Freeman · R. Christenson (✉)

Department of Civil and Environmental Engineering, University of Connecticut, Storrs, CT, USA

e-mail: rchrste@engr.uconn.edu

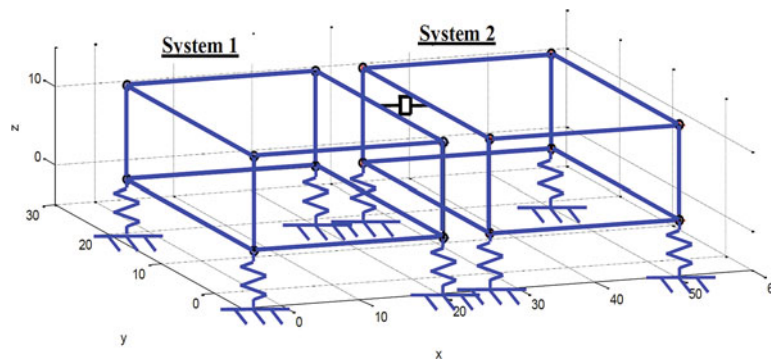


Fig. 11.1 Adjacent rigid body structures connected with viscous damper

Table 11.1 Parameters for adjacent rigid body structures

Parameter	Structure 1	Structure 2
Mass, m_i	159.43 N-sec ² /m	84.1 N-sec ² /m
x -axis moment of inertia, I_{xx}	6.97 N-sec ² -m	4.05 N-sec ² -m
y -axis moment of inertia, I_{yy}	6.97 N-sec ² -m	4.05 N-sec ² -m
z -axis moment of inertia, I_{zz}	10.44 N-sec ² -m	5.50 N-sec ² -m
Horizontal stiffness, $k_{x,i}$	11,390 N/m	11,390 N/m
Lateral stiffness, $k_{y,i}$	35,040 N/m	35,040 N/m
Vertical stiffness, $k_{z,i}$	91,100 N/m	91,100 N/m
Modal damping, ξ_i	1%	1%
Number of isolators	4	4

computer models. Schöbi et al. [6] further refined this approach by utilizing polynomial-chaos kriging with AK-MCS and also implementing a new stopping criterion for the algorithm. Abbiati et al. [2] then merged these methods with hybrid simulations to create the AK-HS method. AK-HS is unique because hybrid tests (which involve some physical component) are used to build the metamodels rather than completely deterministic computer model evaluations. This research will employ a slightly modified AK-HS method to determine the probability of failure of a more complex spring-mass-damper system and examine the performance of the AK-HS method as the number of uncertain parameters in the system increases. The system being examined consists of two adjacent rigid body structures each supported by four base isolating springs and connected with a viscous damper. In addition, each of the eight springs supporting the structures have some lateral, horizontal, and vertical stiffness. Figure 11.1 shows an illustration of the complete system. Table 11.1 lists the various system parameters when the system is modeled as two adjacent six degree-of-freedom structures.

The connected system is excited by a force applied to the top of Structure 2 in the x -direction. The purpose of the connected damper is to create dissipative forces using the relative motion of the structures to reduce the force transmissibility of the system. Previously, Botelho and Christenson [7] demonstrated the effectiveness of this connected control method (CCM) of vibration control through analytical and experimental studies of this system. This study will explore how treating the spring stiffnesses as normally distributed random variables affects the performance of the damper. The performance criteria used is the maximum total force transmissibility transmitted through the eight springs to the base. This maximum force transmissibility is defined as the peak of the total force transmissibility frequency response curve. A force transmissibility failure threshold of 25 dB is selected. Prior to conducting actual RTHS tests, purely numerical simulations are conducted to determine the feasibility of using the AK-HS method on this system. Several different cases are examined. First, the horizontal stiffnesses in each structure are treated as two lumped random variables. Next, the horizontal stiffnesses are treated as eight individual random variables. Finally, the horizontal, lateral, and vertical stiffnesses are treated as 24 individual random variables. Table 11.2 lists the means and standard deviations for each of these cases.

Figure 11.2 shows the visual results of Case 1. The leftmost plot shows the MCS conducted using 20,000 full numerical model evaluations (red points denote system failure). The middle plot shows the adaptive kriging MCS which required only 69 numerical model evaluations (represented by black dots). The rightmost plot shows the convergence of the probability of failure as the adaptive kriging process iteratively added sample points. The UQLab software framework [8] was used to create the kriging metamodels during each iteration. For Case 1, the probabilities of failure for the full MCS and the adaptive kriging MCS were identical (error of 0%). For Case 2, 136 model evaluations were required to achieve an error of 0%. For Case 3, 408 model evaluations were required to achieve an error of 0.206%.

Table 11.2 Random variable parameters

	Random variable	Mean (N/m)	Standard deviation (N/m)
Case 1	$k_{x,1}$	11,390	2630
	$k_{x,2}$		
Case 2	$k_{x1,1}, k_{x2,1}, k_{x3,1}, k_{x4,1}$	11,390	2630
	$k_{x1,2}, k_{x2,2}, k_{x3,2}, k_{x4,2}$		
Case 3	$k_{x1,1}, k_{x2,1}, k_{x3,1}, k_{x4,1}$	11,390	2630
	$k_{x1,2}, k_{x2,2}, k_{x3,2}, k_{x4,2}$		
	$k_{y1,1}, k_{y2,1}, k_{y3,1}, k_{y4,1}$	35,040	7880
	$k_{y1,2}, k_{y2,2}, k_{y3,2}, k_{y4,2}$		
	$k_{z1,1}, k_{z2,1}, k_{z3,1}, k_{z4,1}$	91,100	21,020
	$k_{z1,2}, k_{z2,2}, k_{z3,2}, k_{z4,2}$		

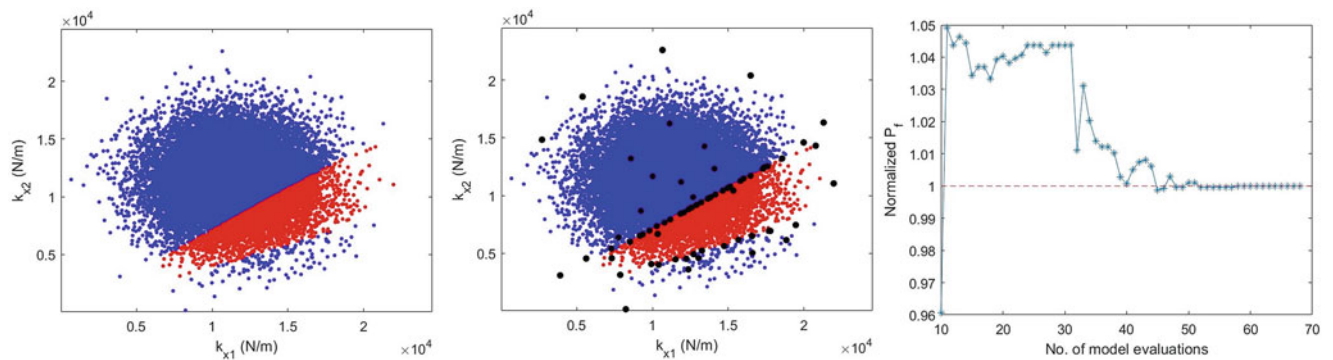


Fig. 11.2 (a) Full MCS (b) Adaptive kriging MCS (c) Convergence of normalized probability of failure



Fig. 11.3 Servo-hydraulic actuator and damper experimental setup

Full RTHS tests using the AK-HS method will be conducted in the Shock and Vibration Laboratory at the University of Connecticut. The physical substructure consists of a D-Series linear viscous damper from Taylor Devices Inc. (Model No. 1 × 2D). This damper is attached to a servo-hydraulic actuator system which consists of a Quincy-Ortman Cylinder attached to a MOOG servo-valve as shown in Fig. 11.3. The actuator is controlled with a Parker Hannifin Corporation analog controller. A PCB force sensor (Model 208C04) will be used to measure the damper force. The dynamic equations of the numerical substructure will be solved by a Speedgoat performance real-time target machine. The Speedgoat machine will also provide displacement commands to the servo-hydraulic actuator system. A Data Physics SignalCalc Mobilyzer dynamic signal analyzer will be used to collect numerical and physical data and derive the frequency response functions automatically.

References

1. Blakeborough, A., Williams, M.S., Darby, A.P., Williams, D.M.: The development of real-time substructure testing. *Philos. Trans. R. Soc. Lond. A Math. Phys. Eng. Sci.* **359**(1786), 1869–1891 (2001)
2. Abbiati, G., Schöbi, R., Sudret, B., Stojadinovic, B.: Structural reliability analysis using deterministic hybrid simulations and adaptive kriging metamodeling. In: 16th World Conference on Earthquake Engineering, paper no. 595 (2017)
3. Kleijnen, J.P.: Kriging metamodeling in simulation: a review. *Eur. J. Oper. Res.* **192**(3), 707–716 (2009)
4. Santner, T.J., Williams, B.J., Notz, W.I.: *The Design and Analysis of Computer Experiments*. Springer Science & Business Media, New York (2003)
5. Echard, B., Gayton, N., Lemaire, M.: AK-MCS: an active learning reliability method combining Kriging and Monte Carlo simulation. *Struct. Saf.* **33**(2), 145–154 (2011)
6. Schöbi, R., Sudret, B., Marelli, S.: Rare event estimation using polynomial-chaos kriging. *ASCE-ASME J. Risk Uncertain. Eng. Syst. A Civ. Eng.* **3**(2), D4016002 (2016)
7. Botelho, R.M., Christenson, R.E.: Reducing resonant vibrations of adjacent base isolation systems using connected control method. In: ASME 2014 International Design Engineering Technical Conferences and Computers and Information in Engineering Conference, pp. V008T11A098–V008T11A098 (2014)
8. Marelli, S., Sudret, B.: UQLab: a framework for uncertainty quantification in Matlab. In: Proceedings of the 2nd International Conference on Vulnerability, Risk Analysis and Management (ICVRAM2014), pp. 2554–2563 (2014)

Chapter 12

Modal Identification Using a Roving Actuator and a Fixed Sensor



Rajdip Nayek, Suparno Mukhopadhyay, and Sriram Narasimhan

Abstract Experimental modal analysis typically use an actuator to apply input force on a structure and multiple fixed sensors to record the responses of the structure. An appealing alternative to using many stationary sensors is to use a roving actuator and a single fixed sensor. In this study, a method to identify the modal properties of a beam from the input-output data obtained using a roving actuator and a fixed accelerometer is presented. In multiple test setups, the roving actuator applies input forces at different points on the beam, while the fixed sensor measures the response at a particular location of the beam during all tests. Using the accumulated input-output measurements, the modal identification of the beam is performed in two distinct steps: identification of natural frequencies and modal damping ratios, followed by an estimation of mode shape components at all excited degrees of freedom. The variability in the estimated modal parameters due to the presence of measurement noise is studied using Monte Carlo simulations.

Keywords Modal identification · Single sensor · Roving input · Input-output balance · Noise-induced uncertainty

12.1 Introduction

Forced vibration modal testing of bridges involve estimating the modal parameters of the bridge from input-output data recorded using one (or more) actuator(s) and a set of sensors. Typically, a dense array of sensors is employed to accurately capture the vibration mode shapes of the bridge. However, using a large number of sensors can be expensive in terms of installation, data storage and processing. An appealing alternative is to use a roving actuator and a single or a small set of stationary sensors. The benefit is that mass normalized mode shapes of the structure can be obtained at all points where the inputs are applied (using Maxwell-Betti's reciprocal work principle). This alternative strategy has generated some research interest in forced vibration testing as well as operational modal testing. Cara et al. [1] presented a modal identification method using input-output measurements from a roving input and a small set of fixed sensors to estimate the state-space model of the structure using maximum likelihood algorithm. Matarazzo et al. [4] proposed a similar maximum likelihood based method for modal identification using mobile sensors from ambient vibration data. In both of the methods, the modal parameters are subsequently derived from the state-space model updated using the measurements. Marulanda and Caicedo [3] proposed a operational modal analysis technique which uses output data measured using two sensors, one fixed and the other mobile. They derived a linear system of equations relating the mode shapes of the structure to the correlation between two output responses. The natural frequencies and damping ratios of the structure are obtained from a single or a small set of measurements, and the arbitrarily normalized mode shapes are obtained as the solution to the linear system.

In this paper, a forced-vibration method which uses a single roving actuator (roving input) and a single fixed sensor for modal identification is presented. The method requires the modal identification procedure to be performed into two steps: (i) identification of natural frequencies and damping ratios using any system/modal identification technique, and (ii) estimation of mode shape components using input-output balance [5]. The uncertainty in the identified modal parameters due to noise in the input-output data is studied using numerical simulations.

R. Nayek (✉) · S. Narasimhan

Department of Civil and Environmental Engineering, University of Waterloo, Waterloo, ON, Canada
e-mail: rnayek@uwaterloo.ca

S. Mukhopadhyay

Department of Civil Engineering, Indian Institute of Technology Kanpur, Kanpur, India

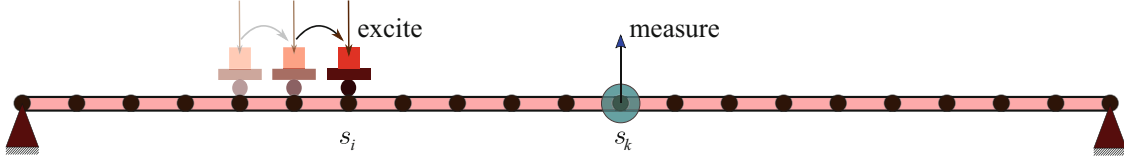


Fig. 12.1 Beam with a mobile actuator and a fixed sensor

12.2 System Model and Measurements

Consider an N degree-of-freedom (dof) finite element (FE) model of a beam (representing a bridge) whose governing dynamic equation is given by:

$$[M] \{\ddot{d}\} + [C] \{\dot{d}\} + [K] \{d\} = \{L\}f \quad (12.1)$$

The matrices $[M]$, $[C]$, and $[K]$, each of dimension $N \times N$, denote the global mass, global damping and global stiffness matrices of the beam. $\{L\}$ is the $N \times 1$ input location vector, with $\{L\}_j = 1$, $\{L\}_k = 0$, $k \neq j$ when the actuator applies an input to the j th dof of the structure.

The input-output measurements are obtained by fixing the sensor (in this case, an accelerometer) at one station s_k and changing the actuator locations s_i from one test to the next, sequentially, as shown in Fig. 12.1. The actuator applies an excitation at s_i and the resulting structural response is measured by the sensor fixed at station s_k . This input-output pair is indexed as $(f_{s_i}, \ddot{d}_{s_k}^{s_i})$, where f_{s_i} indicates the input force at station s_i , and $\ddot{d}_{s_k}^{s_i}$ indicates the output response at station s_k due to force exerted at station s_i . For all selected stations $i = 1, 2, \dots, P$ where the input is applied sequentially, a set of input-output pairs $\{(f_{s_i}, \ddot{d}_{s_k}^{s_i}), i = 1, 2, \dots, P\}$ is obtained.

12.3 Modal Identification

Using modal superposition, the measured acceleration responses $\ddot{d}_{s_k}^{s_i}$ can be expressed in terms of r dominant modes of the beam as:

$$\ddot{d}_{s_k}^{s_i} \approx \sum_{j=1}^r \phi_{s_k, m_j} \ddot{q}_{m_j} \quad (12.2)$$

where ϕ_{s_k, m_j} is the component of the m_j th mode shape at the s_k station. Substituting Eq. (12.2) in Eq. (12.1), and considering mass normalized modes, one obtains r uncoupled modal equations of motion:

$$\ddot{q}_{m_j} + 2\xi_{m_j}\omega_{m_j}\dot{q}_{m_j} + \omega_{m_j}^2 q_{m_j} = \phi_{s_i, m_j} f_{s_i} \quad (12.3)$$

with ξ_{m_j} and ω_{m_j} denoting the identified m_j th modal damping ratio and circular natural frequency of the test structure, respectively. Estimates of ξ_{m_j} and ω_{m_j} can be obtained using common system identification methods such as ERA, SSI, etc. However ϕ_{s_i, m_j} being unknown, \ddot{q}_{m_j} cannot be obtained directly. Instead, a set of r pseudo-modal equations [5] can be obtained by substituting $q_{m_j} = \phi_{s_i, m_j} \tilde{q}_{m_j}$ in Eq. (12.3) as:

$$\ddot{\tilde{q}}_{m_j} + 2\xi_{m_j}\omega_{m_j}\dot{\tilde{q}}_{m_j} + \omega_{m_j}^2 \tilde{q}_{m_j} = f_{s_i} \quad (12.4)$$

which are then solved to obtain what are termed as pseudo-modal acceleration responses, $\ddot{\tilde{q}}_{m_j}$. The measured acceleration response vector, $\ddot{d}_{s_k}^{s_i}$ can then be expressed in terms of the pseudo-modal acceleration responses as:

$$\ddot{d}_{s_k}^{s_i} = \sum_{j=1}^r \phi_{s_k, m_j} \phi_{s_i, m_j} \ddot{\tilde{q}}_{m_j} \quad (12.5)$$

It is found that the pseudo-modal responses are linearly related to the measured point accelerations through the product of mode shape coefficients. Assuming n_t discrete time samples for responses $\ddot{a}_{s_k}^{s_i}$ and \ddot{q}_{m_j} , a linear matrix equation is obtained as expressed below:

$$[G]^{(s_i)} \{\psi\}^{(s_k, s_i)} \approx \{y\}^{(s_i)} \quad (12.6)$$

Here $[G]^{(s_i)}$ is a $n_t \times r$ matrix, where the columns contain the pseudo-modal acceleration responses obtained using input sequence f_{s_i} , $\{\psi\}^{(s_k, s_i)}$ is a $r \times 1$ vector of product of mode shape coefficients corresponding to the s_i th input station and s_k th response station, and $\{y\}^{(s_i)}$ is a $n_t \times 1$ vector of acceleration response measured at the s_k th station due to input at s_i th station. With $n_t > r$, Eq. (12.6) can be solved in a least squares sense to obtain the estimate:

$$\{\hat{\psi}\}^{(s_k, s_i)} = [G]^{(s_i)\dagger} \{y\}^{(s_i)} \quad (12.7)$$

where \dagger represents the Moore-Penrose pseudo-inverse. Repeating Eqs. (12.2), (12.3), (12.4), (12.5), (12.6), and (12.7) for all input-output pairs, the following matrix of mode shape component products is obtained:

$$[\Psi] = \begin{bmatrix} \hat{\phi}_{s_k, m_1} \hat{\phi}_{s_1, m_1} & \hat{\phi}_{s_k, m_2} \hat{\phi}_{s_1, m_2} & \cdots & \hat{\phi}_{s_k, m_r} \hat{\phi}_{s_1, m_r} \\ \hat{\phi}_{s_k, m_1} \hat{\phi}_{s_2, m_1} & \hat{\phi}_{s_k, m_2} \hat{\phi}_{s_2, m_2} & \cdots & \hat{\phi}_{s_k, m_r} \hat{\phi}_{s_2, m_r} \\ \vdots & \vdots & \ddots & \vdots \\ \hat{\phi}_{s_k, m_1} \hat{\phi}_{s_p, m_1} & \hat{\phi}_{s_k, m_2} \hat{\phi}_{s_p, m_2} & \cdots & \hat{\phi}_{s_k, m_r} \hat{\phi}_{s_p, m_r} \end{bmatrix} \quad (12.8)$$

At this point it is to be emphasized that *one should have at least one collocated input-output measurement* (i.e., exciting and measuring at s_k station) to recover the individual mode shape components from the matrix $[\Psi]$. With collocated input-output measurements made at station s_k , the squared mode shape components at s_k can be obtained, from Eq. (12.7), as:

$$\{\hat{\psi}\}^{(s_k, s_k)} = \left[\hat{\phi}_{s_k, m_1}^2, \hat{\phi}_{s_k, m_2}^2, \dots, \hat{\phi}_{s_k, m_r}^2 \right]^T \quad (12.9)$$

and an element-wise square root operation yields mode shape components $\hat{\phi}_{s_k, m_j}$ corresponding to the s_k station and m_j th mode. Then, the measured mode shape matrix, of all r modes at all P sequentially excited stations, is obtained by dividing j th column of $[\Psi]$ by $\hat{\phi}_{s_k, m_j}$, for all $j = 1, 2, \dots, r$, resulting in the following estimate of the mode shape matrix:

$$[\hat{\Phi}] = \begin{bmatrix} \hat{\phi}_{s_1, m_1} & \hat{\phi}_{s_1, m_2} & \cdots & \hat{\phi}_{s_1, m_r} \\ \hat{\phi}_{s_2, m_2} & \hat{\phi}_{s_2, m_2} & \cdots & \hat{\phi}_{s_2, m_r} \\ \vdots & \vdots & \ddots & \vdots \\ \hat{\phi}_{s_p, m_1} & \hat{\phi}_{s_p, m_2} & \cdots & \hat{\phi}_{s_p, m_r} \end{bmatrix} \quad (12.10)$$

12.4 Noise-Induced Uncertainty in Modal Parameter Estimates

12.4.1 Numerical Test Bed

A numerically simulated set of input-output measurement data is obtained for a single span simply-supported Euler-Bernoulli beam with the following properties: $L = 20$ m, $EI = 3.2 \times 10^8$ Nm², $\rho A = 2000$ kg/m. A FE model consisting of 80 elements is used for the simulation of input-output measurements. The natural frequencies for the first four modes are 1.571, 6.283, 14.138, 25.135 Hz and the modal damping ratios for the first four modes are set equal to 2.5%, and 5% for the remaining modes. A total of 19 measurement stations ($s_1 - s_{19}$), equally spaced at 1 m intervals, is considered (as shown in Fig. 12.2). The actuator applies input excitations sequentially at all these 19 stations in 19 different tests. Random excitations bandlimited to 30 Hz are used as vertical input forces at each station. An accelerometer is fixed at station s_{11} (as shown in Fig. 12.2),

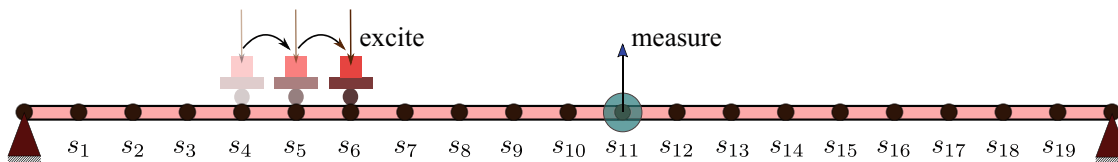


Fig. 12.2 Beam with measurement stations; the mobile actuator roves from one station to another during test to test; the accelerometer remains fixed at station s_{11}

measuring the acceleration responses at that location during all the 19 tests. No noise in measurements is considered in this simulation. The proposed formulation (as discussed in the preceding section) is used to find the mode shapes at the 19 station locations. Modal Assurance Criteria (MAC) is used for comparing the correlation of the estimated mode shapes with the true mode shapes of the beam. The MAC values, comparing the estimated mode shapes with the corresponding FE mode shapes, for the first four mode shapes are obtained as 1.000, 0.999, 0.999 and 0.997, respectively.

12.4.2 Effect of Noise in Measured Data

In practice, the recorded input-output measurement data are corrupted with measurement noise. Presence of noise in measurements induces errors in the estimates of identified natural frequencies and damping ratios. Moreover, as the mode shapes are estimated using the estimates of natural frequencies and damping ratios, the errors in identified natural frequencies and damping ratios also get propagated to the estimates of mode shapes. It is therefore necessary that the effect of different levels of noise in the measured data on the identified modal parameters be studied.

Numerically simulated data from the test bed described previously is used for studying the noise-induced uncertainty in the identified modal parameters. Measurement noise, modelled as zero-mean Gaussian white noise, is added to the input-output data. The noise level is defined as the ratio of the (root mean square) RMS of the noise to the RMS of the noise-free measurement for each measurement time history. Two levels of noise, namely 10% and 20%, are considered here. A set of 200 Monte Carlo simulations of modal parameter identification is performed for each level of measurement noise. In each simulation, the natural frequencies and the damping ratios are first identified from all the 19 noisy input-output data pairs (gathered from the 19 roving input tests). The Eigensystem Realization Algorithm with the Observer Kalman Filter Identification (ERA-OKID) [2] is employed for this purpose, along with the aid of stabilization diagrams. The estimated natural frequencies and damping ratios are then used for mode shape estimation using the proposed approach.

Normalized histogram plots, illustrating the probability distribution of the estimated natural frequencies and damping ratios for the first four modes, are shown in Figs. 12.3 and 12.4, respectively. The probability distribution of the MAC values, comparing the estimated mode shapes with the corresponding FE mode shapes, for the first four modes are shown in Fig. 12.5. The statistics (mean and coefficient of variation) of the identified frequencies, damping ratios, and MAC values are presented in Table 12.1, along with the corresponding values from the FE model.

It is observed that the modal parameter estimates for higher modes show decreasing uncertainty. This can be due to the presence of more energy in higher modes, as is evident from an example acceleration frequency response function, obtained by averaging over a set of 19 input-output measurements, shown in Fig. 12.6. It is also seen that presence of measurement noise induces more uncertainty in the identified damping ratios than in the identified natural frequencies, possibly due to the ability of ERA-OKID to estimate frequencies with higher accuracy than damping. Finally, the MAC values of mode shape estimates have higher variation in cases where the frequency estimation is poor compared to cases where damping ratio estimation is poor. This shows that the mode shapes estimates are more sensitive to errors in identified natural frequencies than to errors in identified damping ratios. Overall the proposed methodology performs reasonably well in presence of noise.

12.5 Conclusions

In this paper, a forced vibration modal testing method using a roving actuator and a single sensor has been investigated. The sensor remains fixed at a location and the roving actuator changes its location from test to test. A time-domain technique, based on input-output balance with pseudo-modal responses, has been developed. A numerical example of mode shape estimation using the approach has been demonstrated. Uncertainty in the identified modal parameters due to presence of

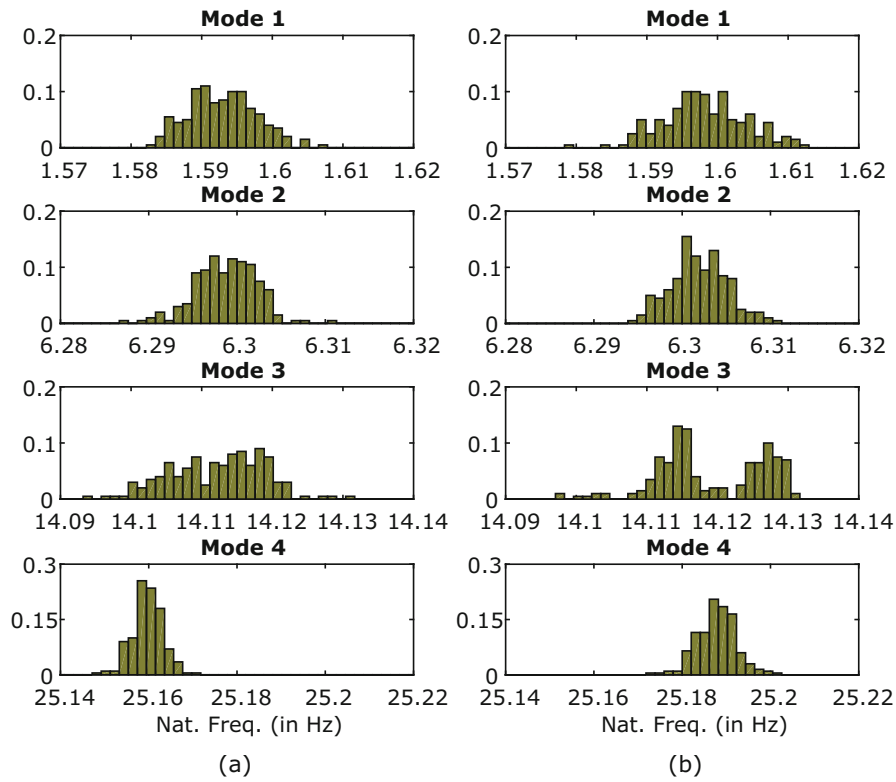


Fig. 12.3 Distribution of identified natural frequencies for modes 1–4 for different levels of noise; (a) Noise level = 10%, (b) Noise level = 20%

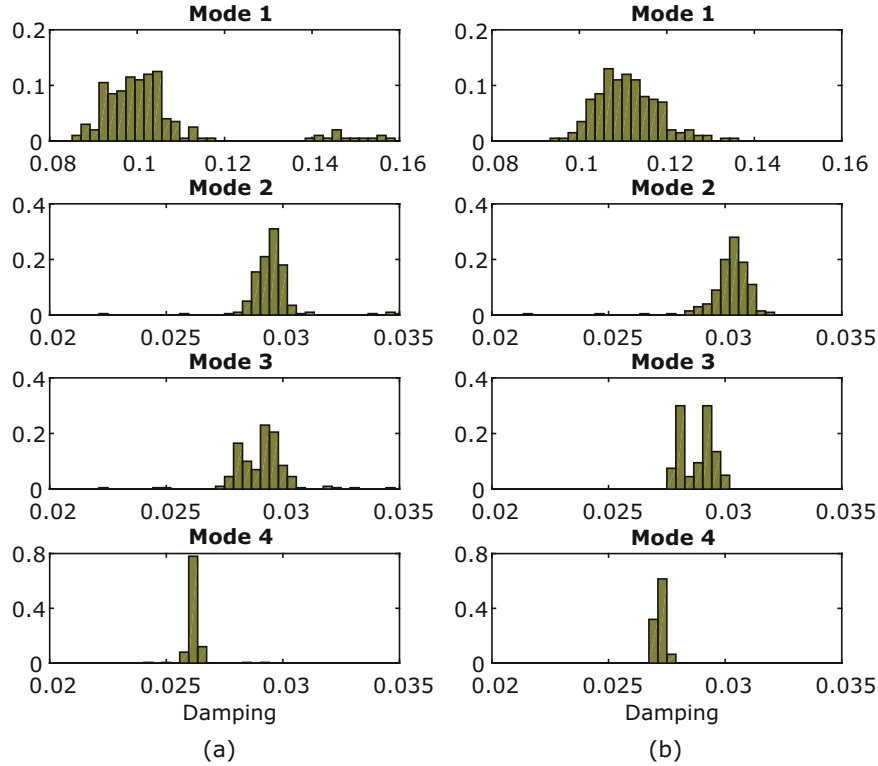


Fig. 12.4 Distribution of identified damping ratios for modes 1–4 for different levels of noise; (a) Noise level = 10%, (b) Noise level = 20%

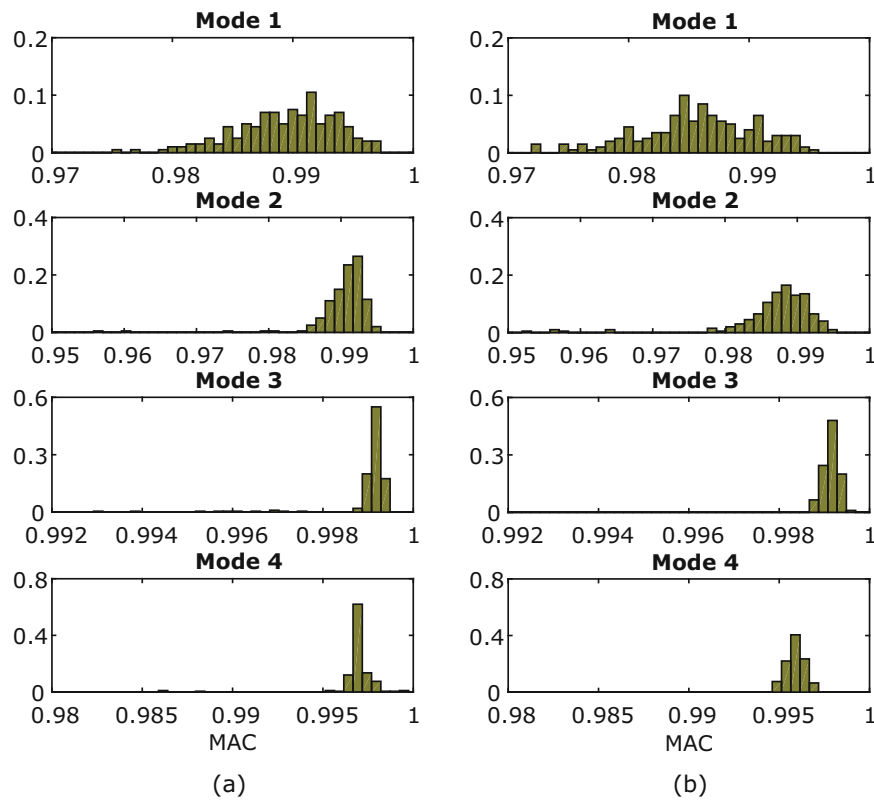


Fig. 12.5 Distribution of MAC values, comparing estimated mode shapes with corresponding FE mode shapes, for modes 1–4 for different levels of noise; (a) Noise level = 10%, (b) Noise level = 20%

Table 12.1 Statistics of identified modal parameters (COV = coefficient of variation)

		FE model	Identified (Noise level = 10%)		Identified (Noise level = 20%)	
			Mean	COV(%)	Mean	COV(%)
Natural frequency (Hz)	Mode 1	1.571	1.593	0.302	1.598	0.359
	Mode 2	6.283	6.299	0.055	6.302	0.051
	Mode 3	14.138	14.112	0.046	14.119	0.053
	Mode 4	25.135	25.160	0.014	25.188	0.027
Damping ratio(%)	Mode 1	2.5	10.320	13.677	11.100	11.359
	Mode 2	2.5	2.952	2.312	3.021	1.953
	Mode 3	2.5	2.901	2.955	2.880	2.817
	Mode 4	2.5	2.622	0.513	2.724	0.645
MAC	Mode 1	1	0.990	0.416	0.986	0.486
	Mode 2	1	0.990	0.411	0.987	0.609
	Mode 3	1	0.999	0.023	0.999	0.016
	Mode 4	1	0.997	0.032	0.996	0.048

different levels of measurement noise has been studied. Mode shape estimates obtained using the proposed approach are found to be more sensitive to errors in natural frequency estimates than to errors in damping ratio estimates. While the proposed method uses only a single actuator and a single sensor, and provides reasonably good estimates of the modal parameters, it needs multiple test set-ups.

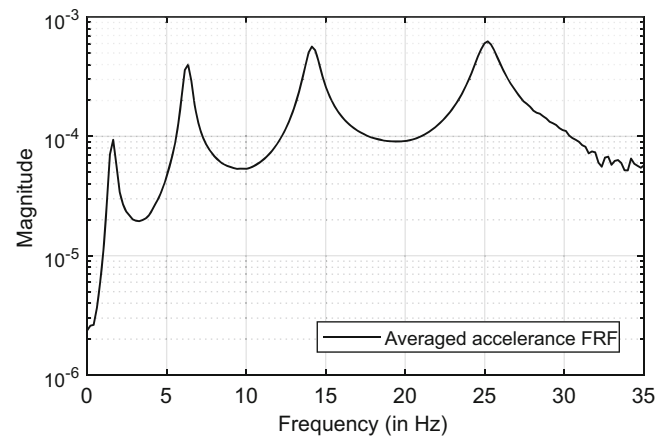


Fig. 12.6 A sample acceleration FRF plot in presence of 20% measurement noise

References

1. Cara, J., Juan, J., Alarcón, E.: Modal identification of structures from roving input data by means of maximum likelihood estimation of the state space model. In: Proceedings of the International Conference on Noise and Vibration Engineering – ISMA 2016 and International Conference on Uncertainty in Structural Dynamics – USD 2016, pp. 2923–2931 (2016)
2. Juang, J.N.: Applied System Identification. Prentice Hall, Englewood Cliffs (1994)
3. Marulanda, J., Caicedo, J.M., Thomson, P.: Modal identification using mobile sensors under ambient excitation. *J. Comput. Civil Eng.* **31**(2), 04016051 (2016)
4. Matarazzo, T.J., Horner, M., Pakzad, S.N.: High-resolution mode shape identification using mobile sensors. In: Topics in Modal Analysis & Testing, pp. 255–260. Springer, Cham (2016)
5. Mukhopadhyay, S., Luş, H., Betti, R.: Modal parameter based structural identification using input–output data: minimal instrumentation and global identifiability issues. *Mech. Syst. Signal Process.* **45**(2), 283–301 (2014)



Chapter 13

Validation of Lightweight Antenna Reflector Model for Environmental Acoustic Testing Operating Conditions

M. Alvarez Blanco, R. Hallez, A. Carrella, K. Janssens, and B. Peeters

Abstract Environmental testing is required in the space industry to evaluate the survivability of space hardware to the launch environment. Such hardware is designed according to high demands in terms of performance and lightweight (e.g. aiming to maximise the payload weight and increase fuel efficiency). Solar panels and antenna reflectors, typically made of carbon fiber reinforced polymers and honeycomb, are examples of sub-systems presenting large surfaces of lightweight materials which are particularly sensitive to acoustic loads. Environmental acoustic testing consists in reproducing the acoustic field of a Launch Vehicle (LV) with acoustic power distribution comparable to the operating conditions. The standard way to reproduce the acoustic loading is the so-called Reverberant Field Acoustic eXcitation (RFAX) test, which is a rather costly and time consuming test method. Therefore, at sub-system level, other dynamic tests than acoustic (especially those for model validation) are performed only if strictly necessary. An alternative to RFAX is Direct Field Acoustic eXcitation (DFAX) testing. This test method has emerged as a more cost-efficient qualification technique which, in addition, presents features to potentially improve the reproducibility of the launch environment (e.g. explicit setting of the acoustic field *spatial correlation* properties). In this paper, Operational Modal Analysis (OMA) is applied aiming to determine the dynamic characteristics of a parabolic-shape antenna reflector for DFAX operating conditions. This approach explores the possibility to exploit data collected during qualification tests also for modal model validation purposes. The objective of this research is the validation of the lightweight antenna reflector model by correlating numerical modal analysis results against OMA results. Modal-based correlation techniques followed by sensitivity analysis, help on error localisation and on the selection of proper model updating parameters. Then, the output of this correlation study allows updating the model, bringing the numerical modal model in better agreement with the experimental data acquired during the environmental acoustic test.

Keywords DFAX · DFAT · OMA · Environmental acoustic testing · Operational modal analysis

13.1 Introduction

Ground based environmental testing is a necessity to ensure the survivability of hardware during launch of spacecrafts (SCs). Testing methodologies for this purpose must provide a safe, effective and efficient control strategy to synthesize the dynamic loads an aerospace structure, – system or component – will encounter during its operational life. In case of the environmental acoustic test, the dynamical loads to be reproduced consist of the ones induced by the sound field inside the SC vehicle's fairing during ignition and lift-off launch stages.

The standard way to reproduce the acoustic loading is the so-called Reverberant Field Acoustic eXcitation (RFAX) test, which is a rather costly and time consuming test method. Therefore, at sub-system level, other dynamic tests than acoustic (especially those for model validation) are performed only if strictly necessary. An alternative to RFAX is Direct Field Acoustic eXcitation (DFAX) testing. DFAX is a testing method which does not require a dedicated facility and consists in setting an array of loudspeakers around the Device Under Test (DUT), as shown in Fig. 13.1. Through Multiple Input Multiple Output (MIMO) closed-loop control strategies, DFAX has shown good performance in achieving the environmental acoustic *test requirements* at the discrete controlled locations of the test volume [2–5]. Such *test requirements* consist only

M. Alvarez Blanco (✉)
Siemens Industry Software NV, Leuven, Belgium

KU Leuven, Department of Mechanical Engineering, Heverlee, Belgium
e-mail: mariano.alvarez_blanco@siemens.com

R. Hallez · A. Carrella · K. Janssens · B. Peeters
Siemens Industry Software NV, Leuven, Belgium

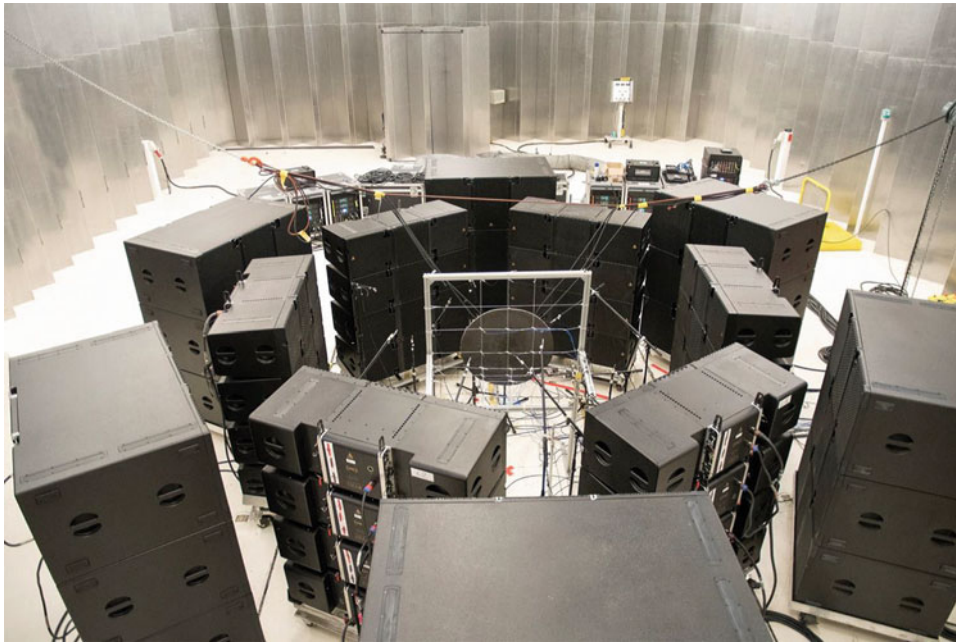


Fig. 13.1 DFAX experimental set-up [1]

of Sound Pressure Level (SPL) profiles, without specifying the structural response of the DUT. This makes sense, since structural responses depend on the DUT design and health-status. To the point that screening out deficiencies of design, parts or materials and workmanship is an objective of environmental testing. Due to this reason, structural responses are not controlled during environmental acoustic tests, but only monitored. However, growing interest has been focused on the structural response produced by DFAX, against more traditional testing methods like Reverberant Field Acoustic eXcitation (RFAX) [1, 6, 7].

The subject of this paper is not related to MIMO acoustic control *per se*, but to the exploitation of the structural vibration data acquired during such a test by means of Operational Modal Analysis (OMA). To the knowledge of the authors, the only previous work exploring a similar approach has focused on analysing the correlation between Experimental Modal Analysis (EMA) and OMA results [1]. In this paper, OMA is also applied aiming to determine the dynamic characteristics of a parabolic-shape antenna reflector for DFAX operating conditions. Nevertheless, the scope is different, since it is explored the possibility to exploit the data collected during qualification tests for numerical modal model validation purposes. Hence, the objective of this research is the validation of the lightweight antenna reflector FE model by correlating numerical modal analysis results against OMA results.

The paper is organised as follows, Sect. 13.2 describes the launching operating conditions and a model to derive the expected structural response of the DUT to acoustic fields with different *spatial correlation* properties. In Sect. 13.3 the expected structural responses are expressed in terms of an output Spectral Density Matrix (SDM), and the analysis is briefly linked to the theoretical aspects of OMA. Section 13.4 introduces the numerical model of the DUT and the (modal) pre-test analysis aiming to determine the optimal location for the sensors to measure the vibration on the DUT. Section 13.5 presents the results of DFAX tests and OMA and analyses the coupling between acoustical and structural dynamics. Next, Sect. 13.6 uses these results to calibrate the numerical model. Modal-based correlation techniques followed by sensitivity analysis, help on error localisation and on the selection of proper model updating parameters. Then, the output of the correlation study allows updating the model, bringing the numerical modal model in better agreement with the experimental data acquired during the environmental acoustic test. Finally, Sect. 13.7 consists of the conclusions of this research.

13.2 Payload Fairing Acoustic Environment: The Operating Conditions

Traditional environmental acoustic testing methodology requires a large reverberant acoustic room (i.e. RFAX). All tests in this kind of facilities are based on the assumption that the sound field is diffuse [8]. A diffuse acoustic field is normally defined as being due to an *infinite* number of uncorrelated plane waves, generated by remote acoustic sources, which, on

average, provide equal incident energy from all directions [9–11]. Since the theoretical distant sources generating these waves are uncorrelated there would be no interference pattern phenomena in such a sound field, and consequently the field would be completely homogeneous and isotropic. Ideally, the sound pressure level (SPL) would be the same at all positions, and temporal correlation functions between linear quantities measured at two points would depend only on the distance between the two points [8]. However, the assumption of diffuseness in a reverberant room for RFAX is only a reasonable approximation for the excitation frequencies above the room's Schroeder frequency. Below this frequency, individual modes of the source room can dominate the pressure field which is not diffuse [11]. As there is not enough overlapping of modes due to low modal density, at least in the lower frequency bands, the acoustic field in this facility might produce partially correlated dynamical loads to the DUT.

Although previous works in reverberant chambers have reported lack of SPL spatial uniformity [4], potential deviation from the correlation coefficient reference and structure responses dependent on specimen locations [12], RFAX is still considered as representative of the non-deterministic acoustic environment inside the SC vehicle's fairing and an appropriate method to evaluate the survivability of a payload during launch. However, on the one hand building a reverberant chamber suitable for spacecraft testing is expensive. On the other hand, transporting a sensitive space structure to an existing facility is risky, costly and time consuming.

An approximation to a perfect diffuse sound field might be generated by a number of loudspeakers driven by uncorrelated noise in a large anechoic room, as described in an experimental investigation [13]. The anechoic facility provides a free-field condition which ensures that the acoustic waves are directly arriving from the acoustic sources without boundary reflections. In the practical realization of such an artificial diffuse sound field, an array of acoustic sources in an ordinary room can be used to reproduce the *spatial correlation* properties of a random pressure field. This is how DFAX testing emerges as a cost-efficient technique for component and subsystem acoustic testing. In order to achieve the *test requirement*, the acoustic field must be controlled by placing an array of control microphones between the loudspeakers and the DUT. In addition, monitoring microphones can also be placed in the test volume to evaluate the spatial uniformity of energy density at the uncontrolled points of the acoustic field.

The principles of DFAX testing with MIMO random control strategies rely on the generation of a limited amount of independent acoustic wavefronts. Although this may call into question the capability of DFAX to reproduce a theoretical diffuse acoustic field, it has been shown that state-of-the-art MIMO control strategies for DFAX can achieve enough SPL spatial uniformity at the discrete controlled locations of the test volume [14]. In addition, such control strategies provide a unique feature to DFAX. They allow to explicitly set as MIMO test target SDM, the *spatial correlation* properties of the aimed acoustic field [15]. In this way, and unlike RFAX, the acoustic field reproduced by DFAX with MIMO may be independent of the facility where the test is conducted. Which brings a unique added value to DFAX, the capability to define launcher dependent environmental acoustic *test requirements* to reproduce more accurately the launching operational conditions. Not just in terms of SPL, but also taking into account *spatial correlation* properties of the acoustic field inside the SC vehicle's fairing.

13.2.1 Payload's Subsystem Structural Response

A DUT was kindly provided by Thales Alenia Space (Toulouse, France). It consisted of the parabolic-shape antenna reflector shown in Fig. 13.2, an essential subsystem of a telecommunication satellite. Subsystems like this one are typically made of carbon fiber reinforced polymers and honeycomb, presenting large surfaces of lightweight materials which are particularly sensitive to acoustic loads. Since the objective of this paper concerns the analysis of the structural dynamics of the DUT, it is meaningful to understand and model the fluid-structure coupling in the test volume. In other words, to model how the acoustic waves load the DUT and to foresee how the structure would response. On the next section, this model allows assessing the suitability of OMA assumptions for the estimation of the modal parameters.

The dynamic behaviour of the DUT can be studied considering the structure as a discrete mechanical system with multiple degrees of freedom. Such system can be described by following matrix differential equations:

$$[\mathbf{M}] \{\ddot{\mathbf{x}}(t)\} + [\mathbf{C}] \{\dot{\mathbf{x}}(t)\} + [\mathbf{K}] \{\mathbf{x}(t)\} = \{\mathbf{F}(t)\} \quad (13.1)$$

where $[\mathbf{M}]$ is the mass matrix, $[\mathbf{C}]$ is the damping matrix, $[\mathbf{K}]$ the stiffness matrix, $\{\mathbf{F}(t)\}$ is the forcing vector as a function of time and $\{\mathbf{x}(t)\}$ is the response vector as a function of time. Introducing the transformation to modal coordinates by Eq. (13.2),

$$\{\mathbf{x}(t)\} = [\Phi] \{\boldsymbol{\eta}(t)\} \quad (13.2)$$



Fig. 13.2 DUT: Antenna reflector kindly provided by Thales Alenia Space

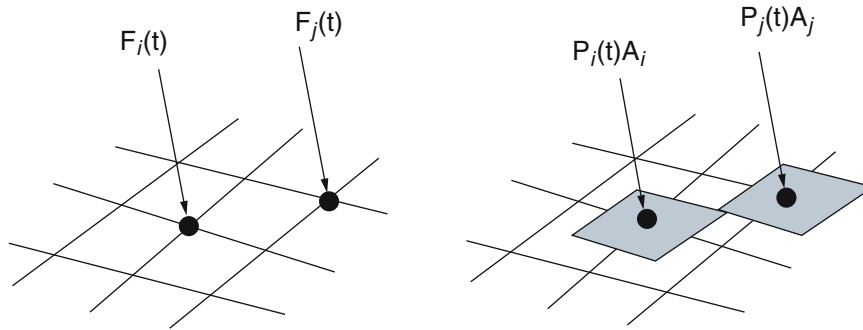


Fig. 13.3 Forces and pressures exciting DOFs and differential areas corresponding to such DOFs [17]

and assuming diagonal form for the generalized damping matrix [16] yield, for a single degree of freedom (DOF) i , the following decoupled equation:

$$\ddot{\eta}_i(t) + 2\zeta_i\omega_i\dot{\eta}_i(t) + \omega_i^2\eta_i(t) = \frac{\{\boldsymbol{\phi}_i\}^T \{\mathbf{F}(t)\}}{m_i} = f_i(t) \quad (13.3)$$

where $i = 1, 2, \dots, n$; $\{\boldsymbol{\phi}\}$ is an eigenvector or mode shape, $[\boldsymbol{\Phi}]$ the modal base, n is the number of generalized coordinates, ζ_i is the modal damping ratio and m_i is the generalized mass.

The cross-correlation between forces $F_i(t)$ exciting DOFs at the surface of the DUT is:

$$R_{F_i F_j}(\tau) = \lim_{T \rightarrow \infty} \frac{1}{2T} \int_{-T}^T F_i(t) F_j(t - \tau) dt \quad (13.4)$$

Such forces can be approximately translated into pressures $P_i(t)$ over differential areas A_i . This is shown in Fig. 13.3 and written in Eq. (13.5) for DOF i .

$$F_i(t) = \int_A P(t) dA \approx P_i(t) A_i \quad (13.5)$$

Combining Eqs. (13.2), (13.3), (13.4), and (13.5) allows to rewrite the cross-correlation in modal coordinates as:

$$R_{f_i f_j}(\tau) = \frac{1}{m_i m_j} \{\boldsymbol{\phi}_i\}^T A_i R_{P_i P_j}(\tau) A_j \{\boldsymbol{\phi}_j\} \quad (13.6)$$

where \cdot^T is the *transpose* operator. Based on the Wiener–Khinchine theorem, the cross-correlation can be Fourier transformed into cross-spectra [18]. Then, the cross-spectra between forces exciting the structure is a function of the acoustic cross-spectra between pressures over the structure's surface.

$$S_{f_i f_j}(\omega) = \frac{1}{m_i m_j} \{\phi_i\}^T A_i S_{p_i p_j}(\omega) A_j \{\phi_j\} \quad (13.7)$$

When MIMO control strategies are applied for DFAX testing, the acoustic cross-spectra can be explicitly defined by the controller user as test target SDM [14]. More specifically, in terms of cross-spectral densities (CSDs), which are function of the *ordinary coherence* $\gamma_{ij}^2(\omega)$ and the *expected phase* $\phi_{ij}(\omega)$ between pressures at the DOFs:

$$S_{p_i p_j}(\omega) = \sqrt{\gamma_{ij}^2(\omega) \text{PSD}_i(\omega) \text{PSD}_j(\omega)} e^{j\phi_{ij}(\omega)} \quad (13.8)$$

where PSD is the pressure power-spectral density at such DOFs. Usually, for DFAX testing these PSDs are set equal, because spatial uniformity of SPL is aimed. Then, Eq. (13.8) can be rewritten in matrix notation involving all the DOFs as:

$$[\mathbf{S}_{pp}(\omega)] = \text{PSD}(\omega) [\mathbf{D}(\omega)] \quad (13.9)$$

where $[\mathbf{D}(\omega)]$ comprehends the *spatial correlation* properties of the acoustic field [11] (e.g. *sinc*($k r_{ij}$) function for a theoretical diffuse field, where k is the wave number and r_{ij} the distance between DOFs [19]). Combining Eq. (13.7) in matrix notation and Eq. (13.9) yields Eq. (13.10):

$$[\mathbf{S}_{ff}(\omega)] = \text{PSD}(\omega) [\mathbf{M}]^{-1} [\mathbf{J}^2(\omega)] [\mathbf{M}]^{-1} \quad (13.10)$$

where $[\mathbf{J}^2]$ is the so-called *joint acceptance* matrix multiplied by the *modal mass* diagonal matrix. The *joint acceptance* can be interpreted as a measure of the coupling between the structure and the acoustic field [18, 20, 21]. This is clearly shown by each element of such matrix, the *joint acceptance* function:

$$J_{ij}^2(\omega) = \{\phi_i\}^T A_i D_{ij}(\omega) A_j \{\phi_j\} \quad (13.11)$$

Finally, the dynamic response of the structure to the acoustic excitation, in a field with certain $[\mathbf{D}(\omega)]$, is determined by Eq. (13.12).

$$[\mathbf{S}_{\eta\eta}(\omega)] = [\mathbf{T}(\omega)] [\mathbf{S}_{ff}(\omega)] [\mathbf{T}^*(\omega)] \quad (13.12)$$

where $[\mathbf{T}(\omega)]$ is the diagonal matrix formulation for the FRFs. Hence, the cross-spectra matrix between physical displacement \mathbf{x} is:

$$[\mathbf{S}_{xx}(\omega)] = [\Phi] [\mathbf{S}_{\eta\eta}(\omega)] [\Phi]^T \quad (13.13)$$

where the diagonal of this matrix retrieves the PSDs for the displacement, while the off-diagonal elements consist of the CSDs.

13.3 Operational Modal Analysis

OMA is used to derive an experimental dynamic model from vibration measurements on a structure in operational conditions. Such model is based on the modal decomposition of the output cross-spectra matrix, $[\mathbf{S}_{xx}(\omega)]$. This matrix was derived in the previous section and can be rewritten by combination of Eqs. (13.10), (13.11), (13.12), and (13.13):

$$[\mathbf{S}_{xx}(\omega)] = [\Phi] [\mathbf{T}(\omega)] [\Phi]^T [\mathbf{S}_{ff}(\omega)] [\Phi] [\mathbf{T}^*(\omega)] [\Phi]^T = [\mathbf{H}(\omega)] [\mathbf{S}_{ff}(\omega)] [\mathbf{H}(\omega)]^H \quad (13.14)$$

where $[\mathbf{H}(\omega)]$ is the FRF matrix relating input-output *physical* magnitudes, \bullet^H is the complex-conjugate transpose operator and $[\mathbf{S}_{\mathbf{FF}}(\omega)]$ the cross-spectra between *physical* forces exciting the structure. It is well known that the modal decomposition of an FRF matrix $[\mathbf{H}(\omega)]$ is [22]:

$$[\mathbf{H}(\omega)] = \sum_{i=1}^n \frac{\{\phi_i\} \{I_i^T\}}{j\omega - \lambda_i} + \frac{\{\phi_i^*\} \{I_i^H\}}{j\omega - \lambda_i^*} \quad (13.15)$$

where $\{I_i\}$ are the *modal participation factors* and λ_i are the *poles*.

The deterministic knowledge of the acoustic excitation on the surface of the DUT is replaced by the assumption that the input is *white noise*. A property of white noise is that it has a constant power spectrum. Hence $[\mathbf{S}_{\mathbf{FF}}(\omega)]$ in Eq. (13.14) should be independent of the circular frequency ω [23]. The modal decomposition of the output spectrum matrix is obtained by inserting Eq. (13.15) into Eq. (13.14) and converting to the partial fraction form [24–26]:

$$[\mathbf{S}_{\mathbf{xx}}(\omega)] = \sum_{i=1}^n \frac{\{\phi_i\} \{\mathbf{g}_i^T\}}{j\omega - \lambda_i} + \frac{\{\phi_i^*\} \{\mathbf{g}_i^H\}}{j\omega - \lambda_i^*} + \frac{\{\mathbf{g}_i\} \{\phi_i^T\}}{-j\omega - \lambda_i} + \frac{\{\mathbf{g}_i^*\} \{\phi_i^H\}}{-j\omega - \lambda_i^*} \quad (13.16)$$

where $\{\mathbf{g}_i\}$ are the *operational reference factors*, which replace the *modal participation factors* in case of output-only data. The goal of OMA is to identify the *right hand side* terms of Eq. (13.16) based on the responses measured during the DFAX testing procedure. This is done by pre-processing the operational data with a non-parametric spectrum estimate like the *weighted correlogram*. Further details on the estimation of spectra from the measured time histories in a modal analysis context can be found in Ref. [24]. Pre-processing this operational data allows using PolyMAX for the estimation of the modal parameters in Eq. (13.16). A detailed description for the application of PolyMAX on OMA can be found in Refs. [23, 27, 28].

As mentioned above, the main theoretical assumption in OMA is that the input is a realization of a stochastic process (*white noise*) [27]. This is not only presuming constant power spectrum, but also conjecturing that off-diagonal elements of $[\mathbf{S}_{\mathbf{FF}}(\omega)]$ in Eq. (13.14) are null at each spectral line. If such assumptions are violated, for instance, if the input contains in addition to *white noise* also some dominant frequency components, these frequency components cannot be separated from the eigenfrequencies of the system and will be identified as such [23]. In addition, if constant but fully correlated inputs excite the structure at some frequencies, these frequency components may not be separated from the eigenfrequencies of the system either. In DFAX such kind of violations can be exploited to identify acoustic standing waves in the field, as it is explained below in Sect. 13.5.

13.4 Specimen Numerical Model

The DUT is an antenna reflector composed of composites materials. These composites are sandwich structures with external surfaces having high strength limit and a core made of a very light-weight material. In case of this antenna reflector, the core consists of a honeycomb structure designed according to the pressures to which the sandwich structure is subjected in operating conditions.

13.4.1 Pre-test Analysis for OMA

Since it is necessary to acquire useful data to estimate the modal model of the DUT, pre-testing is the former step to design a proper OMA setup. In a DFAX test where OMA is also aimed, the structural responses should be measured in such a way that all modes are measured and clearly identified out of the observed dynamics (i.e. observability assumption in modal analysis and orthogonality of modal eigenvectors) [22]. Pre-test analysis helps minimizing the amount of measured degrees of freedom (DOFs) while *spatial aliasing* is avoided [22]. Nevertheless, such analysis needs a preliminary FE-model to make available a modal basis in a large number of DOFs. Then, the test conditions can be mimicked by retaining the modal information in a set of chosen measuring DOFs. Lack of reliable information regarding the material properties of the DUT during the pre-test stage constrained the design of the preliminary FE model. Therefore, for mesh design and

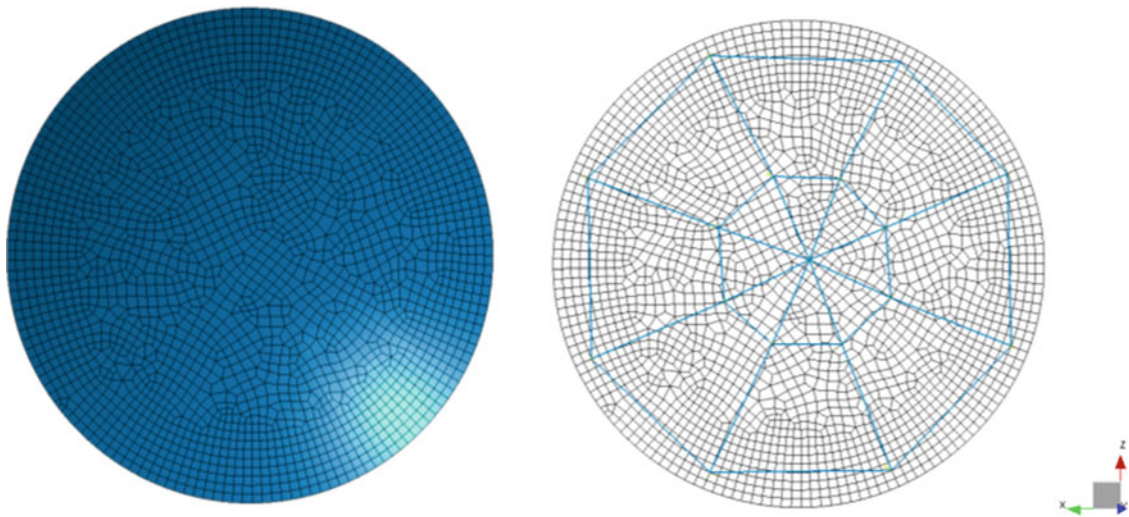


Fig. 13.4 Left: FE model of the DUT. Right: wireframe of transducers on the DUT

placement of measuring DOFs, it was assumed the specimen had axisymmetric parabolic-shape and was made of a unique set of orthotropic materials (i.e. orthotropic external skins and orthotropic core). The preliminary FE-model designed in LMS Virtual.Lab is shown on the left of Fig. 13.4.

Although in launching operational conditions this kind of antenna reflector is attached to a larger structure, or full system (i.e. satellite), the environmental acoustic tests to qualify this component are commonly performed with free-free boundary conditions [7]. Therefore, these were the boundary conditions used to design the model. The mesh of the preliminary structural model consists of 2329 shell quadrilateral linear elements. From this FE-model are derived the structural modal vectors with their corresponding resonance frequencies. Figure 13.5 shows the simulation of the antenna deformation (magnitude). This kind of nodes and antinodes visualization helped to design the wireframe shown on the right of Fig. 13.4, where 17 accelerometers were arranged in two rings on the external surface of the DUT. Until 1020 Hz, the modes present shapes like shown on the top-left plot in Fig. 13.5, but with increasing amount of nodal lines along the specimen diameter. As in environmental acoustic testing the acoustic dynamical loads are generally reproduced up to 10,000 Hz, it is attempted to extend the structural dynamic analysis up to, at least, 1500 Hz. Therefore, with this objective in mind, measurement DOFs need to be located in the inner ring on the specimen, as shown on the right of Fig. 13.4. Such statement is supported by the bottom left and right mode shapes in Fig. 13.5, which show antinodes in this region of the DUT. Further analysis, based on the Auto-Modal Assurance Criterion (Auto-MAC) matrix shown in Fig. 13.6, indicates that extending the bandwidth of analysis to 1500 Hz with 17 sensors (arranged as shown in Fig. 13.4) could compromise the assumption of observability in modal analysis. However, increasing the amount of sensors was not considered feasible due to the lack of equipment availability besides, eventual mass loading of the light-weight structure was trying to be avoided.

13.5 DFAX Testing and OMA

In the frame of the DFAX test campaign conducted at Siemens PLM's semi-anechoic facility in Leuven, Belgium, an elaborated test programme was performed:

- Open-loop (OL) tests: the MIMO controller is not active; the loudspeakers are driven by independent shaped random noise.
- Closed-loop (CL) tests: the MIMO controller is active and the objective is to reproduce a pre-defined power and cross spectral density matrix at 12 (or 16) control microphones in order to reproduce acoustic fields with different *spatial correlation* properties (target SDM).
- Different loudspeaker driving strategies: the amount of active loudspeakers remains the same, but the number of independent drives sent to the loudspeakers varies (6, 9 or 12). The number of control microphones is linked somehow to the number of drives and equals respectively 12, 12 and 16.
- Tests at multiple excitation/SPLs. For instance, closed-loop tests were performed at 101, 104, 107, 110, 113 dB.

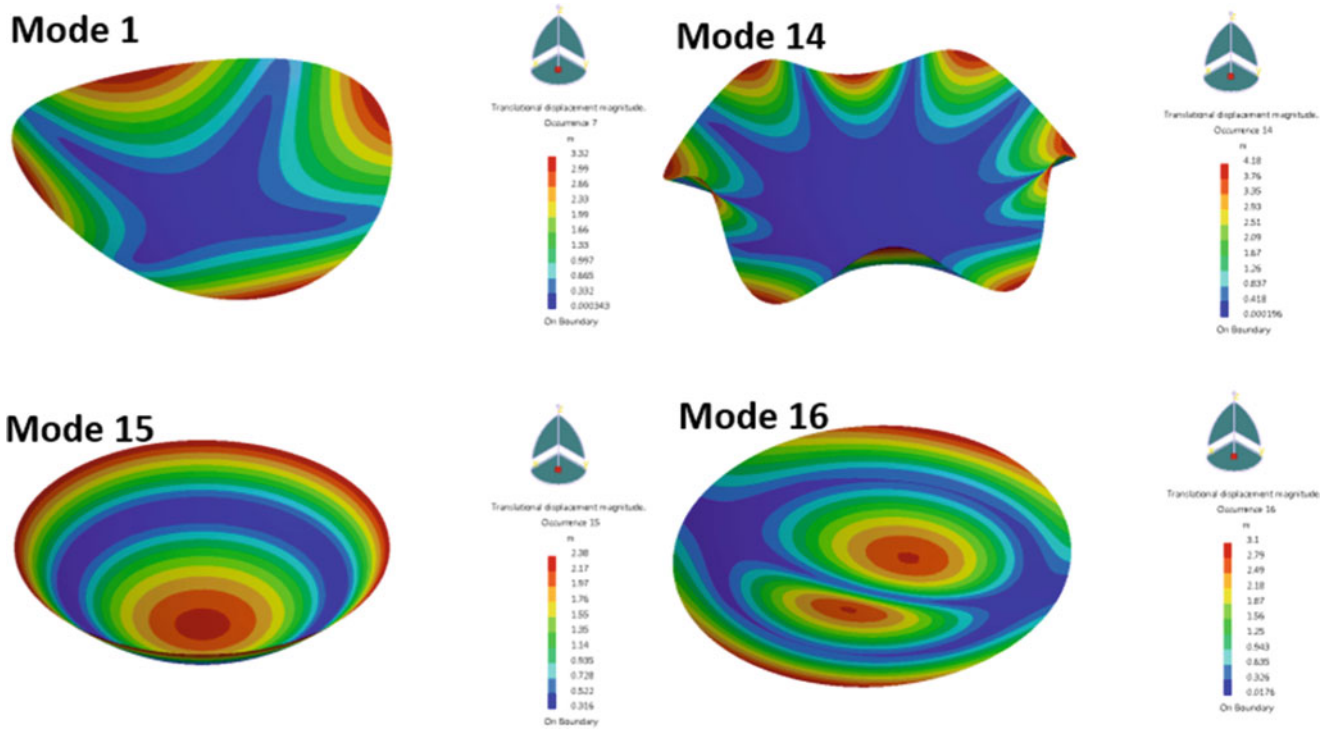


Fig. 13.5 Visualization of simulated mode shapes (magnitude) for the preliminary model of the DUT. Top-left corresponds to eigenfrequency: 169.7 Hz. Top-right: 1013.1 Hz. Bottom-left: 1248.9 Hz. Bottom-right: 1368.5 Hz

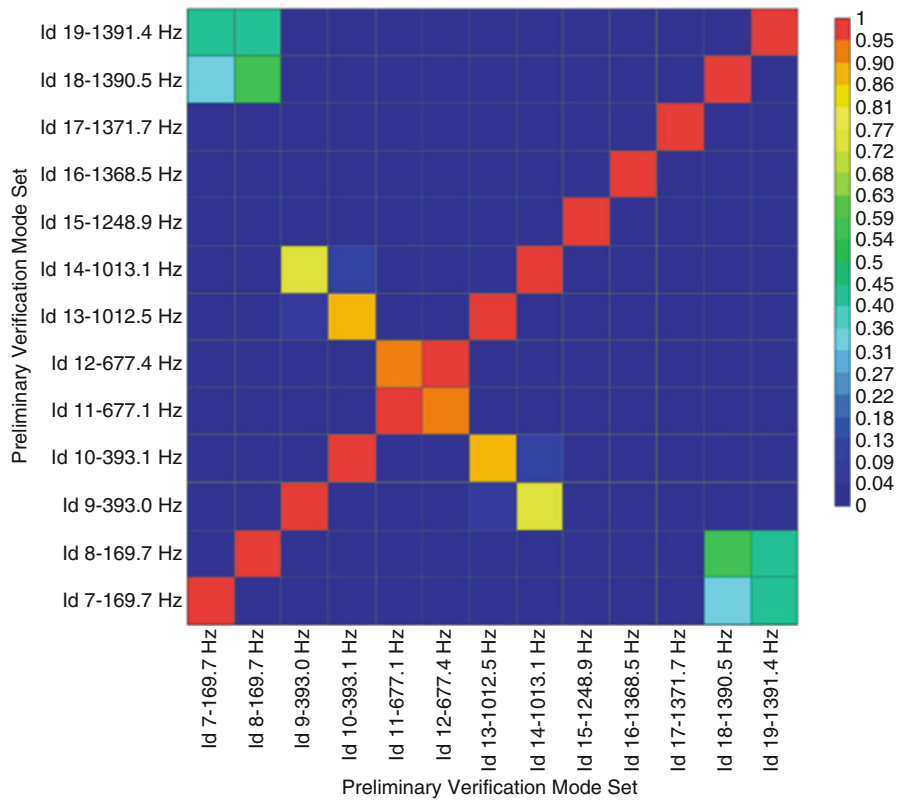


Fig. 13.6 Auto-MAC matrix for preliminary model of the DUT

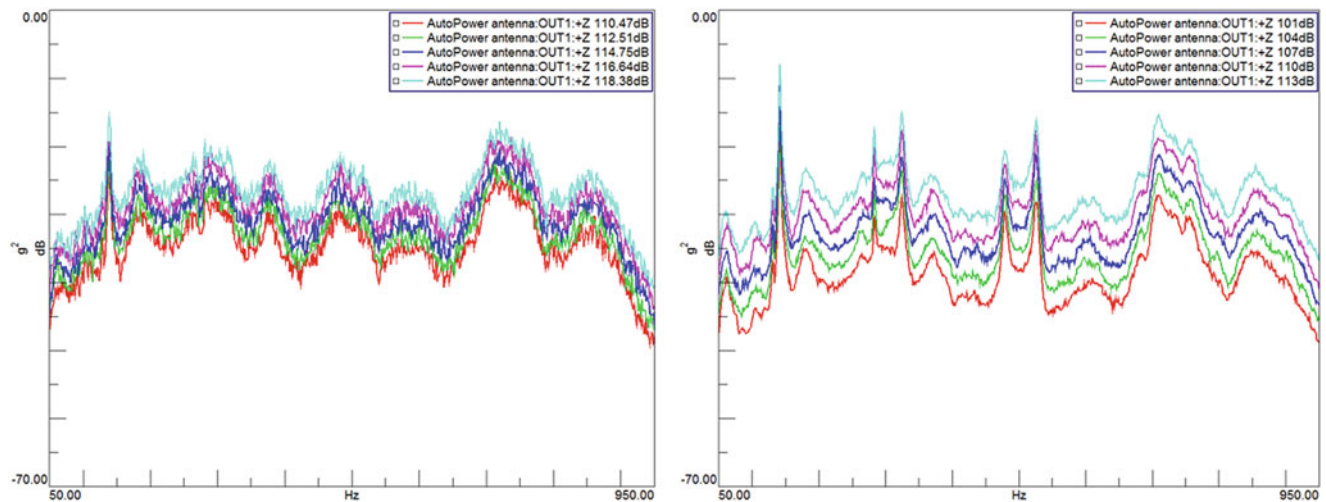


Fig. 13.7 Acceleration power spectra measured at the DUT for five different sound pressure levels Left: OL 12. Right: CL 12

The DFAX test set-up is shown in Fig. 13.1. The loudspeakers and amplifiers were provided by DV2, a company that provides sound engineering services and equipment for indoor and outdoor concerts. Although the DFAX application is a bit atypical, standard sound system equipment was used. The acoustic field was instrumented with 34 microphones and the specimen was equipped, as described in detail on the previous section, with 17 accelerometers. The data was acquired using LMS SCADAS hardware and LMS Test.Lab MIMO Random Control software. A subset of the test results are discussed in the following.

On the left, Fig. 13.7 shows the power spectra measured at one location at the DUT for open-loop tests with 12 drives (OL 12) and 5 different SPLs. On the right of the same figure, the power spectra measured at the same location but for closed-loop tests with 12 drives (CL 12), and similar SPLs. The curves on the left look “noisier” since the length of the OL test was shorter than in case of CL tests, while frequency resolution, averaging and windows settings for the estimation of the PSDs were the same. Figure 13.8 shows the Operational PolyMAX stabilization diagrams from which the modes can be objectively selected. The diagram on the left corresponds to OL 12 and the one on the right to CL 12. The *sum of cross-spectra* from OL 12 shows, consistently with curves in Fig. 13.7, a “noisier” shape and lower magnitude at the peaks. However, although the sharp definition of the CL 12 curve on the right foresees an easier analysis for modes picking, stabilization diagrams for the same model order (80) show that clearer diagram is obtained for OL 12 than for CL 12. This may be due to the validity of the white noise assumption for OMA. Although in both cases, OL and CL, the loudspeakers are driven by shaped random noise, in OL the 12 drives are uncorrelated (i.e. independent). While in case of CL 12 they are partially correlated. Correlation between drives does not (necessarily) translates into correlation between structural loads. Nevertheless, since measuring the distribution of acoustic pressure loads exactly on the surface of the DUT is not industrially feasible, it is fair to assume that OL 12 will excite the DUT closer to white noise (i.e. so-called “rain on the roof” excitation in vibro-acoustic) than CL 12, especially at mid-high frequency.

Figure 13.9 allows comparing the mode sets estimated for CL 12 (y-axis) and for OL 12 (x-axis) tests through a MAC matrix. Pink blocks highlight a subset of modes following certain correlation pattern. Since these modes were selected from the PolyMAX stabilization diagrams, they should correspond to *physical* modes [29]. However, such pattern is showing high correlation between very distant eigenfrequencies, suggesting the modes may not belong strictly to the structural system, but to the acoustic field, namely, the fluid bounded by the loudspeakers array. Previous publications have pointed out that acoustic standing waves and interference patterns may generate acoustic pressure nodes and antinodes in the test volume during environmental acoustic testing [1, 12]. Such standing waves may be a consequence of the cylindrical shape of the loudspeakers array (see Fig. 13.11) and the geometry of the room where the test is being carried out. Since in this research the room is a semi-anechoic facility, special attention is given to the loudspeaker configuration in order to explain if the “additional modes” appearing on the OMA mode sets are indeed due to acoustic modes loading coherently the structure.

Figure 13.10 shows the mode shapes for modes 4, 9, 10 and 13 of the CL 12 mode set. The first three of them look like rigid body modes, while the last one starts showing some flexural motion (dynamics). This difference is because at lower frequency acoustic waves are likely to excite the surface of the structure in a correlated way. Therefore, producing a rigid-body-like motion. In this respect, previous publication highlights the importance of understanding *low/high frequency* as a

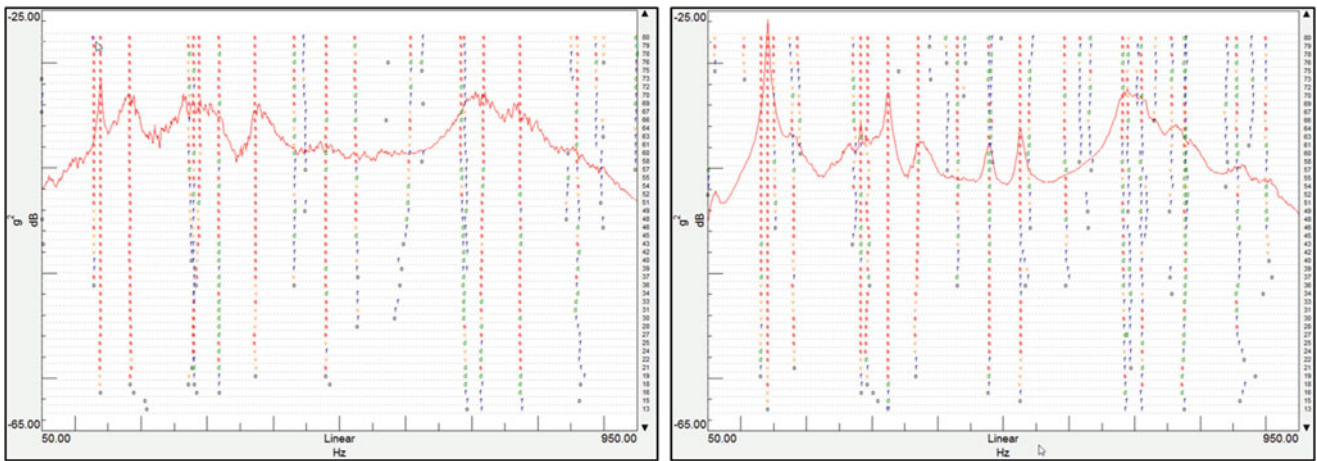


Fig. 13.8 Operational PolyMAX stabilization diagram. Left: OL 12. Right: CL 12

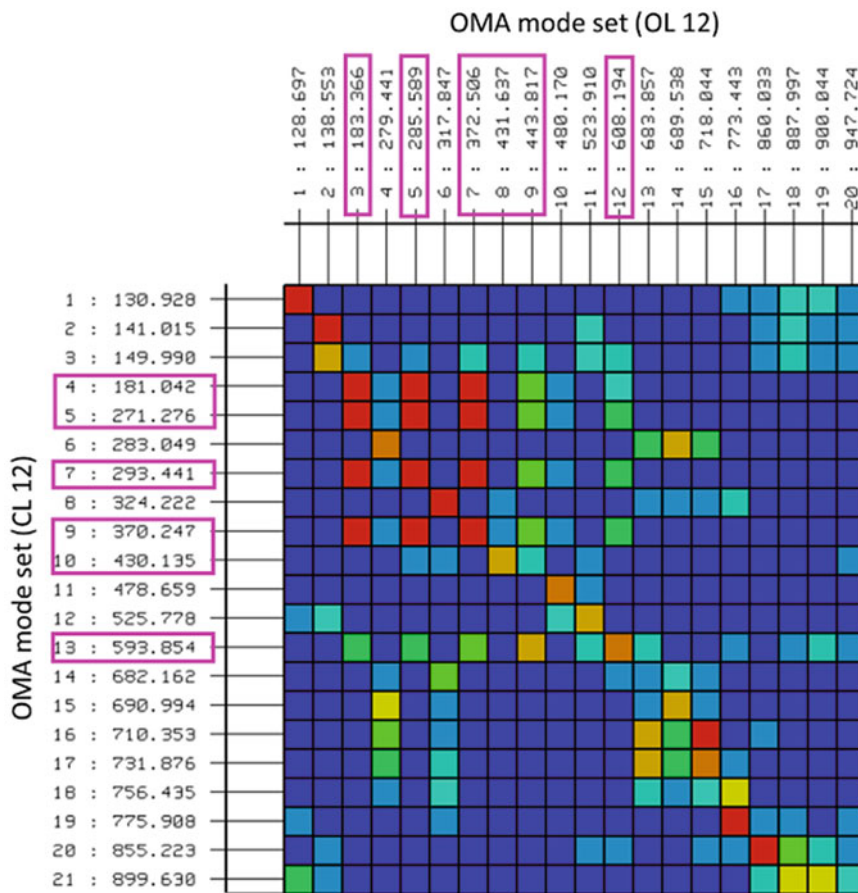


Fig. 13.9 MAC matrix between CL 12 and OL 12 mode sets

relative concept in vibro-acoustics. A concept which is mainly dependent on the dimension of the structures involved in the fluid-structure interaction. Then, the lower the frequency, or the more comparable the *acoustic wavelength* to the size of the DUT (diameter = 0.7 m), the higher the expected correlation between acoustic loads [17].

A meaningful proof supporting the hypothesis of acoustic modes producing the “additional structural modes” is that the latter appear in both mode sets: CL 12 and OL 12 [1]. This means that such “additional modes” are not dependent on the partial correlation generated by the MIMO controller, which may induce acoustic interference patterns in the field. On the

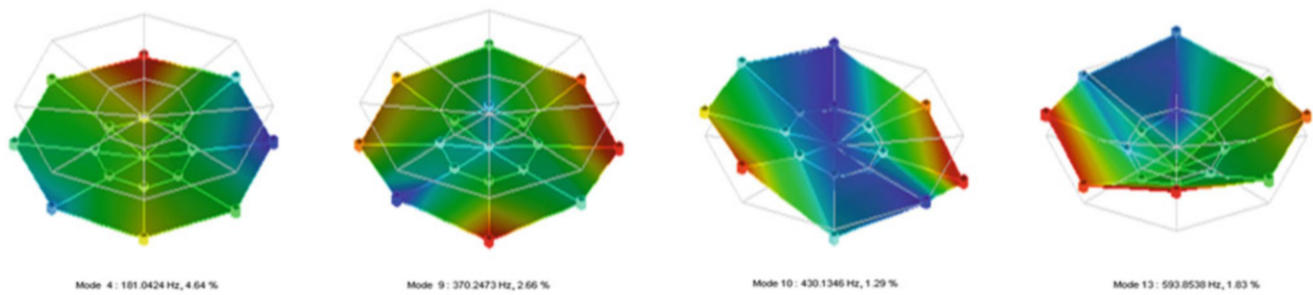


Fig. 13.10 “Additional modes” obtained from the DFAX data. Their eigenfrequencies correspond, from left to right, to: 181.0, 370.2, 430.1, 593.9 Hz [1]

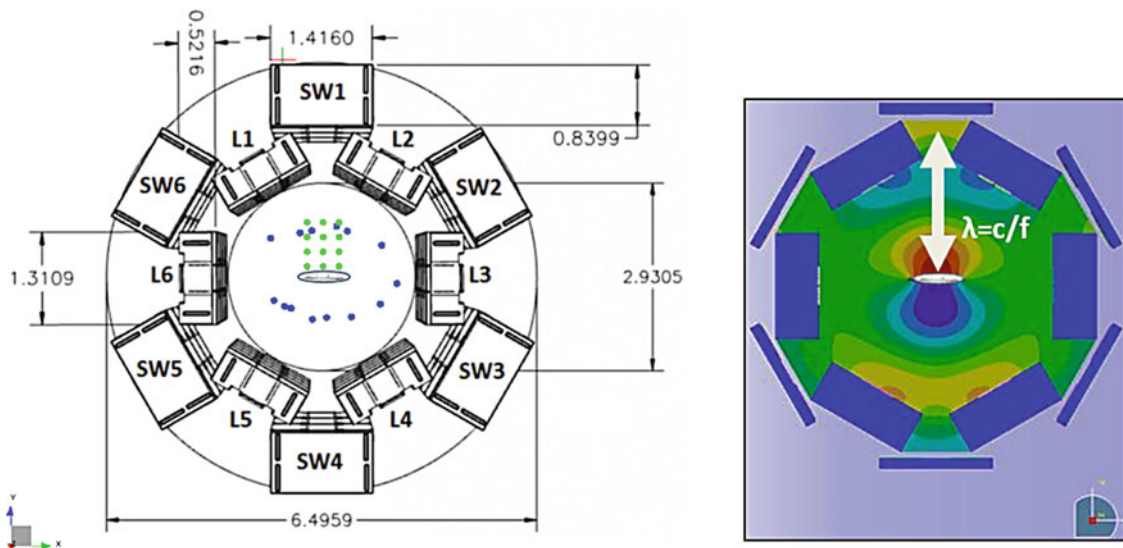


Fig. 13.11 Top-view of the DFAX electroacoustic setup. Left: Microphones placement, blue dots for control and green for monitoring. Right: Simulated acoustic modal analysis, cross-section of the pressure field at frequency 173.6 Hz; where c is the speed of sound, λ the acoustic wavelength and f the frequency

contrary, these “additional modes” are produced only due to the boundary and the atmospheric conditions (i.e. the latter determine the speed of sound, therefore, the acoustic wavelength). And such conditions did not change significantly between CL 12 and OL 12 tests.

In order to further analyse this phenomenon, Fig. 13.11 shows a top-view of the DFAX electroacoustic setup and an horizontal cross-section of the pressure field for frequency 173.6 Hz. On the left, it can be observed the placement of the loudspeakers (L1–6) and the sub-woofers (SW1–6), and the location of the control microphones 1–16 (blue dots) and monitoring microphones 17–34 (green dots). On the right of the same figure, acoustic modal analysis was simulated by a FE model designed in LMS Virtual.Lab. The presence of periodical pressure nodes at the predicted pressure field seems to evidence acoustic modes in the cavity between loudspeakers. Actually, the highlighted distance between antinodes corresponds to the wavelength of an acoustic standing wave exciting the DUT surface coherently. This may explain the presence of “additional modes” on the OMA mode sets. The small difference with respect to the first “additional mode” from the CL 12 mode set (181 Hz) or OL 12 mode set (183.3 Hz) can be attributed to uncertainties on the impedance assigned to the loudspeakers cabinets. Such impedance was defined assuming rigid boundary conditions for the fluid domain, which may not be exactly the case.

The monitor microphones shown as green dots on the left of Fig. 13.11 were distributed in two grids. Figure 13.12 shows in detail the horizontal ($H_{x,x}$) and vertical ($V_{x,x}$) grids where these 18 microphones were placed. The vertical grid was especially close to the surface of the structure, at 0.2 m from the vertex of the parabolic-shape DUT. Its objective was to capture the acoustic radiation of the specimen. On the other hand, the purpose of the horizontal grid was to measure the pressure gradient in front of the DUT to identify standing waves. Distance between microphones in both grids was 0.2 m.

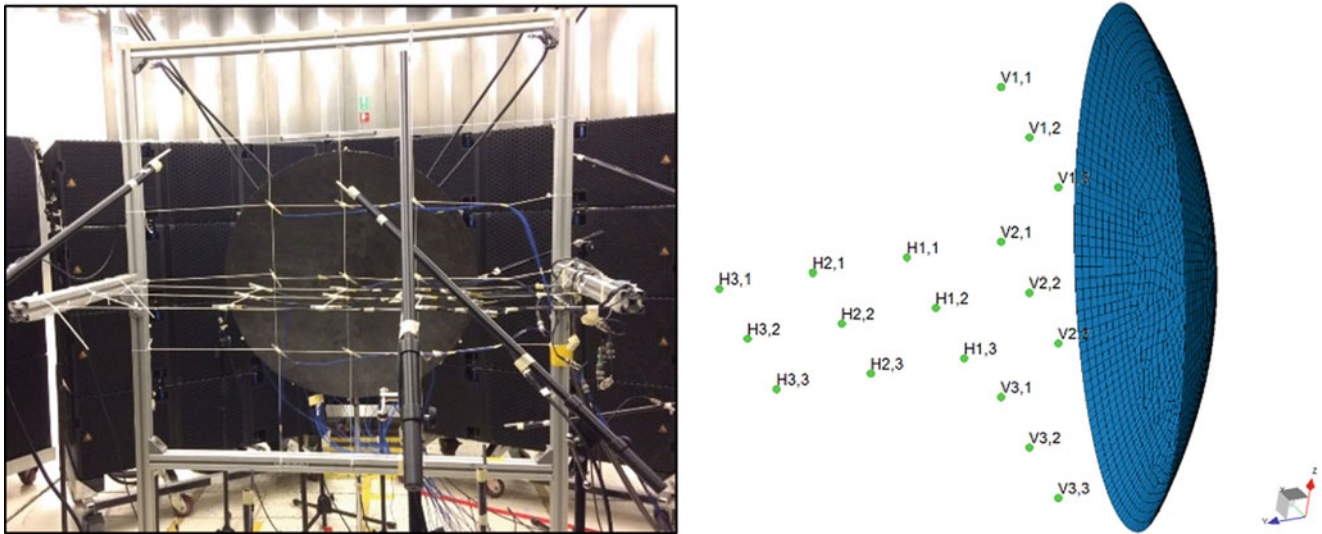


Fig. 13.12 Monitoring microphones on grids. Left: Experimental setup. Right: Detailed monitoring microphones placement, distance between sensors and between vertical grid to the DUT was 0.2 m

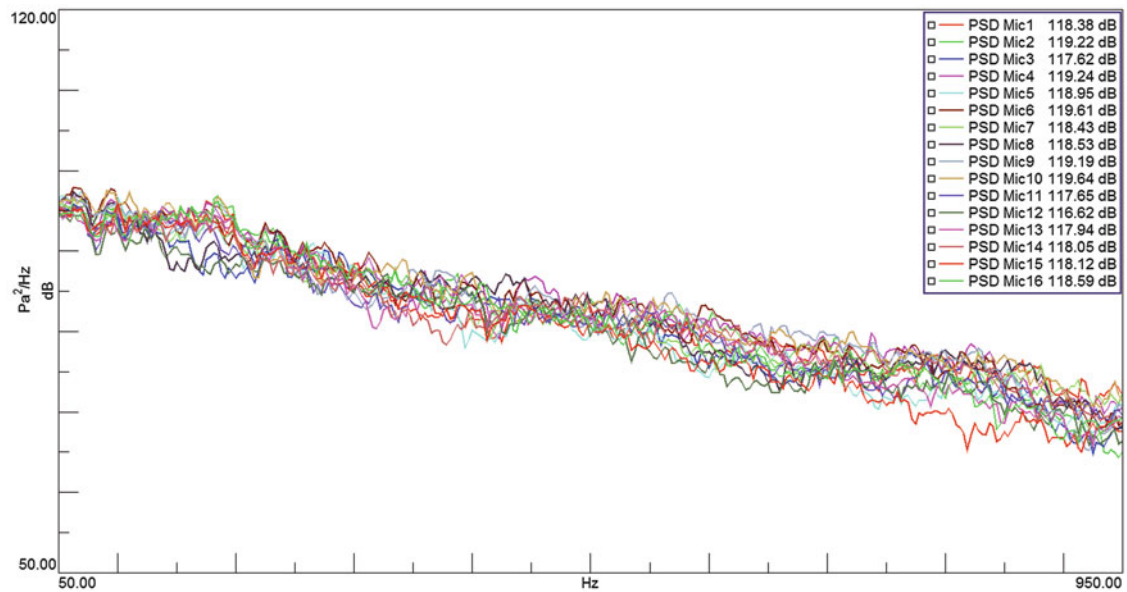


Fig. 13.13 Pressure power spectral density measured at microphones 1–16 (OL 12–118 dB SPL)

Figure 13.13 shows the pressure PSD at microphones 1–16 for OL 12. Although such shaped spectrum is not exactly white noise, it is smooth enough for OMA to provide good results [1, 23]. However, for acoustic control purposes these responses prove that OL is not a feasible control strategy for DFAX testing, since the PSD dispersion overpass the typical testing tolerances (e.g. ± 3 dB). At 183.4 Hz Fig. 13.13 shows a prominent lack of uniformity, which approximately corresponds to the result from the simulated acoustic modal analysis shown in Fig. 13.11. Experimental results in Fig. 13.14 show the horizontal (top) and vertical (bottom) pressure fields at the monitoring microphones of the grids (i.e. linear interpolation). On the top-left, the result for horizontal pressure field at 183.4 Hz is consistent with the expected from the simulations, since high pressure at the surface of the DUT slowly decreases along the grid in positive y -axis direction.

Figure 13.15 shows the pressure PSD at the monitoring microphones. On the left, the sensors at the horizontal grid show changes on pressure magnitude over a plane which was placed at 1.3 m high from the ground (i.e. at the center of the DUT, see scheme in Fig. 13.12). The cursors on the plot highlight the frequencies corresponding to the so-called “additional modes” of the OMA mode sets.

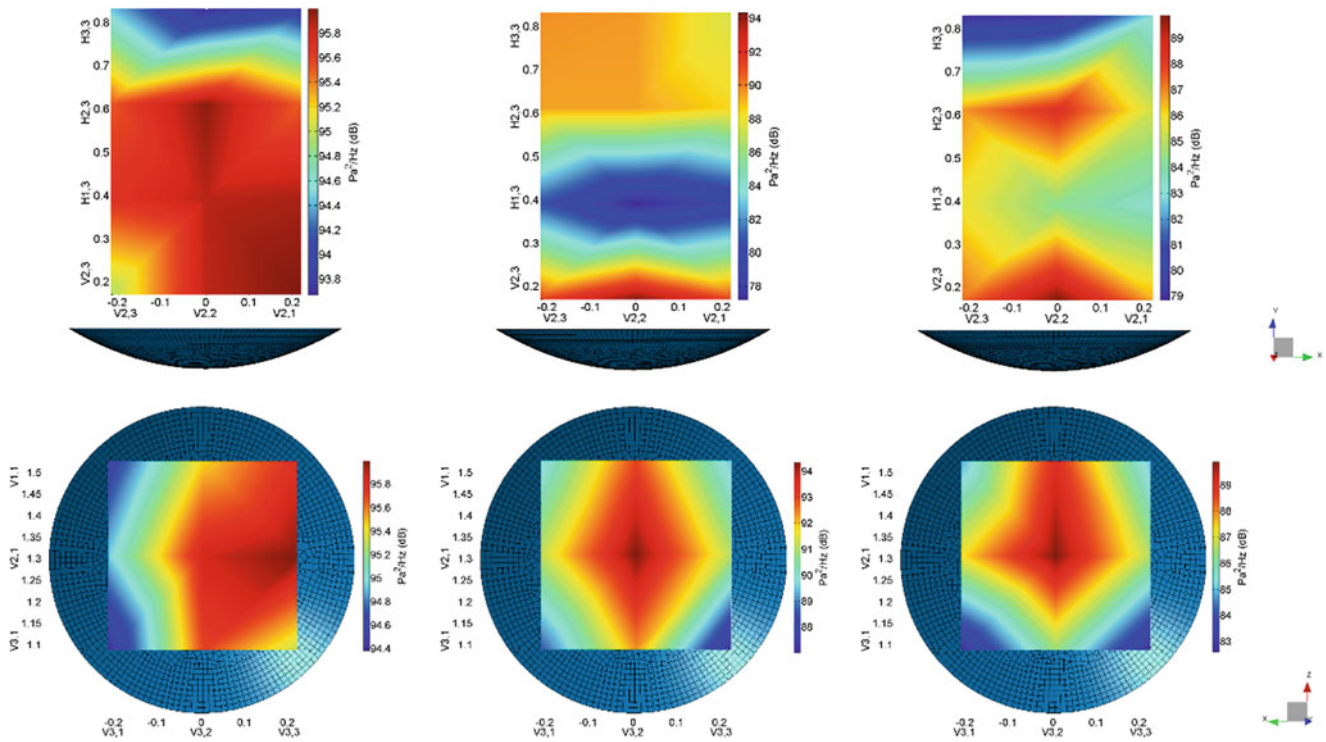


Fig. 13.14 Pressure field measured at the monitoring microphones on the grids. From left to right plots on top correspond to: 183.4, 372.5, 443.8 Hz. From left to right plots on the bottom correspond to: 183.4, 372.5, 443.8 Hz (OL 12–118 dB SPL)

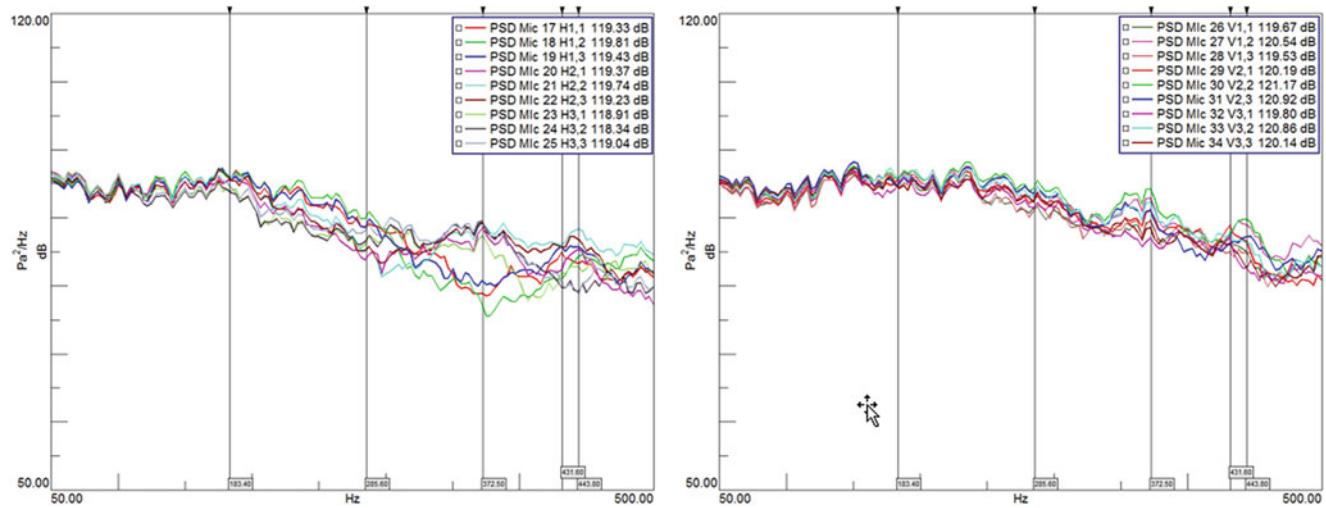


Fig. 13.15 Pressure power spectral density measured at monitoring microphones on the grids. Left: Horizontal grid. Right: Vertical grid (OL 12–118 dB SPL)

Unlike at 183.4 Hz, where the pressure gradient was small on the horizontal grid, at 372.5 Hz the PSD dispersion in Fig. 13.15 is large. Plots on the middle of Fig. 13.14 allow visualizing the spatial distribution of pressure PSD. The vertical grid at 372.5 Hz shows high pressure concentrated at the center of the DUT (V2,2). Then, the horizontal grid at the same frequency shows how the pressure drops along a nodal line (0.42 m), exactly at $\lambda/4$ (0.22 m) from the vertical grid (0.2 m). Then the pressure rises again at around 0.64 m from the DUT’s vertex (0 m), as expected. This is evidencing another acoustic standing wave, an harmonic of the first “additional mode”. PSD results from the horizontal grid, on the left of Fig. 13.15, also show large PSD dispersion at 443 Hz. On the right of Fig. 13.14, the vertical grid at this frequency shows high pressure concentrated at the center of the DUT (V2,2), like at 372.5 Hz. However, at 443 Hz the horizontal grid shows two nodal lines

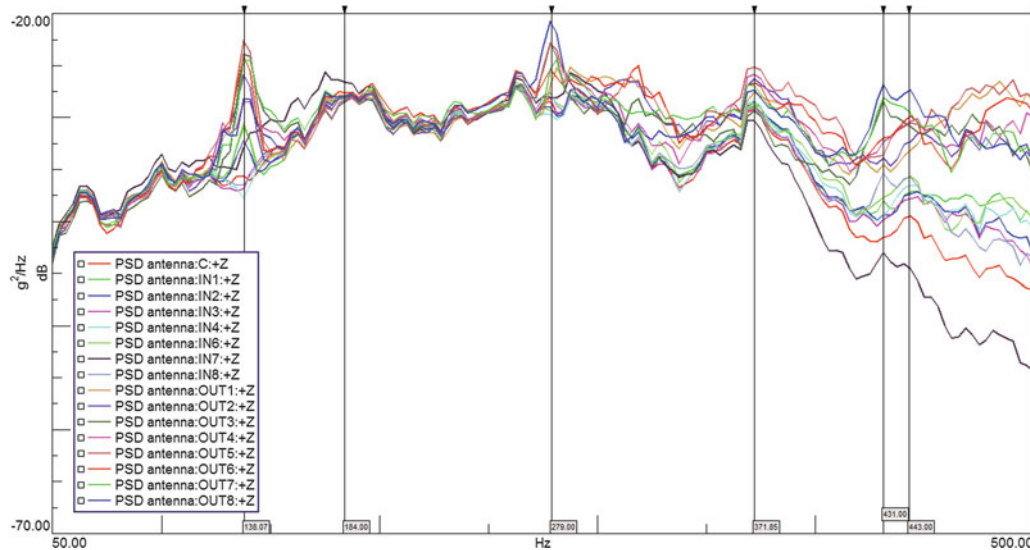


Fig. 13.16 Acceleration power spectral density measured at the DUT (OL 12– 118 dB SPL)

separated by $\lambda/2$ (0.38 m), also evidencing the presence of an acoustic standing wave. (Wavelength calculation was done assuming $c = 340$ m/s).

Finally, Fig. 13.16 shows the acceleration PSDs estimated from the time histories captured through the 16 accelerometers on the DUT for OL 12. Although the dominant peaks clearly correspond to structural modes (i.e. 138 and 279 Hz), acoustic modes (i.e. 183.4 and 372.5 Hz) seem to contribute significantly to the RMS acceleration. In this figure, it is also interesting to notice that lack of uniformity of structural responses is only observed at the eigenfrequencies of the structural modes and at *high frequency*. At resonance frequencies this is the expected since the motion of the structure follows certain mode shapes (e.g. predictions available in Fig. 13.5) and, naturally, each sensor will capture different motion amplitudes. Nevertheless, at *high frequency*, over 250 Hz (diameter $\sim \lambda/2$) or ever higher, the responses get gradually more and more non-uniform. This might be due to the fact that the acoustic waves load more and more incoherently the structure. Another explanation can be derived from the pre-test analysis in Sect. 13.4.1. According to the mode shapes of the preliminary FE-model of the DUT in Fig. 13.5, from 169 Hz towards 1013 Hz the specimen is not expected to show significant dynamics at the inner ring of sensors. Certainly, curves belonging to these sensors are the ones dropping faster in magnitude along the frequency axis in Fig. 13.16.

13.6 Model Calibration and Update

Validation of the structural FE-model of the DUT is attempted by calibrating the numerical results against OMA results during DFAX tests. The output of this correlation analysis allows updating the model bringing the numerical model in better agreement with the experimental data.

As the dynamic characteristics of the models are defined in terms of modal parameters, the correlation target is to improve the match between: model mass, modal frequencies and mode shapes. Generally, the modelling uncertainties might be related with: materials, geometry and boundary conditions. This paper focuses the correlation analysis, and the subsequent update, on geometry and materials properties. The correlation vocabulary used further on uses the term *reference model* for the experimental data and *verification model* for the numerical data.

13.6.1 Modal-Based Correlation Analysis

Operational Modal Analysis was applied to the acceleration responses measured on the DUT during the DFAX testing procedure. The idea behind OMA is that the responses are sufficient to characterise the system (up to the input-output

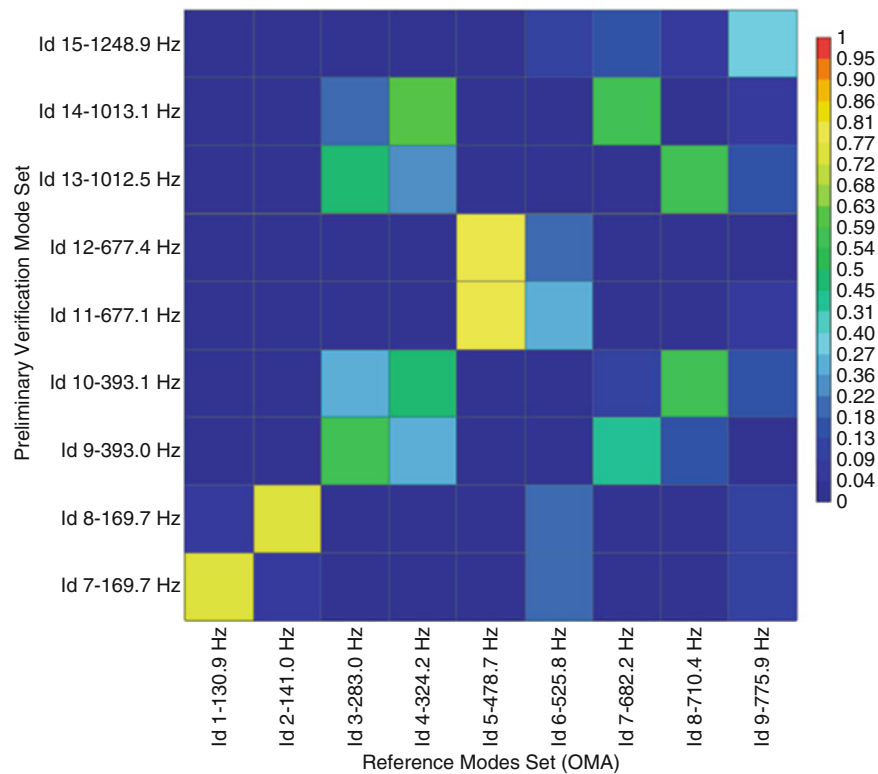


Fig. 13.17 MAC matrix between *reference* (x-axis) and *verification* (y-axis) models

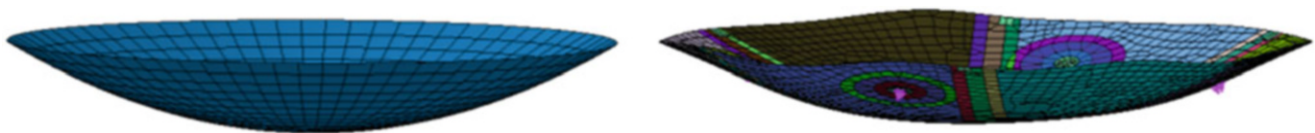


Fig. 13.18 Left: preliminary structural model. Right: updated structural model

scaling). An estimation of the modal parameters of the DUT through Operational PolyMAX (CL 12) provided the structural *reference* model for the calibration. Analysis in previous section allowed to remove the so-called “additional modes” from the *reference* mode set because they are produced by acoustic standing waves. In this way, only modal parameters corresponding to structural modes are used for validation of the numerical modal model.

A *preliminary verification* modal model was obtained from the preliminary structural model. Simulated mode shapes for such model are shown above, in Fig. 13.5. Figure 13.17 shows the Modal Assurance Criterion (MAC) matrix between the *reference* (x-axis) and *verification* (y-axis) mode sets. This MAC is evidencing very poor correlation for *reference* modes Id 3–9, which might be due to wrong assumptions regarding the materials composing the preliminary model.

After the DFAX test campaign, Thales Alenia Space contributed significantly with detailed information about the DUT mechanical properties. This allowed updating the preliminary model. Such update concerned the geometry and the material composition of the antenna reflector. Figure 13.18 shows, from left to right, the evolution of the FE-model. An *updated verification* modal model was obtained from this updated design. Its correlation against the *reference* model is shown in Fig. 13.19.

The MAC matrix in Fig. 13.19 shows that the correlation for the first four modes of the *verification* mode set is notably improved. Eigenfrequencies are in much better agreement to the experimental data, especially for the first modes. However, *verification* mode Id 11, as well as *reference* modes Id 6 and 9 do not show clear correlation. This may be related with observability issues, since the auto-MAC matrix for the *reduced verification* model on the right of Fig. 13.19 shows a similar correlation pattern along this frequency range, evidencing that identification of modes would not be easy. Such violation of the observability assumption, together with uncertainties inherent to the tests (e.g. noise), could explain the imperfect correlation between modal models.

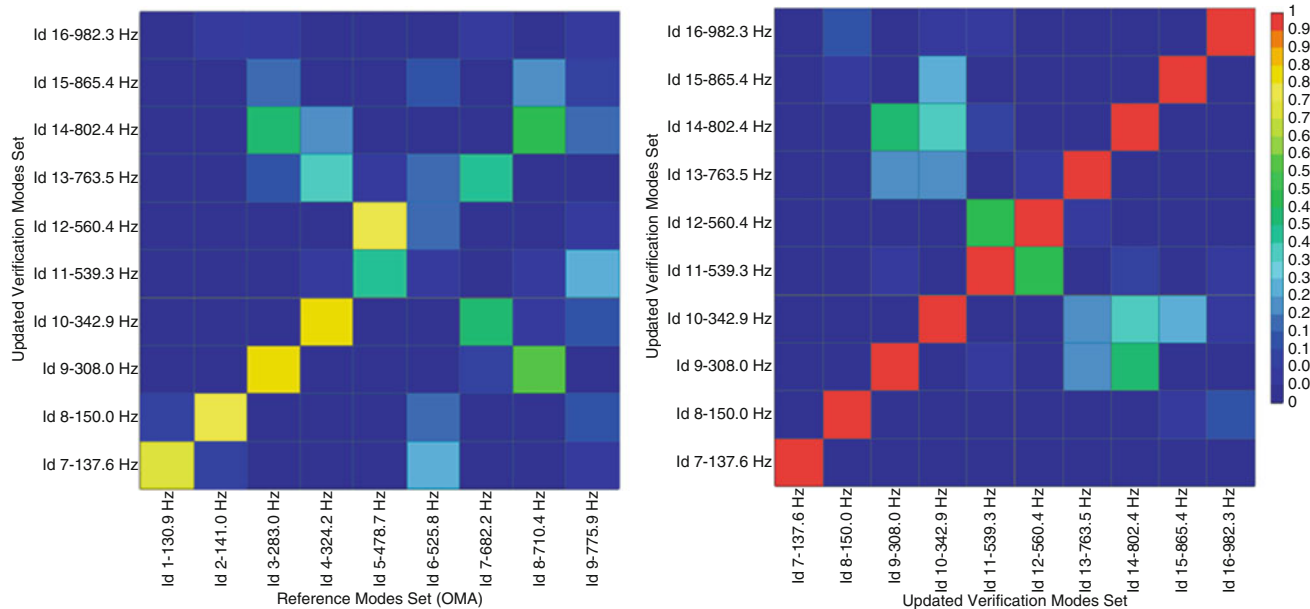


Fig. 13.19 Left: MAC matrix between *reference* (x-axis) and updated *verification* (y-axis) models. Right: auto-MAC of updated *verification* model

13.6.2 Sensitivity-Based Model Update

The first four structural eigenfrequencies on the left of Fig. 13.19, *reference* mode Id: 7, 8, 10, 12, still show a significant frequency difference between numerical and experimental eigenvalues. To overcome that, further update is aimed through sensitivity-based optimisation. First step consisted in setting a Nastran SOL200 sensitivity case. This is performed to identify which material parameters might be leading to the observed mismatch between models. Then, the most sensitive parameters are used as inputs of an iterative optimisation procedure.

The FE-model shown on the right of Fig. 13.18 is composed of five materials. An isotropic one (Iso) and four orthotropic materials (M1–M4). The latter are arranged in plies, with different thicknesses and orthotropic axes orientations. Among others, the following mechanical parameters of the materials (M1–M4) can be modified: modulus of elasticity in the longitudinal direction (E1), modulus of elasticity in the lateral direction (E2), Poisson’s ratio (N12), in-plane shear modulus (G12), transverse shear modulus for shear in 1-Z plane (G1Z), transverse shear modulus for shear in 2-Z plane (G2Z) and mass density (RHO).

A parameter is called sensitive if the first partial derivatives of modal parameters or system matrices to this parameter are large in absolute value. The set of the most sensitive parameters is probably the best one for a fast convergence to an updated model that correlates better with the experimental data. Figure 13.20 shows the mode frequency sensitivity analysis of the verification model with respect to the parameters enumerated above, where, for example, M1.RHO corresponds to the mass density of the orthotropic material 1. The higher sensitivity is observed at high frequency (updated *verification* mode Id: 12–14).

In order to further update the numerical model, it is performed a LMS Virtual.Lab optimisation. The input variables are the results of the sensitivity analysis, while the correlation targets for this optimisation are the *reference* model eigenfrequencies for the first four structural modes (*verification* mode Id: 7, 8, 10, 12). These modes were chosen because the frequency difference between mode sets was small enough to be attributed to uncertainties in terms of material properties. On the contrary, correlation between higher order modes may be compromised by other kind of uncertainties, still not discovered at the current status of this research. Therefore, optimisation of material properties are not implemented for such high order modes. Next to setting the correlation targets for the optimisation, a set of simulated experiments are performed (i.e. 3-level full factorial, Latin-Hypercube). Then, a *mathematical model* is designed from the simulated experiments and the sensitivity analysis. Finally, a Sequential Quadratic Programming (SQP) algorithm is used to iteratively minimise the difference between the targets and the numerical eigenfrequencies. The process finishes with a set of optimised material properties, reaching a maximum frequency difference of 4.04 Hz for *reference* mode Id: 10.

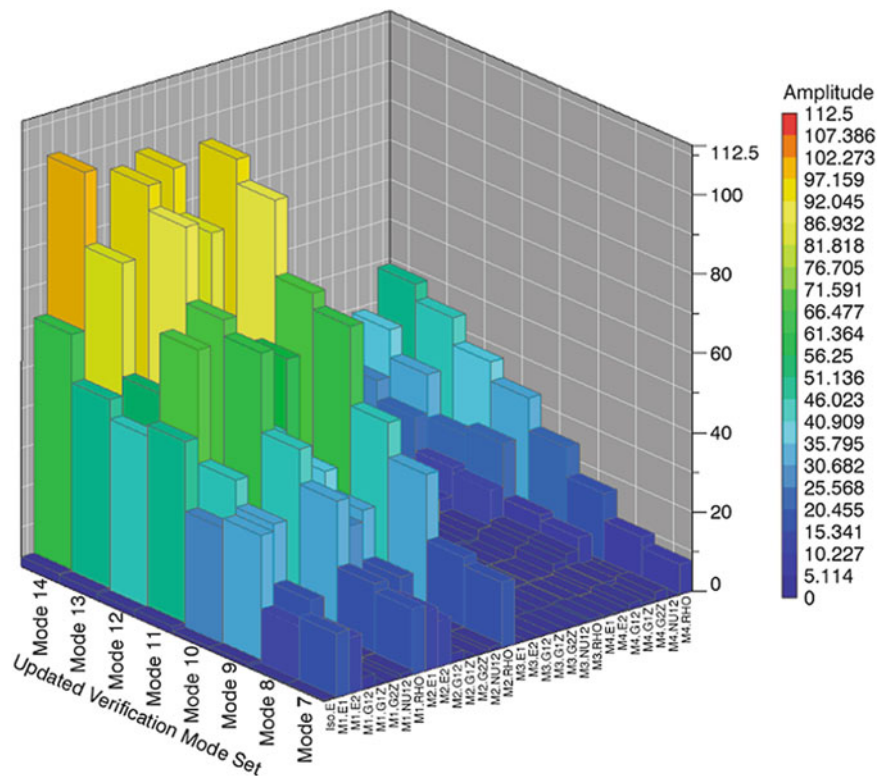


Fig. 13.20 Normalised mode frequency sensitivity

13.7 Conclusions

Lightweight space components, like the antenna reflector studied in this research, need to be qualified through environmental tests to prove they are able to survive the dynamical loads encountered during operating conditions. Representative dynamic acoustic loads on the specimens are typically specified through a test requirement covering the frequency range between 22 and 10,000 Hz. Nevertheless, the scope of this study was to validate the numerical model of the DUT up to 1000 Hz.

This paper proves that for validation purposes it is possible to identify the modal parameters of a spacecraft specimen by applying Operational Modal Analysis to environmental acoustic testing data. The quality of the OMA results increase when thorough pre-test analysis is performed. Furthermore, the success of the model updating is strongly dependent on the preliminary model used for pre-test. Not only because a good model (i.e. low uncertainties) would need less updating effort, but mostly because proper pre-testing determines the quality of the experimental data acquired through OMA, which yields the experimental modal model. Non-exhaustive exploitation of the pre-test stage may lead to violation of the observability modal analysis assumption, limiting the scope of the validation in terms of frequency range, like observed in this research. For future measurements on lightweight structures, the pre-test stage should be exploited more efficiently, lighter tri-axial transducers should be used for the test, and, for curved structures like this antenna reflector, special attention should be given to the orientation of transducers' sensitivity axes.

It is highlighted a significant advantage associated to the use of OMA during DFAX testing. The coupling between the structure and the acoustic environment can be investigated while testing. This aspect was deeply exploited in this paper and enabled to study the acoustic field through the DUT structural dynamics, since the occurrence of acoustic standing waves and interference patterns showed up as "additional modes" in the structural responses. These modes can be easily removed from the structural mode set along the DFAX testing procedure, without hindering the model validation objective.

In this paper it was also shown that acoustic modal analysis of the cavity bounded by the loudspeakers array can be useful to identify potential standing waves. Even a simple simulation with basic assumptions regarding the boundary conditions can highlight pressure nodes and antinodes in the field, potentially leading to lack of SPL spatial uniformity.

In terms of correlation analysis model updating sequence, from the lessons learned in this study, further procedures should combine the following approaches: *Modification Prediction Analysis* to evaluate mass loading of the DUT, then *Sensitivity-based Optimization* setting as correlation targets the eigenfrequencies of all the modes included in the bandwidth of study, as well as mode shapes derived from *MAC Sensitivity Analysis*. Finally, *Modal-based Correlation Analysis* against the experimental modal model obtained through OMA during the DFX test.

Acknowledgements The authors gratefully acknowledge the European Commission for its support in the frame of the Marie Curie program through the ITN ANTARES project (GA 606817) in collaboration with Siemens Industry Software NV and KU Leuven. A special thank you also to the RTD team of Test Division at Siemens PLM and to Christophe Fabries from Thales Alenia Space (Toulouse, France) for their support during and after the test campaign.

References

- Peeters, B., Alvarez Blanco, M., Musella, U., Waimer, S., Di Lorenzo, E., Carrella, A.: Identifying the structural behaviour of a specimen during spacecraft acoustic testing by operational modal analysis. In: 7th International Operational Modal Analysis Conference (2017)
- Larkin, P.: Developments in direct-field acoustic testing. *J. Sound Vib.* (2014)
- Meric, A., Markowicz, B.: Direct field acoustic testing at SSL. In: 29th Aerospace Testing Seminar (2015)
- Bo, Z., Zuluaga, W., Fecheté, L.: Direct field acoustic noise test of a solar wing, a pathfinder test for SSL. In: 29th Aerospace Testing Seminar (2015)
- Brévar, B., Fabries, C., Carrella, A., Janssens, J., Debille, J.: Direct field acoustic experiment on satellite subsystem. In: 29th Aerospace Testing Seminar (2015)
- Kolaini, A., Doty, B., Chang, Z.: Reverberant acoustic testing and direct field acoustic testing: acoustic standing waves and their impact on structural responses. In: Spacecraft and Launch Vehicle Dynamic Environments Workshop (2012)
- Fabries, C., Brevart, B., Carrella, A., Alvarez Blanco, M., Dal Fitto, D., Scharfenberg, S.: Experimental validation of direct field acoustic testing. In: 14th European Conference on Spacecraft Structures, Materials and Environmental Testing (2016)
- Jacobsen, F., Roisin, T.: The coherence of reverberant sound fields. *J. Acoust. Soc. Am.* **108**(1), 204–210 (2000)
- Schultz, T.: Diffusion in reverberation rooms. *J. Sound Vib.* **16**(1), 17–28 (1971)
- Jacobsen, F.: The diffuse soundfield. Report No. 27, Acoustics Laboratory, Technical University of Denmark (1979)
- Elliott, S.J., Cédric, M., Gardonio, P.: The synthesis of spatially correlated random pressure fields. *J. Acoust. Soc. Am.* **117**(3), 1186–1201 (2005)
- Kolaini, A.R., O’Connell, M.R., Tsoi, W.B.: Acoustically induced vibration of structures: reverberant vs. direct acoustic testing. In: Aerospace Testing Conference (2009)
- Veit, L., Sander, H.: Production of spatially limited diffuse sound field in an anechoic room. *Audio Eng. Soc.* **35**(3), 138–143 (1987)
- Alvarez Blanco, M., Janssens, K., Bianciardi, F.: Experimental verification of projection algorithms and optimization routines for acoustic field uniformity enhancement in MIMO direct field acoustic control. In: ISMA International Conference on Noise and Vibration Engineering (2016)
- Alvarez Blanco, M., Janssens, K., Bianciardi, F.: Target spectrum matrix definition for multiple-input-multiple-output control strategies applied on direct-field-acoustic-excitation tests. In: 13th International Conference on Motion and Vibration Control (2016)
- Center of Aerospace Structures, University of Colorado Boulder, on-line (2017)
- Wijker, J.: *Random Vibration in Spacecraft Structures Design*. Springer (2009)
- Heinrich, W., Hennig, K.: *Zufallsschwingungen mechanischer Systemen* (1978)
- Cook, R., Waterhouse, R.V., Berendt, R.D., Edelman, S., Thompson, M.C.: Measurement of correlation coefficients in reverberant sound fields. *J. Acoust. Soc. Am.* **27**(6), 1071–1077 (1955)
- Himmelblau, H., Fuller, M.C., Sharton, T.D.: Assessment of space vehicle aeroacoustic vibration prediction, design and testing. In: McDonnell Douglas Aeronautics Company – NASA Contractor Report, CR-1596 (1970)
- Shi, Q.: The effectiveness of reverberant acoustic test by investigating the sound characteristics and vibration responses in comparison between test and flight telemetry acoustic data. In: Aerospace Testing Seminar (2015)
- Heylen, W., Lammens, S., Sas, P.: *Modal analysis theory and testing*. Department of Mechanical Engineering, Katholieke Universiteit Leuven, Leuven, Belgium (2013)
- Peeters, B., Van der Auweraer, H., Vanhollenbeke, F., Guillaume, P.: Operational modal analysis for estimating the dynamic properties of a stadium during a football game. *J. Shock Vib.* **11**, 395–409 (2004)
- Hermans, L., Van der Auweraer, H., Guillaume, P.: A frequency-domain maximum likelihood approach for the extraction of modal parameters from output-only data. In: ISMA International Conference on Noise and Vibration Engineering, pp. 367–376 (1998)
- Hermans, L., Van der Auweraer, H.: Modal testing and analysis of structures under operational conditions: industrial applications. *Mech. Syst. Signal Process.* **13**(2), 193–216 (1999)
- Peeters, B.: System identification and damage detection in civil engineering. PhD thesis, Department of Civil Engineering, K.U. Leuven, Belgium. www.bwk.kuleuven.ac.be/bwm (2000)
- Peeters, B., De Roeck, G.: Stochastic system identification for operational modal analysis: a review. *ASME J. Dyn. Syst. Meas. Control.* **123**(4), 659–667 (2001)
- Di Lorenzo, E., Petrone, G., Manzato, S., Peeters, B., Desmet, W., Marulo, F.: Damage detection in wind turbine blades by using operational modal analysis. *Struct. Health Monit.* **15**, 289–301 (2016)
- Peeters, B., Van der Auweraer, H., Guillaume, P., Leuridan, J.: The PolyMAX frequency-domain method: a new standard for modal parameter estimation? *Shock Vib.* **11**, 395–409 (2004)



Chapter 14

Confidence in the Prediction of Unmeasured System Output Using Roll-Up Methodology

Kyle Neal, Chenzhao Li, Zhen Hu, Sankaran Mahadevan, Joshua Mullins, Benjamin Schroeder, and Abhinav Subramanian

Abstract This research is concerned with how to use available experimental data from tests of lower complexity to inform the prediction regarding a complicated system where no test data is available. Typically, simpler test configurations are used to infer the unknown parameters of an engineering system. Then the calibration results are propagated through the system model to predict the uncertainty in the system response. However, it is important to note that parameter estimation results are affected by the quality of the model used to represent the test configuration. Therefore, it is necessary that the model of the test configuration be also subjected to rigorous validation testing. Then the calibration and validation results for the test configurations need to be integrated to produce the distributions of the parameters to be used in the system-level prediction. Such a systematic roll-up methodology that integrates calibration and validation results at multiple levels of test configurations has been previously established (Sankararaman and Mahadevan, *Reliab Eng Syst Saf* 138:194–209, 2015).

The current work develops an approach to quantify the confidence in the use of lower-level test data (through the roll-up methodology) in predicting system-level response. The propagated roll-up distributions are compared against simulated output distributions from a calibrated system model based on synthetic data; this comparison is done through the model reliability metric (Rebba and Mahadevan, *Reliab Eng Syst Saf* 93(8):1197–1207, 2008) and results in a quantified roll-up confidence. Then an optimization procedure is formulated to maximize the roll-up confidence by selecting the most valuable calibration and validation tests at the lower levels. The proposed methods for both the forward and inverse UQ problems are applied to the multi-level Sandia dynamics challenge problem (Red-Horse and Paez, *Comput Methods Appl Mech Eng* 197(29–32):2578–2584, 2008).

This work is funded by Sandia National Laboratories.

Keywords Multi-level system · Bayesian · Roll-up · Uncertainty quantification · Resource allocation

14.1 Extended Abstract

There are certain critical engineering systems where experiments cannot be directly conducted on the full system, such as aircraft, weapons systems, space rovers, etc. Experimental testing restrictions can be due to cost of testing, international and governmental testing requirements, or physical limitations in the testing equipment and environment. However, the individual components and subsystems of this complex system may be readily conducive to experimentation. The first challenge addressed in this work is how to use available experimental data from levels of lower complexity to inform the prediction regarding a complicated system where no test data is available. The second challenge confronted is that, before any experiments have been conducted, how to best allocate an available budget to lower level tests in order maximize confidence in the roll-up prediction.

K. Neal · C. Li · S. Mahadevan (✉) · A. Subramanian
Department of Civil and Environmental Engineering, Vanderbilt University, Nashville, TN, USA
e-mail: sankaran.mahadevan@vanderbilt.edu

Z. Hu
Department of Industrial and Manufacturing Systems Engineering, University of Michigan, Dearborn, MI, USA

J. Mullins · B. Schroeder
Sandia National Laboratories, Albuquerque, NM, USA

A key assumption in this work is that the levels of lower complexity share one or more model parameters with the complex system whose performance is being predicted. Model calibration focuses on the inference of model parameters so that the prediction by the computational model matches the experimental data [4]. Here Bayesian inference is used for model calibration:

$$f''(\boldsymbol{\theta}) \propto L(\boldsymbol{\theta})f'(\boldsymbol{\theta}) \quad (14.1)$$

If all the parameters to be calibrated are denoted as $\boldsymbol{\theta}$, Eq. (14.1) of Bayesian inference indicates that the joint posterior distribution $f''(\boldsymbol{\theta})$ is proportional to the product of likelihood function $L(\boldsymbol{\theta})$ and prior distribution $f'(\boldsymbol{\theta})$.

After obtaining the posterior distribution of model parameters in the model calibration, some analysts directly propagate the posterior distributions through the computational model of the system of interest to predict the system output, while others incorporate model validation in the uncertainty quantification of model parameters claiming that it provides information to understand the limitation of calibration [5]. In this work, model validation is performed on the models of each test configuration. Among several available quantitative validation metrics, the model reliability metric is implemented here since it gives an easily interpretable probability value that can be used in the roll-up methodology [1, 2].

The roll-up approach developed by Sankararaman and Mahadevan [6] provides a framework for integrating the results from calibration and validation into the distribution for each model parameter, to be used in system-level prediction:

$$\begin{aligned} f(\boldsymbol{\theta} \mid D_1^{C,V}, D_2^{C,V}) &= P(G_1)P(G_2)f(\boldsymbol{\theta} \mid D_1^C, D_2^C) + P(G'_1)P(G_2)f(\boldsymbol{\theta} \mid D_2^C) \\ &+ P(G_1)P(G'_2)f(\boldsymbol{\theta} \mid D_1^C) + P(G'_1)P(G'_2)f(\boldsymbol{\theta}) \end{aligned} \quad (14.2)$$

In Eq. (14.2), $P(G_i)$ is the probability of the model at Level i being valid, calculated using the model reliability metric. The term $P(G'_i)$ is the complementary probabilities of model being invalid, calculated as $1 - P(G_i)$. The integrated (roll-up) distribution from Eq. (14.2) is then propagated through the system model to predict the quantity of interest. This completes the forward problem.

In the inverse problem, no experimental tests have yet been conducted. This is where resource allocation is necessary. Tests can be conducted at multiple lower levels and can be used for either calibration or validation of the lower level models. Additionally, there are different associated costs for each type of test and a total budget for testing that cannot be exceeded. The objective is thus to select lower level tests that, when rolled-up, accurately predict the quantity of interest with the least amount of uncertainty, or said differently, minimize bias and variance in the roll-up prediction.

A method is developed in this study to assess how well the roll-up prediction of the QOI agrees with the “perfect” QOI prediction. The “perfect” QOI prediction replicates the ideal case where system level tests are available, by synthetically generating data at the system level to compare with the roll-up prediction. Several different metrics could be considered for such assessment, including KL Divergence, sensitivity comparison, or the model reliability metric. In this work, the model reliability metric is used since it has a clear interpretation and offers a quantitative basis for decision-making. The model reliability metric was previously developed for the purpose of model validation [2], and is extended in this work to assess the roll-up prediction.

Roll-up confidence is used as the objective in test resource allocation. The number of tests at each of the lower levels and whether the tests are used to calibrate model parameters or validate the lower level models is decided based on maximizing the roll-up confidence. Of course, this is subject to a budget constraint.

The methods developed for both the forward problem and the inverse problem are applied to the Sandia dynamics challenge problem [3] (Fig. 14.1).

This example consists of three levels with each of the levels having in common three masses joined by springs and dashpots. The three levels are distinguished by their boundary conditions and input excitations. The stiffnesses and damping coefficients are the model parameters requiring calibration and the quantity of interest is the peak acceleration of the topmost mass at the third (system) level.

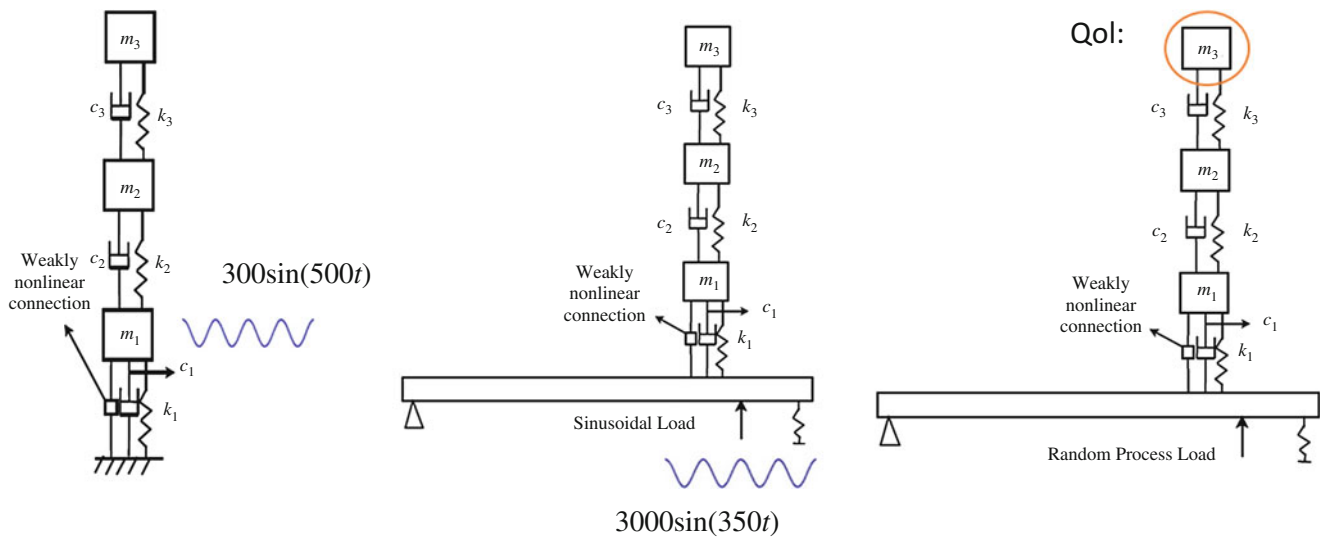


Fig. 14.1 Sandia dynamics challenge problem setup [3]

References

1. Sankararaman, S., Mahadevan, S.: Integration of model verification, validation, and calibration for uncertainty quantification in engineering systems. *Reliab. Eng. Syst. Saf.* **138**, 194–209 (2015)
2. Rebba, R., Mahadevan, S.: Computational methods for model reliability assessment. *Reliab. Eng. Syst. Saf.* **93**(8), 1197–1207 (2008)
3. Red-Horse, J.R., Paez, T.L.: Sandia National Laboratories validation workshop: structural dynamics application. *Comput. Methods Appl. Mech. Eng.* **197**(29–32), 2578–2584 (2008)
4. Kennedy, M., O’Hagan, A.: Bayesian calibration of computer models. *J. R. Stat. Soc.* **63**(3), 425–464 (2001)
5. Trucano, T.G., Swiler, L.P., Igusa, T., Oberkampf, W.L., Pilch, M.: Calibration, validation, and sensitivity analysis: what’s what. *Reliab. Eng. Syst. Saf.* **91**(10–11), 1331–1357 (2006)
6. Sankararaman, S., Mahadevan, S.: Comprehensive framework for integration of calibration, verification and validation. In: 53rd AIAA/ASME/ASCE/AHS/ASC Structures, Structural Dynamics and Materials Conference, pp. 1–12 (2012)



Chapter 15

Application of the Transfer Matrix Method for the Analysis of Lateral Vibrations of Drillstrings with Parameter Uncertainties

Ilja Gorelik, Mats Wiese, Lukas Bürger, Sebastian Tatzko, Hanno Reckmann, Andreas Hohl, and Jörg Wallaschek

Abstract To compare the susceptibility of different drillstring assemblies to lateral vibrations while taking parameter uncertainties into consideration, a computationally efficient model based on the transfer matrix method (TMM) in combination with a modal reduction is proposed in this study. Changing boundary conditions along the drilling trajectory are taken into account by combining the linear dynamic analysis from the TMM model with a static solution obtained from a finite element model. The statistical evaluation of the results enables a comparison of the dynamic behavior of different drillstring configurations during an early design stage.

Keywords Transfer matrix method · Lateral drillstring vibrations · Parameter uncertainties · Monte Carlo simulations · Robust design

15.1 Introduction

Due to their extremely large ratio between length and diameter, drillstrings for oil and gas exploration are highly prone to vibrations. As pointed out in [1], drillstring vibrations can be classified as axial, torsional and lateral vibrations. For each vibration mode, at least one self-excited phenomenon can be allocated to: bit bounce (axial), stick-slip (torsional), forward/backward whirl and snaking (lateral). Many situations are known to trigger vibrations including changes between soft and hard rock formations [2], pressure fluctuations in the surrounding drilling fluid, nonlinear relation between driving torque and bit speed [3], gravitational forces [4, 5] and mass imbalance of the drillstring components [6]. Self-excited phenomena adversely affect the drilling process and cause malfunctions of electronic components within the drilling tools, drill bit damage or even drillstring ruptures. According to [7] about one third of all electronic component failures within the drillstring are caused by vibration. As stated by [8, 9] most vibration-related malfunctions were encountered within the lower part of the drillstring, the bottom hole assembly (BHA). Lateral vibrations are especially detrimental, because they result in impacts with the borehole wall and exhibit high alternating bending stress.

To respond to this challenge, modelling and prediction of potentially harmful vibration regimes subject to operational parameters, such as rotation rate, weight on bit (WOB) and flow rate, have received considerable attention. Numerous mathematical models with different levels of complexity and purpose have been developed. Examples of lumped parameter models, that consider one or a few modes and for lateral dynamics describe the behavior of a particular section within the drillstring, can be found in [3, 4, 10, 11]. These types of models helped to gain a better understanding of the generation mechanisms for the vibration phenomena and revealed influencing factors. More sophisticated drillstring models, which account for the distributed nature of the drillstring and the course of the well trajectory, are mainly based upon the finite element method and play an important role during the early planning and design of a drilling operation. These models are used to calculate internal static loads and estimate critical driving speeds through modal and harmonic analysis [12, 13].

One of the long-term objectives is to mitigate drillstring oscillations using an automated system. This system would predict harmful vibration states based on downhole measurements and/or mathematical models of the system and provide recommendations for an optimal setting of operational parameters. A promising realization of such a system for the

I. Gorelik (✉) · M. Wiese · L. Bürger · S. Tatzko · J. Wallaschek

Department of Mechanical Engineering, Institute of Dynamics and Vibration Research, Leibniz Universität Hannover, Hannover, Germany
e-mail: gorelik@ids.uni-hannover.de

H. Reckmann · A. Hohl
Baker Hughes a GE Company, Celle, Germany

suppression of stick-slip oscillations is reported in [14]. The authors showed that a 1-DOF torsional pendulum with a nonlinear torque characteristic at the bit, can reproduce the complex torsional dynamics of the entire drillstring if the model parameters are identified from downhole measurements. A good review of automated drilling systems and control strategies is given in [1]. However, it also shows, that the presented concepts mainly focus on the mitigation of torsional vibrations. This focus is due to the fact, that the main influence parameters, such as surface/downhole torque, RPM and WOB can be gathered from measurements. The realization of such a system for lateral vibrations is very challenging due to several reasons. Bending vibrations are not transmitted to the surface and are not detectable from surface measurement data [15]. Usually, only one downhole measurement tool capable of capturing accelerations and bending moments is included in the drillstring assembly. In this situation, even if the measurement data indicates no significant vibration levels at the sensor position, high accelerations and bending rates may still occur at other positions along the drillstring. Furthermore, as stated in [3–5], the occurrence of harmful self-excited lateral vibrations strongly depends on parameters that cannot be measured, such as friction coefficients between the borehole wall and the eccentricity of mass imbalance of the drillstring components. For these reasons, the mitigation of lateral vibrations is mainly focused upon the determination of critical driving speeds to avoid resonance conditions. However, changing boundary conditions along the drilling trajectory introduce uncertainties, even for linear dynamic analysis.

In spite of these facts, most drillstring dynamics models neglect uncertainties within the model parameters and use deterministic values. Alternatively, this study presents a methodology that enables consideration of parameter uncertainties during the numerical analysis of drillstring lateral dynamics and allows comparison of different design alternatives for a specified well trajectory. To the best of our knowledge, this capability has not been available in the field of drilling dynamics.

This study provides a brief description of the underlying model in the first section. Due to its computational advantages over the finite element method, the transfer matrix method is chosen to model the lateral dynamics of the bottom hole assembly. A further reduction of the computational costs for the determination of the forced response is achieved by modal superposition. The influence of changing contact positions between the drillstring and the borehole wall along a drilling trajectory is considered by a static solution carried out with a finite element model. Next, the standard deviation for the lateral natural frequencies and displacements is evaluated for a given set of uncertain parameters. These results are used to determine ranges for critical driving speeds and to compare the robustness of different drillstring geometries. The achieved results are summarized in the last section.

15.2 Methodology

15.2.1 Modelling

The transfer matrix method (TMM) was developed by Holzer [16] in the early 1920s for the calculation of torsional oscillations of machine shafts. Based on the principle of Holzer's method, Myklestad [17] developed a new method to determine the natural frequencies and mode shapes for bending vibrations of beams. The core of this method is based upon the setup of the transfer matrix, which analytically describes how the state variables at one end are transferred to the other end of the beam (Fig. 15.1a). After this is done, the individual transfer matrices can then be assembled by simple matrix multiplication to form an entire structure. Unlike the finite element method, the size of the system of equations does not depend on the number of the used degrees of freedom. The size of the transfer matrices is only determined by the order of the underlying differential equations (4×4 for beam). This capability is probably one of the biggest advantages of the TMM over the finite element method. According to [18] this method is especially suitable for periodic, chain-like structures.

A brief description of the transfer matrix method and the underlying equations will be given here. For a detailed description of this method and the derivation of the necessary equations, please refer to [18, 19]. To describe flexural vibrations of drillstrings with the help of the transfer matrix method, each segment of the drillstring is considered as a uniform beam with constant material density ρ , cross-sectional area A , Young's modulus E and length ℓ (see Fig. 15.1a). Neglecting shear deformations, the following homogeneous, partial differential equation is obtained in accordance with Euler-Bernoulli beam theory

$$\mu \ddot{w}(x, t) + EI w''''(x, t) = 0, \quad (15.1)$$

with w being the lateral deflection and μ the mass distribution. In this study we neglected the influence of the axial compression force on the eigenfrequencies. After the separation of spatial and time-dependent variables and the application of the general solution

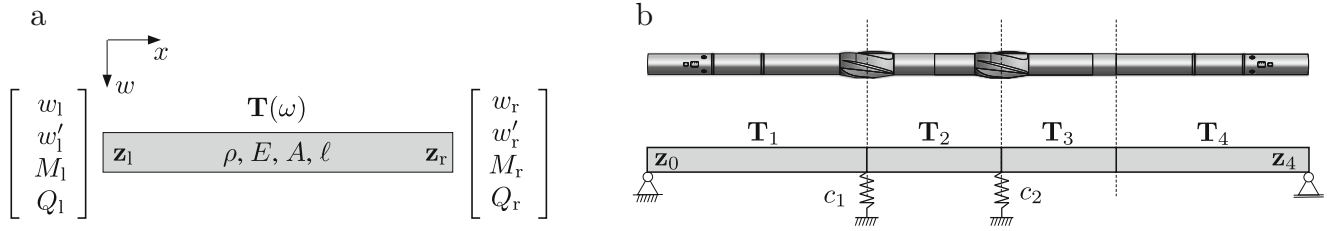


Fig. 15.1 (a) Definition of state variables at left and right boundary of beam element. (b) Representation of drillstring section with two stabilizers by means of transfer matrices

$$W(x) = K_1 \cosh(\lambda x) + K_2 \cos(\lambda x) + K_3 \sinh(\lambda x) + K_4 \sin(\lambda x) \quad (15.2)$$

for the spatial differential equation, the constants K_1 - K_4 can be expressed in terms of the state variables at the left and right boundary of the beam. The four resulting equations can be arranged in matrix form as follows

$$\mathbf{T}(\omega) = \frac{1}{2} \begin{bmatrix} C + c & \frac{1}{\lambda}(S + s) & -\frac{1}{\lambda^2}(C - c) & -\frac{1}{\lambda^3}(S - s) \\ \lambda(S - s) & C + c & -\frac{1}{\lambda}(S - s) & -\frac{1}{\lambda^2}(C + c) \\ -\lambda^2(C - c) & -\lambda(S - s) & C + c & \frac{1}{\lambda}(S + s) \\ \lambda^3(S - s) & -\lambda^2(C - c) & \lambda(S - s) & C + c \end{bmatrix}. \quad (15.3)$$

With the abbreviations

$$C = \cosh(\lambda x), \quad c = \cos(\lambda x), \quad s = \sin(\lambda x), \quad S = \sinh(\lambda x), \quad \lambda = \sqrt[4]{\frac{\mu \omega^2}{EI}} \quad (15.4)$$

the matrix in expression (15.3) represents the dynamic transfer matrix of the beam, with λ denoting the eigenvalues and ω an arbitrary angular frequency of the beam motion. Drillstring stabilizers, which have approximately the same diameter as the borehole, are modelled as discrete stiff or rigid ($c = \infty$) intermediate supports (Fig. 15.1b). After separating the variables and applying the exponential trial function for the time-dependent term, the following expression is obtained from Eq. (15.1)

$$EIw'''' - \omega^2 \mu w = \sum_{i=1}^m \delta(x - x_i) \Delta Q(x_i), \quad (15.5)$$

with δ being the *Dirac*-delta function, which takes the value one as soon the variable x coincides with a position x_i of a stabilizer/intermediate support. The index m defines the total number of stabilizers or intermediate supports. At every location the spring stiffness c_i causes a discontinuity within the shear force $Q(x)$, of which the magnitude can be expressed in terms of the lateral deflection w_i at the spring location as follows

$$\Delta Q(x_i) = c_i w(x_i) \quad (15.6)$$

15.2.2 Modal Analysis

The calculation of the eigenfrequencies and the corresponding mode shapes will be explained with the help of the system depicted in Fig. 15.1b. At first the linear system of equations comprising the state vector \mathbf{z}_4 and \mathbf{z}_0 is set up as follows

$$\mathbf{z}_4 = \mathbf{T}_4 \mathbf{T}_3 \mathbf{T}_2 \mathbf{T}_1 \mathbf{z}_0 + \mathbf{T}_4 \mathbf{T}_3 \mathbf{T}_2 \begin{bmatrix} 0 \\ 0 \\ 0 \\ \Delta Q(x_1) \end{bmatrix} + \mathbf{T}_4 \mathbf{T}_3 \begin{bmatrix} 0 \\ 0 \\ 0 \\ \Delta Q(x_2) \end{bmatrix}. \quad (15.7)$$

Applying the boundary conditions ($w_0 = M_0 = w_1 = M_1 = 0$) to the expression above, the following set of equations is obtained

$$\begin{bmatrix} 0 \\ 0 \\ 0 \\ 0 \end{bmatrix} = \mathbf{T}_M(\omega) \begin{bmatrix} w'_0 \\ Q_0 \\ \Delta Q(x_1) \\ \Delta Q(x_2) \end{bmatrix}. \quad (15.8)$$

Values for ω , which satisfy the following condition

$$\det(\mathbf{T}_M(\omega)) = 0 \quad (15.9)$$

are eigenfrequencies of the system. To obtain the corresponding mode shapes, the eigenfrequencies are substituted into Eq. (15.8) and solved for the unknown state variables and shear forces resulting from the intermediate supports. In a subsequent step the state variables can be calculated at any position along the structure.

15.2.3 Forced Response Analysis and Modal Reduction

For the forced response analysis, the mass proportional term ($\alpha\mu$) of the *Rayleigh*-damping and a mass imbalance excitation is added to expression (15.5) resulting in

$$EIw'''' - \Omega^2 \mu w + j\Omega \alpha \mu w = \sum_{i=1}^m \delta(x - x_i) \Delta Q(x_i) + \sum_{k=1}^p \delta(x - x_k) \varepsilon_k m_{\varepsilon,k} \Omega^2. \quad (15.10)$$

The amplitude of the p discrete excitation forces is defined by the corresponding eccentricity ε_k , mass m_k and the squared excitation frequency Ω . The procedure for the setup of the linear system of equations is very similar to the one for the modal analysis. However, the main difference is that the discontinuity in the shear force, created by an excitation force, and the vibration frequency Ω are known quantities. To obtain the operational mode shapes within a specified frequency range, the unknown state variables in \mathbf{z}_0 must be determined for every new value of Ω . For that reason, modal reduction is applied in order to further decrease the necessary computational time for the harmonic analysis and enable the consideration of parameter uncertainties.

The above described modal analysis allows the calculation of the mass normalized modal matrix $\tilde{\Phi}$, which contains the N considered mode shapes and the diagonal spectral matrix Λ comprising the N corresponding eigenfrequencies. By means of these matrices the coupled equations of motion

$$\mathbf{M}\ddot{\mathbf{w}} + \mathbf{D}\dot{\mathbf{w}} + \mathbf{K}\mathbf{w} = \mathbf{f}. \quad (15.11)$$

of the discretized structure, can be transformed to N decoupled equations in the modal domain as follows

$$\underbrace{\text{diag}(-\mathbf{I}\Omega^2 + j\Omega\alpha\mathbf{I} + \Lambda)}_{n=1\dots N} \hat{\mathbf{q}} = \hat{\mathbf{f}}. \quad (15.12)$$

From the expression above, the modal amplitudes yield

$$\hat{\mathbf{q}} = \mathbf{S}^{-1} \hat{\mathbf{f}}. \quad (15.13)$$

with $\hat{\mathbf{f}}$ being the vector of modal forces and \mathbf{S} the dynamic stiffness matrix. With $\hat{\mathbf{q}}$, the physical amplitudes for every state variable can be determined as follows

$$\begin{bmatrix} w \\ w' \\ M \\ Q \end{bmatrix} = \begin{bmatrix} \tilde{\Phi}_w \hat{\mathbf{q}} \\ \tilde{\Phi}_{w'} \hat{\mathbf{q}} \\ \tilde{\Phi}_M \hat{\mathbf{q}} \\ \tilde{\Phi}_Q \hat{\mathbf{q}} \end{bmatrix}. \quad (15.14)$$

Please note that for this last step the modal matrix for each individual state variable must be applied. Because the transfer matrix method automatically provides all spatial derivatives of the lateral deflection w , these are also available from the results of the modal analysis. This is a further advantage of the transfer matrix method over the finite element method.

Besides all the positive features of the transfer matrix method, such as computational efficiency and exact calculation of the inner loads, some disadvantages exist. One major drawback of the transfer matrix method, is the occurrence of numerical instabilities that are strongly linked to the frequency range and overall length of the structure under investigation. For the treatment of drillstring dynamics, the structure length is crucial. The reason for this lies in the different order of magnitudes of the trigonometric and hyperbolic functions contained in the transfer matrix and the limited working precision of the used programming environment (here MATLAB was used). One possible method to overcome this problem is suggested in [19, 20]. The method reduces the segment length by introducing additional intermediate state variables. It was implemented here as well. Please refer to the above mentioned references for a detailed description. In the course of this study, the method was further improved by adding an adaptive control of the number of necessary subdivisions to avoid numerical instabilities.

15.3 Application and Results

The intended purpose of this section is to show how the previously described transfer matrix model can be utilized in order to compare different drillstring designs with each other and to provide additional information on the reliability of calculated results in the presence of parameter uncertainties. This could be of importance for a calculation of critical driving frequencies.

15.3.1 Simulation Procedure

For the following example, the four different drillstring geometries, as shown in Fig. 15.3d, are chosen. The geometry I represents the base case and from there slight changes are introduced that result in the other three configurations II–IV. The alterations comprise additional stabilizers and the insertion of an element with a smaller outer diameter right above the bit. All geometries represent only the bottom hole assembly just below the drillpipes.

The simulation procedure starts with the definition of the drilling trajectory along against which the different drillstring designs are compared. Here, for each geometry the drilling trajectory depicted in Fig. 15.2c is used. As it can be seen, the trajectory comprises a vertical, inclined and curved section. In a subsequent step the uncertain parameters are defined by their range and type of distribution. For this example the location x_k of each imbalance excitation and its amplitude defined by the parameters ε_k and $m_{\varepsilon,k}$, are considered as uncertain. Moreover, it is assumed that due to friction between the drillstring and the borehole walls the actual weight-on-bit (WOB) deviates from the measured value and therefore is regarded as a further uncertainty. Because it is unlikely that the borehole diameter D_B remains constant over the full trajectory length, it is added as a further uncertain parameter. For all mentioned parameters a uniform distribution within the specified ranges is assumed. To generate the random parameter values a Sobol sequence is applied. For each parameter 250 samples X are generated and stored in the sampling matrix \mathbf{P} . Because 20 excitation forces are considered, the dimension of \mathbf{P} yields 250×62 . For all BHA configurations a free-free boundary condition is chosen and 10 modes are retained for modal reduction. The forced response is calculated within a frequency range between 0.1 and 6 Hz.

The main calculation loop comprises two parts: the transfer matrix model for the dynamic analysis and a finite element model for the calculation of the static deformation along the defined drilling trajectory. In this example the well trajectory is discretized with 40 points. As soon as the sampling matrix \mathbf{P} is defined, the calculation begins with a static analysis at the first trajectory position. The output of the static calculation comprises contact locations between the drillstring and the borehole wall, that are then transferred to the TMM model. For reasons of simplification, it is assumed that these contacts remain closed even when the structure is excited. Based on this assumption, rigid intermediate supports are introduced at

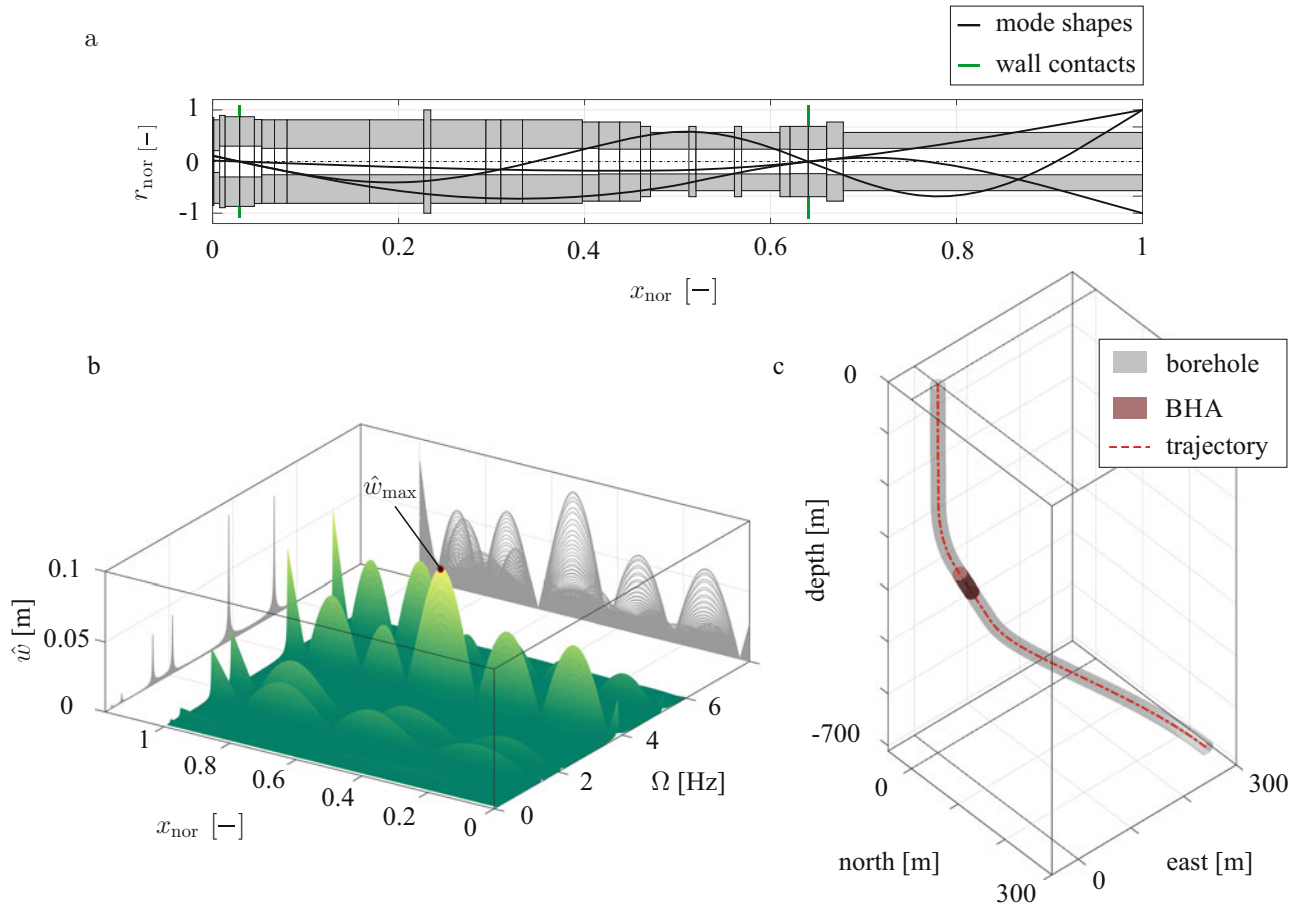


Fig. 15.2 (a) Drillstring geometry and first three calculated mode shapes for one specific subset of \mathbf{P} and position along the well trajectory. (b) Results of the forced response analysis for one subset of \mathbf{P} . (c) Drilling trajectory and current location of drillstring geometry from (a)

these locations and the modal (Fig. 15.2a) and harmonic analysis are subsequently executed. This combination of static and harmonic analysis is repeated for every row of \mathbf{P} and for every position along the drilling trajectory. As it can be seen from Fig. 15.2b, the vibration mode shapes and the frequency response functions are obtained from every harmonic analysis. For post-processing, all calculated eigenfrequencies and the maximum lateral deflections \hat{w}_{max} (see Fig. 15.2b) are stored.

15.3.2 Evaluation and Discussion

The comparison of the different drillstring configurations is based upon the evaluation of the signal-to-noise-ratio (SNR) η , which was proposed within the framework of the *Taguchi*-method. This quantity is a representation of a quadratic loss function on the decibel scale and enables assessment of the robustness of a process. It penalizes the deviation of the process output (\hat{w}_{max}) from a desired target value ($\hat{w}_{\text{max}} = 0$) and its variability. Depending on the type of target value a different SNR is applied. Here, a drillstring configuration is considered as robust, when the maximum lateral deflection takes the smallest possible value. In that case the SNR yields

$$\eta = -10 \log \left(\frac{1}{s} \sum_{s=1}^X \hat{w}_{\text{max},s}^2 \right). \quad (15.15)$$

Please refer to [21, 22] for a more detailed description of the *Taguchi*-method. Given the expression above, the robustness for each of the four drillstring configurations can be evaluated along the drilling trajectory. Besides the maximum lateral deflection, also the occurring bending moment is evaluated in the same manner. For both output values the robustness measure

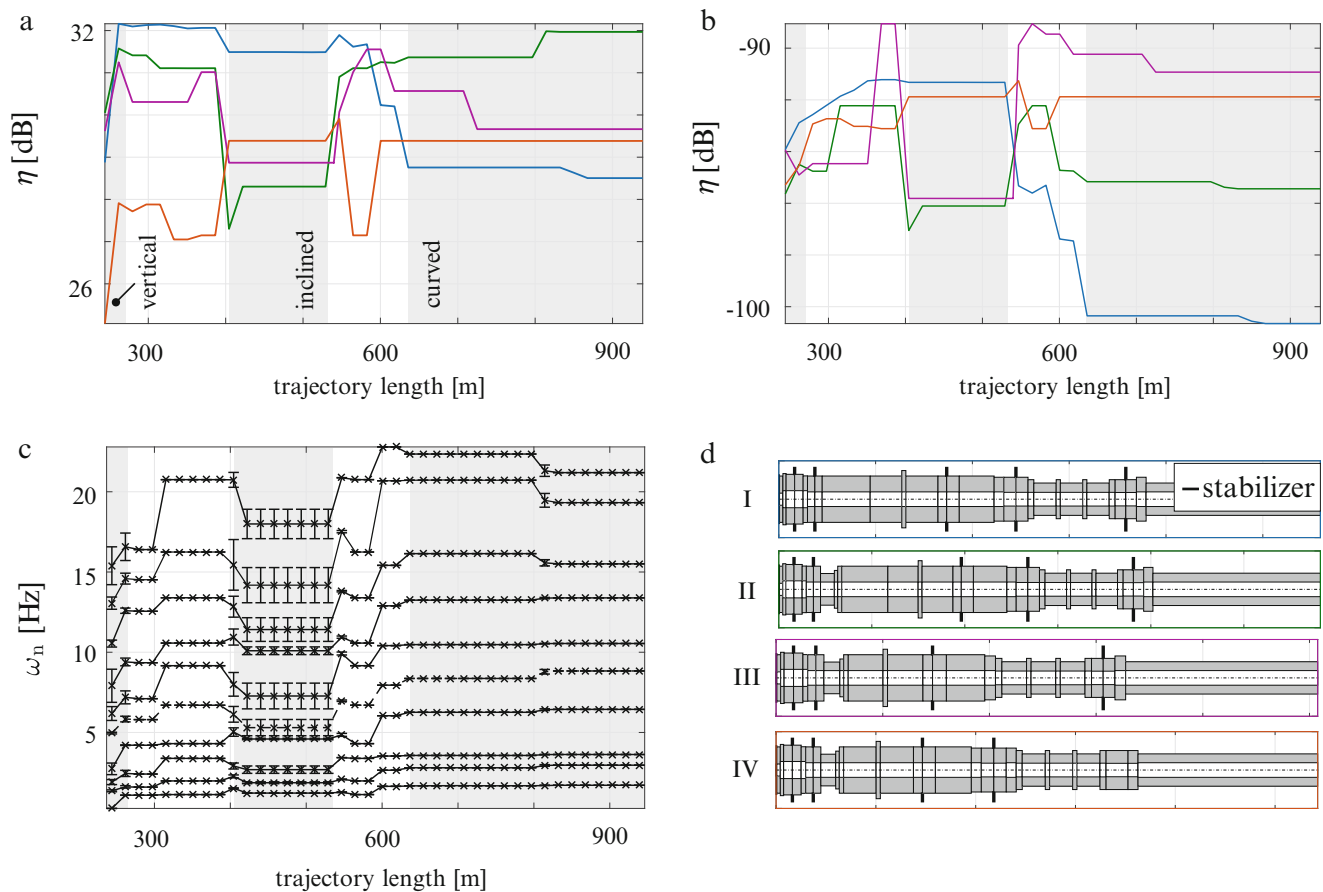


Fig. 15.3 Comparison of drillstring configurations along the specified drilling trajectory. (a) SNRs with respect to the maximum occurring lateral deflection. (b) SNR with respect to the maximum occurring bending moment. (c) Eigenfrequencies and their standard deviation (indicated by errorbars) for configuration II. (d) Drillstring configurations

η is depicted along the drilling trajectory in Fig. 15.3a, b respectively. Each drillstring configuration performs differently in terms of robustness at distinct positions along the trajectory. The changes between the vertical, inclined and curved sections (see Fig. 15.3a, b) can be clearly distinguished because the SNRs either drop or increase significantly at these locations. Amongst the configurations under investigation, configuration I is the only one without the more-flexible element above the bit, which turns it more rigid compared to the other designs. This is reflected by the higher SNRs for the deflection in the vertical and inclined section, because here the additional rigidity affects the maximum amplitude positively. However, as indicated by Fig. 15.3b, the increased stiffness influences the maximum bending moments adversely in the curved section. The same holds true for the maximum deflection of configuration I in the curved segment of the borehole trajectory. Here, the higher bending stiffness prevents other components than the stabilizers from establishing a wall contact, leading to higher amplitudes and a lower SNR. These results suggest, that the SNRs are mainly affected by the trajectory characteristic and by the changing wall contact locations. Because a modal analysis is performed for every parameter combination, the eigenfrequencies and their standard deviation can be determined at every position along the trajectory. Figure 15.3c shows the evolution of the eigenfrequencies along the borehole for configuration II. Comparison of these results to the SNR curves reveals a similar behavior for the eigenfrequencies within the individual sections of the trajectory. Because the results of the modal analysis are solely influenced by the calculated contact locations from static analysis, the presumption, that the robustness is mainly affected by the trajectory characteristic, can be confirmed. The variability or standard deviation of the eigenfrequencies originates from the variation of the WOB and borehole diameter D_B . As indicated by the higher standard deviations, the eigenfrequencies are especially sensitive towards variations of the WOB and borehole diameter within the vertical and inclined sections of the drilling trajectory. Between the different sections and within the curved section, the eigenfrequencies remain at one level with practically no variability. Furthermore, an increase of the eigenfrequencies can be observed within those sections. Due to the curvature, the bottom hole assembly is deformed and establishes more contacts with the borehole wall, which causes the mentioned increase. In addition, the resulting pre-stress leads to higher contact

forces and a less-sensitive reaction of the contact locations towards variations of the axial force and the borehole diameter. Due to the absence of this pre-stress effect in the straight vertical and inclined sections, fewer wall contacts, with an increased sensitivity towards changes in WOB and borehole diameter are established, leading to lower eigenfrequencies with a higher variability.

In conclusion, the representation of the SNR values in Fig. 15.3 enables a direct comparison of the different drillstring configurations along a specified borehole trajectory while taking parameter uncertainties into consideration. However, the results also suggest, that there is no BHA configuration that performs equally well in terms of robustness along the entire drilling trajectory. Moreover, as seen in Fig. 15.3c, the calculated eigenfrequencies and therefore the critical driving speeds, may be subject to significant variations due to parameter uncertainties and the trajectory characteristic. The latter ones should be included for the modal analysis in order to determine possible ranges for critical speeds rather than one single value.

15.4 Summary and Conclusion

This study presents a methodology that enables comparison of different drillstring configurations in terms of their robustness towards lateral vibrations along a specified borehole trajectory. To achieve this goal, a computationally efficient model, based on the transfer matrix method, was developed and implemented. To account for the influence of the drilling trajectory on the results of the dynamic analysis, this model was combined with a static calculation to determine the locations of the contacts between drillstring and borehole wall. At these locations rigid intermediate supports were introduced for the subsequent dynamic calculation. These calculations approximated the nonlinear behavior due to intermittent wall contacts by piecewise linear sub models. By using this modeling procedure, Monte Carlo Simulations were conducted for four different drillstring configurations and a set of uncertain parameters (WOB, borehole diameter, excitation position and amplitude). To compare the designs with each other, the signal-to-noise-ratio (SNR) proposed within the framework of the Taguchi-method was used. The described methodology enables a comparison of different design alternatives while considering parameter uncertainties. Furthermore, the method demonstrates how different drilling trajectory sections (vertical, inclined, curved) affect the reliability of the calculated eigenfrequencies. The study also shows the transfer matrix method, in combination with modal reduction, to be a powerful tool for numerical analysis of lateral drillstring dynamics. Due to its computational efficiency, it also enables the application of variance-based methods for global sensitivity analysis (GSA). First tests with the model from this investigation showed promising results.

Acknowledgements The author would like to thank Baker Hughes and the German Federal Ministry for Economic Affairs and Energy (BMWi) for funding this research (Project Number FKZ 0324015).

References

1. Saldivar Márquez, M.B., Boussaada, I., Mounier, H., Niculescu, S.-I.: Analysis and Control of Oilwell Drilling Vibrations: A Time-Delay Systems Approach. Springer, Cham (2015)
2. Brett, J.F., Warren, T.M., Behr, S.M.: Bit whirl – a new theory of PDC bit failure. *SPE Drill. Eng.* **5**, 275–281 (1990)
3. Jansen, J.: Nonlinear dynamics of oilwell drillstrings. PhD thesis, TU Delft (1993)
4. Gorelik, I., Höhn, O., Neubauer, M., Wallaschek, J.: Model and method for a time-efficient analysis of lateral drillstring dynamics. In: Proceedings of ASME Turbo Expo 2015: Turbine Technical Conference and Exposition (2015)
5. Stroud, D.R.H., Lines, L.A., Minett-Smith, D.J.: Analytical and experimental backward whirl simulations for rotary steerable bottom hole assemblies. In: SPE/IADC Drilling Conference and Exhibition (2011)
6. Dykstra, M., Chen, D.-K., Warren, T., Azar, J.: Drillstring component mass imbalance: a major source of downhole vibrations SPE drilling and completion. *SPE* **11**, 234–241 (1996)
7. Reckmann, H., Jogi, P., Kpetehoto, F., Chandrasekaran, S., Macpherson, J.: MWD failure rates due to drilling dynamics. In: IADC/SPE Drilling Conference and Exhibition (2010)
8. Baryshnikov, A., Calderoni, A., Ligrone, A., Ferrara, P.: A new approach to the analysis of drillstring fatigue behaviour, SPE drilling & completion. *Soc. Pet. Eng.* **12**, 77–84 (1997)
9. Sweet, R.: Case history of drillstem failures offshore West Africa SPE drilling engineering. *Soc. Pet. Eng.* **7**, 55–58 (1992)
10. Christoforou, A., Yigit, A.: Dynamic modeling of rotating drillstrings with borehole interaction. *J. Sound Vib.* **206**, 243–260 (1997)
11. Yigit, A., Christoforou, A.: Stick-slip and bit-bounce interaction in oil-well drillstrings. *Trans. ASME J. Energy Resour. Tech.* **128**, 268–274 (2006)
12. Heisig, G.: Zum statischen und dynamischen Verhalten von Tiefbohrsträngen in räumlich gekrümmten Bohrlöchern. PhD Thesis, Technische Universität Braunschweig, Institut für Technische Mechanik (1993)

13. Spanos, P.D., Payne, M.L.: Advances in Dynamic Bottomhole Assembly Modeling and Dynamic Response Determination SPE/IADC Drilling Conference. Society of Petroleum Engineers, New Orleans (1992)
14. Rudat, J., Dashevskiy, D.: Development of an innovative model-based stick/slip control system. In: SPE/IADC Drilling Conference and Exhibition. Society of Petroleum Engineers (2011)
15. Spanos, P., Chevallier, A., Politis, N., Payne, M.: Oil and gas well drilling: a vibrations perspective. *Shock vib. Digest* **35**, 85–103 (2003)
16. Holzer, H.: Die Berechnung der Drehschwingungen und ihre Anwendung im Maschinenbau. Springer, Berlin (1921)
17. Myklestad, N.O.: A new method of calculating natural modes of uncoupled bending vibration of airplane wings and other types of beams. *J. Aeronaut. Sci.* **11**, 153–162 (1944)
18. Pestel, E.C., Leckie, F.A.: Matrix Methods in Elastomechanics. McGraw-Hill, New York (1963)
19. Gasch, R., Knothe, K., Liebich, R. (eds.): *Strukturodynamik – Diskrete Systeme und Kontinua*. Springer, Berlin (2012)
20. Bestle, D., Abbas, L., Rui, X.: Recursive eigenvalue search algorithm for transfer matrix method of linear flexible multibody systems. *Multibody Sys. Dyn.* **32**, 429–444 (2014); Springer, Netherlands
21. Phadke, M.S.: *Quality Engineering Using Robust Design*. Prentice Hall International, Englewood Cliffs (1989)
22. Park, G., Hwang, K.-H., Lee, T.-H., Lee, K.H.: Robust design: an overview. *AIAA J.* **44**, 181–191 (2006)

Chapter 16

Consolidation of Weakly Coupled Experimental System Modes



Robert N. Coppolino

Abstract Normal modes of thin-walled axisymmetric shell structures are characterized by (1) overall body and (2) shell breathing families. By utilization of “body” deformation trial vectors, the two modal families are readily identified and separated. Local non-symmetrical structural features and/or imperfections cause body and breathing modes to mix (weak coupling) to form “fragmented” body mode clusters. Employment of singular value decomposition of experimental body mode cluster kinetic energies is found to consolidate the “fragments” back to ideally axisymmetric system body modes.

Keywords Weakly · Coupled · Modes · Reduction · Consolidation

16.1 Introduction

Natural frequencies and mode shapes of thin shell construction launch vehicle assemblies (and other structures, notably offshore jacket platforms) are ideally grouped in (a) body mode families (e.g. bending, axial, torsion and “bulge” [especially fluid-filled tanks]) and (b) breathing mode families. Breathing modes tend to occur well within the frequency band of fundamental body modes. In addition, breathing modes (especially those associated with singly curved, cylindrical regions) are strongly sensitive to static internal pressure and “weight” structural loading. In contrast, body modes tend to be insensitive to static loadings (as a general rule). Structural features and imperfections (especially in joints) tend to produce structural modes of thin shell structures with mixed body and breathing characteristics, which are sometimes referred to as “weakly coupled” or “fragmented” modes [1]. The mixed character modes often appear as repeated body modes, differing from one another merely due to the magnitude and phase of breathing kinetic energy contributions.

Consolidation of mixed body-breathing modes of a detailed thin shell structure finite element model is easily accomplished by application of either the Harmonic Reduction (HR) [2] or Modified Guyan Reduction (MGR) [3] method, which directly estimates approximate body dominant modes, while suppressing shell breathing modal characteristics. However, corresponding experimental modes of mixed body-breathing character are difficult to categorize and discern.

Due to the likelihood that measured thin shell structure modes will be of mixed body-breathing character, (1) a modal test requires thorough instrumentation and exciter resources to clearly map the subject system’s modes and (2) a sufficiently detailed finite element model that describes all anticipated body and breathing modes in the frequency band of interest. Employment of a systematic modal test planning procedure (e.g., RKE [4] and IRKE [5]) defines an instrumentation array that will properly map all modes in the frequency band of interest.

This paper introduces a procedure for consolidation of mixed character (body-shell breathing) experimental modes that processes modal kinetic energy clusters via singular value decomposition. The estimated consolidated body natural frequencies and mode shapes are found to be in close agreement with both HR and MGR consolidated body modes of an illustrative example shell structure.

R. N. Coppolino (✉)
Measurement Analysis Corporation, Torrance, CA, USA
e-mail: rcoppolino@macorp.net

16.2 Nomenclature

Symbol	Definition	Subscript	Definition
F	force	[] _L	lower frequency modes
K	stiffness	[] _b	body modes
KE	kinetic energy	[] _r	remaining, breathing modes
M	mass	[] _n	modal
OR	orthogonality	[] _c	consolidated modes
U	displacement		
f	frequency	Acronym	Definition
m	generalized mass	CGR	Classical Guyan Reduction
p	sensitivity parameter	DOF	Degree of Freedom
q	modal displacement	HR	Harmonic Reduction
u	generalized displacement	MGR	Modified Guyan Reduction
Γ	force allocation array	TAM	Test Analysis Model
I	identity matrix		
Φ	mode shape		
Ψ	displacement allocation array		
γ	modal cluster SVD eigenvalue		
λ	eigenvalue		
v	modal cluster SVD eigenvector		
φ	generalized mode shape		

16.3 Model Order Reduction Techniques and System Mode Classification Metrics

Classical Guyan Reduction (CGR) [6] has been a mainstay in the aerospace community since its introduction in 1965. CGR was originally intended to permit modal analysis of “large” finite element models that were beyond the practical solution capabilities of most computers. Since that time, computers and numerical methods have achieved the capability to treat extremely large, sparse real and complex eigenvalue problems. The primary reason for continued employment of CGR today is for definition of the Test-Analysis Model (TAM) mass matrix that corresponds to the planned measured response array for modal testing [4, 5].

16.3.1 Harmonic Reduction (HR)

A noteworthy alternative to CGR is a technique termed “Harmonic Reduction” or HR [2], which was an attempt to efficiently and effectively reduce large-order NASTRAN hydroelastic propellant tank models. In that endeavor, discrete DOFs were replaced with harmonic “patches” that defined displacement transformations of the type,

$$\{U\} = \begin{bmatrix} \Psi_{11} & 0 & \dots & 0 \\ 0 & \Psi_{22} & \dots & 0 \\ \dots & \dots & \dots & \dots \\ 0 & 0 & \dots & \Psi_{kk} \end{bmatrix} \begin{Bmatrix} U_1 \\ U_2 \\ \dots \\ U_k \end{Bmatrix} = [\Psi_{HR}] \{u\} \quad (16.1)$$

Employing $[\Psi_{HR}]$ as Ritz vectors, the reduced HR stiffness and mass matrices are

$$[K_{HR}] = [\Psi_{HR}]^T [K] [\Psi_{HR}], [M_{HR}] = [\Psi_{HR}]^T [M] [\Psi_{HR}]. \quad (16.2)$$

16.3.2 Modified Guyan Reduction (MGR)

Modified Guyan Reduction (MGR) [3] is the direct result of a conversation with Dr. Paul Blesloch of ATA, who informed the writer of difficulties encountered with Classical Guyan Reduction (CGR) during test planning for a complex structure modeled, in-part, with 3-D elastic solid elements. Recalling that CGR is based on static deflection patterns associated with point loads, coupled with the fact that 3-D elastic deflections under concentrated loadings are infinite, a distributed “patch” load approach (MGR) was defined to circumvent the CGR difficulty. Since 2011, the new, MGR method has been applied to other challenging situations and continuing evaluations have produced related developments.

Consider the general distribution of static loads described by the matrix equation,

$$\{F\} = \begin{bmatrix} \Gamma_{11} & 0 & \dots & 0 \\ 0 & \Gamma_{22} & \dots & 0 \\ \dots & \dots & \dots & \dots \\ 0 & 0 & \dots & \Gamma_{kk} \end{bmatrix} \begin{Bmatrix} F_1 \\ F_2 \\ \dots \\ F_k \end{Bmatrix} = [\Gamma] \{F_\Gamma\}, \quad (16.3)$$

where the individual load patches, $[\Gamma_{ii}]$, represents unit load patterns (over each specific geometric patch) that are mathematically the transposes of rigid body deflection patterns. The static displacement due to the above defined loading is

$$\{U\} = [K]^{-1} \{F\} = [K^{-1}\Gamma] \{F_\Gamma\}. \quad (16.4)$$

Pre-multiplication of this result by the transpose of unit loadings yields,

$$\{U_\Gamma\} = [\Gamma]^T [K]^{-1} \{F\} = [\Gamma^T K^{-1} \Gamma] \{F_\Gamma\}, \{F_\Gamma\} = [\Gamma^T K^{-1} \Gamma]^{-1} \{U_\Gamma\}. \quad (16.5)$$

Substitution of this result into Eq. 16.4 yields the (load patch based) MGR transformation,

$$\{U\} = [K^{-1}\Gamma] [\Gamma^T K^{-1} \Gamma]^{-1} \{U_\Gamma\} = [\Psi_{MGR}] \{U_\Gamma\}. \quad (16.6)$$

Employing $[\Psi_{MGR}]$ as Ritz vectors, the MGR stiffness and mass matrices are

$$[K_{MGR}] = [\Psi_{MGR}]^T [K] [\Psi_{MGR}], [M_{MGR}] = [\Psi_{MGR}]^T [M] [\Psi_{MGR}]. \quad (16.7)$$

It should be noted that, in the limiting case of concentrated, point patch loads, the present formulation reduces to CGR.

16.3.3 Approximate Modes of the Reduced Order System

Regardless of the selected model reduction strategy (CGR, HR, MGR), the original system is using the generic reduction transformation,

$$\{U\} = [\Psi] \{u\} \quad (16.8)$$

Resulting in the generic reduced order mass and stiffness matrices,

$$[K_{\Psi\Psi}] = [\Psi]^T [K] [\Psi], [M_{\Psi\Psi}] = [\Psi]^T [M] [\Psi]. \quad (16.9)$$

The modal transformation resulting from analysis of the reduced-order system is therefore,

$$\{\mathbf{u}\} = [\boldsymbol{\varphi}] \{\mathbf{q}\} \quad (16.10)$$

with corresponding approximate natural frequencies (for orthonormal modal vectors),

$$(2\pi f_n)^2 = \{\boldsymbol{\varphi}_n\}^T [\mathbf{K}_{\Psi\Psi}] \{\boldsymbol{\varphi}_n\} \quad (16.11)$$

Approximate mode shapes, expressed in terms of the original unreduced DOF set are

$$[\Phi_{\Psi}] = [\Psi] [\boldsymbol{\varphi}] \quad (16.12)$$

16.3.4 Body and Breathing Modes of Axisymmetric Shell Structures

The shell structure, shown below in Fig. 16.1, serves as an illustrative example system for the present discussion. It consists of five substructures, namely (1) a lower cylindrical skirt (fully fixed at its base), (2) a lower hemispherical bulkhead, (3) lower cylindrical section, (4) upper cylindrical section, and (5) upper hemispherical bulkhead. The overall dimensions of the aluminum structure are length, $L = 100$ inches, radius, $R = 20$ inches, and wall thickness, $h = 0.4$ inches. It should be noted that this illustrative example structure does not represent a realistic design. The rather high thickness-to-radius ratio, $h/R = 1/50$, was selected to produce less shell breathing modes in the base frequency band ($f < 2000$ Hz) than typical aerospace systems, while including modes of sufficient complexity to illustrate key aspects of quantitative normal mode metrics.

There are a variety of metrics for characterization of normal modes, namely (a) modal effective mass (for a supported structure), (b) directional kinetic energy distribution, (c) component kinetic and strain energy distribution (when the structure is appropriately segmented into separate individual components), and (d) kinetic energy distribution in terms of “body” and “breathing” modes. While all of the above characterization metrics are discussed in references 7 and 8, the present discussion focuses on the fourth category.

Consider the following seven “body” geometric patterns for the example shell axial stations (which may be used for either HR or MGR purposes) (Fig. 16.2).

The seven patterns are associated with cross-sectional lateral (“TX” and “TY”), and axial (“TZ”) translations, pitch, yaw and torsional (“RX”, “RY”, and “RZ”) rotations, and radial bulge (“TR”) translation. In “circumferential harmonic terms, the above seven patterns represent $n = 0$ and 1 motions (or load patterns).

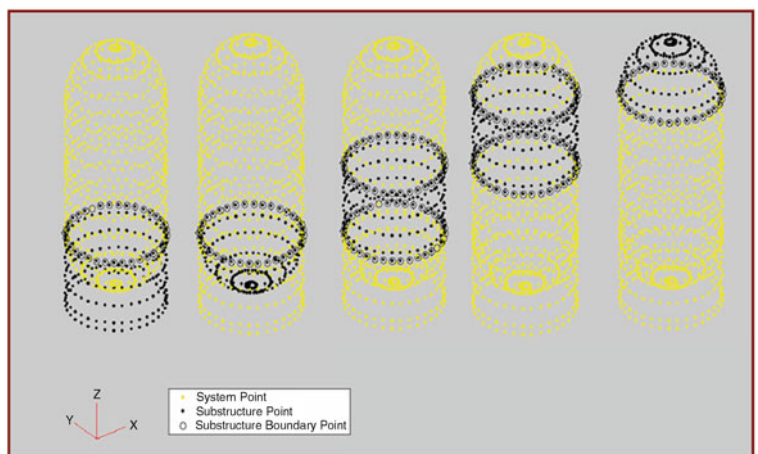


Fig. 16.1 Illustrative example axisymmetric shell structure

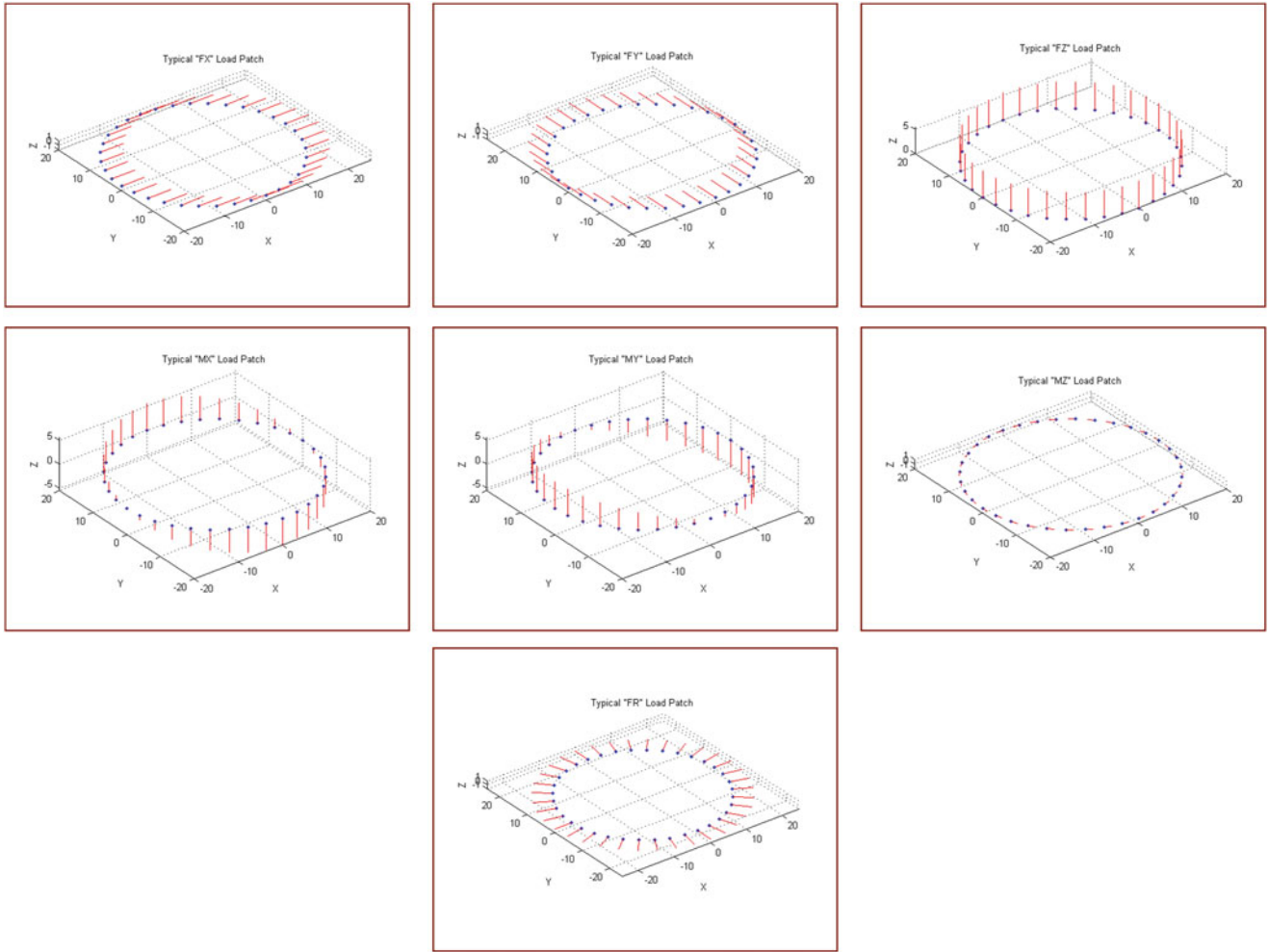


Fig. 16.2 Shell axial station “Body” geometric patterns

By organizing the above described geometric patterns as a body displacement transformation matrix, $[\Psi_b]$, the discrete lower frequency FEM shell displacements, $[\Phi_L]$, are expressed as,

$$[\Phi_L] = [\Psi_b] [\varphi_b] + [\Phi_r] \quad (16.13)$$

where $[\Psi_b]$ may be either defined as $[\Psi_{HR}]$ or $[\Psi_{MGR}]$. In actuality, $[\Psi_{HR}]$ has been selected for the present discussion and illustrative example analysis.

Employing linear least-squares analysis, as follows, each system normal mode may be partitioned into “body” and (remainder) “breathing” components.

$$\begin{aligned} [\Psi_b^T M \Phi_L] &= [\Psi_b^T M \Psi_b] [\varphi_b] + [\Psi_b^T M \Phi_r] = [\Psi_b^T M \Psi_b] [\varphi_b] + [0] \rightarrow [\varphi_b] = [\Psi_b^T M \Psi_b]^{-1} [\Psi_b^T M \Phi_L] \\ [\Phi_b] &= [\Psi_b] [\varphi_b], [\Phi_r] = [\Phi_L] - [\Phi_b], [\Phi_b^T M \Phi_r] = [0] \quad (\text{orthogonality of body and breathing}) \end{aligned} \quad (16.14)$$

Due to orthogonality of the body and breathing modal displacement components, the following kinetic energy metrics are defined:

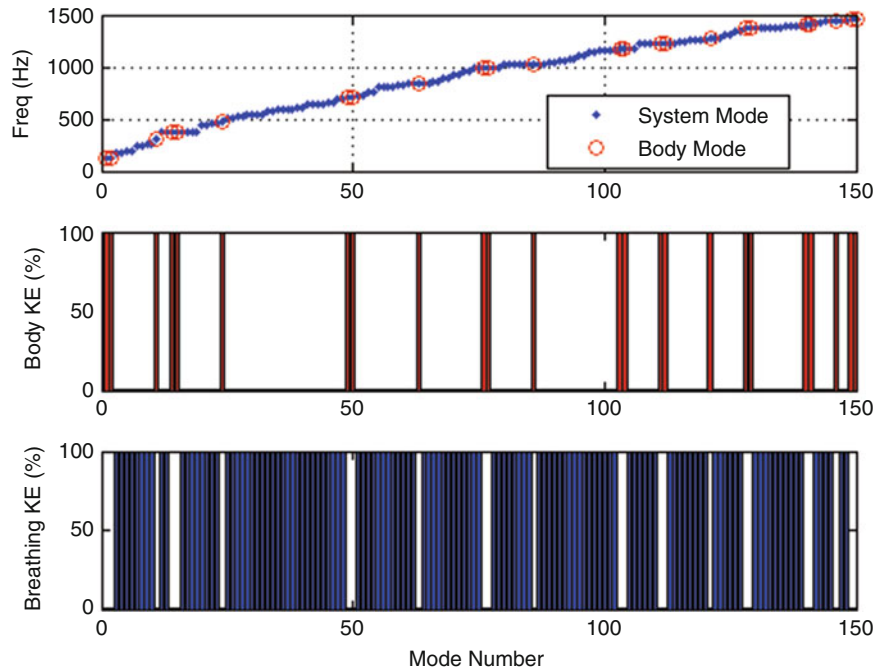


Fig. 16.3 Axisymmetric shell structure modal frequencies and kinetic energy metrics

$$\begin{aligned}
 [I_L] &= [\Phi_L^T M \Phi_L] = [\Phi_b^T M \Phi_b] + [\Phi_r^T M \Phi_r] \quad (\text{Total modal KE} = \text{total body KE} + \text{total breathing KE}) \\
 [M \Phi_L] \otimes [\Phi_L] &= [M \Phi_b] \otimes [\Phi_b] + [M \Phi_r] \otimes [\Phi_r] \quad (\text{Body and breathing KE distributions})
 \end{aligned} \tag{16.15}$$

The total modal kinetic energy and partial kinetic energies for each individual mode are the diagonal terms of the first matrix equation set of “equation” 16.15. A summary of ideal axisymmetric shell structure modal frequencies and kinetic energy metrics is presented below in Fig. 16.3.

16.3.5 MGR and HR Approximations for the Perfectly Axisymmetric Shell Structure

HR and MGR strategies produce approximate modal solutions for body dominant modes, which are summarized below in Table 16.1, along with exact body dominant modes for the ideal axisymmetric shell structure. The MGR modal kinetic energy distributions, based on partial generalized displacement (TX, TY, TZ, RX, RY, RZ, and TR) sums clearly indicate the nature of each body dominant mode.

The above results indicate that MGR based natural frequencies follow exact structure body dominant modal frequencies more accurately than the HR based approximation.

16.3.6 Body and Breathing Modes of a Perturbed Axisymmetric Shell Structure

As a general rule, as-built geometrically axisymmetric shell structures are not structurally axisymmetric due to local design features and imperfections. The effects of typical perturbations are evaluated herein by addition of a “X = 0” axial line of added mass (total value is 1.85% of the baseline shell rigid body mass) on the example shell (previously illustrated in Fig. 16.1). A summary of perturbed axisymmetric shell structure modal frequencies and kinetic energy metrics is presented below in Fig. 16.4.

Applying the body-breathing metrics (Eqs. 16.13, 16.14, and 16.15) to the perturbed shell structure to categorize modes that are body kinetic energy dominant, forty-nine (49) modes of the perturbed system are found to have “body” kinetic energy in excess of 2%. The 49 perturbed system modes are now compared to the 24 pure “body” modes of the ideal axisymmetric

Table 16.1 Comparison of exact, HR and MGR body modes

Exact			Harmonic reduction		MGR		MGR KE distribution						
Mode	Freq (Hz)	Type	Mode	Freq (Hz)	Mode	Freq (Hz)	TX	TY	TZ	RX	RY	RZ	TR
1	122.20	Bend-Y	1	122.20	1	122.20		96		4			
2	122.20	Bend-X	2	122.20	2	122.20	96				4		
11	315.24	Torsion	3	315.24	3	315.24						100	
14	377.21	Bend-Y	4	377.21	4	377.23		91		9			
15	377.21	Bend-X	5	377.21	5	377.24	91				9		
24	467.77	Axial	6	467.78	6	467.78			100				
49	706.65	Bend-Y	7	706.84	7	706.86		91		9			
50	706.65	Bend-X	8	706.85	8	706.87	91				9		
63	841.31	Torsion	9	841.35	9	841.35						100	
76	997.48	Lateral-Y	10	999.12	10	997.81		60		40			
77	997.50	Lateral-X	11	999.14	11	997.83	60				40		
86	1029.90	Axial	12	1031.30	12	1030.10			94				6
103	1169.60	Lateral-Y	13	1174.20	13	1170.00		60		40			
104	1169.60	Lateral-X	14	1174.30	14	1170.10	60				40		
111	1223.50	Bend-Y	15	1233.80	15	1224.10		91		9			
112	1223.50	Bend-X	16	1233.80	16	1224.10	91				9		
121	1273.40	Axial-Bulge	17	1281.00	17	1273.60			78				22
128	1368.30	Bend-Y	18	1395.10	18	1369.10		95		5			
129	1368.40	Bend-X	19	1395.10	19	1369.20	95				5		
140	1402.80	Lateral-XY	20	1416.30	20	1404.50	7	8		45	40		
141	1402.80	Lateral-XY	21	1416.30	21	1404.50	8	8		40	44		
146	1440.40	Bulge-Axial	22	1466.60	22	1440.40			45				55
149	1452.70	Lateral-XY	23	1467.50	23	1453.60	33	43		14	11		
150	1452.70	Lateral-XY	24	1484.70	24	1453.60	43	33		11	14		

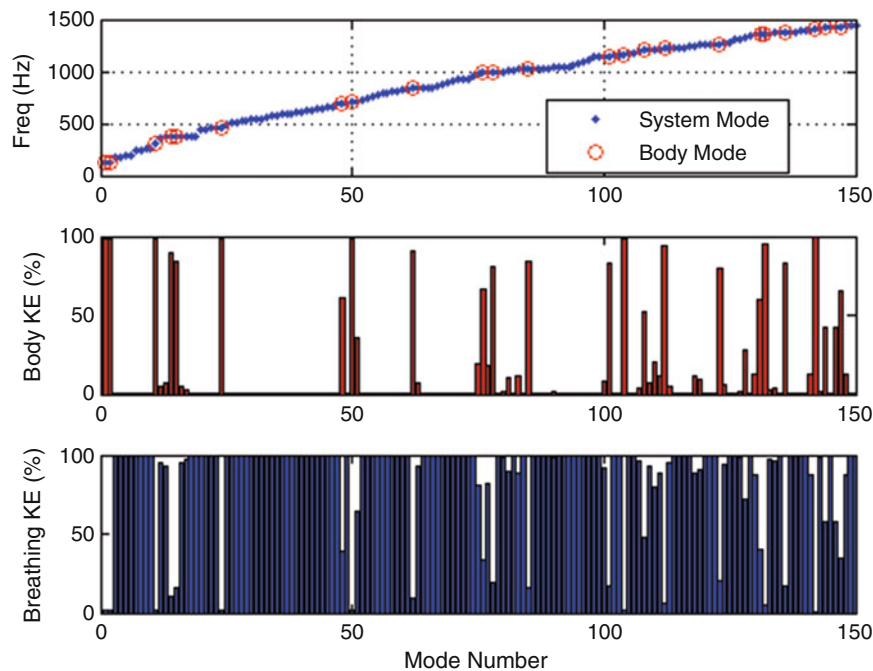


Fig. 16.4 Perturbed shell structure modal frequencies and kinetic energy metrics

structure employing the cross-orthogonality matrix (using the axisymmetric structure mass matrix as a reference). Results showing absolute values of cross-orthogonality in excess of 5% are provided in below in Table 16.2.

Table 16.2 Cross-orthogonality of ideal axisymmetric & perturbed shell body dominant modes

		Ideal Axisymmetric Shell																						
Mode	Freq (Hz)	1	2	11	14	15	24	49	50	63	76	77	86	103	104	111	112	121	128	129	140	141	146	149
		122.20	122.20	315.24	377.21	377.21	467.77	706.65	706.65	841.31	997.48	997.50	1029.9	1169.6	1169.6	1223.5	1223.5	1273.4	1368.3	1368.4	1402.8	1402.8	1440.4	1452.7
1	120.97	99																						
2	121.13		99																					
11	312.43			99																				
12	359.94				24																			
13	367.98				27																			
14	373.97					95																		
15	374.65					92																		
16	375.36						23																	
17	377.43						16																	
24	463.45							99																
48	695.39								78															
50	701.56									99														
51	706.21							60																
62	833.52									95														
63	836.13									26														
75	967.62										44													
76	986.08										82		7											
77	992.77											43												
78	994.38											90												
81	1001.8											31												
83	1017.4												34											
85	1020.4												91											
100	1148.6													29										
101	1149.7													91										
104	1166.4														99		5							
107	1187.2																							
108	1200.1													9										6
109	1205.5													7										
110	1210.2													12										
111	1212.5													8										
112	1219.5																							
113	1221.3																							
118	1237.1																							
119	1252.5																							
123	1266.5																							
124	1275.8																							
128	1322.5																							
130	1352.8																							
131	1363.1																							
132	1366.3																							
133	1366.4																							
134	1368.8																							
136	1373.7																							
141	1395.2																							
142	1402.0																							
144	1419.6																							
146	1422.6																							
147	1433.2																							
148	1434.8																							

Introduction of a perturbation to the ideal axisymmetric shell structure has the effect of “fragmenting” or “splitting” the ideal axisymmetric system’s body-dominant modes. The naming and characterization of experimental body-dominant modes is no longer a straightforward process. Moreover, estimation of specific experimental “body” mode frequencies is problematic.

16.3.7 Additional Modal Sensitivity Trends for the Perturbed Shell Structure

Additional insight into modal sensitivity for the example shell structure is gained by variation of the magnitude of added line mass from 0 to 3.7% (the sensitivity parameter, p, varies from 0 to 2). Sensitivity of all system modes in the 0–1400 Hz frequency band, along with tagged modal subsets with body kinetic energy $\geq 25\%$, $\geq 50\%$, and $\geq 75\%$ respectively, is illustrated below in Fig. 16.5.

The above results indicate that body dominant (body KE $\geq 75\%$) modal frequencies are generally insensitive to added line mass (0–3.7% of total system mass), while some breathing mode frequencies (especially body KE $\leq 25\%$) exhibit much greater frequency sensitivity.

16.4 Body Mode Consolidation

While there appears to be a series of options for understanding and categorization of structural modes for shell-type structures (as well as other built-up systems), “fragmentation” or “splitting” of body dominant modes represents a challenge that cannot necessarily be easily circumvented when modal data is experimental.

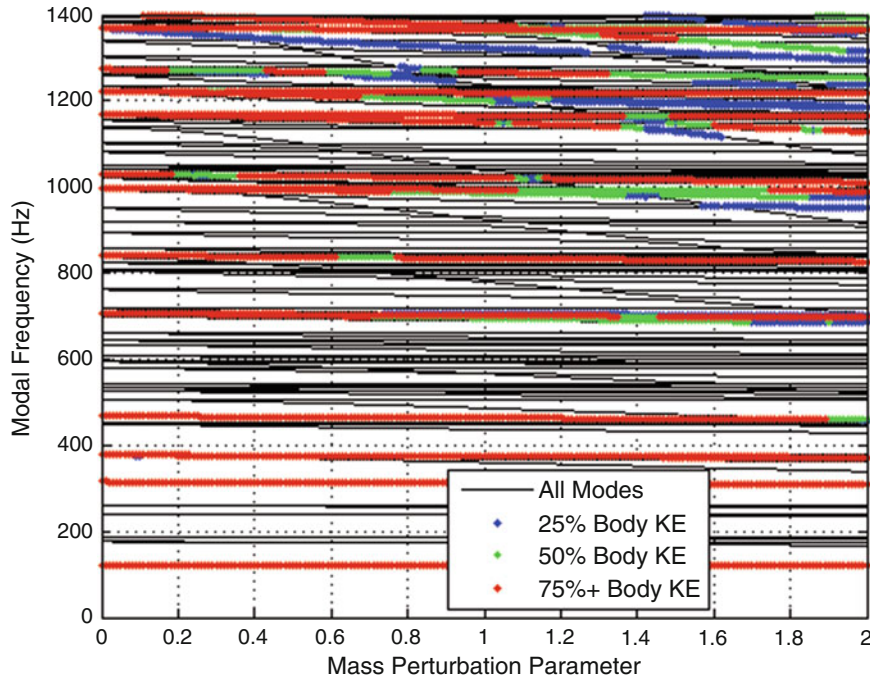


Fig. 16.5 Sensitivity of perturbed shell system modes to added line mass

16.4.1 Modal Cluster Definition Using the Perturbed Shell Model Example

Recalling the previous discussion in Sect. 16.3.4, the body displacement transformation matrix, $[\Phi_b]$, is used to decompose the discrete lower frequency FEM shell modal displacements, $[\Phi_L]$, into “body” and remaining (“breathing”) components, respectively,

$$[\Phi_L] = [\Phi_b] + [\Phi_r], \text{ where } [\Phi_b] = [\Psi_b][\varphi_b]. \quad (16.16)$$

Since the “body” and “breathing” modal components are mutually orthogonal (see Eqs. 16.13, 16.14, and 16.15), the modal orthogonality matrix (which is also the modal kinetic energy matrix) is the sum of two components, namely,

$$[\text{OR}] = [m_b] + [m_r] = [I], \text{ where } [m_b] = [\Phi_b^T M \Phi_b], [m_r] = [\Phi_r^T M \Phi_r]. \quad (16.17)$$

The process of mode consolidation focuses on mathematical operations on “clusters” within the body mode orthogonality matrix, $[m_b]$, and the associated lower eigenvalues of the complete structural system, $[\lambda_L]$.

The body mode orthogonality matrix, $[m_b]$, for the perturbed example shell structure ($p = 1$) from the previous section is depicted below in Fig. 16.6 as a Matlab “pseudocolor” graphic of absolute values for $[m_b]$.

It should be noted that the body modes were normalized to unit modal mass to generate a version of $[m_b]$ with unit diagonal terms, thus accentuating the repeated nature of clustered modes. Apparently repeated and highly coupled body mode clusters are readily “tagged” among the 49 body modes (selected based on individual body mode kinetic energy, $[m_b]_{ii} \geq 10\%$, body modes that have not been renormalized).

The following rule is employed to define body mode clusters, with their selection depicted in Fig. 16.7:

$$|m_b|_{ii} \geq 0.10, |m_b|_{ij} \geq 0.10 \text{ for } i \neq j. \quad (16.18)$$

Eight body mode clusters are defined using the above defined criteria. They are depicted below for body dominant modes 1–22 and 23–49, respectively in Tables 16.3 and 16.4.

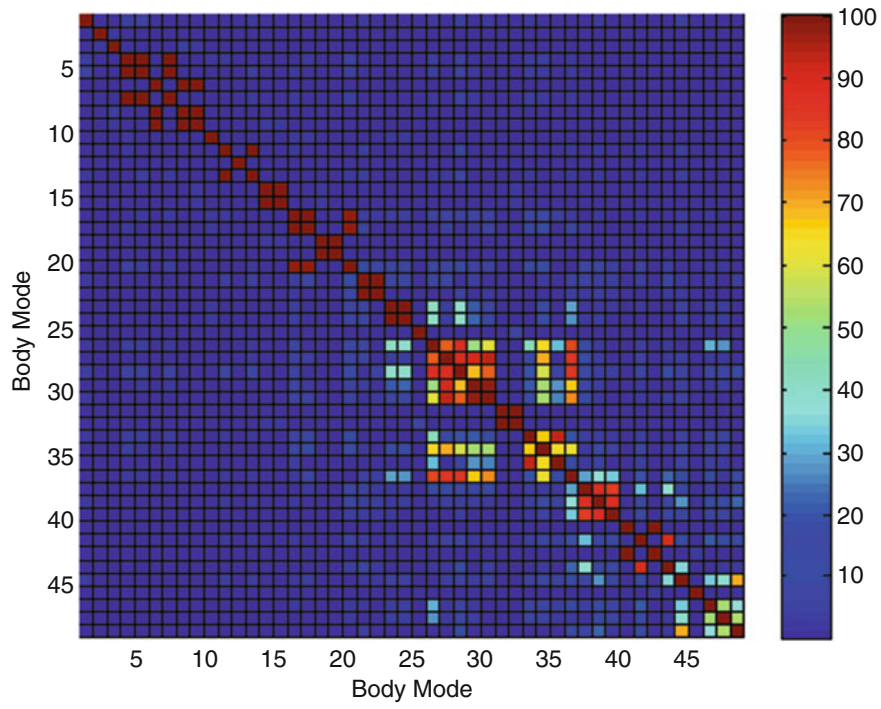


Fig. 16.6 Body mode orthogonality matrix, $[m_b]$, absolute values

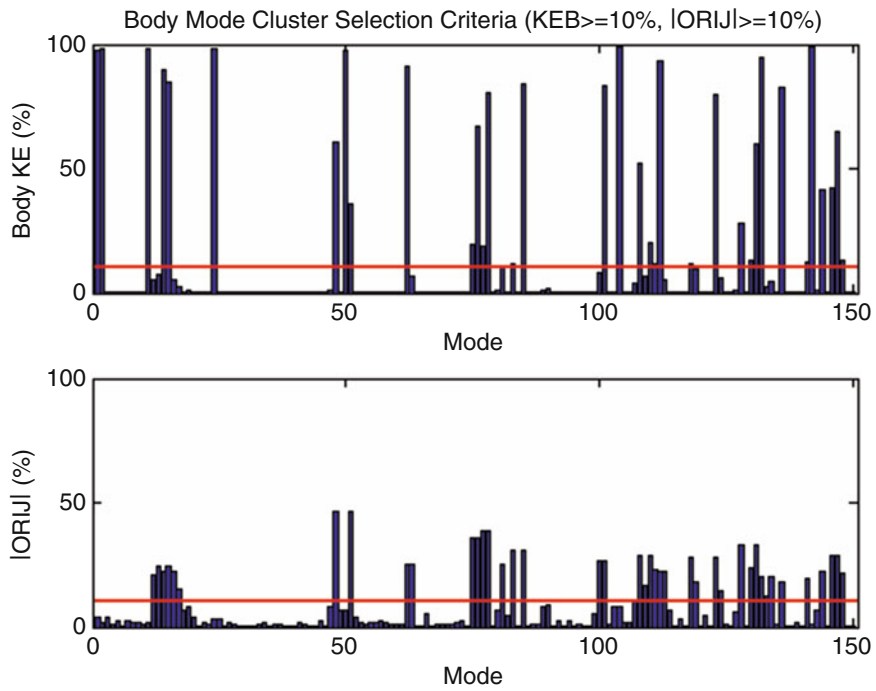


Fig. 16.7 Body mode cluster selection criterion (note $KEB = |m_b|_{ii}$, $|ORIJ| = |m_b|_{ij}$)

Table 16.3 Mode clusters for body dominant modes 1–22

Perturbed (Selected Modes)				Body Mode Orthogonality Matrix																							
Mode	Freq (Hz)	diag (OR)	coup(OR)	1	2	3	4	5	6	7	8	9	10	11	12	13	14	15	16	17	18	19	20	21	22		
1	120.97	98	2	98	0	0	1	-2	0	0	0	0	-1	1	0	1	0	0	0	0	0	0	0	0	-1	0	
2	121.13	98	2	0	98	-2	0	0	0	0	0	0	0	0	0	0	0	0	0	0	0	0	0	0	0	0	
11	312.43	98	2	0	0	-2	98	0	0	-1	0	-1	0	0	0	0	0	0	0	0	0	0	0	0	0	0	
12	359.94	5	21	1	0	0	0	5	6	0	21	0	0	0	0	0	0	0	0	0	0	0	0	0	0	0	
13	367.98	7	25	-2	0	0	0	6	7	0	25	0	0	0	0	1	0	0	0	0	0	0	0	0	0	0	
14	373.97	90	22	0	0	-1	0	0	0	90	0	-22	-15	0	0	0	1	0	0	0	0	0	0	0	0	0	
15	374.65	84	25	0	0	0	0	21	25	0	84	0	0	0	1	0	1	0	0	-1	0	0	0	-1	0	0	
16	375.36	5	22	0	0	-1	0	0	0	-22	0	5	4	0	0	0	0	0	0	0	0	0	0	0	0	0	
17	377.43	3	15	0	0	0	0	0	0	-15	0	4	3	0	0	0	0	0	0	0	0	0	0	0	0	0	
24	463.45	98	2	-1	0	0	0	0	0	0	0	0	0	98	0	0	0	0	0	-1	-1	0	0	0	0	0	
48	695.39	61	46	1	0	0	0	0	0	0	1	0	0	0	61	0	-46	0	0	-1	0	0	0	0	0	-1	0
50	701.56	98	0	0	0	0	0	0	0	0	0	0	0	0	98	0	0	0	0	0	0	0	0	0	0	0	
51	706.21	36	46	1	0	0	0	0	1	0	1	0	0	0	-46	0	36	0	0	0	0	0	0	0	0	1	0
62	833.52	91	25	0	0	0	0	0	0	1	0	0	0	0	0	0	91	25	0	0	0	1	0	0	0	0	
63	836.13	7	25	0	0	0	0	0	0	0	0	0	0	0	0	0	25	7	0	0	0	0	0	0	0	0	
75	967.62	20	36	0	0	0	0	0	0	0	-1	0	0	-1	-1	0	0	0	0	20	36	0	0	-14	-1	1	
76	986.08	67	36	0	0	0	0	0	0	0	0	0	0	-1	0	0	0	0	0	36	67	0	0	-25	-2	-1	
77	992.77	19	39	0	0	0	0	0	0	0	0	0	0	0	0	0	1	0	0	0	0	19	-39	0	0	0	
78	994.38	81	39	0	0	0	0	0	0	0	0	0	0	0	0	0	0	0	0	0	0	-39	81	0	0	0	
81	1001.81	10	25	0	0	0	0	0	0	0	-1	0	0	0	0	0	0	0	0	-14	-25	0	0	10	-1	-5	
83	1017.37	12	31	-1	0	0	0	0	0	0	0	0	0	-1	0	0	1	0	0	-1	-2	0	0	-1	12	31	
85	1020.38	84	31	0	0	0	0	0	0	0	0	0	0	0	0	0	0	0	0	1	-1	0	0	-5	31	84	

Table 16.4 Mode clusters for body dominant modes 23–49

Perturbed (Selected Modes)				Body Mode Orthogonality Matrix																											
Mode	Freq (Hz)	diag (OR)	coup(OR)	23	24	25	26	27	28	29	30	31	32	33	34	35	36	37	38	39	40	41	42	43	44	45	46	47	48	49	
100	1148.56	8	26	8	-26	0	2	1	-3	-3	-1	0	0	0	-2	0	-2	0	0	1	0	0	0	0	1	0	0	1	-1	0	0
101	1149.73	83	26	-26	83	0	-7	-2	10	9	3	0	0	0	5	-1	6	1	-1	-1	0	0	0	0	-2	0	-2	3	1	1	
104	1166.38	99	1	0	0	99	0	0	0	0	0	0	-1	0	0	0	0	0	0	0	0	0	0	0	0	0	0	0	0	0	
107	1187.16	4	11	2	-7	0	4	11	-4	4	4	0	0	-3	4	-6	-4	-1	0	0	0	0	0	0	0	0	-4	3	0	-2	
108	1200.07	52	29	1	-2	0	11	52	-17	29	23	0	0	-3	15	0	-15	-4	-1	-1	0	1	0	-2	-1	0	-1	1	-1	0	
109	1205.54	7	17	-3	10	0	-4	-17	7	-8	-7	0	0	2	-5	2	5	2	0	-1	0	0	0	-2	0	0	1	1	-2	1	
110	1210.18	20	29	-3	9	0	4	29	-8	20	15	0	0	3	7	11	-7	-2	-1	0	0	0	0	0	0	-1	0	1	-1	0	
111	1212.47	12	23	-1	3	0	4	23	-7	15	12	0	0	2	6	8	-6	-2	0	0	0	0	0	1	-1	0	0	0	0	1	
112	1219.50	93	22	0	0	0	0	0	0	0	0	93	22	0	0	0	0	0	0	0	0	0	0	0	0	0	0	0	0	0	
113	1221.28	5	22	0	0	-1	0	0	0	0	0	22	5	0	0	0	0	0	0	0	0	0	0	0	0	0	0	0	0	0	
118	1237.13	12	28	0	0	0	-3	-3	2	3	2	0	0	12	-7	28	2	1	1	1	0	0	0	0	1	0	1	-2	0	1	
119	1252.53	10	18	-2	5	0	4	15	-5	7	6	0	0	-7	10	-18	-5	0	-2	1	0	0	0	-1	-1	0	1	-1	0	2	
123	1266.47	80	28	0	-1	0	-6	0	2	11	8	0	0	28	-18	80	2	1	2	0	0	-1	0	-1	2	0	-2	1	-1	-2	
124	1275.81	6	15	-2	6	0	-4	-15	5	-7	-6	0	0	2	-5	2	6	-4	3	-6	0	-1	0	5	-1	0	2	0	-2	1	
128	1322.55	28	33	0	1	0	-1	-4	2	-2	-2	0	0	1	0	1	-4	28	-17	33	0	3	0	-18	2	0	-1	0	-3	1	
130	1352.82	13	24	0	-1	0	0	-1	0	0	-1	0	0	0	1	-2	2	-17	13	-24	0	-1	0	5	3	0	-2	-3	7	-2	
131	1363.11	60	33	1	-1	0	0	-1	-1	0	0	0	0	1	1	0	-6	33	-24	60	0	-2	0	11	-2	0	-3	-3	2	-1	
132	1366.26	95	20	0	0	0	0	0	0	0	0	0	0	0	0	0	0	0	0	95	0	20	0	0	0	0	0	0	0	0	
133	1366.43	2	12	0	0	0	0	1	0	0	0	0	0	0	0	0	-1	-1	3	-1	-2	0	2	0	-12	1	0	2	-1	-1	
134	1368.84	4	20	0	0	0	0	0	0	0	0	0	0	0	0	0	0	0	0	20	0	4	0	0	0	0	0	0	0	0	
136	1373.70	83	18	0	0	0	0	-2	-2	0	1	0	0	0	-1	-1	5	-18	5	11	0	-12	0	83	-11	0	0	-1	-2	-1	
141	1395.25	12	20	1	-2	0	0	-1	0	-1	-1	0	0	1	-1	2	-1	2	3	-2	0	1	0	-11	12	0	-8	-9	20	-5	
142	1402.03	99	0	0	0	0	0	0	0	0	0	0	0	0	0	0	0	0	0	0	0	0	0	0	99	0	0	0	0	0	
144	1419.64	42	22	1	-2	0	-4	-1	1	1	0	0	0	1	1	-2	2	-1	-2	-3	0	2	0	0	-8	0	42	-22	-19	22	
146	1422.59	42	29	-1	3	0	3	1	1	-1	0	0	0	-2	-1	1	0	0	-3	-3	0	-1	0	-1	-9	0	-22	42	-29	-9	
147	1433.20	65	29	0	1	0	0	-1	-2	0	0	0	0	0	0	-1	-2	-3	7	2	0	-1	0	-2	20	0	-19	-29	65	-14	
148	1434.82	13	22	0	1	0	-2	0	1	1	1	0	0	1	2	-2	1	1	-2	-1	0	1	0	-1	-5	0	22	-9	-14	13	

16.4.2 Decomposition of Modal Clusters Using SVD (Mode Consolidation Theory)

Consider an individual modal cluster (see Tables 16.3 and 16.4) that is defined by the following matrix data:

[Φb] = “body” mode shape cluster (see Eq. 16.16)

[λ] = eigenvalues for the system modes from which the cluster is defined

[mb] = “body” mode cluster generalized mass matrix (see Eq. 16.17).

Generalized eigenvectors associated with [mb] are defined based on the following singular value decomposition operations:

$$[m_b] [\tilde{u}_b] = [\tilde{u}_b] [\gamma_b], \text{ where } [\tilde{u}_b^T] [\tilde{u}_b] = [I] \text{ and } [\tilde{u}_b^T] [m_b] [\tilde{u}_b] = [\gamma_b], \tag{16.19}$$

and the calculated eigenvalues are sequenced in descending order ($\gamma_{b,1} \geq \gamma_{b,2} \geq \gamma_{b,3} \geq \dots$). By employing a cut-off criterion ($\gamma_{b,i} / \gamma_{b,1} \geq \text{tol}$), a truncated subset of eigenvalues and eigenvectors are kept. Finally, the truncated set of cluster eigenvectors is rescaled as,

$$[v_b] = [\tilde{u}_b] [\gamma_b]^{1/2}, \text{ resulting in } [v_b^T] [v_b] = [\gamma_b] \text{ and } [m_b] \approx [v_b] [v_b^T]. \tag{16.20}$$

Table 16.5 Consolidated body mode set orthogonality

Mode		1	2	3	4	5	6	7	8	9	10	11	12	13	14	15	16	17	18	19	20	21	22	23
	Freq (Hz)	Orthogonality (%)																						
1	120.97	100	0	0	0	0	-1	0	0	0	0	0	0	0	0	0	0	0	0	0	0	0	0	0
2	121.13	0	100	-2	0	0	0	0	0	0	0	0	0	0	0	0	0	0	0	0	0	0	0	0
3	312.43	0	-2	100	0	1	0	0	0	0	0	0	0	0	0	0	0	0	0	0	0	0	0	0
4	373.36	0	0	0	100	0	1	0	0	0	1	0	0	0	0	0	0	-1	0	0	0	0	0	0
5	374.14	0	0	1	0	100	0	0	0	-1	0	0	0	0	0	0	0	0	0	0	0	0	0	0
6	463.45	-1	0	0	1	0	100	0	0	0	-2	0	0	-2	0	1	0	0	0	0	0	0	0	-1
7	699.42	0	0	0	0	0	0	100	0	0	0	0	1	0	0	0	0	0	0	1	0	0	1	0
8	701.56	0	0	0	0	0	0	0	100	0	0	0	0	0	0	0	0	0	0	0	0	0	0	0
9	833.71	0	0	0	0	-1	0	0	0	100	0	-1	0	0	0	0	0	0	0	0	0	0	0	0
10	983.97	0	0	0	1	0	-2	0	0	0	100	0	-1	-1	0	0	0	-1	0	0	0	0	0	0
11	994.07	0	0	0	0	0	0	0	0	-1	0	100	0	0	0	0	0	0	0	0	0	0	0	0
12	1020.02	0	0	0	0	0	0	1	0	0	-1	0	100	1	0	1	0	0	0	3	0	0	-1	0
13	1149.62	0	0	0	0	0	-2	0	0	0	-1	0	1	100	0	0	0	-1	-1	0	0	0	0	-4
14	1166.38	0	0	0	0	0	0	0	0	0	0	0	0	0	100	0	0	0	0	0	0	0	0	0
15	1210.08	0	0	0	0	0	1	0	0	0	0	0	1	0	0	100	0	0	0	0	0	0	0	1
16	1219.59	0	0	0	0	0	0	0	0	0	0	0	0	0	0	0	100	0	0	0	0	0	0	0
17	1260.33	0	0	0	-1	0	0	0	0	0	-1	0	0	-1	0	0	0	100	0	0	0	0	0	2
18	1359.92	0	0	0	0	0	0	0	0	0	0	0	0	-1	0	0	0	0	100	0	0	0	0	0
19	1375.75	0	0	0	0	0	0	1	0	0	0	0	3	0	0	0	0	0	0	100	0	0	0	0
20	1381.47	0	0	0	0	0	0	0	0	0	0	0	0	0	0	0	0	0	0	0	100	0	0	0
21	1387.15	0	0	0	0	0	0	0	0	0	0	0	0	0	0	0	0	0	0	0	0	100	0	0
22	1415.87	0	0	0	0	0	0	1	0	0	0	0	-1	0	0	0	0	0	0	0	0	0	100	0
23	1422.53	0	0	0	0	0	-1	0	0	0	0	0	0	-4	0	1	0	2	0	0	0	0	0	100

The body dominant modal frequencies are finally “consolidated” employing “strain energy” weighted summing employing Rayleigh quotients and associated SVD eigenvectors as,

$$\lambda_{c,i} = \frac{\{\mathbf{v}_{b,i}\}^T [\boldsymbol{\lambda}] \{\mathbf{v}_{b,i}\}}{\{\mathbf{v}_{b,i}\}^T \{\mathbf{v}_{b,i}\}} \rightarrow f_{c,i} = \frac{\sqrt{\lambda_{b,i}}}{2\pi}, \quad (16.21)$$

where the “c” subscript is used to denote the “consolidated” mode quantity. The corresponding consolidated system mode shapes associated with the consolidated modal frequencies are computed as follows:

$$\begin{aligned} \{\tilde{\Phi}_{c,i}\} &= [\Phi_b] \{\mathbf{v}_{b,i}\} \quad (\text{Non-normalized, consolidated system mode shape}) \\ m_{c,i} &= \{\tilde{\Phi}_{c,i}\}^T [M] \{\tilde{\Phi}_{c,i}\} \quad (\text{Non-normalized modal mass, with respect to the system (TAM) mass matrix}) \\ \{\Phi_{c,i}\} &= \{\tilde{\Phi}_{c,i}\} / m_{c,i} \quad (\text{Unit mass normalized, consolidated system mode shape}) \end{aligned} \quad (16.22)$$

The above development is apologetically “heuristic”. However, it appears to provide consistent, satisfying results for the example perturbed shell structure (with $p = 1$ and SVD tol = 0.01), as evidenced in orthogonality of the consolidated body modes shown below in Table 16.5.

16.4.3 Further Results of the Mode Consolidation Exercise

General consistency and integrity of the present mode consolidated methodology are further indicated in a comparison of various results for the perturbed shell structure below in Table 16.6.

Table 16.6 Comparison of various modal approximations for the perturbed shell structure

Baseline (O)		Perturbed (P)		Consolidated (C)		Modified Guyan Reduction (MGR)			Harmonic Reduction (HR)		
Mode	Freq (Hz)	Mode	Freq (Hz)	Mode	Freq (Hz)	Mode	Freq (Hz)	COR	Mode	Freq (Hz)	COR
1	122.20	1	120.97	1	120.97	1	121.02	100	1	121.02	100
2	122.20	2	121.13	2	121.13	2	121.14	100	2	121.13	100
11	315.24	11	312.43	3	312.43	3	312.38	100	3	312.38	100
14	377.21	15	374.65	4	373.36	4	373.37	100	4	373.35	100
15	377.21	14	373.97	5	374.14	5	374.19	100	5	374.17	100
24	467.77	24	463.45	6	463.45	6	463.50	100	6	463.50	100
49	706.65	48	695.39	7	699.42	7	698.99	100	7	698.99	100
50	706.65	50	701.56	8	701.56	8	701.74	100	8	701.70	100
63	841.31	62	833.52	9	833.71	9	833.72	100	9	833.72	100
76	997.48	76	986.08	10	983.97	10	983.00	100	10	984.52	100
77	997.50	78	994.38	11	994.07	11	994.38	100	11	995.48	100
86	1029.94	85	1020.38	12	1020.02	12	1020.47	100	12	1021.74	100
103	1169.56	101	1149.73	13	1149.62	13	1151.88	100	13	1156.45	100
104	1169.59	104	1166.38	14	1166.38	14	1166.83	100	14	1170.61	100
111	1223.46	108	1200.07	15	1210.08	15	1205.31	99	15	1215.82	99
112	1223.49	112	1219.50	16	1219.59	16	1220.14	100	16	1228.84	100
121	1273.43	123	1266.47	17	1260.33	17	1261.37	99	17	1268.71	99
128	1368.34	131	1363.11	18	1359.92	18	1344.84	94	18	1371.89	91
129	1368.41	132	1366.26	19	1375.75	20	1379.78	84	19	1391.51	80
140	1402.79	136	1373.70	20	1381.47	19	1367.05	76	20	1391.78	74
141	1402.83	142	1402.03	21	1387.15	21	1403.83	76	21	1415.61	74
146	1440.38	147	1433.20	22	1415.87	23	1427.86	78	23	1453.68	82
149	1452.66	144	1419.64	23	1422.53	22	1426.94	88	22	1453.35	9

(O) = Baseline System Body Modes	Cross-Orthogonality (COR) : Reference Modes=Consolidated (C)
(P) = Perturbed System Body-Dominant Modes (p=1)	Reference Mass = Baseline [MFF]
(C) = Perturbed System Consolidated Body Modes (Reference)	
(MGR) = Modified Guyan Reduction (Perturbed System)	
(HR) = Harmonic Reduction (Perturbed System)	

The above results lead to the following observations for the perturbed shell structure:

1. The body dominant modes are remarkably insensitive to introduction of the “line mass” perturbation. This suggests that “features” and “imperfections” in a real structure’s make-up may not significantly alter its “body dominant” modes (which are perhaps a reasonable target mode set for practical V&V).
2. Deviation of the last six “body dominant” modal frequencies among the various approximations (especially Consolidated vs. MGR) may be a symptom of truncation in the mode consolidation process, which employs modes up to 1500 Hz; a more authentic consolidation in this range may require inclusion of some modes above 1500 Hz.
3. Modified Guyan Reduction (MGR) appears to be slightly more accurate than Harmonic Reduction (HR).
4. While mixed body and breathing modes for a shell structure are generally unavoidable, mode consolidation may offer an efficient and effective alternative for test mode “comprehension”.
5. Moreover, employment of body mode consolidation and MGR may produce an abbreviated, more direct path for test-analysis reconciliation (V&V), which avoids complexities and sensitivities inherent in shell breathing modes.

The reader is cautioned that the present mode consolidated methodology is quite new and it requires additional exercising and potential refinements before it can be applied routinely.

16.5 Concluding Remarks

Thin shell structures have many breathing modes interspersed among fewer overall body dominant lateral (bending), torsion, and axial-bulge dominant modes within the typically accepted 0–60 Hz frequency band for full-scale launch vehicles. Due to high sensitivity of body (especially bending) modes to configuration features and imperfections (and static pressure and “g” loads), body dominant “target modes” often adopt mixed body-shell breathing (and local appendage) characteristics, which are difficult to discern and verify. Review, comprehension, and categorization of system modes should be treated using two distinct strategies for FEM predictions and experimental modal data, respectively. Modified Guyan Reduction (MGR) or Harmonic Reduction (HR) represents two related options for estimation of body modes (not requiring consolidation operations) for the system FEM. The newly introduced Mode Consolidation (MC) procedure, in contrast, appears to resolve the often noticed “repeated body mode” phenomenon occurring in experimental modal analysis of thin-walled shell structures. It is anticipated that Mode Consolidation will gradually gain acceptance in the technical community as a result of applications in modal testing and inevitable refinements of the strategy.

Acknowledgements The Modified Guyan Reduction concept was strongly influenced by conversations, during the mid 1980's, with Robert T. Lahey, who had previously developed and applied a load patch procedure at Lockheed Aircraft Company. Dr. Sheldon Rubin, formerly with The Aerospace Corporation, studied weak coupling in launch vehicle structures over many years since the mid 1970's. Rubin's personal notes, under the same title as this paper, followed a different line of thought focusing on launch vehicle flight data based on sparsely allocated instrumentation. It is unfortunate that both Lahey's and Rubin's key contributions in model order reduction and mode consolidation, respectively, have not been published in the open literature.

References

1. Klosterman, A.: Modal surveys of weakly coupled systems. SAE Technical Paper 760876 (1976)
2. Coppelino, R.: A numerically efficient finite element hydroelastic analysis. NASA CR-2662 (1976)
3. Coppelino, R.: DOF reduction strategy for large order finite element models. IMAC XXIX (2011)
4. Coppelino, R.: Automated response DOF selection for mapping of experimental normal modes. IMAC XVI (1998)
5. Tuttle, R., Cole, T., Lollock, J.: An automated method for identification of efficient measurement Degrees-of-Freedom for mode survey testing. AIAA 2005-2344 (2005)
6. Guyan, R.: Reduction of stiffness and mass matrices. AIAA J. **3**(2), 380-381 (1965)



Chapter 17

Fatigue Monitoring and Remaining Lifetime Prognosis Using Operational Vibration Measurements

Costas Papadimitriou, Eleni N. Chatzi, Saeed Eftekhar Azam, and Vasilis K. Dertimanis

Abstract A framework is presented for real-time monitoring of fatigue damage accumulation and prognosis of the remaining lifetime at hotspot locations of new or existing structures by combining output-only vibration measurements from a permanently installed, optimally located, sparse sensor network with the information build into high-fidelity computational mechanics models. To produce fatigue damage accumulation maps at component and/or system level, valid for the monitoring period, the framework integrates developments in (a) fatigue damage accumulation (FDA) and (b) stress time histories predictions under loading and structural modeling uncertainties based on monitoring information (Papadimitriou et al., *Struct Control Health Monit* 18(5):554–573, 2011). Methods and computational tools include, but are not limited to, the use of Kalman-type filters for state and stress response reconstruction based on the sensor information (Eftekhar Azam et al., *Mech Syst Signal Process* 60:866–886, 2015; Lourens et al., *Mech Syst Signal Process* 29:310–327, 2012), as well as stress cycle counting techniques, S-N curves and fatigue damage accumulation laws (Miner, *Appl Mech Trans (ASME)* 12(3):159–164, 1945; Palmgren, *VDI-Z* 68(14):339–341, 1924) to estimate fatigue from the reconstructed stress time histories at numerous hot spot locations. The FDA maps provide realistic fatigue estimates consistent with the actual operational conditions experienced by an individual structure. Combined with models of future loading events and their uncertainties, assumed or rationally estimated during the long-term monitoring period, the continuously updated FDA maps can be used to predict the remaining fatigue lifetime maps and associated uncertainties. Developments are valuable for planning cost-effective maintenance strategies, eventually reducing the life-cycle maintenance cost.

Keywords Fatigue prediction · Kalman filtering · Operational vibrations · Uncertainty quantification · Bayesian inference

17.1 Accounting for Loading and Modeling Uncertainties

Consider a structure that is subjected to time varying load events $f_l(t)$. The estimation of the fatigue damage d_l due to the l -th load event depends on the load time history, the structural model and the fatigue model. These models involve uncertainties that ought to be accounted for in the estimation of the fatigue. The proposed methodology for fatigue damage accumulation due to an event takes into account the parametric uncertainties associated with these models. Loading uncertainties may arise due to uncertain amplitude and frequency characteristics of the excitation, such as the parameters of the spectrum introduced to provide a stochastic model of the excitation. For example, for the loads applied on a wind turbine the parameters of the spectral density of the wind forces may be uncertain. In simple traffic loads applied on bridges the uncertain parameters may be associated with the speed and weight of the trains or automobiles crossing a railway or a motorway bridge. Structural model uncertainties are associated with the mass and stiffness related properties. For example, uncertain parameters can be the modulus of elasticity of the material, the yield stress, the stiffness and damping of isolation devices, the parameters of nonlinear models of the material behavior (hysteretic models, friction coefficients, etc.). Uncertainties are also involved in fatigue models. For example, one could introduce uncertainties in the parameters involved in the S-N models, the prediction error from these models, as well as in the model associated with the linear damage accumulation rule [4, 5]. It is assumed that the load models, structural models and the fatigue damage models depend respectively on parameter sets $\underline{\psi}$, $\underline{\theta}$ and $\underline{\varphi}$

C. Papadimitriou (✉) · S. Eftekhar Azam
Department of Mechanical Engineering, University of Thessaly, Volos, Greece
e-mail: costasp@uth.gr

E. N. Chatzi · V. K. Dertimanis
Institute of Structural Engineering, Department of Civil, Environmental and Geomatic Engineering, ETH Zürich, Zürich, Switzerland

with their uncertainties quantified by PDFs $\pi(\underline{\psi})$, $\pi(\underline{\theta})$ and $\pi(\underline{\varphi})$. Using information from load data D_L and structural vibration data D_S (e.g. acceleration, displacement and strains) obtained during monitoring from a sensor network or during individual component tests, the uncertainties can be updated using Bayesian inference techniques [6, 7] to posterior PDFs $p(\underline{\psi}|D_L)$ and $p(\underline{\theta}|D_S)$. Similarly, using information from fatigue experimental data D_F , uncertainties are updated to the posterior PDF $p(\underline{\varphi}|D_F)$.

17.2 Conditional Fatigue Damage Estimates

The fatigue damage $d_l(\underline{\psi}, \underline{\theta}, \underline{\varphi})$ for an l -th load event, conditioned to the values of the parameters $\underline{\psi}$, $\underline{\theta}$ and $\underline{\varphi}$, can be obtained using stochastic fatigue assessment methods [1] or cycle counting methods [8]. Specifically, using the linear damage accumulation law [4, 5], the damage at a point in the structure subjected to variable amplitude stress time history is

$$d_l(\underline{\psi}, \underline{\theta}, \underline{\varphi}) = \sum_i^{k_l(\underline{\psi}, \underline{\theta})} \frac{n_{i,l}(\underline{\psi}, \underline{\theta})}{N_{i,l}(\underline{\varphi})} \quad (17.1)$$

where $n_{i,l}(\underline{\psi}, \underline{\theta})$ is the number of cycles at a stress level σ_i , $N_{i,l}(\underline{\varphi})$ is the number of cycles required for failure at a stress level σ_i , and $k_l(\underline{\psi}, \underline{\theta})$ is the number of stress levels identified in a stress time history. It should be noted that $n_{i,l}(\underline{\psi}, \underline{\theta})$ and $k_l(\underline{\psi}, \underline{\theta})$ depend on the load time history and the structural model, and so they depend on the load and structural model parameters $\underline{\psi}$ and $\underline{\theta}$, respectively. The number of cycles $N_{i,l}(\underline{\varphi})$ required for failure in terms of the stress level σ_i is obtained from S-N fatigue curves available from laboratory experiments on simple specimens subjected to constant amplitude loads. Thus $N_{i,l}(\underline{\varphi})$ depends on the fatigue model parameters $\underline{\varphi}$. The number of cycles $n_{i,l}(\underline{\psi}, \underline{\theta})$ is obtained by applying rainflow cycle counting methods. To account for a non-zero mean stress in (17.1), the Goodman relationship can be used.

17.3 Robust Fatigue Damage Estimates Using Monitoring Data

Robust fatigue estimates are predictions of fatigue damage to load events that take into account the uncertainties in the loading, structural model and fatigue model parameters. Prior to the data, these uncertainties are usually postulated based on engineering judgement and quantified by the prior PDFs $\pi(\underline{\psi})$, $\pi(\underline{\theta})$ and $\pi(\underline{\varphi})$. External loads are usually not representative of the actual loads applied on the structure, while structural models are not calibrated to match the actual structural behavior. Such models and uncertainties can lead to completely inaccurate results for the fatigue damage accumulation and fatigue reserve prognosis that eventually misguide maintenance decisions. The information obtained from a monitoring system is valuable to predict strain and fatigue at hotspot locations of the structure that are consistent with the actual behavior of the structure subjected to various loads during the monitoring period. Specifically, combining output-only vibrations measurements from a limited number of measured locations with the information build into a computational mechanics model, one can use the Kalman-type filter techniques [2, 3] to predict the strains at all critical (hotspot) locations without knowing the spatial and temporal variation of the loads applied on the structure. Moreover, one can also exploit the information from the measured time histories to calibrate the finite element model and update the parameters of the model and the uncertainties so that the predictions are based on the calibrated model and parameter uncertainties instead of a nominal model that might not be representative of the actual behavior of the structure. Finally, using a permanent monitoring system, model degradation can be continually traced by analyzing the monitoring information and the calibrated models at its damaged state can be identified along with the uncertainties so that the prediction of strains are continually based on the current, possibly deteriorating, state of the structure to constantly provide accurate estimates of the fatigue damage accumulation using the fatigue damage accumulation maps [8].

Thus, the posterior uncertainty in the fatigue damage d_i taking into account load, structural model and fatigue model uncertainties, as well as the monitoring and material test data $D = (D_L, D_S, D_F)$, is obtained from the total probability theorem

$$p(d_i|D) = \int p(d_i|\underline{\psi}, \underline{\theta}, \underline{\varphi}) p(\underline{\psi}|D_L) p(\underline{\theta}|D_S) p(\underline{\varphi}|D_F) d\underline{\psi} d\underline{\theta} d\underline{\varphi} \quad (17.2)$$

which is as an average of the conditional probability distribution $p(d_i|\underline{\psi}, \underline{\theta}, \underline{\varphi})$ weighting by the posterior (or prior) PDF of the load/model parameters. The multidimensional integral (17.2) can be computed using sampling techniques (e.g [9]).

17.4 Remaining Fatigue Lifetime Prognosis and Maintenance Planning Under Uncertainty

The use of the information acquired during the monitoring period for fatigue damage prognosis depends on the type of structure (e.g. airframe, building, railway or motorway bridge, wind turbine, car frame) and the type of loading events applied on the structure. One important consideration is whether or not the information in the monitoring period can be used to infer fatigue for the period before a permanent monitoring system was installed and also for making prognosis of the remaining fatigue lifetime. Estimating fatigue damage accumulation for the pre-monitoring period is very important for a number of structures such as civil infrastructure since the idea of installing monitoring systems is only recent and thus the fatigue damage accumulation before the monitoring system has been installed is unknown. As a result, the prognosis of the remaining fatigue lifetime is not possible due to unknown fatigue damage accumulation in the structure. This is feasible only for certain type of structures for which the loads have a ‘repeatable’ pattern that can be identified during the monitoring period. One such type of important structures are, for example, the railway steel bridges. Output vibration measurements derived from a strategically placed network of sensors (e.g. strain, acceleration sensors) in a bridge can provide on an hourly, daily, monthly and yearly basis, fatigue damage accumulation maps based on actual operational loads (train passages on the bridge). Projecting the number of train passages on an hourly, daily, monthly and yearly basis to the past (before the monitoring system was installed) and the future, and assuming that similar loading patterns occur on a daily, monthly and yearly basis, with the only difference the number of daily train passages that can be known from the companies record, one can make an estimate of the fatigue damage accumulation before the monitoring period, as well as make prognosis of the remaining fatigue life given that the model of the bridge does not deteriorate.

Developments based on the monitoring system are very important for planning cost-effective maintenance strategies of a large number of structures based on the actual condition of the structure and not on statistical models that have been derived by processing data from a group of structures (e.g. fleet of aircrafts), failing to be representative of the actual condition in a member of the group. Potential applications of the proposed framework cover a large number of important metallic structures, including railway/motorway steel bridges, offshore structures, wind turbines, ground and air vehicles (airframes). Processing of the monitoring information for estimating the fatigue damage accumulation and prognosing remaining fatigue lifetime is valuable for optimizing inspection intervals and component replacement strategies based on the actual behavior of an individual structure, eventually reducing the life-cycle maintenance cost.

References

1. Papadimitriou, C., Fritzen, C.P., Kraemer, P., Ntotsios, E.: Fatigue predictions in entire body of metallic structures from a limited number of vibration sensors using Kalman filtering. *Struct. Control. Health Monit.* **18**(5), 554–573 (2011)
2. Eftekhar Azam, S., Chatzi, E., Papadimitriou, C.: A dual Kalman filter approach for state estimation via output-only acceleration measurements. *Mech. Syst. Signal Process.* **60**, 866–886 (2015)
3. Lourens, E., Papadimitriou, C., Gillijns, S., Reynders, E., De Roeck, G., Lombaert, G.: Joint input-response estimation for structural systems based on reduced-order models and vibration data from a limited number of sensors. *Mech. Syst. Signal Process.* **29**, 310–327 (2012)
4. Miner, M.A.: Cumulative damage in fatigue. *Appl. Mech. Trans. (ASME)*. **12**(3), 159–164 (1945)
5. Palmgren, A.: Die Lebensdauer von Kugellagern. *VDI-Z.* **68**(14), 339–341 (1924)
6. Yuen, K.V.: *Bayesian Methods for Structural Dynamics and Civil Engineering*. John Wiley & Sons, Singapore (2010)
7. Behmanesh, I., Moaveni, B., Lombaert, G., Papadimitriou, C.: Hierarchical Bayesian model updating for structural identification. *Mech. Syst. Signal Process.* **64–65**, 360–376 (2015)

8. Papadimitriou, C., Lourens, E., Lombaert, G., De Roeck, G., Liu, K.: Prediction of fatigue damage accumulation in metallic structures by the estimation of strains from operational vibrations. Third International Symposium on Life-Cycle Civil Engineering (IALCCE'12), Vienna, Austria (2012)
9. Ching, J., Chen, Y.C.: Transitional Markov chain Monte Carlo method for Bayesian model updating, model class selection, and model averaging. *J. Eng. Mech.* **133**(7), 816–832 (2007)



Chapter 18

Feasibility of Applying Phase-Based Video Processing for Modal Identification of Concrete Gravity Dams

Qi Li, Gaohui Wang, Aral Sarrafi, Zhu Mao, and Wenbo Lu

Abstract Hydraulic structures have been considered as one of the most essential civil infrastructures, and play a critical role in developing countries throughout the history for water storage and electricity generation. Due to the importance and the catastrophic consequences of unexpected failures in hydraulic infrastructures, monitoring and maintenance of dams should be handled very meticulously and with high precision. Among several measurement techniques as a specific modern non-contact sensing technology, optical/video information is getting more and more attention to interpret structural responses and system status awareness. By means of processing the acquired video, a full-field system information is available which may be applied later to Experimental Modal Analysis, Structural Health Monitoring (SHM), System Identification, etc. Such non-contact full-field sensing technologies avoid the installation of a gigantic number of conventional sensors in the occasions of large dimension. Within this context, the feasibility of applying Phase-Based Motion Estimation (PME) and video magnification has been studied for structural identification purposes on the concrete gravity dam subject to white noise excitations. Firstly, the PME and motion magnification algorithms are validated by the comparison of a lab-scale cantilever beam test and the numerical simulation. Next, the modal dynamic procedure in ABAQUS is carried out and the time history response of the dam is obtained. Then the simulated motion video of the dam is exported and processed using PME and magnification. The video processing results are finally compared with the results from frequency procedure in ABAQUS. The results obtained prove the concept of using PME and video magnification as a successful methodology in the modal identification of large-scale concrete gravity dams.

Keywords Phase-Based Motion Estimation · Video Magnification · Concrete Gravity Dam · Modal Identification · Numerical Simulation

18.1 Introduction

As a water retaining structure designed to restrict flow of water into a specific region, dams provide essential benefits such as supplying drinking water, irrigation, hydropower, flood control, and recreation. However, during their service life, dams are likely to have a variety of defects, which would cause great economic loss or even catastrophic consequences. Hence, monitoring and maintenance of dams should be handled very meticulously and with high precision.

The structural vibration characteristics, such as frequencies, damping ratios, and modal shapes, may reflect the structural damages. Therefore, the vibration-based SHM technology is widely concerned in dam structures [1–4]. However, most of the studies traditionally require physically-attached wired or wireless sensors for vibration measurement of dam structures. These methods are costly and time-consuming for both installation and maintenance. Moreover, only discrete measurements at limited locations are feasible and the spatial sensing resolution is low [5]. Therefore, alternative measurement (e.g. non-contact techniques) should be considered to avoid testing difficulties and increase the spatial resolution of acquired data [6].

As a specific modern non-contact sensing technology, optical/video information is getting more and more attention to interpret structural responses and system status awareness for its convenience and efficiency [7–11]. Phase-based video

Q. Li · G. Wang (✉) · W. Lu

State Key Laboratory of Water Resources and Hydropower Engineering Science, Wuhan University, Wuhan, China
e-mail: wanggaohui@whu.edu.cn

A. Sarrafi · Z. Mao

Structural Dynamics and Acoustic Systems Laboratory, Department of Mechanical Engineering, University of Massachusetts Lowell, Lowell, MA, USA

methods have been used to identify modal information on a variety of different structures in previous works [5, 12–14]. However, less attention has been paid to large-scale concrete structures.

The objective of this paper is to demonstrate whether the PME and video magnification methods can be used with high-speed camera video to visualize and quantify the vibrational mode shapes of large-scale dam structures. The PME and motion magnification algorithms are validated by the comparison of a lab-scale cantilever beam test and numerical simulation of concrete dam structure. Due to the lack of experimental data, the modal dynamic procedure in ABAQUS is carried out and the time history response of the dam is obtained. The simulated motion video of the dam is exported and processed using PME and video magnification. The identified natural frequencies and mode shapes of the dam are finally compared with the results from the frequency procedure in ABAQUS.

18.2 Theory Background

The phase-based motion estimation method as an alternative motion estimation technique was put forward by Jepson and Fleet in 1990 [15]. The main idea of the PME is derived from the Fourier transform shift theorem, which indicates that any motion in the spatial domain of a real function represents itself as a variation of the phase in the frequency domain. In this method, the acquired sequence of images can be mapped onto a complex domain using

$$C_\theta = I(x, y, t) \otimes (G_\theta + iH_\theta) \quad (18.1)$$

where $I(x, y, t)$ is the intensity value and \otimes is the convolution operator. G_θ and H_θ are real and imaginary parts of the Gabor wavelet in direction of θ . All the images are mapped onto a 2D complex map C_θ for different orientations and scales. The complex map can be written in polar form to extract the amplitude and phase values at each pixel using

$$C_\theta = A_\theta(x, y, t) e^{i\Phi_\theta(x, y, t)} \quad (18.2)$$

where $A_\theta(x, y, t)$ is the local spatial amplitude and $\Phi_\theta(x, y, t)$ is the phase, which contains the local spatial motion information in a specific direction based on the orientation of the Gabor Wavelet.

Phase-based motion magnification, proposed by Wadhwa et al. [16], applies a band-pass temporal filter to phase signals $\Phi_\theta(x, y, t)$ and amplifies it to get a new set of phase values. It is acknowledged that if the center of the filter's frequency band is set to be the structural natural frequency or close to the natural frequency, the obtained video will mostly contain the operating deflection of the structure at one of its approximate resonant frequencies if the modes are reasonably well separated [13]. The magnified video is paused during a frame with the maximum deflection of the structure. The Canny edge detection routine is implemented to determine the edges of the structure. In this way, quantitative data can be obtained and compared with the operational deflection shapes derived from numerical simulation.

18.3 Verification Test

18.3.1 Experimental Test on a Cantilever Beam

In order to apply the PME and video magnification algorithms for structural dynamics identification, a lab-scale cantilever beam (which is made of carbon steel and the dimension of the beam is 260 mm × 25 mm × 3 mm) test setup has been prepared. The identified natural frequencies and mode shapes of the beam are then compared with the numerical results to validate the PME and motion magnification algorithms.

The experimental setup shown in Fig. 18.1 was used as the test-bed to capture the sequence of images from the vibrating cantilever beam. The beam was excited by an impact hammer. After inducing the excitation to the beam, the motion of the beam was recorded by a single CMOS high speed camera. The frame rate of the camera is 2500 frames per second. Therefore, the natural frequencies and operating mode shapes of the beam can be extracted up to 1250 Hz without causing any aliasing according to the Nyquist criteria.

The obtained sequence of images from the vibrating cantilever beam was processed by the PME algorithm firstly to extract the dynamic response of the beam. The estimated motion signals via phase-based video processing were transferred to the frequency domain using the Fast Fourier Transform (FFT). The frequency domain representation of the motion is shown in Fig. 18.2, from which the natural frequencies of the beam can be acquired through identifying the peaks. The identified first four natural frequencies of the beam are 34.18 Hz, 212.4 Hz, 594.5 Hz, and 1167 Hz respectively.

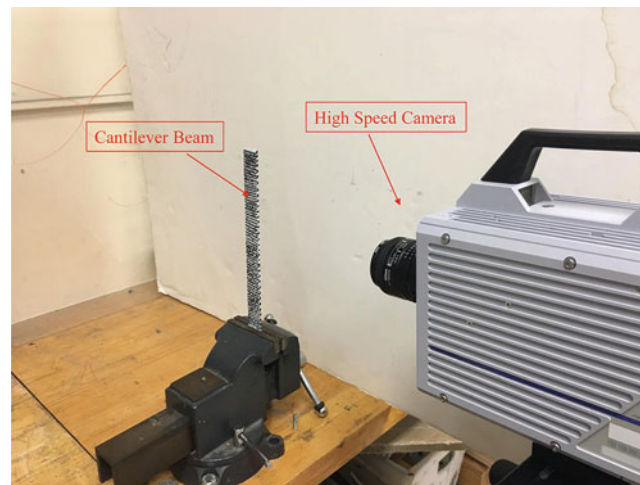


Fig. 18.1 The CMOS high speed camera and the cantilever beam

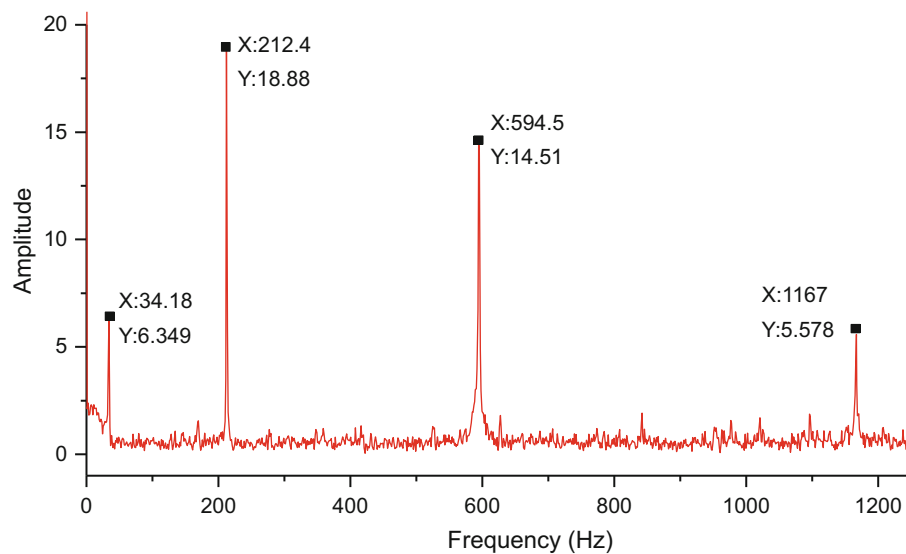


Fig. 18.2 Frequency domain representation of estimated motions obtained from the phase-based motion estimation for the dam

After identifying the first four natural frequencies of the beam, the video magnification algorithm was applied to the sequence of images. Different frequency bands were selected to visualize the operating deflection shape of the cantilever beam corresponding to the selected natural frequency. As mentioned above, if the center frequency for the motion magnification process is selected to be one of the natural frequencies, the resulting video will mostly contain the operating deflecting shape of the cantilever beam corresponding to the selected mode. The source video was processed with frequency bands of 32.68–35.68 Hz, 210.9–213.9 Hz, 592.5–596.5 Hz, and 1165–1169 Hz and amplification factors of 3, 25, 25, and 100. The motion magnified video is paused during a frame with the maximum deflection of the beam and snap shots of the magnified videos are shown in Fig. 18.3.

18.3.2 Numerical Simulation and Comparison

In order to validate the proposed methods, numerical simulation of the cantilever beam is conducted and compared with the experimental results obtained above. The cantilever beam, which is made of carbon steel, is assumed to be linear elastic. The dimension of the beam is 260 mm × 25 mm × 3 mm. The mass density of the beam is 7850 kg/m³, Young's modulus is 195 GPa, and Poisson's ratio is 0.28. The calculation is conducted in the 2D planar modeling space. The element size

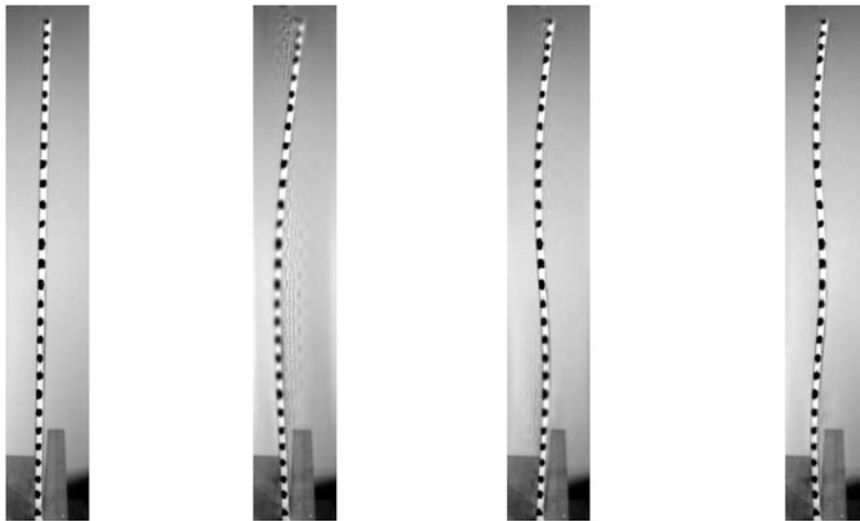
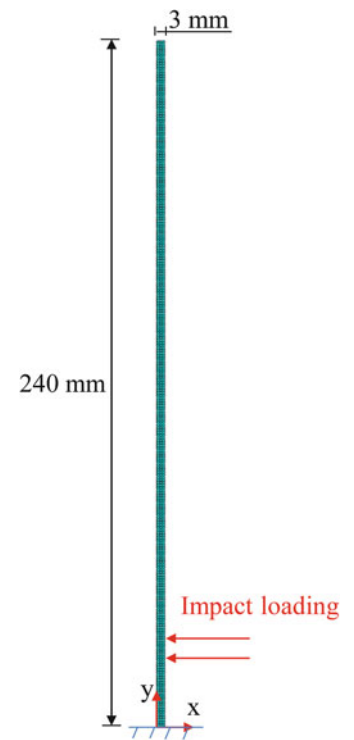


Fig. 18.3 Snap shots of the magnified video of the beam: (a) 34.18 Hz, (b) 212.4 Hz, (c) 594.5 Hz, and (d) 1167 Hz

Fig. 18.4 Calculating diagram of the cantilever beam



is 1 mm and the whole model contained 780 elements. The lower part of the beam is subjected to impact loading and the bottom of the beam is considered as fixed in all directions. The calculating diagram is shown in Fig. 18.4. The calculated natural frequencies and mode shapes of the cantilever beam are shown in Fig. 18.5.

The natural frequencies of the cantilever beam estimated from the video measurements compared to those estimated from the numerical simulation are shown in Table 18.1. It can be easily found that the errors between the two results are very small. The camera extracted operational deflection shapes compare well to those calculated from the numerical simulation. The Modal Assurance Criterion (MAC) values for the comparison between the numerical simulation and edge detected motion magnified video screenshot operational mode shapes are shown in Table 18.2. Therefore, the PME and motion magnification algorithms can be validated.

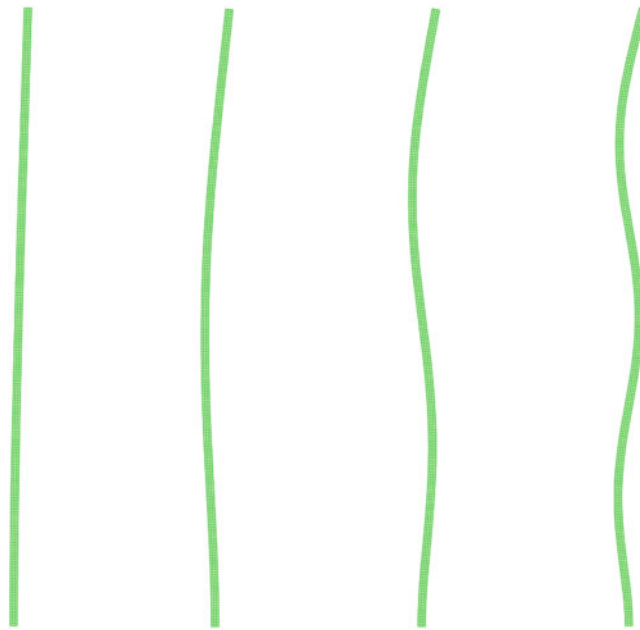


Fig. 18.5 Mode shapes of the cantilever beam

Table 18.1 The natural frequencies of the cantilever beam estimated from the video measurements compared to those estimated from the numerical simulation

Mode number	Numerical simulation (Hz)	PME (Hz)	Error (%)
1	33.69	34.18	1.45
2	211.0	212.4	0.66
3	590.3	594.5	0.71
4	1155	1167	1.04

Table 18.2 MAC values for the comparison between the numerical simulation and edge detected motion magnified video screenshot operational mode shapes

Numerical Simulation	Edge detected			
	33.69 Hz (%)	211.0 Hz (%)	590.3 Hz (%)	1155 Hz (%)
33.69 Hz	99.62	4.14	10.52	25.81
211.0 Hz	3.23	97.96	4.43	7.74
590.3 Hz	4.40	1.57	97.04	5.64
1155 Hz	6.00	8.46	10.32	89.77

18.4 Modal Identification of the Concrete Gravity Dam

18.4.1 Numerical Model Setup

In order to explore the feasibility of applying phase-based video processing for dam structure dynamics characterization, a simple dam model is established in this section due to lack of field test data. The concrete gravity dam is assumed to be a linear elastic body. The maximum dam height is 103 m. The mass density, Young's modulus, and Poisson's ratio of the concrete material are 2643 kg/m^3 , 31GPa, and 0.2, respectively. The calculation is also conducted in the 2D planar modeling space. Finite element model for the tallest section of the dam is shown in Fig. 18.6. The mesh of the dam is adequately refined at the base and near the changes change in downstream slope because they are weak parts of the dam and the subsequent damage analysis would be carried out. The whole model contains 2928 elements. The foundation of the dam is taken as being rigid. The upper part of the dam is assumed to be subjected to a white noise excitation.

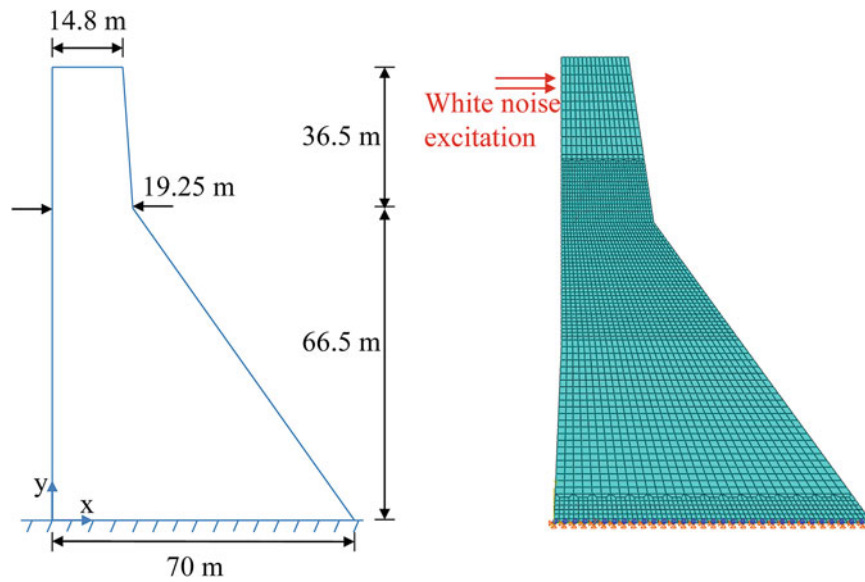


Fig. 18.6 Configuration of the geometric and numerical models

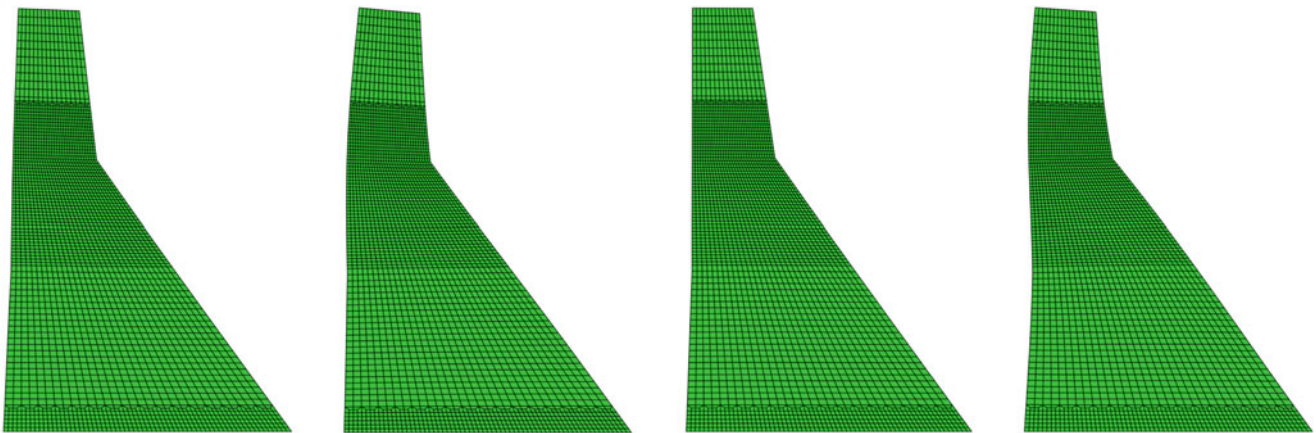


Fig. 18.7 Mode shapes of the concrete gravity dam: (a) 3.14 Hz, (b) 8.35 Hz, (c) 11.05 Hz, and (d) 16.16 Hz

18.4.2 Modal Identification

Frequency procedure is conducted firstly to extract the natural frequencies and mode shapes of the concrete gravity dam. The calculated natural frequencies and mode shapes of the concrete gravity dam are shown in Fig. 18.7. The first four natural frequencies of the dam are 3.14 Hz, 8.35 Hz, 11.05 Hz, and 16.16 Hz respectively. It should be noted that because the third mode of the dam is mainly vertical deformation and no amplification applied to the mode shape, nearly no deformation can be observed in Fig. 18.7c.

Due to lack of experimental data, then the modal dynamic procedure is carried out and the time history response of the dam can be obtained. Next, the simulated motion video of the dam is exported from the ABAQUS and then processed using PME and magnification. The obtained first four natural frequencies of the dam are 3.13 Hz, 8.40 Hz, 11.52 Hz, and 16.21 Hz respectively. The frequency domain representation of the motion is shown in Fig. 18.8. The magnified frequency bands are selected as 2.94–3.34 Hz, 7.85–8.85 Hz, 10.85–11.25 Hz, and 15.16–17.16 Hz and amplification factors of 3, 25, 50, and 200. Snap shots of the motion magnified videos are shown in Fig. 18.9.

The natural frequencies of the concrete gravity dam estimated from the video measurements compared to those estimated from the numerical simulation are shown in Table 18.3. The MAC values for the comparison between the numerical simulation and edge detected motion magnified video screenshot operational mode shapes are shown in Table 18.4. It should

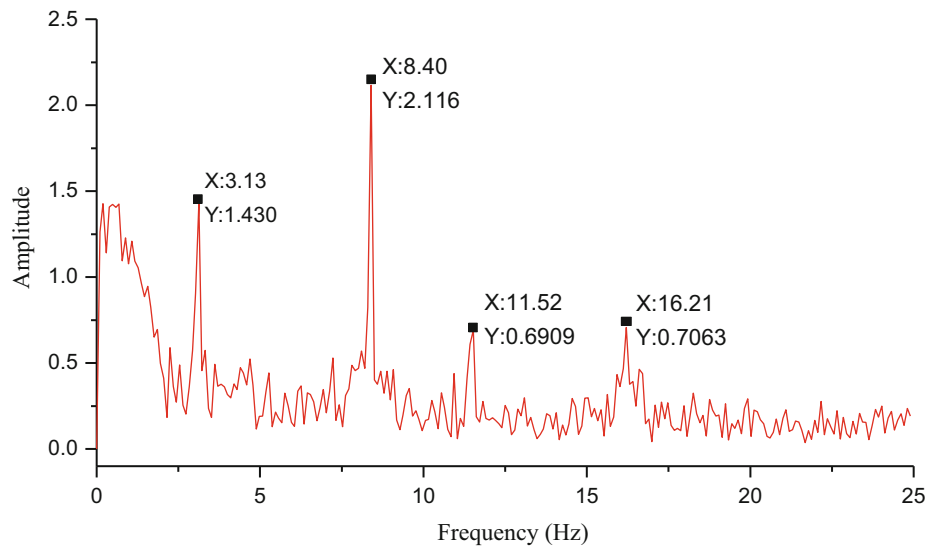


Fig. 18.8 Frequency domain representation of estimated motions obtained from the phase-based motion estimation for the dam

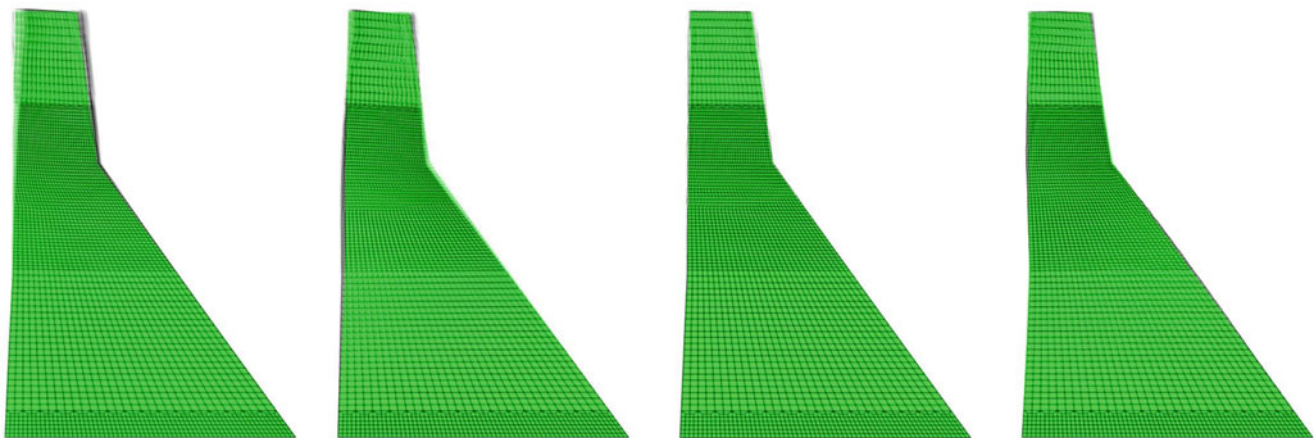


Fig. 18.9 Snap shots of the magnified video of the dam: (a) 3.13 Hz, (b) 8.40 Hz, (c) 11.52 Hz, and (d) 16.21 Hz

Table 18.3 The natural frequencies of the concrete gravity dam estimated from the video measurements compared to those estimated from the frequency procedure

Mode number	Numerical simulation (Hz)	PME (Hz)	Error (%)
1	3.14	3.13	3.18
2	8.35	8.40	0.60
3	11.05	11.52	4.25
4	16.16	16.21	0.31

be noted that because the third mode of the dam is mainly vertical deformation and it makes no sense to calculate the MAC value between the vertical mode shape and horizontal mode shapes, some MAC values are not given in Table 18.4. From Tables 18.3 and 18.4, it can be found that the identified natural frequencies and mode shapes of the dam from video method are in good consistent with the results from the frequency procedure. Hence, the feasibility of applying the phase-based video processing on the modal identification of large-scale dam structures is confirmed.

Table 18.4 MAC values for the comparison between the frequency procedure results and edge detected motion magnified video screenshot operational mode shapes

Numerical Simulation	Edge detected			
	3.141 Hz (%)	8.345 Hz (%)	11.05 Hz (%)	16.16 Hz (%)
3.141 Hz	93.38	25.46	–	8.58
8.345 Hz	5.81	95.82	–	33.62
11.05 Hz	–	–	95.98	–
16.16 Hz	2.28	22.66	–	95.95

18.5 Conclusions

In this paper, modal identifications of a cantilever beam and a concrete gravity dam are conducted through video processing methods. It is demonstrated that the PME and video magnification methods may be used with video measurements to quantify the vibrational mode shapes of large-scale hydraulic structures. A lab-scale cantilever beam test is carried out firstly and compared with the numerical simulation, through which the PME and motion magnification algorithms are validated. Due to the lack of experimental data, then the modal dynamic procedure in ABAQUS is carried out and the time history response of the dam is obtained. The simulated motion video of the dam is exported and processed using PME and video magnification. The identified natural frequencies and mode shapes of the dam are finally compared with the results from the frequency procedure in ABAQUS. It is found that the identified natural frequencies and mode shapes of the dam from the video method are in good consistent with the results from the frequency procedure. Hence, the feasibility of applying the phase-based video processing on the modal identification of concrete gravity dams is confirmed.

References

- Sevim, B., Bayraktar, A., Altunisik, A.C.: Finite element model calibration of berke arch dam using operational modal testing. *J. Vib. Control*. **17**, 1065–1079 (2011)
- Sevim, B., Altunisik, A.C., Bayraktar, A.: Experimental evaluation of crack effects on the dynamic characteristics of a prototype arch dam using ambient vibration tests. *Comput. Concr.* **10**, 277–294 (2012)
- Oliveira, S., Toader, A.M., Vieira, P.: Damage identification in a concrete dam by fitting measured modal parameters. *Nonlinear Anal. Real World Appl.* **13**, 2888–2899 (2012)
- Altunişik, A.C., Günaydin, M., Sevim, B., Bayraktar, A., Adanur, S.: Retrofitting effect on the dynamic properties of model-arch dam with and without reservoir water using ambient-vibration test methods. *J. Struct. Eng.* **142**, 04016069 (2016)
- Yang, Y., Dorn, C., Mancini, T., Talken, Z., Kenyon, G., Farrar, C., et al.: Blind identification of full-field vibration modes from video measurements with phase-based video motion magnification. *Mech. Syst. Signal Process.* **85**, 567–590 (2017)
- Poozesh, P., Niezrecki, C., Baqersad, J.: An acoustic-array based structural health monitoring technique for wind turbine blades. In *SPIE Symposium on Smart Structures & Materials/NDE and HealthMonitoring*, San Diego, CA (2015)
- Chang, C.C., Ji, Y.F.: Flexible videogrammetric technique for three-dimensional structural vibration measurement. *J. Eng. Mech.* **133**, 656–664 (2007)
- Sutton, M.A., Orteu, J.J., Schreier, H.: *Image Correlation for Shape, Motion and Deformation Measurements: Basic Concepts, Theory and Applications*. Springer Science & Business Media, Berlin (2009)
- Morlier, J., Michon, G.: Virtual vibration measurement using KLT motion tracking algorithm. *J. Dyn. Syst. Meas. Control.* **132**, 91–93 (2010)
- Caetano, E., Silva, S., Bateira, J.: A vision system for vibration monitoring of civil engineering structures. *Exp. Tech.* **35**, 74–82 (2011)
- Feng, M.Q., Asce, F., Fukuda, Y., Feng, D., Asce, S.M., Mizuta, M.: Nontarget vision sensor for remote measurement of bridge dynamic response. *J. Bridg. Eng.* **20**, 04015023 (2015)
- Chen, J.G., Davis, A., Wadhwa, N., Durand, F., Freeman, W.T., Büyükoztürk, O.: Video camera-based vibration measurement for civil infrastructure applications. *J. Infrastruct. Syst.* **23**, B4016013 (2017)
- Chen, J.G., Wadhwa, N., Cha, Y.J., Durand, F., Freeman, W.T., Buyukozturk, O.: Modal identification of simple structures with high-speed video using motion magnification. *J. Sound Vib.* **345**, 58–71 (2015)
- Poozesh, P., Sarrafi, A., Mao, Z., Avitabile, P., Niezrecki, C.: Feasibility of extracting operating shapes using phase-based motion magnification technique and stereo-photogrammetry. *J. Sound Vib.* **407**, 350–366 (2017)
- Fleet, D.J., Jepson, A.D.: Computation of component image velocity from local phase information. *Int. J. Comput. Vis.* **5**, 77–104 (1990)
- Wadhwa, N., Rubinstein, M., Freeman, W.T.: Phase-based video motion processing. *ACM Trans. Graph.* **32**, 1–10 (2013)



Chapter 19

Using 2D Phase-Based Motion Estimation and Video Magnification for Binary Damage Identification on a Wind Turbine Blade

Aral Sarrafi and Zhu Mao

Abstract Videos (sequence of images) as three-dimensional signals may be considered as a very rich source of information for several applications in structural dynamics identification and structural health monitoring (SHM) systems. Within this paper high-speed cameras are used to record the sequence of images (video) of a baseline and damaged wind turbine blade (WTB) while vibrating due to the external loadings. Among several computer vision algorithms for motion extraction from the videos, phase-based motion estimation technique is used to extract the response of both the baseline and damaged wind turbine blade. Modal parameters (natural frequencies and operating deflection shapes) were used as damage sensitive features in order to detect the occurrence of damage in the wind turbine blade. The first four natural frequencies of the both baseline and damaged wind turbine blade are extracted by analyzing the estimated motion provided by the phase based motion estimation in the frequency domain. The motion magnification algorithm is also utilized to visualize and extract the operating deflection shapes of the wind turbine blade which may be used later as an indicator of the presence of damage. It has been shown that changes in the dynamic behavior of the wind turbine blade will result to deviations in the nominal natural frequencies and operating deflection shapes, and the damaged wind turbine blade can be differentiated from the baseline WTB using this non-contact measurement approach.

Keywords Phase-based motion estimation · Video Magnification · Wind Turbine Blade · Structural Health Monitoring · Modal Analysis

19.1 Introduction

Modal parameters including natural frequencies, mode shapes and damping ratios are among the most widely used features in vibration based damage detection [1]. Vibration based structural health monitoring (SHM) approach utilizes the changes in the modal parameters in order to obtain the health status of the structures and detect the deviations in the dynamic behavior [2]. Therefore, performing an accurate and fast experimental modal analysis (EMA) or operational modal analysis (OMA) test is an essential step for vibration based damage detection [3]. Likewise other SHM approaches such as ultrasonic wave propagation [4, 5] or thermal imaging, excitation of the structure and recording the response is an essential part in vibration based SHM as well. Traditionally, accelerometers and laser vibrometers are being used to record the response of structures due to the external loads as the raw data for modal parameter estimation [6, 7]. There are several drawbacks associated with each of the traditional measurement techniques. Instrumentation of large structures with accelerometers is very time consuming and labor intensive, on the other hand, for relatively lightweight structures, the mass-loadings being induced from the mounted accelerometers can deviate the original dynamic response, which is not suitable for accurate estimation of modal parameters [8]. As a non-contact measurement equipment, laser vibrometers can avoid the mass loading effects and the instrumentation of the structure is also eliminated; however, several measurement points have to be performed sequentially which may lead to very long testing time especially for large-scale structures [9].

As an alternative measurement technique, digital cameras can offer full-field and instantaneous measurement capabilities [10]. Camera-based measurements are non-contact which means there will be no mass loading effects on the structure. Moreover, the measurement is full field and instantaneous that can reduce the testing time dramatically unlike the laser

A. Sarrafi · Z. Mao (✉)

Structural Dynamics and Acoustic Systems Laboratory, Department of Mechanical Engineering, University of Massachusetts Lowell, Lowell, MA, USA

e-mail: zhu_mao@uml.edu

vibro-meter, which is only able to make the measurements sequentially [11, 12]. Considering the advantageous associated with optical measurements, applications of digital cameras in engineering applications have been increasing [13, 14].

The main difficulty in working with camera-based measurements is that the displacement signals are not explicitly available from the video or the recorded sequence of images, and specific algorithms from computer vision known as motion estimation have to be utilized to interpret the captured sequence of images into meaning full displacement signals, which is necessary for modal parameter estimation [15, 16]. There are numerous motion estimation techniques available and each has its own advantageous [17–19].

Within this paper phase-based, motion estimation [20] is used to extract the motion of the vibrating structure from sequence of images. Moreover, phase based motion magnification has been used to extract the operating deflection shapes of the structures [21–23]. In recent year phase-based motion processing have been gaining more attention for structural dynamics applications because of its unique features such as providing very accurate visual perception of the mode shapes of the structure and robustness to noise [24–28].

Within this study, a binary damage occurrence detection is performed on a 2.3 m long Skystream wind turbine blade (WTB). The type of induced damage to the WTB blade is an additive mass to mimic the icing condition on the tip of the WTB. It is shown that the changes in the natural frequencies and the location of the nodes and anti-nodes of the operating deflection shapes can potentially lead to damage detection.

The first section of the paper discusses some of the fundamental equations and considerations in phase based motion estimation and motion magnification. Followed by the second section, introducing the test setup. In the third section, the results are presented and discussed briefly. The papers aims to highlight some of capabilities and potential applications of phase-based motion processing in structural dynamics identification and structural health monitoring.

19.2 Phase-Based Motion Processing

The main indication of phase based motion estimation is similar to the shift theorem in Fourier transform. The Fourier transform shift theorem indicates that any shift in the spatial domain of a function would result to variations in phase in the frequency domain representation of the same function.

$$F[f(x-a, y-b)] = e^{j2\pi(au+bv)} F(u, v) \quad (19.1)$$

In Eq. (19.1), it is assumed that the Fourier transformation of function $f(x, y)$ is $F(u, v)$. As it is clear, a shift in spatial domain will represent itself as proportional variations in phase in the frequency domain representation of the function. The same idea can be applied for phase-base motion estimation in 2D images as 2D discrete spatial functions. The major difference between the phase-based motion estimation and the Fourier transform shift theorem is that instead of using sinusoids, Gabor wavelets will be used to map the spatial domain functions to the frequency domain.

$$g(x, y) = G_\theta + jH_\theta \quad (19.2)$$

There are several types of Gabor wavelet that can be used for motion estimation, and design of Gabor wavelet can affect the accuracy and sensitivity of the motion estimation procedure [29]. The pair of Gabor wavelets used in this study are as follows:

$$G_0(x, y) = 0.9213(2x^2 - 1)e^{-(x^2+y^2)} \quad (19.3)$$

$$H_0(x, y) = (-2.205x + 0.9780x^3)e^{-(x^2+y^2)} \quad (19.4)$$

$$G_{90}(x, y) = 0.9213(2y^2 - 1)e^{-(x^2+y^2)} \quad (19.5)$$

$$H_{90}(x, y) = (-2.205y + 0.9780y^3)e^{-(x^2+y^2)} \quad (19.6)$$

The orientation of the Gabor wavelet determines the direction of sensitivity for extracting the motion [29]. For example, the Gabor wavelet with orientation of zeros is only sensitive to the motion in x direction and the motions in y-direction will not be extracted using the Gabor wavelet with orientation zero. The sequence of images captured from the vibrating structure will be convolved with a pair of Gabor wavelets based on the direction of the anticipated motion θ . Therefore, each frame of the video will be mapped on to a complex valued domain with real and imaginary parts of:

$$REAL_{\theta}(u, v, t) = \sum_x \sum_y I(x, y, t) G_{\theta}(x - u, y - v) \quad (19.7)$$

$$IMAG_{\theta}(u, v, t) = \sum_x \sum_y I(x, y, t) H_{\theta}(x - u, y - v) \quad (19.8)$$

Convolving images at all frames from the video with Gabor wavelets will map the images on to complex domain and the phase for each of the complex valued numbers can be found:

$$\phi_{\theta}(u, v, t) = \arg \left[REAL_{\theta}(u, v, t), IMAG_{\theta}(u, v, t) \right] \quad (19.9)$$

Similar to the Fourier transform shift property any motion in spatial domain will be reflected as variation of phase in the complex domain and the variations will be proportional to the motion. Therefore, the motion from time (t) to $(t + 1)$ can be estimated by subtracting the phase planes as in Eq. (19.9):

$$\delta_{t,t+1}^{\theta} = \alpha [\phi(u, v, t + 1) - \phi(u, v, t)] \quad (19.10)$$

In Eq. (19.10) α is a calibration factor, which is not the concern of our study, since the natural frequencies can be extracted from the un-calibrated data as well.

Motion magnification (video magnification) also works because the motion information is preserve with in the phase variations. In motion magnification algorithm, the phase plane signals $\phi_{\theta}(u, v, t)$ are processed with a band-pass filter. In other words, the phase temporal variations in a specific frequency band is amplified and all the other temporal variations out of the selected pass-band are suppressed. Reconstructing a new video using the band-pass filtered phase series will result to a new video with magnified motions with in the selected frequency band. Respectively, if the center frequency of the band-pass filter is selected as one of the natural frequencies of the structure, the resulting video will represent a visual perception of the operating deflection shape corresponding to the selected natural frequency [22, 26, 27].

19.3 Experimental Test-Setup

The experimental test bed shown in Fig. 19.1 was used as the test-bed to capture the sequence of images from the vibrating wind turbine blade. The cantilevered wind turbine blade was excited by a modal impact hammer. After inducing the excitation to the wind turbine blade, a single four-megapixel (2048×2048 CMOS sensor) PHOTRON high-speed camera (mounted above) equipped with 14-mm lens was used to capture the sequence of images from the vibrating structure at 500 frames per second (fps). According to the accelerometer data and the validated FEM model of the subjected wind turbine blade, the 9th Eigen frequency of the wind turbine is approximately 145 Hz. With a 500 fps frame rate, any aliasing up to 9th mode will be avoided, which can be considered a sufficient frequency range based on the fact that the contribution of the higher order modes in the overall dynamic response is negligible. The distance between the high-speed camera and the wind turbine blade is approximately 1.8 m and this working distance enables the high speed camera to include the full length of the wind turbine blade within its field of view as shown in Fig. 19.1c. It is also worth mentioning that the force signal of the modal hammer was not recorded, since the intent was to extract the unscaled operating deflection shapes, and the force spectrum is not required. The same test-bed was used for the damaged case in which the additive was attached to the tip of the WTB to mimic the icing condition on the tip.

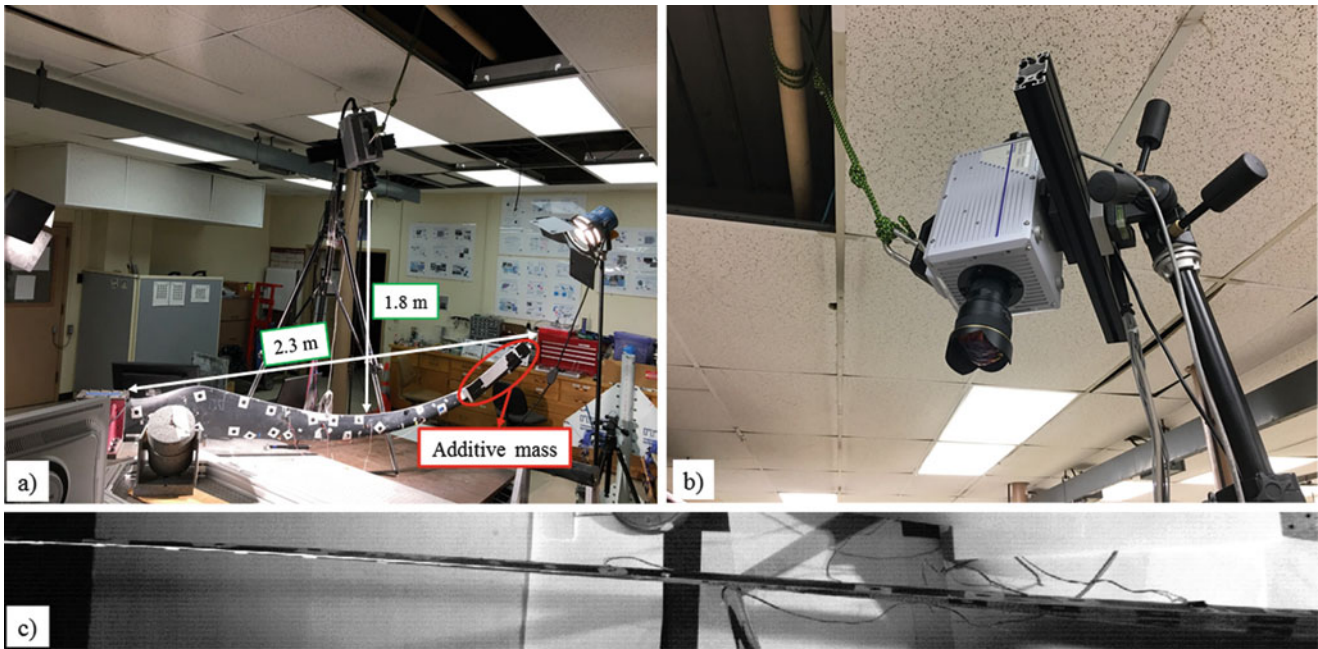


Fig. 19.1 (a) 2.3-m Skystrem 4.7 clamped wind turbine blade; (b) Another view of the test bed; the approximate distance between wind turbine blade and camera is 1.8-m; (c) field of view for the high-speed camera after applying image enhancement

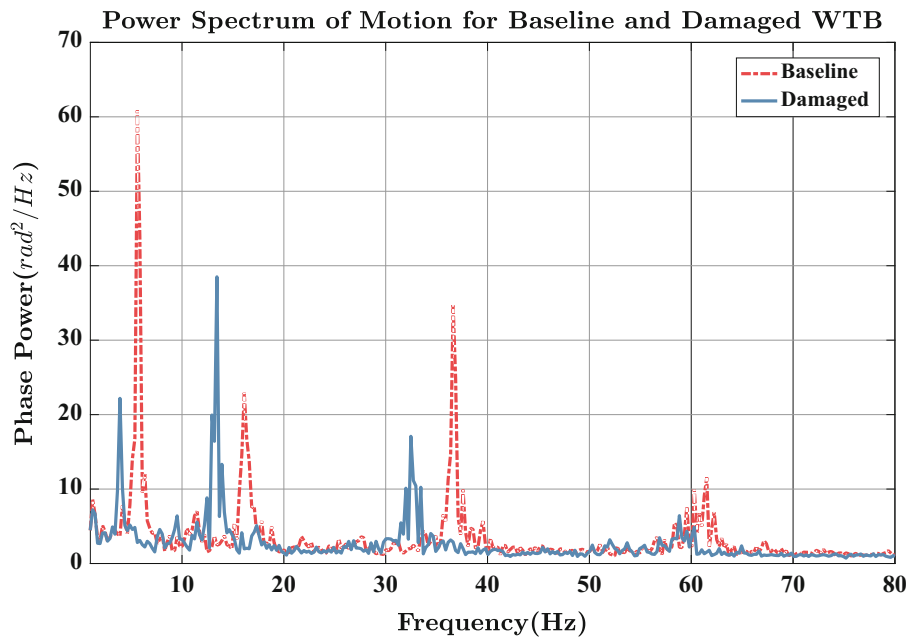


Fig. 19.2 Power spectrum of response for baseline and damaged wind turbine blade

19.4 Results and Discussion

The recorded sequence of images from vibrating wind turbine blade has been processed using the phase based motion estimation. The subtle motions in the spatial domain are extracted in terms of variations in phase as discussed in the theoretical background section. At this point, the phase variations are proportional to the actual displacements of the wind turbine blade and the data is un-calibrated. However, the natural frequencies are independent of the calibration factor. Therefore, by converting the phase signal to frequency domain as shown in Fig. 19.2 the natural frequencies of the WTB for both the baseline and damaged cases can be extracted using a simple peak picking.

The peaks in the power spectrum plot of phase variations (Fig. 19.2) are the natural frequencies of the structures for both the baseline and the damaged wind turbine blades. As it is clear attaching the additive mass as an induced damage to the WTB causes the natural frequencies to decrease as expected. The natural frequencies and the percentage of deviations in the damaged case are available in Table 19.1.

As mentioned in the theories associated with the phase based motion magnification the ODSs of the WTB can be visualized by mean of magnifying the motions with in specific frequency bands. In phase based motion magnification, the center frequency for the band-pass filter should be selected as one of the natural frequencies of the structure. In this case, the resulting motion magnified video will represent the operating deflection shape of the structure.

In order to obtain a more informative visualization of the operating deflection shapes two snap shots of the vibrating wind turbine blade after applying the motion magnification are fused together and represented in the Figs. 19.3, 19.4, 19.5, and 19.6. Selected snap shots for image fusion are from the ODS at its maximum deflection in the videos. As it is clear, the motion magnified and fused frames of the vibrating wind turbine blade can provide valuable information such as location of the nodes and anti-node, which can be used later for damage detection. The same procedure can be applied on the damaged wind turbine blade the results for the damaged wind turbine blade are not provided.

Table 19.1 Extracted natural frequencies of baseline and damaged wind turbine blade from peak picking

Baseline WTB (Hz)	Damaged WTB (Hz)	% of deviation
5.86	3.91	33.28
15.63	13.67	12.54
37.11	33.2	10.54
60.55	58.59	3.24

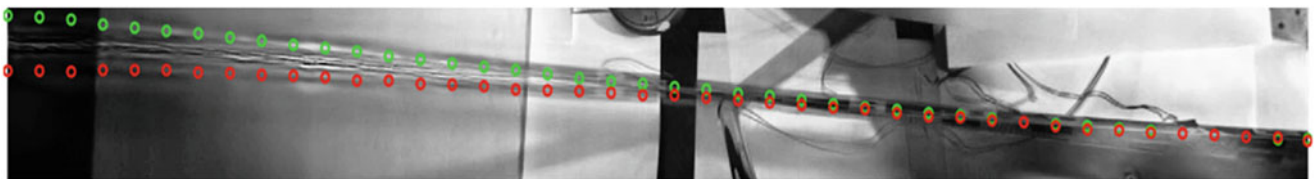


Fig. 19.3 Fused snap shots of first ODS at two of its maximum deflection positions; frequency = 5.85 Hz

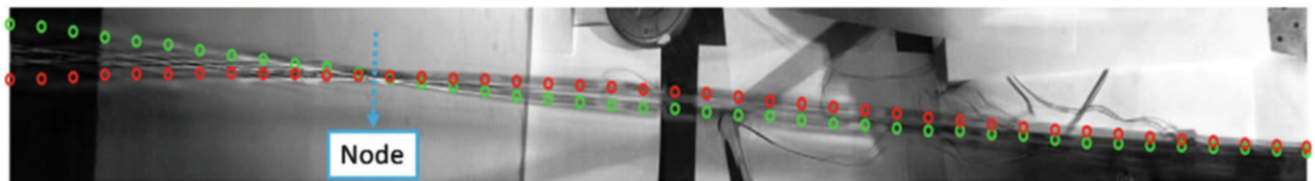


Fig. 19.4 Fused snap shots of second ODS at two of its maximum deflection positions; frequency = 15.63 Hz

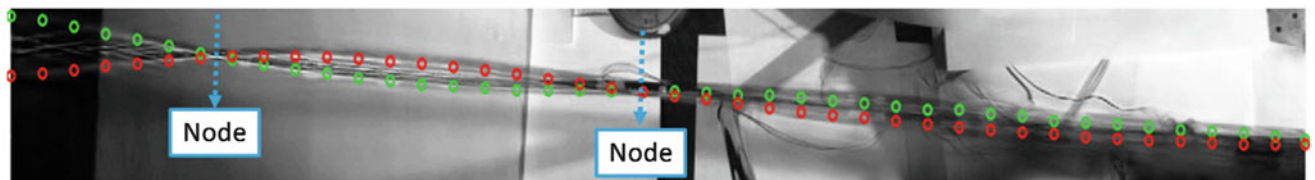


Fig. 19.5 Fused snap shots of third ODS at two of its maximum deflection positions; frequency = 37.11 Hz

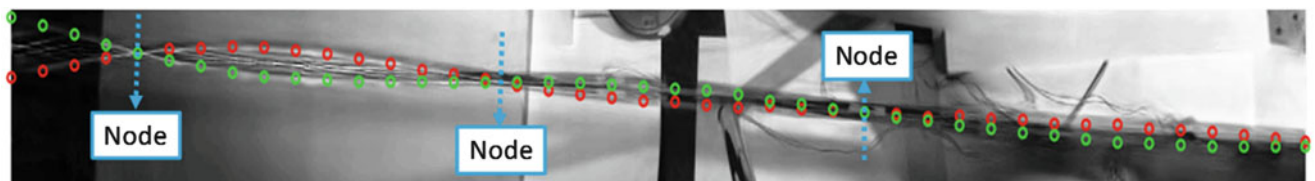


Fig. 19.6 Fused snap shots of fourth ODS at two of its maximum deflection positions; frequency = 60.55 Hz

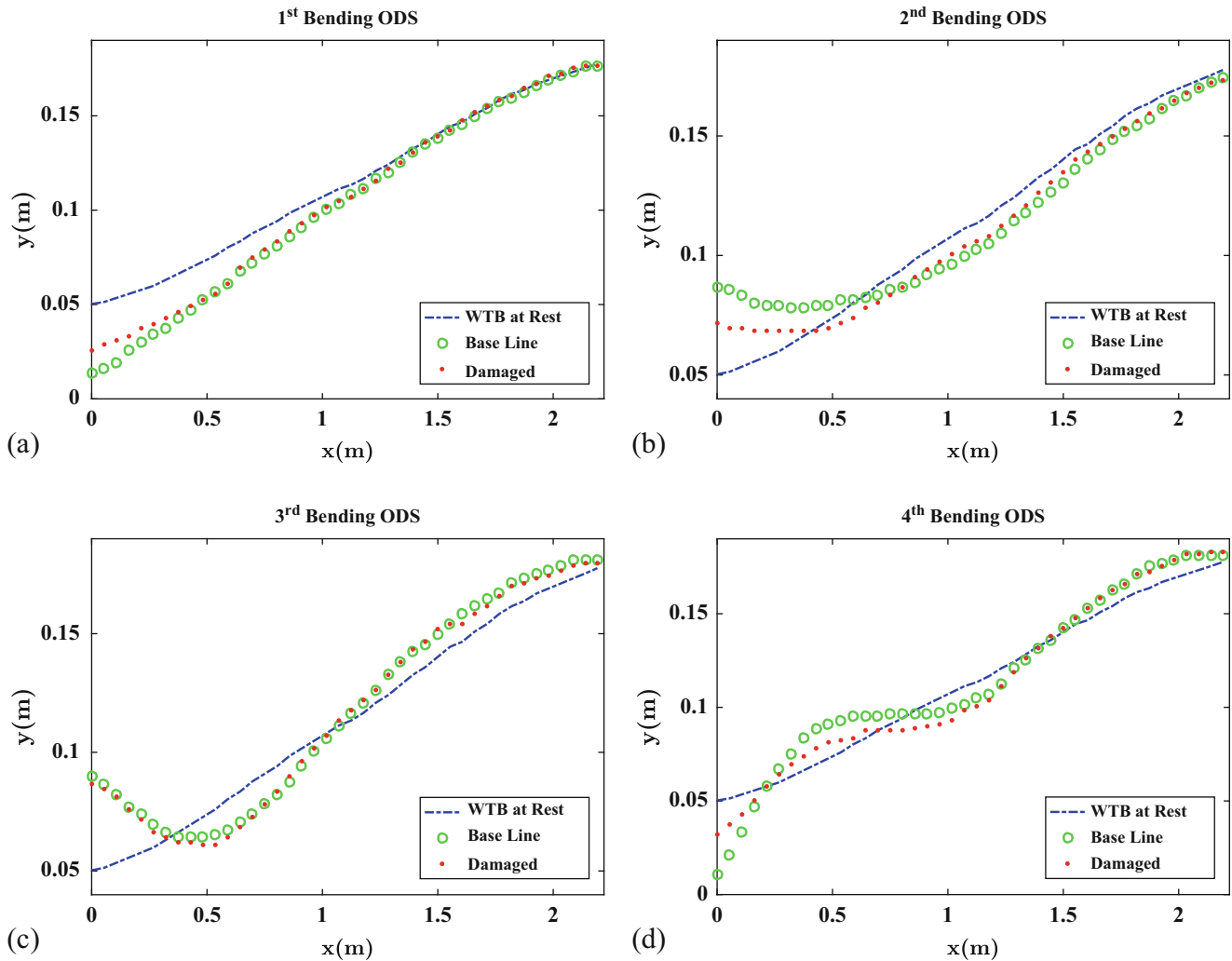


Fig. 19.7 (a) 1st Bending ODS for baseline and damaged WTB, (b) 2nd Bending ODS for baseline and damaged WTB, (c) 3rd Bending ODS for baseline and damaged WTB, (d) 4th Bending ODS for baseline and damaged WTB

Other than visual perceptions in Figs. 19.3, 19.4, 19.5, and 19.6 that the video magnification can provide, the quantitative ODSs of the wind turbine blade can be estimated using an edge detection algorithm. The edge detection algorithm is not fully automated and some of the detected points as data points for ODSs need to be deleted from the data set and may be changed manually (some of the captured edges are associated with the background and not the wind turbine blade). Figure 19.7 shows the extracted quantified operating deflection shapes after removing the outliers manually, for both the baseline and damaged wind turbine blade. The deviations in the location of the nodes and anti-nodes as well as the overall layout of the ODS can be used as damage sensitive feature.

19.5 Conclusion

Within this paper the features for vibration based damage detection on a 2.3 m long Skystream wind turbine blade has been studied. It has been shown that the deviations in natural frequencies and operating deflection shapes can be used as practical damage sensitive features for vibration based structural health monitoring. As a non-contact measurement system, camera-based measurement system in conjunction with phase-based motion estimation and motion magnification was used to estimate the natural frequencies of the structure. Visual perception of the ODS were presented using phase based motion magnification and image fusion techniques. The visual perception of mode shapes or ODSs can provide valuable information

such as location of nodes and anti-node, which can be later used as damage sensitive features as well. For engineering decision makings, having a reliable estimate of the quantitative ODSs is necessary. Therefore, edge detection was utilized on the motion-magnified videos to extract the quantitative ODSs. It has been shown that the deviations in ODSs are also visible due to the induced damage. In conclusion the natural frequencies estimated from phase-based motion estimation and the ODS provided by the motion magnification can be considered as a potential pair of features for vibration based damage detection. For further studies the proposed features can be fed to a machine learning algorithm to classify the damaged and undamaged cases which will complete the loop of autonomous SHM.

References

1. Doebling, S.W., Farrar, C.R., Prime, M.B.: A summary review of vibration-based damage identification methods. *Shock Vib. Dig.* **30**, 91–105 (1998)
2. Fan, W., Qiao, P.: Vibration-based damage identification methods: a review and comparative study. *Struct. Health Monit.* **10**, 83–111 (2011)
3. Reynders, E.: System identification methods for (operational) modal analysis: review and comparison. *Arch. Comput. Meth. Eng.* **19**, 51–124 (2012)
4. Ebrahimkhanlou, A., Salamone, S.: Acoustic emission source localization in thin metallic plates: a single-sensor approach based on multimodal edge reflections. *Ultrasonics*. **78**, 134–145 (2017)
5. Ebrahimkhanlou, A., Dubuc, B., Salamone, S.: Damage localization in metallic plate structures using edge-reflected lamb waves. *Smart Mater. Struct.* **25**, 085035 (2016)
6. Ewins, D.J.: *Modal Testing: Theory and Practice*, vol. 15. Research Studies Press, Letchworth (1984)
7. Chiariotti, P., Martarelli, M., Castellini, P.: Exploiting continuous scanning laser Doppler Vibrometry in timing belt dynamic characterisation. *Mech. Syst. Signal Process.* **86**, 66–81 (2017)
8. Baqersad, J., Poozesh, P., Niezrecki, C., Avitabile, P.: Photogrammetry and optical methods in structural dynamics—a review. *Mech. Syst. Signal Process.* **86**, 17–34 (2016)
9. Castellini, P., Martarelli, M., Tomasini, E.P.: Laser Doppler Vibrometry: development of advanced solutions answering to technology’s needs. *Mech. Syst. Signal Process.* **20**, 1265–1285 (2006)
10. Ebrahimkhanlou, A., Farhidzadeh, A., Salamone, S.: Multifractal analysis of crack patterns in reinforced concrete shear walls. *Struct. Health Monit.* **15**(1), 81–92 (2016)
11. Poozesh, P., Baqersad, J., Niezrecki, C., Avitabile, P., Harvey, E., Yarala, R.: Large-area photogrammetry based testing of wind turbine blades. *Mech. Syst. Signal Process.* **86**, 98–115 (2016)
12. Sarrafi, A., Mao, Z.: Wind turbine blade damage detection via 3-dimensional phase-based motion estimation. *Struct. Health Monit.* **2017**, 2545–2552 (2017)
13. Cheli, F., Mazzoleni, P., Pezzola, M., Ruspini, E., Zappa, E.: Vision-based measuring system for rider’s pose estimation during motorcycle riding. *Mech. Syst. Signal Process.* **38**, 399–410 (2013)
14. Baqersad, M., Hamed, A., Mohammadafzali, M., Ali, H.: Asphalt mixture segregation detection: digital image processing approach. *Adv. Mater. Sci. Eng.* **2017**, 1–6 (2017)
15. Sarrafi, A., Poozesh, P., Mao, Z.: A comparison of computer-vision-based structural dynamics characterizations. In: *Model Validation and Uncertainty Quantification*, vol. 3, pp. 295–301. Springer, Cham (2017)
16. Javh, J., Slavič, J., Boltežar, M.: The subpixel resolution of optical-flow-based modal analysis. *Mech. Syst. Signal Process.* **88**, 89–99 (2017)
17. Fleet, D., Weiss, Y.: Optical flow estimation. In: *Handbook of Mathematical Models in Computer Vision*, pp. 237–257. Springer, Boston (2006)
18. Baker, S., Matthews, I.: Lucas-kanade 20 years on: a unifying framework. *Int. J. Comput. Vis.* **56**, 221–255 (2004)
19. Horn, B.K., Schunck, B.G.: Determining optical flow. *Artif. Intell.* **17**, 185–203 (1981)
20. Fleet, D.J., Jepson, A.D.: Computation of component image velocity from local phase information. *Int. J. Comput. Vis.* **5**, 77–104 (1990)
21. Wadhwa, N., Rubinstein, M., Durand, F., Freeman, W.T.: Phase-based video motion processing. *ACM Trans. Graph. (TOG)*. **32**, 80 (2013)
22. Chen, J.G., Wadhwa, N., Cha, Y.-J., Durand, F., Freeman, W.T., Buyukozturk, O.: Modal identification of simple structures with high-speed video using motion magnification. *J. Sound Vib.* **345**, 58–71 (2015)
23. Wadhwa, N., Rubinstein, M., Durand, F., Freeman, W. T.: Riesz pyramids for fast phase-based video magnification. US Patent 9,338,331, 2016
24. Yang, Y., Dorn, C., Mancini, T., Talken, Z., Kenyon, G., Farrar, C., et al.: Blind identification of full-field vibration modes from video measurements with phase-based video motion magnification. *Mech. Syst. Signal Process.* **85**, 567–590 (2017)
25. Yang, Y., Dorn, C., Mancini, T., Talken, Z., Theiler, J., Kenyon, G., et al.: Reference-free detection of minute, non-visible, damage using full-field, high-resolution mode shapes output-only identified from digital videos of structures. *Struct. Health Monit.* **0**, 1475921717704385 (2017)
26. Sarrafi, A., Poozesh, P., Niezrecki, C., Mao, Z.: Mode extraction on wind turbine blades via phase-based video motion estimation. In *SPIE Smart Structures and Materials+ Nondestructive Evaluation and Health Monitoring*, pp. 101710E-101710E-12 (2017)
27. Poozesh, P., Sarrafi, A., Mao, Z., Avitabile, P., Niezrecki, C.: Feasibility of extracting operating shapes using phase-based motion magnification technique and stereo-photogrammetry. *J. Sound Vib.* **407**, 350–366 (2017)
28. Sarrafi, A., Mao, Z.: Uncertainty quantification of phase-based motion estimation on noisy sequence of images. In *SPIE Smart Structures and Materials+ Nondestructive Evaluation and Health Monitoring*, pp. 101702M-101702M-8 (2017)
29. Freeman, W.T., Adelson, E.H.: The design and use of steerable filters. *IEEE Trans. Pattern Anal. Mach. Intell.* **13**, 891–906 (1991)



Chapter 20

Hierarchical Bayesian Calibration and Response Prediction of a 10-Story Building Model

Mingming Song, Iman Behmanesh, Babak Moaveni, and Costas Papadimitriou

Abstract This paper presents Hierarchical Bayesian model updating of a 10-story building model based on the identified modal parameters. The identified modal parameters are numerically simulated using a frame model (exact model) of the considered 10-story building and then polluted with Gaussian white noise. Stiffness parameters of a simplified shear model - representing modeling errors - are considered as the updating parameters. In the Hierarchical Bayesian framework, the stiffness parameters are assumed to follow a probability distribution (e.g., normal) and the parameters of this distribution are updated as hyperparameters. The error functions are defined as the difference between model-predicted and identified modal parameters of the first few modes and are also assumed to follow a predefined distribution (e.g., normal) with unknown parameters (mean and covariance) which will also be estimated as hyperparameters. The Metropolis-Hastings within Gibbs sampler is employed to estimate the updating parameters and hyperparameters. The uncertainties of structural parameters as well as error functions are propagated in predicting the modal parameters and response time histories of the building.

Keywords Hierarchical Bayesian · FE model updating · Response prediction · Modeling errors · Uncertainty quantification and propagation

20.1 Introduction

Finite model (FE) is often used to predict the response of built structural systems; however, even complicated and detailed FE model cannot provide the same structural response as its measured counterpart. This response prediction discrepancy can be mitigated and minimized by FE model updating method [1]. FE Model updating method was first applied in a deterministic manner in which model's parameters are calibrated to match model-predicted data features with measured counterparts through an optimization process, then an "optimized" model can be obtained. This deterministic model updating approach has provided many successful applications due to the simple application nature [2–5]. However, effective parameters (e.g., stiffness, mass) of structural systems, especially for civil structures, have been found to show evident variability due to the changing in-service environment such as wind excitation, temperature, rain, and human activity [6–8]. This variability in modeling parameters is referred as "inherent variability" in this study and is separated from other sources of uncertainties such as measurement noise and identification errors. Presence of the inherent variability in structural parameters conflicts with the concept of a unique solution for the "optimized" model. Therefore, it is preferred to perform model updating in a probabilistic manner.

Bayesian model updating based on Bayesian inference is one of the most common approaches for probabilistic model updating. Bayesian approach has many advantages over the deterministic method, including uncertainty quantification of model parameters, uncertainty propagation in response prediction and model class selection [9, 10]. Some successful applications of this method for structural model updating can be found in [11–15]. However, many of the previous studies neglect the inherent variability of structural parameters due to changing ambient and environmental condition (which may or may not be significant based on the structure and varying conditions) and consider the main sources of uncertainties as

M. Song · B. Moaveni (✉)

Department of Civil and Environmental Engineering, Tufts University, Medford, MA, USA
e-mail: babak.moaveni@tufts.edu

I. Behmanesh

Building Structures, WSP USA, New York, NY, USA

C. Papadimitriou

Department of Mechanical Engineering, University of Thessaly, Volos, Greece

measurement noise and identification errors. The limitations of the classical Bayesian model updating formulations have been discussed by the authors in [16] and show that the model parameters' uncertainties can be decreased unlimitedly by feeding more and more datasets into the process, which is not expected for civil structures. Note that this limitation is specific to civil structures where the modeling parameters show inherent variability due to changing in-service conditions. The Hierarchical Bayesian model updating is capable of estimating the structural inherent variability, measurement noise and modeling error by introducing and updating hyperparameters. Several pioneering applications have been made recently and its advantage over classical Bayesian approach has been demonstrated [17–22]. FE models calibrated through Hierarchical Bayesian approach are capable of predicting structural response more accurately by accounting for and propagating the inherent variability, measurement noise and modeling errors.

This paper presents a Hierarchical Bayesian model updating framework and an application to a numerical 10-story building model. The inherent variability in structural stiffness parameters are considered as hyperparameters in the Hierarchical Bayesian model. Metropolis-Hastings (MH) within Gibbs sampling method is used to sample the posterior conditional probability density functions (PDFs) since the posterior joint PDF cannot be evaluated analytically. A 10-story frame building model is built and used to generate modal parameters which are used as “identified” datasets for model updating. Then a simplified 10 degree-of-freedom (DOF) shear building model is created and calibrated using the proposed model updating strategy. Due to the presence of modeling error in this application, the error function covariance matrix was overestimated to account for error bias. This prompts a second model updating process with non-zero mean error function. The modal parameters and displacement/acceleration time history predictions of calibrated model are significantly improved through the second model updating process.

20.2 Hierarchical Bayesian Model Updating Framework

20.2.1 Formulation of Hierarchical Bayesian Model Updating

The real-world civil structures always show inherent variability in the structural stiffness and mass, due to the changing in-service environmental conditions, including wind excitation, rain, temperature and human's activities. In this paper, only the inherent variability in structural stiffness is considered, but the proposed Hierarchical Bayesian model updating framework has the capability to estimate the inherent mass variability (mainly due to human activity) as well in a similar manner.

Figure 20.1 presents the proposed Hierarchical Bayesian model. The changing in-service condition causes the variability in structural stiffness, which in turn causes the uncertainty in identified modal parameters, e.g., natural frequencies

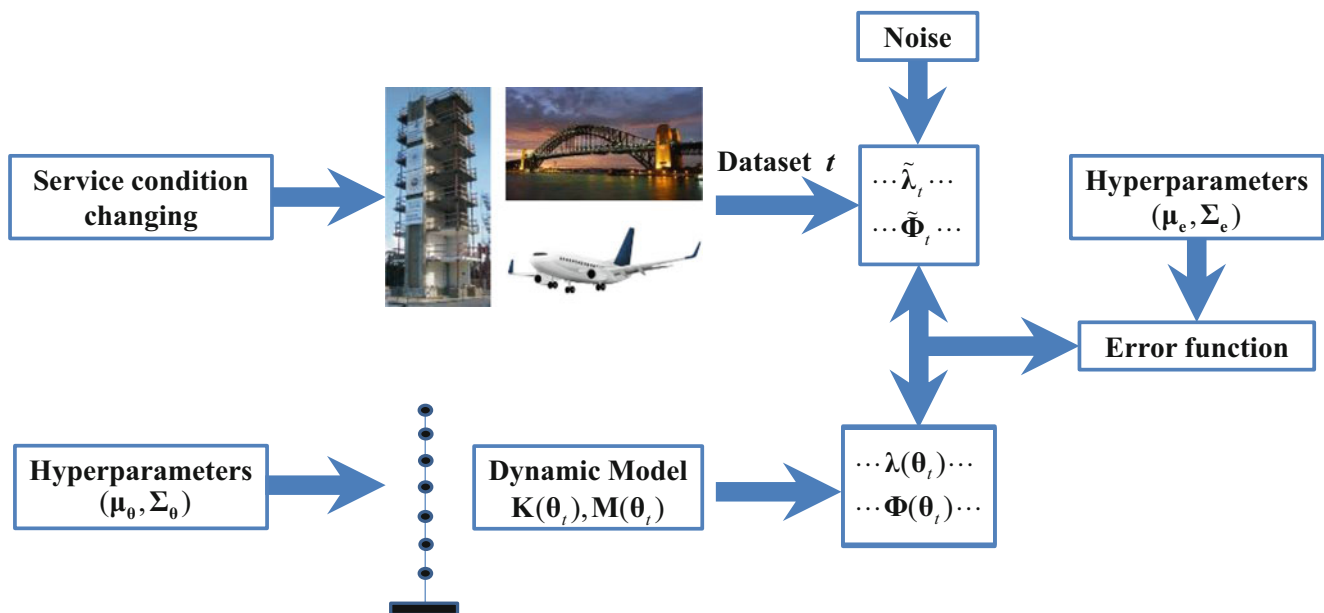


Fig. 20.1 Graphical representation of the proposed Hierarchical Bayesian model

and mode shapes. In addition to this inherent variability, other sources of uncertainties exist in the modal parameters identification process, including measurement noise and identification error. The changing in-service condition is modeled as hyperparameters of a representative dynamic model of the real structure. For civil engineering structures, based on past studies and author's experience, Gaussian distribution with mean $\boldsymbol{\mu}_\theta$ and covariance matrix $\boldsymbol{\Sigma}_\theta$ is considered as a reasonable distribution for the stiffness vector $\boldsymbol{\theta}_t$ of the dynamic model. Error function is defined as the difference between model-predicted modal parameters with their identified counterparts, and it is assumed to follow a Gaussian distribution with mean $\boldsymbol{\mu}_e$ and covariance matrix $\boldsymbol{\Sigma}_e$.

If there is no modeling error in the dynamic model, the variability of error function only comes from the noise, then it is reasonable to assume $\boldsymbol{\mu}_e = \mathbf{0}$, as shown in Eq. (20.1):

$$\mathbf{e}_t = \begin{bmatrix} \mathbf{e}_{\lambda_t} \\ \mathbf{e}_{\Phi_t} \end{bmatrix} \sim N(\mathbf{0}, \boldsymbol{\Sigma}_e) \quad (20.1)$$

where \mathbf{e}_t is the error function for dataset t , including two parts: eigen-frequency error \mathbf{e}_{λ_t} and mode shape error \mathbf{e}_{Φ_t} , which are vectors and consist of errors for different modes. The errors for each mode are defined as:

$$e_{\lambda_m} = \frac{\tilde{\lambda}_{tm} - \lambda_m(\boldsymbol{\theta}_t)}{\lambda_m(\boldsymbol{\theta}_t)} \quad (20.2)$$

$$\mathbf{e}_{\Phi_m} = \frac{\tilde{\Phi}_{tm}}{\|\tilde{\Phi}_{tm}\|} - a_{tm} \frac{\boldsymbol{\Gamma} \Phi_m(\boldsymbol{\theta}_t)}{\|\boldsymbol{\Gamma} \Phi_m(\boldsymbol{\theta}_t)\|} \quad (20.3)$$

$$a_{tm} = \frac{\tilde{\Phi}_{tm} \cdot \boldsymbol{\Gamma} \Phi_m(\boldsymbol{\theta}_t)}{\|\tilde{\Phi}_{tm}\| \cdot \|\boldsymbol{\Gamma} \Phi_m(\boldsymbol{\theta}_t)\|} \quad (20.4)$$

in which, the subscript m refers to mode number, $\tilde{\lambda}_{tm}$ ($\tilde{\lambda}_{tm} = (2\pi\tilde{f}_{tm})^2$, where \tilde{f}_{tm} is identified natural frequency in Hz) and $\tilde{\Phi}_{tm}$ are identified eigen-frequency and mode shape in dataset t , $\lambda_m(\boldsymbol{\theta}_t)$ and $\Phi_m(\boldsymbol{\theta}_t)$ are model-predicted counterparts. $\boldsymbol{\Gamma}$ is called picking matrix, which picks the corresponding components of $\Phi_m(\boldsymbol{\theta}_t)$ and makes it comparable with $\tilde{\Phi}_{tm}$. a_{tm} is a scaling factor, and defined in Eq. (20.4). Note that, in the case that modeling error exists, the assumption of $\boldsymbol{\mu}_e = \mathbf{0}$ might be violated, which can be overcome by a second model updating process with non-zero $\boldsymbol{\mu}_e$ evaluated from the first model updating process, see the application in Sect. 20.3. The reason why $\boldsymbol{\mu}_e$ is not updated with other model parameters is that, it might cause convergence issue due to the potential compensation effect between $\boldsymbol{\mu}_e$ and $\boldsymbol{\mu}_\theta$.

The $\boldsymbol{\Sigma}_e$ is covariance matrix and assumed to be a diagonal matrix which means no correlation between different error function components, as shown in Eq. (20.5):

$$\boldsymbol{\Sigma}_e = \begin{bmatrix} \ddots & & & \\ & \ddots & & \\ & & \sigma_{e_i}^2 & \\ & & & \ddots \end{bmatrix} \quad (20.5)$$

Note that, the full matrix $\boldsymbol{\Sigma}_e$ can also be considered and updated in this framework.

Based on Bayes' theorem, the posterior probability function is proportional to the product of likelihood function and prior function, Eq. (20.6) can be derived straightforward:

$$p(\boldsymbol{\theta}_t, \boldsymbol{\mu}_\theta, \boldsymbol{\Sigma}_\theta, \boldsymbol{\Sigma}_e \mid \tilde{\lambda}_t, \tilde{\Phi}_t) \propto p(\tilde{\lambda}_t, \tilde{\Phi}_t \mid \boldsymbol{\theta}_t, \boldsymbol{\mu}_\theta, \boldsymbol{\Sigma}_\theta, \boldsymbol{\Sigma}_e) p(\boldsymbol{\theta}_t, \boldsymbol{\mu}_\theta, \boldsymbol{\Sigma}_\theta, \boldsymbol{\Sigma}_e) \quad (20.6)$$

$$\propto p(\tilde{\lambda}_t, \tilde{\Phi}_t \mid \boldsymbol{\theta}_t, \boldsymbol{\Sigma}_e) p(\boldsymbol{\theta}_t \mid \boldsymbol{\mu}_\theta, \boldsymbol{\Sigma}_\theta, \boldsymbol{\Sigma}_e) p(\boldsymbol{\mu}_\theta, \boldsymbol{\Sigma}_\theta, \boldsymbol{\Sigma}_e) \quad (20.7)$$

$$\propto p(\tilde{\lambda}_t, \tilde{\Phi}_t \mid \boldsymbol{\theta}_t, \boldsymbol{\Sigma}_e) p(\boldsymbol{\theta}_t \mid \boldsymbol{\mu}_\theta, \boldsymbol{\Sigma}_\theta) p(\boldsymbol{\mu}_\theta) p(\boldsymbol{\Sigma}_\theta) p(\boldsymbol{\Sigma}_e) \quad (20.8)$$

Equation (20.7) can be derived from Eq. (20.6) based on the fact that the identified modal parameters only depend on the structural stiffness $\boldsymbol{\theta}_t$ and the error function, therefore, the condition on hyperparameters $\boldsymbol{\mu}_\theta$, $\boldsymbol{\Sigma}_\theta$ can be dropped. Since the structural stiffness only depend on its hyperparameters, therefore, the condition on $\boldsymbol{\Sigma}_e$ can be dropped and by assuming $\boldsymbol{\mu}_\theta$, $\boldsymbol{\Sigma}_\theta$, $\boldsymbol{\Sigma}_e$ are independent in their joint prior distribution, Eq. (20.8) is readily derived from Eq. (20.7).

In the case that multiple datasets are available, by assuming that all datasets are independent and structural stiffness at different time instants is independent, Eq. (20.9) can be derived:

$$p\left(\boldsymbol{\Theta}, \boldsymbol{\mu}_\theta, \boldsymbol{\Sigma}_\theta, \boldsymbol{\Sigma}_e \mid \tilde{\boldsymbol{\lambda}}, \tilde{\boldsymbol{\Phi}}\right) \propto \prod_{t=1}^{N_t} p\left(\tilde{\boldsymbol{\lambda}}_t, \tilde{\boldsymbol{\Phi}}_t \mid \boldsymbol{\theta}_t, \boldsymbol{\Sigma}_e\right) p\left(\boldsymbol{\theta}_t \mid \boldsymbol{\mu}_\theta, \boldsymbol{\Sigma}_\theta\right) p\left(\boldsymbol{\mu}_\theta\right) p\left(\boldsymbol{\Sigma}_\theta\right) p\left(\boldsymbol{\Sigma}_e\right) \quad (20.9)$$

in which, $\boldsymbol{\Theta} = \left[\boldsymbol{\theta}_1 \dots \boldsymbol{\theta}_t \dots \boldsymbol{\theta}_{N_t}\right]$, $\tilde{\boldsymbol{\lambda}} = \left[\tilde{\boldsymbol{\lambda}}_1 \dots \tilde{\boldsymbol{\lambda}}_t \dots \tilde{\boldsymbol{\lambda}}_{N_t}\right]$ and $\tilde{\boldsymbol{\Phi}} = \left[\tilde{\boldsymbol{\Phi}}_1 \dots \tilde{\boldsymbol{\Phi}}_t \dots \tilde{\boldsymbol{\Phi}}_{N_t}\right]$. N_t is the total number of datasets.

To simply the formulation process, uniform prior distribution is used for $\boldsymbol{\mu}_\theta$ and conjugate prior distributions are used for $\boldsymbol{\Sigma}_\theta$ and $\boldsymbol{\Sigma}_e(\sigma_{e_i}^2)$:

$$p\left(\boldsymbol{\mu}_\theta\right) \propto 1 \quad (20.10)$$

$$\boldsymbol{\Sigma}_\theta \sim \text{Inverse-Wishart}\left(\boldsymbol{\Sigma}_{\theta_0}, v_1\right) \quad (20.11)$$

$$\sigma_{e_i}^2 \sim \text{Inverse-}\chi^2\left(v_2, \sigma_{e_0}^2\right) \quad (20.12)$$

in which, $\boldsymbol{\Sigma}_{\theta_0}$, v_1 , v_2 , $\sigma_{e_0}^2$ are parameters of the prior distributions. There are no universal optimal values for them, and should be adjusted based on specific applications. The posterior distribution function is the compromise of the likelihood function and prior functions; therefore, these parameters of prior distributions always have impact on the final posterior distribution. Careful selection and tuning these parameters based on prior knowledge is recommended, and if the total number of datasets is large enough, the effect of likelihood function should dominate the posterior distribution and the impact of prior distribution can be minimized.

The joint posterior distribution can then be derived from Eq. (20.9) by combining the prior distributions Eqs. (20.10, 20.11, and 20.12) and the assumed likelihood functions:

$$p\left(\boldsymbol{\Theta}, \boldsymbol{\mu}_\theta, \boldsymbol{\Sigma}_\theta, \boldsymbol{\Sigma}_e \mid \tilde{\boldsymbol{\lambda}}, \tilde{\boldsymbol{\Phi}}\right) \propto |\boldsymbol{\Sigma}_\theta|^{-\frac{N_t+v_1+N_p+1}{2}} \prod_{i=1}^{N_e} (\sigma_{e_i}^2)^{-\frac{N_t+v_2+2}{2}} \exp\left[\sum_{t=1}^{N_t} (\mathbf{J}_{e_t} + \mathbf{J}_\theta) - \frac{1}{2} \text{tr}\left(\boldsymbol{\Sigma}_{\theta_0} \cdot \boldsymbol{\Sigma}_\theta^{-1}\right) - \sum_{i=1}^{N_e} \frac{v_2 \sigma_{e_0}^2}{2\sigma_{e_i}^2}\right] \quad (20.13)$$

$$\mathbf{J}_{e_t} = -\frac{1}{2} \mathbf{e}_t^T \boldsymbol{\Sigma}_e^{-1} \mathbf{e}_t \quad (20.14)$$

$$\mathbf{J}_\theta = -\frac{1}{2} (\boldsymbol{\theta}_t - \boldsymbol{\mu}_\theta)^T \boldsymbol{\Sigma}_\theta^{-1} (\boldsymbol{\theta}_t - \boldsymbol{\mu}_\theta) \quad (20.15)$$

where N_p is the number of components in stiffness vector $\boldsymbol{\theta}$, N_e is the number of components in error function \mathbf{e}_t , which is equal to $(1 + N_s)N_m$, and N_m and N_s denote number of identified modes and number of components in each identified mode shape, respectively.

20.2.2 Metropolis-Hastings within Gibbs Sampling

The joint posterior probability function Eq. (20.13) cannot be evaluated analytically, since it is only known to a scaling factor and needs multiple integrations to obtain the scaling factor. Markov Chain Monte Carlo (MCMC) method is a stochastic sampling method and can be used to generate samples from Eq. (20.13). Gibbs sampling method is one of the MCMC

algorithms and is usually more efficient than Metropolis-Hastings (MH) algorithm, due to its high sample acceptance ratio (100%), but it requires deriving all the posterior conditional PDFs. Posterior conditional PDFs are not always available and depend on the specific applications. For this study, thanks to the conjugate prior distributions used, the posterior conditional PDFs are derived and listed below:

$$p(\boldsymbol{\theta}_t | \boldsymbol{\mu}_\theta, \boldsymbol{\Sigma}_\theta, \boldsymbol{\Sigma}_e, \tilde{\boldsymbol{\lambda}}_t, \tilde{\boldsymbol{\Phi}}_t) \propto \exp(\mathbf{J}_{e_t} + \mathbf{J}_{\theta_t}) \quad (20.16)$$

$$p(\boldsymbol{\mu}_\theta | \boldsymbol{\Theta}, \boldsymbol{\Sigma}_\theta, \boldsymbol{\Sigma}_e, \tilde{\boldsymbol{\lambda}}, \tilde{\boldsymbol{\Phi}}) = N\left(\frac{1}{N_t} \sum_{t=1}^{N_t} \boldsymbol{\theta}_t, \frac{1}{N_t} \boldsymbol{\Sigma}_\theta\right) \quad (20.17)$$

$$p(\boldsymbol{\Sigma}_\theta | \boldsymbol{\Theta}, \boldsymbol{\mu}_\theta, \boldsymbol{\Sigma}_e, \tilde{\boldsymbol{\lambda}}, \tilde{\boldsymbol{\Phi}}) = \text{Inverse-Wishart}(\boldsymbol{\Sigma}_{\theta_0} + \mathbf{S}, v_1 + N_t) \quad (20.18)$$

$$p(\sigma_{e_t}^2 | \boldsymbol{\Theta}, \boldsymbol{\mu}_\theta, \boldsymbol{\Sigma}_\theta, \tilde{\boldsymbol{\lambda}}, \tilde{\boldsymbol{\Phi}}) = \text{Inverse-}\chi^2\left(v_2 + N_t, \frac{v_2 \sigma_{e_0}^2 + N_t V_i}{v_2 + N_t}\right) \quad (20.19)$$

$$\mathbf{S} = \sum_{t=1}^{N_t} (\boldsymbol{\theta}_t - \boldsymbol{\mu}_\theta) (\boldsymbol{\theta}_t - \boldsymbol{\mu}_\theta)^T \quad (20.20)$$

$$V_i = \frac{1}{N_t} \sum_{t=1}^{N_t} e_{t_i}^2 \quad (20.21)$$

Gibbs sampling method samples only one parameter each step. There are multiple ways to decide the order of parameters to sample, either random choose one parameter each time, or sample the parameters in turn recurrently. In this study, the parameters are sampled in order $\boldsymbol{\Theta} \rightarrow \boldsymbol{\mu}_\theta \rightarrow \boldsymbol{\Sigma}_\theta \rightarrow \boldsymbol{\Sigma}_e$ recurrently. The sampling of Eq. (20.16) requires another MCMC algorithm since its full analytical expression is unknown and MH algorithm is applied here. The proposal distribution in MH algorithm is chosen as a normal distribution whose covariance matrix is adjusted to keep the acceptance ratio at a level recommended by [23]. Equations (20.17, 20.18, and 20.19) can be sampled directly since they are standard distributions. Therefore, MH within Gibbs sampling method is used to sample the derived posterior conditional PDFs in this study. Note that, each sample generated by MH within Gibbs contains all the updating parameters, i.e., $\boldsymbol{\Theta}, \boldsymbol{\mu}_\theta, \boldsymbol{\Sigma}_\theta, \boldsymbol{\Sigma}_e$.

20.3 Application to a 10-Story Building Model

20.3.1 Description of the 10-Story Building Model

For the purpose of verification and demonstration, the proposed Hierarchical Bayesian model updating framework is applied to a 10-story frame building model (the exact model) shown in Fig. 20.2a. Blue dots denote the considered accelerometers, i.e., measurements. The building foundation is constrained in horizontal and vertical direction and has rotational springs to constrain the rotation. The stiffness of the rotational spring is $k_r = 2 \times 10^5$ kN/m, story height is 3 m throughout the building, width of the building is 10 m, and the mass of each slab is 4×10^3 kg. The considered member sizes and material properties are summarized in Table 20.1. The Young's modulus of each structural member is assumed to follow a Gaussian distribution with means and standard deviations summarized in Table 20.1. The stiffness of each structural member is assumed independent, but the stiffness of two columns on the same story is assumed to be equal.

Based on the assumed Gaussian distribution of material properties, 100 datasets of modal parameters are generated. The frame model is used to generate the exact modal parameters which are then polluted with Gaussian white noise to simulate the "identified data" for the purpose of model updating. The added noise level is 0.5% in coefficient-of-variation. In the identified data, only first three modes are considered (assuming other modes are not identified), and only the mode shape components corresponding to the accelerometers (blue dots) are considered, i.e., at stories 2, 4, 6, 8 and 10. Note that, the accelerometers are assumed to have only horizontal measurement. The histograms of the 100 sets of "identified" natural

Fig. 20.2 (a) 10-story frame building model; (b) 10 DOF shear building model

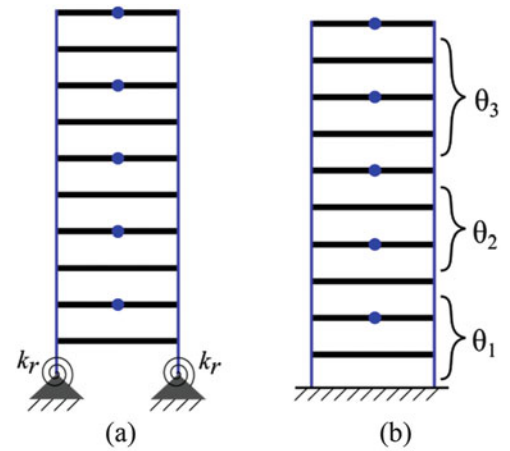


Table 20.1 Member sizes and material properties of 10-story frame building model

Structural members		Cross-section (m × m)	Young's modulus (GPa)	
			Mean	Std
Columns	Story (1–3)	0.3 × 0.3	50	3
	Story (4–6)	0.25 × 0.25	40	2
	Story (7–10)	0.2 × 0.2	30	1
	Slabs (all stories)	0.5 × 0.5	25	1

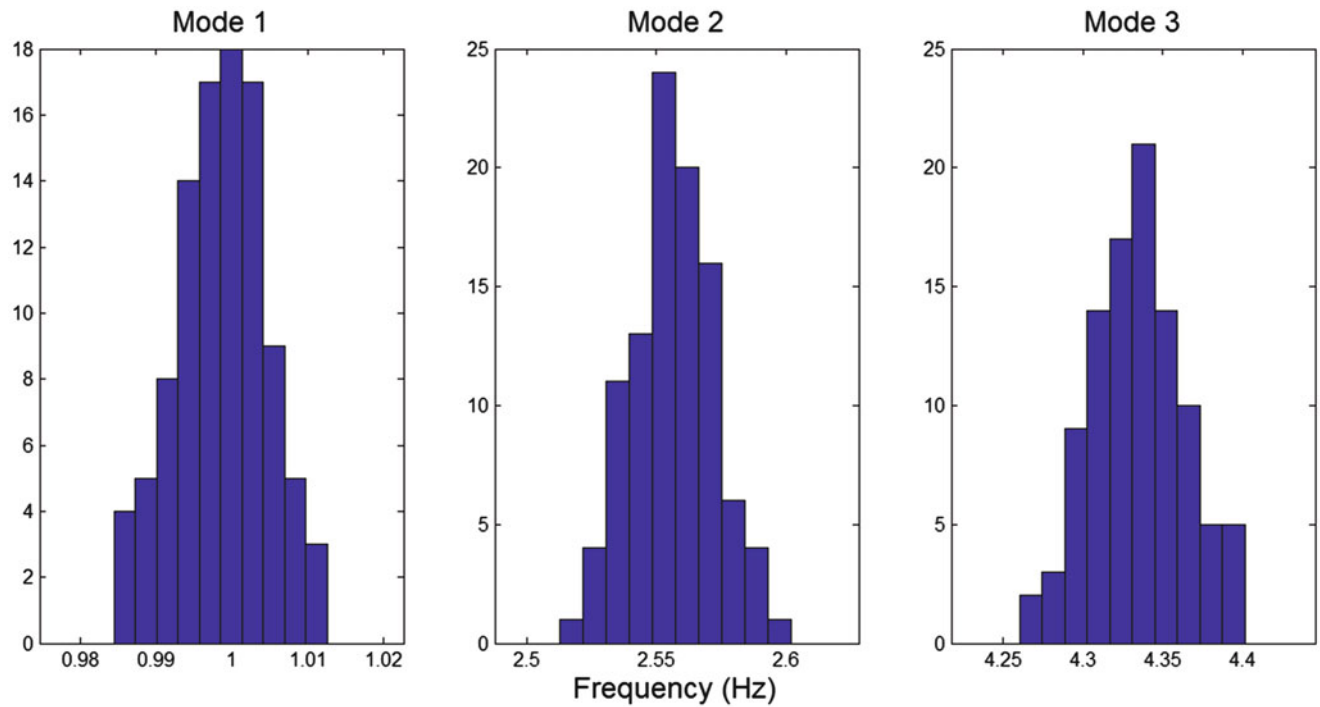


Fig. 20.3 Histogram of natural frequencies of first three modes

frequencies for the first three modes are shown in Fig. 20.3. The first three mode shapes of the frame building model (all members at their mean stiffness) are shown in Fig. 20.4.

A 10 DOF shear building model is considered to represent the building for the purpose of introducing modeling error, as shown in Fig. 20.2b. The base of the shear building is considered as fixed, slabs are assumed to be rigid, and the columns are grouped into three substructures (story 1–3, 4–6 and 7–10 as shown in Fig. 20.2b), with three updating parameters $\theta_1 \sim \theta_3$ assigned for the Young's modulus of the substructures. The grouping strategy or substructuring is often adopted in real

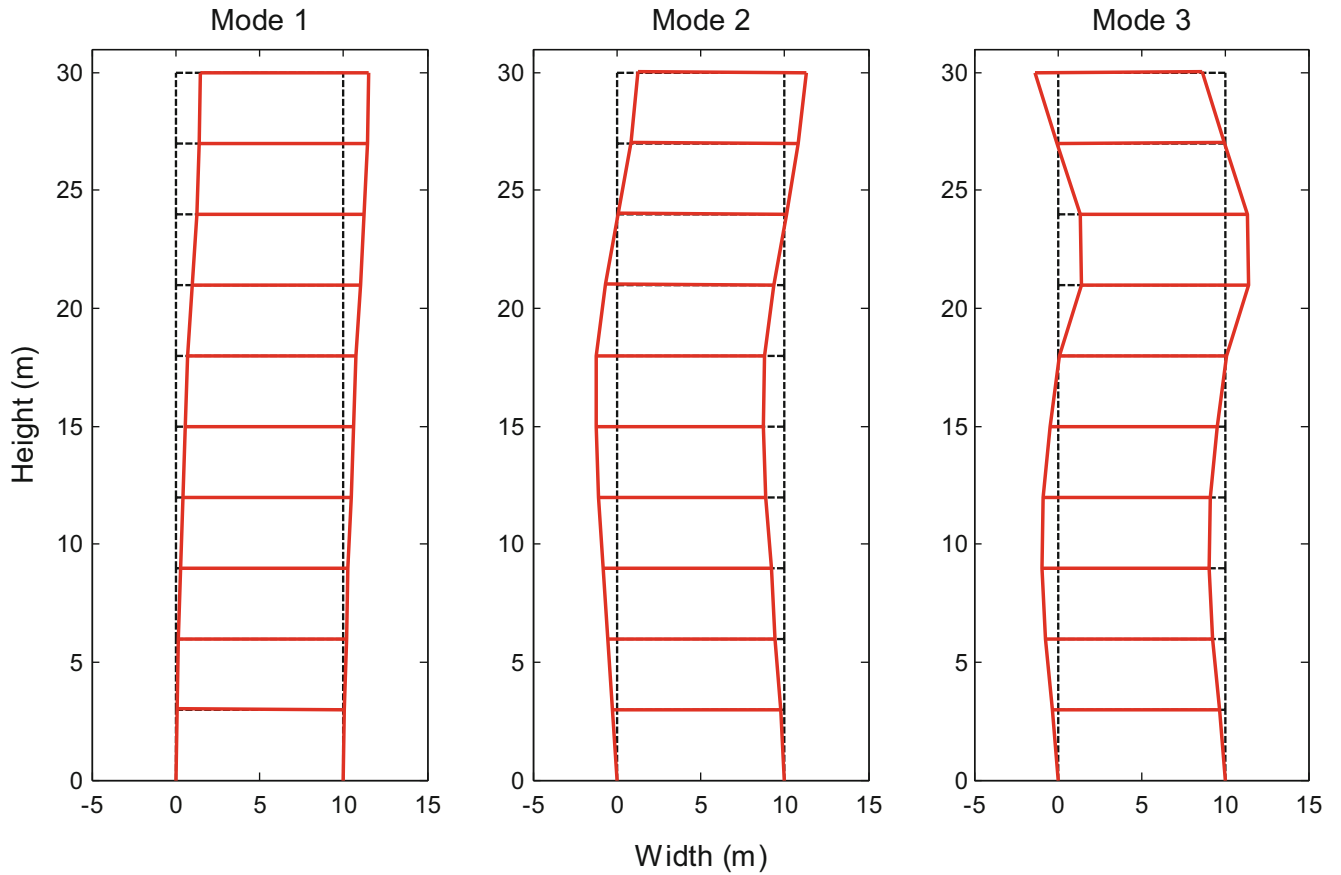


Fig. 20.4 First three mode shapes of the 10-story frame building model

structural applications to reduce the number of parameters and avoid the potential ill-condition of the inverse problem, but it will introduce additional modeling errors into the problem due to the smearing effect of grouping.

20.3.2 Model Updating with $\mu_e = 0$

The proposed Hierarchical Bayesian model updating framework is applied to estimate the stiffness parameters $\theta = [\theta_1, \theta_2, \theta_3]^T$ and the associated hyperparameters of the 10 DOF shear building model using the “identified” modal parameters. The parameters of prior distributions in Eqs. (20.11 and 20.12) are chosen as:

$$v_1 = 3, \Sigma_{\theta_0} = \begin{bmatrix} 1^2 & & \\ & 1^2 & \\ & & 1^2 \end{bmatrix}, v_2 = 1, \sigma_{e_0}^2 = 1 \times 10^{-6}, \quad (20.22)$$

The proposed MH within Gibbs sampling method is used to sample the derived conditional posterior PDFs Eqs. (20.16, 20.17, 20.18, and 20.19). It is found that 20,000 samples are large enough to provide sample statistics with desired precision, and the first 5000 samples are discarded as burn-in samples. Burn-in strategy provides better sample estimate of updating parameters by discarding the initial few transitional samples. The samples of μ_{θ} and Σ_{θ} (σ_{θ_i}) (after burn-in) are shown in Fig. 20.5. Note that, for Σ_{θ} , only standard deviations σ_{θ_i} of each updating parameter is shown here. It can be observed that, the samples are distributed similar to Gaussian distributions.

After the samples are generated, sample statistics (e.g., sample mean, mode, standard deviation) can be derived accordingly. Note that sample mode is also referred as maximum-a-posteriori (MAP) value. The MAPs are evaluated as the parameters’ values which maximize the kernel PDFs derived from the samples. The histograms and kernel PDFs of μ_{θ}

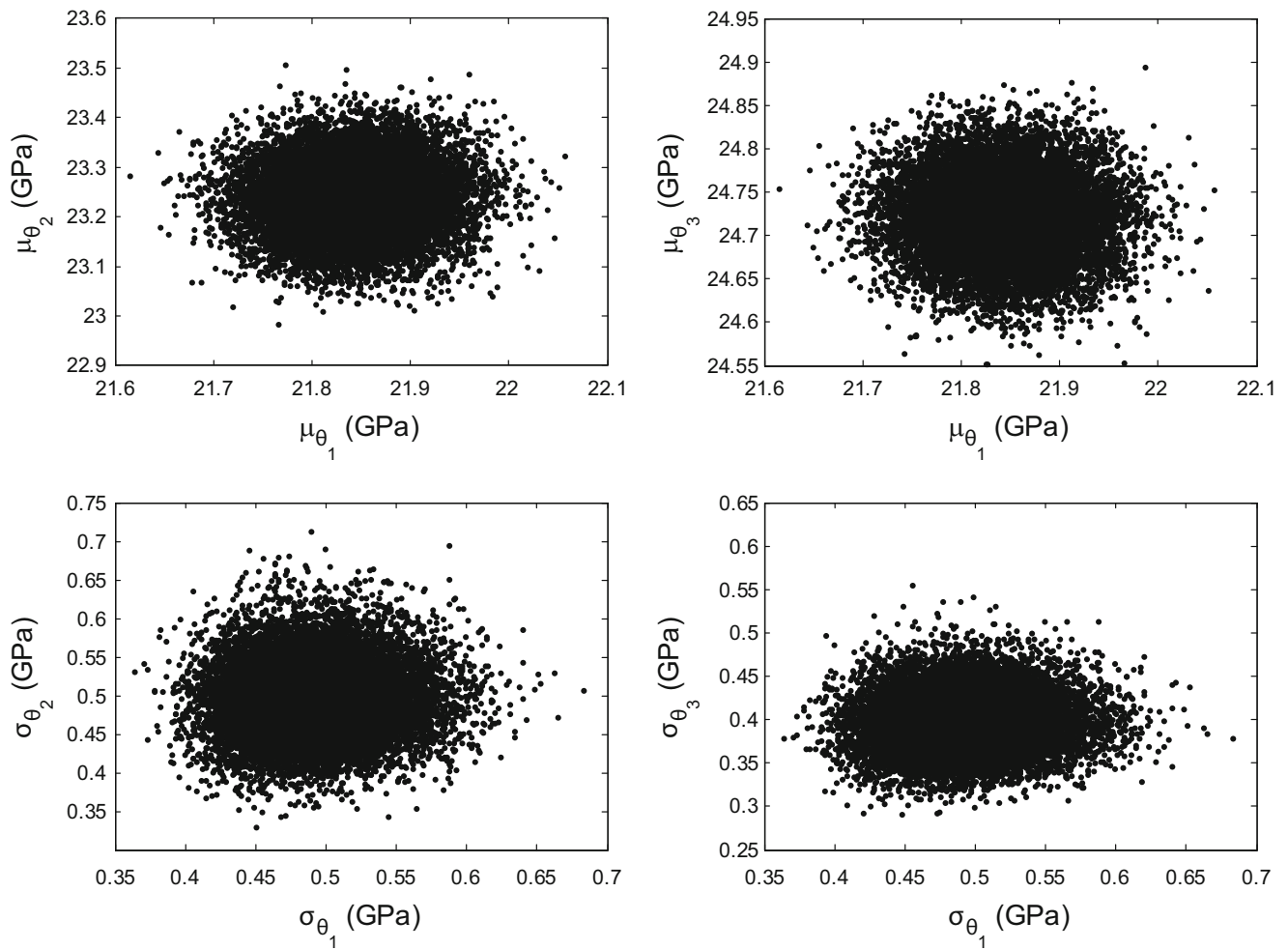


Fig. 20.5 Samples of μ_{θ} and Σ_{θ} (σ_{θ_i}) (after burn-in)

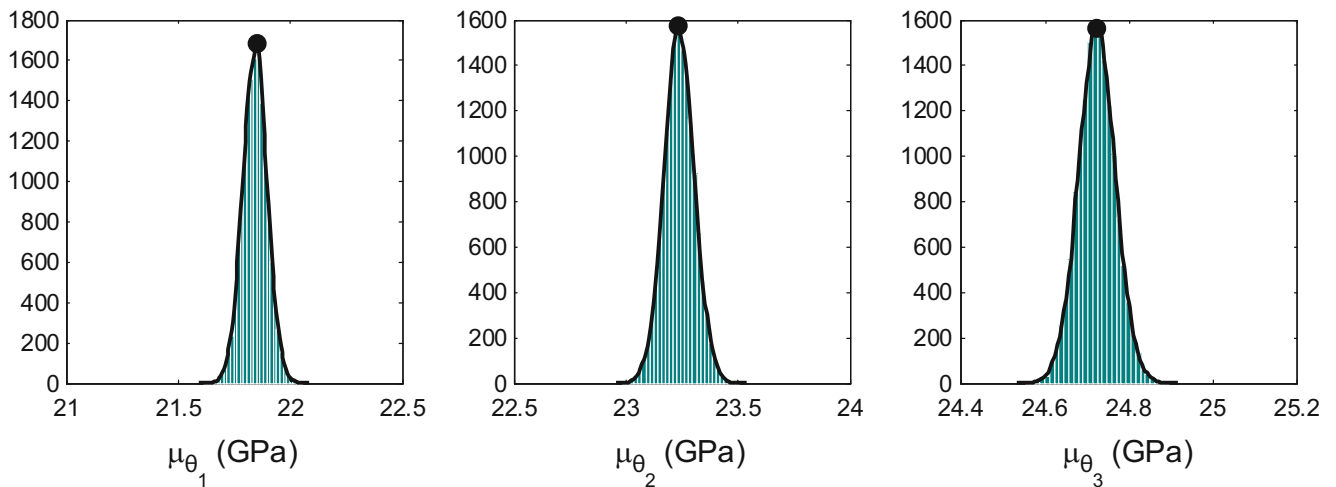


Fig. 20.6 Histograms and kernel PDFs of μ_{θ} (after burn-in)

are shown in Fig. 20.6. Note the kernel PDFs are normalized such that their peaks (MAPs shown as black dots) have the same height of the highest bins of the histograms. It can be observed that the samples of μ_{θ} seem to follow a Gaussian distribution.

Table 20.2 MAPs of Hierarchical model updating with $\mu_e = \mathbf{0}$ and $\mu_e \neq \mathbf{0}$, and evaluated μ_e

MAPs of updating parameters	With $\mu_e = \mathbf{0}$	With $\mu_e \neq \mathbf{0}$	μ_e (Evaluated) ($\times 10^{-2}$)	
$\hat{\mu}_\theta$ (GPa)	$\hat{\mu}_{\theta_1}$	21.85	21.85	
	$\hat{\mu}_{\theta_2}$	23.23	23.31	
	$\hat{\mu}_{\theta_3}$	24.72	24.67	
$\hat{\Sigma}_\theta$ ($\hat{\sigma}_{\theta_i}, \hat{\rho}_{ij}$)	$\hat{\sigma}_{\theta_1}$ (GPa)	0.48	0.49	
	$\hat{\sigma}_{\theta_2}$ (GPa)	0.49	0.50	
	$\hat{\sigma}_{\theta_3}$ (GPa)	0.40	0.36	
	$\hat{\rho}_{12}$	0.01	-0.12	
	$\hat{\rho}_{13}$	0.10	0.03	
	$\hat{\rho}_{23}$	0.11	-0.10	
$\hat{\Sigma}_e$ ($\hat{\sigma}_{e_i}$) ($\times 10^{-3}$)	$\hat{\sigma}_e(\lambda_1)$	25.1	5.9	-2.36
	$\hat{\sigma}_e(\lambda_2)$	0.8	7.7	0.01
	$\hat{\sigma}_e(\lambda_3)$	55.0	10.0	5.39
	$\hat{\sigma}_e(\phi_{1,1})$	0.8	0.5	-0.02
	$\hat{\sigma}_e(\phi_{2,1})$	5.4	2.8	0.47
	$\hat{\sigma}_e(\phi_{3,1})$	2.0	2.7	0.08
	$\hat{\sigma}_e(\phi_{4,1})$	3.5	2.7	-0.22
	$\hat{\sigma}_e(\phi_{5,1})$	2.1	2.2	0.01
	$\hat{\sigma}_e(\phi_{1,2})$	6.3	4.2	0.45
	$\hat{\sigma}_e(\phi_{2,2})$	5.9	5.6	-0.21
	$\hat{\sigma}_e(\phi_{3,2})$	5.4	4.1	0.37
	$\hat{\sigma}_e(\phi_{4,2})$	8.1	8.1	-0.06
	$\hat{\sigma}_e(\phi_{5,2})$	6.2	5.3	0.37
	$\hat{\sigma}_e(\phi_{1,3})$	21.9	12.7	1.63
	$\hat{\sigma}_e(\phi_{2,3})$	5.4	5.1	0.07
	$\hat{\sigma}_e(\phi_{3,3})$	14.6	7.2	-0.92
	$\hat{\sigma}_e(\phi_{4,3})$	12.0	6.4	0.90
	$\hat{\sigma}_e(\phi_{5,3})$	9.8	9.5	-0.20

The MAPs of μ_θ , Σ_θ ($\sigma_{\theta_i}, \rho_{ij}$), Σ_e (σ_{e_i}) are reported in Table 20.2. For $\hat{\sigma}_{e_i}$, the corresponding component of error function is shown in parenthesis. λ_i refers to the eigen-frequency error component, and $\phi_{i,j}$ refers to the mode shape error component, i.e., component i of mode shape j . From Table 20.2, it can be observed that $\hat{\mu}_{\theta_i}$ and $\hat{\sigma}_{\theta_i}$ are smaller than the actual mean and standard deviations shown in Table 20.1. This can be due to (a) the smearing effect of grouping strategy which neglects the independence of members stiffness values resulting in underestimation of $\hat{\sigma}_{\theta_i}$, and (b) the modeling errors in the shear building model cause underestimation of $\hat{\mu}_{\theta_i}$. The $\hat{\rho}_{ij}$ are accurately estimated close to zero. The $\hat{\sigma}_{e_i}$ are generally estimated larger than the added Gaussian white noise level, i.e., 0.5% for $\hat{\sigma}_e(\lambda_1)$ and $\hat{\sigma}_e(\lambda_3)$, mainly due to the modeling error of the shear building model.

Based on the definition of error function in Eqs. (20.2 and 20.3), the model-predicted modal parameters can be evaluated from Eqs. (20.23 and 20.24):

$$\tilde{\lambda}_{tm} = \lambda_m(\theta_t) + \lambda_m(\theta_t) e_{\lambda_{tm}} \quad (20.23)$$

$$\frac{\tilde{\Phi}_{tm}}{\|\tilde{\Phi}_{tm}\|} = a_{tm} \frac{\Gamma \Phi_m(\theta_t)}{\|\Gamma \Phi_m(\theta_t)\|} + \mathbf{e}_{\Phi_{tm}} \quad (20.24)$$

in which, θ_t represents the Young's modulus of the three substructures in the shear building model and follows a normal distribution $\theta_t \sim N(\hat{\mu}_\theta, \hat{\Sigma}_\theta)$. Eigen-frequency error $e_{\lambda_{tm}}$ and mode shape error $\mathbf{e}_{\Phi_{tm}}$ follow a zero-mean Gaussian distribution $\mathbf{e}_t \sim N(\mathbf{0}, \hat{\Sigma}_e)$.

The comparison between the calibrated shear building model prediction of natural frequencies (400 predictions) and simulated "identified data" is shown in Fig. 20.7. The black dots correspond to the same 100 data points used in the model

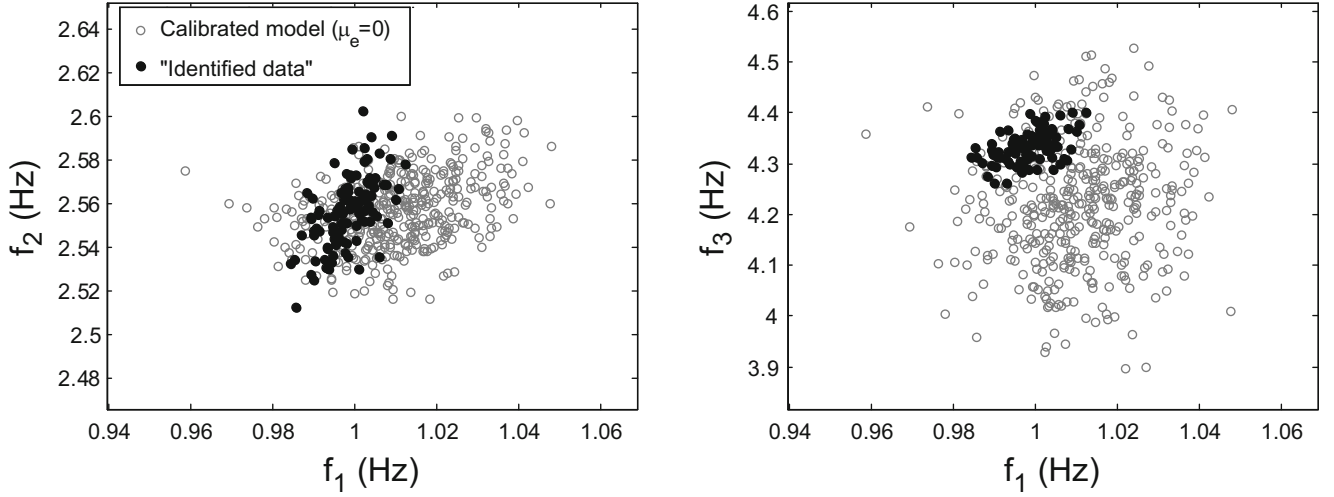


Fig. 20.7 Comparison of natural frequencies of calibrated model ($\mu_e = \mathbf{0}$) with data

updating process. It can be observed that the calibrated model predicted natural frequencies cover the scatter of actual data but they provide a much larger variability as shown in the estimated $\hat{\Sigma}_e$ at Table 20.2. It is also observed that the centers of two clouds (black vs gray) are not aligned, especially for modes 1 and 3, indicating bias in error function. Based on this observation, another model updating is performed in the following section where $\mu_e \neq \mathbf{0}$ is considered and its value is estimated.

20.3.3 Model Updating with $\mu_e \neq \mathbf{0}$

In this section, the model updating process is repeated with $\mu_e \neq \mathbf{0}$ to account for the observed bias in error functions. μ_e is evaluated from Eq. (20.25):

$$\mu_e = \frac{1}{N_t} \sum_{t=1}^{N_t} \hat{\mathbf{e}}_t \quad (20.25)$$

where $\hat{\mathbf{e}}_t$ is equal to the error function evaluated from Eqs. (20.2 and 20.3) using $\hat{\boldsymbol{\theta}}_t$ obtained from Sect. 20.3.2. The calculated μ_e is shown in Table 20.2.

The model updating with $\mu_e \neq \mathbf{0}$ follows almost the same process, except for the following minor modification made for Eqs. (20.14) and (20.21):

$$\mathbf{J}_{e_t} = -\frac{1}{2}(\mathbf{e}_t - \mu_e)^T \boldsymbol{\Sigma}_e^{-1} (\mathbf{e}_t - \mu_e) \quad \text{Before : Eq.(14) : } \mathbf{J}_{e_t} = -\frac{1}{2}\mathbf{e}_t^T \boldsymbol{\Sigma}_e^{-1} \mathbf{e}_t \quad (20.26)$$

$$V_i = \frac{1}{N_t} \sum_{t=1}^{N_t} (e_{t_i} - \mu_{e_i})^2 \quad \text{Before : Eq.(21) : } V_i = \frac{1}{N_t} \sum_{t=1}^{N_t} e_{t_i}^2 \quad (20.27)$$

The MAPs of model updating with $\mu_e \neq \mathbf{0}$ are summarized and compared with previous process in Table 20.2. It can be seen that, $\hat{\boldsymbol{\mu}}_\theta$ and $\hat{\boldsymbol{\Sigma}}_\theta$ do not show significant change. However, $\hat{\boldsymbol{\Sigma}}_e$ is reduced for most of the components, especially for $\hat{\sigma}_e(\lambda_1)$ and $\hat{\sigma}_e(\lambda_3)$, and the values for $\hat{\sigma}_e(\lambda_1 \sim \lambda_3)$ are closer to the added white noise level, i.e., 0.5%. The comparison

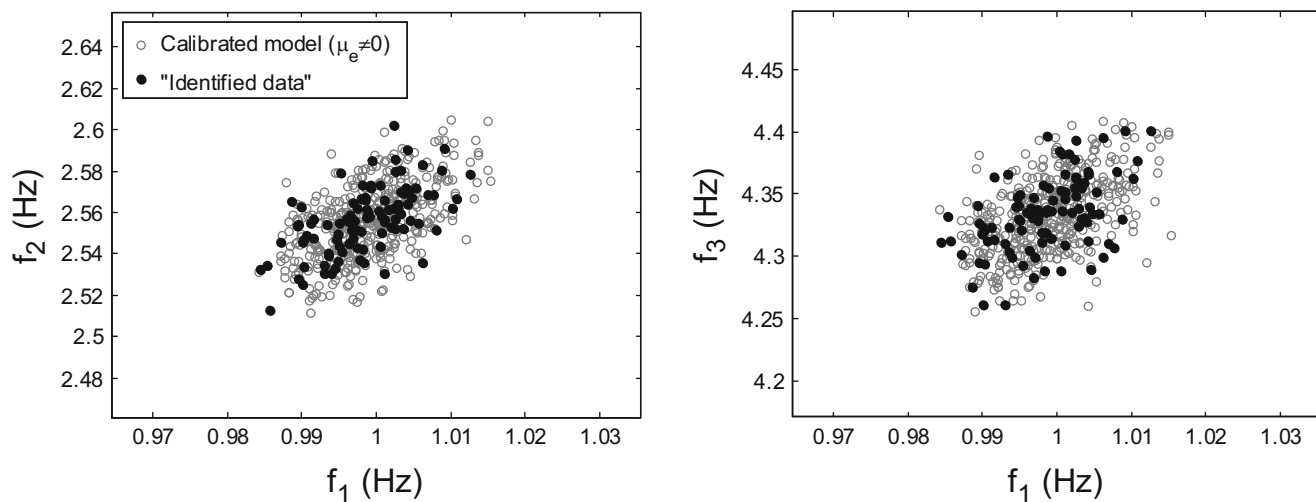


Fig. 20.8 Comparison of natural frequencies of calibrated model ($\mu_e \neq \mathbf{0}$) with data

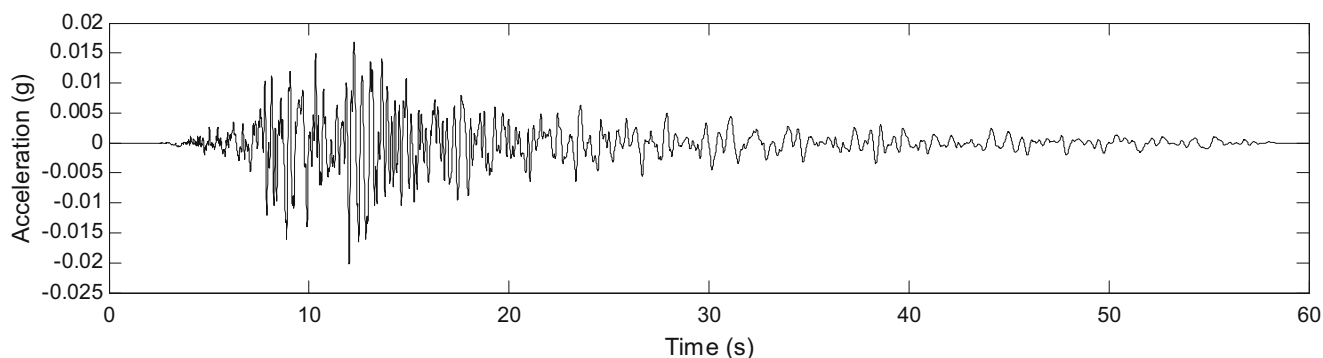


Fig. 20.9 Acceleration time history of 2009 L'Aquila Italy earthquake

between model predicted natural frequencies (400 predictions) from calibrated model ($\mu_e \neq \mathbf{0}$) with simulated data is shown in Fig. 20.8. It can be observed that, the predicted natural frequencies match their counterparts very well and there is a tighter fit compared to Fig. 20.7.

20.4 Time History Predictions

The calibrated shear models are used to predict the dynamic response of the building to a small magnitude earthquake. The selected ground motion is the record at Antrodoco station during the 2009 L'Aquila Italy earthquake. The acceleration record of this earthquake is shown in Fig. 20.9. The response time history is estimated using modal superposition and the uncertainty of model parameters ($\mu_\theta, \Sigma_\theta$) as well as errors (μ_e, Σ_e) are propagated in the predicted time histories. Note that only contributions of the first three modes are considered in the predictions which introduces another source of error in predictions. The modal parameters are obtained using Eqs. (20.23 and 20.24), with two cases of error function \mathbf{e}_t ($\mu_e = \mathbf{0}$ and $\mu_e \neq \mathbf{0}$). The error function \mathbf{e}_t only includes the error for mode shape components at story 2, 4, 6, 8 and 10 (i.e., location of sensors). For time history predictions at other stories, the maximum value of $\hat{\sigma}_e(\phi_{i,j})$ ($i = 1 \dots 5, j = 1, 2, 3$) is selected and used, and $\mu_{e_i} = 0$ is always used for unknown mode shape components. The predicted response is also sensitive to the variability/uncertainty of modal damping ratios, therefore, a coefficient-of-variation of 30% is assumed for the first three modal damping with mean values of 2%. Note that this variability can be obtained from system identification results from experimental data. For predictions from the exact model, no variability is considered for damping ratios.

The comparisons of displacement/acceleration time histories from the exact model and calibrated models are shown in Figs. 20.10 and 20.11 for stories 10 and 9, respectively. Note that there is sensor on story 10, but not for story 9 which makes

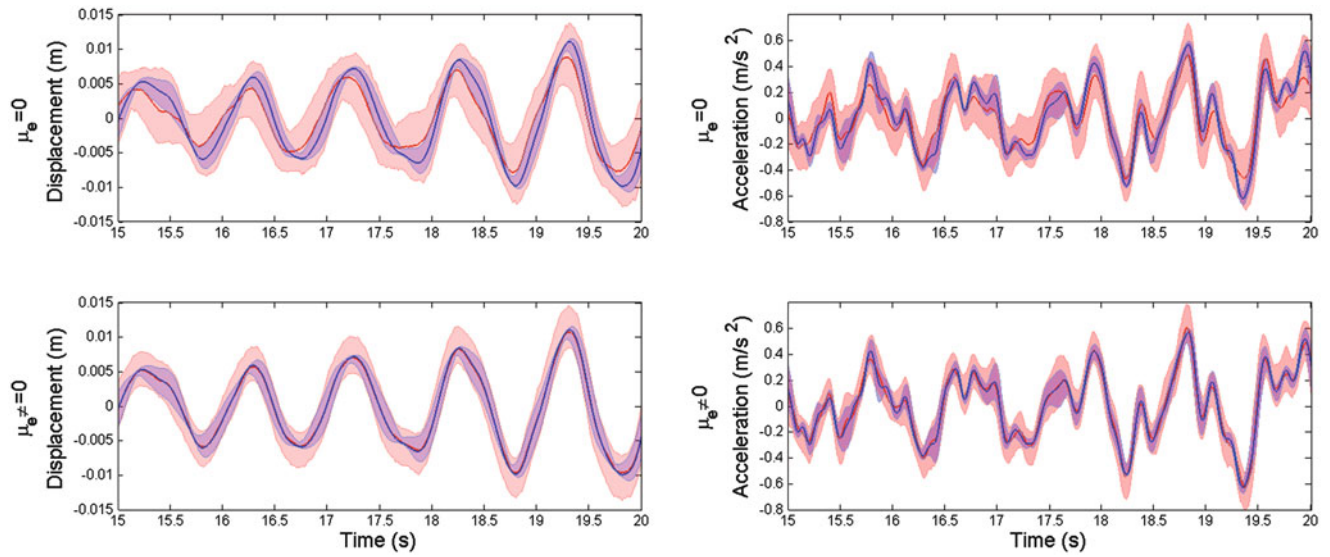


Fig. 20.10 Comparison of predicted displacement/acceleration time histories at story 10 from the exact model and calibrated models (zoom-in for 15–20 s)

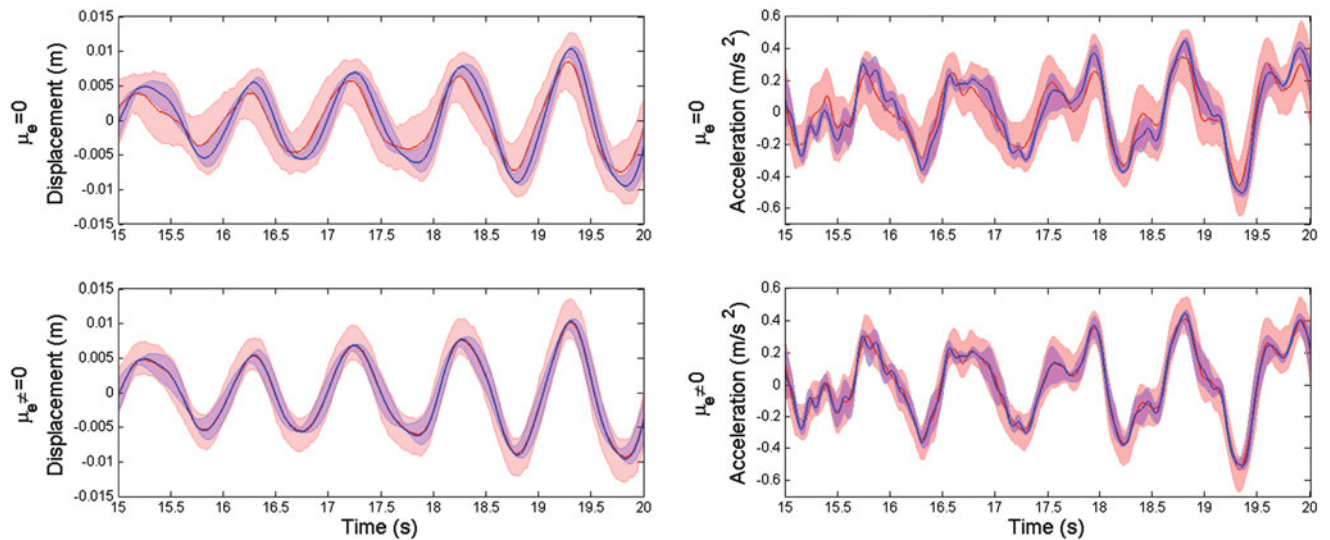


Fig. 20.11 Comparison of predicted displacement/acceleration time histories at story 9 from the exact model and calibrated models (zoom-in for 15–20 s)

its prediction more complex. The top and bottom graphs in each figure show the predictions from calibrated model with $\mu_e = \mathbf{0}$ and $\mu_e \neq \mathbf{0}$, respectively. The red and blue shaded areas refer to predictions from the calibrated models and exact model, respectively. The shaded areas denote the 95% confidence interval of predictions. The red and blue center lines in the middle of shaded areas show the median values of predictions. The variability in the exact model prediction comes from the underlying probability distribution of material properties (Table 20.1). From Figs. 20.10 and 20.11, it can be observed that, the predictions from both calibrated models ($\mu_e = \mathbf{0}$ and $\mu_e \neq \mathbf{0}$) are capable of covering the variability of their counterparts from exact model for story 10 (where measurement data was available) and story 9 (where no measurement data was available), but predictions from calibrated model with $\mu_e \neq \mathbf{0}$ show smaller variability and match the results of exact model better.

20.5 Conclusions

This paper presents a Hierarchical Bayesian model updating framework and an application to a 10-story building model. Hierarchical Bayesian model updating algorithm has the capability of estimating the inherent variability in structural parameters by introducing hyperparameters in the dynamic model. MH within Gibbs sampling method is used to sample the posterior conditional PDFs. The application to the 10-story frame building model shows that the proposed framework is capable of providing accurate confidence bounds when predicting response time histories using calibrated models with modeling errors. However, the confidence bounds or the uncertainty in response predictions is reduced (i.e., providing a tighter fit) when the updating process explicitly accounts for the error bias, i.e., when considering $\mu_e \neq 0$.

Acknowledgements Partial support of this study by the National Science Foundation Grant 1254338 is gratefully acknowledged. The opinions, findings, and conclusions expressed in this paper are those of the authors and do not necessarily represent the views of the sponsors and organizations involved in this project.

References

1. Friswell, M., Mottershead, J.E.: *Finite Element Model Updating in Structural Dynamics*. Springer Science & Business Media, 2013
2. Brownjohn, J.M., Xia, P.-Q.: Dynamic assessment of curved cable-stayed bridge by model updating. *J. Struct. Eng.* **126**, 252–260 (2000)
3. Teughels, A., De Roeck, G.: Structural damage identification of the highway bridge Z24 by FE model updating. *J. Sound Vib.* **278**, 589–610 (2004)
4. Reynders, E., Roeck, G.D., Gundes Bakir, P., Sauvage, C.: Damage identification on the Tilff bridge by vibration monitoring using optical fiber strain sensors. *J. Eng. Mech.* **133**, 185–193 (2007)
5. Song, M., Yousefianmoghadam, S., Mohammadi, M.E., Moaveni, B., Stavridis, A., Wood, R.L.: An application of finite element model updating for damage assessment of a two-story reinforced concrete building and comparison with lidar. *Struct. Health Monit.* Nov 7:1475921717737970 (2017)
6. Alampalli, S.: Effects of testing, analysis, damage, and environment on modal parameters. *Mech. Syst. Signal Process.* **14**, 63–74 (2000)
7. Clinton, J.F., Bradford, S.C., Heaton, T.H., Favela, J.: The observed wander of the natural frequencies in a structure. *Bull. Seismol. Soc. Am.* **96**, 237–257 (2006)
8. Moaveni, B., Behmanesh, I.: Effects of changing ambient temperature on finite element model updating of the Dowling Hall Footbridge. *Eng. Struct.* **43**, 58–68 (2012)
9. Sohn, H.: A Bayesian probabilistic approach for structure damage detection. *Earthq. Eng. Struct. Dyn.* **26**(12), 1259–1281 (1997)
10. Beck, J.L., Katafygiotis, L.S.: Updating models and their uncertainties. I: Bayesian statistical framework. *J. Eng. Mech.* **124**, 455–461 (1998)
11. Ching, J., Beck, J.L.: New Bayesian model updating algorithm applied to a structural health monitoring benchmark. *Struct. Health Monit.* **3**, 313–332 (2004)
12. Yuen, K.V., Beck, J.L., Au, S.K.: Structural damage detection and assessment by adaptive Markov chain Monte Carlo simulation. *Struct. Control. Health Monit.* **11**, 327–347 (2004)
13. Muto, M., Beck, J.L.: Bayesian updating and model class selection for hysteretic structural models using stochastic simulation. *J. Vib. Control.* **14**, 7–34 (2008)
14. Ntotsios, E., Papadimitriou, C., Panetos, P., Karaiskos, G., Perros, K., Perdikaris, P.C.: Bridge health monitoring system based on vibration measurements. *Bull. Earthq. Eng.* **7**, 469 (2009)
15. Behmanesh, I., Moaveni, B., Papadimitriou, C.: Probabilistic damage identification of a designed 9-story building using modal data in the presence of modeling errors. *Eng. Struct.* **131**, 542–552 (2017)
16. Behmanesh, I., Moaveni, B., Lombaert, G., Papadimitriou, C.: Hierarchical Bayesian model updating for structural identification. *Mech. Syst. Signal Process.* **64**, 360–376 (2015)
17. Jiang, X., Mahadevan, S.: Bayesian hierarchical uncertainty quantification by structural equation modeling. *Int. J. Numer. Methods Eng.* **80**, 717–737 (2009)
18. Ballesteros, G., Angelikopoulos, P., Papadimitriou, C., Koumoutsakos, P.: Bayesian hierarchical models for uncertainty quantification in structural dynamics. *Vulnerability Uncertain Risk Quantification, Mitigation Manage.* 1615–1624 (2014)
19. Nagel, J.B., Sudret, B.: Hamiltonian Monte Carlo and borrowing strength in hierarchical inverse problems. *ASCE-ASME J Risk. Uncertain. Eng. Sys. Part A Civ. Eng.* **2**, B4015008 (2015)
20. Wu, S., Angelikopoulos, P., Papadimitriou, C., Moser, R., Koumoutsakos, P.: A hierarchical Bayesian framework for force field selection in molecular dynamics simulations. *Phil. Trans. R. Soc. A.* **374**, 20150032 (2016)
21. Behmanesh, I., Moaveni, B.: Accounting for environmental variability, modeling errors, and parameter estimation uncertainties in structural identification. *J. Sound Vib.* **374**, 92–110 (2016)
22. Huang, Y., Beck, J.L., Li, H.: Bayesian system identification based on hierarchical sparse Bayesian learning and Gibbs sampling with application to structural damage assessment. *Comput. Methods Appl. Mech. Eng.* **318**, 382–411 (2017)
23. Roberts, G.O., Rosenthal, J.S.: Optimal scaling for various Metropolis-Hastings algorithms. *Stat. Sci.* **16**, 351–367 (2001)

Chapter 21

Scaling and Structural Similarity Under Uncertainty



Mo E. Asl, Christopher Niezrecki, James Sherwood, and Peter Avitabile

Abstract Fiber reinforced composite structures require extensive experimental evaluation for validation due to their heterogeneous properties and manufacturing variability. A scaled model replicating the structural characteristics of its full-scale parent structure facilitates and expedites the assessment of the mechanical performance of large composite structures. This study primarily investigates the problems associated with the design of a scaled model and its similarity to its full-scale parent structure when there is uncertainty in the design parameters. A successful design should be robust to its assumptions and the sources of uncertainty. In this study, scaled-down composite I-beams are designed from their reference full-scale I-beam representing the spar caps and the shear web structure inside a utility-scale wind turbine blade. Similitude analysis is used in conjunction with Info-Gap theory to design scaled composite I-beams under uncertainty in the design parameters. The scaling laws for the strain field of the composite I-beam are derived and used as a metric to design scaled models that are robust to the uncertainties in the design parameters. The range of influence of uncertainty in different design parameters is investigated. The effect of uncertainty on accuracy of the scaled model in predicting the strain field of the full-scale structure is studied under uncertainty in all design parameters and the strain field of the full-scale I-beam is predicated using that of the scaled model for the worst-case scenario.

Keywords Wind turbine blade · Subcomponent · Similitude · Uncertainty · Scaling

21.1 Introduction

Certification of the utility-scale wind turbine blades starts with coupon testing of the materials and is finalized with the full-scale testing of the blade. Coupon testing is not fully representative of the structural performance of the blade and full-scale testing is time consuming and very expensive (i.e. on order of hundreds of thousands of dollars). Sub-component testing can bridge the leap between full-scale and coupon testing and expedite introducing of the new materials into the wind industry if meaningful small-scale tests can be designed that are representative of the critical regions of the wind turbine blade.

Several studies have been perused to investigate and design small-scale subcomponents emulating a wind turbine blade. Mandell et al. [1] fabricated and tested composite I-beams with shear webs and flanges emulating the cross-section region of a wind turbine blade. The root section of the blade was studied by Cairns et al. [2] in which the specimens representing a single insert of a blade to hub joint were evaluated by using a pull out test. Mandell et al. [3] conducted a study on sandwich panel terminations and skin-stiffener intersections. The objective was to estimate skin-stiffener fracture loads and evaluate the performance at the transition location between sandwich panel and normal laminate by using tension tests.

The design of sub-component tests for the adhesive joints and bond-line of the wind turbine blades were the focus of a few studies. Sayer et al. [4] designed an asymmetric three-point bending test was performed on what is called a Henkel beam. The idea was to introduce a comparable amount of shear and normal stress to the bond-line to certify the adhesive performance. Later, the Henkel beam was tested for a parametric study to investigate the influence of the bond-line thickness between web and flanges on the beam flexural strength [5].

The designed subcomponent (referred to as the “model”) regardless of the size and complexity needs to correlate with the full-scale component (referred to as “prototype”, see Fig. 21.1). The correlation between the scaled model and the prototype must be based on the structural parameters that describe the response of the system under study [6]. Similitude theory can extract scaling laws from the governing equations of the system to predict the response of the prototype from those of the scaled-down model. In order to take advantage of the scaling laws, a properly scaled model should be designed to work

M. E. Asl (✉) · C. Niezrecki · J. Sherwood · P. Avitabile
Department of Mechanical Engineering, University of Massachusetts Lowell, Lowell, MA, USA
e-mail: Mohamad_eydanasl@student.uml.edu

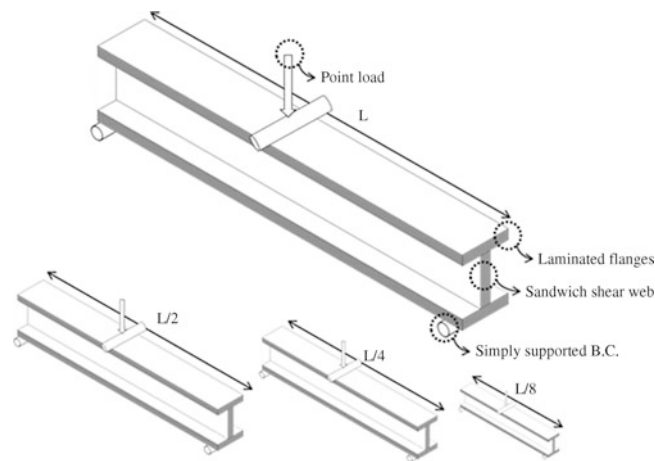


Fig. 21.1 Prototype (top) and Models with different scales and layups (bottom)

well with the derived scaling law. The designed scaled model needs to predict the response of the prototype accurately using the derived scaling laws. Otherwise, the experimental data of the scaled model cannot be correlated with the prototype and therefore the scaled-down model will not be representative of its corresponding prototype. As the model is not always an exact scaled-down replica of the prototype, a deliberate methodology should be implemented to design scaled models. The design of a scaled-down laminated composite structure is a challenge because the thickness of the plies in the laminates is fixed and cannot be scaled to any desired ratio. Therefore, a deliberate methodology needs to be applied to design a scaled composite structure which is representative of its full-scale parent. To study the degree of similarity between the scaled-down model and the full-scale prototype, the structural response of the scaled model can be mapped to those of the prototype using the scaling laws. Comparison of the response of the prototype with the mapped response of the model indicates the degree of the similarity between the scaled model and the full-scale prototype.

Similitude analysis can provide the necessary and sufficient conditions for the similarity of the two structures with different scales. The similarity conditions can be obtained using either dimensional analysis or direct use of the governing equations. To study the buckling of the laminated plates using the scaled models, Simitses and Rezaeepazhand [7] derived the similarity conditions for the buckling of the orthotropic and symmetric cross-ply laminated plates using the governing equations to demonstrate the credibility of similitude analysis. They applied the same approach to extract the scaling laws for the vibration of scaled laminated rectangular plates [8] and to investigate the effect of axial and shear loads on the stability of the scaled laminated rectangular plates [9, 10]. Later, the same method was extensively used in their works regarding the prediction of vibration response of laminated shells [11, 12]. According to their results, ply-level scaling of a laminated plate yields scaled models with perfect accuracy in predicting the response of the prototype. However, a systematic approach to design the partially similar scaled models was lacking. In two previous works by the authors [13, 14], a clear methodology was proposed to design the partially similar models for a simply supported laminated plate. The derived scaling laws were used as a metric to measure the correlation between the scaled models and the prototype. The accuracy of the designed scaled models in predicting the response of the prototype was shown to be proportional to the discrepancy of the models in satisfying the requirements of the similarity. The same approach was improved in the later studies [15, 16] to design scaled composite I-beams representative of the spar caps and the shear web of a utility-scale wind turbine blade using partial similarity [17–20]. Experimental validation of the similarity of the strain fields in the designed I-beams using the distorted layup scaling technique was demonstrated in a three-point quasi-static bending test [21].

Moreover, the applicability of the proposed scaling methodology was demonstrated for frequency-domain characterizations [22] and testing of innovative recyclable materials for wind turbine blades [23].

The best candidates for the design of the subcomponent test for wind turbine blade are the portions of the blade that are structurally critical. The spar caps and the shear web of the wind turbine blade carry the majority of the aerodynamic loads and make an interesting case study for subcomponent testing of the blade. In this study, the I-beam geometry of a utility-scale wind turbine blade [24] near its max chord is considered as the prototype and scaled-down beams are designed from the prototype under uncertainty in the design parameters. This area was chosen for analysis because many failures in blades occur near maximum the chord, and the area of interest is responsible for carrying most of the aerodynamic loads. The scaling laws for design of a scaled composite I-beam are derived using similitude analysis and a range of variation is defined for each design parameter. The effect of uncertainty in the design parameter are investigated by predicting the strain field

of the full-scale prototype from that of the scaled model. The nominal strain field of the prototype is analytically calculated for a three-point bending configuration and the nominal strain field is compared to the predicted strain values by the scaled model with uncertainty in its design parameters. The effect of each design parameter is investigated for overprediction and underprediction cases and accuracy of the scaled model is examined for the worst-case scenario.

21.2 Governing Equations

In this section, the governing equations for the deflection of a shear deformable thin-walled composite I-beam with a sandwich web are introduced based on a variational formulation, and a closed-form solution is derived for the strain distribution in the flanges of the I-beam placed in a three-point bending configuration. The scaling law for the strain field is derived and its fidelity in predicting the strain field of the prototype is discussed.

Neglecting all coupling effects due to the symmetric geometry, the equations governing the bending with respect to x -axis are given by [25]:

$$(GA_x)_{com} (V'' + \Psi'_x) = p \quad (21.1a)$$

$$(EI_x)_{com} \Psi''_x - (GA_x)_{com} (V' + \Psi_x) = 0 \quad (21.1b)$$

where Ψ_x denotes the rotation of the cross section with respect to x -axis shown in Fig. 21.2, V the displacement in y direction, p the point load, the prime ($'$) is used to indicate differentiation with respect to z , $(GA_x)_{com}$ and $(EI_x)_{com}$ are composite shear and flexural rigidity with respect to x -axis, respectively which could be expressed as:

$$(EI_x)_{com} = [A_{11}^\alpha y_\alpha^{(2)} - 2B_{11}^\alpha y_\alpha + D_{11}^\alpha] b_\alpha + \frac{b_3^{(3)}}{12} A_{11}^3 \quad (21.1c)$$

$$(GA_x)_{com} = A_{55}^\alpha b_\alpha + A_{66}^3 b_3 \quad (21.1d)$$

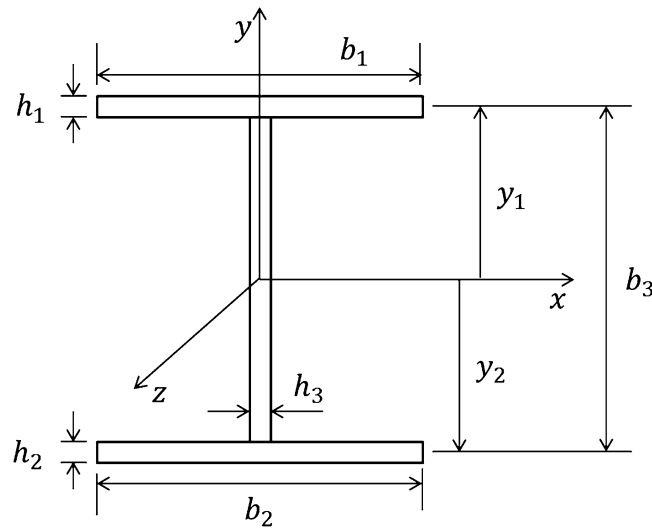


Fig. 21.2 Geometry and coordinate of the I-beam

where A_{11} , A_{66} , A_{55} , B_{11} and D_{11} are elements of extensional, coupling and bending stiffness matrices for a composite layup. The superscript in the parenthesis () denotes the power of the exponent, and repeated index denotes summation. Index α varies from 1 to 3 where the indices 1 and 2 represent the top and bottom flanges, and 3 is for the web, respectively as shown in Fig. 21.2 and b_α denotes width of the flanges and web. Equations (21.1c) and (21.1d) can be written for a geometrically symmetric I-beam with respect to x and y axis including symmetric and balanced laminated flanges and the web as:

$$(EI_x)_{com} = \left[2A_{11}^f y_1^{(2)} + 2D_{11}^f \right] b_f + \frac{b_w^{(3)}}{12} A_{11}^w \quad (21.1e)$$

$$(GA_x)_{com} = 2A_{55}^f b_f + 2A_{55}^w b_w + A_{66}^w b_w \quad (21.1f)$$

where f and w represent the flange and the web respectively. The closed-form solution of the normal strain ε_{zz} and transverse deflection for the uncoupled Eq. (21.1) may be directly calculated for the simply-supported boundary condition and the point load as [26]:

$$\varepsilon_{zz} = y \cdot \Psi'_x \quad (21.2)$$

To derive the scaling laws, all variables of the governing equations of the model (x_m) are assumed to be connected to their corresponding values in prototype (x_p) by one to one mapping. Then the scale factor may be defined as $\lambda_x = x_p/x_m$ and standard similitude procedure [7] can be applied to the Eq. (21.2) that results in the following scaling law:

$$\lambda_{\varepsilon_{zz}} = \frac{\lambda_p \lambda_y \lambda_z}{\lambda_{(EI_x)_{com}}} \quad (21.3)$$

Where λ_p , λ_z , λ_y and $\lambda_{(EI_x)_{com}}$ denote load, length, height and flexural rigidity ratios of the prototype to those of the scaled-down model.

The prototype geometry and lay-up scheme considered in this study emulates the spar caps and the shear web of the Sandia 10 MW wind turbine blade [24] near its max chord. This area was chosen for analysis because many failures in the utility scale blades occur near maximum chord due to the flap-wise bending, and the area of interest is responsible for carrying most of the aerodynamic loads. The prototype is assumed to be an I-beam consisting of two identical laminated plates having an overall dimension of 29.3 m \times 2.446 m \times 1.5 m with layup $[\pm 45_2/0_{46}]_s$ and ply thickness of $t = 1.36$ mm. The shear web is a sandwich panel with the foam thickness of 160 mm and two face sheets with layup $[\pm 45]_{50}$ with an overall thickness of 17.5 mm. Because the blade is tapered throughout its length and the geometry of the structure changes significantly, the geometry of the full-scale component (i.e. first 1/3 of the Sandia blade from its root) was averaged to simplify analysis. All computations are implemented for the glass/epoxy materials with following material characteristics [24]: $E_1 = 41.8$ GPa, $E_2 = E_3 = 14$ GPa, $G_{12} = G_{13} = 2.63$ GPa, $G_{23} = 1.83$ GPa, $\nu_{12} = \nu_{13} = 0.28$, $\nu_{23} = 0.47$. To design a scaled-down model of the considered prototype, the Distorted Layup Scaling method [15] was used to find an appropriate layup for the model. The scale of the model considered is 1/50 of the prototype (i.e. $l_p/l_m = 50$) that resulted in an overall dimension of 58.6 cm \times 4.93 cm \times 3 cm for the model with two unidirectional plies for each flange and a ply thickness of $t = 1.36$ mm.

21.3 Numerical Observations

To investigate the fidelity of the derived scaling law in predicting the strain field of the prototype from that of the scaled-down model, effect of uncertainty in design parameters was evaluated based on the info-gap theory. The design parameters were ranged from their nominal values and the accuracy of the derived scaling law in predicting the strain of the prototype from that of the scaled model was investigated. Table 21.1 lists the design parameters considered in the uncertainty analysis including their nominal values and their range of variations. Uncertainty in the design parameters can be modeled as an envelope-bound model [27] to constrain the uncertain deviations to an expandable envelope as the following:

Table 21.1 Definition of the design parameters considered in the uncertainty analysis

Variable	Description	Nominal	Range of variation
E_1	Young modulus	41.8 GPa	37.8–46 GPa
y	Height of the beam	25 mm	24–26 mm
l	Length of the beam	535 mm	533–537 mm
b	Width of the flange	30 mm	29–31 mm

$$U(\alpha, \tilde{u}) = \{u : |u - \tilde{u}| \leq \alpha \psi\}, \alpha \geq 0 \quad (21.4a)$$

Where ψ is a known function chosen from prior information determining the shape of the envelope and the size of the envelope is determined by α the uncertainty parameter. $U(\alpha, \tilde{u})$ indicates the set of design variables u whose deviation from their nominal values \tilde{u} is not greater than the range of variation of the design variable $\alpha\psi$. Considering the dominant design parameters for the laminated I-beam geometry, four variables were selected with their nominal values and their range listed in Table 21.1. Based on the number of the selected variables and their constant range of variation, Eq. (21.4a) can be expressed as a four-dimensional hyper-cube:

$$U(\alpha, \tilde{u}) = \{u : \alpha \cdot \psi_L \leq u - \tilde{u} \leq \alpha \cdot \psi_U\} \quad (21.4b)$$

Where u denotes one of the design parameter in Table 21.1, \tilde{u} is the nominal value of the considered design parameter and α indicates the horizon of uncertainty ranging from zero to unity. ψ_L and ψ_U are the weights defined such that the design parameter u varies in its full range when α varies from zero to unity.

For each of the selected design parameters, the normal strain at the midpoint of the bottom flange of the I-beam was calculated for both model and the prototype using Eq. (21.2). Then the strain of prototype was predicted using the derived scaling law Eq. (21.3) while the design parameters for the model were varying in their range of variation. The predicted strain values were normalized based on the nominal strain of the prototype. As the uncertainty parameter α increase from zero to unity, the values of the design parameters listed in Table 21.1 range from their nominal values to their defined upper and lower bounds.

The deviation of the predicted strain values for the prototype with respect to the uncertainty in the design parameters was investigated. Effect of deviation of each design parameter from its nominal value on predicted strain of the prototype was studied as shown in Fig. 21.3. The discrepancy in predicted strain of the prototype with uncertainty in all the considered design parameters was also investigated as shown in Fig. 21.3. For the case that all parameters were varying in their defined range, the worst case scenario was searched which resulted in two data points for each value of the uncertainty parameter α corresponding to over-prediction and under-prediction of the strain of the prototype. As shown in Fig. 21.3, uncertainty in Young's modulus was the dominant factor on discrepancy of predicting the strain of the prototype compared to the other design parameters. Uncertainty in the Young's modulus showed 8% and 10% under-prediction and over-prediction of the strain respectively for α equal to unity. Uncertainty in all of the design parameters combined together resulted in 12.5% under-prediction and 14.5% over-prediction for the worst case scenarios and α equal to unity.

To determine the bounds of uncertainty in the design parameters for a robust model, an error margin was considered for discrepancy of the predicted strain of the prototype from that of the model. Assuming maximum 5% error in prediction as a criterion for a robust model, the margin of uncertainty for design parameters can be identified as shown in Fig. 21.4 in highlighted green area. Models with less than 36% uncertainty in their design parameters will guarantee an accurate prediction of the strain field of their prototype (i.e. less than 5% discrepancy in prediction). The deviation of the predicted strain values from the nominal strain axis is not symmetric because the ranges of variation for the design parameters are not necessarily symmetric. Therefore, considering the lower value of the uncertainty parameter α between the under-prediction and over-prediction values (i.e. $\alpha = 38\%$ and $\alpha = 36\%$) ensures that prediction error does not exceed the 5% margin in both cases.

To demonstrate the effect of uncertainty on the accuracy of the derived scaling laws, a numerical study was conducted. The strain distribution of the scaled beam and its full-scale prototype were calculated for the midline of the bottom flange along the length of the model and the full-scale prototype in a three-point loading configuration. The load for scale model

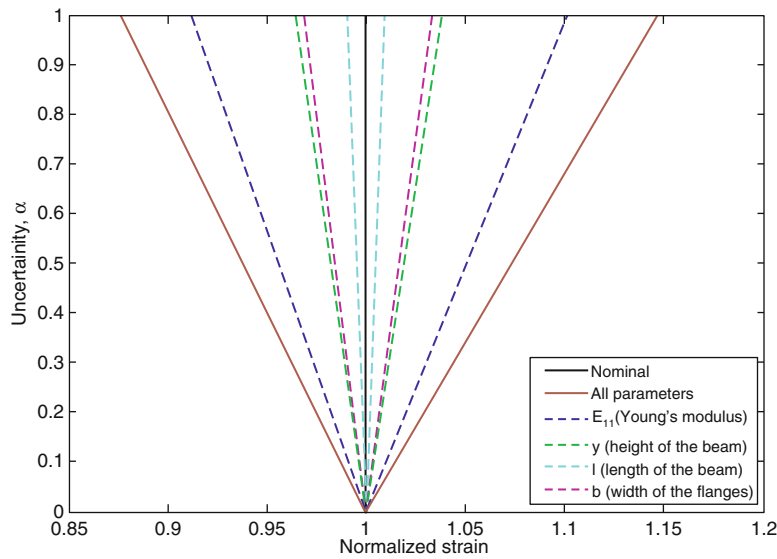


Fig. 21.3 Deviation of the predicted strain of the prototype from its nominal value when the uncertainty in the design parameters of the model increases

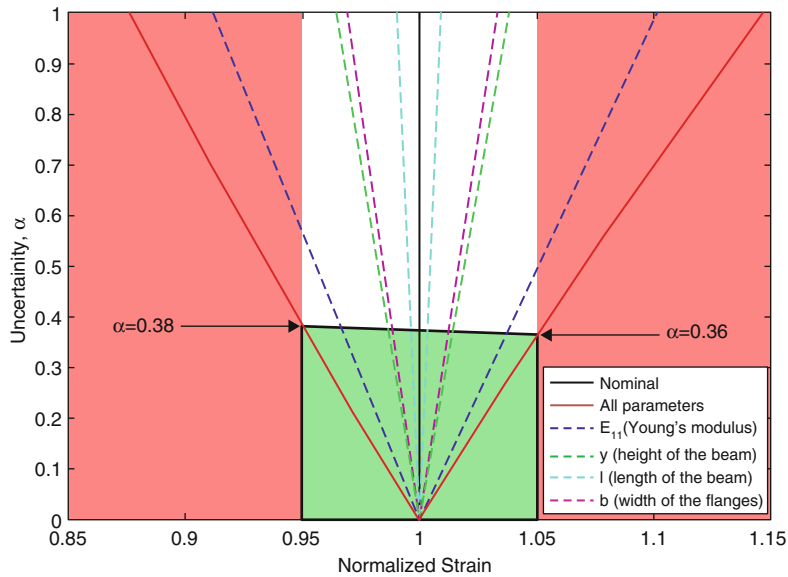


Fig. 21.4 Green: uncertainty range that ensures less than 5% discrepancy in predicting the strain of the prototype. Red: models in this area could yield more than 5% discrepancy in predicting the strain of the prototype

was $p = 175$ lbf (i.e. $p = 778.4$ N) and for the prototype the load was calculated based on Eq. (21.3) for equivalent strain between the model and the prototype (i.e. $\lambda_p = p_p/p_m = \lambda_l^2$). The derived scaling law Eq. (21.3) was used to predict the strain distribution in the prototype from that of the scaled model under uncertainty in the design parameters of the model. Figure 21.5 shows the accuracy in the predicted strain values of the prototype for $\alpha = 0$ and $\alpha = 0.4$ when there is uncertainty in all the parameters. As shown in Fig. 21.5, the strain distribution of the prototype is accurately predicted from that of the scaled model when there is no uncertainty in the design parameters (i.e. $\alpha = 0$). However, the accuracy in the prediction of the strain field decreases as the uncertainty in the design parameters of the model increases. As shown in Fig. 21.5, for $\alpha = 0.4$ the strain distribution can be over predicted or under predicted up to 6% and 5% respectively.

Based on the numerical results, the uncertainty in the design parameters of the scaled model can affect the accuracy of the scaled model in predicting the structural response of its full-scale prototype. Although other parameters such as discrepancy in the experimental data collected from the model and inaccuracy in the governing equations can also affect the prediction of the structural response of the full-scale prototype from that of its scaled model, the numerical analysis conducted in this study

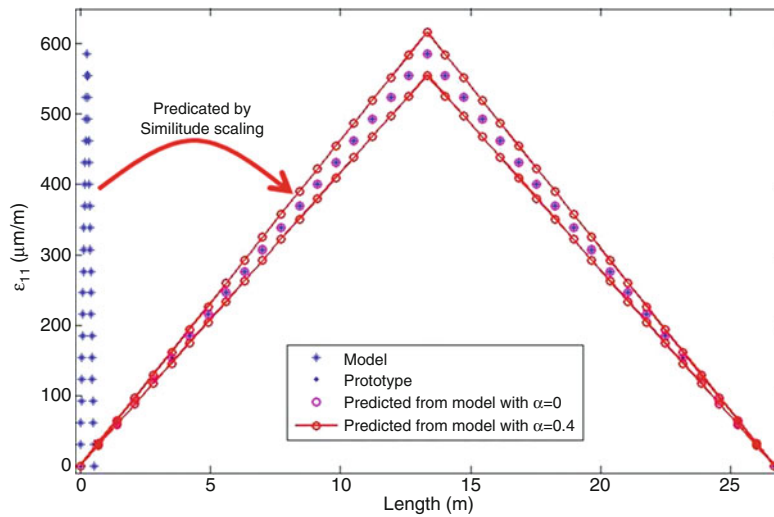


Fig. 21.5 Predicating the normal strain on the midline of the bottom flange of the prototype from those of the model with uncertainty in the design parameters of the model for a three-point bending loading configuration. Blue asterisks: nominal strain distribution of the scaled model. Blue dots: nominal strain distribution of the prototype. Magenta circles: predicted strain of the prototype by applying the scaling law Eq. (21.3) to the nominal strain values of the model for $\alpha = 0$. Red circle–line: predicted strain of the prototype by applying the scaling law Eq. (21.3) to the nominal strain of the model with uncertainty $\alpha = 0.4$ in all parameters

suggests that the uncertainty in the design parameters of the scaled model is also an important factor to be considered. Although the uncertainty in the structural characteristics and design parameters may not be completely eliminated, knowing the range of the influence of the uncertainty on the accuracy of the scaled model is critical in the design of a scaled model that is structurally similar to its prototype and can accurately replicate the structural response of its full-scale prototype on a smaller scale.

21.4 Conclusions

In this paper, the design of a scaled composite laminated model under uncertainty in the design parameters was studied. A scaled composite I-beam replicating the spar-caps and the shear web geometry of a utility-scaled wind turbine blade was designed using a distorted layup scaling technique. The robustness of the designed scaled-down model in predicting the strain distribution of its full-scale prototype was investigated. The dominant design parameters were selected and their range of variation was defined. A robustness analysis was pursued based on the envelope-bound model and info-gap theory. The discrepancy in the strain prediction of scaled-model was quantified for uncertainty in the design parameters. The accuracy of the derived scaling laws in predicting the strain field of the full-scale prototype was investigated and it was shown that the uncertainty in the design parameters is a factor in the design of scaled composite laminated models.

Acknowledgments This material is based upon work supported by the National Science Foundation under Grant Number 1230884 (Achieving a Sustainable Energy Pathway for Wind Turbine Blade Manufacturing). Any opinions, findings, and conclusions or recommendations expressed in this material are those of the authors and do not necessarily reflect the views of the particular funding agency. The authors are grateful for the support obtained.

References

1. Mandell, J.F., Creed Jr., R.J., Pan, Q., Combs, D.W., Shrinivas, M.: Fatigue of fiberglass generic materials and substructures. *Wind Energy*. **207**, 207–213 (1994)
2. Cairns, D.S., Skramstad, J.D., Mandell, J.F.: Evaluation of hand lay-up and resin transfer molding in composite wind turbine blade structures. *International SAMPE Symposium and Exhibition: SAMPE*; pp. 967–980 (1999)
3. Mandell, J.F., Combs, D.E., Samborsky, D.D.: Fatigue of fiberglass beam substructures. *Wind Energy*. **16**, 99 (1995)

4. Sayer, F., Post, N., Van Wingerde, A., Busmann, H.G., Kleiner, F., Fleischmann, W., et al.: Testing of adhesive joints in the wind industry. European Wind Energy Conference and Exhibition 2009, pp. 288–315 EWEC (2009)
5. Sayer, F., Antoniou, A., Van Wingerde, A.: Investigation of structural bond lines in wind turbine blades by sub-component tests. *Int. J. Adhes. Adhes.* **37**, 129–135 (2012)
6. Ilbeigi, S., Chelidze, D.: Reduced order models for systems with disparate spatial and temporal scales. In: *Rotating Machinery, Hybrid Test Methods, Vibro-Acoustics & Laser Vibrometry*, vol. 8, pp. 447–455. Springer International Publishing (2016.) https://books.google.com/books/about/Rotating_Machinery_Hybrid_Test_Methods_V.html?id=yoSQDAAAQBAJ&printsec=frontcover&source=kp_read_button#v=onepage&q&f=false
7. Simitzes, G.J., Rezaeepazhand, J.: Structural similitude for laminated structures. *Compos. Eng.* **3**, 751–765 (1993)
8. Rezaeepazhand, J., Simitzes, G.J.: Use of scaled-down models for predicting vibration response of laminated plates. *Compos. Struct.* **30**, 419–426 (1995)
9. Rezaeepazhand, J., Simitzes, G.J., Starnes Jr., J.H.: Design of scaled down models for stability of laminated plates. *AIAA J.* **33**, 515–519 (1995)
10. Simitzes, G.J., Rezaeepazhand, J.: Structural similitude and scaling laws for buckling of cross-ply laminated plates. *J. Thermoplast. Compos. Mater.* **8**, 240–251 (1995)
11. Rezaeepazhand, J., Simitzes, G.J., Starnes Jr., J.H.: Design of scaled down models for predicting shell vibration response. *J. Sound Vib.* **195**, 301–311 (1996)
12. Rezaeepazhand, J., Simitzes, G.J.: Structural similitude for vibration response of laminated cylindrical shells with double curvature. *Compos. Part B.* **28**, 195–200 (1997)
13. Asl, M.E., Niezrecki, C., Sherwood, J., Avitabile, P.: Predicting the vibration response in subcomponent testing of wind turbine blades. In: *Special Topics in Structural Dynamics*, vol. 6, pp. 115–123. Springer, Cham (2015)
14. Asl, M.E., Niezrecki, C., Sherwood, J., Avitabile, P.: Application of structural similitude theory in subcomponent testing of wind turbine blades. *Proceedings of the American Society for Composites*, pp. 8–10 (2014)
15. Asl, M.E., Niezrecki, C., Sherwood, J., Avitabile, P.: Similitude analysis of composite I-beams with application to subcomponent testing of wind turbine blades. In: *Experimental and Applied Mechanics*, vol. 4, pp. 115–126. Springer, Cham (2016)
16. Asl, M.E., Niezrecki, C., Sherwood, J., Avitabile, P.: Design of scaled-down composite I-beams for dynamic characterization in subcomponent testing of a wind turbine blade. In: *Shock & Vibration, Aircraft/Aerospace, Energy Harvesting, Acoustics & Optics*, vol. 9, pp. 197–209. Springer International Publishing, Cham (2016)
17. Asl, M., Niezrecki, C., Sherwood, J., Avitabile, P.: Experimental and theoretical similitude analysis for flexural bending of scaled-down laminated I-beams. *Composite Structures* (2017)
18. Asl, M.E., Niezrecki, C., Sherwood, J., Avitabile, P.: Similitude analysis of thin-walled composite I-beams for subcomponent testing of wind turbine blades. *Wind Engineering*. **0**, 0309524X17709924 (2017)
19. Eydani Asl, M., Niezrecki, C., Sherwood, J., Avitabile, P.: Vibration prediction of thin-walled composite I-beams using scaled models. *Thin-Walled Structures*. **113**, 151–161 (2017)
20. Asl, M.E., Niezrecki, C., Sherwood, J., Avitabile, P.: Scaled composite I-beams for subcomponent testing of wind turbine blades: An experimental study. *Mechanics of Composite and Multi-functional Materials*. **6**, 71–78 (2018)
21. Asl, M., Niezrecki, C., Sherwood, J., Avitabile, P.: Similitude analysis of the strain field for loaded composite I-beams emulating wind turbine blades. *Proceedings of the American Society for Composites: Thirty-First Technical Conference* (2016)
22. Asl, M.E., Niezrecki, C., Sherwood, J., Avitabile, P.: Similitude analysis of the frequency response function for scaled structures. In: *Model Validation and Uncertainty Quantification*, vol. 3, pp. 209–217. Springer, Cham (2017)
23. Asl, M.E., Niezrecki, C., Sherwood, J., Avitabile, P.: Static performance assessment of recyclable bio-based resin for wind turbine blades using sub-component testing. In: *Proceedings of the American Society for Composites—Thirty-second Technical Conference* (2017)
24. Griffith, D.T., Ashwill, T.D.: The Sandia 100-meter all-glass baseline wind turbine blade: SNL100-00. Sandia National Laboratories, Albuquerque, Report NoSAND2011-3779 (2011)
25. Reddy, J.N.: *Mechanics of Laminated Composite Plates and Shells: Theory and Analysis*. CRC Press, Boca Roten, Florida (2004). <https://www.crcpress.com/Mechanics-of-Laminated-Composite-Plates-and-Shells-Theory-and-Analysis/Reddy/p/book/9780849315923>
26. Lee, J.: Flexural analysis of thin-walled composite beams using shear-deformable beam theory. *Compos. Struct.* **70**, 212–222 (2005)
27. Ben-Haim, Y.: *Info-gap Decision Theory: Decisions Under Severe Uncertainty*. Academic Press, San Diego (2006). <https://www.amazon.com/Information-Gap-Decision-Theory-Uncertainty/dp/0120882515>



Chapter 22

Bayesian History Matching for Forward Model-Driven Structural Health Monitoring

P. Gardner, C. Lord, and R. J. Barthorpe

Abstract Computer models are widely utilised in many structural dynamics applications, however their use depends on calibration to observational data. A complexity in calibrating a computer model is that even when the ‘true’ input parameters to the model are known, there may be model discrepancy caused by the simplification or absence of certain physics. As a consequence the calibration technique employed must incorporate a mechanism for dealing with model discrepancy. Bayesian history matching is a process of using observed data in order to identify and discard areas of the computer model’s parameter space that will result in outputs that are unlikely given the observational data. This is performed using an implausibility metric that encompasses uncertainties associated with observational measurements and model discrepancy. The method employs this metric to identify a non-implausible space (i.e., parameter combinations that are likely to have produced the observed outputs). A maximum a posteriori (MAP) approach can be used to obtain the calibrated computer model outputs from the non-implausible space. Model discrepancy between the calibrated computer model and observational data can then be inferred using a Gaussian process (GP) regression model. This paper applies Bayesian history matching in order to calibrate a computer model for forward model-driven structural health monitoring (SHM). Quantitative metrics are used to compare experimental and predictive damage features from the combined Bayesian history matching and GP approach.

Keywords History matching · Calibration · Model discrepancy · Emulator · Gaussian processes

22.1 Introduction

Forward-model driven structural health monitoring (SHM) is a framework whereby a validated computer model is used, in a forward manner, to simulate damaged state data [1]. The computer model predictions are used to train machine learning techniques which, when shown real world observations, are capable of classifying the new data into categories such as the existence of damage, location, type and extent [2]. The success of a forward model-driven framework relies upon a computer model that is statistically representative of real world observations. Consequently, calibration and validation of this computer model is vital for producing robust decisions about structural health.

All computer models contain simplifications or the absence of certain physical processes; summarised by Box in ‘All models are wrong, but some are useful’ [3]. In order to account for missing physics in the calibration process, model discrepancy must be considered [4, 5]. A forward model-driven approach to SHM therefore requires a method in which model discrepancy is accounted for, producing predictions from the computer model that are statistically representative.

Bayesian history matching is a calibration methodology that reduces the computer model input space whilst accounting for model discrepancy [6–10]. The method can be used to reduce the non-implausible parameter space and produce samples of the computer models predictive distribution. A maximum a posteriori (MAP) estimate of the predictive distribution from the Bayesian history matching process provides an approximation of the ‘most probable’ calibrated computer model output given the uncertainties in the system. This MAP estimate of the output can be combined with a Gaussian process (GP) regression model in order to infer the functional form of the model discrepancy [1]. The combined output provides an approximation of the full predictive distribution whilst considering the systems uncertainties and accounting for model discrepancy.

The focus of this paper is the application of Bayesian history matching in order to calibrate a five storey building structure under several pseudo-damage scenarios. The contribution of this paper is the use Bayesian history matching and a GP regression model to calibrate and infer model discrepancy in a finite element (FE) model. This approach allows the estimation

P. Gardner (✉) · C. Lord · R. J. Barthorpe
Dynamics Research Group, Department of Mechanical Engineering, University of Sheffield, Sheffield, UK
e-mail: pagardner1@shef.ac.uk

of an approximate complete predictive distribution for the computer model whilst accounting for the uncertainties and model discrepancy in the system. Finally, the approximate predictive distribution from the approach is validated against the experimental distributions. The paper outline is as follows: Sect. 22.2 describes the Bayesian history matching methodology used in the paper with details on the calibration and inference of the model discrepancy using a Gaussian process emulator. Section 22.3 presents the experimental case study, the problem setup as well as demonstration and validation of results. Finally, a discussion and conclusions are presented in Sect. 22.4 and areas of further research are highlighted.

22.2 Bayesian History Matching

History matching is a term that originates from the oil industry and describes methods that adjust input parameters of computer models (herein referred to as *simulators*) in order to closely match data from historical production of a reservoir. Many of these approaches as reviewed by Oliver and Chen [11] are similar to the model updating methods used in SHM [12]. Craig et al. adapted the history matching approaches, outlining a Bayesian methodology that searched for all, rather than a single parameter match [6]. Bayesian history matching has been developed and applied to a variety of applications from understanding Galaxy formation [7, 8] to complex social models of HIV transfer in populations [9, 10]. The strength of this approach is that, unlike a likelihood based method, inputs and outputs from the model can be removed and added in each iteration without invalidating the analysis. Additionally, the ability to reduce the non-implausible parameter space (parameters which produce outputs similar to the experimental data) means that it is often a useful pre-calibration tool for likelihood based techniques such as Markov chain Monte Carlo based approaches. Bayesian history matching uses an implausibility metric, assessing whether a given parameter combination was not likely to have produced the output, in order to remove parts of the input space. Implausibility is a measure of distance from the experimental data to the simulator data over the processes uncertainties. This allows the creation of a statistical model form as shown in Eq. (22.1) [4].

$$\mathbf{z}_j(\mathbf{x}) = \eta_j(\mathbf{x}, \boldsymbol{\theta}) + \delta_j + e_j \quad (22.1)$$

Where $\mathbf{z}_j(\mathbf{x})$ is the j th experimental output given inputs \mathbf{x} , $\eta_j(\mathbf{x}, \boldsymbol{\theta})$ is the j th simulator given \mathbf{x} and parameters $\boldsymbol{\theta}$. The model discrepancy is δ and e is the observational uncertainty. Equation 22.1 assumes that $\eta(\mathbf{x}, \boldsymbol{\theta})$, δ and e are independent. In order to speed up computation, Bayesian history matching utilises emulators – a statistical model of a simulator [13]. Here, a GP regression model is used as an emulator as shown in Eq. (22.2). A GP emulator is an interpolation method that fits the simulator data exactly and also informs about the introduced code uncertainty when interpolating, due to its Bayesian formulation. A Gaussian process is a distribution over the function space and therefore allows inference to take place directly in the space of functions. This means it can be thought of as a non-parametric statistical model.

$$\eta_j(\mathbf{x}, \boldsymbol{\theta}) \sim \mathcal{GP}_j(m(\mathbf{x}, \boldsymbol{\theta}), c[(\mathbf{x}, \boldsymbol{\theta}), (\mathbf{x}', \boldsymbol{\theta}')]) \quad (22.2)$$

Where \mathcal{GP} is a GP with mean function $m(\cdot)$ and covariance function $c(\cdot, \cdot)$. In the interest of conciseness the reader is referred to [13–16] for information on GPs and their use as emulators. The posterior mean of the emulator prediction, $\mathbb{E}^*[\mathcal{GP}(\mathbf{x}, \boldsymbol{\theta})]$ can be used in order to evaluate the distance between experimental and simulator data. The posterior variance of the emulator, $V_c(\mathbf{x}, \boldsymbol{\theta})$, considered as code uncertainty, is also incorporated within the implausibility measure. As a results the substitution of an emulator will not eliminate parts of the parameter space due to poor emulator predictions, until the code uncertainty is reduced. GP emulators are single output and therefore must be constructed for each simulator output. Each emulator is validated using diagnostics metrics proposed by Bastos and O’Hagan in [16]. For a single output the implausibility metric is assessed using Eq. (22.3).

$$I_j(\mathbf{x}, \boldsymbol{\theta}) = \frac{|\mathbf{z}_j(\mathbf{x}) - \mathbb{E}^*[\mathcal{GP}_j(\mathbf{x}, \boldsymbol{\theta})]|}{[V_{o,j} + V_{m,j} + V_{c,j}(\mathbf{x}, \boldsymbol{\theta})]^{1/2}} \quad (22.3)$$

Where, V_o , V_m and $V_c(\mathbf{x}, \boldsymbol{\theta})$ are the variances associated with the observational, model discrepancy and code uncertainties. There are two extensions of this metric for multiple output scenarios. The first is maximum implausibility and the second is a multivariate form, Eqs. (22.4) and (22.5) respectively.

Algorithm 1 Bayesian history matching for wave k

$\theta^k \sim \text{GMLHC}$	▷ Draw parameters from GMLHC
$\mathbf{y}^k = \eta(\mathbf{x}, \theta^k)$	▷ Run the simulator at parameters
Draw n samples $\theta_s^k \sim \mathcal{U}(\min(\theta^k), \max(\theta^k))$	▷ Sample parameter space
for $j = 1 : \text{no. of outputs do}$	
Train and validate $\mathcal{GP}_j(\mathbf{x}, \theta^k)$	▷ Train and validate emulators
$[\mathbb{E}^*[\mathcal{GP}_j(\mathbf{x}, \theta_s^k)], V_{c,j}(\mathbf{x}, \theta_s^k)] = \mathcal{GP}_j(\mathbf{x}, \theta_s^k)$	▷ Emulator predictions at n samples of θ^k
Calculate $I_j(\mathbf{x}, \theta_s^k)$	▷ Assess implausibility of samples
end for	
Calculate $I_{\max}(\mathbf{x}, \theta_s^k)$	
for $m = 1 : n$ do	
if $I_{\max}(\mathbf{x}, \theta_{s,m}^k) < c$ then	
$\theta_{nl}^k = \theta_{s,m}^k$	▷ Keep non-implausible samples
end if	
end for	
bounds = $[\min(\theta_{nl}^k), \max(\theta_{nl}^k)]$	▷ Obtain new GMLHC bounds
if any $(V_{c,j}^k(\mathbf{x}, \theta) < (V_{o,j} + V_{m,j}))$ or $\text{isempty}(\theta_{nl}^k)$ then	
Stop	▷ Stop if stopping criteria are met
end if	

$$I_{\max}(\mathbf{x}, \theta) = \arg \max_j I_j(\mathbf{x}, \theta) \quad (22.4)$$

$$I(\mathbf{x}, \theta) = (\mathbf{z}(\mathbf{x}) - \mathbb{E}^*[\mathcal{GP}(\mathbf{x}, \theta)])^T (V_o + V_m + V_c(\mathbf{x}, \theta))^{-1} (\mathbf{z}(\mathbf{x}) - \mathbb{E}^*[\mathcal{GP}(\mathbf{x}, \theta)]) \quad (22.5)$$

A large implausibility value (for all the implausibility metrics) indicates that the parameter set was very unlikely to produce an output that matched the experimental data given all the processes uncertainties. This means that by assessing the implausibility against a threshold, parts of the space can be eliminated. As stated in by Andrianakis et al. a sensible cut-off c is defined for the single and maximum implausibilities by Pukelsheim's 3σ rule [9] – any continuous unimodal distribution contains 99.73% of probability mass within three standard deviations from its mean [17]. For the multivariate case this can be set as a high percentile from a chi-squared distribution with j degrees of freedom [9].

After assessing the implausibility, any remaining non-implausible space is sampled from in order to propose a new input and parameter space design; the simulator is then evaluated at these points. In this paper the parameter space design is a generalised maximin Latin hypercube (GMLHC) [18], this method ensures that the design produces emulator predictions with lower predictive variance at the edges of the parameter space. Bayesian history matching can be run iteratively in waves until one of two stopping criteria are met. If all the space is identified as implausible, the model discrepancy can be increased in order to identify whether the simulator form is inadequate, leading to better model selection. The second criteria is when the emulator variance is smaller than the remaining (observational and model discrepancy) uncertainties in the system. Algorithm 1 outlines the approach used in this paper.

22.2.1 Calibrated Simulator Prediction and Model Discrepancy Estimation

Bayesian history matching produces a set of non-implausible samples; contained within this set will be the posterior of the parameters given the data, $p(\theta|\mathbf{z})$. The non-implausible samples from the final wave can be used as an approximation of this posterior. The resulting emulator outputs for the final non-implausible set are estimates of the predictive simulator distribution, given the uncertainties described. A MAP estimate of the predictive distribution for each output will be adopted as the 'most probable' calibrated simulator.

The calibrated simulator will have the limitation that even given the calibrated parameter set the simulator will not produce outputs that fully describe the experimental data due to model discrepancy. In order to infer the functional form of the model discrepancy a GP regression model (with noise) can be fitted to the MAP estimate of the predictive distribution and the same training experimental data points used in the Bayesian history matching process. The resulting prediction provides a Gaussian approximation of the predictive distribution of the simulator accounting for the assumed uncertainties.

22.3 Five Storey Building Structure

Predictions of modal frequencies for different damage extents were performed on a five storey building structure. The focus of this paper is demonstrating that the distributions of these predictions are representative of those obtained experimentally: the most important consideration in forward model-driven SHM. Modal testing of a representative five storey building structure, made from aluminium 6082, was performed under different pseudo-damage extents, in this case added masses. The structure (Fig. 22.1a) had masses in increments of 0.1 kg, from 0 to 0.5 kg, fixed to the first floor (Fig. 22.1b). The structure was excited with Gaussian noise with a 409.6 Hz bandwidth via an electrodynamic shaker. Sampling rate and sample time were chosen to allow a frequency resolution of 0.05 Hz. Accelerometers were placed at each of the five floors in order to obtain the first five bending modes. Forty averages were acquired for each measurement and ten repeats were performed for each damage extent, in order to estimate the distribution of the modal frequencies. Feature selection found that the second and third bending natural frequencies, ω_2 and ω_3 , were most sensitive to the presence of damage. As a consequence these features were the target outputs of the simulator.

The simulator, a modal FE model, was run for the six damage extents. The second and third bending natural frequencies were extracted from the simulator as the outputs \mathbf{y} . Prior bounds on the parameters, θ , shown in Table 22.1, were $\pm 10\%$ of typical material properties for aluminium 6082. The inputs were added mass in kg, $\mathbf{x} = \{0, 0.1, \dots, 0.5\}$.

22.3.1 Calibration via Bayesian History Matching

Calibration of the simulator was performed using Bayesian history matching as outlined in Algorithm 1. The experimental data $\mathbf{z}(\mathbf{x}_z)$ used in the Bayesian history matching process were the mean natural frequencies when $\mathbf{x}_z = \{0, 0.3, 0.5\}$ kg. The unseen validation set were the full repeat measurements when $\mathbf{x}_z = \{0.1, 0.2, 0.4\}$ kg. This highlights that with a small subset of damage data predictions can be made using forward model-driven SHM.

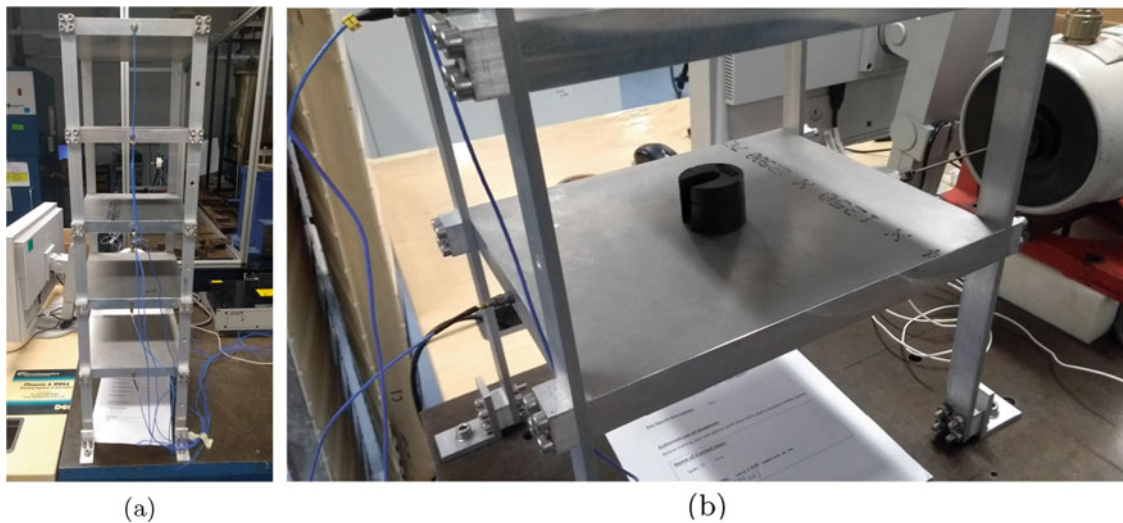


Fig. 22.1 (a) Five storey building structure setup (b) pseudo-damage – added masses

Table 22.1 Calibration parameter prior bounds

Parameter	Lower bound	Upper bound
Elastic modulus, E , GPa	63.9	78.1
Poissons ratio, ν	0.297	0.363
Density, ρ , kg/m ³	2493	3047

Table 22.2 Uncertainties in implausibility measure

Uncertainty	ω_2	ω_3
Observational V_o	0.02	0.08
Model discrepancy V_m	0.01	0.01

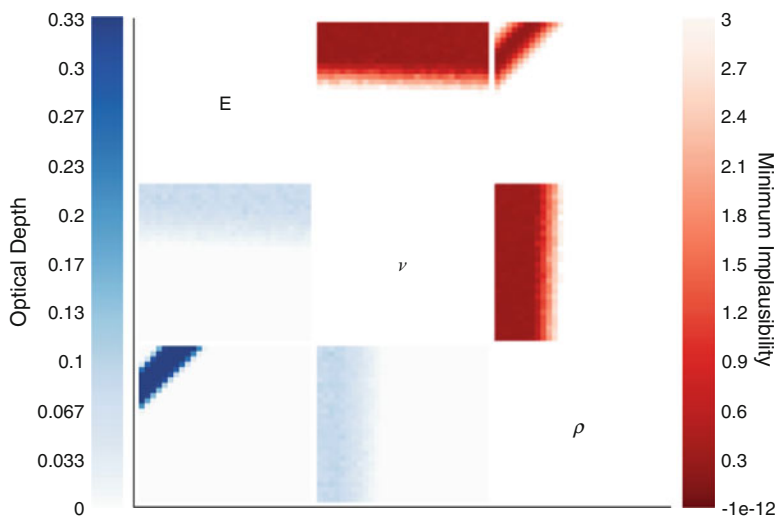


Fig. 22.2 Minimum implausibility and optical depth plots for the first wave of Bayesian history matching. Each quadrant is a comparison of two parameter combinations for the given metric, e.g., the top right and bottom left quadrant are ρ against E for minimum implausibility and optical depth respectively

Two separate 50 and 10 point GMLHC designs (one for training the emulators and one for validation) were obtained in order to fill the initial parameter space. The simulator was run with these parameters combinations for the six inputs, \mathbf{x} . The simulator outputs were used to train and validate two emulators for ω_2 and ω_3 . Constant mean and a squared exponential covariance functions were applied in the emulator due to the smooth functional form of the simulator. A small nugget of $\nu = 1 \times 10^{-6}$ was implemented in order to improve the numerical stability of the emulator whilst minimally affecting the solution as shown by Andrianakis and Challenor [19]. The maximum implausibility metric with a 3σ threshold was implemented. The variances used in the implausibility metric are presented in Table 22.2. A sample size of 500,000, drawn from a 3 dimensional uniform distribution, were used in order to assess the parameter space.

The first wave calculated a non-implausible space $\approx 6.5\%$ of the original space, highlighting the method’s strength in removing unlikely parameters from the analysis. After the first wave the second stopping criteria was met (code uncertainty was less than the remaining uncertainties). This means that the functional form of the emulator was well defined from the GMLHC parameter space and accurately interpolated across the complete parameter space. In order to visualise the non-implausible space, minimum implausibility and optical depth plots were created. These plots divided the parameter space into bins in which the samples are placed. Minimum implausibility is the lowest implausibility found in the bin for each parameter combination. If the number of samples is large enough, these plot provide an estimate of what parts of the input space can be discarded irrespective of the other parameters. The optical depth plots are constructed in a similar method to the minimum plausibility but instead show an estimate of the probability of a point being non-implausible given the bin’s set of parameters. This is the ratio of the number of non-implausible points divided by the number of samples in the bin. Figure 22.2 demonstrates these plots for the first wave. Here it can be seen that high values of elastic modulus and low values of density are identified as non-implausible with Possion’s ratio being relatively insensitive to the outputs. There is a clear linear correlation between the non-implausible space of the elastic modulus and density, displayed in the bottom left and top right quadrants of Fig. 22.2.

The non-implausible samples from the first wave can be used to approximate the predictive densities for simulator outputs, presented in Fig. 22.3. Here both densities are shown to be negatively skewed. The right of Fig. 22.3 shows the predictive densities at the experimental input data points, \mathbf{x}_z where the red circles are the experimental data points $\mathbf{z}(\mathbf{x}_z)$. The experimental data points lie slightly below the distribution’s mode and close to the mean, but firmly within the non-implausible distribution.

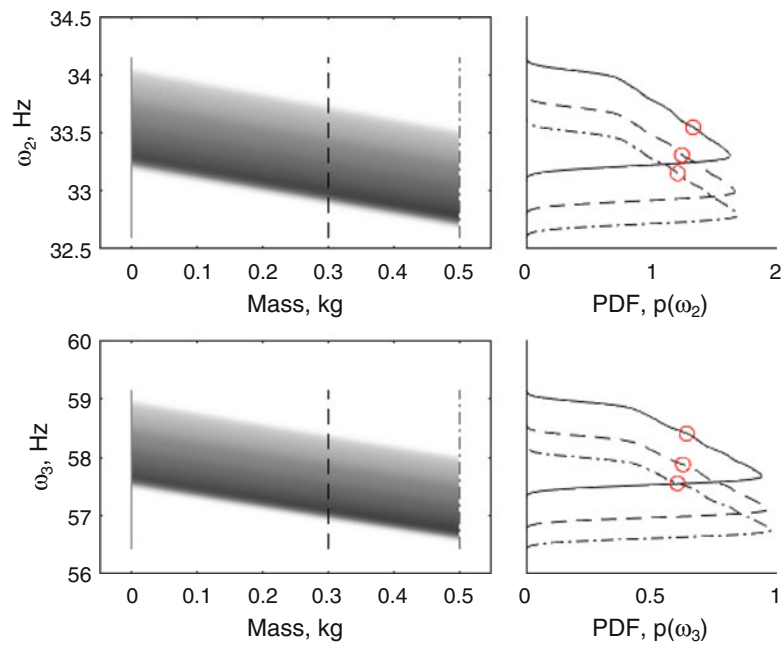


Fig. 22.3 Density of outputs from non-implausible samples (left) and kernel density estimates (KDEs) of the predictive distribution (right); o are experimental data points. Slices of the densities at the training experimental inputs \mathbf{x}_z are shown for the 0 kg (—), 0.3 kg (---), and 0.5 kg (---) masses

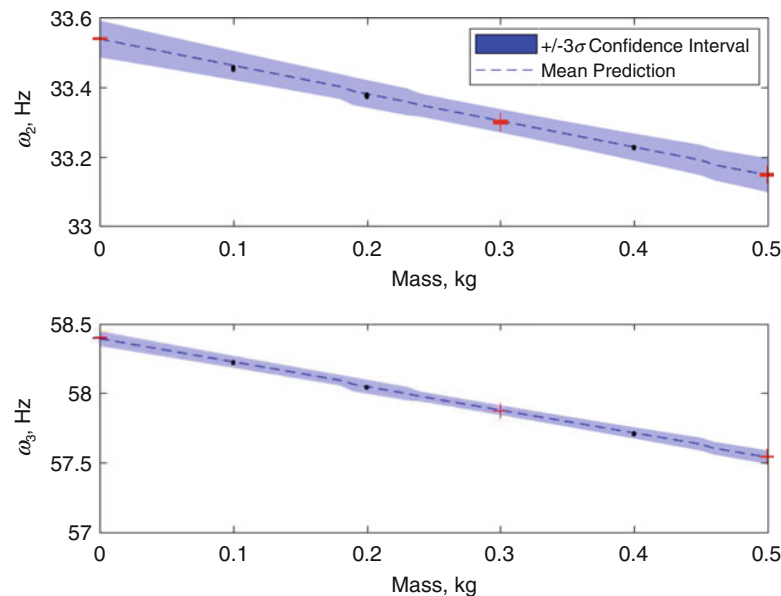


Fig. 22.4 Predictive distributions from the combined Bayesian history matching and GP approach, + are experimental training points, · are experimental test points

The MAP estimates of the predictive distributions for each output from Fig. 22.3 were used as inputs for two independent GP regression models (with noise). These GPs were utilised to infer the model discrepancy and observational uncertainty for each output (ω_2 and ω_3). The modelling assumptions for both GPs were zero mean and squared exponential covariance functions; this represented the belief that no knowledge of the mean functional forms were known a priori but the functions were believed to be relatively smooth. Figure 22.4 presents the two GP outputs for each natural frequency, both showing good agreement with the experimental data.

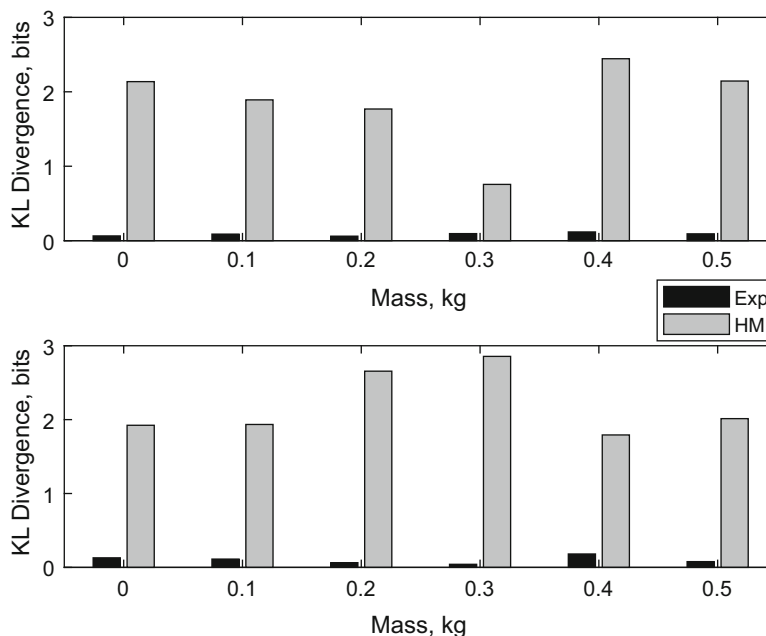


Fig. 22.5 KL-divergence compared to the KDEs from the experimental data. Exp denotes Gaussian approximation of experimental data (black); HM denotes the predictive distribution of the combined Bayesian history matching and GP approach (grey)

22.3.2 Validation of Predictive Distributions

Validation of the predictive distributions is an important aspect of forward model-driven SHM. Ensuring that the predictive distributions of the calibrated simulator are valid for the experimental data provides confidence that the simulator outputs may be used in training a classifier to perform SHM. In order to validate the predictive distributions, normalised mean squared errors and KL-divergences have been calculated.

The normalised mean squared errors (NMSEs) for each output compared to the experimental data were 0.04 and 0.02. This demonstrates the very good agreement between the experimental data and the predictive distribution's means. The mean percentage difference in the variances for each output were 0.2% and 0.8% demonstrating that for the lower order statistical modes the predictive distribution is in good agreement with the experimental data.

To validate the performance of both a Gaussian approximation of the experimental data and the predictive distributions for each output, the Kullback-Leibler (KL) divergence was employed. KL-divergence is a measure of relative entropy and can be defined as the average number of extra bits (binary digits) required to encode the data given that distribution q is used to model the 'true' distribution p . A KL-divergence equal to zero implies $q = p$. In both cases the KDE of the experimental data was taken to be the 'true' distribution. Figure 22.5 presents the KL-divergence for each output (top ω_2 , bottom ω_3). It can be seen that a Gaussian approximation of the experimental data is appropriate for these two features, indicated by near zero KL-divergence. Additionally, the KL-divergence for the predictive distributions for each output are below 3 and most are close to 2. This means that very few additional bits would be needed in order to encode the kernel density estimate (KDE) fully. It is noted that the performance of the KL-divergence is similar throughout the damage extents demonstrating good predictive performance away from the training experimental data. The summed KL-divergence for the Gaussian approximations of the experimental data for each output were 0.5 and 0.6 whereas the predictive distributions were 11.1 and 13.0. Finally, a visual comparison in Figs. 22.6 and 22.7 of the distributions for each damage extent confirms good mean predictions and slightly large variance estimates in the predictive distributions compared to the experimental data.

22.4 Discussion and Conclusions

Predictions of damage extents for two natural frequencies of a representative five storey building structure were performed using a combined Bayesian history matching and GP regression model approach. One wave of Bayesian history matching was required in order to find a non-improbable parameter space. Samples from this space generated an approximate predictive

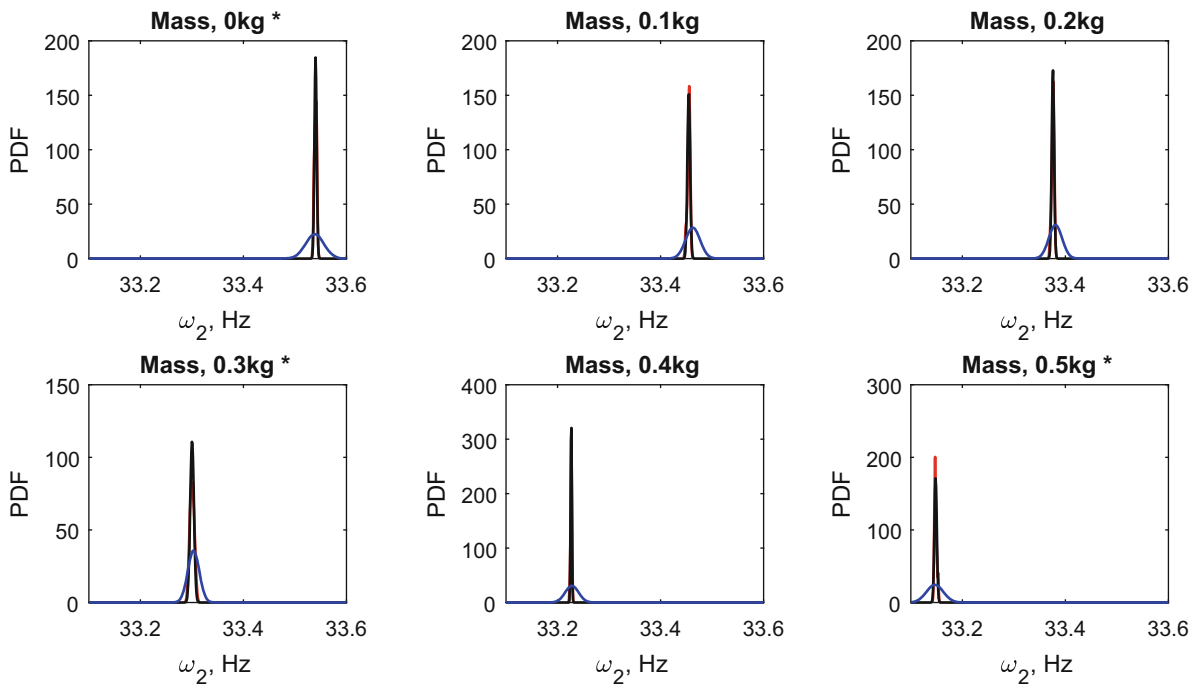


Fig. 22.6 Predictive distributions compared to experimental data for ω_2 ; KDE from experimental data (red), Gaussian approximation of experimental data (black), predictive distribution from Bayesian history matching and GP approach (blue); * denotes inputs used as training data

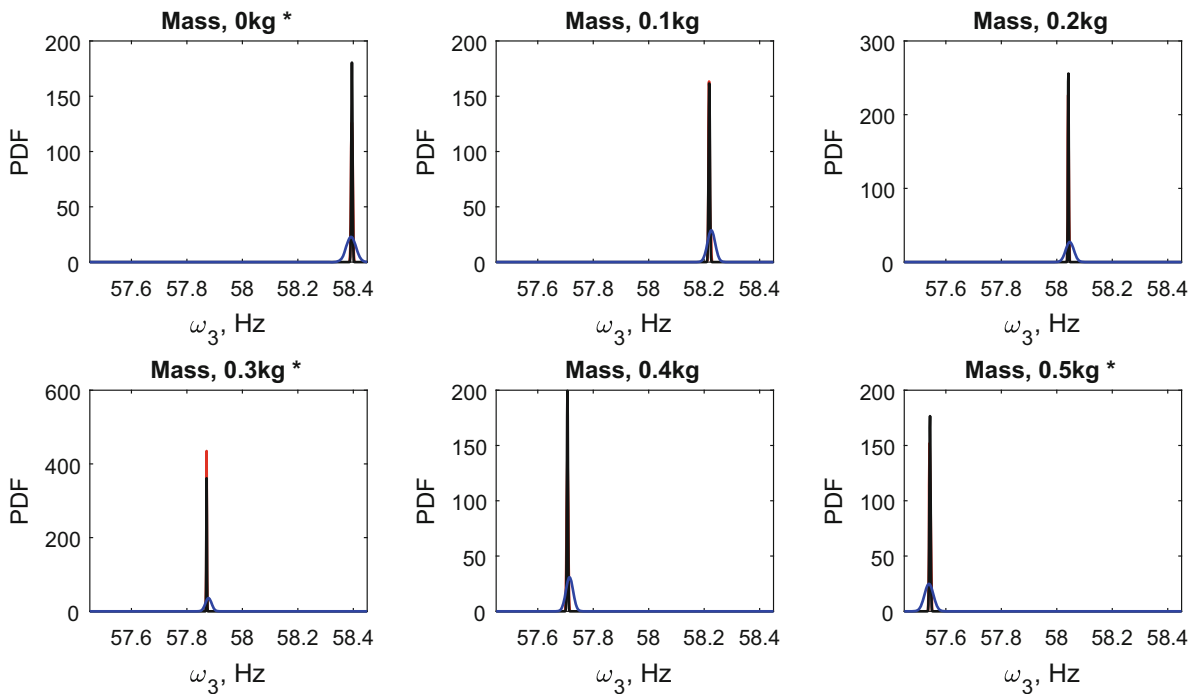


Fig. 22.7 Predictive distributions compared to experimental data for ω_3 ; KDE from experimental data (red), Gaussian approximation of experimental data (black), predictive distribution from Bayesian history matching and GP approach (blue); * denotes inputs used as training data

distribution for each output from which a MAP estimate was taken. Two GP models were built in order to infer the model discrepancy and observational uncertainties. The predictive distributions from the combined approach for each output were validated and demonstrated to be representative of the experimental data, as shown in low NMSEs and low KL-divergences, on and unseen test set. This highlights the approaches effectiveness as a method for forward model-driven SHM.

It is noted Bayesian history matching is likely to be of greater benefit in more complex cases, especially when less is known about the parameter space and the quality of the simulator. The method also has similar difficulties to conventional calibration techniques as the functional form of the emulator restricts the non-implausible space, unless the model discrepancy variance is increased. Bayesian calibration with bias correction, another calibration technique that considers model discrepancy, has the strength that the method allows more flexibility in inferring calibrated parameters whilst simultaneously estimating the functional form of the model discrepancy [4, 20].

Areas for further research are predominately associated with improving Bayesian history matching. To speed up the algorithm computationally, sparse GP emulators could be implemented [21]. Additionally, better methods of sampling the non-implausible space such as a maximum entropy approach could be used. This would mean that new simulator runs are only implemented at points that provide the most information gain. A method for accurately estimating the posterior of the parameters $p(\theta | \mathbf{z})$ from the non-implausible space should be investigated. This would allow sensitivity analysis and a full Bayesian treatment of the outputs to be conducted, rather than a MAP estimate.

References

1. Gardner, P., Barthorpe, R.J., Lord, C.: The development of a damage model for the use in machine learning driven SHM and comparison with conventional SHM methods. In: Proceedings of ISMA2016 International Conference on Noise and Vibration Engineering, pp. 3333–3346 (2016)
2. Rytter, A.: Vibrational based inspection of civil engineering structures. Ph.D. dissertation (1993)
3. Box, G.E.P., Draper, N.R.: Empirical Model-Building and Response Surfaces. Wiley, New York (1987)
4. Kennedy, M.C., O’Hagan, A.: Bayesian calibration of computer models. *J. R. Stat. Soc. Ser. B (Stat. Methodol.)* **63**(3), 425–464 (2001)
5. Brynjarsdóttir, J., O’Hagan, A.: Learning about physical parameters: the importance of model discrepancy. *Inverse Prob.* **30**(11), 114007 (2014)
6. Craig, P.S., Goldstein, M., Seheult, A.H., Smith, J.A.: Pressure matching for hydrocarbon reservoirs: a case study in the use of Bayes linear strategies for large computer experiments. In: Case Studies in Bayesian Statistics. Lecture Notes in Statistics, pp. 37–93. Springer, New York (1997)
7. Vernon, I., Goldstein, M., Bower, R.G.: Galaxy formation: a Bayesian uncertainty analysis. *Bayesian Anal.* **5**(4), 619–669 (2010)
8. Vernon, I., Goldstein, M., Bower, R.: Galaxy formation: Bayesian history matching for the observable universe. *Stat. Sci.* **29**(1), 81–90 (2014)
9. Andrianakis, I., Vernon, I.R., McCreesh, N., McKinley, T.J., Oakley, J.E., Nsubuga, R.N., Goldstein, M., White, R.G.: Bayesian history matching of complex infectious disease models using emulation: a tutorial and a case study on HIV in Uganda. *PLoS Comput. Biol.* **11**(1), e1003968 (2015)
10. Andrianakis, I., Vernon, I., McCreesh, N., McKinley, T.J., Oakley, J.E., Nsubuga, R.N., Goldstein, M., White, R.G.: History matching of a complex epidemiological model of human immunodeficiency virus transmission by using variance emulation. *J. R. Stat. Soc. Ser. C (Appl. Stat.)* **66**(4), 717–740 (2017)
11. Oliver, D.S., Chen, Y.: Recent progress on reservoir history matching: a review. *Comput. Geosci.* **15**(1), 185–221 (2011)
12. Friswell, M.I.: Damage identification using inverse methods. *Philos. Trans. R. Soc. A Math. Phys. Eng. Sci.* **365**(1851), 393–410 (2007)
13. O’Hagan, A.: Bayesian analysis of computer code outputs: a tutorial. *Reliab. Eng. Syst. Saf.* **91**(10–11), 1290–1300 (2006)
14. O’Hagan, A., Kingman, J.: Curve fitting and optimal design for prediction. *J. R. Stat. Soc. Ser. B (Methodol.)* **40**(1), 1–42 (1978)
15. Rasmussen, C.E., Williams, C.K.I.: Gaussian processes for machine learning. *Int. J. Neural Syst.* **14**(2), 69–106 (2004)
16. Bastos, L.S., O’Hagan, A.: Diagnostics for Gaussian process emulators. *Technometrics* **51**(4), 425–438 (2009)
17. Pukelsheim, F.: The three sigma rule. *Am. Stat.* **48**(2), 88–91 (1994)
18. Dette, H., Pepelyshev, A.: Generalized Latin hypercube design for computer experiments. *Technometrics* **52**(4), 421–429 (2010)
19. Andrianakis, I., Challenor, P.G.: The effect of the nugget on Gaussian process emulators of computer models. *Comput. Stat. Data Anal.* **56**(12), 4215–4228 (2012)
20. Gardner, P., Barthorpe, R.J., Lord, C.: Bayesian calibration and bias correction for forward model-driven SHM. In: Proceedings of IWSHM2017 International Workshop of Structural Health Monitoring, pp. 2019–2027 (2017)
21. Titsias, M.: Variational learning of inducing variables in Sparse Gaussian processes. *Aistats* **5**, 567–574 (2009)

Chapter 23

Augmented Reality for Next Generation Infrastructure Inspections



JoAnn P. Ballor, Oscar L. McClain, Miranda A. Mellor, Alessandro Cattaneo, Troy A. Harden, Philo Shelton, Eric Martinez, Ben Narushof, Fernando Moreu, and David D. L. Mascareñas

Abstract Most infrastructure in America is approaching or has exceeded the intended design life. As infrastructure ages, danger is presented to the citizens and the environment. Disasters like the failure of the Oroville Dam emphasize the importance of preventing failure of infrastructure. Despite Structural Health Monitoring (SHM) emerging as the key discipline to evaluate the integrity of structures, human-based visual inspections remain the dominant technique. Main factors behind the slow adoption of the SHM technology are its high installation and maintenance costs, the low confidence level of decision makers in the technology, and the structural community's familiarity with visual inspections. One major drawback to visual inspection is that it can be highly subjective, relying on a small number of manually recorded data points. Inspectors use tape measures, digital cameras, and human senses. These tools are inadequate to capture and document the state of infrastructure at the resolution needed for tracking damage progression. When working with infrastructure, it is desirable to have high-resolution measurement techniques to detect, localize, and characterize the state of a structure. The present work investigates Augmented Reality (AR) to minimize visual inspection drawbacks. AR is a technology that can superimpose holograms onto the real world. In this work an AR headset is used to enhance the ability of human inspectors to perform infrastructure inspections. The headset features RGB and depth cameras, accelerometers, wireless communication, microphones, and stereo sound. These sensors can capture a high-resolution 3D measurement of the infrastructure being inspected along with RGB photos that can be overlaid on the geometry. The 3D measurement can be used to analyze the state of the structure over time, and track damage progression. The 3D model can also be used as a base to overlay data captured with diverse sensors. The proposed technique will ultimately improve inspectors' ability to assess risk on site, make informed decisions faster, analyze defect growth over time, and create high-resolution documentation of structural inspections that will reduce the variability that occurs. Overall, AR is a promising technique for infrastructure inspection, mapping infrastructure on site, generating models, and providing consistency between inspectors. This technology has considerable potential for improving the quality of infrastructure inspections.

J. P. Ballor
Michigan State University, Materials Engineering, East Lansing, MI, USA
e-mail: ballorj2@msu.edu

O. L. McClain
Southern University and A&M College, Chemistry, Baton Rouge, LA, USA
e-mail: oscar_mcclain_00@subr.edu

M. A. Mellor
University of California San Diego, Structural Engineering, La Jolla, CA, USA
e-mail: mmellor@ucsd.edu

A. Cattaneo (✉) · T. A. Harden
Los Alamos National Laboratory, Applied Engineering Technologies, Los Alamos, NM, USA
e-mail: cattaneo@lanl.gov; harden@lanl.gov

P. Shelton · E. Martinez · B. Narushof
Engineering Division, Public Works Department Los Alamos County, Los Alamos, NM, USA
e-mail: philo.shelton@lacnm.us; eric.martinez@lacnm.us; ben.narushof@lacnm.us

F. Moreu
Department of Civil Engineering, University of New Mexico, Centennial Engineering Center 3056 MSC01 1070, 210 University Blvd NE, Albuquerque, NM, USA
e-mail: fmoreu@unm.edu

D. D. L. Mascareñas
Los Alamos National Laboratory, Engineering Institute, Los Alamos, NM, USA
e-mail: dmascarenas@lanl.gov

Keywords Augmented reality · Structural inspection · Structural health monitoring · Non-destructive evaluation · Microsoft HoloLens

23.1 Introduction

A large portion of infrastructure in America has exceeded or will exceed its intended design life in the following years [1]. For example, New Mexico is the home of many 100-year-old fracture-critical steel railroad bridges [2]. These bridges present the possibility of failure without regular and detailed inspections [2].

Although human-based inspections are largely adopted, a number of factors are negatively affecting the results obtained with this approach. Variations in training and experience, as well the information inspectors choose to report after an inspection may cause inaccuracies and lack of consistency when the same infrastructure is inspected by different teams [3, 4].

In the field of engineering, there is a push to embrace new technology to help engineers produce the best work possible [5]. Augmented reality, a technology which allows the user to see computer generated images superimposed on the real world, has the potential to minimize inspection inconsistencies. The augmented reality device used in this paper is the Microsoft HoloLens [6]. Augmented reality differs from virtual reality by allowing the user to be able to see the real world with overlaid holographic images (holograms).

This paper will explore augmented reality capabilities in order to create a tool for more consistent inspections. Using the capabilities of the HoloLens, a model of a structure can be created. Inspection data and measurements made by the HoloLens can then be combined with the model. This model can be used by future inspectors, improving consistency of inspections over time. The experimental procedure and results obtained with the current work are presented in the next sections.

23.2 Experimental Procedures

In the field of infrastructure inspection there is a need for improved measurement tools and a standardized system for reporting results. The following apps were developed to address the current needs of the inspection community. The Microsoft HoloLens was used as the augmented reality headset. All the apps presented in the current section were created with the help of the game development platform Unity and Microsoft Visual Studio. The apps created are categorized as either measurement apps or data storage apps. The measurement apps were created for the purpose of improving accuracy and efficiency of inspection measurement, as well as improving measurement reporting. Data storage apps were developed to store information about a structure which can then be reviewed, shared between inspectors, and used in additional data analysis.

23.2.1 *Measurement Apps*

23.2.1.1 **Surface Area App**

The surface area measuring app was designed to calculate the surface area of specific regions of sidewalks. The types of surface areas the app would need to measure are horizontal and vertical surface areas, to measure flat sidewalks and curbs. To accomplish these tasks, the app needs to be capable of measuring irregular shapes, such as multi-sided polygons. In order to address these needs, two algorithms were developed to measure horizontal and vertical surface areas. The user can define these surface areas through the placement of holograms to define the edges of the surface areas. The remaining of the current subsection provides details about the implementation of the horizontal and vertical surface area measurement algorithms, as well as a complete description of the user feedback for hologram placement and the output files generated by the app. Limitations of the current surface area measurements algorithms are highlighted.

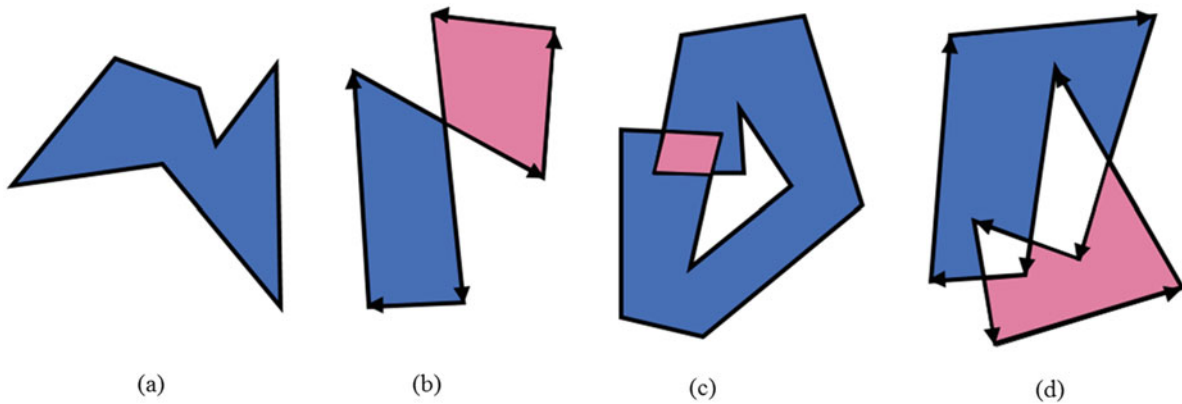


Fig. 23.1 Figure (a) is an example of a polygon where the algorithm can calculate the area [7]. Figures (b–d) are examples of polygons the horizontal algorithm is not able to calculate [7]

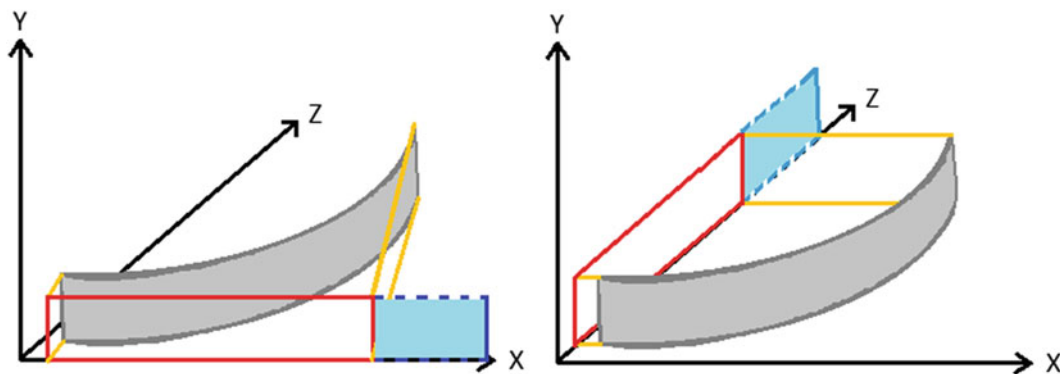


Fig. 23.2 An example of how vertical surface area could be lost to projection error

Horizontal Surface Area Measurement Algorithm

The polygon surface area algorithm by Finley was adapted into C# code to measure the surface area of horizontal polygons [7]. Using the x- and z-coordinates of user-placed holographic markers, the horizontal surface area of the defined polygon can be calculated [7]. Figure 23.1 shows an example of the type of polygon area that can be calculated. X- and z-coordinates were chosen because the HoloLens defines the x-z plane as a horizontal plane. This approach would meet the need to measure horizontal surface areas with irregular shapes. Limitations of this algorithm are that the polygon cannot cross itself, as seen in Fig. 23.1. Also it should be noted that the user-defined surface area is projected onto the x-z plane, ignoring any vertical gradient present. This projection introduces some error into the measurement.

Vertical Surface Area Measurement Algorithm

The horizontal polygon algorithm could not be adapted to a vertical algorithm because it takes coordinate points from 2 planes, so a vertical surface area, such as a curb, would have to be projected on either the x-y or z-y plane. If an angle existed between the curb and the projected plane, significant surface area could be lost. This is illustrated in Fig. 23.2. The vertical algorithm was developed to limit vertical surface area projection error.

The user-placed vertical surface markers consist of “top” and “bottom” markers, which define the top edge and the bottom edge of the vertical surface to be measured. The horizontal distance between top markers is found using the distance formula and the x- and z-components of the vector between two markers, as in Eq. 23.1.

$$d = \sqrt{(x_2 - x_1)^2 + (z_2 - z_1)^2} \quad (23.1)$$

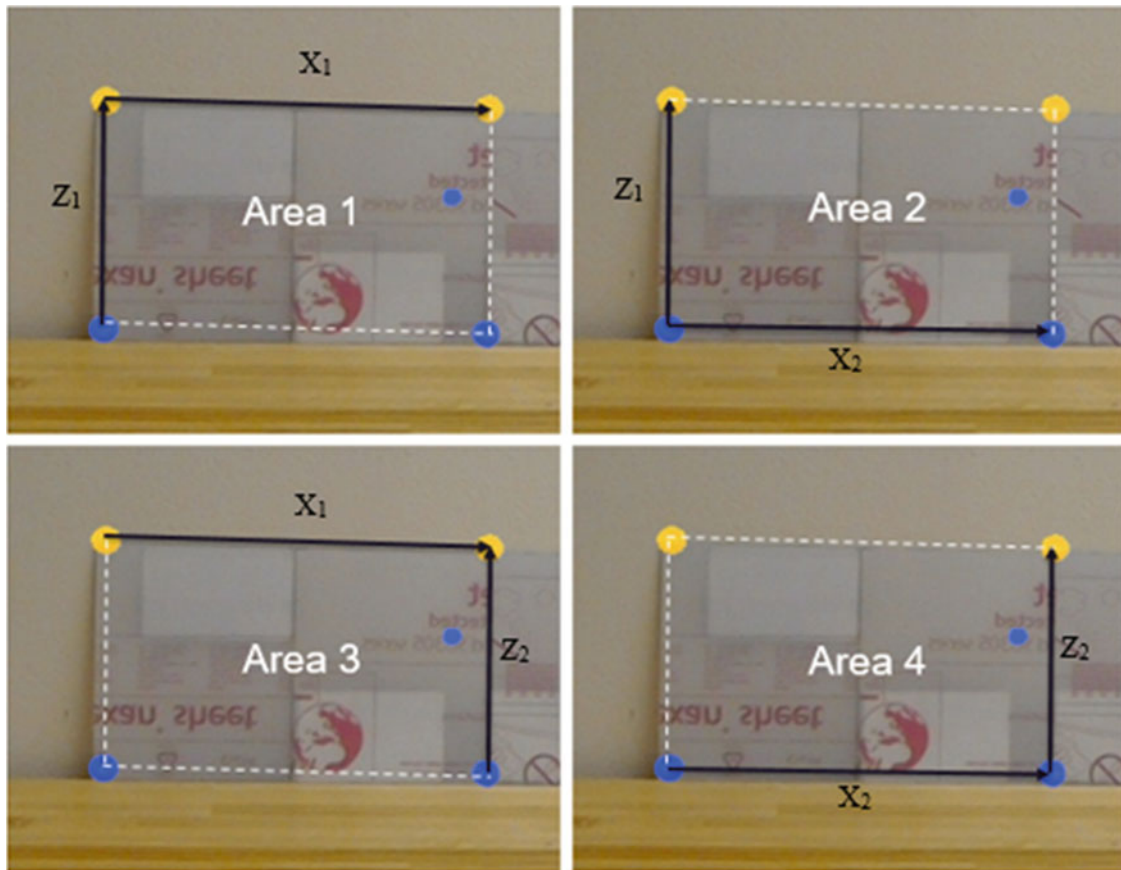


Fig. 23.3 An example of 2 top and 2 bottom markers placed to define a vertical surface area. Also shown are the four areas calculated to get a final average surface area

Similarly, the distance between the bottom markers is computed. The vertical distance between the top and bottom markers is found by taking the y-component of the vector connecting them. With the markers placed as shown in Fig. 23.3, the area of four rectangles defined by the top and bottom markers is averaged to get a final area.

$$\text{Area 1} = X_1 * Z_1 \quad (23.2)$$

$$\text{Area 2} = X_2 * Z_1 \quad (23.3)$$

$$\text{Area 3} = X_1 * Z_2 \quad (23.4)$$

$$\text{Area 4} = X_2 * Z_2 \quad (23.5)$$

$$\text{Final Area} = \frac{\text{Area 1} + \text{Area 2} + \text{Area 3} + \text{Area 4}}{4} \quad (23.6)$$

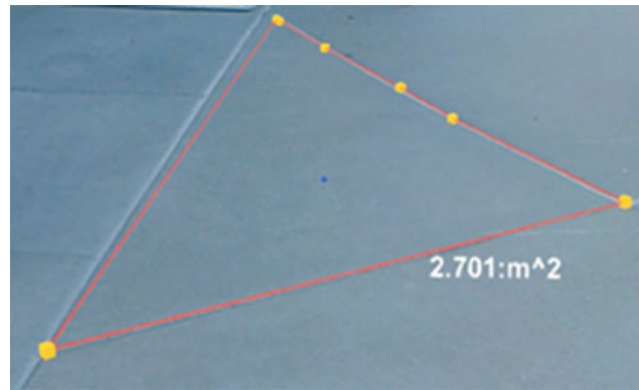


Fig. 23.4 An example of what the user would see when defining a horizontal surface area using the Surface Area App

The surface area measurement algorithm still contains some inherent error because the height of the area is found using only the vector y-component; angles between the surface area and the y-axis are ignored. Also, the algorithm assumes that the user-defined area is a rectangle. This limits the complexity of vertical surface area shapes that can be measured.

User Feedback and Output Files

Three types of markers were created for the surface area app. A yellow cube with side lengths of 3 cm is the marker for defining horizontal surface area. A yellow sphere with a diameter of 3 cm is the marker for defining the top edge of a vertical surface, and a blue sphere with a 3 cm diameter is the marker used for defining the bottom edge of a vertical surface. Visual feedback from both the shape and the color of the marker helps the user keep track of the type of markers he/she has already placed. When calculating surface area, the markers are connected with a red line to provide the user with feedback on the total surface area the app is measuring. The surface area calculated is also instantly displayed in a textbox on screen for the user to view. An example of what the user would see is shown in Fig. 23.4.

Text files with date and time information, marker coordinate positions, and the calculated surface areas are generated automatically for the user. These files allow the user to engage in extra data processing if desired.

23.2.1.2 Depth App

A depth measuring app was developed as a tool for evaluating structural health. The depth of a crack or pothole is one indicator of structural deterioration and damage progression. To properly monitor structural health, damage must be periodically quantified. The depth app aims at allowing the user to efficiently measure and record the magnitude of damage to a structure. Details about the depth measurement algorithm, user feedback and output files are provided hereafter.

Depth Measurement Algorithm

Depth is calculated using 4 user-defined points. The first three markers are placed in order to establish a reference plane for the depth measurement. The last point is placed at the depth that the user wants to measure. The shortest vector is then calculated between the depth marker and the defined plane. The magnitude of that vector is reported to the user as the depth. Figure 23.5 illustrates the three steps taken by the depth measurement algorithm and a screenshot of the scene viewed by the user.

User Feedback and Output Files

Once four markers have been placed the depth will be calculated. The depth is instantly displayed in a textbox on screen for the user to view. Similar to the Surface Area App, text files with date and time information, marker coordinate positions, and the calculated depth are generated automatically for the user. These files allow the user to engage in extra data processing if desired.



Fig. 23.5 An illustration of how depth is calculated along with what the user would see when the app is in use

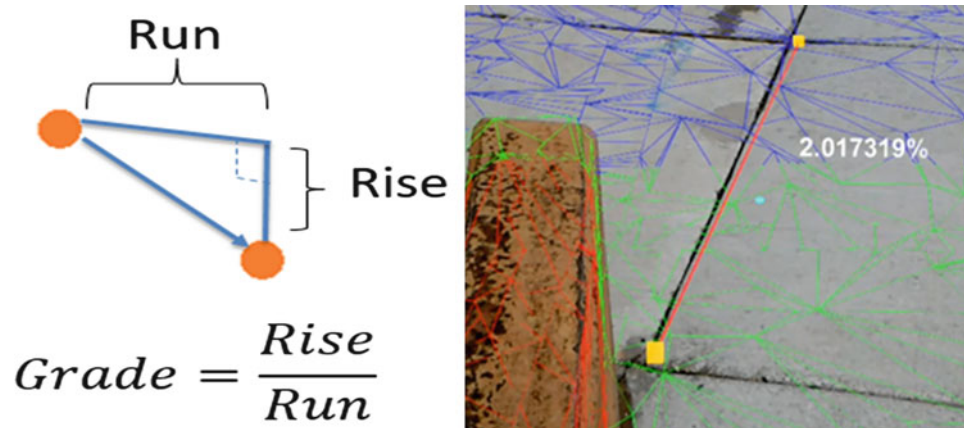


Fig. 23.6 An illustration of how grade is calculated along with what the user would see when the app is in use

23.2.1.3 Grade App

Grade is calculated as the amount of vertical height change over a horizontal distance, which can be calculated as the slope of a line. This is found by creating a ratio between the horizontal and vertical change between set points. The purpose of this app is to allow the user to calculate the grade of a sidewalk to determine if it meets building code. Details about the grade app are provided in the next two subsections.

Grade Algorithm

The grade algorithm works by finding the vector that connects two user-defined points. The slope of the vector is calculated by using the y-component of the vector as the “rise” of the slope. The “run” is calculated by using the x- and z-components of the vector and the distance formula from Eq. 23.1. Grade is then found by dividing the “rise” by the “run”. Since grade is reported as a percentage, the rise over run is then multiplied by 100%. Figure 23.6 illustrates how grade is calculated as well as what the user sees when using the app.

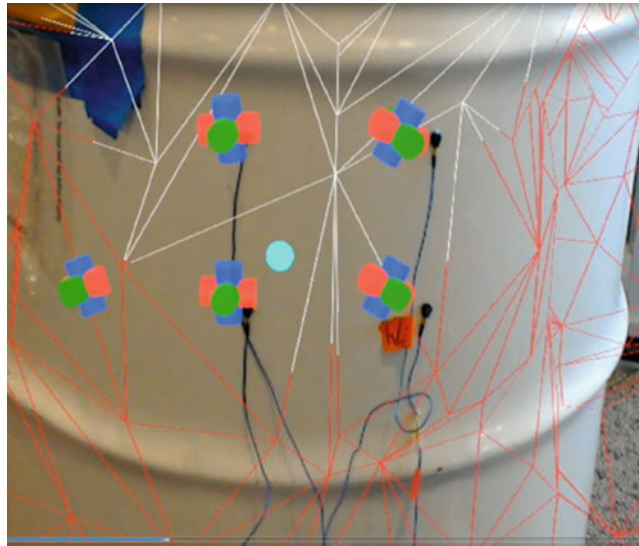


Fig. 23.7 Accelerometer App markers placed on a barrel with accelerometers attached

User Feedback and Output Files

Once two markers have been placed, a grade can then be calculated. The grade is instantly displayed in a textbox on screen for the user to view. Text files with date and time information, marker coordinate positions, and the calculated grade are generated automatically for the user. These files allow the user to engage in extra data processing if desired.

23.2.2 Data Storage Apps

23.2.2.1 Accelerometer Location App

The accelerometer location app is meant to be used as a tool for documenting accelerometer location and orientation on a structure for the purpose of modal analysis. The app enables the user to place a holographic marker onto a structure to permanently record the location and orientation of an accelerometer at its installation. User feedback and output files details follow.

User Feedback and Output Files

The marker created consists of three cylinders which are aligned to form axes as seen in Fig. 23.7. These cylinders are also color coordinated to correspond to the axes defined by Unity. When a marker is placed, the y-axis is automatically aligned to be normal to the surface that it is placed on. Once the user has placed all markers at the desired locations and orientations of each accelerometer on the structure, a text file is created. This text file contains individual marker locations in local coordinates created by the HoloLens. The text file also outputs the orientation vectors for each marker based upon the respective orientation of their axes.

23.3 Future Work

After creating the apps previously mentioned, the team found several areas of structural inspection where augmented reality could also be of use. The two main areas of future potential were found to be modal analysis, particularly accelerometer placement, and file storage of inspection results. With regard to the first point, a model of the structure could be created on the computer, and accelerometers could be placed on the model. The model would then be projected on the real structure

using augmented reality, showing the user where and in what orientation the accelerometers should be placed. With regard to the second point, the HoloLens can be programmed to generate world anchor holograms. A world anchor is a type of hologram specific to the HoloLens that can be placed by the user, and, once placed, this hologram remains permanently at this defined location. If the user reopens the app at a later time, the world anchor would appear in the same location where it was saved. As a result of its ability to have a permanent location, world anchors can be used as a tool for information storage.

23.4 Conclusions

Augmented reality has the potential to help structural inspections meet the needs of a constantly growing and developing modern world dependent on its infrastructure. The research presented shows how the game development platform Unity and Microsoft Visual Studio can be successfully used to develop a set of apps to enable infrastructure inspections with a Microsoft HoloLens augmented reality headset.

Current inspections are subject to variability, and are in need of a standardized system for reporting inspection results. An answer to this need can be provided with augmented reality apps created to perform inspection measurements, such as measuring surface area and grade, as well as to store information pertaining to a structure, such as accelerometer placement.

Aside from the apps already created, there is potential for the development of future apps to further explore the measurement and data storage capabilities of augmented reality.

Acknowledgements This project was funded through the Los Alamos Dynamics Summer School program of the Los Alamos National Laboratory Engineering Institute under the direction of Charles Farrar. This work would not have been possible without the help of the Los Alamos County, Sudeep Dasari, Ben Katko, and Brian Bleck.

References

1. ASCE Committee on America's Infrastructure: 2017 Infrastructure Report Card, American Society of Civil Engineers (2017)
2. Daumueller, A.N., Jauregui, D.V., Roach, D.P.: Development of a Structural Health Monitoring System for Life Assessment of Critical Transportation Infrastructure. Sandia National Laboratories, Albuquerque (2012)
3. Washer, G.A., Chang, C.A.: Guideline for Implementing Quality Control and Quality Assurance for Bridge Inspection, June 2009. [Online]. Available: [http://onlinepubs.trb.org/onlinepubs/nchrp/docs/NCHRP20-07\(252\)_FR.pdf](http://onlinepubs.trb.org/onlinepubs/nchrp/docs/NCHRP20-07(252)_FR.pdf). Accessed June 2017
4. Agrawal, A.K., Washer, G.A.: Consistency of the New York State Bridge Inspection Program, Albany (2013)
5. Lab, F.F.: Reflecting on the Future of Design at the IABSE Conference, 2017. [Online]. Available: <https://formfindinglab.wordpress.com/2017/05/03/reflecting-on-the-future-of-design-at-the-iabse-conference/>. Accessed June 2017
6. Microsoft: HoloLens for Research, Microsoft, 2017. [Online]. Available: <https://www.microsoft.com/en-us/research/academic-program/hololens-for-research/#>. Accessed 5 July 2017
7. Finley, D.R.: Ultra-Easy Polygon Area Algorithm With C Code Sample, 2006. [Online]. Available: http://alienryder.com/polygon_area/. Accessed June 2017



Chapter 24

A Distribution-Based Damping Estimation Method for Random Vibration Response and Its Applications

Ibrahim A. Sever

Abstract In this paper, a damping estimation method based on distribution of zero-crossing times and its applications are presented. The method is empirically derived and it is based on Rice distribution operating on probability distribution of zero-crossings. The method's assertion is that a relationship exists between said probability distribution and the bandwidth of a mechanical system and this can be used as a means of increasing confidence in more traditional damping estimation methods. The method is applicable to responses that are due to broadband random excitation featuring a mono-harmonic response. Given that a multitude of modes will be active in aero-engines; its application has to be preceded with a suitable band-pass filter to isolate modes of interest. Such filtering is shown to affect the damping estimates. Some controlled laboratory tests are performed to verify the accuracy of the method and to study the effects of preceding filtering amongst other factors such as modal density, data length etc. The performance of the method is compared with Fourier transform based damping estimation methods. The results of application of the method to real engine measurements and carefully controlled laboratory tests are also presented.

Keywords Damping estimation · Rice distribution · Random excitation · Operational data · Zero crossing

24.1 Introduction

Controlling vibration amplitudes is essential in machinery operating in harsh conditions where safety is paramount. Operating environment of aero engines is a good example to this and often necessitates introduction of dissipation mechanisms to keep vibration response below harmful levels. These dissipation mechanisms may be introduced deliberately, such as in the case of under-platform dampers used in high pressure turbine stages, or may occur naturally, such as in the case of blade-disc contact. Whatever the mechanism, the analysts rely on accurate estimates of damping available to perform representative forced response calculations, which in turn are used to assess suitability of design from vibration view point.

Given the complex nature of interactions in aero engines, producing reliable damping estimates is often a challenge. The task is further complicated by the fact that in real engine measurements, upon which the said methods are operating, the exact excitation forces are unknown. In the absence of this information, some assumptions about the character of prevailing excitation forces will have to be made. Since the method introduced here relies on underlying excitation force being random broadband in nature, it is important that this is verified before any damping estimation is attempted. When excited by a random input, the mode of interest will act as a band-pass filter resulting in a normal distribution of instantaneous values. In this case the peak response amplitudes will follow the Rayleigh distribution [1] given in Eq. (24.1). Therefore random input requirement of the excitation can be assessed by fitting Eq. (24.1) to probability distribution of the response peaks.

$$P(\delta; \sigma) = \frac{\delta}{\sigma^2} \cdot e^{-\frac{1}{2} \left(\frac{\delta}{\sigma}\right)^2} \quad (24.1)$$

Figure 24.1a shows a Zmod (i.e. spectrogram) showing two modes measured from a real engine test. The measurements are acquired on an external component of a civil engine using strain gauges under gradually increased engine speed conditions. Rayleigh distributions for both modes were constructed after narrow-band filtering of the individual modal responses and Eq. (24.1) fitted using Marquardt-Levenberg nonlinear curve fitting algorithm, [2]. Figure 24.1b shows an adequate degree of correlation whereby confirming the random broadband nature of underlying excitation. However, the same

I. A. Sever (✉)
Rolls-Royce plc, Derby, UK
e-mail: ibrahim.sever@rolls-royce.com

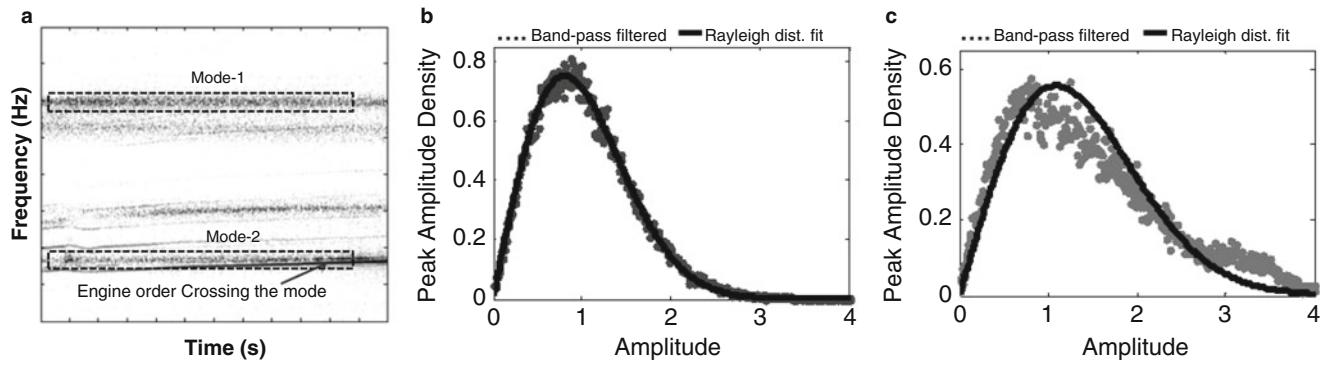


Fig. 24.1 (a) Zmod measured from a real engine component, peak amplitude density and Rayleigh distribution fits for (b) Mode-1, and, (c) Mode-2 shown on the Zmod

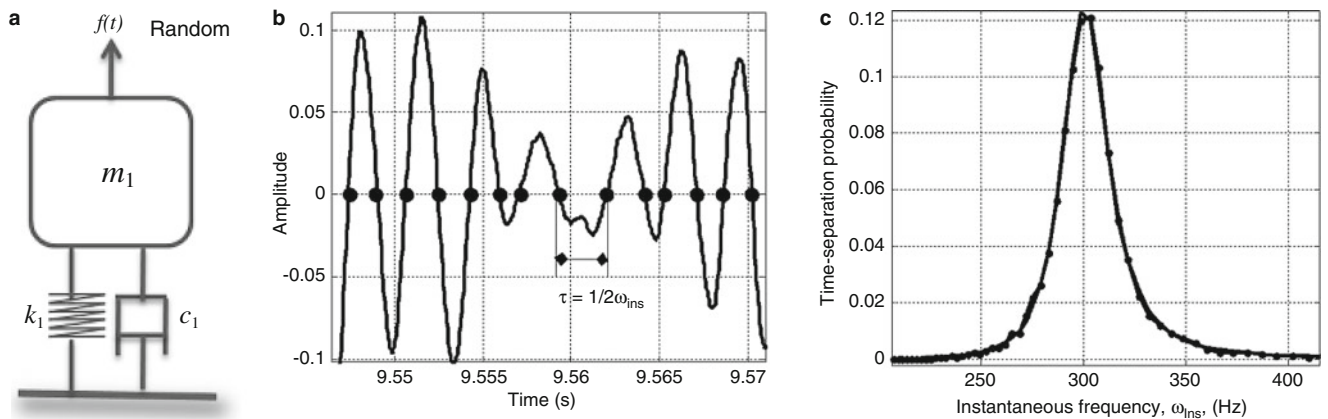


Fig. 24.2 (a) SDOF system with random excitation, (b) its response showing zero-crossings, and (c), distribution of instantaneous frequencies computed from these crossings [...Computed distribution, —Fitted distribution]

cannot be said for Fig. 24.1c. Upon close inspection it can be seen that a nearby strong engine order excitation introduces a bias in peak amplitude distribution. Therefore use of the method for this mode is not justified.

24.2 Damping Estimation from Time-Separation Distribution

The connection between the bandwidth of an ‘ideal’ band pass (electrical) filter to the characteristics of the time separation distribution from the resulting narrowband signal has been made in the classic paper by Rice, [4]. Utilising Rice’s original notation, for an ideal narrow band-pass filter the probability, p , that the distance between two successive zeros lies between τ and $\tau + \Delta\tau$ is approximately;

$$p = \frac{\Delta\tau}{2} \cdot a \sqrt{\frac{1}{(1 + a^2(\tau - \tau_{nat})^2)^3}} \tag{24.2}$$

where $\tau_{nat} = \frac{1}{2 \cdot \omega_{nat}}$ is half the period of natural frequency. For electrical systems, the bandwidth is approximated by the parameter value ‘ a ’. Figure 24.2a shows an SDOF mechanical system. The response of this system to random forcing is computed and locations of zero-crossings in the response are identified as shown in Fig. 24.2b. Time-separation probability distribution of these crossing for a natural frequency of 300 Hz, mass of 0.1 kg and a Q value of 100 is given by the dotted line in Fig. 24.2c. Best fit to the given probability distribution using Eq. (24.2) is also plotted in Fig. 24.2c, as a solid line. It is evident from the plot that the probability distribution is accurately described by Eq. (24.2).

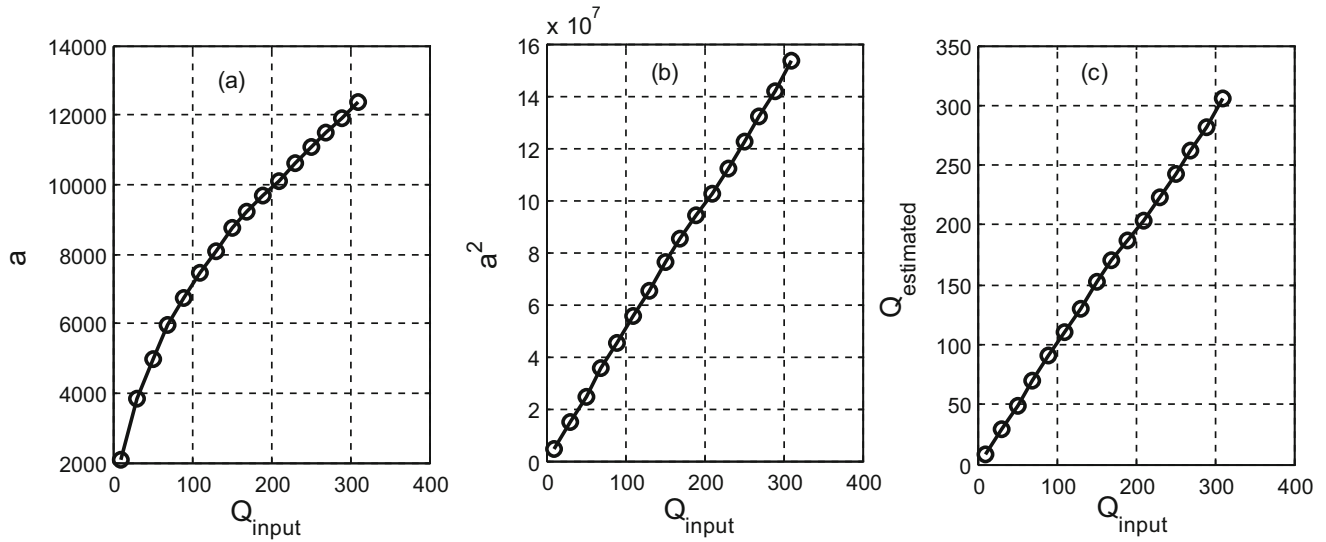


Fig. 24.3 (a) Variation of parameter “a”, (b) “a²” with respect to input Q value, and, (c) Estimated Q value against input Q value

The contribution of this paper is its attempt to appropriate abovementioned concept for mechanical systems as a means of damping estimation. The main concept and empirical identification of bandwidth and damping from a given zero-crossing distribution are presented below. The adaptation of method and its application to simulated, laboratory and operational data, as well as its limitations and scope are also presented.

In an attempt to find a relationship for bandwidth and damping in case of mechanical systems from distribution given above, the SDOF model shown in Fig. 24.2a is used. The idea is to construct an association involving frequency of the mode in the narrowband response and parameter “a” empirically. For this purpose the SDOF model given above is simulated for a range of damping Q values (20–300). The SDOF system is designed to have a natural frequency of 200 Hz and a lumped mass of 1 kg. The simulation range for Q values is kept wide enough to cover possible observations in practice. For each case the SDOF model is simulated to a random input for 20 s. This input is kept the same for all cases. Zero-crossing time distribution for each case is constructed. Once again, Eq. (24.2) is fitted to data. Variation of input Q value as a function of fit parameter “a” is plotted in Fig. 24.3a. The plot reveals a smooth nonlinear relationship which is quadratic in nature. In an attempt to describe this relationship better, input Q is plotted against a² in Fig. 24.3b. The plot now demonstrates a near-perfect linear variation. Given this relationship, it becomes possible to “scale” the “a²” term with a constant featuring natural frequency, such that the slope of this linear relationship is as close to 1 as possible (i.e. an estimate for Q value). A suitable relationship is found when a² term is multiplied by $\frac{\tau_{\text{nat}}^2}{\pi}$, as shown in Fig. 24.3c. The slope of linear variation shown in Fig. 24.3c is nearly 1. As a result the empirical description for estimation of Q value using time separation distribution resulting from a narrowband signal is suggested in the following form:

$$Q_e \cong \frac{1}{\pi} \cdot a^2 \cdot \tau_{\text{nat}}^2 \quad (24.3)$$

Since parameters a and τ_{nat} are obtained directly from fitting Eq. (24.2) to time-separation probability distribution, estimate for damping in the form of Q_e can readily be obtained.

24.2.1 Time-Separation Distribution of Narrow-Band Filtered Response

Although the applicability of the time-separation method is shown on an SDOF system, in practice acquired vibration responses will feature a multitude of harmonic content at different natural frequencies. For the method to work in these cases, total response will have to be band-pass filtered around the mode of interest. To study the effect of narrow-band filtering on time-separation method, the SDOF system introduced above is designed and used with following properties: $m_1 = 0.1$ kg, $\omega = 2000$ Hz, $Q = 100$. Its response to a random input is then simulated for a 20 s period. The response obtained is filtered

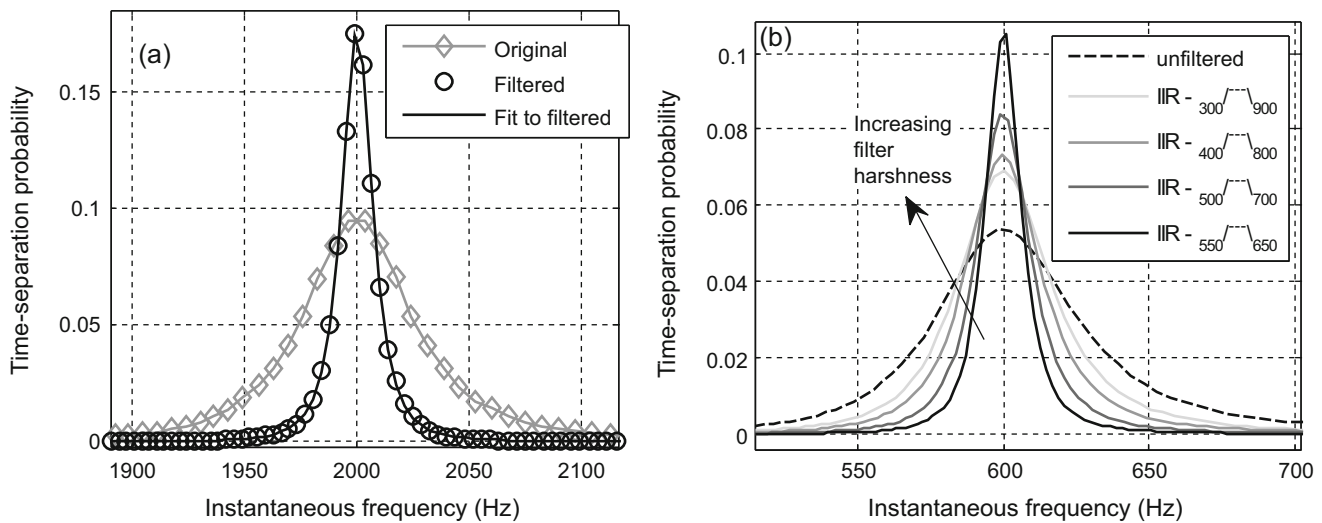


Fig. 24.4 (a) Unfiltered and filtered time-separation probability distribution, (b) Effect of increased filter harshness on time-separation probability distribution

using an equiripple FIR band-pass filter, [3], around the natural frequency. For both un-filtered and filtered responses time-separation probability distributions are obtained. Figure 24.4 shows the comparison of distributions before and after filtering. Also shown in the figure is the fitted distribution to the filtered data.

Figure 24.4 presents a surprising picture. The effect of filtering on distribution obtained is significant. This is unexpected as the bandwidth of the designed mechanical SDOF system is 3 Hz which is much smaller compared with filter bandwidth of 240 Hz used here. The reason for this is that when the high-frequency component of response is filtered, the nature of zero-crossing intervals change significantly. Crossing time intervals which were much shorter when unfiltered (i.e. outliers in original distribution), are removed in case of filtered response and are moved towards the mean of the distribution.

An important observation from Eq. (24.2) is that, time-separation distribution is only a function of parameter “a” and system natural frequency. In other words, filtered response distribution is identical to the unfiltered distribution in characteristics but its parameter “a” is simply scaled by a constant. This is more clearly demonstrated in Fig. 24.4b where the response for a different SDOF system with a natural frequency of 600 Hz is filtered with a series of band-pass filters which are progressively getting narrow in the pass band. It is evident that kurtosis of the distribution increases as the harshness of the filters increase. Therefore, any scaling constant must be a function of filter characteristics and a correction factor will have to be identified in relation to unfiltered case for each filter individually. The question of whether such a correction factor can be derived in a robust manner such that it can be used in real cases with confidence is explored in the following sections.

24.2.2 Identification of Filter Correction Factor

The process followed in correction factor identification for a given filter is as follows: First an SDOF system with desired natural frequency is designed where a rough estimate for expected damping value is assumed. Using time-separation damping estimation method damping from simulation of this system is estimated. Subsequently the simulated response is passed through the filter for which the correction factor is to be identified. Time-separation method is then applied to the filtered response and a new damping estimation is obtained. The correction factor for the filter at hand is then simply a ratio of these two damping estimates.

The process is applied to an SDOF system with $\omega_n = 300$ Hz, $m = 0.1$ kg, and $Q = 100$, simulated for 20 s at a sampling rate of 25 kHz. Correction factor is identified for band-pass FIR filter with following properties: First transition band of 250–270 Hz and second transition band of 330–350 Hz (i.e. pass-band = 270–330 Hz), stop-band attenuation of 20 dB, and, pass-band ripple of 0.1 dB. For this case the response from simulation is first filtered with the given band-pass filter and then time-separation damping estimation is applied to the filtered time domain data. Damping value with applied correction factor is identified as 92.3. The deviation of this value from the original Q value of 100 is 7.7% and the deviation from Q value identified using time-separation for un-filtered response is 6.7%.

Table 24.1 Q values estimated by application of correction factors identified from simulations of an SDOF system with different Q values

$Q_{\text{Reference}}$	20	30	40	50	70	100	130	150	170	200	300
C_f	10.5	9.8	9.4	9.2	8.9	8.6	8.4	8.4	8.4	8.4	8.7
$Q_C (Q_{\text{Filtered}}/C_f)$	79.9	85.6	89.2	91.1	94.2	97.5	99.8	99.8	99.8	99.8	96.4
$(Q_C/Q_{UE}) * 100$	19.3	13.5	9.8	7.9	4.8	1.5	0.9	0.9	0.9	0.9	2.6
$(Q_C/Q_O) * 100$	20.1	14.4	10.8	8.9	5.8	2.5	0.2	0.2	0.2	0.2	3.6

24.2.3 Dependency of Correction Factor on Damping Value

Table 24.1 provides a number of correction scenarios for the SDOF model given above with different Q values. Here the correction factors, C_f (the ratio of Q values after and before filtering), are identified for a range of Q values starting from 20 to 300 using the band-pass filter given above. For very low Q values deviations up to 20% are observed. As the Q values increase stability of correction factor also increases.

Given the evident stability of correction factor with varying Q values, the SDOF system is simulated for the Q of 100 and filtered and then corrected in turn by different C_f factors in Table 24.1 to quantify the dependency of Q value to choice of reference Q value. Estimated Q values (Q_C) and their deviation from original value (Q_O) of 100, and, estimate from unfiltered response (Q_{UE}) of 98.9 are given in Table 24.1. Estimates calculated using correction factors for Q values ranging from 50–300 are all within 10% of original design value. Therefore it is concluded that correction factor is reasonably insensitive to choice of Q value within this range.

24.2.4 Effect of Choice of SDOF System on Filter Correction Factor

Effect of filtering on zero-crossing time-distribution was studied earlier with an SDOF system. A detailed examination was carried out to see if correction factors obtained for different SDOF systems with the same natural frequency would yield the same damping value. To this end, mass value was gradually varied from 0.1 kg to 5 kg and stiffness value adjusted accordingly for a natural frequency of 300 Hz. Correction factors obtained from different SDOF systems showed variations smaller than 1%. Therefore it is concluded that the choice of SDOF system is not a critical parameter in determination of the correction factor.

24.2.5 Effect of Modal Density on Filter Correction Factor

Effect of proximity of neighbouring/bracketing modes on the filtering correction factors was explored. To this end, a number of 3-DOF systems were designed. Natural frequency separation for these systems were gradually decreased (i.e. modal density increased) to simulate close modes scenarios. Each system was then simulated and their responses at 1st DOF were filtered and passed through time separation damping estimation algorithm. Properties of these systems, together with identified correction coefficients and filter properties are given in Table 24.2. Also given in this table are an equivalent SDOF system and its correction coefficient as reference. It is evident from the table that when the modes of the system are well separated and filter cut-off frequencies are sufficiently far away from neighbouring modes, correction coefficients for 3-DOF system are very close to that of reference SDOF system. However, as the cut off frequencies get closer to bracketing mode frequencies, as is the case in System-4, significant deviations are observed.

The same process is repeated with a much harsher band-pass filter to see if the C_f from all 3-DOF systems can be aligned with that from the SDOF system. The results for this case are given in “Filter-2” column of Table 24.2. As the new filter is now much harsher, the resultant filtering coefficients are much larger. Nevertheless, all systems now result in similar correction coefficients with maximum deviation from reference SDOF system being less than 9%.

Table 24.2 Effect of modal density on identification of filter coefficient [IIR Filter-1: $F_s = 25,000$ Hz, $F_{c1} = 280$ Hz, $F_{c2} = 320$ Hz, Order = 4, IIR Filter-2: $F_s = 25,000$ Hz, $F_{c1} = 290$ Hz, $F_{c2} = 310$ Hz, Order = 3]

	m1,m2,m3 (kg)	k1,k2,k3 (N/m)	c1,c2,c3 (kg/s)	$\omega_1,\omega_2,\omega_3$ (Hz)	Q1,Q2,Q3	Filter 1		Filter 2	
						Q2 _C	C _f	Q2 _C	C _f
Sys-1	0.788381	1935330	10	100	285.2	1772.3	17.8	3622.2	36.3
	0.455614	1599560	10	300	99.8				
	1.19597	1921130	10	500	55.6				
Sys-2	1.19312	4020170	0.34 0.34 0.34	200	2693.4	1737.6	17.4	3583.5	35.9
	0.578852	1759710		300	99.9				
	0.0174768	60468.6		400	1345.6				
Sys-3	2.51416	10122900	0.202 0.202 0.202	250	146.0	1630.0	16.2	3541.9	35.2
	0.134519	461284		300	100.6				
	0.0064339	19756.6		350	435.2				
Sys-4	4.23869	15444700	0.058 0.058 0.058	270	183.0	1181.7	11.8	3322.0	33.2
	0.0877328	310571		300	100.2				
	0.00167354	5703.85		330	261.7				
SDOF	1	3,553,060	18.8496	300	100	1763.3	17.6	3640.8	36.4

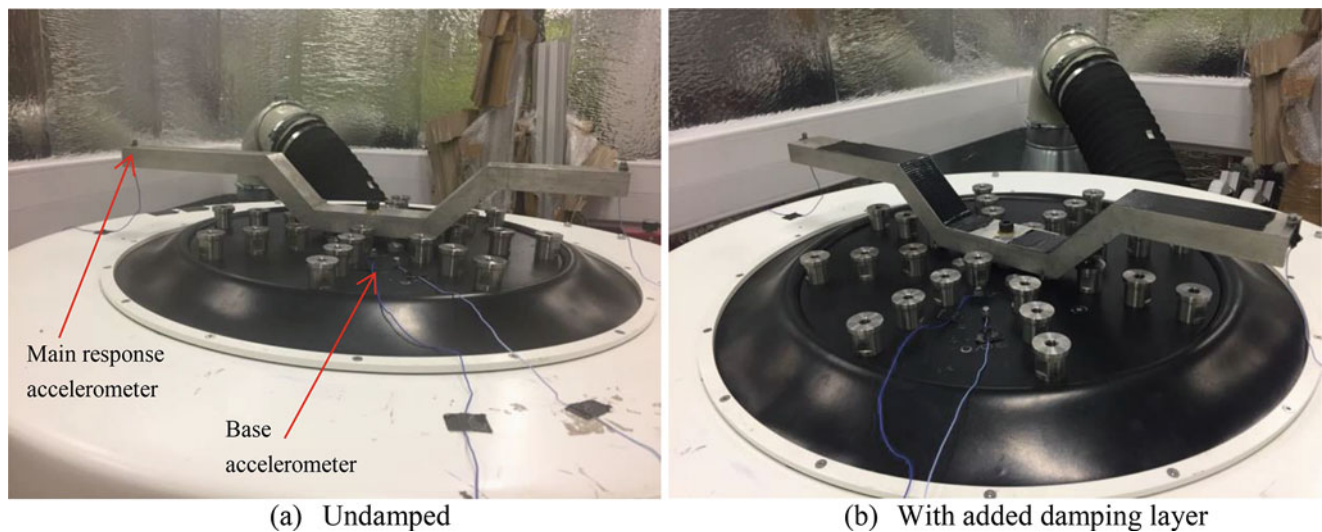


Fig. 24.5 Shaker test setup for undamped and damped configurations

24.2.6 Application of Time-Separation Damping Estimation Method to Laboratory Measurements

In order to evaluate the applicability and effectiveness of the method, a number of carefully controlled laboratory tests were carried out. The test setups used, an undamped and a damped configuration, are given in Fig. 24.5. To this end a simple aluminum test piece with a number of distinct modes in the frequency range of interest was mounted directly onto a shaker. The damped configurations were obtained by application of a damping layer, seen as black patches in Fig. 24.5b and foam material. Main response was measured by an accelerometer attached to the tip of the specimen. Since the way in which the specimen was connected to the shaker made it very difficult to install a force gauge, a base accelerometer was utilised for use in construction of Frequency Response Functions (FRF). Fig. 24.5a shows instrumentation details.

The idea in testing the undamped and damped configurations given above was to obtain a range of data for various degrees of damping in the system and to see if the proposed method captured the change in damping as reliably as the traditional methods would. Before random vibration tests were carried out, a number of sweep sine tests were carried out to identify natural frequencies. A sample FRF from a sine sweep testing of undamped configuration is given in Fig. 24.6a. A number of well separated modes are clearly visible. In this study, the mode at 1240 Hz was targeted for damping estimation comparisons.

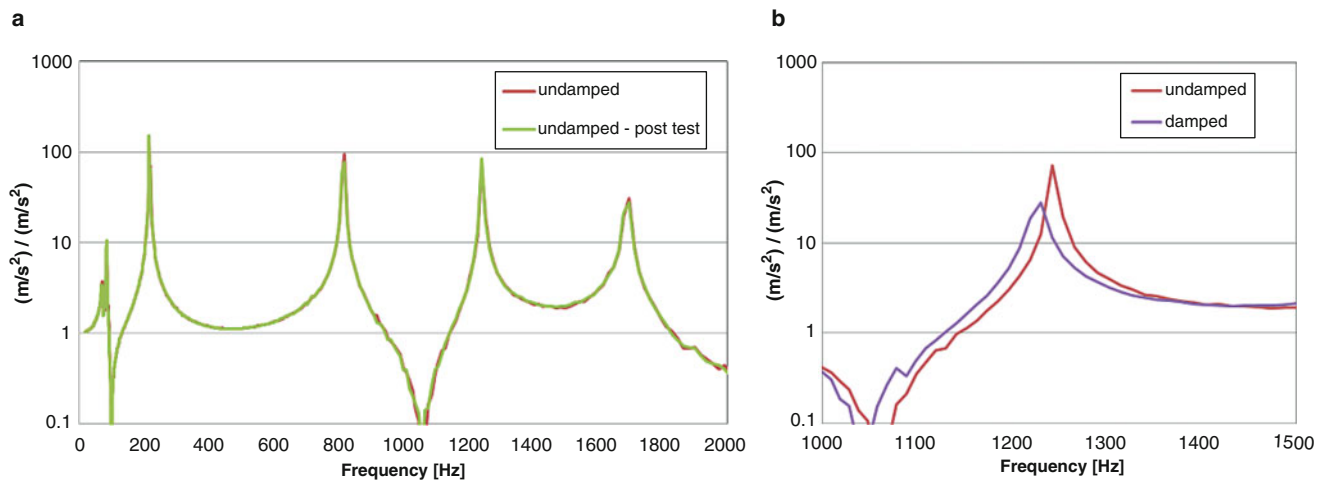


Fig. 24.6 (a) FRFs of undamped specimen before and after the test campaign, (b) response of mode of interest in the presence of various damped configurations

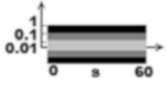
Table 24.3 Comparison of damping estimates for the mode at 1244 Hz in undamped configuration

Gain	Random, Undamped					
	Q _{PSD}		Q _{LineFit}		Q _{ZCTD}	
	Unfiltered	Filtered	Unfiltered	Filtered	Uncorrected	Corrected
0.01	361	357	409	420	1806	401
0.1	355	355	418	423	1935	430
1	420	420	469	450	2040	453


The change in response of this mode to undamped and damped configurations is also given in Fig. 24.6b. Reduction in amplitude, as well as in natural frequency, is evident to increasing damping which should form a good verification test for the method at hand.

Random response measurements were first carried out for the undamped configuration. To evaluate the effect of response amplitude, the tests were carried out for 3 different input gain factors, each an order of magnitude higher than the previous. Acquisition time for each gain setting was 60 s at a sampling rate of 52 kHz. The results of the damping estimation for mode shown in Fig. 24.6b from averaging of PSD estimates using only the response measurements and from line fit curve fitting using FRFs, together with estimates from the Zero-crossing Time Distribution (ZCTD) method introduced here are given in Table 24.3. Band-pass filter used throughout these analyses is a 4th order Butterworth IIR filter with cut off frequencies at 1000 Hz and 1600 Hz for a sampling rate of 52 kHz. Since the ZCDT method requires band-pass filtering of the mode of interest, damping estimates for PSD and line-fit methods are calculated for filtered responses as well. An SDOF system with a mass of 1 kg, stiffness of 6.11E + 7 N/m, and Q of 400 is used to calculate a correction factor of 4.5 for ZCDT method. “Corrected” estimates given in tables below are therefore obtained by dividing the “Uncorrected” results by this factor. The results from Table 24.3 show that corrected ZCDT results differ from PSD and line-fit methods, at most, by 10% and 5%, respectively. Here the results from line-fit method are likely to be more accurate as they are derived from system FRFs whereas PSD method operates on response output measurements alone. A decrease in damping is evident as the input gain is increased for all methods, though decrease is more uniform in case of ZCDT method. Line-fit results show a greater influence of filtering compared with those from PSD. However the variation is nevertheless not significant.

The process was repeated for the damped configuration as well. The same band-pass filter is used which also means that the correction factor for ZCTD method is also the same. Once again, random excitation is applied to the system for each value of gain separately. The results of the damping estimates in this case are given in Table 24.4. It is immediately evident that addition of damping tape and foam increased the damping in the mode on average by 4 folds. Frequency of the mode has also decreased by about 1.5% to 1226 Hz. The maximum deviation in damping estimates increased to 20% between PSD and ZCTD, and to 10% between line-fit and ZCTD methods. Although the differences have doubled, given the variations often

Table 24.4 Comparison of damping estimates for the mode at 1226 Hz in damped configuration


Gain	Random, Damped					
	Q _{PSD}		Q _{LineFit}		Q _{ZCTD}	
	Unfiltered	Filtered	Unfiltered	Filtered	Uncorrected	Corrected
0.01	122	122	108	108	441	98
0.1	120	120	113	112	449	100
1	120	120	114	114	434	96

Table 24.5 Comparison of damping estimates for the mode at 1226 Hz in damped configuration for varying response amplitudes


Interval	Response amp. (m/s ²)	Random, Damped, variable amplitude					
		Q _{PSD}		Q _{LineFit}		Q _{ZCTD}	
		Unfiltered	Filtered	Unfiltered	Filtered	Uncorrected	Corrected
0–60 s	0.3–0.8	115	115	113	113	430	96
0–10 s	0.35	86	86	111	107	387	86
10–20 s	0.4	103	104	112	111	421	94
20–30 s	0.45	107	107	113	110	390	87
30–40 s	0.5	110	110	111	111	458	102
40–50 s	0.6	116	116	110	112	458	102
50–60 s	0.7	123	123	111	113	450	100

observed in damping estimates in operating environments, these levels of agreement are still very encouraging. Unlike the undamped case, damping values do not show any noticeable dependence on vibration response amplitude. This is probably due to already significant degree of added damping.

Forcing levels and, as a consequence, response amplitudes often vary significantly in operating environment. As such it may not always be possible to have access to large number of samples at the same condition. In such cases it is favourable to have methods that can perform equally well with smaller sample sizes. To evaluate such scenarios, the test setup is excited by a random input with linearly increased gain during the acquisition period. Response levels in this case are increased from 0.3 to 0.8 m/s² in a linear manner. The recorded signal is then split into 6 segments and damping estimation methods are applied to each sub set as well as the full signal. The results are given in Table 24.5. The largest variations in damping values have been observed for the PSD method. This is not surprising as reliable estimates from PSD rely on large number of averages which in turn require longer signal lengths. On the other hand estimates from line-fit and ZCTD are more stable even if they differ by around 10%.

24.2.7 Application of Time-Separation Damping Estimation Method to Operational Data

The data set used in this section is acquired from a deceleration manoeuvre engine test. The raw time-domain data is processed at sampling rate of 25 kHz. A Zmod for one of the channels from this manoeuvre is given in Fig. 24.7. The modes at 765 Hz, 500 Hz and 360 Hz, as indicated on the Zmod, are selected for analysis. First 2 modes are analysed for 30–80 s interval, and the mode at 360 Hz is analysed for 50–90 s interval as they show reasonably stationary behaviour in these intervals, respectively. Table shown in Fig. 24.7 gives a summary of filter parameters used and correction factors obtained. Maximum difference in damping values estimated using time-separation and PSD based methods is 10%.

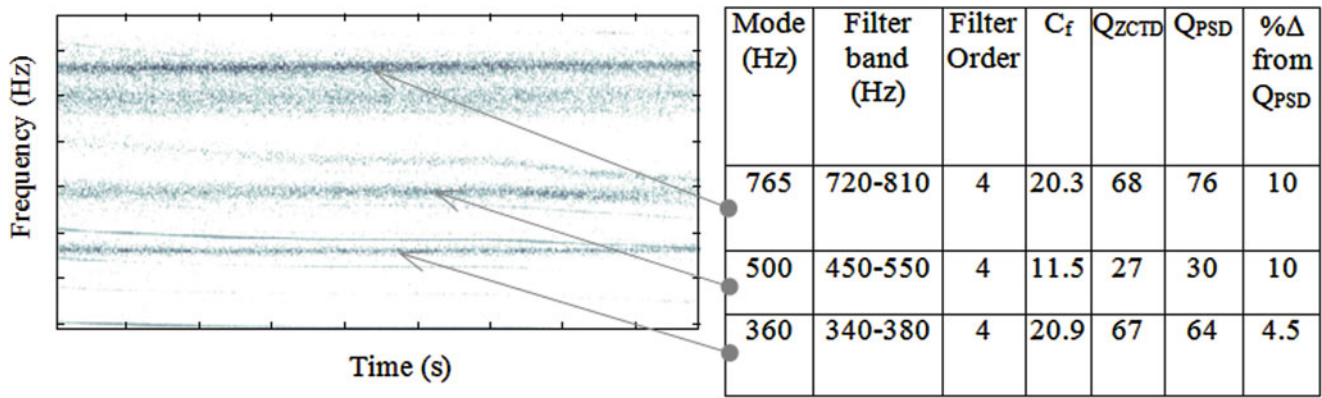


Fig. 24.7 Zmod showing target modes, and, comparison of damping estimations from time-separation distribution and standard PSD SDOF curve fit methods

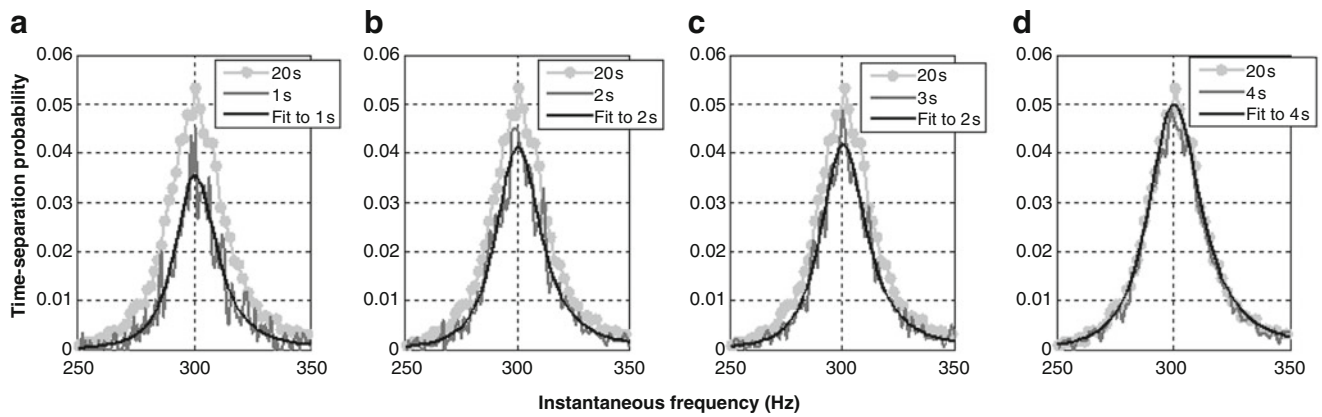


Fig. 24.8 Sensitivity of Time Separation damping estimation methods to time-domain data length used

24.2.8 Sensitivity of Time-Separation Method to Data Length

Sensitivity of time separation damping estimation method to signal length used in construction of time-separation distribution is also investigated. For this purpose an SDOF system with a natural frequency of 300 Hz is excited by a random input and simulated for a 20 s period. Figure 24.8 shows damping estimates from 1, 2, 3 and 4 seconds-long segments taken from this simulation. Also shown on these plots is the original distribution for whole 20 s of simulation. It is evident from distribution and subsequent damping estimates that 1 s segment does not capture the process accurately. However, as the segment length is increased distribution converges very rapidly to original distribution with 4 s segment providing near full convergence.

24.2.9 Effect of Signal Length on Damping Estimation – Operational Data

Dependency of damping estimations to length of signal used is investigated on the same engine data used in Sect. 24.2.6. For this purpose the mode at 765 Hz is used. Data samples of 10, 5, 2, 1 and 0.5 s are evaluated by time-separation distribution and the standard PSD curve fitting methods. Estimates for natural frequencies and damping values are given in Table 24.6. As the signal lengths get shorter, PSD based method deviates from expected value significantly whilst time-separation estimates are always within 10%.

Table 24.6 Effect of signal length on damping estimation by PSD and time-separation

Sample size	ω_{TS} (Hz)	Q_{ZCTD}	% dev from Q_{Exp}	ω_{PSD} (Hz)	Q_{PSD}	% dev from Q_{Exp}
10 s	763.1	85	-7.6	764.5	84	-6.3
5 s	763.4	86	-8.9	764.8	94	-19.0
2 s	762.6	75	5.1	763.8	85	-7.6
1 s	762.5	73	7.6	762.7	49	38.0
0.5 s	761.1	76	3.8	759.8	148	-87.3

24.3 Discussion and Concluding Remarks

Obtaining reliable damping estimates from real engine running measurements is very difficult. Responses acquired are often non-stationary due time-dependent running conditions. In addition the forcing functions are complicated and not precisely known. In the absence of input force data, estimates obtained are a function of response amplitude at which they are extracted and are only valid at those amplitudes. The argument here is that this may be acceptable from practical assessment point of view if these amplitudes can be assumed to be representative of the normal operating conditions. Nevertheless, the absence of precise forcing measurements requires that certain assumptions will have to be made about the character of the forcing to enable calculation of damping estimates. In this paper the focus is on the broadband random vibration measurements.

This paper is dedicated to a new damping estimation method operating on broadband random vibration response and utilising Rice distribution of zero-crossing time intervals. This method is particularly important since it provides estimates that are independent of the way in which PSD based estimates are obtained. As such it is very useful in verifying estimates and gaining confidence in damping values produced. Nevertheless its application is less straight forward. The method is derived empirically for a practical range of damping values. Care should be taken to ensure it is being applied within the boundaries of its scope. As the method is applicable to mono harmonic signals, it is almost always preceded by narrow-band filtering to isolate the mode of interest. Narrowband filtering is shown to have significant effects on zero-crossing distribution; however, a means of accounting for this effect is also given. The performance of the method on laboratory and operational data is compared with that of PSD-based and line-fit methods and a good correlation is obtained. It is shown to outperform PSD-based methods when suitable signal durations are short, providing reasonable estimates for signals that are up to an order of magnitude shorter. The effort made here amounts to first attempt at exploring applicability of this method. More work is needed to extend its reach to a much wider damping range (i.e. very low and very high) as well as reducing its sensitivity to narrow-band filtering.

Acknowledgement The author is grateful to Rolls-Royce plc. for giving permission to publish this work. The author is also grateful to Dr. H. Kurt-Elli whose original work has provided the foundation for this publication, and, to Dr. Christoph Schwingshackl for his help with the laboratory tests.

References

1. Newland, D.E.: An Introduction to Random Vibrations, Spectral & Wavelet Analysis, 3rd edn. Dover Publications Inc. Mineola, NY (2005)
2. Marquardt, D.: An algorithm for least-squares estimation of nonlinear parameters. *SIAM J. Appl. Math.* **11**(2), 431–441 (1963)
3. Rorabaugh, C.: *Digital Filter Designer's Handbook*. McGraw Hill, New York, NY (1993)
4. Rice, O.S.: Mathematical analysis of random noise. *Bell Syst. Tech. J.* **24**(1), 46–156 (1945)



Chapter 25

A Case Study for Integrating Comp/Sim Credibility and Convolved UQ and Evidence Theory Results to Support Risk Informed Decision Making

G. Orient, V. Babuska, D. Lo, J. Mersch, and W. Wapman

Abstract A case study highlighting the computational steps to establish credibility of a solid mechanics model and to use the compiled evidence to support quantitative program decisions is presented. An integrated modeling and testing strategy at the commencement of the CompSim (Computational Simulation) activity establishes the intended use of the model and documents the modeling and test integration plan. A PIRT (Phenomena Identification and Ranking Table) is used to identify and prioritize physical phenomena and perform gap analysis in terms of necessary capabilities and production-level code feature implementations required to construct the model. At significant stages of the project a PCMM (Predictive Capability Maturity Model) assessment, which is a qualitative expert elicitation based process, is performed to establish the rigor of the CompSim modeling effort. These activities are necessary conditions for establishing model credibility, but they are not sufficient because they provide no quantifiable guidance or insight about how to use and interpret the modeling results for decision making. This case study describes a project to determine the critical impact velocity beyond which a device is no longer guaranteed to function. Acceleration, weld failure and deformation based system integrity metrics of an internal structure are defined as QoIs (Quantities of Interest). A particularly challenging aspect of the case study is that predictiveness of the model for different QoIs is expected to vary. A solid mechanics model is constructed observing program resource limitations and analysis governance principles. An inventory of aleatory, computational and model form uncertainties is assembled, and strategies for their characterization are established. Formal UQ (Uncertainty Quantification) over the aleatory random variables is performed. Validation metrics are used to evaluate discrepancies between model and test data. At this point, the customers and the CompSim team agree that the model is useful for qualitative decisions such as design trades but its utility for quantitative conclusions including demonstration of compliance with requirements is not established. Expert judgment from CompSim SMEs is elicited to bound the effects of known uncertainties not currently modeled, such as the effect of tolerances, as well as to anticipate unknown uncertainties. The SME judgement also considers the expected accuracy variation of the different QoIs as recorded by previous organizational history with similar hardware, gaps identified by the PIRT, and completeness of PCMM evidence. Elicitation of the integrated team consisting of system engineering and CompSim practitioners results in quantified requirements expressed as ranges on acceptance threshold levels of the QoIs. Evidence theory is applied to convolve quantitative and qualitative uncertainties (aleatory UQ, numerical, model form uncertainties and SME judgement) resulting in belief and plausibility cumulative distributions at several impact velocities. The process outlined in this work illustrates a structured, transparent, and quantitative approach to establishing model credibility and supporting decisions by an integrated multi-disciplinary project team.

Keywords Computational simulation credibility · Nonlinear structural dynamics · Uncertainty quantification · Evidence theory · Risk informed decision

25.1 Necessary Conditions for Computational Simulation Credibility

Reliance on complex full system multi-physics models in design and qualification phases of programs developing high consequence systems has only relatively recently become a reality. Advances in modeling technologies, especially availability of HPC (High Performance Computing) clusters are enabling factors. As the barriers and cost to computational simulation

G. Orient (✉) · V. Babuska · D. Lo · J. Mersch · W. Wapman
Sandia National Laboratories, Albuquerque, NM, USA
e-mail: georien@sandia.gov

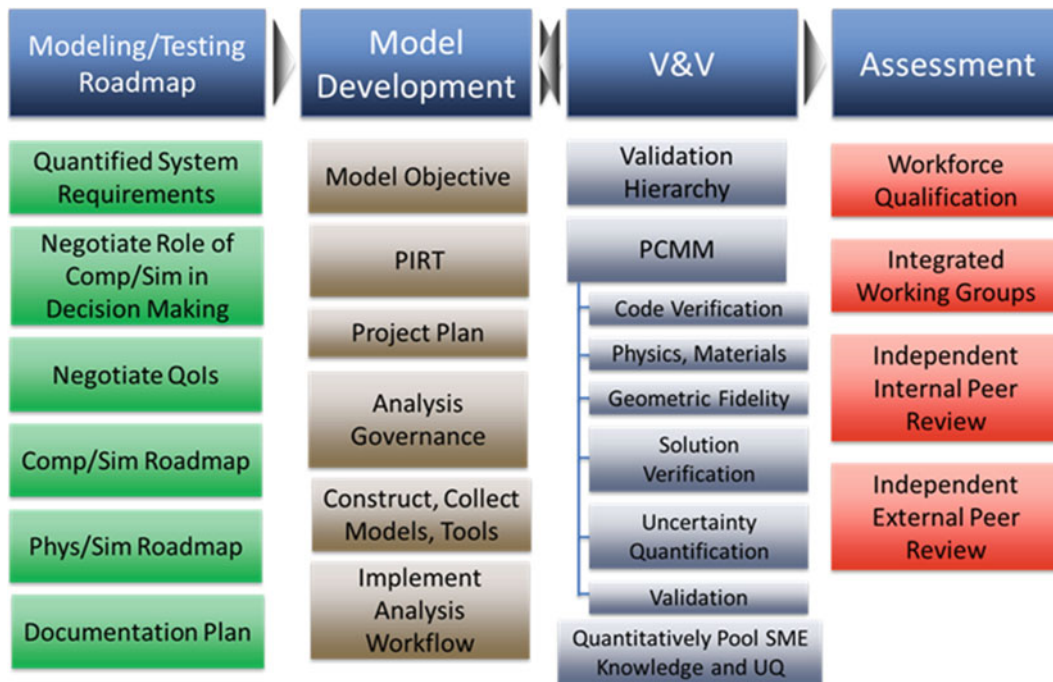


Fig. 25.1 CompSim credibility framework

have drastically reduced, the cost of full system tests has continued to rise, resulting in an increased need for credible simulation models. A practical framework for model credibility assessment is shown in Fig. 25.1.

Traditionally the credibility element of validation and verification (V&V) is by a process health assessment approach such as Technology Readiness Levels, NASA's Credibility Assessment Scale or Sandia National Laboratories' Predictive Credibility Maturity Model (PCMM) [1]. The latter can be viewed as a quality process for CompSim, and it provides a framework to organize credibility evidence in six categories:

Code Verification – Does the analysis code reproduce closed-form results?

Physics and Material Model Fidelity – Are “closure models” (constitutive etc.) credible?

Representation and Geometric Fidelity – Is the geometric abstraction acceptable for the intended use?

Solution Verification – Does the analysis code solve the governing field equations correctly?

Uncertainty Quantification – What is the effect of input uncertainties on QoIs?

Validation – How well do model predictions match experimental data? How does the validation hierarchy support credibility?

The credibility framework provides the necessary conditions for using CompSim results with confidence, however the reality is that not all physics phenomena related to the lifecycle of a mechanical system spanning from fabrication to usage in the field are modeled. Examples may include assembly tolerances, preloads, differences between as designed and as built systems, aging etc. Predicting unit-to-unit variation remains a challenge. The key challenge of credibility is that the mission space is large, system responses are nonlinear and/or discontinuous while experimental data are sparse. The framework needs to be augmented to quantitatively integrate organizational knowledge about the product to assess risk in a quantitative fashion. This will be done through an exemplar to make the process tangible.

25.2 Nonlinear Dynamics Exemplar

Consider crushing a structure as shown in Fig. 25.2. A canister is being crushed between two steel plates, and the system engineers ask the CompSim team to determine the maximum speed of the impactor without Loss of Function (LoF). Only a handful of experiments are planned, and there are fundamental differences between the current and legacy systems. The event is modeled with explicit dynamics FEM approach.

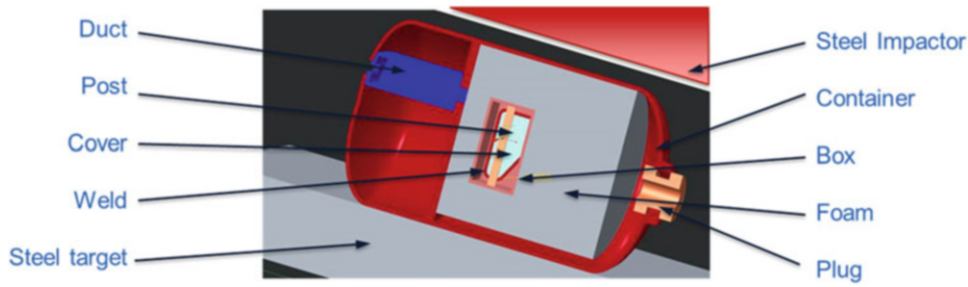


Fig. 25.2 Nonlinear structural dynamics exemplar

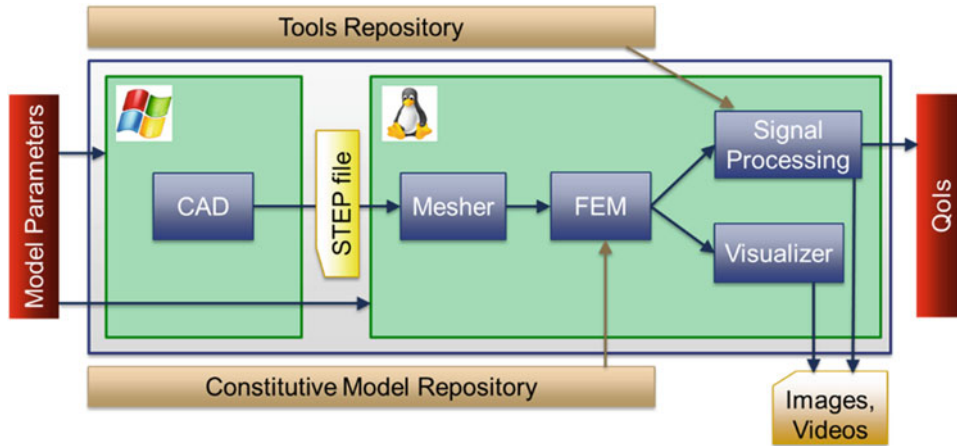


Fig. 25.3 Analysis workflow

The system engineering and the CompSim teams first discuss what loss of function means in this case, and agree on a QoI which is the maximum of the volume averaged acceleration of the part labeled “Post”. This QoI is expected to be noisy, and a signal conditioning approach and its parameters are established.

In the model construction phase a parametric analysis workflow is capable of mapping the model input parameters to QoIs is assembled. This step is critical, since robust parametric execution of the model including post processing is a pre-requisite to UQ. The analysis workflow uses repositories of tools, material data and other sources of institutional knowledge, and it is configuration controlled in an enterprise repository. A notional schema of such analysis workflow is illustrated in Fig. 25.3.

The systems engineering group determines the threshold of concern beyond which function of the device cannot be guaranteed. This is a key part of the process, and it involves mining institutional knowledge about systems similar to the current design. System performance is measured by the predicted amount of margin.

Damage is not catastrophic in a given scenario if

$$M_{QoI} F_{Model} < \frac{R_{QoI}}{F_{Req}} \quad N = \frac{\frac{R_{QoI}}{F_{Req}} - M_{QoI} F_{Model}}{R_{QoI}} > 0$$

M_{QoI} : QoI from Model Response.

F_{Model} : Model Confidence Factor. How accurate is the model? May change as model matures.

R_{QoI} : QoI-Specific Acceptance Requirement.

F_{Req} : Requirement Derating (Confidence) Factor. How well requirements are known? May change as program matures.

N : Normalized Margin; allows comparison of requirements in different units. Positive values indicate criterion is met.

Note that increasing either the model confidence factor of the requirement derating factor will decrease the margin. Two factors are used, since they are determined by different teams. The model confidence factor is owned by the modeling team, while the requirement derating factor is set by the systems engineering team. While this formulation is similar to traditional margin of safety calculations the fundamental difference is that the required factors of safety are determined through many

decades of hardware experience with similar systems. In this case only a handful of experiments are budgeted, similarity with previous systems is ambiguous and the model confidence and requirement derating factors need to be established carefully.

25.3 Uncertainty Quantification

The first step is establishing a quantitative inventory of the “known unknowns”. This is a significant task, and it may involve constitutive and perhaps sub-system experiments. Uncertainties may be classified as aleatory (inherent) and epistemic (lack of knowledge) categories.

Model feature

Constitutive modeling

Model form uncertainty (strain rate dependence, failure model)

Uncertainty within a model form

Interface conditions (friction)

Actual impact velocity, cylinder clocking angle

Signal conditioning parameters (sampling, filtering)

Spatial discretization (mesh)

Numerical uncertainty (processor count, time stepping etc.)

NOT a model feature

Geometric variability within drawing tolerances

Assembly loads

Residual stresses due to welding

Off-spec parts

Subsequently, a UQ method is used to establish a probabilistic lower bound of the normalized margin. The results from an incremental LHS study are shown in Fig. 25.4. The insets at the different impact velocities represent the CDF (Cumulative Distribution Function) of the normalized margin. This Figure implies that impact loss of function didn't occur at impact velocity of v_2 . Additionally, the UQ study provides probabilistic sensitivity metrics such as partial correlation or rank correlation factors that account for both the slope of the response surface and the uncertainty in the input variables. In general, deterministic sensitivity metrics measuring only the slope of the response may be misleading. The order and the sign of the sensitivity metrics for the exemplar were found to change at different impact speeds illustrating why a deterministic worst case cannot be established for all impact velocities.

While UQ is highly informative, and it is an important part of the credibility evidence, several shortcomings must be acknowledged at this point. UQ cannot account for the uncertainties that the model doesn't capture, and it doesn't express (i.e. unknown unknowns) the diversity of SME (Subject Matter Expert) judgment regarding the accuracy of the model.

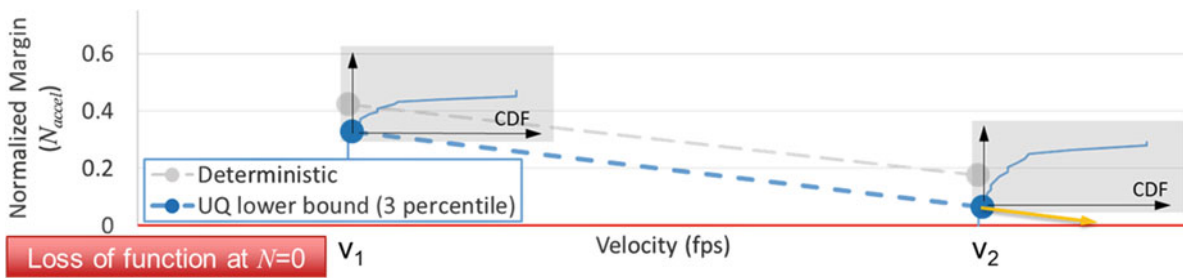


Fig. 25.4 Prediction of loss of function

25.4 Application of Evidence Theory

Evidence theory is a general framework for reasoning with uncertainty, and its results are expressed in terms of belief and plausibility. In practical terms, instead of a single CDF a lower bound (belief) and an upper bound (plausibility) CDF are constructed. In the current use scenario belief/plausibility characterization of loss of function is sought. A panel of SMEs is assembled, and they are asked about their judgment regarding the accuracy of the prediction. Such judgement must be supported by evidence. For example, uncertainty in the acceleration time history may be compared with two physical tests (validation) as illustrated in Fig. 25.5. The evidence shows that the model with uncertainty may underpredict or overpredict the test data. Alternative forms of evidence may be past experiences, results from a solution verification effort such as a mesh convergence study. The panel of experts in this case returned a consistent yet somewhat diverse assessment of the predictiveness of the model. Their assessment representing the state of knowledge is shown in Fig. 25.6.

The two key pieces of information (formal UQ and SME elicitation) can now be combined using a tool that implements the Dempster-Shafer evidence theory algorithm [2] implemented in Dakota [3] to produce belief and plausibility cumulative distributions at each impact velocity. As illustrated on Fig. 25.7 at the lower impact velocity it was found there is a plausibility of about 0.2 of violating the requirements represented by $N < 0$. The belief CDF is entirely above the $N = 0$ line, meaning the device is believed to meet requirements. While the assessment based on only UQ indicated that impact velocity of v_2 is safe, the convolved UQ and SME judgment suggests that even at the lower impact velocity of v_1 there is a plausibility of violating the system requirements.

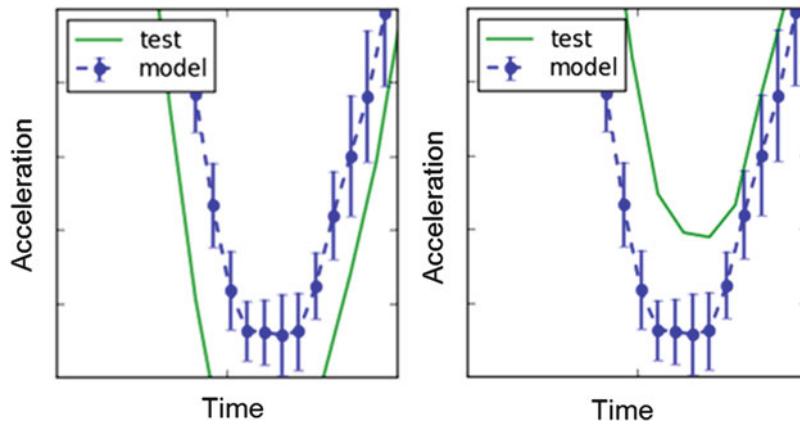


Fig. 25.5 Model validation

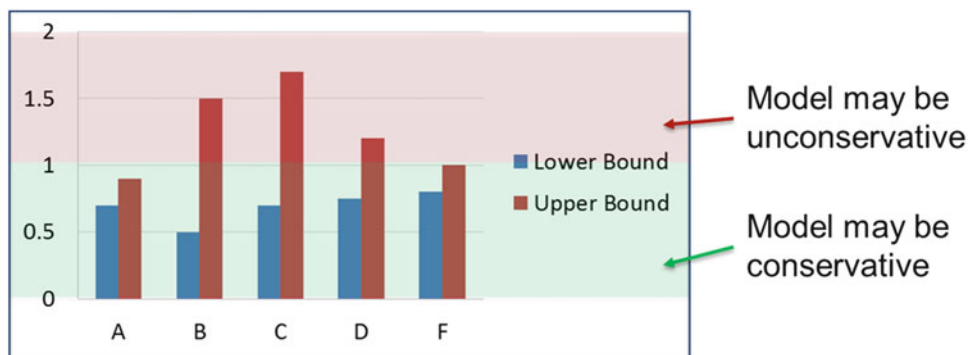


Fig. 25.6 SME panel results

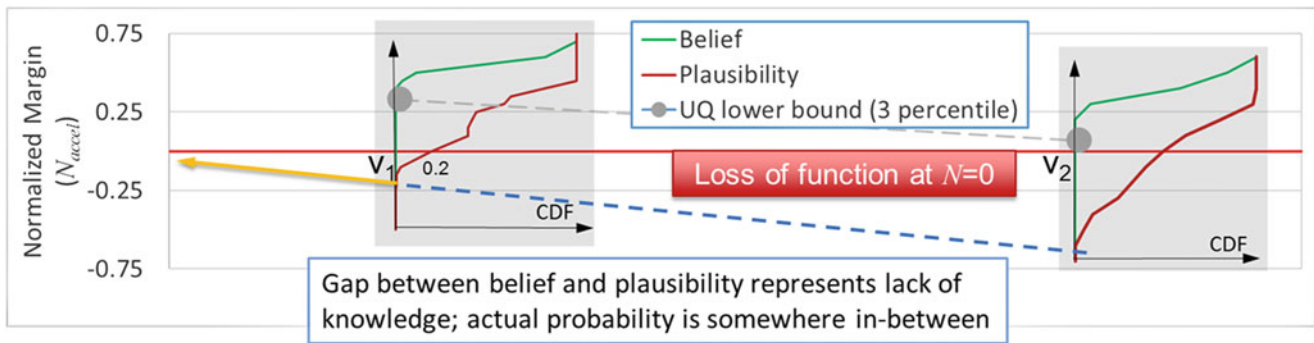


Fig. 25.7 Belief and plausibility of violating system requirements

25.5 Risk Informed Decisions

The integrated system engineering/modeling team can now make risk informed decisions. Several options emerge:

If no plausibility of violating requirements is acceptable search LoF well below v_1 . This may require additional computationally intensive UQ at lower velocities. It may result in unacceptably low threshold velocity for loss of function. Accept plausible negative margin. The belief CDF is indicating no violation of system requirements. Accompanied with a detailed cost analysis this may be an acceptable decision for medium consequence systems.

Redesign the system. If the plausibility of requirement violation is not acceptable, and the overall schedule can absorb this, such decision may be prudent.

Re-evaluate system requirements. Plausibility of violating the requirement was shown, and re-assessing them may be done first. Where did they come from, is their translation into QoI appropriate, what are the historical precedences?

Deep dive into SME judgment. The reason for the separation between belief and plausibility is lack of knowledge expressed by the SMEs in their assessment. Does evidence support their assessment?

25.6 Summary

The standard practices of model credibility such as PCMM provide a body of evidence regarding the suitability of a CompSim model to support high risk program decisions. Uncertainty quantification providing uncertainty estimates of the quantities of interest as well as realistic sensitivity metrics with respect to the model input parameters is part of this evidence package. By eliciting SME judgment relative to the accuracy of the model, and convolving their input with that of formal UQ using evidence theory integrated teams are empowered to make risk informed program decisions. Fundamentally, all the knowledge the organization possesses from material databases characterizing constitutive model uncertainty, fabrication variability to tacit knowledge of experienced system engineers and analysts are unified with this approach to support qualification of high risk engineering systems.

References

1. Oberkampf, W.L., Pilch, M., Trucano, T.: Predictive Capability Maturity Model for Computational Modeling and Simulation SAND2007-5948 Sandia National Laboratories, Albuquerque, NM (2007)
2. Oberkampf, W.L., Helton, J.C.: Evidence theory for engineering applications. Technical Report SAND2003-3559P, Sandia National Laboratories, Albuquerque, NM (2003)
3. Dakota: A Multilevel Parallel Object-Oriented Framework for Design Optimization, Parameter Estimation, Uncertainty Quantification, and Sensitivity Analysis. SAND2014-4633 Sandia National Laboratories, Albuquerque, NM (2017)



Chapter 26

Material Parameter Identification and Response Prediction of Shearing Process for Flying Shear Machine Based on Model Validation

Hongbo Huang, Qintao Guo, Mingli Yu, Yanhe Tao, Yelan Wang, and Ming Zhan

Abstract This paper studies on the simulation of a certain type of flying shear machine's the shearing process. In the finite element simulation, chip formation and cutting ability is not only affected by the high temperature of bar itself and impact velocity of cutter, but also affected by the material itself stress-strain curve under different strain rate and fracture model. Even if the same temperature and impact velocity for high temperature bar, due to the uncertainty of different parameters under different strain rate stress-strain curves, different fracture model, different critical damage factor, the maximum shear force and shear punch depth are not the same. Therefore, in order to obtain a more accurate finite element model and response prediction, it is necessary to identify the uncertainties of the parameters for the material constitutive model and fracture criterion.

According to the principle of equivalent energy, the research group designed a kind of falling hammer punching test rig, and the high temperature (700–900°C) bars of 1Cr18Ni9Ti, $\phi 10$ and $\phi 20$ bars experiments were conducted with multiple groups of shock shear tests. With the aid of the data acquisition instrument, the acceleration parameter of impact shearing process is collected. At the same time, for punching and shearing test numerical simulation was conducted based on nonlinear metal forming finite element analysis.

By $\phi 20$ bars punching test results and simulation results and model updating method, the parameter identification method about stress-strain curve under different strain rate and critical damage factor in material fracture criterion of high temperature bar in punching process is studied. And then the prediction for shearing process of $\phi 10$ was verified by comparing with the test result. After obtaining reasonable and accurate material parameters, for the real flying shear machine, the numerical simulation of $\phi 160$ high temperature bar is carried out under the equivalent impact mass and shear speed. The parameter identification method has practical significance to predict and optimize the shearing performance of different types of flying shear for shearing section steel with different materials and different sections. The results show that: the validation method based on the combination of test data and model updating is effective, which can be applied to discriminate and predict material parameters of similar structures of shearing high temperature bar in engineering.

Keywords Flying shear machine · Shearing test · Nonlinear finite element simulation · Model validation · Response prediction

26.1 Introduction

Flying shear machine is a heavy metallurgical machinery, which is used to shear the bar and plate of transverse movement in continuous production. In order to determine the shear capacity of flying shear, the maximum shear force of materials is mainly calculated by empirical formula in the past. Such as: According to the strength theory, the former Soviet Union M.A.saiikob considered the comprehensive factors of blade clearance, blunt blade, deformation degree, contact friction and so on, shear stress calculation formula is established and verified by experiment [1]; MITSUBISHI heavy industries, Japan's

H. Huang · Q. Guo (✉) · M. Yu · Y. Tao · M. Zhan

College of Mechanical and Electrical Engineering, Nanjing University of Aeronautics and Astronautics, Nanjing, China
e-mail: guo_qintao@nuaa.edu.cn

Y. Wang

Nanjing High Accurate Drive Equipment Manufacturing Group Co., Ltd. ("NGC"), Nanjing, China

IHI company also put forward the corresponding [2, 3] calculation method of shear force and shear moment; Based on a large number of experimental research, the empirical formula and calculation chart including various factors are established by Crasmann, which are used to calculate the shear force under different conditions. On the domestic front, after a lot of test and analysis, Liu Haichang [4] pointed out that the common Nosalia formula of shearing force does not take into account the shear impact in the flying shear force parameter study, and proposed the simple calculating method for calculation of flying shear mechanical parameters; In shear force test and analysis of crank flying shears, in order to obtain the shear force signal of the blade, Xi'an Heavy Machinery Research Institute Li Yanfeng [5] did proper technical improvement, including the temperature compensation and thermal radiation problems, clarified the relationship between shear force and process parameters; The shear energy required for the workpiece is provided by the kinetic energy released by the transmission system and the power of the motor, based on the law of energy conservation, Lu Fu [6] established the shear force calculation model of the four link crank flying shear. The study of shear force and the simulation of shear process are described in the reference above, most of them are based on single experimental study or numerical simulation analysis. Therefore, there is a lack of systematic calibration comparison between simulation and experiment and unable to carry out simulation based prediction.

The innovation of this paper is to use computer finite element technology to simulate the shearing process, and combine model validation technique to provide detailed and reliable mechanical parameters and process parameters for flying shears design and predict the shear process of different sizes, the design of the flying shear would be more convenient and accurate. Zhang [7] fully introduced the validation method of structural dynamics model and its research abroad. Although a lot of research work on model validation has been carried out, this method is still in its initial stage [8], and there are still a lot of key work to be studied, because it's a challenging job to answer how far the computational simulation can describe the objective world.

The main research contents of this paper: in order to verify a certain type of crank flying shear machine performance, as a result of the energy needed to cut the steel per unit area is the same in the process of cutting, research group designed punching test rig with exquisite structure, simple principle, high precision; Based on large deformation commercial finite element software, simplified workpiece-blade model is established for simulation study on the punching process of stainless steel bars, comparing the simulated maximum shear force curve with the experimental data curve under different process parameters to identify the simulation parameters, thus an effective maximum shear force simulation prediction method is obtained.

26.2 Design and Experiment of Punching Test Rig

26.2.1 The Design Principle of Punching Test Rig

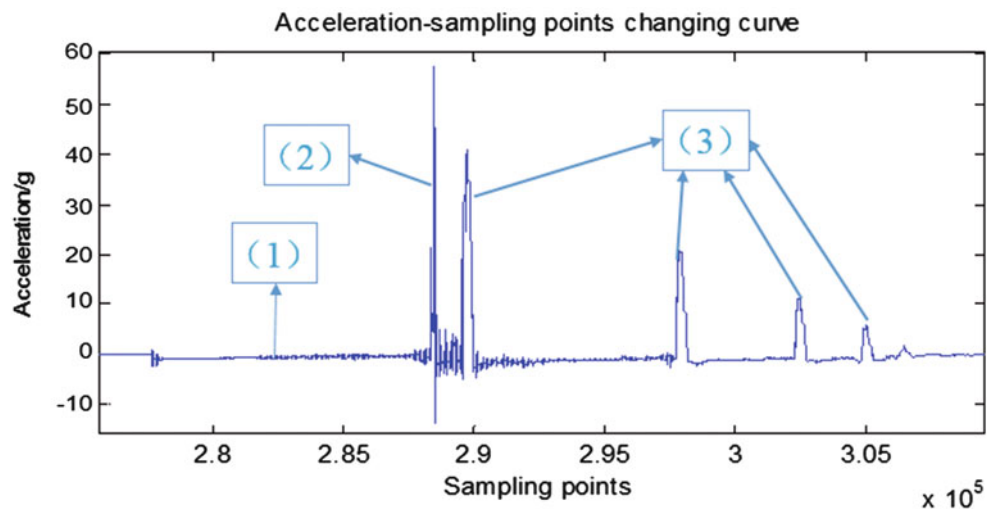
Drop hammer impact test, also called drop weight test, its working principle is to lift a certain weight of heavy hammer to a certain height and free fall, converting the gravitational potential energy of a drop hammer into kinetic energy and impacting test pieces at a certain speed to verify the impact resistance of this workpiece.

Combined with the actual test equipment, in order to ensure the stability and safety of the drop hammer, we need to make sure to drop vertically in the actual falling process, and make the drop impact point and the workpiece force bearing points correct, so we'll have to set up a guide upright column to meet the above requirements. However, the effect of the friction between drop hammer and guide column on the whole impact test should be taken into account. In the drop weight impact test, the foreign researchers carried out a comparative test with a high-speed camera. It is found that the contact velocity between the falling weight and the workpiece is very close to that calculated by the free falling body, the error is less than 5%, so the friction between hammer and guide in the process of falling is very small compared to energy loss of impact so that it can be negligible.

Therefore, the mathematical model of drop hammer impact test is as follows:

$$P = mgh = \frac{1}{2}mv^2$$

In the process of realization, it requires impact hammer falling stably and has higher lead sag to adjust lifting height of drop hammer according to the different acceleration sensor and the impact velocity. At the same time, the safety of operation should be taken into full consideration. Punching test rig is shown in Fig. 26.1:

Fig. 26.1 Punching test rig**Fig. 26.2** Acceleration-sampling points changing curve

26.2.2 Test Result of Punching Test Rig

Figure 26.2 shows the acceleration-sampling point signal collected by the acceleration sensor in the process of punching and shearing:

From the Fig. 26.2, the punching process is divided into three phases:

1. Glide stage: the initial acceleration is g , because of the resistance of sliding bearing, the acceleration decreases gradually;
2. Shear stage: the cutter begins to shear the bar, the shear blade is subjected to the reverse acceleration, and the speed of the blade decreases sharply;
3. Rebound stage: after cutting the bar, the shear blade hit the damping pad, gradually rebound, and slow down until stop;

26.3 Punching Simulation of Commercial Finite Element Software

26.3.1 Introduction of Commercial Finite Element Software

Large deformation commercial finite element software is a highly modular and integrated finite element simulation system, which mainly includes three modules: preprocessor, simulator and postprocessor:

Preprocessor: mainly consists of three sub modules:

1. Data input module, which is convenient for interactive input of data. For example, initial conditions such as initial velocity field, temperature field, boundary condition, punch stroke and friction coefficient;
2. Automatic partition and automatic repartition module of grid;
3. The data transfer module: After remeshing, the data of stress, strain, velocity field and boundary condition can be transferred between the old and new meshes, so as to ensure the continuity of calculation.

Simulator: true finite element analysis process is completed in the simulation of the processor, when running, firstly through the finite element discretization, equilibrium equation, constitutive relation and boundary conditions are transformed into a set of nonlinear equations, and then through the direct iteration method and Newton-Raphson method to solve the problem, save the results in binary form and the user can obtain the required results in the post processor.

Post processor: the postprocessor is used to display the calculation results, the result can be graphic form, can also be a digital text mixed form, the results obtained can be each step's the finite element mesh; equivalent stress, equivalent strain; velocity field, temperature field and pressure stroke curve.

26.3.2 Rigid Plastic Finite Element Method

26.3.2.1 Basic Assumptions of Rigid Plastic Materials and Rigid Plastic Finite Element Principle

For the actual metal plastic forming process, the elastic deformation part is far less than the plastic deformation, its elastic deformation can be ignored, so the material model is simplified as the rigid plastic model. Some processes in the deformation are idealized so that they can be dealt with mathematically. In this case, the material should meet the following assumptions:

1. Ignoring the elastic deformation of materials;
2. The deformation flow of materials obeys the flow law of Levy-Mises;
3. The material is homogeneous isotropic;
4. The material satisfies the volume incompressibility;
5. Ignoring the volume force and inertia force;
6. The boundary between the rigid zone and the plastic zone is given by the loading condition;

26.3.2.2 Fundamental Equations for Rigid Plastic Finite Element Analysis

When the plastic deformation occurs, the rigid plastic material should satisfy the following basic equation [9]:

1. Equilibrium equation

$$\sigma_{ij,i} = 0 \quad (26.1)$$

2. Velocity-strain rate relation

$$\dot{\epsilon}_{ij} = \frac{1}{2} (v_{i,j} + v_{j,i}) \quad (26.2)$$

3. Constitutive equation

$$\dot{\epsilon}_{ij} = \dot{\lambda} \sigma'_{ij} \quad \dot{\lambda} = \frac{3}{2} \frac{\dot{\bar{\epsilon}}}{\bar{\sigma}} \quad (26.3)$$

here: $\bar{\sigma} = \sqrt{\frac{3}{2}(\sigma'_{ij}\sigma'_{ij})^{1/2}}$ is equivalent stress; $\dot{\bar{\epsilon}} = \sqrt{\frac{3}{2}(\dot{\epsilon}_{ij}\dot{\epsilon}_{ij})^{1/2}}$ is equivalent strain rate;

4. Mises yield condition

$$\bar{\sigma} = f(\bar{\epsilon}, \dot{\bar{\epsilon}}, T) \quad (26.4)$$

5. Volume incompressible condition

$$\dot{\epsilon}_V = \dot{\epsilon}_{kk} = 0 \quad (26.5)$$

6. Stress boundary conditions and Velocity boundary conditions

$$\begin{aligned} \sigma_{ij}n_j &= \bar{p}_i \quad S \in S_p \\ v_i &= \bar{v}_i \quad S \in S_v \end{aligned} \quad (26.6)$$

For a rigid plastic boundary value problem, in all admissible velocity fields satisfying geometric equations, volume incompressible conditions and velocity boundary conditions, its real solution makes functional (26.7) obtain stationary value,

$$\Pi = \int_V \bar{\sigma} \dot{\bar{\epsilon}} dV - \int_{S_p} p_i v_i dS \quad (26.7)$$

That is, the first order variation is zero.

The penalty function method is used to introduce the volume incompressible condition into the functional and form a new functional:

$$\Pi = \int_V \bar{\sigma} \dot{\bar{\epsilon}} dV + \frac{\alpha}{2} \int_V (\dot{\epsilon}_{ij} \delta_{ij})^2 dV - \int_{S_p} p_i v_i dS \quad (26.8)$$

When the function is stationary, the equation is a nonlinear function of velocity, and Newton-Raphson is used to linearize the equation. Finally, the solution of the deformation of a cell can be obtained by the stationary value of the corresponding functional:

$$[S]_{n-1}^e \{\Delta u\}_n^e = \{R\}_{n-1}^e \quad (26.9)$$

Each element of the element stiffness matrix $[S]_{n-1}^e$ and element load matrix $\{R\}_{n-1}^e$ is filled into the corresponding position of the whole stiffness matrix $[S]_{n-1}$ and the whole load matrix $\{R\}_{n-1}$ according to the node number, the basic equation of rigid plastic finite element for solving the whole deformation domain is obtained:

$$[S]_{n-1} \{\Delta u\}_n = \{R\}_{n-1} \quad (26.10)$$

26.3.2.3 Fracture Criterion

In the process of punching shear, the material is subjected to shear separation in the plastic deformation state, and the tensile stress in the shear zone at the later stage of deformation leads to fracture. This paper uses Normalized Cockcroft & Latham fracture criterion in finite element simulation analysis [12], corresponding formula is:

$$\int_0^{\bar{\epsilon}_f} \frac{\sigma_1}{\bar{\sigma}} d\bar{\epsilon} = C \quad (26.11)$$

where:

σ_1 : Maximum principal stress; $\bar{\sigma}$: Mean stress; $\bar{\epsilon}_f$: The total plastic strain at fracture;
 $\bar{\epsilon}$: Equivalent plastic strain; C: The area after the regularization of stress-strain curve;

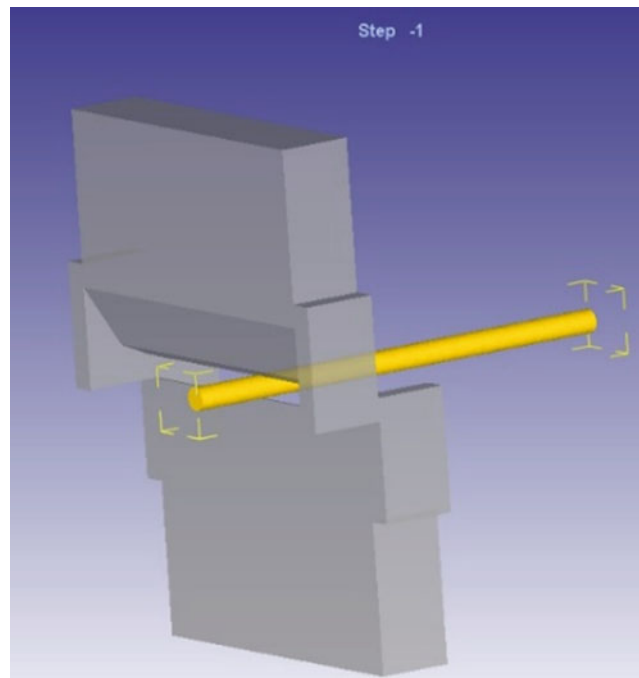


Fig. 26.3 Schematic diagram of simulation model

The Normalized Cockcroft & Latham criterion is obtained by integrating the stress variables along plastic deformation path. It is difficult to obtain the variable values of each point and moment in the tensile test. The critical damage value C of ductile fracture is usually determined through the method of combining simulation with experiment.

26.3.3 Example of Operation Process of Commercial Finite Element Software

Example: The blade and counterweight mass 70 kg are used as the impact mass, the bar diameter is 20 mm, the bar temperature is 882°C, and the height is 850 mm. The finite element simulation is carried out. The operation process is as follows:

Firstly, import model obtained through other CAD/CAE software into the commercial finite element software system, the geometry model interface format is STL format file. After import, model is shown in Fig. 26.3.

Secondly, meshing and boundary conditions set: in finite element software, if the mesh subdivision program is used, only tetrahedral element can be obtained, this is mainly to consider the convenience and shortcut of remeshing. But it also receives the hexahedral mesh generated by the external program. The mesh can control the density of the grid, reduce the number of the grid further, and do not cause serious grid distortion in the region of severe deformation, such as Fig. 26.4 (Table 26.1).

The simulation parameter settings of this example are shown in Table 26.2.

After the simulation operation, click the DB file on the main control interface and enter the post-processing interface in the Post Processor column. The stress nephogram of the workpiece and the stroke load curve of the upper blade can be obtained.

It can be seen from Fig. 26.5: The blade and the counterweight 70 kg as the impact of quality, bar diameter is 20 mm, temperature is 882°C, height is 850 mm, impact finite element simulation begins. Taking Normalized Cockcroft&Latham fracture criterion critical damage factor 0.45. In the seventy-second step of simulation iteration, the hammer energy consumption is complete, and the $\Phi 20$ bar is not sheared fully. In shearing process, the maximum effective stress reached 347 MPa, the maximum shear force on the blade is about $5.69e + 4$ N, the blade punching depth is 14.3 mm.

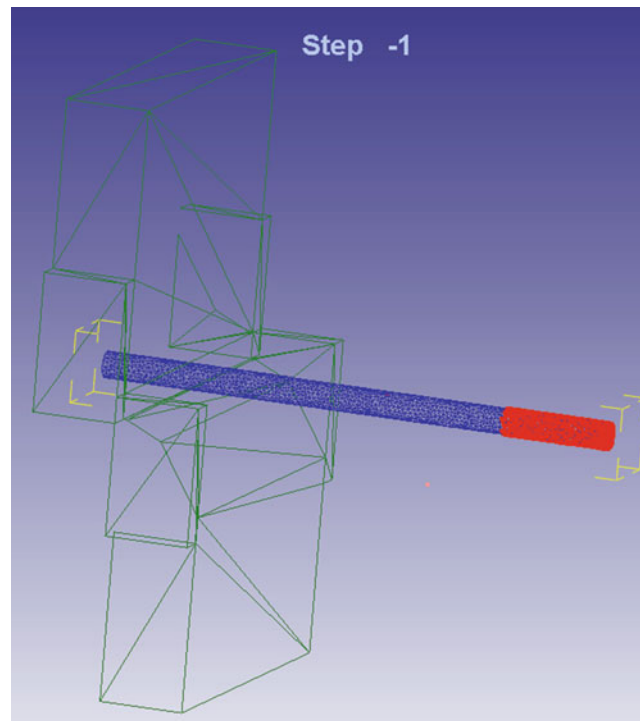


Fig. 26.4 The mesh and boundary conditions

Table 26.1 The mesh and boundary conditions

Mesh and boundary conditions	Result
The number of nodes	5082
The number of elements	20,966
Boundary conditions	Limiting the radial motion of one end of the bar

Table 26.2 Parameter setting table for numerical simulation

Thirdly: Simulation parameter setting

Finite element simulation property	Corresponding settings
Bar diameter	20 mm
Bar material	AISI.304
Bar temperature	882 °C
Material constitutive model	$\bar{\sigma} = \bar{\sigma}(\bar{\varepsilon}, \dot{\bar{\varepsilon}}, T)$
Material yield function	Von Mises
Fracture criterion	Normalized Cockcroft&Latham
Critical damage value	0.45
Friction coefficient between cutter and bar	Hot forging(dry)0.7
Equivalent cutter quality	70 kg
Total energy	583,100 N mm
Step length	0.2 mm
Iteration steps	130

Fourth: Simulation results

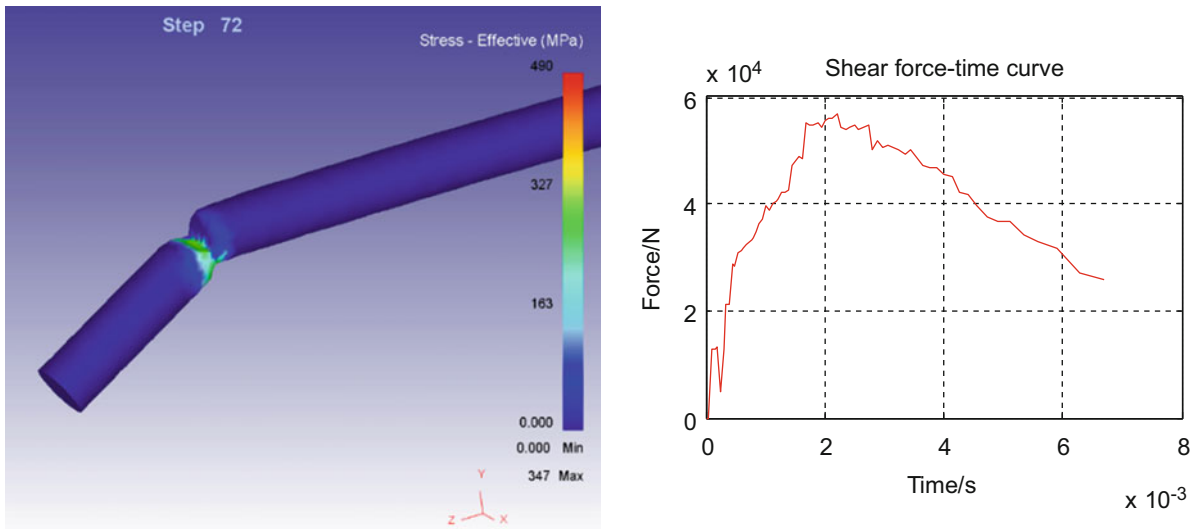


Fig. 26.5 Simulation result chart

26.4 Model Updating Based on Response Surface Methodology

26.4.1 Finite Element Model Updating Theory Based on Response Surface Methodology

In order to obtain an accurate finite element simulation model, the response surface model updating method [10, 11] is proposed. The polynomial response surface model is constructed by using the parametric model and the full factorial design, the polynomial coefficient is determined by the least square method and the fitting accuracy of the response surface is tested. The objective function is constructed by the error between the calculated results and the experimental results, and the response surface is fitted to identify the influencing factors, the modified parameter is taken into the finite element model and the accurate model is obtained.

The basic function of the response surface is to describe the implicit functional relationship between the design variables and the response variables of the computational model, according to the test design method of response surface, the best response surface design sample point need to be selected to ensure that the whole design space covers all the working conditions of the project. Meanwhile, the choice of better response surface fitting method is also one of the important contents of response surface modeling. So far, the method of establishing response surface model is mainly divided into interpolation class and regression class method, as well as artificial neural network and radial basis function with different degrees of regression and interpolation fitting by special methods, Gauss process response surface and so on. The commonly used response surface inspection criteria are shown in Table 26.3.

Among them, y , y_{rsm} , N were response truth values, response surface prediction values, response surface design points, respectively. The size of the $RMSE$ represents the accuracy of the response surface, according to the actual circumstances, $RMSE = 0.01$ indicates that the difference between truth and response surface is about 1% of the average amplitude; R^2 reflect reflects the overall difference between truth value and response surface, Its numerical value is the scalar value between 0~1, the higher the R^2 value is, the higher the prediction accuracy of the response surface will be; MSE and EISE are similar to RMSE, but no obvious physical significance like $RMSE$.

26.4.2 Examples: Finite Element Model Updating of Punching Structure Based on Response Surface Methodology

It can be seen by the parameter setting Table 26.2 in the numerical simulation of Sect. 2.3, The parameters affecting the simulation model mainly include:

1. Stress-strain curves of bars (as shown in Fig. 26.6) influence factor μ (assuming that the allowable curve has a linear error of up to 10%);
2. Fracture criterion and materials critical damage value C ;

Taking impact the quality of 70 kg, bar diameter 20 mm, temperature 882°C, punching test impact height 850 mm as an example, impact coefficient of the stress-strain curves is 0.975, critical damage value C is 0.18, The punching structure finite element model updating analysis process based on response surface methodology is as follows:

26.4.2.1 Fitting Gauss Curve of Test and Simulation Data Points

The test data points and the simulation data points are fitted by MATLAB’s cftool tool Gaussian curve, as shown in Fig. 26.7: The evaluation index of fitting curve is shown in Table 26.4:

Table 26.3 Common inspection criteria of response surface

Inspection criteria	Corresponding formula
1 RMSE	$\sqrt{\sum_N (y - y_{rsm})^2 / (N \cdot \bar{y})}$
2 R ²	$1 - \frac{\sum_{j=1}^N (y_{rsm}(j) - y(j))^2}{\sum_{j=1}^N (y_{rsm}(j) - \bar{y})^2}$
3 MSE	$\sum_N (y - y_{rsm})^2$
4 EISE	$\sum_N (y - y_{rsm})^2 / N$

Fig. 26.6 Stress-strain curve

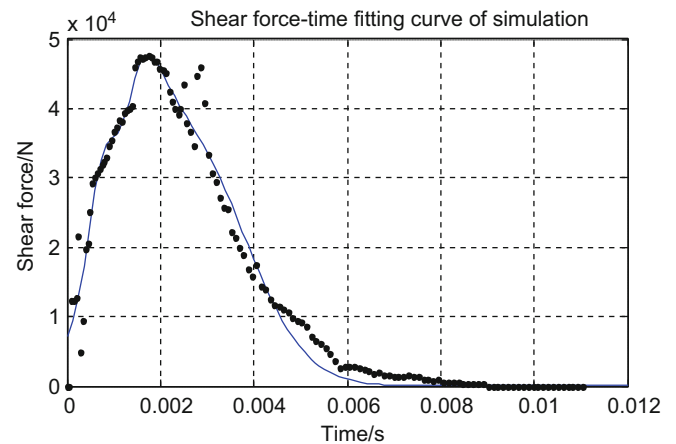
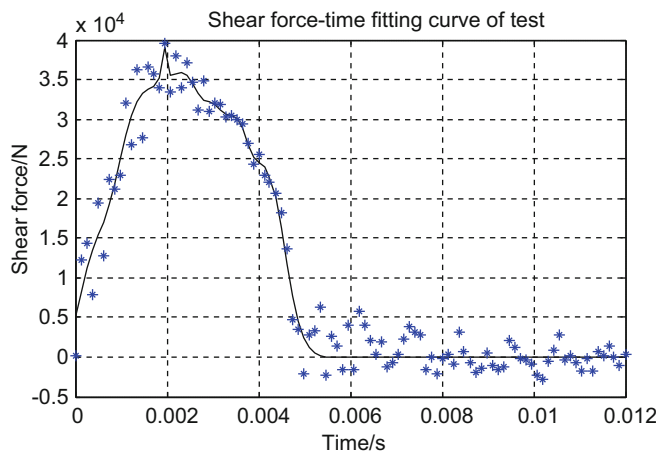
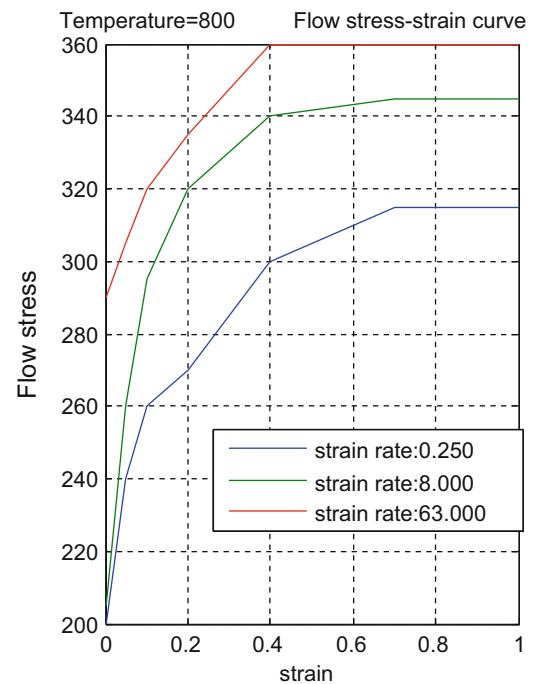


Fig. 26.7 Shear force-time fitting curve of test and simulation

Table 26.4 Fitting curve evaluation index

	Test fitting curve	Simulation fitting curve
SSE	5.429e + 08	9.266e + 08
R-square	0.9721	0.9765
Adjusted R-square	0.9637	0.9737
RMSE	2673	2814

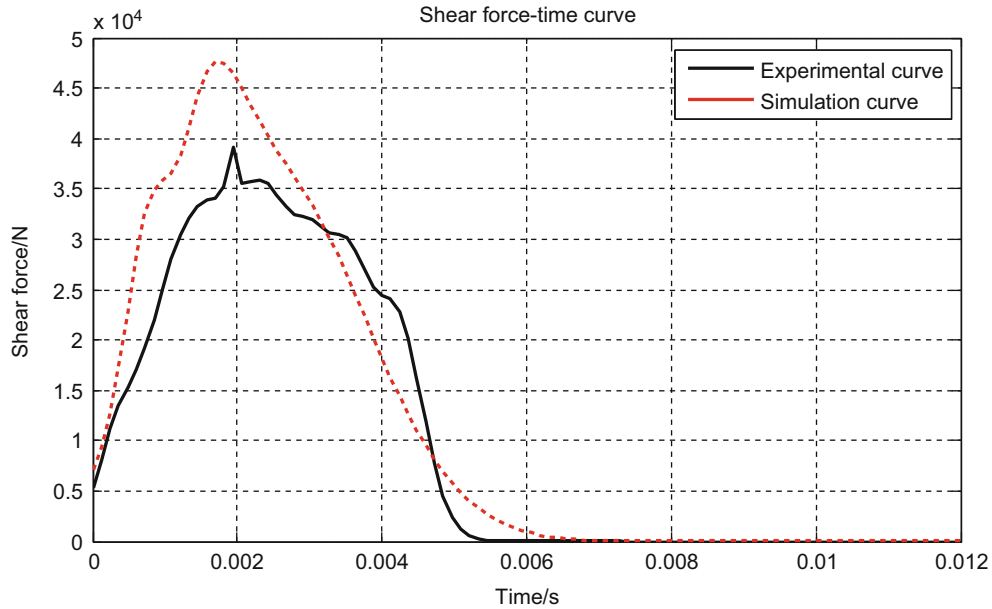


Fig. 26.8 Comparison of fitting curves

Table 26.5 Calculation results of RMS under different influencing factors

$\mu \backslash C$	0.12	0.15	0.18	0.21	0.24	0.27	0.30	0.33
0.9	11,395	8954	7651.9	5948.8	5792.8	7979.4	11,351	17,095
0.925	10,596	8337.8	6353.9	5739.8	6001.6	11,191	13,095	16,825
0.95	9593.7	8111.1	6233.7	6536.3	7738.7	10,213	14,637	17,095
0.975	10,633	7787.8	5777.6	6688.9	8572.3	6591.3	13,823	18,659
1	10,896	7424.1	6985.2	7094	6740	9561.4	9688.3	10,851
1.025	10,829	7848.8	7069.6	7505.3	7724.6	8909.3	8478.9	17,761
1.05	10,578	7111.6	7455.1	7864.8	13,400	15,439	16,454	20,559
1.075	10,846	8924.2	8611.2	10,111	12,426	18,512	19,707	15,821
1.1	10,506	9050.6	7673.1	8772	11,975	14,096	20,021	19,696

26.4.2.2 Establishment of Evaluation Index and Response Surface for Test and Simulation Curve Matching

Definition of test and simulation curve (see Fig. 26.8) matching degree evaluation index RMS:

$$RMS = \sqrt{\frac{\sum_{i=1}^N (y_i - n_i)^2}{N}} \tag{26.12}$$

The full factor test design method is used to determine the influence factor of stress-strain curve and the critical damage value. The results are listed in Table 26.5.

According to Table 26.5, the response surface is obtained by MATLAB cftool tool fitting surface, as shown in Fig. 26.9: Evaluation index of fitting response surface: SSE: 7.229e + 07; R-square: 0.9396; Adjusted R-square: 0.9309; RMSE: 1080.

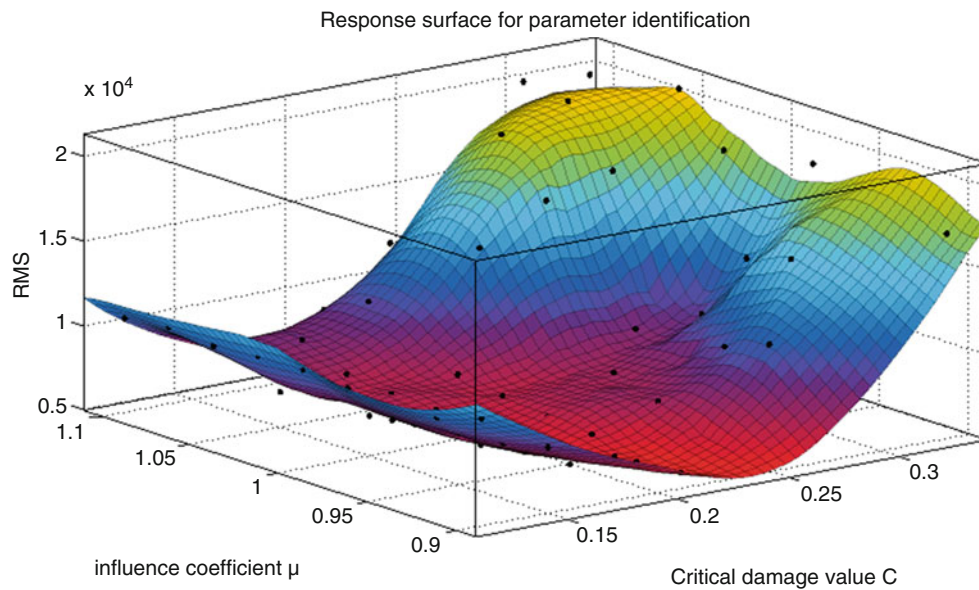


Fig. 26.9 Response surface for parameter identification

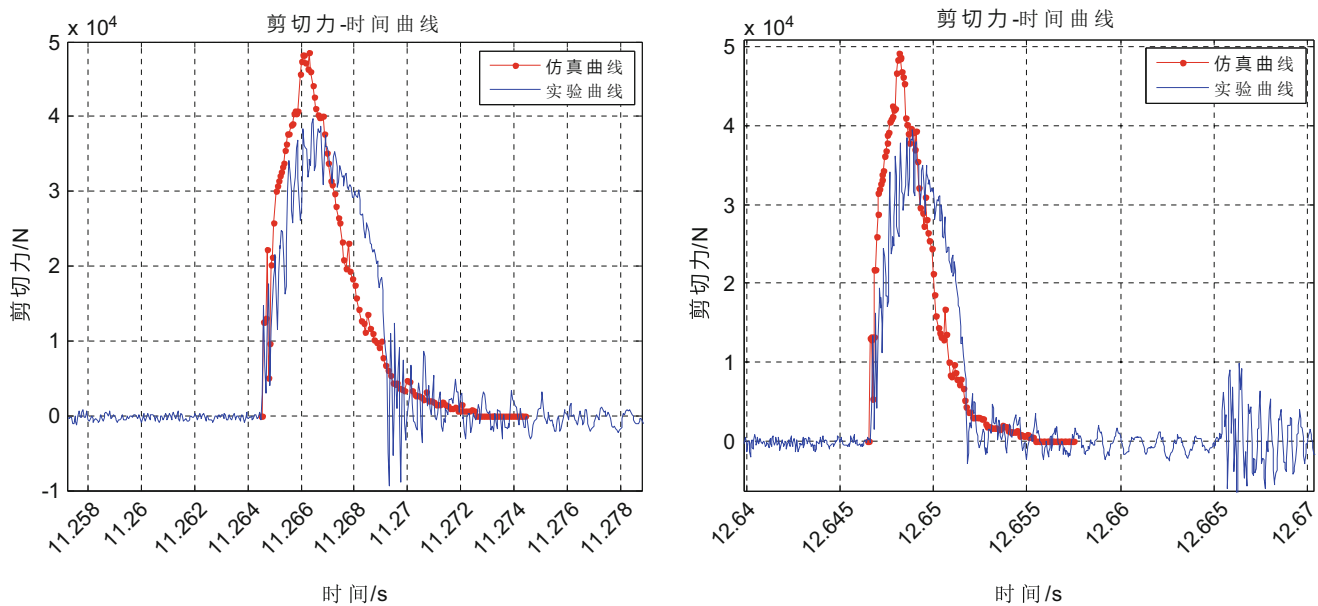


Fig. 26.10 Shear force-time curve ($\Phi 20$ mm_882 $^{\circ}$ C_850 mm/20 mm_857 $^{\circ}$ C_800 mm)

26.4.3 Comparison of Shear Force Curves

After the study and adjusting the simulation parameters, model updating based on response surface methodology, it can be found that the fracture criterion Normalized Cockcroft & Latham has the greatest influence on the shear results. Comparison between the results of multi group test and simulation shows that the Normalized Cockcroft & Latham fracture criterion damage factor value is 0.18, stress-strain curve effect coefficient is 0.975, simulation and test agree well.

Several groups simulation and experimental shear force curves are listed below:

As can be seen from Fig. 26.10: by experiment and simulation of the $\varphi 20$ bar, the shear force time history curves are basically consistent, the maximum shear force magnitude is 10^4 N, the punching time is about 0.015 s. Therefore, the simulation results reflect the experimental shear force curve better.

26.4.4 Comparison of Shear Depth and Fracture Quality and Verification of Reliability of Identification Parameters

As shown in Tables 26.6 and 26.7, the shear simulation parameters of the bars with a diameter of 10 mm and 20 mm are given, and the critical damage factor is 0.18, influence factors of stress-strain curve μ is 0.975. The fracture of the simulation and test are shown in Figs. 26.11 and 26.12.

It can be seen from Figs. 26.11 and 26.12 that the fracture shape and depth are basically consistent with experiment and simulation of the $\phi 10$ and $\phi 20$ bars, so the simulation results reflect the quality of the fracture better.

Table 26.6 Table of shear parameters of $\Phi 10$ bar

Group	Bar temperature/ $^{\circ}$ C	Height/mm	Result
N3	630	90	Without fracture
N4	590	140	Fractured

Table 26.7 Table of shear parameters of $\Phi 20$ bar

Group	Bar temperature/ $^{\circ}$ C	Height/mm	Result
N13	752	597	Without fracture
N14	790	600	Without fracture



$\Phi 10$ Fracture-Group N22



$\Phi 10$ Fracture-Group N23

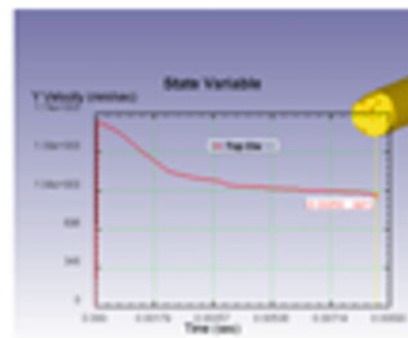
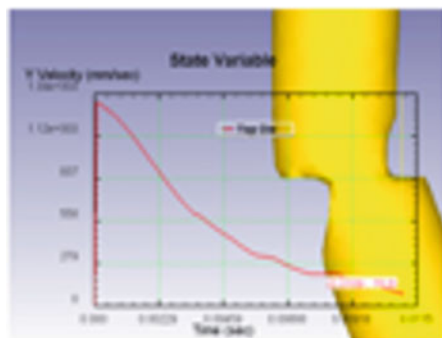


Fig. 26.11 Comparison diagram between $\Phi 10$ bar test and simulation fracture

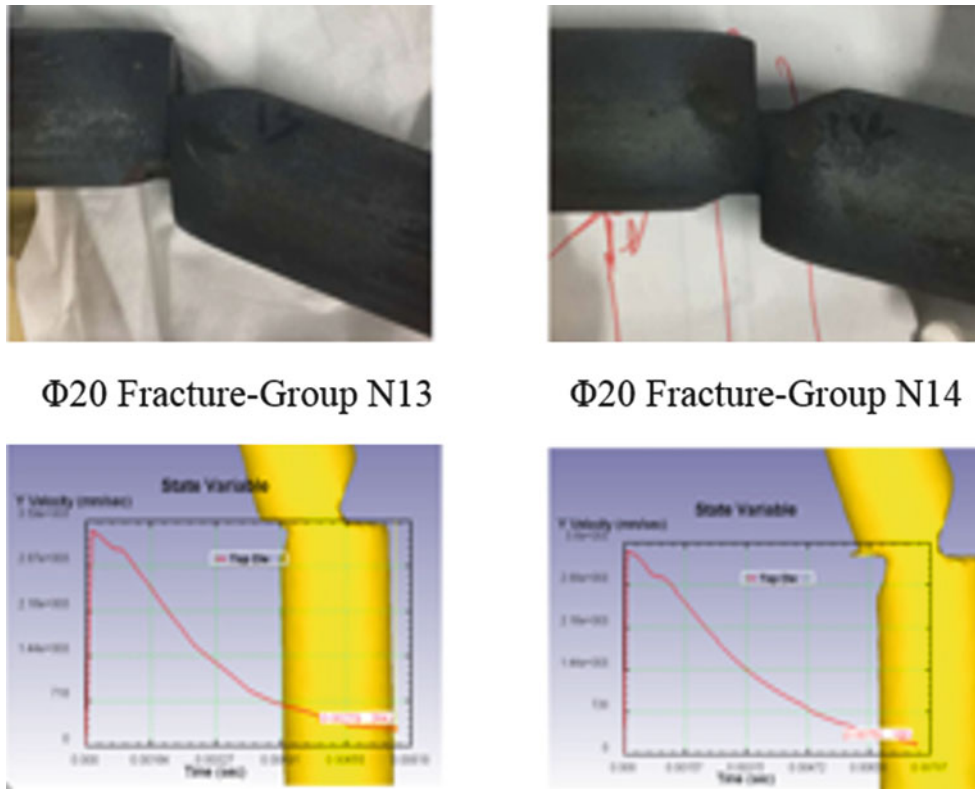


Fig. 26.12 Comparison diagram between Φ20 bar test and simulation fracture

Table 26.8 The mesh and boundary conditions

Mesh and boundary conditions	Result
The number of nodes	12,504
The number of elements	55,675
Boundary conditions	Restrict the radial movement of both ends of bar

Thirdly: Simulation parameter setting

26.5 Response Prediction and Evaluation of Shear Capacity of Φ160 Bar for Real Flying Shear

26.5.1 Response Prediction of Shear Capacity of Φ160 Bar

Example: Flying shear is equivalent to the quality of blade 120 t, which is used as the impact mass, the bar diameter is 160 mm, the bar temperature is 900°C, and the impact velocity is 900 mm/s. The finite element simulation is carried out. The operation process is as follows:

Firstly, import model obtained through other CAD/CAE software into the commercial finite element software system, the geometry model interface format is STL format file. After import, model is shown in Fig. 26.13.

Secondly, meshing and boundary conditions set: in finite element software, if the mesh subdivision program is used, only tetrahedral element can be obtained, this is mainly to consider the convenience and shortcut of remeshing. But it also receives the hexahedral mesh generated by the external program. The mesh can control the density of the grid, reduce the number of the grid further, and do not cause serious grid distortion in the region of severe deformation, the steel is refined by local mesh refinement, such as Fig. 26.14 (Table 26.8).

The simulation parameter settings of this example are shown in Table 26.9.

After the simulation operation, click the DB file on the main control interface and enter the post-processing interface in the Post Processor column. The stress nephogram of the workpiece and the stroke load curve of the upper blade can be obtained.

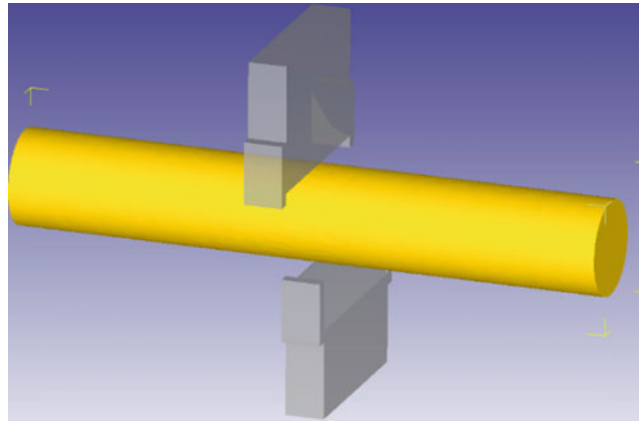


Fig. 26.13 Schematic diagram of simulation model

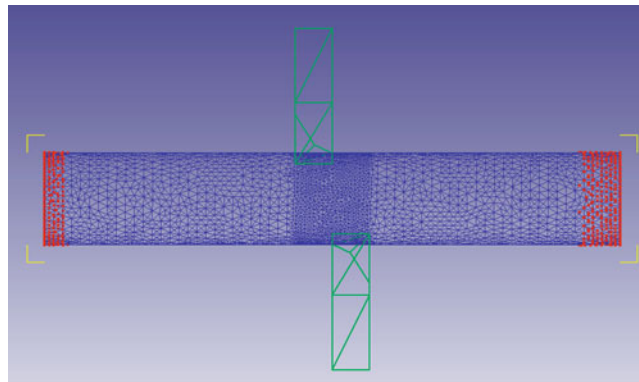


Fig. 26.14 The mesh and boundary conditions

Table 26.9 Parameter setting table for numerical simulation

Finite element simulation property	Corresponding settings
Bar diameter	160 mm
Bar material	AISI.304
Bar temperature	900 °C
Material constitutive model	$\bar{\sigma} = \bar{\sigma}(\bar{\varepsilon}, \dot{\bar{\varepsilon}}, T)$
Material yield function	Von Mises
Fracture criterion	Normalized Cockcroft & Latham
Critical damage value	0.18
Friction coefficient between cutter and bar	Hot forging(dry)0.7
Equivalent cutter quality	125 t
Total energy	1.25e + 08 N mm
Step length	0.5 mm
Iteration steps	330

Fourth: Simulation results

It can be seen from Fig. 26.15: Flying shear is equivalent to the quality of blade 120 t, which is used as the impact mass, the bar diameter is 160 mm, the bar temperature is 900°C, and the impact velocity is 900 mm/s. The finite element simulation is carried out. The maximum shear force is about 2.58E + 6 N, the shear depth is about 33.3 mm, which is not enough to shear the bar.

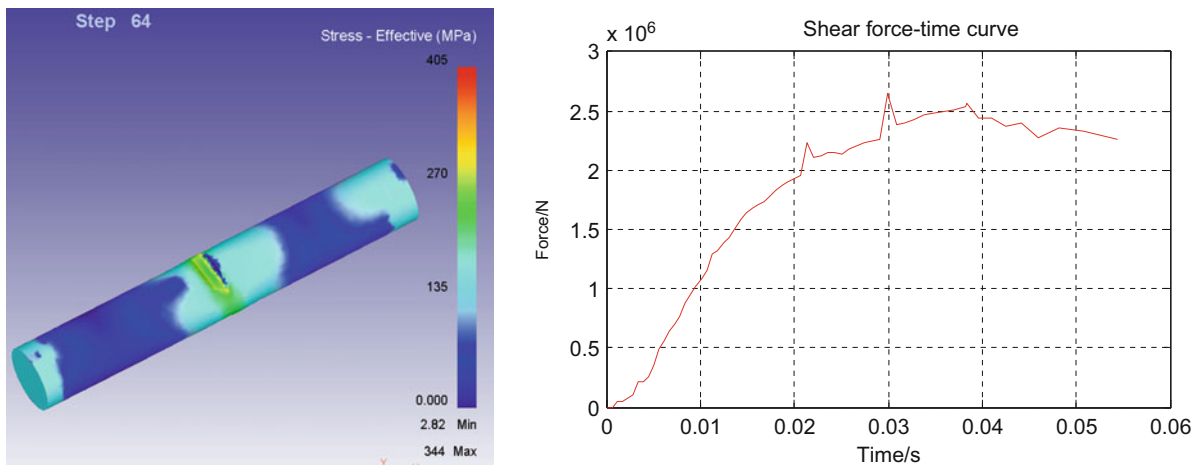


Fig. 26.15 Simulation result chart

26.5.2 Evaluation and Improvement Scheme of Shear Capacity of $\phi 160$ Bar for Real Flying Shear

The simulation results show that the shear capacity of the flying shear in the design stage needs to be improved, so the following improvement scheme is proposed:

1. Adjusting the inertia moment of the flywheel so as to improve the equivalent blade quality of the whole flying shear drive system;
2. The flywheel is adjusted from the low speed stage of the reducer to the high speed stage, so as to improve the equivalent blade quality of the whole flying shear drive system;
3. Adjust the size of the shearing mechanism, so that the blade contact bar earlier, so as to improve the shear speed of the flying shear;
4. In order to improve steel walking speed, the shear speed of flying shear will be increased correspondingly in the case of satisfying the coordination between flying shear process and steel walking speed.

26.5.3 Simulation Example of Improved Scheme

According to the 4.2 section improvement Scheme (2): the flywheel is adjusted from the retarder low speed stage to the reducer high speed stage, the equivalent mass of the transmission system is 228.6 t, and the rest parameters are set the same with the 4.1 section, the simulation results are as follows:

It can be seen from Fig. 26.16: Flying shear is equivalent to the quality of blade 228.6 t, which is used as the impact mass, the bar diameter is 160 mm, the bar temperature is 900° C, and the impact velocity is 900 mm/s. The finite element simulation is carried out. The maximum shear force is about $2.6E + 6$ N, the shearing process takes about 0.15 s.

26.6 Conclusion

By $\phi 20$ bars punching test results and simulation results and model updating method, the parameter identification method about stress-strain curve under different strain rate and critical damage factor in material fracture criterion of high temperature bar in punching process is studied. And then the prediction for shearing process of $\phi 10$ and $\phi 20$ was verified by comparing with the test result. After obtaining reasonable and accurate material parameters, for the real flying shear machine, the numerical simulation of $\phi 160$ high temperature bar is carried out under the equivalent impact mass and shear speed. The parameter identification method has practical significance to predict and optimize the shearing performance of different types

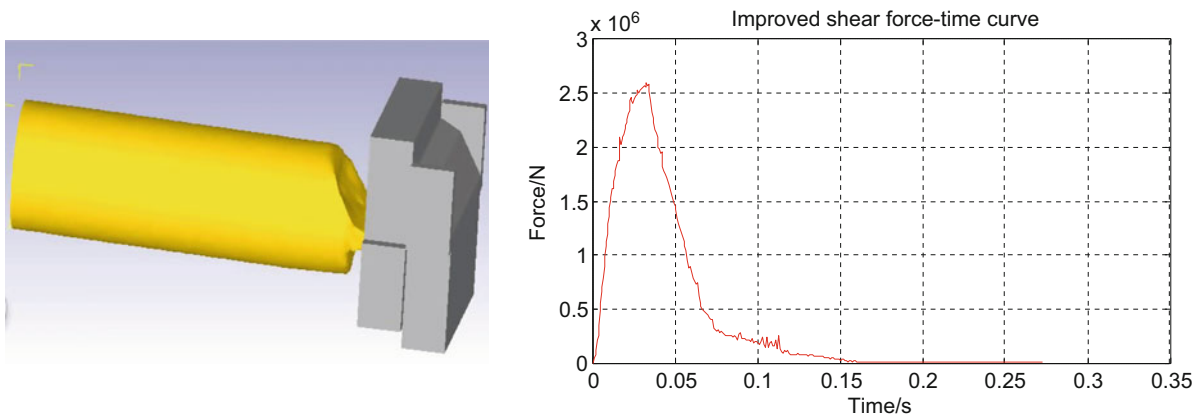


Fig. 26.16 Simulation result chart

of flying shear for shearing section steel with different materials and different sections. The results show that: the validation method based on the combination of test data and model updating is effective, which can be applied to discriminate and predict material parameters of similar structures of shearing high temperature bar in engineering.

References

1. Servo: System improve flying shear process precision. *Des. Fax. Mag.* **18**(11), 55–76 (2003)
2. Faulkner, L.L., Logan Jr., E.: *Handbook of Machinery Dynamics*, pp. 61–89. Marcel Dekker, New York (2001)
3. Bhat, R.B., Dukki Pati, R.V.: *Advanced Dynamics*, pp. 15–78. Alpha Science International Ltd, Pangbouns (2001)
4. Haichang, L., Jianchun, W., Kangqiang, L., et al.: Study on mechanical parameters of flying shear [J]. *China Metall.* **16**(4), 38–39 (2006)
5. Yanfeng, L., Qiang, L., Lvqi, B., et al.: Measurement and analysis of shearing force of four link crank flying shear [J]. *Heavy Mach.* **03**, 38–41 (2001)
6. Fu, L., Zhanfu, C., Weichen, Y. Shear force analysis of four link crank flying shear [J]. *Heavy Mach.* **6**, 43–46 (2009)
7. Ling-mi, Z.: Computational simulation and model validation and their applications in structural environment and strength [J]. *Streng. Environ.* **29**(2), 42–47 (2002)
8. Hemez, F.M., Doebling, S.W: Model validation and uncertainty quantification [A]. *Proceedings of IMAC-XIX [C]*. Kissimmee: The 19th International Modal Analysis Conference.:1153–1158 (2001)
9. Yang, T.: *Modeling and Simulation Analysis of Rigid Plastic Finite Element Modeling of Milling [D]*. Kunming University of Science and Technology, Yunnan (2007)
10. Qintao, G., Lingmi, Z., Qingguo, F.: Response surface method and its experimental design for deterministic computational simulation [J]. *J. Aeronaut.* **27**(1), 55–61 (2006)
11. Qingguo, F., Xiaolin, H., Heling, S.: Implementation and application of response surface finite element model updating [J]. *Vib. Meas. Diagn.* **30**(2), 132–134 (2010)
12. Wenjie, C., Qing, Z., Zhujun, D., et al.: Numerical simulation of ECAP crack initiation trend based on Normalized C&L criterion [J]. *Forging. Stamp. Technol.* **35**(05), 159–163 (2010)



Chapter 27

Probabilistic Maintenance-Free Operating Period via Bayesian Filter with Markov Chain Monte Carlo (MCMC) Simulations and Subset Simulation

Michael Shiao, Tzi-Kang Chen, and Zhu Mao

Abstract This paper presents a probabilistic approach via Bayesian-filter (BF) with Markov chain Monte Carlo (MCMC) simulations and subset simulation (SS), to determine the probabilistic maintenance-free operating period (MFOP) for probabilistic lifing assessment of aircraft fatigue critical components. State transition function representing virtual damage growth of a component and measurement function representing the SHM measurements of the component are defined. State transition function is described by a typical Paris equation for fatigue crack propagation. Measurement functions are assumed in this study, which describe the relationship between the damage features derived from SHM signals and the damage sizes. Damage tolerance (DT) and risk-based methodologies are used for fracture-based reliability assessment. Random samples for posterior joint probability density function of initial flaw size and crack growth rate are generated with information obtained through structural health monitoring (SHM) systems. Subset simulation (SS) is used in conjunction with MCMC in order to determine the small probability of failure with high efficiency. The results have shown that the MCMC-SS combined methodology is two orders of magnitude more efficient than that of MCMC alone.

Keywords Bayesian filter · BF · Markov chain Monte Carlo · MCMC · Probabilistic lifing · Fatigue · Damage tolerance · DT · Probabilistic · Risk · Reliability · Subset simulation

Nomenclature

a_0	Crack size at time 0
BF	Bayesian Filter
c	Crack growth rate in Paris eq.
C	Constant is for jump distribution in Metropolis algorithm
CV	Coefficient of variation
CDF	Cumulative distribution function
DT	Damage tolerance
F_k	k^{th} subset
m	Number of subsets for subset simulation
\bar{m}	Paris Law constant
MCMC	Markov chain Monte Carlo
MCS	Monte Carlo simulation
MFOP	Maintenance free operating period
p	Probability
PDF	Probability density function
POF	Probability of failure
\bar{R}	A specified reliability

M. Shiao · T.-K. Chen
Army Research Laboratory, Aberdeen Proving Ground, Adelphi, MD, USA

Z. Mao (✉)
Structural Dynamics and Acoustic Systems Laboratory, Department of Mechanical Engineering, University of Massachusetts Lowell, Lowell, MA, USA
e-mail: zhu_mao@uml.edu

R_t	Reliability of a component at time t
RUL	Remaining useful life
SS	Subset simulation
SHM	Structural health monitoring
STDV	Standard deviation
t'	The time at which the last SHM measurement was conducted
T	Remaining useful life
z	SHM measurements
σ_ω	Standard deviation of measurement noise ω
Δt_m	SHM measurement interval
ΔK	The range of stress intensity factor
\hat{a}	Damage feature extracted from SHM signals
α	Constant in measurement function
β	Constant in measurement function
$\bar{\alpha}$	Acceptance ratio in Metropolis algorithm
θ	Model parameters
Θ	Uncertain parameters
ν	Process noise
ω	Measurement noise

27.1 Introduction

Army Research Laboratory is conducting researches to develop a probabilistic approach and framework to determine the critical information for real-time risk assessment and risk management regarding aircraft life cycle management of fatigue critical components. Using health state information from health monitoring systems, combined with physics-based damage models, a comprehensive life assessment may be formulated. This new approach allows regulators to make informed judgments regarding potential extending the current design life of critical rotorcraft components while operating under safe and reliable conditions. It also provides new tools to design and manage fatigue critical components of the next generation rotorcraft for low cost, light weight and high reliability.

The assessment requires uncertainty modeling, physics-based modeling, health state quantification, and probabilistic methodologies development. Uncertain design parameters, such as material properties, usages, geometries, damage propagation, manufacture-related uncertain parameters, etc., as well as uncertainties related to health state quantification need to be statistically determined. One of the major issues for this research is the technical challenge in applying probabilistic lifing methods to quantify the health state, while the component is continuously degraded. In this paper, we use the probabilistic lifing approach based on Bayesian filters (BF) with advanced simulation methods for high accuracy and efficiency.

BF has become a broad topic involving many scientific areas. There exist a number of excellent tutorials on BFs and Monte Carlo filters [1–6], and also researches for BF applications on fatigue crack/damage growth scenarios [7–11]. BF is a probabilistic approach to quantify the uncertain damage state of a component recursively over time using incoming measurements and a mathematical damage progression model. In this paper, we investigate and demonstrate the applications of Bayesian filtering-based lifing approach with Markov chain Monte Carlo (MCMC) and subset simulation (SS) to determine the probabilistic maintenance-free operating period (MFOP). MCMC methods [12, 13] are a class of algorithms for sampling based on the construction of Markov chain from the target probability distribution for which direct sampling is difficult. In addition, aircraft require ultra-reliability for high performance. Small probability of failure computation with high accuracy is critical. This motivates the authors to investigate the efficiency and robustness of the new probabilistic approach by implementing SS into BF/MCMC framework studied earlier by the author [14].

The paper is structured as follows. Sections 27.2 and 27.3 discuss the BF and MCMC simulations respectively. Section 27.4 introduces SS for small probability computation. Section 27.5 demonstrates the efficiency and accuracy of the proposed methodology with case studies to determine the probabilistic maintenance-free operating period. Section 27.6 provides a summary of the study.

27.2 Bayesian Filters

Bayesian filters are the methods to solve Bayesian inference numerically, where probability distributions are intractable in closed form. BF with MCMC approximates the probability distributions of unknowns using a large number of samples. As the number of samples increases toward infinity, the approximated probability distributions will converge to the actual. Bayesian filtering-based probabilistic life methodology requires the information of the evolution of damage signals and damage extent in time to estimate the relationship between features extracted from monitoring signals and damage extent for MFOP prediction of a degrading system. Since it is a process to forecast future risks based on current system health states, uncertainty associated with the forecasting needs to be quantified and propagated. This approach describes the system state in terms of discrete probability distribution using a set of simulations representing state values (realizations). Each simulation has an assigned probability representing its probability of occurrence. The general process of BF is based on a state transition function f and a measurement function h shown in Eqs. 27.1 and 27.2.

$$a_j = f(a_{j-1}, \theta, v_j) \quad (27.1)$$

and

$$z_j = h(a_j, \omega_j) \quad (27.2)$$

where j is the time step index, a_j is the damage state, θ is the vector of model parameters, z_j is the SHM feature estimated from health monitoring signals, and v_j and ω_j are the process and measurement Gaussian noises with zero-mean respectively. The state function f is referred to as a damage progression model. The measurement function h describes the relationship between the collected SHM features and damage states. BF estimates and updates unknown parameters as a form of the probability density function (PDF) based on the Bayes' theorem

$$p(\Theta|z) \propto p(z|\Theta) p(\Theta) \quad (27.3)$$

where Θ is the hyperparameter vector which includes all the unknown parameters to be updated, z is the vector of observed features, $p(z|\Theta)$ is the PDF value of z conditional on the given Θ , $p(\Theta)$ is the prior PDF of Θ . Equations 27.1, 27.2 and 27.3 will be used recursively at each time step j to propagate and update various uncertainties by BF. The MFOP for a specified reliability can be determined by a general purpose probabilistic methodology considering all uncertainties including those with posterior PDFs.

27.3 Markov Chain Monte Carlo (MCMC) Simulations

In our previous study [15], samples are randomly generated by traditional Monte Carlo simulations based on prior probability distributions. Posterior probability distributions are determined via simulations using Eqs. 27.1, 27.2 and 27.3. In another paper [14], we employ Markov chain Monte Carlo (MCMC) methods to generate random samples from unknown posterior probability distributions. The MCMC technique is a family of algorithms used to produce approximate random samples from a probability distribution, which is too difficult to sample directly. In this paper, MCMC is also adopted for random simulations, which is the Metropolis algorithm for obtaining a sequence of random samples from the posterior joint probability distribution. This algorithm has been widely used in Bayesian applications for its simplicity and efficiency.

The Metropolis algorithm is performed based on the following iterative procedure:

- (a) At iteration $i = 0$, select a vector X_0 (arbitrarily or based on prior knowledge) consisting of realizations of random variables in the study as the initial sample.
- (b) For each following iteration $i > 0$,
 1. Generate a candidate vector X' randomly from the joint probability distribution function $g(X'|X_{i-1})$ where function g is referred to as the proposal density function or jumping distribution. As a special case of Metropolis-Hastings algorithm, the proposal function g in the Metropolis algorithm is symmetric. A usual choice is to let g be a Gaussian distribution with mean equal to X_{i-1} .
 2. Calculate the acceptance ratio $\bar{\alpha} = q_x(X')/q_x(X_{i-1})$. The ratio will be used to decide whether to accept or to reject the candidate. $q_x(X')$ is a function proportional to the posterior probability density of model parameters θ .

3. If $\bar{\alpha} \geq 1$, the candidate is more likely than X_{i-1} ; automatically accept the candidate by setting $X_i = X'$.
4. If $\bar{\alpha} < 1$, accept the candidate with probability $\bar{\alpha}$; if the candidate is rejected, set $X_i = X_{i-1}$, instead.

Generated random samples are then inputted to a probabilistic damage tolerance analysis framework to determine the probabilistic maintenance free operating period.

27.4 Small Failure Probability Computation by Subset Simulation (SS)

Rotorcraft requires ultra-reliability for its fatigue critical components. Therefore, small probability computation with high efficiency is essential. It is well known that Monte Carlo simulations is not efficient method for small probability computation. This is also true for MCMC simulations. In the following section, we will introduce a subset simulation (SS) concept [16, 17] with MCMC simulations to improve the efficiency for small probability computation.

The failure of a component due to fracture is of great concerns and is defined as a probabilistic event F at which a function g_t is less than zero. Function g_t is defined as

$$g_t = K_{FT} - K_t \quad (27.4)$$

where K_{FT} is the fracture toughness and K_t is the stress intensity factor at time t . K_t as defined in Eq. 27.5.

$$K_t = \sigma_{\max} \sqrt{\pi a_t} \quad (27.5)$$

In the equation, σ_{\max} is the maximum flight stress and a_t is the crack size at time t . a_t is defined in Eq. 27.6 as

$$a_t = a_{t-1} + c (\Delta K_{t-1})^{\bar{m}} \Delta t, \quad \Delta K_{t-1} = \Delta \sigma \sqrt{\pi a_{t-1}} \quad (27.6)$$

where c is the random crack growth rate and \bar{m} is a constant. a_0 is the random crack size at time 0. $\Delta \sigma$ is the stress range and ΔK is the range of stress intensity factor. In our study, K_{FT} and σ_{\max} are also considered as random variables. The probability of failure $P_f(t)$ at time t is thus computed by Eq. 27.7.

$$P_f(t) = P(g_t < 0) \quad (27.7)$$

Aircraft are required to maintain high reliability during operations. It is desirable to determine the maintenance-free operating period with high reliability or small probability of failure. The probability of failure may range from 10^{-7} to 10^{-3} , depending on the criticality of the fatigue critical aircraft components. In this paper, we will use subset simulation (SS) with random samples generated by Markov chain Monte Carlo simulations for small probability computation as explained in the following.

Subset simulation first defines m subsets F_k where $k = 1, m$ in the sampling domain as depicted in Fig. 27.1 in a 2-D sampling domain.

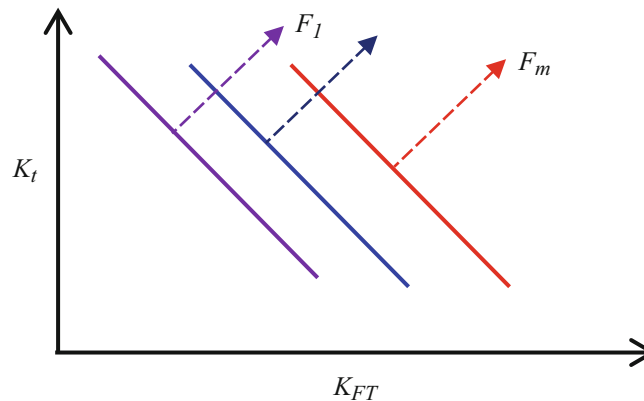


Fig. 27.1 Subsets in A 2-D Sampling Domain.

F_k is defined by Eq. 27.8.

$$F_k = \{g_t < y_k\} \quad (27.8)$$

where y_k are constants representing intermediate thresholds and $y_m = 0$. Each solid color line divides the sampling domain into two subsets. The dashed line with the same color indicates the subset F_k where $g_t < y_k$. F_m is also called failure domain. Therefore, Eq. 27.7 can also be written as Eq. 27.9.

$$P_f(t) = P(F_m) \quad (27.9)$$

The subsets F_k satisfy the following two equations.

$$F_1 \supset F_2 \supset F_3 \supset \dots \supset F_m \quad (27.10)$$

and

$$F_k = \bigcap_{i=1}^k F_i, k = 1, \dots, m. \quad (27.11)$$

The probability of failure is computed by the following equation [16, 17].

$$P_f(t) = P(F_m) = P\left\{\bigcap_{k=1}^m F_k\right\} = P(F_1) \prod_{k=1}^{m-1} P(F_{k+1}|F_k) \quad (27.12)$$

The computational efficiency using subset simulation is achieved by a multiplication of conditional probabilities $P(F_{k+1}|F_k)$ other than the direct computation of the small probability $P(F_m)$. Conditional probabilities $P(F_{k+1}|F_k)$ are computed by random simulations using MCMC simulations. It is important to control the values of the conditional probabilities $P(F_{k+1}|F_k)$ in order to take the advantage of SS. The strategy is to select the intermediate thresholds $\{y_k: k = 1, m-1\}$ such that the $P(F_{k+1}|F_k)$ are equal to a fixed value P_0 . In our study we select $P_0 = 0.10$, as a reasonable pick without losing generality.

27.5 Case Study

In order to use Bayesian filter to solve Bayesian inference, a state transition function and a measurement function need to be defined first. In this study, a Paris Law-based crack growth model is used to define the state transition function as shown in Eq. 27.13.

$$a_t = a_{t-1} + c (\Delta K_{t-1})^{\bar{m}} \Delta t + v, \quad \Delta K_{t-1} = \Delta \sigma \sqrt{\pi a_{t-1}} \quad (27.13)$$

where c is the random crack growth rate and \bar{m} is a constant. a_0 is the random crack size at time 0. $\Delta \sigma$ is the stress range and ΔK is the range of stress intensity factor. The process noise v in state transition function in Eq. 27.13 is not explicitly necessary, since it can be handled through the uncertainty in model parameters.

Next, a general process to define a measurement function is briefly described below. Typically one would establish a relationship between the inspection feature (usually termed as \hat{a}) and the 'true' measured crack length, a . This relationship is established using linear regression as follows [18–20]. Let $x = q_1(a)$ and $y = q_2(\hat{a})$ where q_1 and q_2 are either linear or nonlinear functions selected such that x and y are linearly related. The relationship between the a and \hat{a} is then estimated as:

$$y = \alpha + \beta^* x + \omega \quad (27.14)$$

where α and β are constants and ω is the measurement noise. In our study, without losing generality we let $x = a$ and $y = \hat{a}$ for simplicity. The measurement function in Bayesian filter thus becomes

$$\hat{a}_t = \alpha + \beta^* a_t + \omega_t \quad (27.15)$$

Table 27.1 Mean and standard deviation of fracture toughness and maximum stress

	Mean	Standard deviation
K_{Ic}	100	10
σ_{max}	75	7.5

The initial crack size a_0 , crack growth rate c in Eq. 27.13 and ω_t are random variables for the study. ω_t are normally distributed random variables with zero-mean and standard deviation σ_ω . The unknown hyperparameter Θ in Eq. 27.3 includes the damage state a , model parameters $\theta = (a_0, c)$ and measurement noise ω .

To start the BF process using MCMC, model parameters $\theta_i = (a_{0,i}, c_i)$ are selected arbitrarily or based on prior knowledge for $i = 0$. The likelihood of measurement (observation) \hat{a}_k at time k of the i^{th} iteration with model parameters $\theta_i = (a_{0,i}, c_i)$ is shown in Eq. 27.16.

$$p(\hat{a}_k | a_{k,i}(a_{0,i}, c_i, k)) = \frac{1}{\sqrt{2\pi}\sigma_\omega} \exp\left[-\frac{1}{2}\left(\frac{\hat{a}_k - (\alpha + \beta^* a_{k,i}(a_{0,i}, c_i, k))}{\sigma_\omega}\right)^2\right], \text{ where } k = 1, \dots, t \quad (27.16)$$

The posterior probability of each realization pair $(a_{0,i}, c_i)$ at time k with a new measurement \hat{a}_k is updated recursively in time using Eqs. 27.13 and 27.16 as shown in Eq. 27.17.

$$p(a_{0,i}, c_i | \hat{a}_{1:k}) \propto p(\hat{a}_k | a_{k,i}(a_{0,i}, c_i, k)) p(a_{0,i}, c_i | \hat{a}_{1:k-1}), \text{ where } k = 1, \dots, t \quad (27.17)$$

and $\hat{a}_{1:k} = [\hat{a}_1, \hat{a}_2, \dots, \hat{a}_k]$. By successive substitution of Eq. 27.17, the updated joint probability density function of $(a_{0,i}, c_i)$ at $k = t$ is shown in Eq. 27.18.

$$p(a_{0,i}, c_i | \hat{a}_{1:t}) \propto \left\{ \prod_{k=1}^t p(\hat{a}_k | a_{k,i}(a_{0,i}, c_i, k)) \right\} p(a_{0,i}, c_i) \quad (27.18)$$

The function q_x in Metropolis algorithm is thus approximated by

$$q_x(a_{0,i}, c_i) = \left\{ \prod_{k=1}^t p(\hat{a}_k | a_{k,i}(a_{0,i}, c_i, k)) \right\} p(a_{0,i}, c_i) \quad (27.19)$$

Equation 27.19 is the shape of the posterior joint probability density function of initial crack size a_0 and crack growth rate c . It will be used to generate random samples using MCMC.

Our next step is to compute conditional probabilities $P(F_{k+1} | F_k)$ by Markov chain Monte Carlo simulations. Both K_{FT} in Eq. 27.4 and maximum stress σ_{max} in Eq. 27.5 are normally distributed random variables with means and standard deviations defined in Table 27.1. The prior probabilistic distributions of initial crack size a_0 and the log of crack growth rate c are assumed to be uniformly distributed.

The reliability of a component at time t , R_t , is determined by Eq. 27.20.

$$R_t = 1 - POF(K_t > K_{Ic}) \quad (27.20)$$

POF in Eq. 27.20 represents the probability of failure (POF) where $K_t > K_{FT}$. The MFOP T for a specified reliability \bar{R} after SHM was conducted at time t' is thus determined by finding the T in Eq. 27.21.

$$\bar{R} = 1 - POF(K_{t'+T} > K_{Ic}) \quad (27.21)$$

In the following, studies will be performed for a simulated measurement with measurement intervals Δt_m is set at 50 flights and measurement noise σ_ω is set to be 0.001 as shown in Fig. 27.2. Also α is equal to 0.04 and β is equal to 0.4 for the measurement function in Eq. 27.14. The probabilistic maintenance-free operating period will be studied at $t' = 2000$ and 2500 flights respectively.

As discussed earlier, random samples are generated based on the shape of the posterior joint probability density function as shown in Eq. 27.19. Subset simulation is implemented in order to compute small probability of failure for ultra-reliable

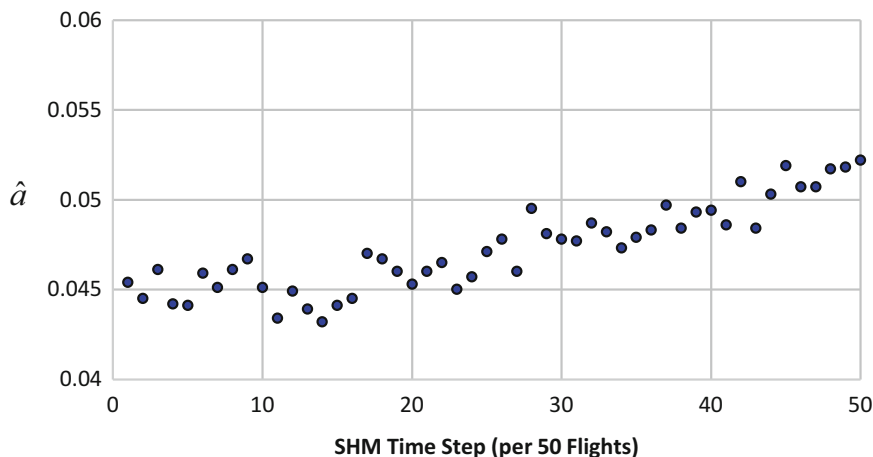


Fig. 27.2 Simulated measurement function

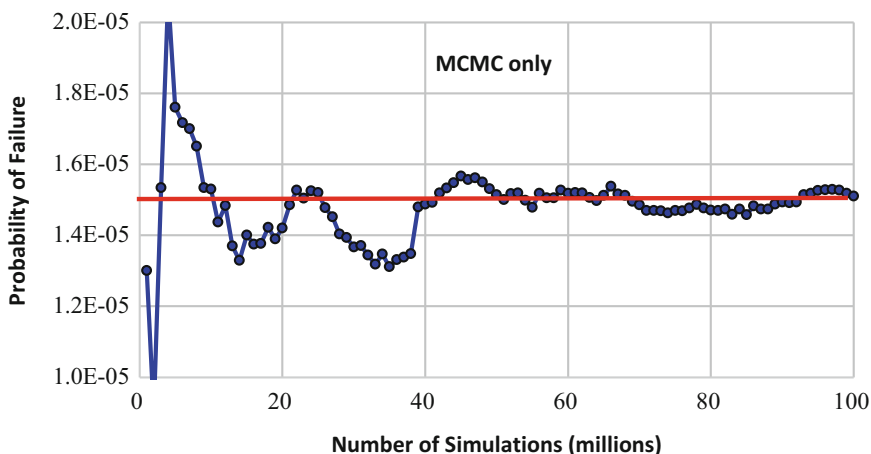


Fig. 27.3 Convergence study for probability prediction using MCMC alone

aircraft fatigue critical components. The computation steps are explained next. To start the subset simulation, we first assign an appropriate value for the conditional probabilities. In our study, we let it be around 0.10. The optimal value can be determined by a separate study. We also let the number of the random samples for the conditional probability computation be N . With this setup, we then generate N samples from entire sampling domain by MCMC to compute $P(F_1)$ in Eq. 27.12. The threshold y_1 is selected by finding the $(0.1 N)^{\text{th}}$ smallest value of g_t shown in Eq. 27.4.

Once y_1 is determined, we execute MCMC again to generate another N random samples from the sub-sampling domain F_1 , where F_1 is defined in Eq. 27.8. This step is repeated until the $(0.1 N)^{\text{th}}$ smallest value of g_t is less than 0. At this time, we let k be m and set y_m to be zero. MCMC is executed for the last time to determine the conditional probability $P(F_m|F_{m-1})$. Once all the conditional probabilities of failure are determined, the probability of failure is then computed by Eq. 27.12.

We will now demonstrate this approach with the last SHM conducted at $t' = 2500$ flights and the probability of failure to be determine at MFOP = 1400 flights. To evaluate the efficiency and accuracy of subset simulation, we first run MCMC only to determine the probability of failure similar to traditional Monte Carlo simulations. The results are shown in Fig. 27.3, in which 100 million random simulations are conducted. It can be seen that the convergence is roughly achieved at 50 million MCMC simulations. The converged probability of failure is 1.50E-05.

Our next step is to run MCMC with SS for the same problem. We select three cases for the study. Each case uses a different number of MCMC simulations for conditional probability calculation as defined in Table 27.2. Table 27.2 also shows the intermediate thresholds for all three cases per the steps discussed above. From the study, five intermediate thresholds are obtained for each case and their values are very close from case to case as shown in the table.

The same analysis for each case is repeated 100 times but with new random samples. The mean, standard deviation and correlation of variation (CV) are shown in Table 27.3. It is seen that the results in Case 1 has the highest CV, and in Case 3 the

Table 27.2 Intermediate thresholds selected for respective conditional probability computation

	Case 1	Case 2	Case 3
Random samples per conditional probability computation	10 thousands	100 thousands	1 million
y_1	40	41	41
y_2	27	28	28
y_3	16	17	17
y_4	7	8	8
y_5	0	0	0

Table 27.3 Predicted probability of failure with 100 repeated analyses

	Case 1	Case 2	Case 3
Random samples per conditional probability computation	10 thousands	100 thousands	1 million
Mean	1.49E-05	1.41E-05	1.43E-05
Standard deviation	3.91E-06	1.14E-06	4.12E-07
Correlation of variation	0.26	0.08	0.03

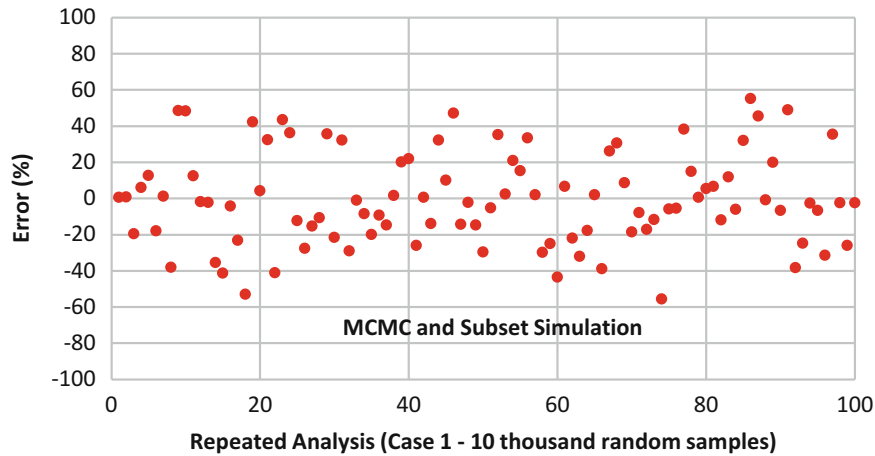


Fig. 27.4 Error (%) for respective analyses using MCMC/SS in Case 1

smallest CV. Case 2 has modest CV. Also, results from Cases 1 by MCMC/SS are within $\pm 60\%$ of converged MCMC results as shown in Fig. 27.4. Results from Cases 2 and 3 are within $\pm 20\%$ and $\pm 10\%$ of converged MCMC results respectively as shown in Figs. 27.5 and 27.6. From this study, we decide to use 100 thousand random samples for conditional probability computation for the remaining study since the predicted probability of failure is bounded within $\pm 20\%$ of converged MCMC results.

As discussed before, it requires roughly 50 million MCMC simulations to obtain the converged failure probability as shown in Fig. 27.3. It requires to determine 5 probabilities using MCMC/SS to obtain a prediction which is within $\pm 20\%$ of converged MCMC results. Each probability is computed with 100 thousand MCMC simulations. As can be seen, MCMC/SS is two orders of magnitude more efficiency than MCMC alone.

In the following study, we will perform two studies with last SHM measurement conducted at 2000 flights and 2500 flights respectively. For each study and for a set of given total flights, the probability of failure are determined based on MCMC/SS procedure. The results are shown in Fig. 27.7. From the figure, we can determine the MFOP for $R = 0.999$ for last SHM measurement conducted at 2000 flights which is approximately 1650 flights. As for the study where last SHM measurement was conducted at 2500 flight, the MFOP for 0.99 reliability can be readily determined to be 1670 flights.

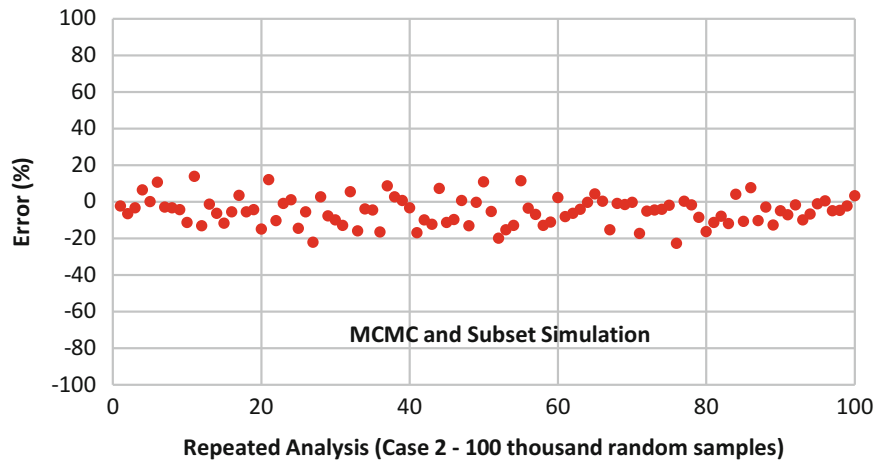


Fig. 27.5 Error (%) for respective analyses using MCMC/SS in Case 2

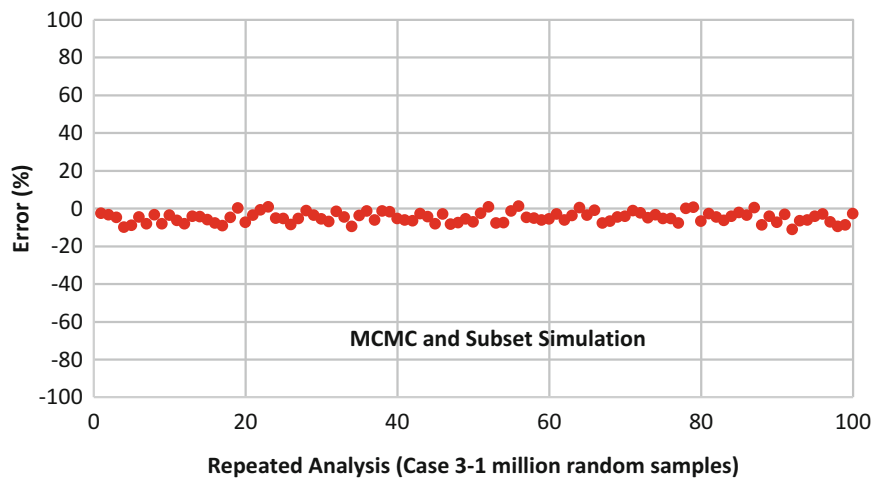


Fig. 27.6 Error (%) for respective analyses using MCMC/SS in Case 3

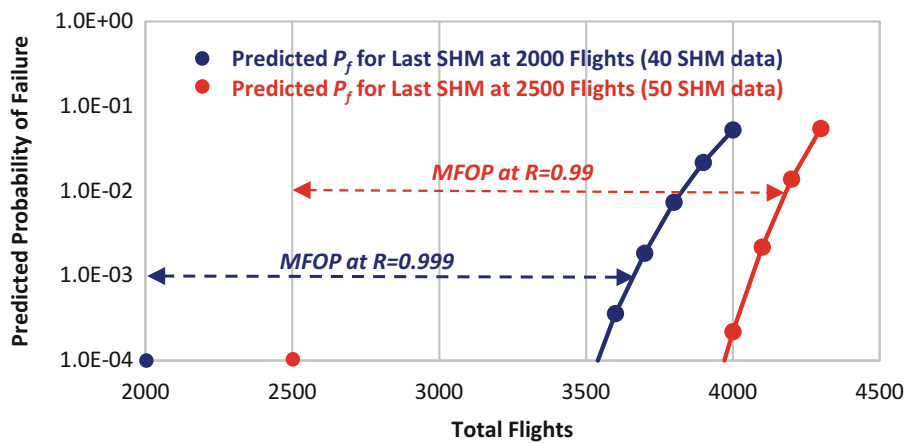


Fig. 27.7 Probabilistic maintenance-free operating period using MCMC/SS

27.6 Summary

Probabilistic maintenance-free operating period (probabilistic MFOP) is determined via Bayesian-filter (BF) with random simulations using Markov chain Monte Carlo (MCMC) and subset simulation for small failure probability computation. The proposed probabilistic lifing method was explored and demonstrated for its robustness in probabilistic life prediction. Random samples are generated by MCMC since only the shape of the joint posterior probability density function of initial crack size and crack growth rate are obtained by Bayes' theory with new information obtained through structural health monitoring (SHM) systems. State transition function is described by a typical Paris equation for fatigue crack propagation for demonstration purpose. Measurement functions are assumed in this study, which describe the relationship between the features derived from SHM signals and the damage sizes. In our approach, damage tolerance and risk-based methodology is applied for a fracture-based reliability assessment. Since ultra-reliability is required for rotorcraft fatigue critical components, subset simulation is utilized in conjunction with MCMC for small failure probability computation with high efficiency. The study has shown that MCMC with subset simulation is two orders of magnitude more efficient than MCMC alone for small probability computation.

References

1. Arulampalam, M.S., Maskell, S., Gordon, N., Clapp, T.: A tutorial on particle filters for online nonlinear/non-Gaussian Bayesian tracking. *IEEE Trans. Signal Processing*. **50**(2), 174–188 (2002)
2. Baraldi, P., Compare, M., Saucio, S., Zio, E.: Fatigue crack growth prognostics by particle filtering and ensemble neural networks. *Proceedings of First European Conference of the Prognostics and Health Management Society 2012, PHM-E'12*, ISBN – 978-1-936263-04-2, July 3–5, Dresden, Germany (2012)
3. Chen, Z.: Bayesian filtering: from Kalman filters to particle filters and beyond. *Statistics*. **182**(1), 1–69 (2003.) 2903
4. Doucet, A., Godsill, S., Andrieu, C.: On sequential Monte Carlo sampling methods for Bayesian filtering. *Stat. Comput.* **10**(3), 197–208 (2000)
5. Doucet, A., de Freitas, N., Murphy, K., Russell, S.: Rao-Blackwellised particle filtering for dynamic Bayesian networks. *The Sixteenth Conference on Uncertainty in Artificial Intelligence (UAI2000)*, UAI-P-2000-PG-176-183, (2000)
6. Tanizaki, H.: In: Rao, C.R., Shanbhag, D.N. (eds.) *Nonlinear and Non-Gaussian State-Space Modeling with Monte Carlo Techniques: A Survey and Comparative Study*. *Handbook of Statistics*, North-Holland (2000)
7. An, D., Choi, J.-H., Kim, N.-H.: Prognostics 101: a tutorial for particle filter-based prognostics algorithm using Matlab. *Reliab. Eng. Syst. Saf.* **115**(2013), 161–169 (2013)
8. He, D., Bechhoefer, E., Demsey, P., Ma, J.: An integrated approach for gear health prognostics. *68th American Helicopter Society, International Annual Forum 2012*, May 1–3, Fort Worth, Texas (2012)
9. Orchard, M.E., Vachtsevanos, G.J.: A particle filtering approach for on-line fault diagnosis and failure prognosis. *Trans. Inst. Meas. Control*. **31**(3–4), 221–246 (2009)
10. Chen, T.-Z.: An integrated prognostic and diagnostic model for airframes. *52nd AIAA/ASME/AHS/ASC Structures, Structural Dynamics and Materials Conference*. April 4–7, Denver, CO (2011)
11. Haile, M.A., Riddick, J.C., Assefa, A.H.: Robust particle filters for fatigue crack growth estimation in rotorcraft structures. *IEEE Trans. Reliab.* **65**(3), 1438–1448 (2016)
12. Khan, Z., Balch, T., Dellaert, F.: An MCMC-based particle filter for tracking multiple interacting target. In *ECCV*. **4**, 279–290 (2004)
13. Renard, B., Garreta, V., Lang, M.: An application of Bayesian analysis and Markov chain Monte Carlo methods to the estimation of a regional trend in annual maxima. *Water Resour. Res.* **42**(W12422), 2006 (2006). <https://doi.org/10.1029/2005WR004591>
14. Shiao, M., Chen, T.: Health-Informed Uncertainty Quantifications via Bayesian Filters with Markov Chain Monte Carlo Simulations for Fatigue Critical Rotorcraft Components. *2017 PHM Annual Conference* (2017)
15. Shiao, M., Chen, T., Ghoshal, A.: Probabilistic lifing methods for fatigue management of life-limited propulsion components. *AHS International 72nd Annual Forum & Technology Display*. May 17–19, West Palm Beach, Florida, (2016)
16. Beck, J.L., Au, S.-K.: Estimation of small failure probability in high dimensions by subset simulation. *Probab. Eng. Mech.* **16**(2001), 263–277 (2001)
17. Au, S.-K.: On MCMC algorithm for subset simulation. *Probab. Eng. Mech.* **43**(2016), 117–120 (2016)
18. Department of Defense: *Nondestructive Evaluation System Reliability Assessment*. MIL-HDBK-1823A (2009) <https://www.amazon.com/NONDESTRUCTIVE-EVALUATION-SYSTEM-RELIABILITY-ASSESSMENT-ebook/dp/B00UB1UK2Q>. <https://www.cnde.iastate.edu/mapod/2005%20September/MIL%20HNDB%201823.pdf>
19. Ihn, J.-B., Pado, L., Leonard, M.S., Desimio, M.P., Olson, S.E.: Development and performance quantification of an ultrasonic structural health monitoring system for monitoring fatigue cracks on a complex aircraft structures. *International Workshop on Structural Health Monitoring: From Condition-based Maintenance to Autonomous Structures*. September 13–15, Stanford, California (2011)
20. Kabban, C.M., Greenwell, B.M., Desimio, M.P., Derriso, M.M.: The probability of detection for structural health monitoring systems: repeated measures data. *Struct. Health Monit.* **14**(3), 252–264 (2015)



Chapter 28

Bayesian Model Updating of a Damaged School Building in Sankhu, Nepal

Mehdi M. Akhlaghi, Supratik Bose, Babak Moaveni, and Andreas Stavridis

Abstract This paper discusses Bayesian model updating of a damaged four-story masonry-infilled reinforced concrete structure using recorded ambient vibration data. The building, located in Sankhu, Nepal, was severely damaged during the 2015 Gorkha earthquake and its aftershocks. Ambient acceleration response of the structure was recorded with an array of 12 accelerometers following the earthquake. An output-only system identification method is deployed to extract modal parameters of the building including natural frequencies and mode shapes from the collected ambient vibration data. These dynamic properties are used to calibrate the finite element model of the building which is used to simulate the response during the earthquake. The initial three-dimensional finite element model is created using in-situ inspections. The goal of the Bayesian model updating procedure is to estimate the joint posterior probability distribution of the updating parameters, which are considered as the stiffness of different structural components. The posterior probability distribution is estimated based on the prior probability distribution of these parameters as well as the likelihood of data. The error function in this study is defined as the difference between identified and model-predicted modal parameters. The posterior distributions are estimated using the Markov Chain Monte Carlo stochastic simulation method. Ultimately, the stiffness values are estimated using the Bayesian model updating approach are compared with those from deterministic model updating conducted previously.

Keywords Finite element model updating · System identification · Bayesian inference · Structural health monitoring · Markov Chain Monte Carlo method

28.1 Introduction

Mitigating the effects of natural hazards such as earthquakes, tsunamis, and hurricanes on civil structures has remained as one of the grand challenges in structural and earthquake engineering over the past few decades. A component of this challenge involves assessment of structural health after a natural hazard. Different damage assessment methods based on quantitative and/or qualitative data have been developed to evaluate performance of structures after such extreme events. Their mission is to identify the existence, location and severity of the damage and estimate the remaining life of the structures.

Model updating methods are among the most common approaches for structural performance assessment [1]. However, deterministic model updating methods are not capable of accounting for the uncertainties involved in this process. These uncertainties are introduced by measurement noise, identification errors, and most importantly modeling errors. In the system identification stage, measurement noise in recorded signals and the underlying assumptions in the identification methods (e.g., broadband and stationary input signal in operational modal analysis) contribute to estimation uncertainty. In the modeling stage, simplified modeling assumptions and element discretization that are inevitable in the modeling process, add their own share of uncertainty to the problem [2]. Therefore, Bayesian model updating methods have received increased attention in recent years for probabilistic assessment of structural performance [3, 4]. In Bayesian model updating methods, the posterior probability distribution of updating structural parameters is estimated based on the initial knowledge (i.e., prior distribution) and the acquired data (i.e., likelihood function).

M. M. Akhlaghi · B. Moaveni (✉)

Department of Civil and Environmental Engineering, Tufts University, Medford, MA, USA
e-mail: mehdi.akhlaghi@tufts.edu

S. Bose · A. Stavridis

Department of Civil, Structural and Environmental Engineering, University at Buffalo, Buffalo, NY, USA

The focus of this study is to assess the performance of a reinforced concrete (RC) school building in Nepal that was damaged during the 7.8 M_w , 2015 Gorkha earthquake [5]. A group of researchers, including some of the authors, visited the site of the earthquake shortly after the earthquake and collected field data for several structures, including the school building studied in this paper. In this study, modal parameters of the structure are extracted from ambient acceleration data. This data is used to estimate the material parameters of a three-dimensional finite element (FE) model of the damaged structure using deterministic and Bayesian model updating.

28.2 School Building and Collected Data

This study focuses on a 4-story reinforced concrete frame school building with masonry infill walls located in Sankhu, Nepal (Fig. 28.1). It has eight almost equally spaced concrete frames in the east-west direction and three disproportionately wider frames in the north-south direction.

A set of ambient acceleration data was collected in two setups. In setup A, 45 min of acceleration data were collected for the three upper floors of the building using 12 accelerometers. In each floor, 4 accelerometers were placed in two opposite corners of the floor and in two perpendicular directions. In setup B, 54 min of acceleration data was collected in a similar procedure but for the first three stories of the building. Sensors placed in the third floor were kept in place in both setups so the complete mode shapes can be assembled. The location of these sensors on each floor is demonstrated in Fig. 28.1.

The extent and location of damage in the structure was documented comprehensively by visual inspections as well as LiDAR data acquisition [6]. It has been observed that damage is mostly concentrated in the first story of the building. Figure 28.2 depicts some of the most severely damaged elements in the structure.

28.3 System Identification

Recorded signals are divided into 9-min intervals; leading to 5 sets of acceleration data for setup A and 6 sets of acceleration data for setup B. Each set of data is filtered by a band-pass Finite Impulse Response (FIR) filter [7] of order 4096 between 1 and 10 Hz. Then, to increase the efficiency of the system identification process, the filtered data is down-sampled from the initial sampling frequency of 2048 Hz to 256 Hz. Finally, voltage spikes are removed from the time history data. Out of the 20 total acceleration channels (considering that 4 sensors are shared between the setups) only 11 of them are used for system identification process due to the high levels of noise in the other 9 signals. Figure 28.3 shows the acceleration time history as well as the frequency content of one of the used acceleration channels.

A combination of the Natural Excitation Technique [8] and the Eigensystem Realization Algorithm [9] (NExT-ERA) is used to identify the modal parameters of the building. NExT-ERA is an output only identification method which can be used to estimate modal parameters of structures in the absence of input measurements [10, 11]. In the application of

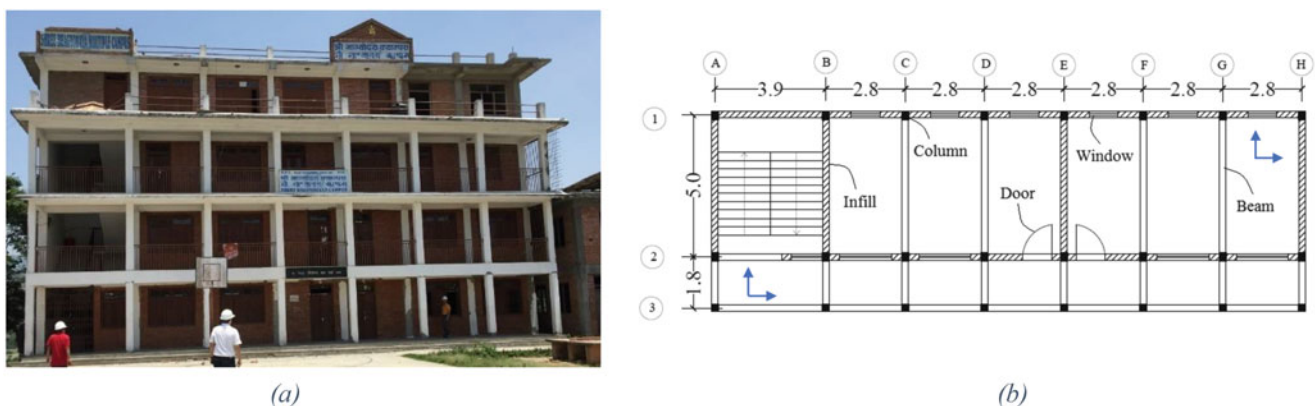


Fig. 28.1 Four-story school building (a) elevation view (b) plan view and location of sensors



Fig. 28.2 Observed damages in the first story of the building (a) Column G2 (b) Column H1 (c) Infill wall H12

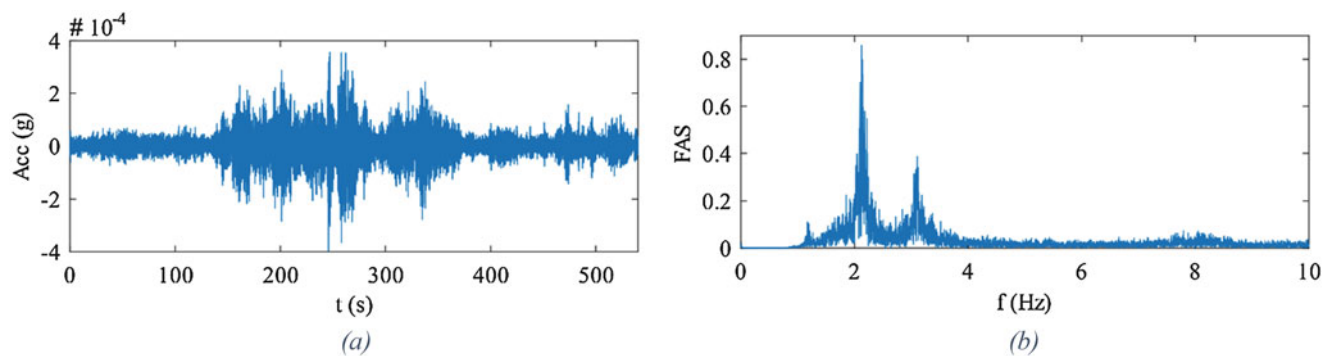


Fig. 28.3 Filtered and down-sampled measurements (a) acceleration time history (b) Fourier Amplitude Spectrum

NExT-ERA, cross power spectral densities between the 11 acceleration channels and two reference channels are computed using 8 equal length Hanning windows with 50% overlap. Free vibration response is then estimated as the inverse Fourier transform of the cross power spectral densities and is considered as the input to the ERA algorithm. A Hankel matrix of size $(11 \times 400) \times (400 \times 2)$ is formed using the free vibration response. Modal parameters are identified through singular value decomposition of the Hankel matrix. In order to select the stable modes of structure, stabilization diagrams are obtained. Figure 28.4 shows a stabilization diagram for one dataset. As it is shown in this diagram, the first stable modes are considered as the prominent modes of the structure.

The same procedure is repeated for each set of data, leading to 11 sets of modal parameters. To reassemble the mode shape data for the two setups, the mode shape values are normalized to one of the mode shape coordinates at the 3rd floor of the building. Table 28.1 shows the mean and coefficient-of-variation (COV) of the natural frequencies, for each setup.

28.4 Deterministic Finite Element Model Updating

Nonlinear three-dimensional finite element model of the building is developed in the OpenSees software [12] based on a newly proposed modeling framework [13, 14], in-situ inspections of the structure, and available experimental data [15, 16]. The RC beams and columns are modeled as beam-column elements discretized into fibers, and masonry infill walls are modeled using diagonal strut elements [17]. Concrete02 material model with a compressive strength of 0.5 ksi and modulus of elasticity of 370 ksi is chosen for infill walls. The same material model with a compressive strength of 1.4 ksi and modulus

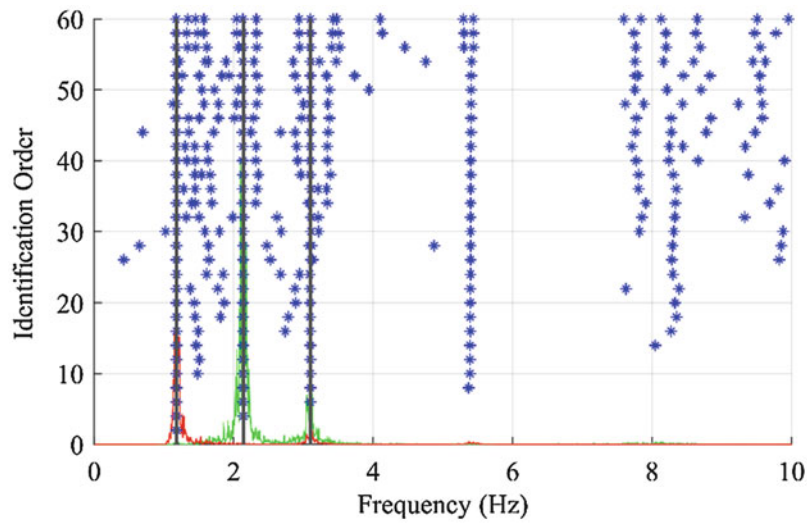


Fig. 28.4 A stabilization diagram and the identified natural frequencies

Table 28.1 Mean and covariance of the natural frequencies

Setup	Mode	Natural frequency [Hz]	
		Mean	COV [%]
A	1	1.19	0.6
	2	2.16	1.3
	3	3.14	0.9
B	1	1.20	0.5
	2	2.16	1.7
	3	3.18	0.8

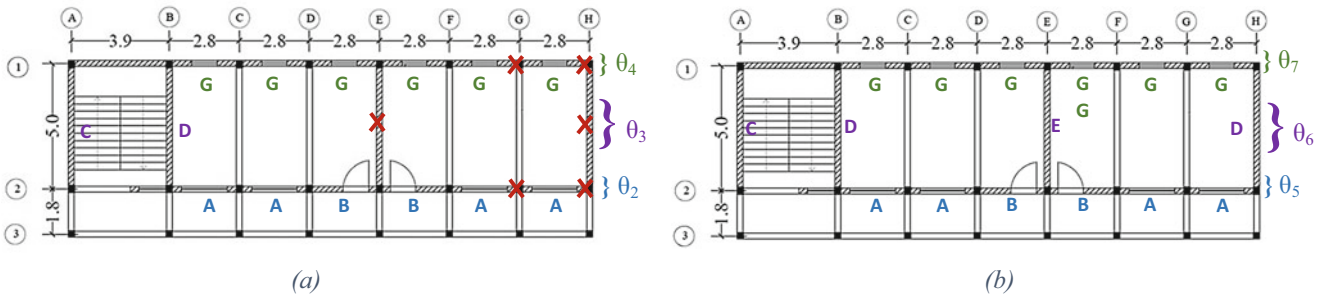


Fig. 28.5 Updating parameters for first two stories (a) Updating parameters for 1st story (b) Updating parameters for 2nd story

of elasticity of 2022 ksi is chosen for the beams and columns of the building. More details on the development of the nonlinear numerical model of the structure can be found in [13, 14].

In this study, severely damaged walls and columns, specifically in the 1st floor, are removed as they would not contribute to the stiffness of the structure under ambient vibrations due to the existence of large cracks. These elements include: H12 and E12 infill walls and H1, H2, G1 and G2 columns (Fig. 28.5). The remaining elements are considered to have an initial stiffness of about 40% of their unloaded and uncracked condition, based on ACI recommendation [18]. In this study, the linear range of behavior of the damaged structure is considered, as this is the range of behavior of the structure recorded during the reconnaissance trip.

Modal parameters of this reference model are calculated and compared to the identified values from the previous section, as shown in the fourth column of Table 28.2. Natural frequencies of the initial model are found to be higher than the identified values which can be attributed to the fact that any loss of stiffness of the elements after the earthquake has been ignored, with the exception of the elements completely removed from the reference model. Modal Assurance Criterion (MAC) values also show good agreement between model and identified mode shapes with MAC value of 0.99 for the 1st mode and an average MAC value of 0.93 for all three modes.

Table 28.2 Modal parameters from the system identification, reference model and the updated models

Modal parameters	Mode	System identification	Reference model	Model with $w_\theta = 0\%$	Model with $w_\theta = 1\%$	Model with $w_\theta = 2\%$	Model with $w_\theta = 5\%$
Frequencies (Hz)	Mode1	1.19	1.30	1.19	1.19	1.19	1.19
	Mode2	2.16	2.69	2.16	2.17	2.17	2.17
	Mode3	3.16	3.39	3.15	3.15	3.15	3.16
MAC values	Mode1	–	0.990	0.992	0.991	0.991	0.991
	Mode2	–	0.886	0.995	0.994	0.993	0.991
	Mode3	–	0.910	0.981	0.983	0.982	0.983
	Average	–	0.929	0.989	0.989	0.989	0.988

Since our model is just considered in its linear range, modulus of elasticity of reinforced concrete material is considered as the updating parameter. The updating parameters θ are defined as the ratio of updated to initial elastic modulus:

$$\theta_i = \frac{E_i^{Updated}}{E_i^{Initial}} \quad (28.1)$$

To limit the number of updating parameters, structural elements are grouped to 9 parameters. Due to their lower influence on the lateral stiffness of the structure, and their relatively lower uncertainty and sensitivity, the beams and columns stiffness are grouped together as one updating parameter, namely θ_1 . Similarly, the undamaged infill walls in the 3rd and 4th floor are grouped together as parameters θ_8 and θ_9 , respectively. As for the infill walls in the 1st and 2nd floors, three updating parameters per floor are considered, $\theta_2 - \theta_7$. The goal of this selection is to investigate if the updating algorithm can distinguish between the two floors and accurately identify the concentration of damage in the first floor. Figure 28.5 shows the updating parameters in the first two floors of the building.

The objective function for the model updating is then expressed as:

$$f(\boldsymbol{\theta}) = \mathbf{r}(\boldsymbol{\theta})^T \mathbf{W} \mathbf{r}(\boldsymbol{\theta}) + (\boldsymbol{\theta} - \boldsymbol{\theta}_0)^T \mathbf{W}_\theta (\boldsymbol{\theta} - \boldsymbol{\theta}_0) \quad (28.2)$$

where $\mathbf{r}(\boldsymbol{\theta})$ is the residual vector and \mathbf{W} is a diagonal weighting matrix to account for the impact of different residuals. The second term in Eq. (28.2) is a regularization term with $\boldsymbol{\theta}_0$ as the initial guess of the updating parameters, and \mathbf{W}_θ as the diagonal matrix of regularization factors. To investigate the effect of this regularization factors on the model updating results, four scenarios are considered with the value regularization factors set to 0, 1, 2 and 5%.

The vector of residuals in this study is defined as:

$$\mathbf{r}(\boldsymbol{\theta}) = \begin{bmatrix} \mathbf{r}_f(\boldsymbol{\theta}) \\ \mathbf{r}_\Phi(\boldsymbol{\theta}) \end{bmatrix} \quad (28.3)$$

$$\mathbf{r}_f(\boldsymbol{\theta}) = \frac{\tilde{\lambda}_i - \lambda_i(\boldsymbol{\theta})}{\tilde{\lambda}_i} \quad (28.4)$$

$$\mathbf{r}_\Phi(\boldsymbol{\theta}) = \frac{\tilde{\Phi}_i}{\|\tilde{\Phi}_i\|} - a_i \frac{\Gamma \Phi_i(\boldsymbol{\theta})}{\|\Gamma \Phi_i(\boldsymbol{\theta})\|} \quad (28.5)$$

where $\mathbf{r}_f(\boldsymbol{\theta})$ is the eigenfrequency residual vector, $\mathbf{r}_\Phi(\boldsymbol{\theta})$ is the mode shape residual vector, $\tilde{\lambda}_i = (2\pi\tilde{f}_i)^2$ refers to the identified natural frequency and $\tilde{\Phi}_i$ refers to the identified mode shape vector of the i th mode. Γ is a matrix which keeps only the observed components of the model-generated mode shapes and a_i is defined as:

$$a_i = \frac{\tilde{\Phi}_i^T \Gamma \Phi_i(\boldsymbol{\theta})}{\|\tilde{\Phi}_i\| \|\Gamma \Phi_i(\boldsymbol{\theta})\|} \quad (28.6)$$

The optimization process is conducted in MATLAB using a constrained minimization algorithm (fmincon), which finds the local minimum of a nonlinear and multivariable function subject to a set of constraints [19]. In our case, the only constraint is the lower and upper bound of the parameters which are chosen to be 0.0 and 2.0, respectively.

Table 28.3 Updated parameter values from the deterministic model updating

Updating parameter	Structural component	Model with $w_\theta = 0\%$	Model with $w_\theta = 1\%$	Model with $w_\theta = 2\%$	Model with $w_\theta = 5\%$
θ_1	All columns and beams	1.39	1.36	1.32	1.20
θ_2	1st story – Frames A, B	0.12	0.16	0.18	0.27
θ_3	1st story – Frames C, D	1.06	0.83	0.78	0.85
θ_4	1st story – Frames F, G	0.30	0.30	0.30	0.30
θ_5	2nd story – Frames A, B	0.36	0.64	0.76	0.85
θ_6	2nd story – Frames C, D, E	0.45	0.65	0.78	0.86
θ_7	2nd story – Frames F, G	1.04	1.01	0.96	0.90
θ_8	3rd story – All frames	1.27	1.13	1.08	1.01
θ_9	4th story – All frames	1.78	1.18	1.12	1.06
Average absolute change of parameters		0.48	0.34	0.31	0.25

Table 28.2 shows the identified modal parameters as well as modal parameters corresponding to the reference model and the updated models. As it can be seen, all updated models, regardless of their corresponding regularization factors, match the identified modal parameters accurately for the three identified modes of the structure.

The updated stiffness parameters, however, don't coincide for the four considered regularization factors. It can be seen in Table 28.3 that the average of absolute changes in the parameters reduces as we move to the larger regularization factors.

Some of the updating results in the case without a regularization term seem to be inaccurate and unrealistic, e.g., the stiffness of the infill walls in the 4th floor is increased by 78%. The updating algorithm with regularization factors seem to be close and realistic. They all point into a drastic loss of stiffness in θ_2 and θ_4 (first story frames A, B, F, G) which is consistent with the on-site observations.

28.5 Bayesian Model Updating

In this section we apply a Bayesian model updating to find the probability distribution of the considered updating parameters in the school building. A detailed description of Bayesian model updating can be found in literature [3]. A brief review is presented here to clarify the process applied in this study. The Bayes theorem can be written as:

$$p(\boldsymbol{\theta}|\mathbf{d}) = cp(\mathbf{d}|\boldsymbol{\theta})p(\boldsymbol{\theta}) \quad (28.7)$$

In this formula, $p(\boldsymbol{\theta}|\mathbf{d})$ is the posterior probability distribution function (PDF) of updating parameters (stiffness ratios here) given the measured data, \mathbf{d} (identified modal parameters here), c is a normalizing constant which reflects the data evidence and ensures that the posterior PDF will integrate to one, $p(\mathbf{d}|\boldsymbol{\theta})$ is the likelihood function and is the probability of observing the specific measured data for any given updating parameters, and $p(\boldsymbol{\theta})$ is the prior PDF which reflects our initial knowledge of the updating parameters. In this study, prior PDF is considered as a normal distribution, assuming independent parameters (θ_i) with mean θ_{i0} and variance $\sigma^2_{\theta_i}$:

$$p(\boldsymbol{\theta}) = \prod_{i=1}^n \exp\left(-\frac{1}{2} \frac{(\theta_i - \theta_{i0})^2}{\sigma_{\theta_i}^2}\right) \quad (28.8)$$

Such prior PDF acts similar to the regularization term used in Eq. (28.2). Likelihood function can be calculated as a product of marginal probability distributions of eigen-frequency and mode shape data assuming their statistical independence.

$$p(\mathbf{d}|\boldsymbol{\theta}) = \prod_{i=1}^m p(\tilde{\lambda}_i|\boldsymbol{\theta}) \cdot p(\tilde{\boldsymbol{\Phi}}_i|\boldsymbol{\theta}) \quad (28.9)$$

Here, m refers to the number of modes.

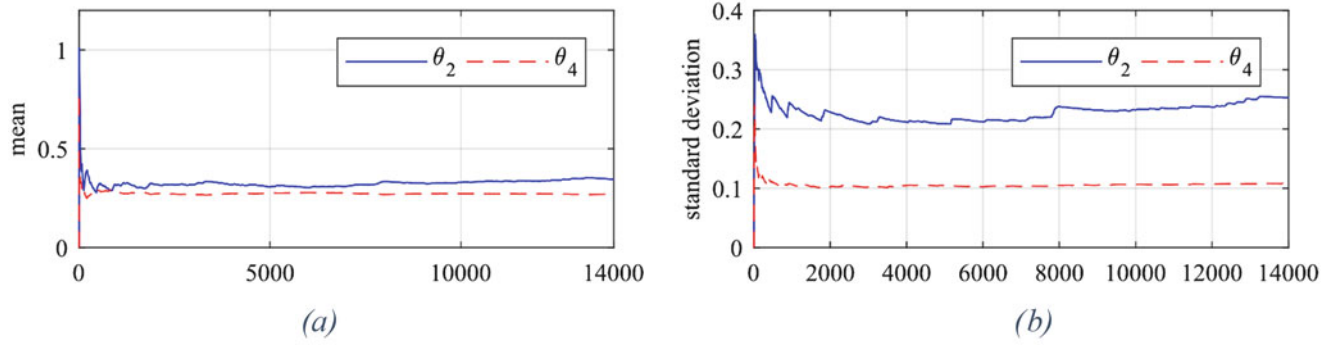


Fig. 28.6 (a) mean and (b) standard deviation of the parameters, based on the sample size

To define the likelihood function, the following error functions are defined and assumed to follow zero mean Gaussian distributions.

$$e_{\lambda_i} = \tilde{\lambda}_i - \tilde{\lambda}_i(\boldsymbol{\theta}) \quad (28.10)$$

$$\mathbf{e}_{\Phi_i} = \frac{\tilde{\Phi}_i}{\|\tilde{\Phi}_i\|} - a_i \frac{\boldsymbol{\Gamma} \Phi_i(\boldsymbol{\theta})}{\|\boldsymbol{\Gamma} \Phi_i(\boldsymbol{\theta})\|} \quad (28.11)$$

Note that the choice of error function and prior PDF provides a similar negative log-posterior function as the deterministic objective function, i.e., the maximum a-posteriori (MAP) estimated are expected to be similar as the optimal deterministic parameters.

Based on these choices of likelihood (i.e., error functions) and prior, the posterior PDF can be represented as:

$$p(\boldsymbol{\theta}|\mathbf{d}) \propto \exp\left(-\frac{1}{2}\mathbf{J}(\boldsymbol{\theta}, \mathbf{d})\right) \quad (28.12)$$

where $\mathbf{J}(\boldsymbol{\theta}, \mathbf{d})$ is:

$$\mathbf{J}(\boldsymbol{\theta}, \mathbf{d}) = \sum_{i=1}^m \frac{(e_{\lambda_i})^2}{\sigma_{\lambda_i}^2} + \sum_{i=1}^m \frac{\mathbf{e}_{\Phi_i}^T \cdot \mathbf{e}_{\Phi_i}}{\sigma_{\Phi_i}^2} + \sum_{i=1}^n \frac{(\theta_i - \theta_{i_0})^2}{\sigma_{\theta_i}^2} \quad (28.13)$$

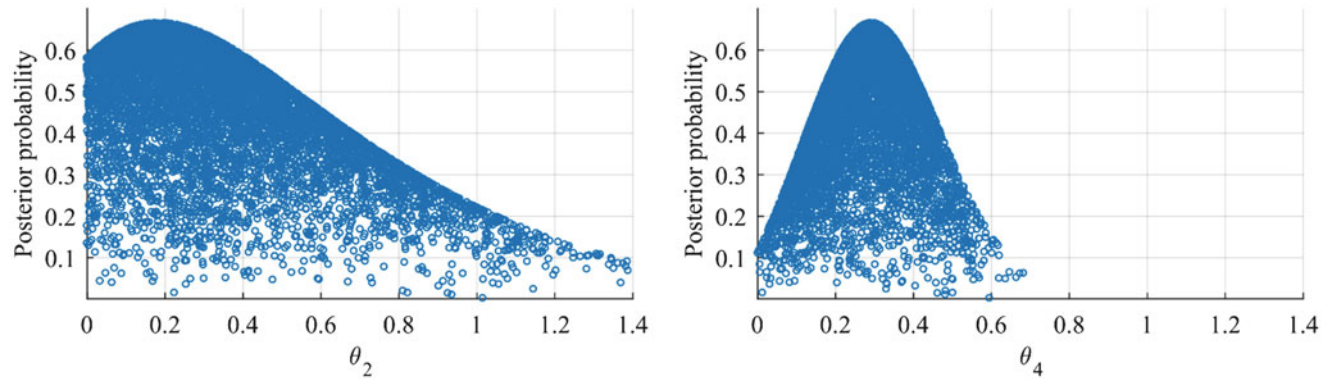
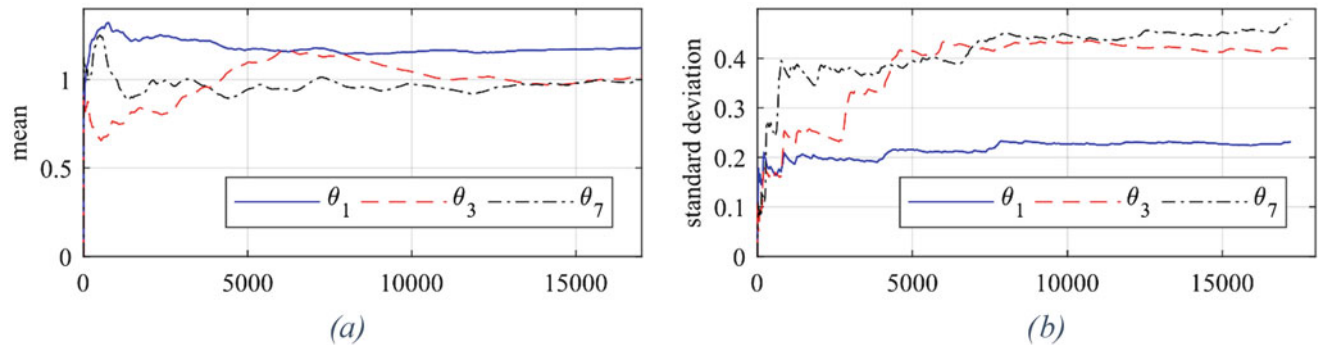
In this equation, σ_{λ_i} is the standard deviation of the i^{th} eigenfrequency, σ_{Φ_i} is the standard deviation of mode shape components for i^{th} mode, and σ_{θ_i} is the standard deviation of i^{th} updating parameter in prior. To sample the posterior PDF in the formulate Bayesian model updating, Markov Chain Monte Carlo (MCMC) is used.

Given the computational cost of MCMC method, we started the Bayesian analysis by updating just two parameters, namely θ_2, θ_4 which refer to the two most damaged substructures. The prior standard variations are selected so the \mathbf{J} function is similar to its deterministic counterpart with 2% regularization factor. The other two standard deviations are also selected based on the values from the equivalent deterministic analysis. The MCMC is implemented using a Gaussian proposal PDF with 0.1 standard deviation and a total of 14,000 are generated. The acceptance ratio of the random walk for the selected proposal PDF is 60%. Figure 28.6 shows the mean and standard deviation of the two updating parameters for accumulating number of samples. The figure shows a fast convergence of the algorithm after just 2000 samples.

Table 28.4 compares the MAP values and optimal values for a similar deterministic case of updating the two considered parameters. It can be seen that the results are almost identical which confirms that the local optimization approach has reached the global minimum for the deterministic application and the MCMC has been successful to sample the high probability region of joint posterior PDF. In the last row of the table, the objective function of the deterministic method is compared with the equivalent value from the Bayesian method, i.e., $1/2 \mathbf{J}(\boldsymbol{\theta}, \mathbf{d})$. As it can be seen, the two values are the same.

Table 28.4 Bayesian (MAP and standard deviation) and deterministic (optimal) model updating results for the bivariate case

Updating parameter	Deterministic model updating ($w_0 = 2\%$)	Bayesian model updating (proposal step = 0.1)
θ_2	0.18	0.18 (<i>std</i> = 0.25)
θ_4	0.29	0.29 (<i>std</i> = 0.11)
Final objective function value	0.409	0.409

**Fig. 28.7** Posterior probability of θ_2 and θ_4 samples**Fig. 28.8** (a) mean and (b) standard deviation of the parameters, based on the sample size

The values of posterior PDFs for all the samples are shown in Fig. 28.7 for each of the updating parameters. Note that, while they have similarities, these plots are not the marginal posterior PDF of updating parameters. The plots also show that the posterior distributions have smaller variability than priors indicating that information is gained about updating parameters from the measured data. It can also be seen that θ_4 has narrower posterior than θ_2 which can be due to the fact that data is more informative (larger sensitivity) about the value of θ_4 . This observation is consistent with results of Table 28.3, where the value of θ_4 is not affected by the regularization factors while θ_2 is somewhat affected. In the table, it is also seen that the optimal values for some parameters with less sensitivity to the measured data are drastically influenced by the regularization term.

The Bayesian model updating is performed again using all the 9 updating parameters defined previously. In this case, the metropolis algorithm used for MCMC has more difficulty to sample to the joint posterior PDF and find the MAP with a reasonable size of samples (<20,000). As it can be seen in Fig. 28.8, in some cases, it takes 10,000 sample points for the mean values to get stable. This makes it challenging to have the parameters with lower sensitivity to data to converge, and therefore the samples may not provide the marginal MAP values for these parameters.

Two different proposal PDFs are used in the implementation of Metropolis algorithm, with standard deviations of 0.05 and 0.1. Table 28.5 reports the MAP values of the updating parameters from both MCMC trials and compares the results with their corresponding deterministic optima. It is observed that the MAP values and deterministic optima are close for parameters with higher sensitivity to the data, while the values are less consistent for others. The objective function values are also close for the three sets of results but are not identical. The fact that objective function values for the Bayesian updating results are higher than the deterministic ones indicates that more samples in the high probability region are needed for accurate estimation of MAP.

Table 28.5 Bayesian (MAP and standard deviation) and deterministic (optimal) model updating results for 9 updating parameters

Updating parameter	Deterministic model updating ($w_0 = 2\%$)	Bayesian model updating (proposal step = 0.05)		Bayesian model updating (proposal step = 0.1)	
		MAP	std	MAP	std
θ_1	1.32	1.23	0.23	1.26	0.23
θ_2	0.18	0.20	0.18	0.17	0.19
θ_3	0.78	1.25	0.54	1.15	0.42
θ_4	0.30	0.31	0.09	0.27	0.09
θ_5	0.76	0.77	0.56	0.87	0.61
θ_6	0.78	0.46	0.54	0.56	0.69
θ_7	0.96	1.03	0.54	0.98	0.48
θ_8	1.08	1.15	0.74	1.07	0.49
θ_9	1.12	1.28	0.59	0.98	0.61
Final objective function value	0.433	0.466		0.474	
Acceptance ratio	–	49%		26%	

28.6 Conclusions

Deterministic and Bayesian finite element model updating studies are performed for performance assessment of an RC building in Nepal, after Gorkha earthquake. The modal parameters of the building are estimated from in-situ recordings of the ambient vibration of the building after the earthquake. An initial model of the structure is developed in OpenSEES software and residuals/ error functions are defined as the difference between the model-predicted and identified modal parameters. The stiffness of different substructures in the building is selected as the updating parameters and their values are tuned to minimize the residuals. The deterministic finite element model updating is performed through a local optimization algorithm with different levels of regularization, to mitigate the unrealistic changes in parameters that are not sensitive to data. The calibrated model provides an accurate match with the identified modal parameters. However, results are sensitive to the regularization factor. The damaged components, as observed in-situ, are detected accurately with small variability of identified stiffness. Bayesian model updating is then conducted using similar residuals, defined as error functions in Bayesian formulation, and a prior PDF which provides comparable regularization as the deterministic case. The Bayesian approach is in excellent agreement with deterministic results when only two updating parameters with adequate sensitivity to data are used. However, the sampling algorithm implemented in the Bayesian approach struggles to find the absolute MAP when all 9 updating parameters are considered. In this case, the results are close to their deterministic counterparts but are not identical. Overall, both methods provide consistent results and are capable of detecting and quantifying damage in the main two damaged substructures θ_2 and, θ_4 .

Acknowledgements Partial support of this study by the National Science Foundation Grants 1254338, 1430180, and 1545595 is gratefully acknowledged. The opinions, findings, and conclusions expressed in this paper are those of the authors and do not necessarily represent the views of the sponsors and organizations involved in this project.

References

- Mottershead, J.E., Friswell, M.I.: Model updating in structural dynamics: a survey. *J. Sound Vib.* **167**(2), 347–375 (1993)
- Moaveni, B., Conte, J.P., Hemez, F.M.: Uncertainty and sensitivity analysis of damage identification results obtained using finite element model updating. *J. Comput. Aided Civ. Infrastruct. Eng.* **24**(5), 320–334 (2009)
- Beck, J.L., Katafygiotis, L.S.: Updating models and their uncertainties. I: Bayesian statistical framework. *ASCE J. Eng. Mech.* **124**(4), 455–461 (1998)
- Behmanesh, I., Moaveni, B.: Probabilistic identification of simulated damage on the Dowling Hall footbridge through Bayesian finite element model updating. *Struct. Control. Health Monit.* **22**, 463–483 (2015)
- Rai, D.C., Singhal, V., Raj, B.S., Sagar, L.: Reconnaissance of the effects of the M7.8 Gorkha (Nepal) earthquake of April 25, 2015. *J. Geom. Nat. Hazards Risk*, Taylor Francis. **7**(1), 1–17 (2015)
- Bose, S., Nozari, A., Mohammadi, M.E., Stavridis, A., Moaveni, B., Wood, R., Gillins, D., Barbosa, A.: Structural Assessment of a school building in Sankhu, Nepal damaged due to torsional response during the 2015 Gorkha earthquake. *Proceedings of International Modal Analysis Conference, 34th IMAC, Orlando, Florida* (2016)

7. Oppenheim, A.V., Willsky, A.S., Young, I.T.: Signals and Systems, p. 256. Prentice-Hall, Inc., ISBN 0-13-809731-3, Englewood Cliffs (1983)
8. Caicedo, J.M., Dyke, S.J., Johnson, E.A.: Natural excitation technique and Eigensystem realization algorithm for phase I of the IASC-ASCE benchmark problem: simulated data. *J. Eng. Mech.* **130**, 49–60 (2004)
9. Juang, J.N., Pappa, R.S.: An eigensystem realization algorithm for modal parameter identification and model reduction. *J. Guid. Control. Dyn.* **8**(5), 620–627 (1985)
10. He, X., Moaveni, B., Conte, J.P., Elgamal, A.: Comparative study of system identification techniques applied to New Carquinez Bridge, Proc. of 3rd International Conference on Bridge Maintenance, Safety, and Management, Porto, Portugal (2016)
11. Moaveni, B., He, X., Conte, J.P., Restrepo, J.I., Panagiotou, M.: System identification study of a 7-story full-scale building slice tested on the UCSD-NEES shake table. *J. Struct. Eng.* **137**(6), 705–717 (2010)
12. McKenna, F., Fenves, G.L., Scott, M.H., Jeremic, B.: Open System for Earthquake Engineering Simulation (OpenSees), Pacific Earthquake Engineering Research Center. University of California, Berkeley (2000)
13. Tempestti, M., Stavridis, A.: Updating the ASCE 41 provisions for Infilled RC frames.” Proc. 2017 SEAOC Convention, San Diego, California, September 2017
14. Martin Tempestti, A.: Stavridis. “Simplified method to assess the lateral resistance of infilled reinforced concrete frames.” Proc. 16th World Conference in Earthquake Engineering, Santiago Chile, January 2017
15. Chaulagain, H., Rodrigues, H., Spacone, E., Varum, H.: Seismic Assessment of RC Structures with Infill Masonry Panels in Nepal – Sensitivity Analysis. Second European Conference on Earthquake Engineering and Seismology, Istanbul, Turkey (2014)
16. Pradhan, P.L.: Composite actions of brick infill wall in RC frame under in-plane lateral load. PhD Dissertation, Tribhuvan University, Pulchowk Campus (2009)
17. Bose, S., Nozari, A., Stavridis, A., Moaveni, B.: Nonlinear modeling of a school at Sankhu for performance assessment during the 2015 Nepal earthquake, 16th World Conference on Earthquake Engineering, Santiago, Chile (2017)
18. ACI 369: Guide for Seismic Rehabilitation of Existing Concrete Frame Buildings and Commentary, American Concrete Institute (2011)
19. MATLAB: R2017a, MathWorks Inc., MA, USA (2017)



Chapter 29

Interpreting the Eigenbasis of Principal Component Analysis to Identify Design Space Regions of Interest

B. Daughton, P. Alexeenko, D. Alexander IV, G. N. Stevens, and E. M. Casleton

Abstract Computational models are a valuable tool for predicting the behavior of complex systems in regimes that are difficult, or infeasible to test. Uncertainties in a model resulting from lack of knowledge regarding parameters needed to define system behavior raise concern in simulations predictions, particularly those in extreme operating regimes. In such cases, calibration and validation of numerical models across a large operational domain is beneficial, but creates a high dimensional domain in which the model must be tested. Statistical decomposition methods present an ability to reduce the dimensionality of a measured or simulated quantity while maintaining relevant correlations across the domain, therefore providing insight to important relationships between input parameters and system response throughout many loading scenarios. Principal Component Analysis (PCA) is a commonly used statistical decomposition method used to produce a low order projection from a higher dimensional space. Herein, we evaluate a specific component of PCA, the eigenvectors providing statistical weighting to explanatory variables, to identify variable model sensitivity across high dimensional operational domains. The concept is demonstrated by simulation of an elasto-plastic material undergoing tensile testing at variable loading conditions. Results indicate that the eigenbasis reveals distinct relationships between a model's behavior and uncertain parameters, even when the relationship is not readily apparent and without relying on any a priori knowledge of system or material behavior.

Keywords Principal Component Analysis · Sensitivity Analysis · Statistical Decomposition · Quantifications of Margins and Uncertainties · Quantities of Interest

29.1 Introduction

Models are traditionally used as forward predictors to understand the behavior of a system under various loadings. Forward modeling requires an understanding of system characteristics, such as material properties, boundary conditions, and coupling among components, which are assumed to be known. However, in reality complete knowledge of system, particularly as they become more complex, is not attainable, and uncertainties are therefore introduced in the model. Such input uncertainties motivate inverse analysis, where unknown or variable system properties may be treated as uncertain model parameters and their “true” values are sought by model calibration. Model calibration is the process of learning values of uncertain input parameters by seeking model inputs that optimize a fit of predictions to experimental measurements. Accompanying model calibration is model validation, which seeks to a calibrated model accurately reflects real-world behavior of the system across many different domains, not just settings at which parameters were calibrated.

Sensitivity analysis is traditionally the first step in any model calibration and validation study, and is employed to determine parameters in a model that account for the most significant degree of uncertainty in the model response. Accurate models are imperative for predicting in extreme environments where an experiment is not environmentally or

B. Daughton
Chemical Engineering Department, New Mexico Institute of Mining and Technology, Socorro, NM, USA

P. Alexeenko
Electrical and Computer Engineering, Cornell University, Ithaca, NY, USA

D. Alexander IV
Department of Mechanical Engineering, Tuskegee University, Tuskegee, AL, USA

G. N. Stevens (✉) · E. M. Casleton
Los Alamos National Laboratory, Los Alamos, NM, USA
e-mail: garrison@lanl.gov

financially feasible. Confidence in these predictions, however, requires sufficient experimental data in testable regimes. Such experiments may themselves be extremely costly. Therefore, efficient design of experiments to ensure optimal testing for model calibration are valuable. Furthermore, maximizing information gain of existing data is also critical. As systems become more complex, a single quantity of interest may span across several operational settings (i.e. temperatures or frequencies) as well as over large spatial and temporal domains. Increasingly, experimental techniques are available to collect full-field measurements across these domains. However, benefits of detailed experimental data cannot be fully realized until calibration and validation metrics are expanded to capture the same full-field, multi-domain behaviors.

Decomposition methods reduce the dimensionality of the data while maintaining information and are particularly useful in large data sets. Our goal is to maximize information gained from experimental data across many operational domains. By combining this information, rather than analyzing each point in an independent manner, we seek to increase our understanding of parameter sensitivity in different domains and therefore best calibrate relevant parameters in their respective domains of high sensitivity. Data is analyzed in this high dimensional space through an innovative application of Principal Component Analysis (PCA), where the intermediate step of the eigenbasis is relied upon for information rather than the traditional approach of analyzing reduced order projections.

The paper is organized as follows. Section 29.2 provides relative background information on model calibration and uncertainty quantification, as well as PCA. Details of the finite element model and embedded material model are provided in Sect. 29.3. Details of the methodology for developing a high-dimensional response matrix and the accompanying decomposition are presented in Sect. 29.4 and results of the decomposition are presented in Sect. 29.5. Finally, Sect. 29.6 concludes with key takeaways and discussion of a path forward for future work.

29.2 Background

29.2.1 *Model Calibration and Uncertainty Quantification in Large Dimensional Space*

Model calibration and uncertainty quantification is necessary because of the inherent error associated with measurement inaccuracies and mathematical models of real-world behavior. When approaching nonlinear real-world behavior analytically, the instability of the model may result in small fluctuations in input values causing large output effects, making the system unpredictable as time progresses.

It is noted by Kabanikhin [1] that model instability is a common behavior of inverse and ill posed problems. Problems are deemed ill posed when there is more than one solution, no solution, or the estimation procedure is unstable causing measurement errors that are greatly augmented in the solution. This is a concern when calibrating the parameters of a mathematical model to reproduce observations because the mathematical analysis is subtle. Large data sets may be used to mitigate this problem, acting as a trial and error method suggested by Tikhonov and Arsenin [2], to approximate solutions for conditionally well-posed problems. The trends of the outputs compared with known information on the physical system, such as boundary conditions and experimental results, to highlight where the mathematical model is providing pseudo-solutions could benefit calibration.

Full-field models become unwieldy because of high-dimensionality. The problems associated with high dimensionality are explored by Donoho [3] and Fan et al. [4], and methods of feature selection are suggested. Because of the computational challenges presented by full-field models, quantification of margins and uncertainties (QMU) may be conducted on surrogate models. Xie and Li explored the use of the integrated Kriging surrogate model for reducing the computational cost of the Monte Carlo method [5]. Allemang et al. explored the creation of surrogate models using PCA [6]. Cross validation in PCA has been explored across various dimensions. Giancarlo et al. [7] and Josse et al. [8] examined the optimal number of components to be retained. Krzanowski discusses selection of important observations and variables [9].

Sensitivity analysis studies how uncertainty in model outputs can be traced back to uncertainty in model parameters [10]. It has varying applications, including selection of assumptions, assessing risk, and identifying important input parameters [11]. This paper is chiefly concerned with the last point. Traditional methods for conducting sensitivity analysis include variance-based, entropy-based, and distribution-based. Of these, variance-based sensitivity analysis is the most closely related to the methodology presented in this paper. However, the methods presented in this paper differ from variance-based sensitivity analysis. For example, Sobol's method decomposes output variance into a sum of input variances of increasing dimensionality [12], while the method presented here looks for correlations between input parameters and directions of maximum variance.

29.2.2 Principal Component Analysis

Principal Component Analysis (PCA) transforms a set of potentially correlated variables into a set of uncorrelated variables called the principal components, which are linear combinations of the original variables [13]. The principal components are selected so that the fewest possible components capture the greatest possible variation in the original data. The coefficients or statistical loadings on the principal components and variances of the principal components are the eigenvectors and eigenvalues of the covariance matrix of the data [13].

While PCA and Exploratory Factor Analysis (EFA) are often treated as synonymous, there are fundamental differences between the two variable reduction methods. PCA retains account for a maximal amount of variance of observed variables, while EFA account for the common variance in the data. PCA incorporates ones on the diagonals of the correlation matrix, while EFA utilizes an adjusted unique factor on the diagonals of correlation matrix. PCA minimizes the sum of squared perpendicular distance to the component axis, and the principal component scores are a linear combination of the observed variables weighted by eigenvectors. EFA estimates factors that influence responses on observed variables, and the observed variables are linear combinations of the underlying and unique factors [14].

29.3 Model Development

29.3.1 Finite Element Model

A uniaxial tensile test is modeled in ABAQUS for sampling different material properties. This output of the test is maximum strain, as measured at the center of the coupon. The material properties specified are Poisson's ratio of 0.35 and a Young's modulus that ranges from 60 GPa to 80 GPa. The coupon is tensioned with varying forces from 10 to 100 N at varying strain rates from 0.15 to 1.5 s⁻¹. Both ends of the coupon are fixed boundaries, which centers the load in the middle of the coupon. The test is performed using a dog bone model that is 180 mm long with a cross sectional area of 50 mm² at center (Fig. 29.1).

29.3.2 Material Model

In order to define the material properties, various stress strain curves were formed and sampled. The elastic region of a stress strain curve is modeled using Young's modulus, however there is no current method that easily models the hardening portion of the stress strain curves. This equation is an accepted model for describing the hardening portion of metals, particularly Aluminum, on a stress strain curve. The Fields-Backofen equation (Eq. 29.1) models stress, σ , as a function of strain, ϵ , and strain rate, $\dot{\epsilon}$ (Eq. 29.1). Uncertain parameters in the Fields-Backofen model include the strength coefficient K , strain hardening exponent, n , and strain rate sensitivity exponent, m [15, 16]. This elasto-plastic model provides an interesting model for the present analysis due to the known change in sensitivity of the model response in the elastic and plastic regimes, as well as the inclusion of strain rate as a control parameter in the Fields-Backhofen model.

Fig. 29.1 Coupon dimensions

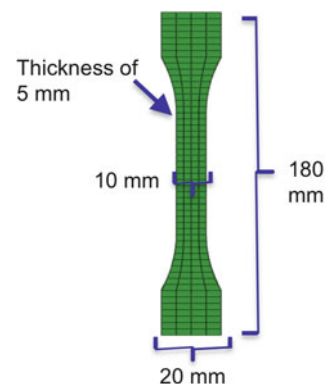
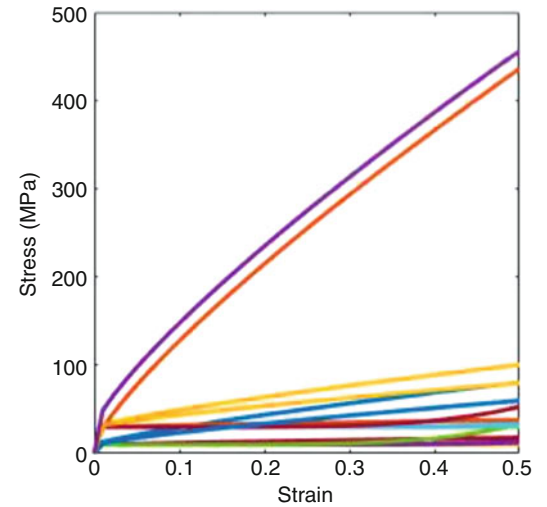


Table 29.1 Control and uncertain model parameter ranges

Variable	Minimum	Maximum
<i>Control parameters</i>		
Strain rate, $\dot{\varepsilon}$ (s^{-1})	0.15	1.50
Force, F (kN)	0.10	100
<i>Uncertain parameters</i>		
Yield stress, σ_Y (MPa)	34.0	500
Young's modulus, E (GPa)	60.0	80.0
Strength coefficient, K	117	2110
Strain hardening exponent, n	0.80	5.00
Strain rate sensitivity exponent, m	0.10	0.70

Fig. 29.2 Sample stress-strain curves for material model generated from two-level full factorial design of parameter space



$$\sigma = K\varepsilon^n \dot{\varepsilon}^m \quad (29.1)$$

29.3.3 Model Parameters

Herein, control parameters, denoted as \mathbf{x} , are those that control the condition at which a test is operating. For the tensile test the control parameters are strain rate and magnitude (force) of the tensile load. Uncertain parameters, denoted as $\boldsymbol{\theta}$, are those defining system properties for which the true value is not known. Ranges for these values are provided in Table 29.1. Figure 29.2 illustrates the variability in stress-strain curves resulting from a two-level full factorial sampling of uncertain model parameters.

29.4 Methodology: Statistical Decomposition of High Dimensional Sample Space

In order to perform statistical decomposition, the data must be arranged into vectors of measured values corresponding to desired explanatory variables. There are two distinct ways in which the data matrix can be evaluated; explanatory characteristics (i.e. material properties) or conversely explanatory controls (e.g. load case). In the first case, uncertain parameters, $\boldsymbol{\theta}$, are the explanatory variables with control settings, \mathbf{x} , generating variable observations. Consider the observations, Y , taken at a single control setting, i , varied across p draws in the uncertain parameter domain. Our observations, Y_i take the form:

$$Y_i = \{\varepsilon(\mathbf{x}_i, \boldsymbol{\theta}_1), \varepsilon(\mathbf{x}_i, \boldsymbol{\theta}_2), \dots, \varepsilon(\mathbf{x}_i, \boldsymbol{\theta}_p)\} \quad (29.2)$$

where $i = 1, 2, \dots, q$ and q is the number of control domain samples. Y_i is therefore a vector of strain responses given the i^{th} draw of control parameters, \mathbf{x} , throughout the full uncertainty domain. Model outputs are then sampled over q control scenarios, forming a $q \times p$ response matrix:

$$\mathbf{Y} = \begin{bmatrix} \varepsilon(\mathbf{x}_1, \boldsymbol{\theta}_1) & \varepsilon(\mathbf{x}_1, \boldsymbol{\theta}_2) & \dots & \varepsilon(\mathbf{x}_1, \boldsymbol{\theta}_p) \\ \varepsilon(\mathbf{x}_2, \boldsymbol{\theta}_1) & \varepsilon(\mathbf{x}_2, \boldsymbol{\theta}_2) & \dots & \varepsilon(\mathbf{x}_2, \boldsymbol{\theta}_p) \\ \vdots & \vdots & \ddots & \vdots \\ \varepsilon(\mathbf{x}_q, \boldsymbol{\theta}_1) & \varepsilon(\mathbf{x}_q, \boldsymbol{\theta}_2) & \dots & \varepsilon(\mathbf{x}_q, \boldsymbol{\theta}_p) \end{bmatrix} \quad (29.3)$$

For statistical decomposition, the covariance matrix of the observations, considering $\boldsymbol{\theta}$ as the explanatory variable, is given by:

$$\begin{bmatrix} \text{Var}(\mathbf{Y}_{1:q,1}) & \dots & \text{Cov}(\mathbf{Y}_{1:q,1}, \mathbf{Y}_{1:q,p}) \\ \vdots & \ddots & \vdots \\ \text{Cov}(\mathbf{Y}_{1:q,p}, \mathbf{Y}_{1:q,1}) & \dots & \text{Var}(\mathbf{Y}_{1:q,p}) \end{bmatrix} \quad (29.4)$$

In the second scenario, control settings, \mathbf{x} , are the explanatory variables with uncertain parameters, $\boldsymbol{\theta}$, creating variable observations. Our observation vector, \mathbf{Y}_j , therefore takes the form:

$$\mathbf{Y}_j = \{\varepsilon(\mathbf{x}_1, \boldsymbol{\theta}_j), \varepsilon(\mathbf{x}_2, \boldsymbol{\theta}_j), \dots, \varepsilon(\mathbf{x}_q, \boldsymbol{\theta}_j)\} \quad (29.5)$$

and the covariance matrix, considering \mathbf{x} as the explanatory variable, becomes:

$$\begin{bmatrix} \text{Var}(\mathbf{Y}_{1,1:p}) & \dots & \text{Cov}(\mathbf{Y}_{1,1:p}, \mathbf{Y}_{q,1:p}) \\ \vdots & \ddots & \vdots \\ \text{Cov}(\mathbf{Y}_{q,1:p}, \mathbf{Y}_{1,1:p}) & \dots & \text{Var}(\mathbf{Y}_{q,1:p}) \end{bmatrix} \quad (29.6)$$

Figure 29.3 illustrates the evolution of the response matrix, \mathbf{Y} . First a sample $i = 1$ is selected from the control domain. The model is then tested with all q material model samples under load case \mathbf{x}_1 (ε_1, F_1) resulting in a distribution of strain predictions at the center of the coupon (red histogram), becoming the response vector \mathbf{Y}_1 , or $\mathbf{Y}_{1:q,1}$ in the response matrix. Next, a new control sample $i = 2$ is taken and the simulation with the full suite of material models is tested with load case \mathbf{x}_2 (ε_2, F_2), forming the second strain distribution (green histogram) and the response matrix is expanded with a second column of observations. Herein, we consider the response matrix by both explanatory controls (Sect. 29.5.1) and explanatory system properties (Sect. 29.5.2).

29.5 Results and Discussion

29.5.1 Explanatory Control Parameters

The heatmap shown in Fig. 29.4 illustrates the strain response under varying control and uncertain parameters. Rows of the heatmap correspond to force conditions, while columns correspond to uncertainty parameter cases. Strain output is represented by color. For example, reading across the fifth row of the figure shows the various strains output by different material parameter cases under a load of approximately 45kN. Similarly, reading down column 80 shows the strain output under various force conditions given the material parameters corresponding to case 80.

Treating the load cases as explanatory in the eigendecomposition is equivalent to asking which load cases are most informative in explaining the variability of the response. From the heatmap, it is clear that at high load conditions there are dramatic variations in output strain, evidenced by the wider range of colors appearing in these regions. By contrast, lower force regions depict strain outputs with lower variations. Clearly, high force regions are more informative than low force regions.

With this intuition in mind, a spectral decomposition was performed on the covariance matrix corresponding to load conditions as explanatory variables (Eqs. 29.2, 29.3 and 29.4). Unsurprisingly, the first principal component captured more

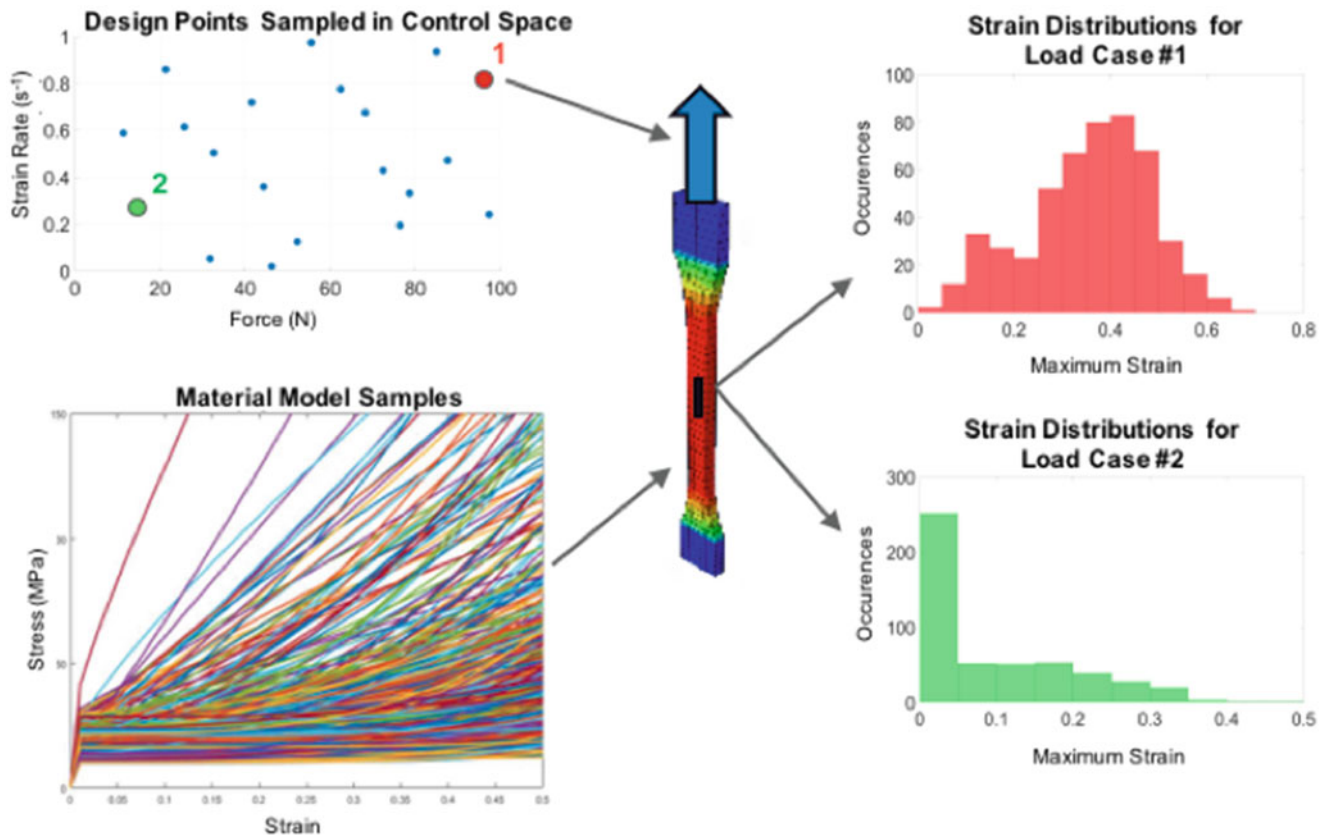


Fig. 29.3 Formation of the observation matrix with variability across control and uncertain parameter domains

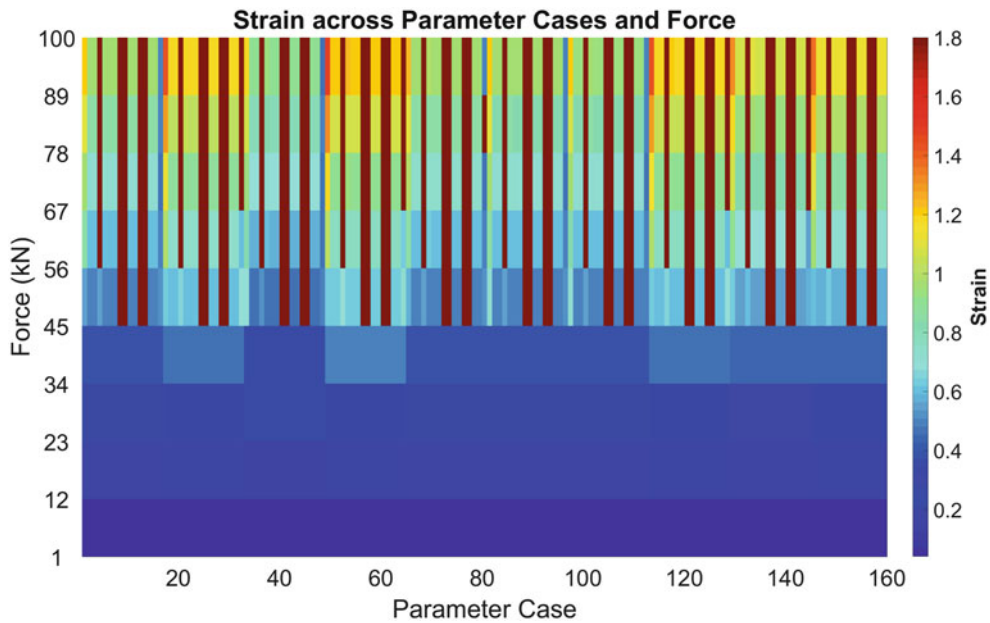


Fig. 29.4 Strain outputs exhibit greater variance at higher applied forces

than 95% of the total variation. Figure 29.5 shows the statistical loadings on the principal eigenvector plotted against force. The result of the decomposition completely agrees with intuition; larger force conditions are associated with higher statistical loadings, while lower forces have nearly zero statistical loading coefficients.

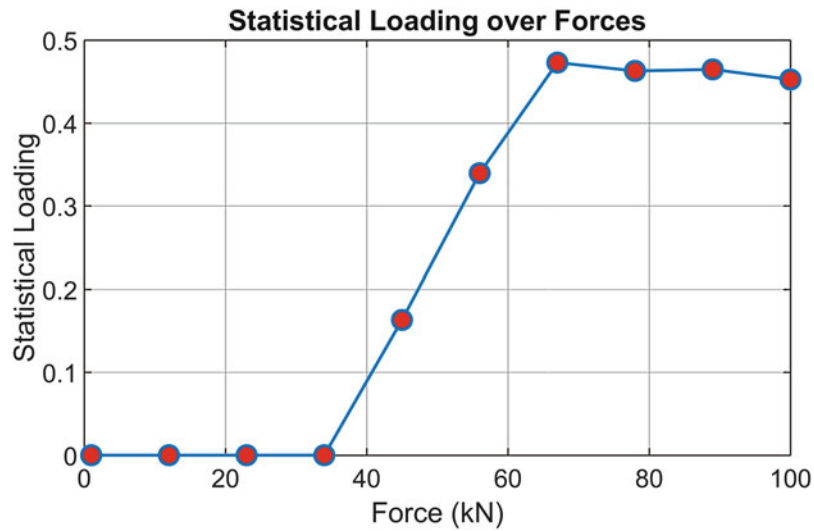


Fig. 29.5 The statistical loading coefficients of the first principal component are greater for more informative forces

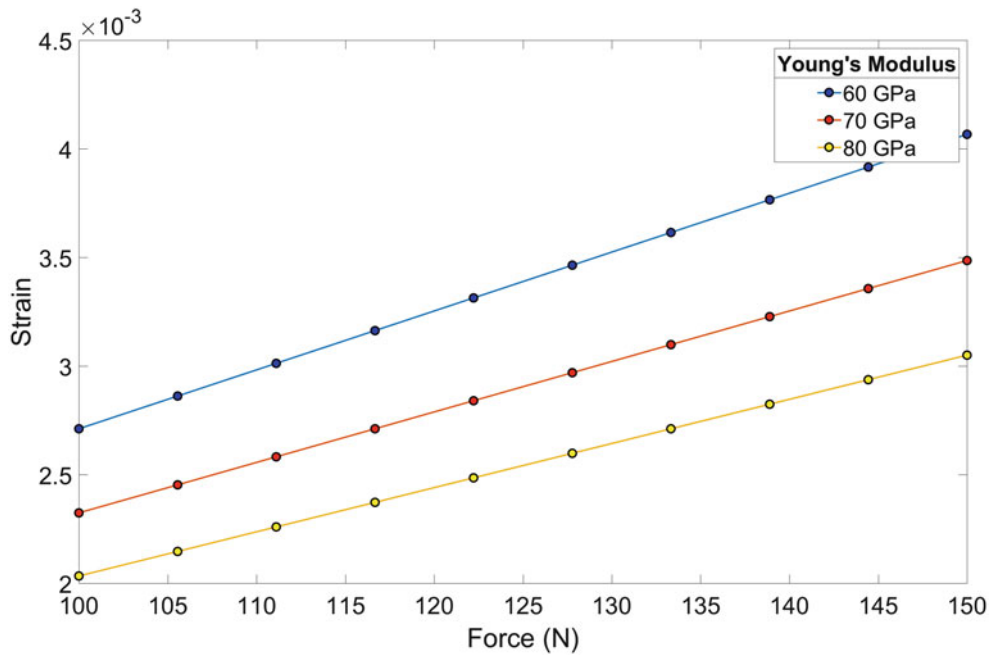


Fig. 29.6 Under low applied force, material behavior is solely determined by Young’s Modulus

29.5.2 Explanatory Uncertain Parameters

29.5.2.1 Elastic Analysis

Instead of considering different material parameters as observations and forces as explanatory variables (as in Sect. 29.5.1), material parameters can be treated as explanatory and varying load conditions will be treated as observations (Eqs. 29.5 and 29.6). In this case, the decomposition seeks to identify which material parameters have the greatest impact on output strain. As a rudimentary test of the capability of the eigenbasis to reveal sensitivity information, samples of varying elastic and plastic parameters under a load of 100–150 Newtons were considered. Under low load conditions, Young’s Modulus is the only parameter that impacts the output strain, as the material remains in the elastic region, as illustrated by Fig. 29.6.

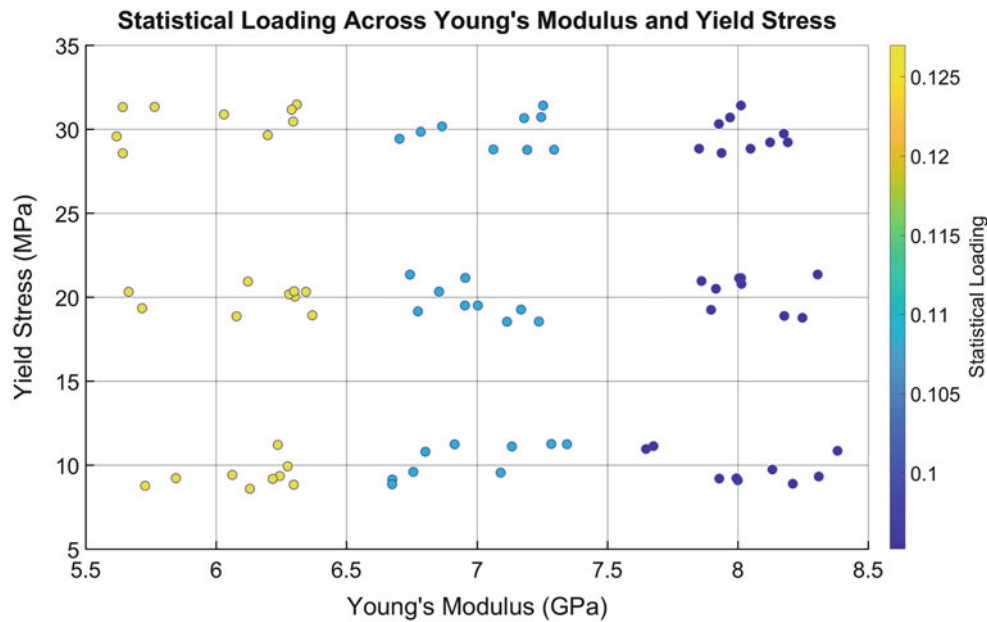


Fig. 29.7 Statistical Loading is correlated with Elastic Modulus and Uncorrelated with other parameters

At each applied force, 81 samples of varying yield stress, K , m , n , and Young's Modulus were tested. However, the figure depicts each force as resulting in only three distinct strain outputs. This happens because in the elastic region, variations in yield stress, K , m , and n , which are plastic parameters, do not impact material behavior and therefore produce identical output strain.

An eigendecomposition was performed on the matrix of output strains, in correspondence with Eqs. 29.5 and 29.6. That is, each applied force was treated as an observation with samples of varying parameters as explanatory variables. As before, the eigenvector associated with the first principal component captures more than 90% of the variation. Plotting the loading coefficients on each entry of the eigenvector against the parameter values to which they corresponded revealed that the loading coefficients were strongly correlated with the relevant parameter (Young's Modulus) and uncorrelated with irrelevant parameters (yield stress, K , m , n). Figure 29.7 illustrates the relationships found.

The eigendecomposition produced a vector with three distinct statistical loading coefficients corresponding to the three distinct Young's Moduli used in the samples. The color of the points in this figure represents the three statistical loading values found. The points in this figure were jittered to better illustrate the number of samples examined, but actually represent only nine distinct coordinates. Reading across increasing Young's Modulus, it is clear that each Young's Modulus represents a distinct and decreasing statistical loading value. Reading across an unrelated parameter, in this case yield stress, illustrates that any given yield stress results in one of the three statistical loading values with equal probability. That is, it is clear from the decomposition that there is no relationship between the yield stress and statistical loading.

29.5.2.2 Elasto-Plastic Analysis

Having demonstrated the ability of statistical loading to reveal intuitive relationships, the natural extension is to explore relationships that are more complex. In particular, it is of interest whether eigendecomposition can reveal relationships that are difficult to identify from raw data and traditionally require insight and exhaustive search to isolate.

Figure 29.8 displays a heatmap illustrating strain output (represented by color) across varied load cases and model parameters. As before, each row represents fixed load conditions, and reading across a row shows the variation in strain output as model parameters are varied. Similarly, each column represents a fixed set of model parameters and reading down a column illustrates the strain response under different load cases holding model parameters constant.

From the raw data presented in Fig. 29.8, it is difficult to identify any clear patterns. The variation is consistent across any visible dimension. However, performing an eigendecomposition successfully identified parameters of interest. The eigenvector associated with the first principal component again captured more than 90% of the variation in the data. Looking for correlations between the parameter values and the coefficients on the eigenvector revealed two dominant terms: K and m , as seen in Fig. 29.9.

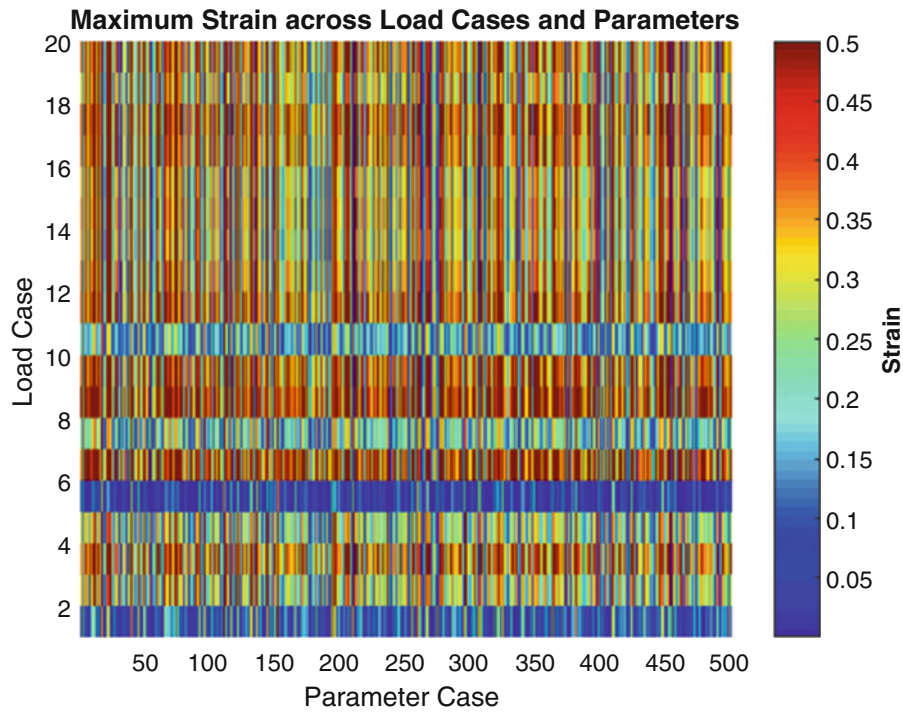


Fig. 29.8 Complex relationships are not obvious in the heatmap

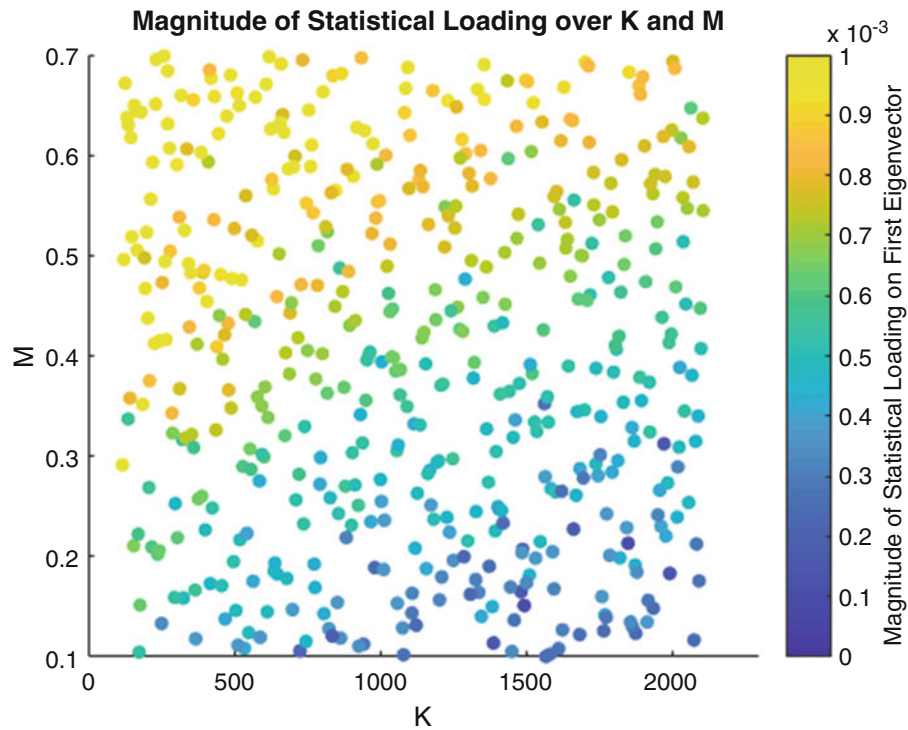


Fig. 29.9 Statistical Loading is shown to be correlated with K and m

As before, statistical loading is represented by color and a relationship is evident in the consistent decrease in statistical loading magnitude across decreasing values of m or increasing values of K . In contrast, Fig. 29.10 shows a plot of statistical loading against K and n , a parameter that does not impact strain output as strongly as others. The relationship between statistical loading and K is still present. Comparing, for instance, the row corresponding to high values of K with a row

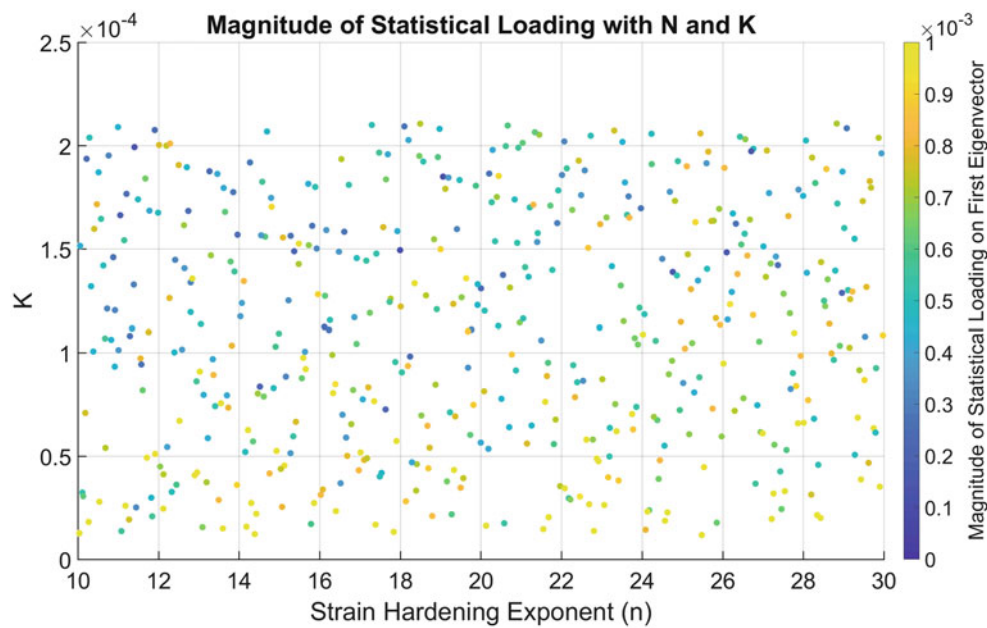


Fig. 29.10 Statistical Loading is shown to be uncorrelated with n

corresponding to lower values of K , it is clear that the average magnitude of statistical loading is greater in the lower row. By contrast, comparing any two columns corresponding to values of the strain hardening exponent yields similar distributions of statistical loading magnitudes, indicating that no strong relationship is present.

29.6 Conclusions and Future Work

The methodology presented herein demonstrated an application of Principal Component Analysis for interpreting underlying relationships causing changing model sensitivities. Although PCA is commonly used for reducing dimensionality of large problem domains, the eigenbasis had not yet been used as a tool to determine regions of interest for model calibration and validation. Results of this study suggest that PCA's eigenbasis can identify parameters of a model that propagate the most uncertainty. This is particularly powerful as spectral decomposition can be used to identify certain causal relationships without relying on a priori knowledge of material or system behavior. The methodology could be used to improve model accuracy or as a guiding mechanism to efficiently design experiments.

Potential extensions of this project include improving the validity of the methodology for application on other systems and models. This would require more data of a different nature to be simulated and analyzed. Relationships identified in the eigenbasis may provide a means of sensitivity analysis to determine model parameters that should be variable throughout an operational domain. Identifying such variability in the nature of parameters throughout a model can lead to more accurate model calibration, as opposed to always assuming constant, averaged values for calibrated parameter values. Expansion of the methodology to such a problem domain is suggested by incorporating temperature dependence to the Fields-Backhofen model.

Acknowledgements We would like to extend our gratitude to Los Alamos National Laboratory and the University of California San Diego for supporting this project through the Los Alamos Dynamics Summer School.

References

1. Kabanikhin, S.I.: Definitions and examples of inverse and ill-posed problems. *J. Inverse Ill-Posed Prob.* **16**(4), 317–357 (2008)
2. Tikhonov, A.N., Arsenin, V.Y.: Solutions of ill-posed problems. *SIAM Rev.* **21**(2), 266–267 (1979)
3. Donoho, D.L.: High-dimensional data analysis: the curses and blessing of dimensionality. *AMS Math Challenges Lecture* (2000)

4. Fan, J., Samworth, R.J., Wu, Y.: Ultrahigh dimensional feature selection: beyond the linear model. *J. Mach. Learn. Res.* **10**, 2013–2038 (2009)
5. Xie, C., Li, G.: Quantification of margins and uncertainties approach for structure analysis based on evidence theory. *Math. Probl. Eng.* **2016**, 1–5 (2016)
6. Allemang, R., Kolluri, M.M., Spottswood, M., Eason, T.: Decomposition-based calibration/validation metrics for use with full-field measurement situations. *J. Strain Anal. Eng. Des.* **51**(1), 14–31 (2016)
7. Diana, G., Tommasi, C.: Cross-validation methods in principal component analysis: a comparison. *Stat. Methods Appl.* **11**(1), 71–82 (2002)
8. Josse, J., Husson, F.: Selecting the number of components in principal component analysis using cross-validation approximations. *Comput. Stat. Data Anal.* **56**(6), 1869–1879 (2012)
9. Krzanowski, W.J.: Cross-validation in principal component analysis. *Biometrics.* **43**(3), 575–584 (1987)
10. Saltelli, A., Chan, K., Scott, E.M.: *Sensitivity Analysis*, vol. 1. Wiley, New York (2000)
11. Pannell, D.J.: Sensitivity analysis of normative economic models: theoretical framework and practical strategies. *Agric. Econ.* **16**(2), 139–152 (1997)
12. Zhang, X.-Y., Trame, M., Lesko, L., Schmidt, S.: Sobol sensitivity analysis: a tool to guide the development and evaluation of systems pharmacology models. *CPT Pharmacometrics Syst. Pharmacol.* **4**(2), 69–79 (2015)
13. Jolliffe, I.T.: *Principal Component Analysis*, 2nd edn. Springer, New York (2002)
14. Suhr, D.D.: Principal Component Analysis vs. Exploratory Factor Analysis, SUGI 30 Proceeding, No. 203–30 (2005)
15. Lin, Y.C., Chen, X.: A Critical review of experimental results and constitutive descriptions for metals and alloys in hot working. *Mater. Des.* **32**(4), 1733–1759 (2011)
16. Kotkunde, N., Deole, A.D., Gupta, A.K., Singh, S.K.: Comparative study of constitutive Modeling for Ti-6Al-4V alloy at low strain rates and elevated temperatures. *Mater. Des.* **55**, 999–1005 (2014)



Chapter 30

Uncertainty Quantification in Nanoscale Impact Experiment in Energetic Materials

Chandra Prakash, I. Emre Gunduz, and Vikas Tomar

Abstract Finite element method is extensively used for the analysis of impact response in complex materials. The prediction from finite element model may exhibit significant difference from that of experiments due to uncertainties in model, experimental measurements, and parameters that are derived based on experiments for model development. The quantification of parametric uncertainties, such as parameters in constitutive relation, associated with the numerical model is an important aspect that needs to be investigated for a credible computational prediction. This work considers uncertainty quantification in finite element modeling of nanoscale dynamic impact problems. A viscoplastic power law constitutive model is obtained from nanoscale impact experiments on Hydroxyl-terminated polybutadiene (HTPB)-Ammonium Perchlorate (AP) samples. The constitutive model is used in a finite element model to simulate impact experiments. The measured response from impact experiment and FEM simulation is used to quantify the parametric uncertainties in the constitutive model for the analyzed HTPB-AP sample.

Keywords Energetic Material · Stress/strain relationship · HTPB · AP · UQ

Uncertainty quantification (UQ) is the study of the error and uncertainty in mathematical and simulation model and their quantification. There are broadly two types that require quantification - probabilistic or statistical uncertainty and systematic uncertainty. Uncertainty quantification makes use of a probabilistic model of a set of input parameters to measure the uncertainty in the output of a model. The uncertainty in the model parameters can be obtained by validating the model with the experimental data. Even though, experimental data usually has uncertainty in the measurement due to equipment as well as local material behavior, it can be used to obtain information about uncertainties in a model. For example, several factors can affect the knowledge of a parameter in a model which may induce significant uncertainty. Experimental Data can be used to reduce such uncertainty through validation as well as by adding constraints in the model parameters.

Parameter uncertainty depends on the complexity of the simulation models. Propagation of errors depends on the interaction of several parameters within the model itself. It is, therefore, important to analyze the combined effect of such parameters on the model. This can be done with the help of probabilistic models. A model represents the system that can be validated or invalidated with experimental data. One of the primary goals of a model is to provide information about the system and predict the outcome in certain condition where it is difficult or costly to measure experimentally. To accurately predict the response of a system, a detailed and precise models are required. However, this makes the system more complex and difficult to analyze.

In this work, we investigate uncertainty quantification (UQ) in a rate dependent stress-strain model of nanoscale impact experiments that uses a viscoplastic constitutive model with parameters derived from the same experiments. Experiments are conducted on Hydroxyl-terminated polybutadiene (HTPB)-Ammonium Perchlorate (AP) energetic material samples that consist of AP particles embedded in HTPB binder. The fabrication of the material is explained in an earlier work in detail [1]. Mechanical properties of energetic materials depend upon size and type of particle used as oxidizer [2].

In order to understand the failure mechanisms along with their mechanical strength, characterization techniques with sufficient resolution are needed. The experimental procedure for measuring particle-binder interface level dynamic properties involves impacting the surface of the material being tested by an impactor (Fig. 30.1). The strain rates in such a setup is typically up to 100 s^{-1} , [3]. The experimental data includes the information of depth of penetration during impacts with time

C. Prakash · V. Tomar (✉)
School of Aeronautics and Astronautics, Purdue University, West Lafayette, IN, USA
e-mail: tomar@purdue.edu

I. E. Gunduz
School of Mechanical Engineering, Purdue University, West Lafayette, IN, USA

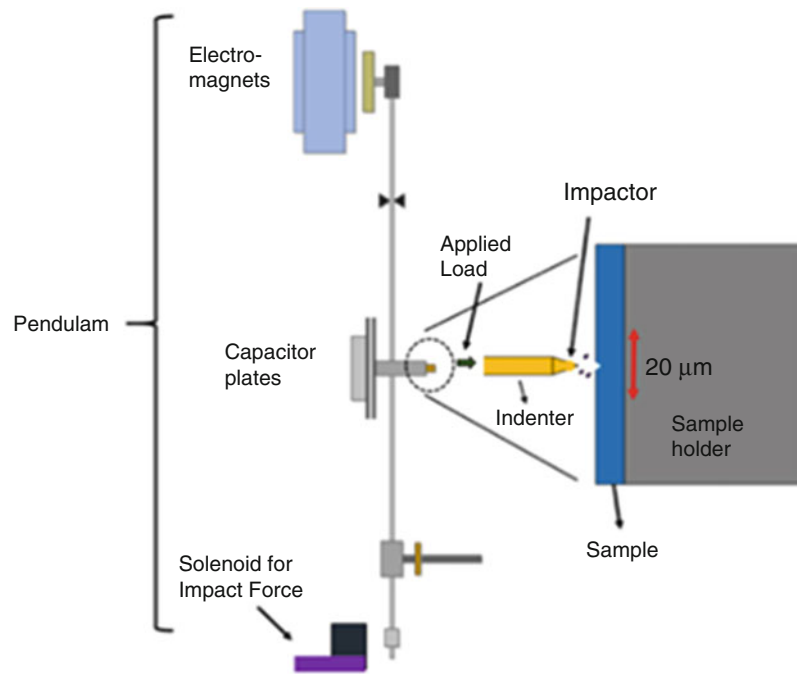


Fig. 30.1 Dynamic impact experimental setup

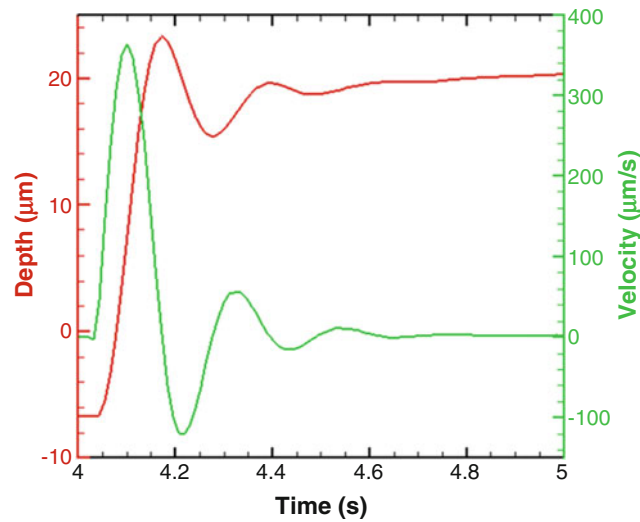


Fig. 30.2 Representative data from one impact test

(Fig. 30.2). The derivative of depth versus time gives the information of velocity during impacts (Fig. 30.2). The advantage of this experiment is that the impacts are aimed at the interfaces in the precision range of nanometers to micrometers. The experimental set up has been described in detail in previous works [1, 3–5]. A typical data obtained from one impact is a depth versus time history as shown in Fig. 30.2. An average strain rate characterizing the impact can be approximated by the expression,

$$\dot{\varepsilon} \approx \frac{V_{in}}{h_{max}}, \quad (30.1)$$

where, h_{max} is the maximum depth and V_{in} is the maximum velocity. The strain and stress are given by [3, 6],

$$\varepsilon = \frac{h_{res}^2}{h_{max}^2} \quad \text{and} \quad (30.2)$$

$$\sigma = \frac{P}{\pi h_{max}^2},$$

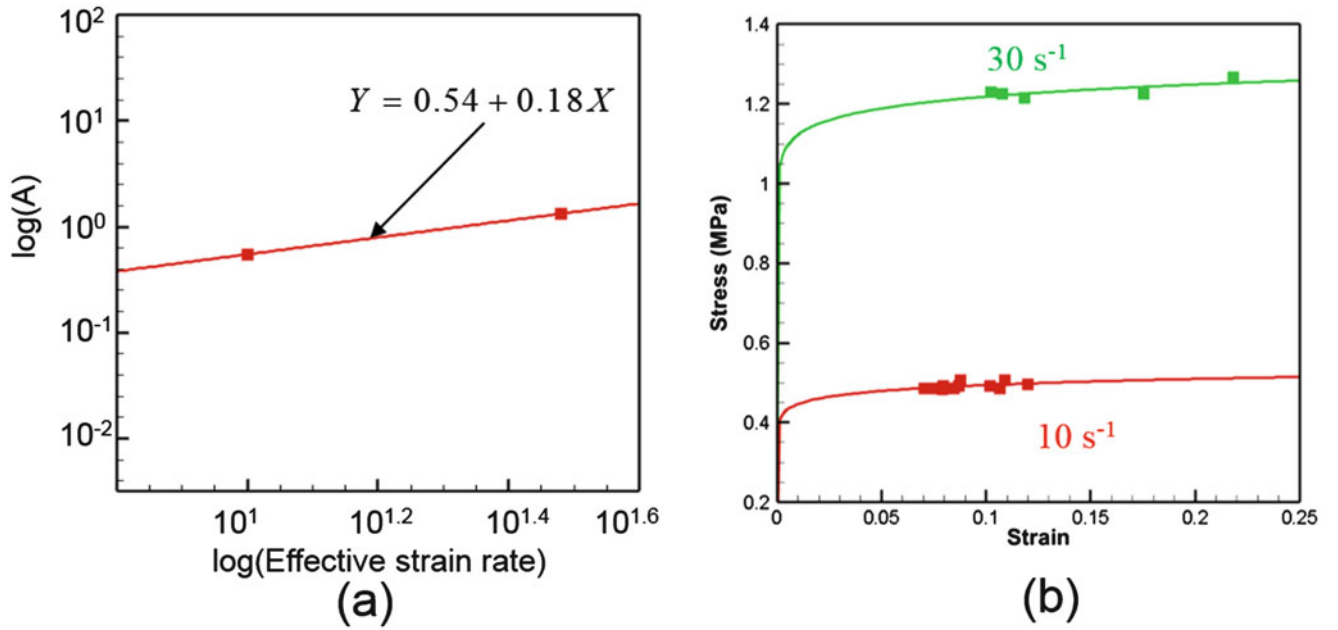


Fig. 30.3 Viscoplastic model parameter estimation and stress-strain curve for HTPB binder as a function of strain rate

where, h_{res} , is the residual depth where the impactor starts to rebound from the sample. The strain rate was found to be in the range of 10 to 100 s^{-1} . The strain rates in the current experiment is varied by increasing the maximum load applied. The impact stress-strain data from experiments is then modeled following viscoplastic constitutive model of Tsai and Sun, [7]. We assume an effective stress-effective viscoplastic strain curve given by a power law model

$$\bar{\sigma} = F\bar{\epsilon}^m\dot{\bar{\epsilon}}^n, \quad (30.3)$$

Where, $\bar{\epsilon}$ and $\bar{\sigma}$ are the equivalent strain and equivalent stress, respectively. Using this procedure on the experimental data for different strain rates, one can obtain the corresponding stress-strain curves shown in Figs. 30.3b. The values of m and n are found from the stress strain data obtained during nanoscale impact test, Fig. 30.3b. Figure 30.3a shows amplitude $A = F\dot{\bar{\epsilon}}^m$, as a function of effective plastic strain rate on the log-log scale for the HTPB binder. The parameters A and m are then determined from these plots as the intercept and the slope, respectively. Once m and A are determined, this model can be extrapolated to predict the material behavior at different strain rates.

In order to validate the viscoplastic power law constitutive model proposed above, a 2-dimensional plane strain finite element simulation is carried out using ABQUS [8] to model the dynamic impact experiment, as shown in Fig. 30.4a. The impactor is chosen to be a spherical impactor of radius $1 \mu\text{m}$, Fig. 30.4b, which is the size used in the experiment. The impactor velocity-time profile was kept to be the same as in experiment with different load. A depth-time curve obtained from the simulation is compared to that from the experiment. The result in Fig. 30.4c show the difference in depth profile obtained from experiment and simulation using the viscoplastic material model. A major source of uncertainty in the model comes from the model form. The difference between model and experimental response is modeled as

$$y^e(X) = y^m(X, \theta) + \delta(X) \quad (30.4)$$

Here, y^e is the experimental observation and y^m is the response from the finite element simulation. The difference between the two responses is termed as model discrepancy (δ). θ is the input parameters (F , m and n) used to measure the uncertainty in the model response. The model discrepancy in this study is assumed to be a function of input variable only [9]. Solution approximation error in the model from finite element discretization is minimized by choosing appropriate mesh sizes. This was done during the analysis but is not shown here due to brevity. Measurement error in the experiment is assumed to be small and not considered in this study. The elastic properties of the particle and matrix are chosen assuming isotropic behavior and are constant throughout the study [1].

The sensitivity of the response to each of the 3 material model parameters, F , m , and n , is studied here. Experimental data was fitted to the power law model to set bounds on the prior distributions of each of these parameters in the calibration. Ten sets of these model parameters were selected using Monte-Carlo sampling with Gaussian Copula and were each used

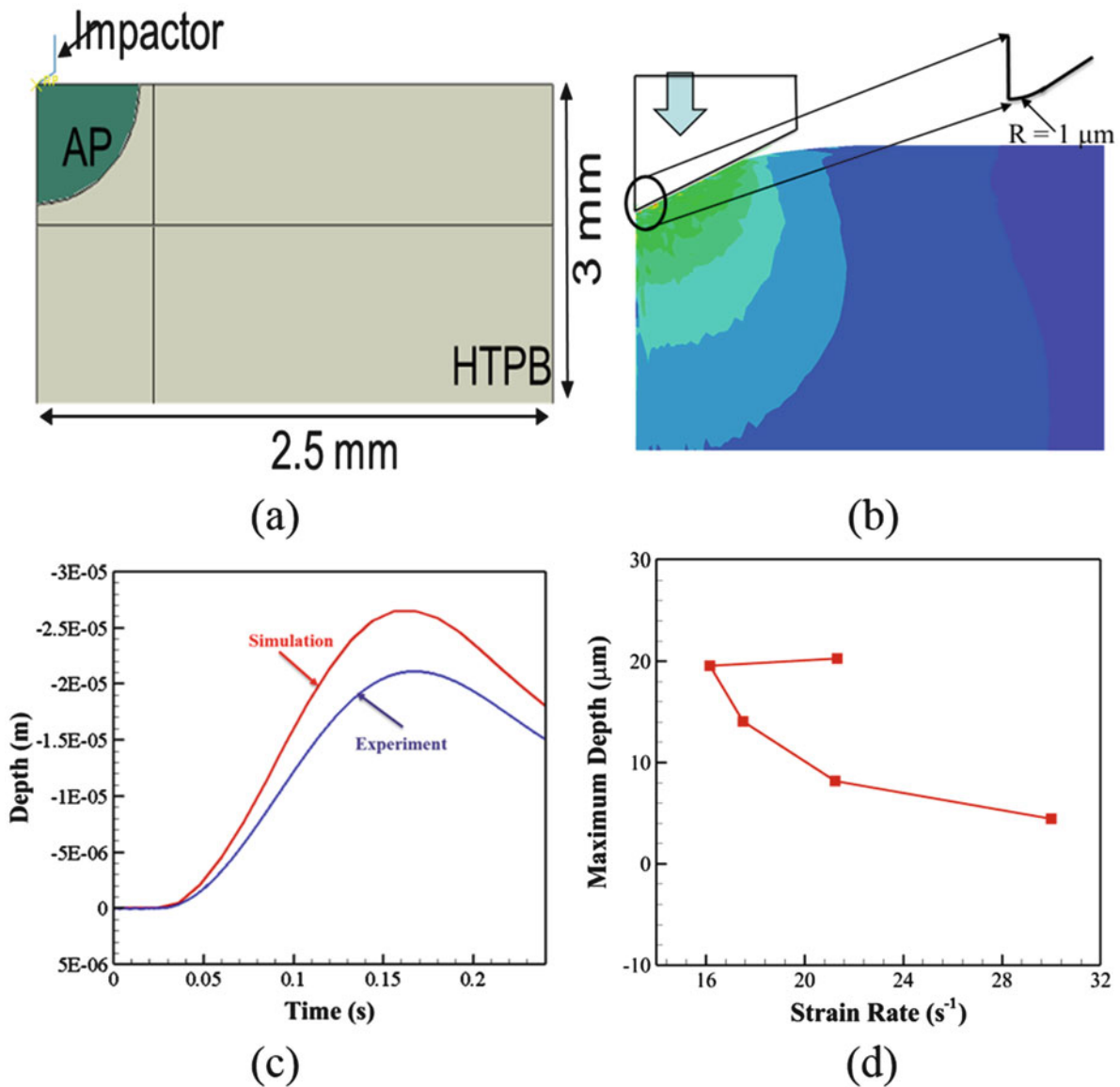


Fig. 30.4 (a) Finite element model of the dynamic impact experiment. (b) Deformed configuration of the sample. (c) Comparison of response from experiment and simulation. (d) Experimental response for different strain rate

to simulate five strain rate input conditions from the experimental data. The experimental data is then used to calibrate the parameters of the damage model and discrepancy function and the standard deviation of the measurement errors. Finally, the uncertainty in the prediction is summarized and quantified.

As shown in Fig. 30.5, a set of independent input parameters were used to identify the bounds for the probabilistic input modelling. In this study we have used a uniform distribution of input parameters with a Monte-Carlo sampling scheme. Table 30.1 shows the parameters used to identify the uncertainty in the model. We then use the UQLab ([10]) software framework to sample the input parameters which is then used in the finite element simulation as described above. (Fig. 30.4).

A Gaussian process (GP) modeling is used to obtain the computer model response at the simulation data points [9]. In this study we have used the Kriging approximation available in UQLab [10] with a cubic polynomial fitting as shown in Fig. 30.7a. This GP model is then used to obtain the model discrepancy at any x . After creating the GP model, the hyper-parameters for the GP model is calculated in order to represent the discrepancy function. Experimental data points were obtained in the dynamic impact test were used for the simulation. Figure 30.7b shows the standard deviation of GP model for different input parameter (θ) used from the sample given in Table-1. As shown in Fig. 30.7a) the Kriging model with cubic polynomial doesn't have a good fit at the high strain rate. One of the reason is that the experimental data available is limited at higher strain rates.

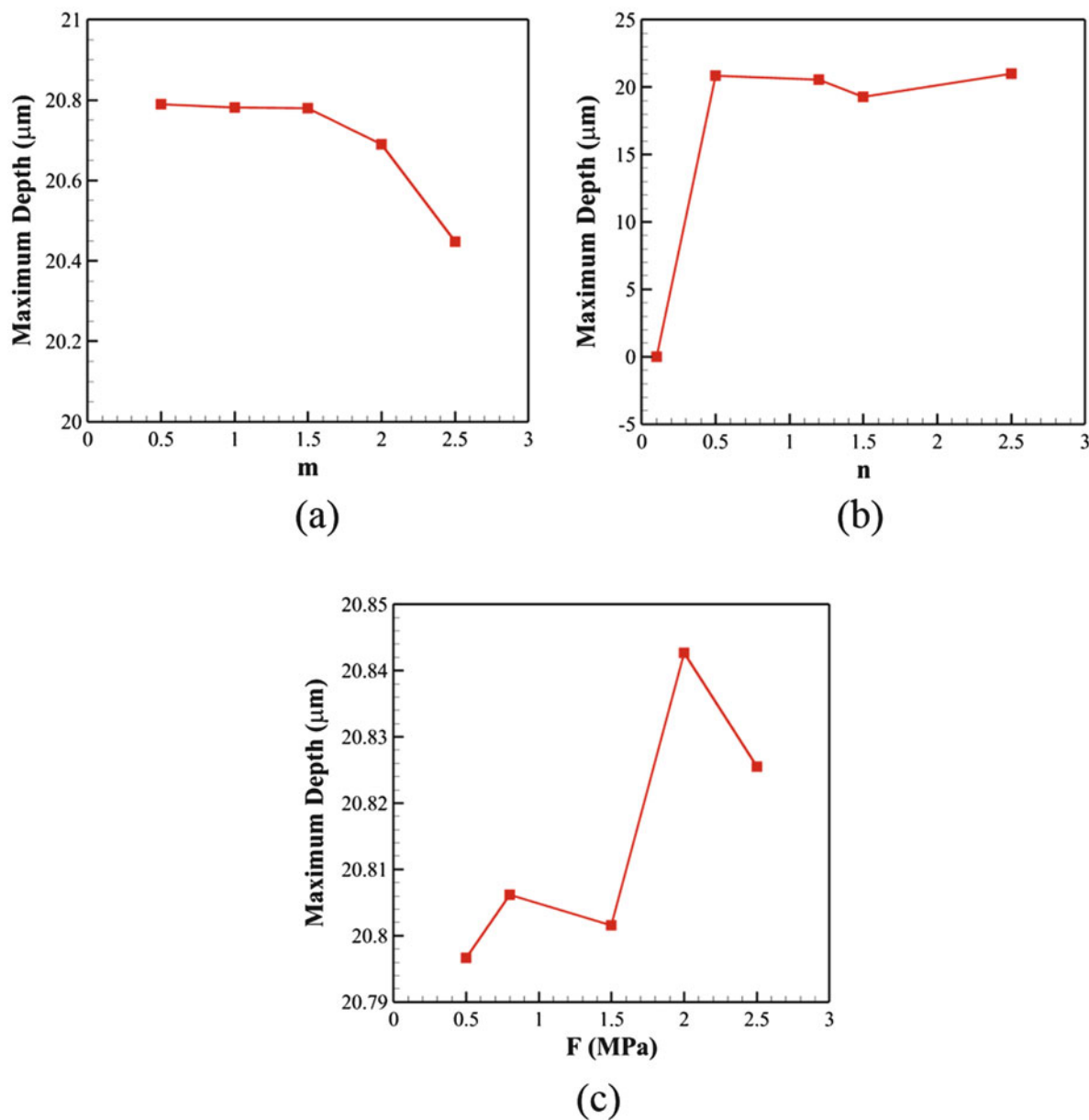


Fig. 30.5 Effect of input parameter (a) m, (b) n, and (c) F on the maximum depth response obtained from simulation

Table 30.1 Model parameter used for the sensitivity analysis

F (MPa)	1.65	1.46	1.33	1.70	1.28	1.58	1.14	1.63	1.96	1.93	1.67
m	0.30	0.14	0.03	0.22	0.22	0.39	0.04	0.17	0.48	0.42	0.38
n	0.71	0.60	0.44	0.29	0.34	0.59	0.20	0.33	0.95	0.72	0.68

In summary, a uniformly distributed data with a Monte-Carlo sampling approach was used to obtain the input model parameters in the rate dependent material model. This approach yielded distributions for the material parameters of the stress-strain model for the constituents and the standard deviation of the measurement errors. Further experimental testing is needed to improve the accuracy of the calibration and to better quantify the measurement errors. As was shown, due to limited data points available at higher strain rates, the error estimates were high. Additional data points are needed to fully characterize the response across the entire parameter input space and reduce the uncertainty contribution from the model.

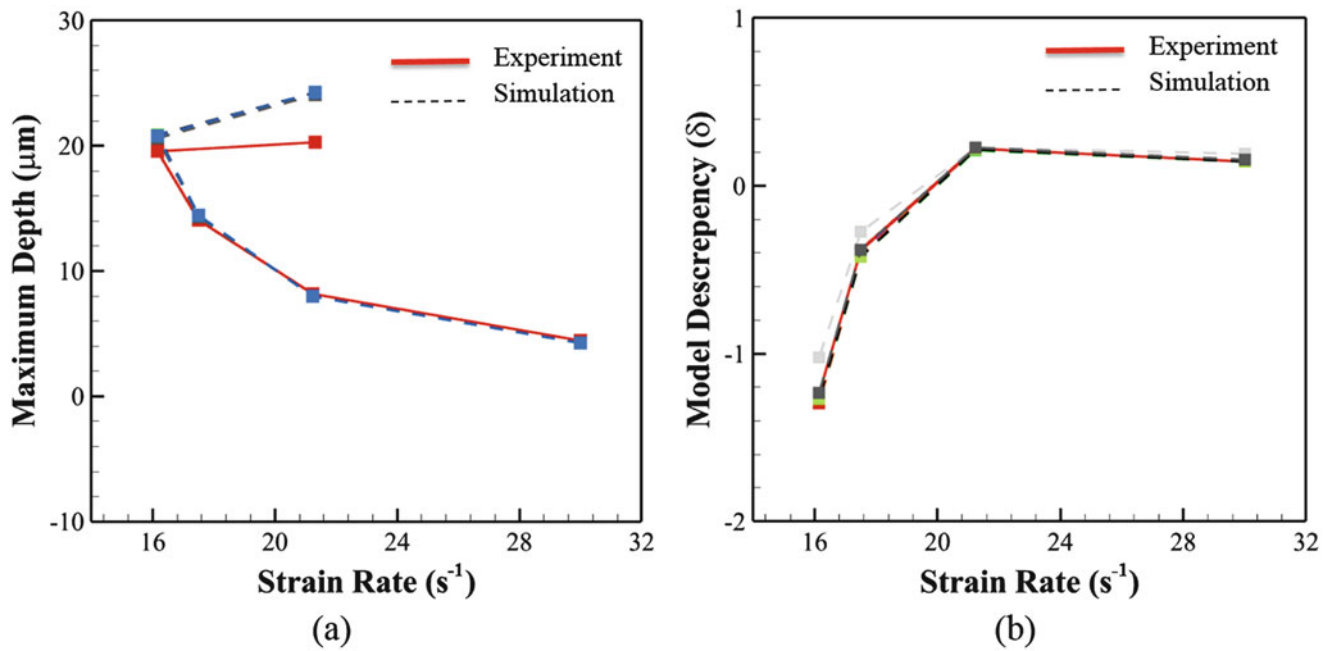


Fig. 30.6 (a) Response obtained from the simulation and (b) the model discrepancy calculated from Eq. (30.4)

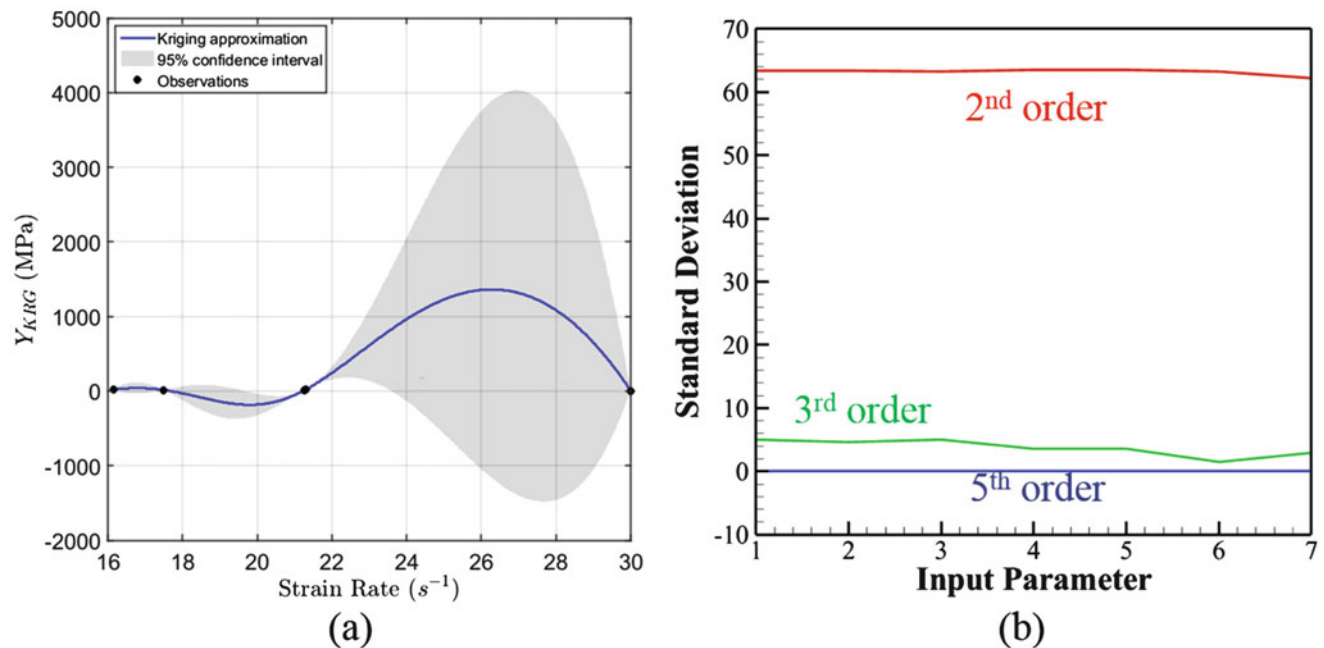


Fig. 30.7 (a) The response from the GP model and (b) the correlation between GP model response and simulation response

Acknowledgments This research was supported by US-AFoSR Grant FA9550-15-1-0202 (Program Manager Dr. Martin Schmidt).

References

- Hu, R., Prakash, C., Tomar, V., Harr, M., Gunduz, I.E., Oskay, C.: Experimentally-validated mesoscale modeling of the coupled mechanical-thermal response of AP-HTPB energetic material under dynamic loading. *Int. J. Fract.* **203**, 1–22 (2016)
- Wiegand, J.H.: Study of Mechanical Properties of Solid Propellant. Arlington, Armed Forces Technical Information Agency (1961)
- Prakash, C., Verma, D., Exner, M., Gunduz, E., Tomar, V.: Strain rate dependent failure of interfaces examined via nanoimpact experiments. In: Challenges in Mechanics of Time Dependent Materials, vol. 2, Conference Proceedings of the Society for Experimental Mechanics Series (2017).

4. Prakash, C., Gunduz, I.E., Tomar, V.: Effect of strain rate and interface chemistry on failure in energetic materials. In: Fracture, Fatigue, Failure and Damage Evolution, vol. 7, Conference Proceedings of the Society for Experimental Mechanics Series (2018)
5. Verma, D., Prakash, C., Tomar, V.: Interface mechanics and its correlation with plasticity in polycrystalline metals, polymer composites, and natural materials. *Procedia Eng.* **173**, 1266–1274 (2017)
6. Verma, D., Exner, M., Tomar, V.: An investigation into strain rate dependent constitutive properties of a sandwiched epoxy interface. *Mater. Des.* **112**, 345–356 (2016)
7. Tsai, J., Sun, C.T.: Constitutive model for high strain rate response of polymeric composites. *Compos. Sci. Technol.* **62**, 1289–1297 (2002)
8. Abaqus: Version 6.14 Documentation. Dassault Systemes Simulia Corp, Providence (2014)
9. Bogdanor, M.J., Mahadevan, S., Oskay, C.: Uncertainty quantification in damage modeling of heterogeneous materials. *Int. J. Multiscale Comput. Eng.* **11**(3), 289–307 (2013)
10. Marrel, A., Iooss, B., Van Dorpe, F., Volkova, E.: An efficient methodology for modeling complex computer codes with gaussian processes. *Comput. Stat. Data Anal.* **52**(10), 4731–4744 (2008)



Chapter 31

Analysis of Contact Dynamics Using Controlled Impact Excitations

Shivang Shekhar, Sudhanshu Nahata, and O. Burak Ozdoganlar

Abstract In the current work, the contact dynamics during impact is analyzed using a repeatable impact excitation system. In general, accurate description of force-deformation relationship during a dynamic impact event necessitates using semi-empirical or empirical models. The validity of these models under different conditions (the shape, material, surface condition, and impact velocity of the impacting bodies) depends on accurate experimental calibration of model parameters. As such, an effective and reproducible calibration approach is critical to obtaining effective contact dynamics models. The prevailing calibration approaches for impact dynamics focus on identifying only one of those parameters, the coefficient of restitution (CoR), and only for limited range of impact conditions. Estimating the contact stiffness and the power law exponent requires direct, precise and simultaneous measurement of force and sub-micron level deformation (indentation). Furthermore, calibration and modeling uncertainty must be well understood to determine the applicability of the contact-dynamics models. To address these challenges, the objective of the current work is to use a repeatable impact excitation system (IES) and interferometry to enable calibration of contact dynamics models. The IES enables precise control of impact velocities, and high-resolution interferometric (Laser Doppler Vibrometer, LDV) measurement of impacted surface and impact tip provides accurate determination of the associated deformations. After describing the approach in detail, we present demonstrative case studies on stainless steel and aluminum surfaces, and obtain the calibration parameters for different models presented in the literature. During the calibration, the force and deformations levels are varied by controlling the velocity of the impact. Furthermore, an uncertainty quantification is conducted to determine uncertainties of determined parameters to better identify the validity of the calibrated model, as well as the capability of the approach. It is concluded that the presented approach is an effective means of calibrating and validating various contact dynamics models at different impact velocities.

Keywords Contact dynamics · Hertzian model · Uncertainty quantification · Model validation · Coefficient of restitution

31.1 Introduction

The theory of contact dynamics has been studied well for a variety of problems, such as granular flows [1–3], multi-contact problems in space-robotics applications [4, 5], and collisions among bodies. Collision between two bodies results in a short-lived excitation, commonly referred as impact. The models governing the contact dynamics for impact dates to the Hertzian theory of contact which is in its original form is derived for collision between two spheres [6]. The theory gives a non-linear force-deformation relationship during impact. Also, there has been extensive literature on theoretical development of the models governing the complex interactions during the impact [7–9]. A detailed characterization of the impact requires the use of an accurate force-deformation relation, estimation of parameters of the model such as contact stiffness and CoR, and quantification of energy dissipation mechanism [10]. Though there is an extensive literature on the theoretical studies and numerical simulations to understand the impact process, accurate experimental investigation is necessary to assess the validity of these models.

S. Shekhar · S. Nahata
Department of Mechanical Engineering, Carnegie Mellon University, Pittsburgh, PA, USA

O. Burak Ozdoganlar (✉)
Department of Mechanical Engineering, Carnegie Mellon University, Pittsburgh, PA, USA

Department of Biomedical Engineering, Carnegie Mellon University, Pittsburgh, PA, USA

Department of Materials Science and Engineering, Carnegie Mellon University, Pittsburgh, PA, USA
e-mail: ozdoganlar@cmu.edu

A majority of the experimental studies on impact focus on determining only the coefficient of restitution [2, 11]. However, the parameter of the Hertzian theory, i.e., contact stiffness depends on accurate determination of contact area during impact which is difficult to determine theoretically for irregular geometries and hence its experimental determination is needed. The existing experimental studies to determine contact stiffness are limited [5, 12] and restricted to the classical assumptions of the Hertzian theory, i.e. interactions between bodies with spherical geometries. For other geometries, such as cones and flat punch indentors, a power law relation was theoretically derived [13]. Following this, this power law relation was parameterized for arbitrary geometries and was used in nanoindentation experiments [14]. It was shown that the contact area assumptions in Hertzian theory does not hold well for arbitrary geometries and hence required an accurate determination of force-deformation relation. However, the power law relation used in [13, 14] lacks an energy dissipative mechanism since the indentation experiments were done quasi-statically. In dynamic impact scenarios, there is some energy loss because of material damping [15]. Hence, a dissipative power law relation is necessary to capture the dynamics of impact while incorporating the complex interactions between objects of varying material and geometry. To summarize, till date, there is no experimental approach to accurately calibrate all the three parameters of the contact model simultaneously. As the majority of models are empirical and/or semi-empirical in nature, accurate use of these models necessitates conducting calibration tests to determine model parameters, particularly for non-spherical shapes.

To address these challenges, the objective of the current work is to experimentally calibrate and investigate the parameters of different contact models by using highly repeatable and controlled impulsive excitations. A set of models, commonly used to represent the force-deformation behaviour, are evaluated. In addition, a parametric model to capture the effects of varying material, geometry and initial velocity is used and compared with the existing models. The parameters of the models are determined experimentally by measuring the force and deformation during impact. In order to compare it with classical impact models, the experiments are conducted using a sphere and a flat test sample. The sphere is attached to a load cell which measures the impact force and a laser Doppler vibrometer (LDV) is used to continuously measure the velocity (and hence deformation) of the colliding bodies during the impact. A non-linear curve fitting is then performed on the obtained force-deformation values to extract the model parameters.

This paper is organized as follows. Section 31.2 summarizes theoretical details of the development of different contact models. Section 31.3 describes the methods which covers the experimental setup, analysis approach and uncertainty analysis in detail. Section 31.4 provides results and discussion of experiments conducted on two different metal surfaces at two different velocities. Lastly, Sect. 31.5 present the conclusions drawn from the study.

31.2 Dynamics of Impact

Impact between two bodies primarily involves two phases: compression and restitution. In the first phase, i.e., compression, both the colliding bodies deform, resulting in momentum transfer until they reach the maximum compression point where the relative velocity becomes zero. During the second phase, i.e., restitution, they separate from each other because of elastic recovery. The elastic nature of the collision is governed by this phase and is typically quantified by CoR. The CoR is defined as the ratio between the velocity of separation and the velocity of approach [9]. During a perfectly elastic collision, the separation follows the same relation with the deformations as during compression and hence there is no energy loss in the restitution forces. The CoR is 1 in this case. However, in almost all practical cases, the collisions are rarely pure elastic. For a partially inelastic case, as shown in Fig. 31.1, the compression (loading) follows a different path than restitution (unloading). This is because the force at a given deformation is also dependent on the rate of deformation. In this case, the separation velocity is lower than the approach and the colliding bodies lose some of the energy during impact. This energy loss can be attributed to various sources such as elastic wave propagation, damping, plasticity, material damping, sound, heat etc. In the current work, following [10], energy dissipation from friction is not considered and therefore, only normal contact force is used for the analysis.

The force-deformation relation which relate the normal contact force (F_{impact}) as a function of the instantaneous relative deformation (δ) and instantaneous relative deformation rate ($\dot{\delta}$) can be written as

$$F_{impact} = f(\delta, \dot{\delta}) \quad (31.1)$$

This relationship is profoundly studied in literature and some of the important models are included here, covering most of the practical contact scenarios. Hertzian theory [9], in its original form deals with the contact between two spheres assuming a circular contact area. It was shown that that the parameters of the force-deformation relation during impact is dependent on many factors, including but not limited to, material properties, geometry of colliding objects and relative velocity before impact [7]. A theoretical analysis resulted in the following non-linear relation

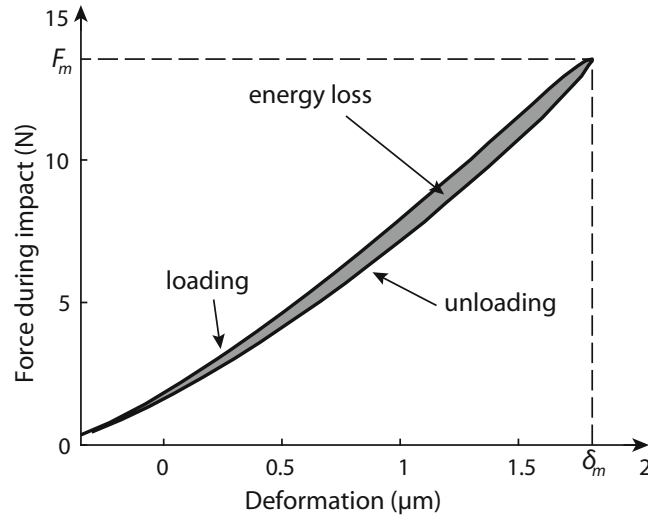


Fig. 31.1 A typical force-deformation curve during impact

$$F_{impact} = K\delta^{\frac{3}{2}}, \quad (31.2)$$

where

$$K = \frac{4}{3\pi(k_i + k_j)} \left(\frac{r_i r_j}{r_i + r_j} \right)^{\frac{1}{2}} \quad (31.3)$$

and

$$k_i = \frac{(1 - \mu_i^2)}{\pi E_i}, \quad (31.4)$$

where, E_i is the moduli of elasticity and μ_i is the Poisson ratio. Note that the impact force is independent of the rate of deformation and hence neglects any energy loss. For a sphere-plate collision, one of the radii is assumed to be very large and hence the expression for K reduces to

$$K = \frac{4}{3\pi(k_i + k_j)} (r_i)^{\frac{1}{2}}. \quad (31.5)$$

Since there is no energy dissipation term in the original Hertzian form, the CoR is equal to 1. Following this, Hunt and Crossley [16] introduced an extra damping term to account for the energy loss during restitution which is dependent on the CoR between the colliding objects. A hysteresis damping is considered which implied that the major source of energy dissipation is assumed to be from the material damping. The force-deformation relation in this case is derived in [10] and a commonly used expression can be written as

$$F_{impact} = K\delta^{\frac{3}{2}} \left(1 + \frac{3(1 - e^2)}{4} \frac{\dot{\delta}}{U_0} \right), \quad (31.6)$$

Where, e is the CoR and U_0 is the relative initial velocity. When the colliding geometries differ from perfect spheres, the coefficient n may not be equal to 3/2 and this led few authors to parameterize n . The most notable being [13] who gave a power law relation between force and deformation, given as

$$F_{impact} = K' \delta^n, \quad (31.7)$$

where K' is a parameter, and unlike K (from Hertzian theory), does not hold any physical significance. For spheres, where $n = 3/2$, K' is given by Eq. (31.3). Hence, the above power law expression is a more generalized form and captures the dependency on the material and arbitrary geometry of both the colliding objects. The theoretical expression of K' for some simpler geometries (spherical ($n = 3/2$), flat ($n = 1$), conical ($n = 2$)) is derived in [13]. However, for complex geometries, the constants K' needs to be determined experimentally [14]. For such cases, these parameters may depend on the maximum deformation which is directly related to the initial relative velocity. Combining all the above information, in the current work, a parameterized model [14] is used along with the addition of a damping term [15], given as

$$F_{\text{impact}} = K' \delta^n \left(1 + \frac{3(1-e^2)}{4} \frac{\dot{\delta}}{U_0} \right). \quad (31.8)$$

31.3 Methods

This section outlines the methods used in characterizing and comparing different models. First, a brief description of the experimental setup is included. Accordingly, the procedure to obtain the force $f(t)$ and the rate of deformation $\dot{\delta}(t)$, during impact, is described. Second, a least-square curve fitting approach to calibrate the parameters of any given model, using obtained force and rate of deformation, is presented. Lastly, uncertainty in the measurement of force and velocity is calculated, followed by model validation using k -fold cross-validation.

31.3.1 Experimental Setup

The experimental setup consists of a test sample, an Impact Excitation System (IES) [17] to provide controllable impact to the test sample and a laser Doppler vibrometer (LDV) to measure rate of deformation (see Fig. 31.2). All the components of the experimental setup are bolted down to a vibration isolation table to suppress ground vibrations. The IES includes a high-frequency load cell (Kistler 9213BX1) to measure the impact force. An LDV system (Polytec OFV-552) measures the velocity of the impact system. A National Instrument data acquisition system is used to collect both the force and velocity data in time domain. The data acquisition is synchronized by using PXI-6115 simultaneous sampling module.

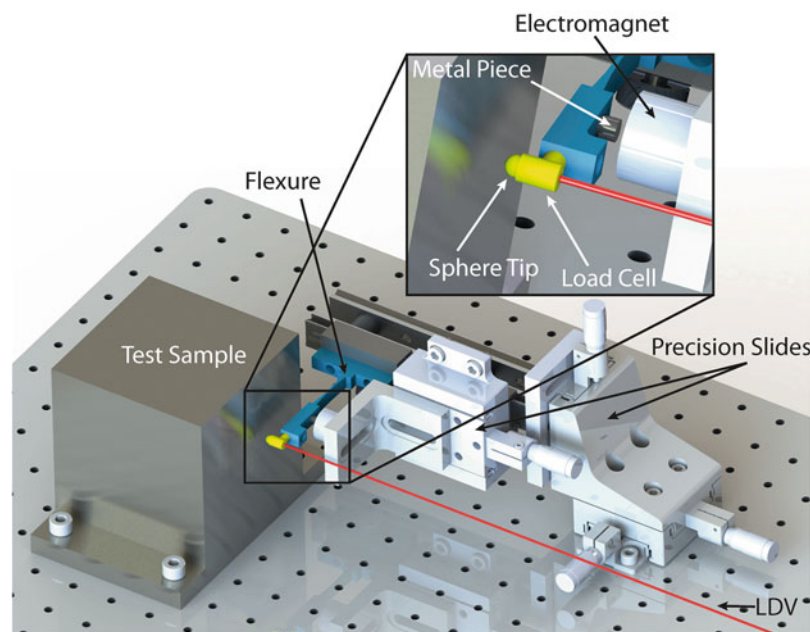


Fig. 31.2 Impact Excitation System (Modified design from [17]) and test sample

Table 31.1 Summary of different models considered in this work

	Coefficient of stiffness (K, K')	Power law exponent (n)	CoR (e)
Model 1 (Eq. (31.2))	Theoretical (K)	1.5	1
Model 2 (Eq. (31.6))	Theoretical (K)	1.5	Experimental
Model 3 (Eq. (31.7))	Experimental (K')	Experimental	1
Model 4 (Eq. (31.8))	Experimental (K')	Experimental	Experimental

The experimental approach involves the use of the IES for providing repeatable and controllable impacts. The design of the IES contains a flexure based body to hold the hammer-load cell combination. A custom-made spherical impact tip is attached to the load cell (bolted). The automation is achieved by using an electromagnet. The electromagnet, when turned ON, engages the hammer by pulling the metal piece towards itself. To provide an impact, electromagnet is turned OFF which releases the hammer. A varied range of force range can be obtained changing the flexure geometry. Given a flexure geometry, the force is controlled by prescribing the gap between the metal piece and the electromagnet and the gap between the hammer-tip and the test sample. The rate of deformation is measured using the LDV by measuring the velocity of the load cell from its (flat) back side.

31.3.2 Parametric Estimation

Table 31.1 summarizes all the different models used in the current work. The time domain force and velocity data from the experimental measurements (unloading curve) is used to calibrate the parameters of different models. For Models 1 and 2, K is determined theoretically which depends on the material properties and the geometry of the colliding objects. To determine K , material properties are obtained from [18] and the geometry measurements are conducted using 3D optical surface profiler (ZYGO NewView 7300).

The theoretical models of CoR have very limited applicability and they are often determined experimentally [12]. Thus, the CoR is experimentally determined by taking the ratio of velocity of separation to the velocity of approach, i.e. the velocity after and before the impact. These CoR values are used for Models 2 and 4. For velocity independent models (Model 1 and Model 3), the CoR is taken as 1. For Models 3 and 4, the values of K' and n are determined experimentally by curve-fitting the force-deformation curve, where the value of CoR is used as the value obtained above for curve fitting.

31.3.3 Uncertainty Analysis and Model Validation

31.3.3.1 Experimental Uncertainty

It is desired to obtain accurate and repeatable experimental data. However, factors such as environmental noise and vibrations, temperature fluctuations and linearity introduce variability in measured data. A detailed quantification of the sources of error is required to comment on the validity of the measured data. Such a calculation of measurement uncertainty for each of the measurand is conducted in this section. Depending on the (assumed) distribution, various coverage factors k_p are used to relate the range of variation (of the measurand) to the standard uncertainty u_i given as

$$u_i = k_p * (\text{range}) \quad (31.9)$$

The value of k_p for normal and rectangular distributions are 0.25 (95.45% confidence) and 0.29 (100% confidence), respectively. Assuming all the contributors are uncorrelated, the combined uncertainty U_i can be characterized by the numerical value obtained by applying the method for the combination of variances [19] given as

$$U_i = \sqrt{\sum_{i=1}^n u_i^2}, \quad (31.10)$$

for n contributors. The measurand in the present work are the force and the velocity measured from the load cell (of impact hammer) and the LDV, respectively.

31.3.3.2 Model Validation Using k -Fold Cross-Validation

Model predictions depend on the accuracy of the model in capturing the correct physics involved in the process and the accurate calibration of model parameters. However, these model parameters are subject to errors arising from the experimental measurements. To obtain generalized model parameters under statistical variations and to estimate the prediction error, a k -fold cross validation technique is used [20].

In this method, the measurement data is randomly divided into 10 equal parts. From the partitioned data, two data sets are created in 70:30 ratio, i.e., 7 parts for training: 3 parts for validation. The training data set is used to calculate model parameters and those parameters are then used on validation data for prediction. This cross-validation procedure is then repeated 10 times, each time with a unique combination of training and validation data. As a result, 10 sets of model parameters are obtained representative of the statistical variation in the measurements.

31.4 Results and Discussion

Following the above approach, experiments are conducted on two different metal surfaces, i.e., Aluminum 6061 T6 alloy and SS304 to characterize, compare and validate the different contact models (see Table 31.1). To analyze the sphere-plate interactions as it is originally used in the Hertzian theory, mirror finish flat surfaces ($R_a < 30$ nm) are used. The radius of the spherical tip used in theoretical contact stiffness calculations (K) is measured to be $2.38 \text{ mm} \pm 0.02\%$. Experimental approach includes providing single hit impact force at two different velocities (28–35 mm/s and 50–58 mm/s) to calibrate the coefficients of the different impact dynamics models as described in Sect. 31.3.2. For each material and velocity combination, 10 repetitions are conducted to quantify statistical uncertainty and conduct model validation. A detailed quantification of experimental uncertainty is presented below followed by determination of model parameters and comparison between model predictions.

The uncertainty in the load cell can be classified [21] into: (1) statistical variation in calibration coefficient, (2) linearity error, (3) cosine error, and (4) sensor + DAQ noise. To estimate statistical variation in calibration coefficient, the impact hammer load cell is calibrated three times against a calibrated load cell. The standard error in calibration is calculated ($df = 2$) as $\pm 0.011 \text{ N/V}$, at a mean calibration value of 1.302 N/V . Assuming uniform distribution, the standard uncertainty is calculated to be 0.005 F N . For force amplitude up to 10 N , the maximum standard uncertainty is 0.05 N . The linearity error of the load cell is $0.21\% \text{ FSO}$, which corresponds to a range of $\pm 0.525 \text{ N}$. Assuming uniform distribution, this corresponds to a standard uncertainty of 0.304 N . The cosine error is the angular misalignment between the impact direction and the workpiece normal. Since the gap between the sphere and the workpiece is close to 0.5 mm , the misalignment angle is estimated to be ≤ 1 deg. For such small angles, cosine is very close to 1 and hence the uncertainty due to cosine error is negligible. The uncertainty in sensor + DAQ noise is found to be $\pm 0.08 \text{ N}$ for frequencies above 100 Hz (frequencies below 100 Hz do not affect impact force magnitude significantly) at a sampling rate of $1.5 \text{e}6$. Assuming gaussian white noise, the standard uncertainty is calculated to be 0.04 N .

Similarly, the uncertainty contributors in velocity measurements from LDV are determined to be: (1) calibration error, (2) cosine error, and (3) LDV + DAQ noise. For a calibrated LDV system, the calibration error is negligible. The cosine error is defined as the angular misalignment between the velocity measurement direction and the workpiece normal. An alignment better than ± 0.02 deg. is realized by mounting the LDV-head to a 6-axis kinematic mount. Therefore, the standard error in velocity measurement due to cosine error can be considered negligible. The uncertainty in LDV + DAQ noise is found to be $\pm 1 \text{ mm/s}$. Again, assuming gaussian white noise, the standard uncertainty is calculated to be 0.5 mm/s .

Considering only the significant sources of uncertainty affecting force and velocity measurements, standard uncertainty for individual contributors is summarized in Table 31.2. The combined uncertainty in force and velocity measurements is found to be 0.31 N and 0.5 mm/s , respectively. Since, velocity is used to calculate displacement (or deformation), the uncertainty in velocity measurement is used to calculate uncertainty in displacement by multiplying it by sampling time ($1/1.5 \text{e}6$). Hence, the uncertainty in displacement is calculated to be 0.33 nm .

For the calculation of K , used in Models 1 and 2, the moduli of elasticity and Poisson ratios for Al6061 and SS304 are obtained from [18] as $E_{Al} = 68.9 \text{ GPa}$ and $\mu_{Al} = 0.33$, $E_{SS} = 193 \text{ GPa}$ and $\mu_{SS} = 0.25$, respectively. Also, since the current analysis focuses on a sphere-plate impact, therefore the contact stiffness K is calculated using Eq. (31.5). These values are reported in Tables 31.3 and 31.4. For experimental determination of parameters, i.e. K' and n for Models 3 and 4, e for Models 2 and 4, the cross-validation approach, as described in Sect. 31.3.3.2 is followed (see Tables 31.3 and 31.4 for results). It is observed that the experimentally calculated parameters are repeatable, as shown by low standard deviations for n and e . A slightly high standard deviation is seen for the parameter K' which is expected because of its direct correlation

Table 31.2 Uncertainty in force and velocity measurements

Measurand	Uncertainty source	Range	Distribution	u_i
Force (N)	Calibration	0.172	Uniform	0.05
	Linearity	1.05	Uniform	0.304
	Cosine	0	Uniform	0
	Load cell + DAQ	0.16	Gaussian	0.04
Combined uncertainty, U_f				0.31
Velocity (mm/s)	Calibration	0	Uniform	0
	Cosine	0	Uniform	0
	LDV + DAQ	2	Gaussian	0.5
Combined uncertainty, U_v				0.5

Table 31.3 Determination of model parameters for Al6061

	K		n		e	
	Low velocity	High velocity	Low velocity	High velocity	Low velocity	High velocity
Al6061						
Model 1	3.66E + 09	3.66E + 09	1.5	1.5	1	1
Model 2	3.66E + 09	3.66E + 09	1.5	1.5	0.989 ± 0.002	0.903 ± 0.002
Model 3	(2.26 ± 0.18) E + 08	(2.50 ± 0.31) E + 07	1.315 ± 0.006	1.148 ± 0.009	1	1
Model 4	(2.26 ± 0.18) E + 08	(2.50 ± 0.31) E + 07	1.315 ± 0.006	1.148 ± 0.009	0.989 ± 0.002	0.903 ± 0.002

Table 31.4 Determination of model parameters for SS304

	K		n		e	
	Low velocity	High velocity	Low velocity	High velocity	Low velocity	High velocity
SS304						
Model 1	6.77E + 09	6.77E + 09	1.5	1.5	1	1
Model 2	6.77E + 09	6.77E + 09	1.5	1.5	0.996 ± 0.003	0.962 ± 0.002
Model 3	(0.90 ± 0.16) E + 09	(1.32 ± 0.31) E + 07	1.395 ± 0.011	1.249 ± 0.016	1	1
Model 4	(0.90 ± 0.16) E + 09	(1.32 ± 0.31) E + 07	1.395 ± 0.011	1.249 ± 0.016	0.996 ± 0.003	0.962 ± 0.002

with the measured force. Hence, the overall uncertainty in the force and displacement measurements propagates the most in K' compared to other parameters. The effect of this uncertainty on the predicted force will be seen from the cross-validation approach.

To predict the force magnitude as a function of displacement for the validation dataset, the parameters obtained from each iteration (10 in total) are used, one at a time. By combining all the prediction lines, a region (band) of uncertainty is thus obtained, as shown in Fig. 31.3. This procedure is repeated for all four models considered in this work. A brief description of information conveyed in Fig. 31.3 is explained below. First, the experimental data from 10 repetitions is plotted as a grey region. Second, a mean (line) curve is calculated for experimental data by averaging the repetitions for a given deformation. Third, the combined uncertainty in force (from Table 31.2) is added to this curve as error bars. Since the combined uncertainty in displacement is very low (less than 1 nm), they are not shown in the plot. Fourth, the prediction region corresponding to output of each of the four models is plotted, using the validation dataset.

From the figure, the experimental data lies within the error bars for low force values. For higher forces, the errors coming from system repeatability, which adds up to the experimental uncertainty, cause increased variations in the experimental data. However, the prediction bands for Model 3 and 4 lies within the error bars thus validating the presented curve-fitting approach and helps in estimating the force well within the uncertainty bands. It is also noted that higher variability in K' (see Tables 31.3 and 31.4) does not translate to the variability in the prediction of force.

Now, following the quantification of uncertainty, a brief discussion on the mean values of the calculated/estimated parameters is presented here. From the values of K , K' , n and e , we can see that the parameters are dependent on the initial relative velocity between the sphere and the plate, as observed in literature [22]. For low velocities, the value of n is similar to the reported value in [14] where indentation experiments were conducted quasi-statically. The value of n is closer to the Hertzian value of 3/2 for the SS-SS impact at low velocity compared to SS-Al impact. The value of n for both materials is found to deviate towards a flat indenter case [13] as the initial velocity is increased. This means that for the interaction between a sphere and a plate, Hertzian theory is accurate only for low velocities and starts deviating as velocity is increased which is consistent to what is seen in literature [10]. Finally, we observe that the difference between the Hertzian model and the power law model is higher for SS-SS impact. This can be owed to the fact that when materials with similar stiffness are

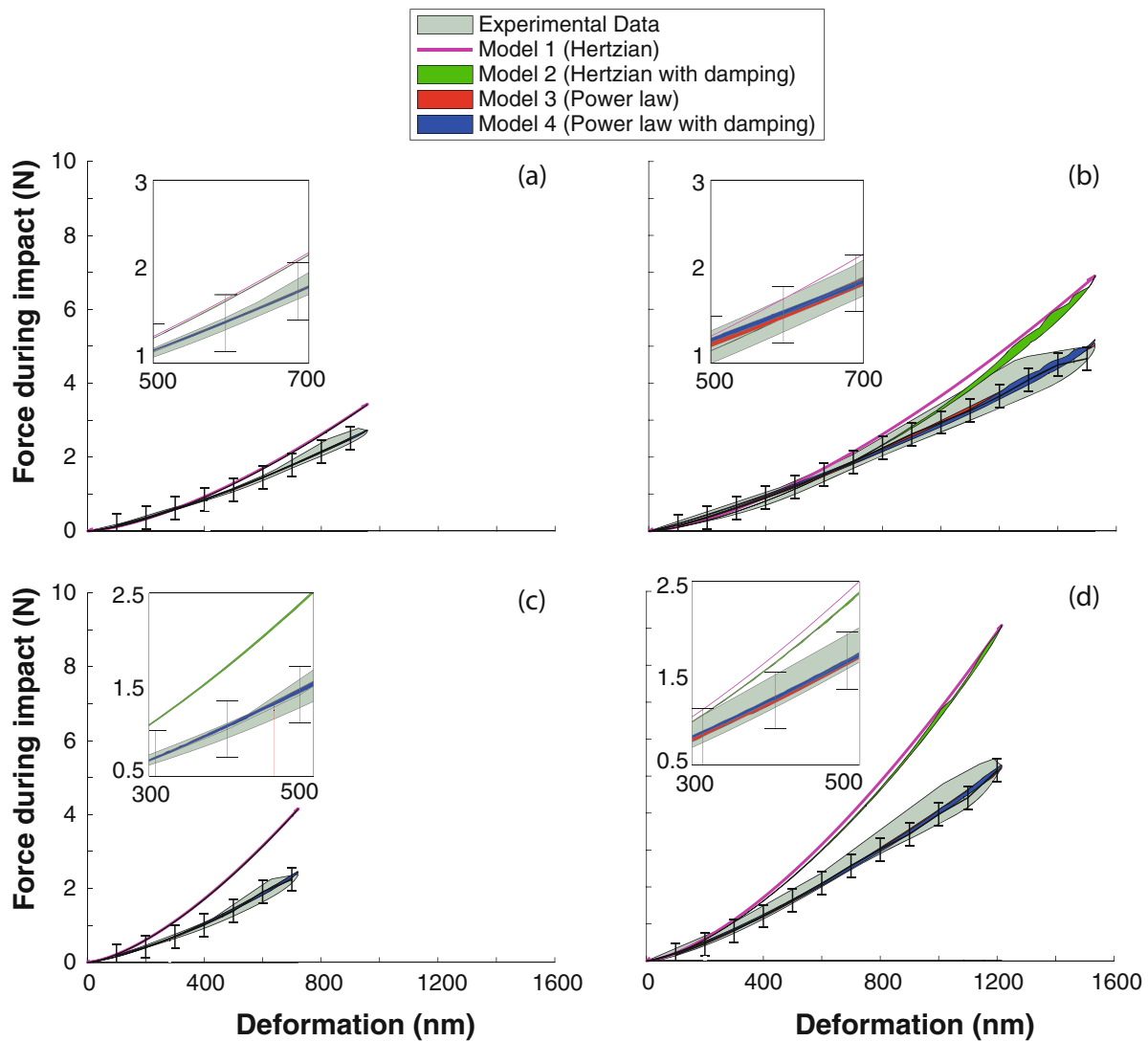


Fig. 31.3 Force deformation curves for different models considered for the analysis including the experimental data for varying material and initial velocity. (a) Al6061 with low velocity, (b) Al6061 with high velocity (c) SS304 with low velocity (d) SS304 with high velocity. The readers are referred to the web version of the paper for colors

used, complex interactions happen because of significant deformations in both the materials. Though the Hertzian theory accounts for the deformations in both the colliding objects, the interactions may no longer follow the circular area of contact assumption postulated in the original Hertzian theory [7].

31.5 Conclusions

The proposed experimental approach is useful in quantifying the uncertainty and validating the different contact models present in the literature. The results obtained are consistent with literature. Hence, by calibrating all the parameters of the impact models simultaneously, the proposed approach is effective in analyzing the contact dynamics with varying material and geometry of colliding objects. Following specific conclusions can be drawn from this study:

- The calibrated coefficients K' , n and e are obtained through experiments within a reasonably small variation. Among the three parameters, the variation in K' is found to be the largest which suggests that it is sensitive to the experimental uncertainty. However, this variation in K' does not affect the predicted forces significantly.

- The uncertainty in all the models are low as seen from the region of uncertainty obtained using k -fold cross-validation.
- The addition of damping term causes model improvements only at high velocities as evident from the CoR values at higher velocities. For lower velocities, the collision is almost elastic and hence energy dissipation is minimum.
- For lower velocities, the power exponent n is closer to 1.5 as given in the Hertzian theory. However, at higher velocities, the value decreases which suggests a behavior closer to a flat indenter ($n = 1$). Overall, for the current experimental setup, the geometry of the sphere behaves somewhere between a flat and a perfect sphere, as expected.
- All the three parameters change significantly with material properties of the test sample. For Al6061, we see lower n values which is consistent to what has been observed in nanoindentation experiments.
- The CoR in both the cases decrease as the velocity increases, similar to what has been consistently reported in literature.

References

1. Di Renzo, A., Paolo, F., Maio, D.: Comparison of contact-force models for the simulation of collisions in DEM-based granular flow codes. *Chem. Eng. Sci.* **59**, 525–541 (2004)
2. Patil, D., Higgs, C.F.: A coefficient of restitution model for sphere – plate elastoplastic impact with flexural vibrations. *Nonlinear Dyn.* **88**(3), 1817–1832 (2017)
3. Weir, G., Tallon, S.: The coefficient of restitution for normal incident, low velocity particle impacts. *Chem. Eng. Sci.* **60**, 3637–3647 (2005)
4. Marhefka, D.W., Member, S., Orin, D.E.: A compliant contact model with nonlinear damping for simulation of robotic systems. *IEEE Trans. Syst. Man Cybern. Part A Syst. Hum.* **29**(6), 566–572 (1999)
5. Van Vliet, J., Sharf, L., Ma, O.: Experimental validation of contact dynamics simulation of constrained robotic tasks. *Inter. J. Robotics Res.* 1–3 (1999)
6. Raman, C.V.: On some applications of Hertz's theory of impact. *Phys. Rev.* **15**(4), 277–284 (1920)
7. Goldsmith, W.: *Impact, the Theory and Physical Behaviour of Colliding Solids*, 1st edn. Edward Arnold (Publishers) Ltd, London (1960)
8. Guban, D.: Inelastic collision and the Hertz theory of impact. *Am. J. Phys.* **68**(10), 920 (2000)
9. Johnson, K.L.: *Contact Mechanics*, 1st edn. Cambridge University Press, Cambridge (1985)
10. Lankarani, H.M., Nikravesh, P.E.: Continuous contact force models for impact analysis in multibody systems. *Nonlinear Dyn.* **5**(2), 193–207 (1994)
11. Seifried, R., Schiehlen, W., Eberhard, P.: The role of the coefficient of restitution on impact problems in multi-body dynamics. *Proc. Inst. Mech. Eng. K J. Multi-body Dyn.* **224**, 279–306 (2010)
12. Gilardi, G., Sharf, I.: Literature survey of contact dynamics modelling. *Mech. Mach. Theory.* **37**, 1213–1239 (2002)
13. Harding, J.W., Sneddon, I.N.: The elastic stresses produced by the indentation of the plane surface of a semi-infinite elastic solid by a rigid punch. In: *Mathematical Proceedings of the Cambridge Philosophical Society*, vol. 41, pp. 16–26. Cambridge University Press (1945)
14. Oliver, W.C., Pharr, G.M.: An improved technique for determining hardness and elastic modulus using load and displacement sensing indentation experiments. *J. Mater. Res.* **7**(6), 1564–1583 (1992)
15. Hunt, K.H.: Coefficient of restitution interpreted as damping in Vibroimpact. *J. Appl. Mech.* **42**(2), 440–445 (1974)
16. Machado, M., Moreira, P., Flores, P., Lankarani, H.M.: Compliant contact force models in multibody dynamics: evolution of the Hertz contact theory. *Mech. Mach. Theory.* **53**, 99–121 (2012)
17. Bediz, B., Korkmaz, E., Burak Ozdoganlar, O.: An impact excitation system for repeatable, high-bandwidth modal testing of miniature structures. *J. Sound Vib.* **333**(13), 2743–2761 (2014)
18. <http://asm.matweb.com/>
19. Evaluation of measurement data—Guide to the expression of uncertainty in measurement: Bureau International des Poids et Mesures (2008)
20. Kohavi, R.: A study of cross-validation and bootstrap for accuracy estimation and model selection. *Ijcai.* **14**(2), 1137–1145 (1995)
21. Schmitz, T.L., Smith, K.S.: *Machining Dynamics: Frequency Response to Improved Productivity*. Boston, Springer (2009)
22. Thornton, C.: Coefficient of restitution for collinear collisions of elastic-perfectly plastic spheres. *J. Appl. Mech.* **64**, 383–386 (1997)



Chapter 32

Extraction of Coupling Stiffness of Specimens Printed with Selective Laser Melting Using Modal Analysis

Brian West, Nicholas E. Capps, James S. Urban, Troy Hartwig, Ben Brown, Douglas A. Bristow, Robert G. Landers, and Edward C. Kinzel

Abstract Modal analysis is an affordable form of nondestructive evaluation (NDE) for many forms of manufacturing. Developments in Additive Manufacturing (AM) have enabled the printing of sophisticated metal parts in processes like Selective Laser Melting (SLM). In most metallic AM processes fabrication is conducted on a build plate, which allows for convenient fixturing for model analysis. However, many build plate contain multiple parts that introduces the challenge of dynamic coupling where the dynamic characteristics of other specimens appear in the frequency analysis of the specimen that is being analyzed. The dynamic coupling can obscure the analysis, especially for prints with multiple identical parts. This work sets a foundation for a method to improve the modal analysis of multiple AM parts fabricated on a single build plate by estimating the coupling stiffness between two specimens with similar modal characteristics.

Keywords Modal Analysis · Selective Laser Melting · Coupling · Additive Manufacturing · Laser Doppler Vibrometry

32.1 Introduction

Recent improvements in Additive Manufacturing (AM), commonly referred to as 3D printing, have allowed a variety of materials to be used to create specimens with exceedingly complex geometries. Currently, there are commercial devices that allow materials such as aluminum, stainless steel, titanium, and refractory metals to be printed using powder bed or powder feeder systems [1]. The ability to manufacture complex parts using metal offers a large opportunity for industries that desire parts with improved structural strength without sacrificing weight. The aerospace industry could especially benefit from this technology because of the inherent low-volume production associated with AM. Because of the low-volume production of the process, it is ideal to have a cost effective and efficient method of part nondestructive evaluation (NDE). Some NDE methods, such as Computed Tomography, have been proven to be effective tools in identifying geometric defects and porosity; however, they are very expensive [2]. Modal analysis is a more cost-effective NDE method that has been applied to a variety of structural dynamics studies within the automotive, aerospace, and civil infrastructure industries [3].

A potential benefit of using modal analysis with metallic AM is the inherent fixturing that exists from the printing process. In processes like Selective Laser Melting (SLM), part warpage can be reduced by incorporating support material that is distributed between the part and the printing substrate. The exact part orientation and distribution of support material is determined by the machine operator in the software before printing. This adds the benefit of allowing a part to be printed in a certain manner to accentuate certain modes present in the part. Another potential benefit is the ability to test multiple specimens on a single substrate at once. Time can be considerably reduced by eliminating the need of fixturing individual parts by placing sequential builds onto a testing platform. With this consideration, a current disadvantage to this method is the dynamic coupling that exists between specimens on the same build plate. Similar to the dynamics of a tuned mass damper, or dynamic vibrational absorber, resonators with nearly identical uncoupled natural frequencies undergo a phenomenon that splits their perceived natural frequencies when coupled together and complicates analysis. This effect is will be referred to in this paper as “mode splitting.”

Figure 32.1 shows an example of how mode splitting reduces the observed sensitivity of one resonator to a change in mass. Two modal analysis simulations were performed with $9.525 \times 3.81 \times 100$ mm stainless steel cantilever beam

B. West · N. E. Capps · J. S. Urban · D. A. Bristow · R. G. Landers · E. C. Kinzel (✉)

Department of Mechanical and Aerospace Engineering, Missouri University of Science and Technology, Rolla, MO, USA
e-mail: kinzele@mst.edu

T. Hartwig · B. Brown

Kansas City National Security Campus, Kansas City, MO, USA

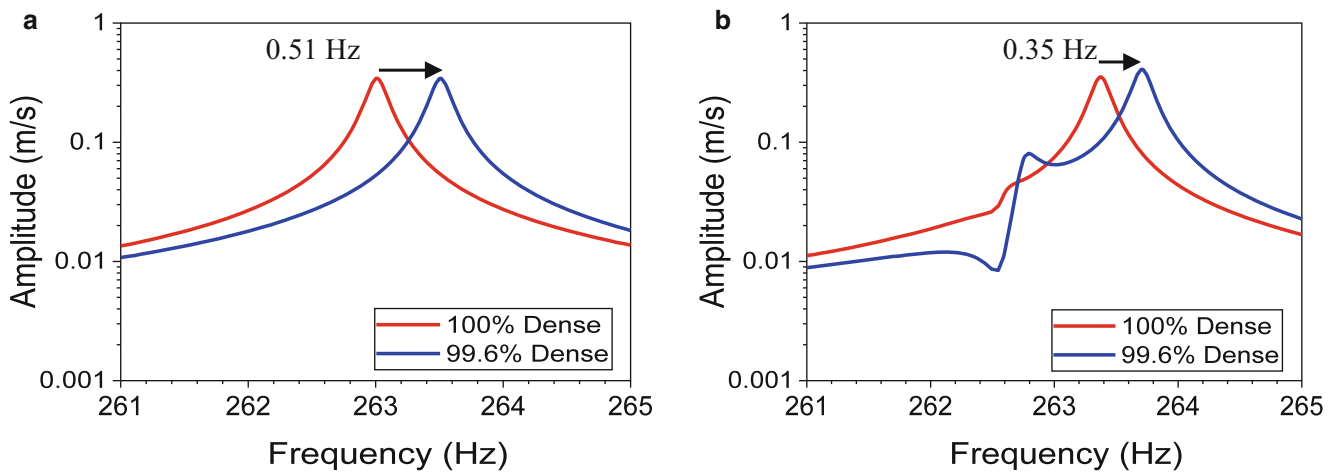


Fig. 32.1 Reduction of resonant frequency sensitivity due to mode splitting. (a) Isolated specimens. (b) Coupled specimens

specimens printed on a build plate with support material. The first simulation was of a single specimen and the second was with two specimens with the same orientation, separated by 10 mm. For both simulations, a single specimen was modeled at 100% and 99.6% of the nominal density. The resulting Frequency Response Function (FRF) plots of the altered specimens, shown in Fig. 32.1, demonstrate that there is a larger frequency difference for the single specimen than the two specimens between tests, meaning it is more sensitive to the changes in mechanical properties. This is an important concept to realize when attempting to modal test specimens multiple specimens on a build plate, as certain changes in frequency may represent different varying mechanical properties for builds with a different number of specimens.

There are very few studies quantifying this effect experimentally, especially with large-scale systems. Most studies that have attempted to quantify mode splitting using strongly coupled micro-scaled electromechanical devices, optical cavities and various quantum systems. Mathew et al. found mode splitting in multiple modes of tension-adjustable resonating graphing drums [4]. Faust et al. observed the effect in strongly coupled modes of a nano-mechanical beam resonator driven to represent a dynamic quantum system [5].

Traditional methods to avoiding mode splitting effects in modal analysis involve removing the specimens from the substrate and testing them individually; however, this will drastically increase the required testing time. An alternative would be to print the specimens with varying support material height so that the inertial characteristics of the specimens change and shift the frequencies away from each other. However, this limits the ability to rapidly qualify a specimen's response against a modal "fingerprint" obtained for a specimen with identical geometry. If an ideal specimen's fingerprint can be identified and the skewing effect imparted by coupling be understood, it is suggested that a coupled specimen's response could be manipulated in a way to compare to the ideal fingerprint and determine whether the part meets its mechanical property requirements.

This study is intended to improve upon methods used in previous studies that found modal analysis to be an effective tool in predicting mechanical properties, including Young's moduli, of specimens printed with SLM [6]. The goal of this paper is to understand the amount of mode splitting, quantified as coupling stiffness. A build with sets of nearly identical resonators containing various features were printed and modal tested. Various specimen features examined the effects of support material, separation, and orientation on coupling. A numerical model was derived to relate the magnitude of mode splitting found in the experimental model to that of a representative coupling stiffness between two idealized mechanical oscillators.

32.2 Experimental Setup

To evaluate the coupling stiffness between two specimens under different conditions, an experimental build, shown in Fig. 32.2a, was printed using SLM with eight cantilever beam specimens, grouped into four pairs of two. Each beam had a nominal cross-section of 9.525×3.81 mm. The four groups' general heights were selected to separate their bending modes from any other group by at least 10%, or approximately 20 Hz, to reduce any coupling effects between any two groups. Each group's specimens were printed as shown in Fig. 32.2. Specimen labels and features are listed in Table 32.1. The numbered order of the groups indicate the general heights in increasing order.

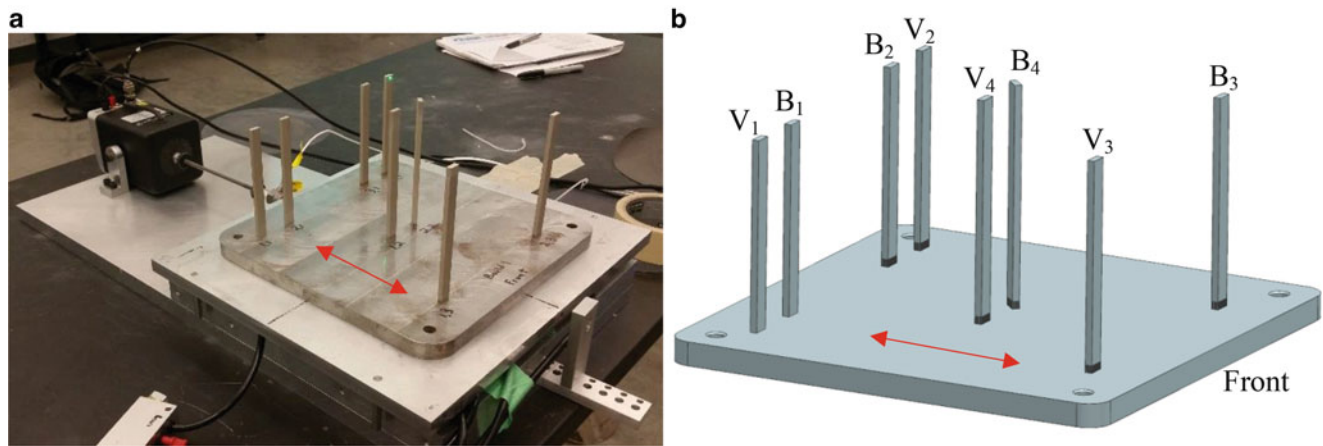


Fig. 32.2 Experimental build. (a) Experimental setup of build on electrodynamic shaker. (b) Specimen location and type labels

Table 32.1 Specimen group and type

Group number	Feature(s)	Specimen	Specimen type
1	No support material	V ₁	Variable
		B ₁	Baseline
2	Support material (control)	V ₂	Variable
		B ₂	Baseline
3	Support material and orientation	V ₃	Variable
		B ₃	Baseline
4	Support material and separation	V ₄	Variable
		B ₄	Baseline

Group 2 was mounted on support material, which is common in most 3D printing applications where support material is used so that specimens may be easily removed from the build plate. Other circumstances may not require support material if the specimen could be better removed with Electrical Discharge Machining (EDM). Groups 1 and 2 were made to compare the effect of support material on coupling, Groups 2 and 3 were made to compare specimen separation, and Groups 2 and 4 were made to compare specimen orientation.

The two specimens in each group consisted of a baseline specimen with constant height and a variable specimen with height that was reduced incrementally over the duration of the experiment by removing material from the top with an EDM. Baseline specimens had heights of 101.30, 105.30, 117.89, and 111.60 mm for Groups 1, 2, 3, and 4, respectively. The variable specimens' heights began with approximately 100.6% of baseline height and were reduced to 99.4% of baseline height over nine EDM cuts. These values were chosen based on a set of ANSYS simulations, one of which is shown in Fig. 32.3, to estimate the optimal variable specimen height range for observing coupling for the first bending mode. Because baseline specimens maintain a constant height, the only frequency shift observed is due to mode splitting. Note the increasing trend of the variable specimen's resonant frequency as its height is removed.

Before each EDM cut, all specimens were measured with a set of calipers four times, once for each vertical side of the specimen, and were averaged together to obtain the specimen heights. The build plate was then placed on a shaker table, shown in Fig. 32.2, supported by air bearings and excited using an electrodynamic shaker with a periodic chirp from 10 to 2000 Hz. The input force into the plate was measured using a force transducer between the shaker and the build plate. A scanning Laser Doppler Vibrometer (LDV) obtained velocity-based Frequency Response Functions (FRF) from the tips of each specimen with a resolution of 9.766 mHz. Coherence was verified near resonances and the FRFs were normalized to the measured input force.

Group FRFs were summed near specimen resonances to classify modes of each specimen. For poorly defined peaks, engineering judgment was used to approximate the mode. In previous experiments, coupling has been observed primarily in the first bending mode. For this reason, only the first bending mode between 180 and 300 Hz was examined. Once the FRF of the specimen was obtained, the variable specimens in each group had approximately 0.04% of the baseline specimen's height removed from their tip.

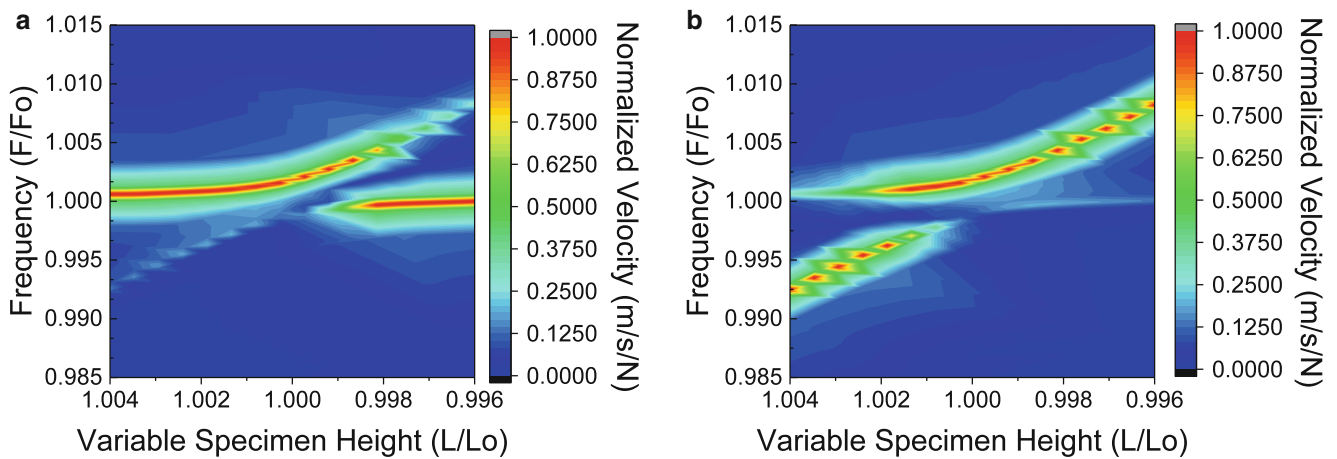


Fig. 32.3 Simulation of control group FRFs show optimal variable specimen height within avoided-crossing pattern as variable specimens are trimmed. Variable specimen height and frequency are normalized to the baseline height and uncoupled resonant frequency, respectively. Velocity for each FRF is normalized to maximum value within frequency range. (a) Baseline Specimen. (b) Variable Specimen

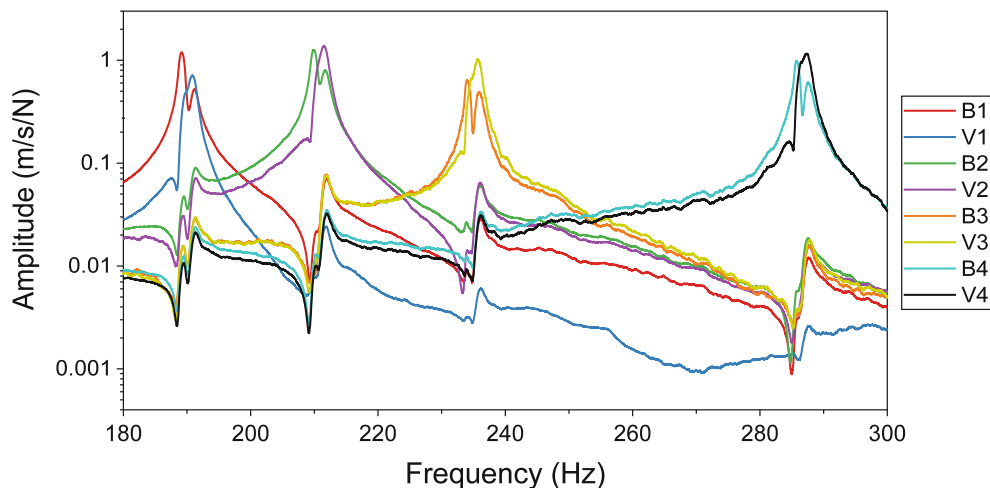


Fig. 32.4 Frequency Response Function of all specimens with variable specimen height at approximately 100.07% of baseline height

The procedure described was repeated nine times, with the final trim leaving the height of the variable specimen at 99.8% of the baseline specimen height. Lengths and FRFs were measured again before completely removing all variable specimens from the build plate via EDM. The resonances of the baseline specimens were then measured to be used for normalization.

32.3 Experimental Results

Figure 32.4 shows an example FRF that was measured using the LDV. The resonant frequencies for Groups 1, 2, 3, and 4 occurred around 190 Hz, 210 Hz, 235 Hz, and 285 Hz, respectively, a separation of at least 10%. To approximate the resonant frequencies for coupled specimens, FRFs of grouped specimens were summed to calculate a ‘total response’ of the system. It can be assumed that a resonance of two coupled specimens would be when their collective responses are maximum. From this, it was defined that the peaks of the summed response would be the resonant frequency.

The experimental FRFs of each specimen were plotted together for all nine cuts, as shown in Figs. 32.5, 32.6, 32.7 and 32.8. Note that the higher frequencies, approximated by the upper black line, represents the mode in which both specimens are traveling in phase and the lower black line represents the mode in which the specimens are traveling out of phase from one another. The avoided crossings can be seen by the peaks of the plots below, especially within Group 1. Noise was attributed to somewhat skewing Groups 2, 3 and 4. The coupling values for all groups ranged from 6.71 to 9.10.

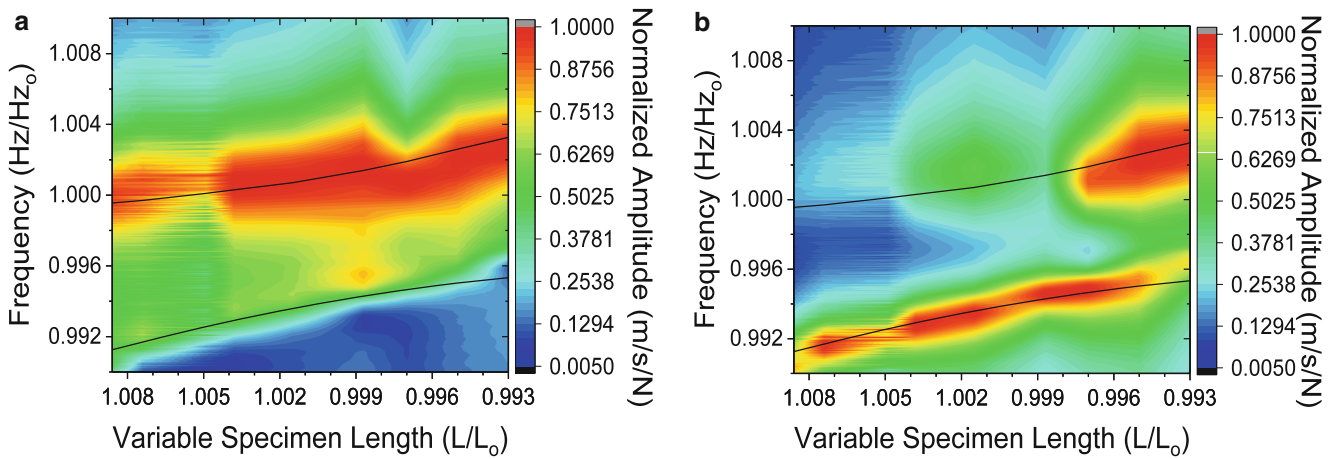


Fig. 32.5 Group 1. Experimental avoided crossing FRF peaks as variable specimens are trimmed. Curve fit from analytical solution; $\Gamma = 9.10$. (a) Baseline Specimen. (b) Variable Specimen

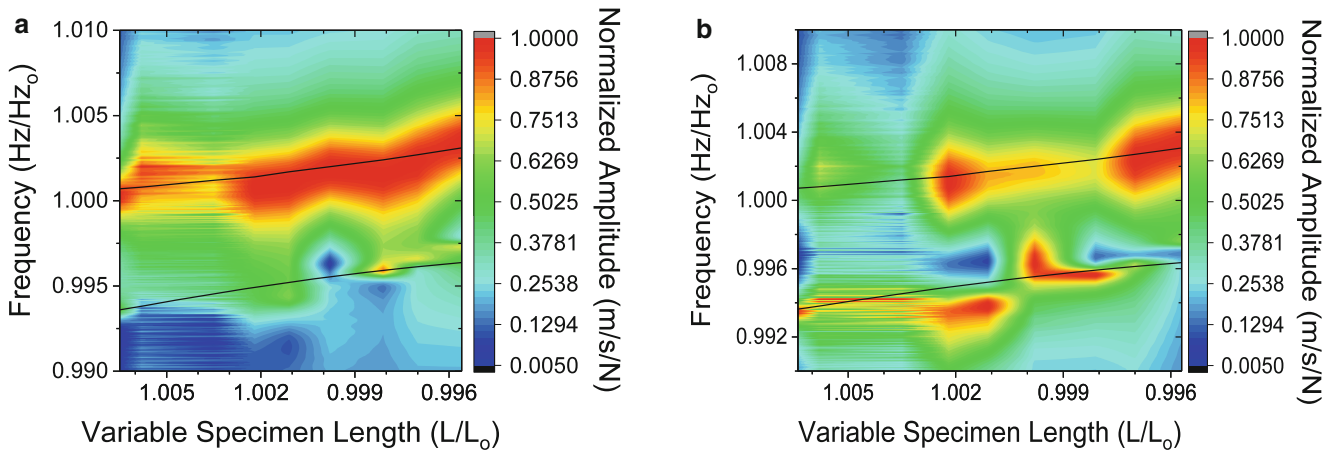


Fig. 32.6 Experimental avoided crossing FRF peaks for Group 2 as variable specimens are cut. Black line is curve fit from analytical solution where $\Gamma = 8.81$. (a) Baseline Specimen. (b) Variable Specimen

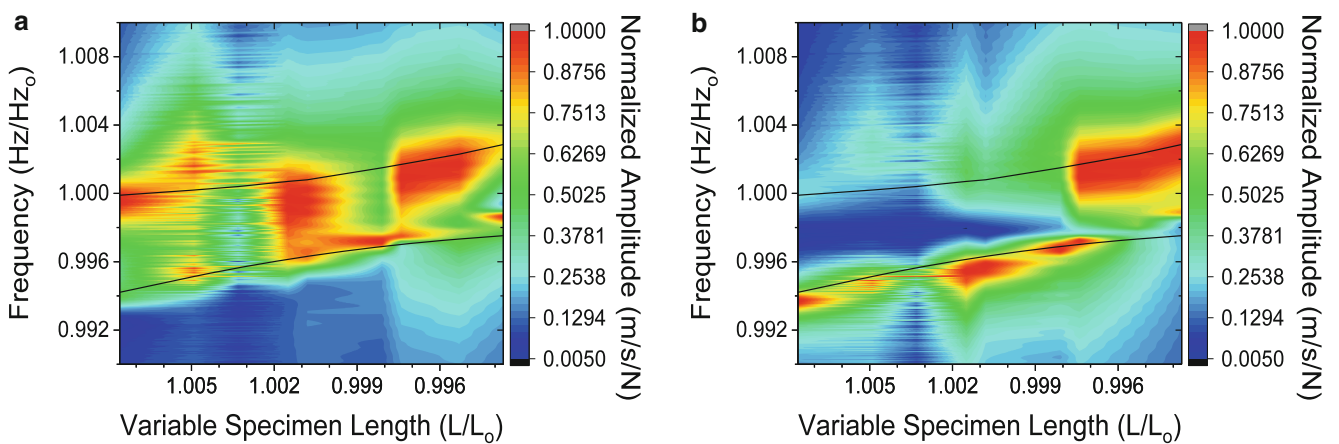


Fig. 32.7 Group 3. Experimental avoided crossing FRF peaks as variable specimens are trimmed. Curve fit from analytical solution; $\Gamma = 7.22$. (a) Baseline Specimen. (b) Variable Specimen

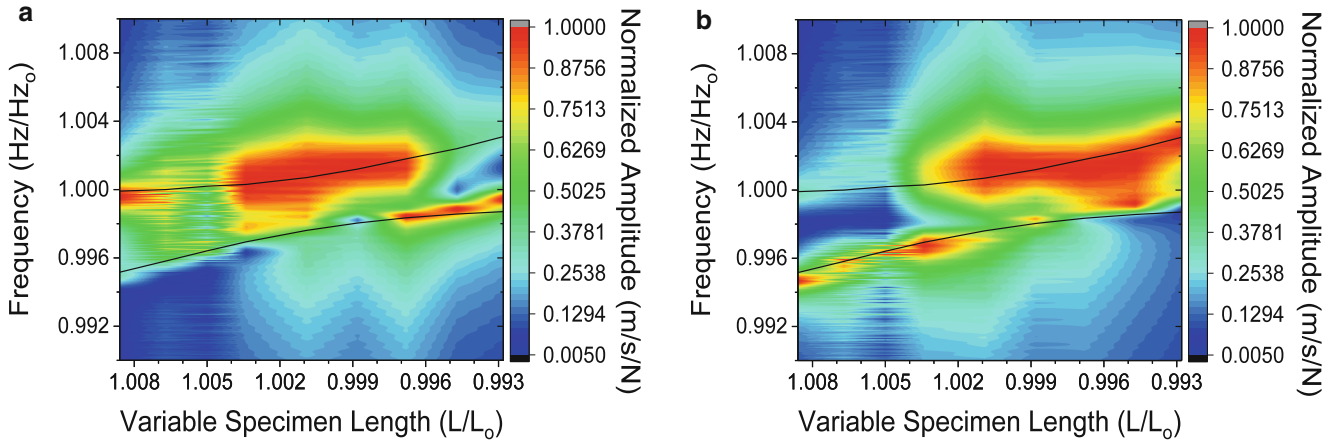


Fig. 32.8 Group 4. Experimental avoided crossing FRF peaks as variable specimens are trimmed. Curve fit from analytical solution; $\Gamma = 6.71$. (a) Baseline Specimen. (b) Variable Specimen

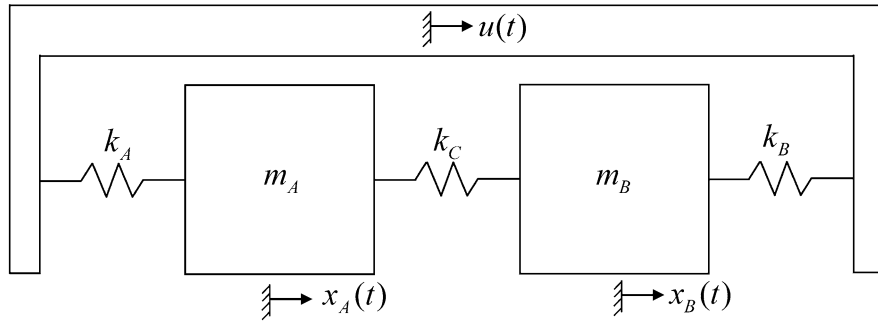


Fig. 32.9 2-DOF coupled mechanical oscillator

32.4 Analytical Model

A representation of the coupled experimental resonators was derived to quantify the amount of coupling present. Similar models have been used in quantifying the coupling of quantum particle systems [7]. The model shown in Fig. 32.9 is an undamped 2-DOF system with two oscillators with masses m_A and m_B , respectively, and stiffnesses k_A and k_B , respectively. The two oscillators are coupled using a spring with stiffness k_C . The build plate is represented by the boundary surrounding the two masses that would be displaced harmonically some distance $u(t)$. The displacements of each mass is $x_A(t)$ and $x_B(t)$.

For an unforced system, take the model shown in Fig. 32.1 with $u(t) = 0$. Equations of motion can be derived and arranged in the matrix form of

$$\mathbf{M}\ddot{\mathbf{x}} + \mathbf{K}\mathbf{x} = 0 \quad (32.1)$$

where the mass and stiffness matrices, respectively, are

$$\mathbf{M} = \begin{bmatrix} m_A & 0 \\ 0 & m_B \end{bmatrix} \text{ and } \mathbf{K} = \begin{bmatrix} k_A + k_C & -k_C \\ -k_C & k_B + k_C \end{bmatrix} \quad (32.2)$$

If the anticipated solution is assumed to be harmonic, it can be expressed in the form of

$$x_i(t) = A \exp(-i\omega_{\pm}t) \quad (32.3)$$

with ω_{\pm} representing the coupled eigenfrequencies. A nontrivial solution can be found by inserting Eq. (32.3) into Eq. (32.1) and taking the determinant of the resulting matrix

$$\det \begin{bmatrix} -m_A \omega_{\pm}^2 + (k_A + k_C) & -k_C \\ -k_C & -m_B \omega_{\pm}^2 + (k_B + k_C) \end{bmatrix} = 0 \quad (32.4)$$

The eigenfrequencies of the result of Eq. (32.4) can be expressed as

$$\omega_{\pm} = \frac{1}{2} \left[(\omega_A^2 + \omega_B^2) \pm \sqrt{(\omega_A^2 - \omega_B^2)^2 + 4\Gamma^2} \right], \quad (32.5)$$

where

$$\omega_A = \sqrt{(k_A + k_C)/m_A}, \omega_B = \sqrt{(k_B + k_C)/m_B}, \quad (32.6)$$

and the coupling stiffness can be expressed as

$$\Gamma = \sqrt{\frac{k_C^2}{m_A m_B}} \quad (32.7)$$

The Γ term can also be used to represent the difference between the frequencies ω_+ and ω_- . This model is assumed to be a reasonable representation of a given coupled pair in the experiment without the consideration of damping because typical damping ratios of the build were found to be no more than 0.03%.

32.5 Results and Discussion

Table 32.2 shows the coupling stiffness obtained in simulation and experimentally for each group.

These results show that the simulation and experiment found that there was a reduction in coupling with the inclusion of support material. This result agrees with what was expected, as the support material has a lower cross-sectional area than the specimens printed directly on the substrate. The larger reduction in coupling based on separation on the build plate was expected, as the build plate's inertia could limit the energy transferred from one specimen to another. Simulation found a substantially larger decrease in coupling for this feature due to the restrictions of boundary conditions because of the frictionless support enforced on the bottom of the substrate. In terms of application, this feature is limiting in that to minimize coupling between specimens, they must be as far apart as possible on a relatively small print area.

A more noteworthy result of the experiment is the reduction in coupling due to change in orientation. A reduction of 23.84% was found and can be considered reasonable for a specimen rotated by 45°, as a rotation of 90° by a nonsymmetrical specimen could almost completely reduce the amount of coupling, depending on the similarities of geometry and inertia. From this, it is justifiable in saying that the greatest reduction in coupling can be attained by changing the orientation of specimens on the substrate and keeping them separated from each other as much as possible.

32.6 Summary and Conclusions

In summary, the method presented was able to quantify coupling between multiple groups of cantilever beam specimens on the same build plate. The results obtained experimentally and by simulation showed that coupling was best reduced by changing the orientation of specimens on the build plate, followed by a similar reduction in increasing the separation between

Table 32.2 Results of measured coupling stiffness

Group	Feature	Simulation coupling stiffness (Γ)	Experimental coupling stiffness (Γ)
1	No support material	7.99	9.10
2	Support material (control)	7.12	8.81
3	Support material and separation	2.66	7.22
4	Support material and orientation	2.42	6.71

specimens. The addition of support material on specimens was found to decrease coupling with the least benefit. All results aligned with the expectations of the experiment and showed that the method presented has the potential to be extended to more complex geometry and a greater number of coupled specimens.

Acknowledgments This work was funded by Honeywell Federal Manufacturing & Technologies under Contract No. DE-NA0002839 with the U.S. Department of Energy. The United States Government retains and the publisher, by accepting the article for publication, acknowledges that the United States Government retains a nonexclusive, paid up, irrevocable, world-wide license to publish or reproduce the published form of this manuscript, or allow others to do so, for the United States Government purposes. This work contains a patent pending technique, U.S. Patent Application Serial No. 14/941,258.

References

1. Frazier, W.E.: Metal additive manufacturing: a review. *J. Mater. Eng. Perform.* **23**(6), 1917–1928 (2014)
2. Van Bael, S., Kerckhofs, G., Moesen, M., Pyka, G., Schrooten, J., Kruth, J.P.: Micro-CT- based improvement of geometrical and mechanical controllability of selective laser melted Ti6Al4V porous structures. *Mater. Sci. Eng. A.* **528**(24), 7423–7431 (2011)
3. Van der Auweraer, H.: Structural dynamics modeling using modal analysis: applications, trends and challenges. *IEEE Instrum. Measur. Technol. Conf.* **3**, 1502–1509 (2001)
4. Mathew, J.P., Patel, R.N., Borah, A., Vijay, R., Deshmukh, M.M.: Dynamical strong coupling and parametric amplification in mechanical modes of graphene drums. *Nat. Nanotechnol.* **11**, 747–751 (2016)
5. Faust, T., Rieger, J., Seitner, M.J., Krenn, P., Kotthaus, J.P., Weig, E.M.: Nonadiabatic dynamics of two strongly coupled nanomechanical resonator modes. *Phys. Rev. Lett.* **109**(3), 037205 (2012)
6. Pribe, J.D., West, B.M., Gegel, M.L., Hartwig, T., Lunn, T., Brown, B., Landers, R., Bristow, D., Kinzel, E.C.: Modal response as a validation technique for metal parts fabricated with selective laser melting. In: *Proceedings 27th International Solid Freeform Fabrication Symposium*, pp. 151–174. (2016)
7. Novotny, L.: Strong coupling, energy splitting, and level crossings: a classical perspective. *Am. J. Phys.* **78**(11), 1199–1202 (2010)



Chapter 33

Quantification of Dynamic Model Validation Metrics Using Uncertainty Propagation from Requirements

Andrew M. Brown, Jeffrey A. Peck, and Eric C. Stewart

Abstract The Space Launch System, NASA's new large launch vehicle for long range space exploration, is presently in the final design and construction phases, with the first launch scheduled for 2019. A dynamic model of the system has been created and is critical for calculation of interface loads and natural frequencies and mode shapes for guidance, navigation, and control (GNC). Because of the program and schedule constraints, a single modal test of the SLS will be performed while bolted down to the Mobile Launch Pad just before the first launch. A Monte Carlo and optimization scheme will be performed to create thousands of possible models based on given dispersions in model properties and to determine which model best fits the natural frequencies and mode shapes from modal test. However, the question still remains as to whether this model is acceptable for the loads and GNC requirements. An uncertainty propagation and quantification (UP and UQ) technique to develop a quantitative set of validation metrics that is based on the flight requirements has therefore been developed and is discussed in this paper. There has been considerable research on UQ and UP and validation in the literature, but very little on propagating the uncertainties from requirements, so most validation metrics are "rules-of-thumb;" this research seeks to come up with more reason-based metrics. One of the main assumptions used to achieve this task is that the uncertainty in the modeling of the fixed boundary condition is accurate, so therefore that same uncertainty can be used in propagating the fixed-test configuration to the free-free actual configuration. The second main technique applied here is the usage of the limit-state formulation to quantify the final probabilistic parameters and to compare them with the requirements. These techniques are explored with a simple lumped spring-mass system and a simplified SLS model. When completed, it is anticipated that this requirements-based validation metric will provide a quantified confidence and probability of success for the final SLS dynamics model, which will be critical for a successful launch program, and can be applied in the many other industries where an accurate dynamic model is required.

Keywords Structural Dynamics · Uncertainty Quantification · Uncertainty Propagation · Modal Test · Probabilistic Analysis

Nomenclature

BME	Best Model Estimate
DOF	Degree-of-Freedom
FEM	Finite Element Model
GNC	Guidance, Navigation, & Control
IMT	Integrated Modal Test
ML	Mobile Launcher
PDF	Probability Density Function
rv	random variable
SLS	Space Launch System
SRB	Solid Rocket Booster
UQ, UP	Uncertainty Quantification and Propagation

A. M. Brown (✉)

NASA/Marshall Space Flight Center, ER41/Propulsion Structural & Dynamic Analysis, Huntsville, AL, USA
e-mail: andy.brown@nasa.gov

J. A. Peck · E. C. Stewart

NASA/Marshall Space Flight Center, EV31/Vehicle Dynamics, Loads, and Strength Analysis, Huntsville, AL, USA

33.1 Introduction

NASA is developing the Space Launch System (SLS) as the first manned extra-orbital vehicle since the Apollo program. Briefly, the system consists of a Core Stage consisting of a liquid hydrogen and oxygen tank and four RS-25 liquid rocket engines; a second stage powered by one RL-10 engines; the manned Orion capsule and command module upper stage; and two advance Solid Rocket Boosters (SRB) attached to the sides of the core stage (see Fig. 33.1). As with any launch vehicle, the structural dynamics finite element model (FEM) is vitally important for a number of reasons. First, the dynamic model is critical for the successful design of a safe guidance, navigation, and control (GNC) system, since in-flight vectoring of the propulsion system must be consistent with system mode shapes. Second, the dynamic model is the central basis for the determination of dynamic loads as they propagate from numerous sources at all phases of the mission, which are used for strength analysis throughout the vehicle.

As the above factors are well-recognized, modal testing of launch vehicle systems has always been a requirement for space flight. However, determining the details of this modal testing is problematic; there are many different configurations and system components to consider, and it is difficult to determine which configuration and which combination of components should be tested. In recent years, for instance, the launch dynamics community has started moving away from traditional “full-up” modal testing of the entire system in favor of testing individual substructures (e.g., the SRB’s, the Core Stage, etc.) and then analytically tying the test-verified components together. As far as testing the proper configuration, it is very difficult to devise a true “flight” configuration, as this would involve devising accurate free-free boundary conditions and would require loading of the propellants into the fuel tanks, which would be dangerous and extremely costly.

The SLS program has made several decisions regarding the above issues. First, the primary modal test of the system (called the Integrated Modal Test, or IMT) will be with the empty SLS mounted on the Mobile Launcher (ML), which itself is a complex structure. The validation of the SLS flight model will be achieved using a probabilistic optimization technique defined as the “Best Model Estimate (BME)” method developed by Stewart [1]. Since the IMT is scheduled for only a couple of months before the first SLS launch, the BME method uses a Monte Carlo analysis of a large pre-determined set of potential SLS models using probabilistic dispersions of primitive geometric variables in the finite element model. Once the IMT is performed, each Monte Carlo sample is compared with the natural frequency and mode shape results, and a Pareto Front is created that identifies the “best model.”

Although a best model would be created, though, no criteria had been established for whether that model was actually accurate enough to be acceptable for the applications to GNC and loads. Although typical model correlation criteria such as “less than 10% variation in natural frequency” and “greater than 0.9 on the Modal Assurance Criteria diagonal” could be applied, these are not tied to the dynamic model requirements.

An effort was therefore initiated to develop a technique that uses the requirements for the dynamic model to generate the metrics for its acceptability. For example, the GNC community has a guideline that says the post-test modeled first bending mode flight frequency must be no less than -3% of the pre-test model first bending mode. The first bending mode can

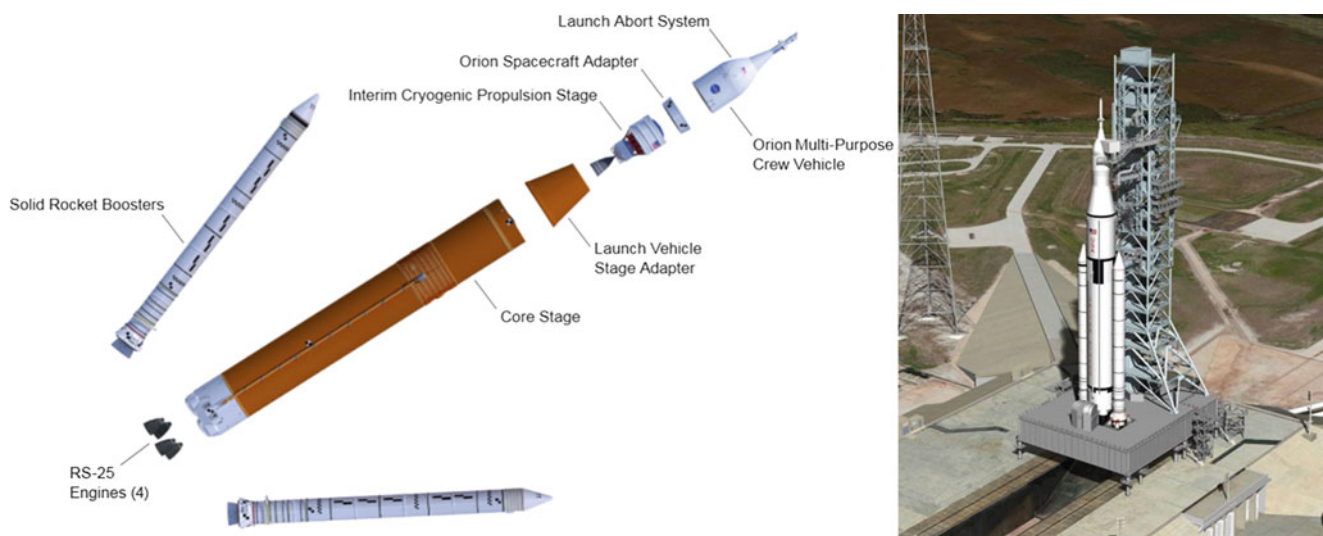


Fig. 33.1 Space Launch System Block I Configuration and mounted on Mobile Launcher

increase in frequency from the pre-test to post-test models with little impact on the GNC community, so no guidelines exist for that case. Although there are other important applications for the dynamic model, it is believed that the GNC requirement is the most stringent and provides a clear metric to be met prior to flight. A technique has therefore been developed to address the need for model acceptability metrics and is described in this document; as this is a work-in-progress, the technique has only been implemented on simplified systems and so this paper should be considered an “extended abstract” rather than as a paper with fully-vetted results. Nevertheless, the technique is unique as a “requirements-based metric” so publication at this time should be valuable to the dynamics community.

33.2 Literature Survey

There has been substantial work in the literature on uncertainty quantification and propagation (UQ, UP), but little on the reverse propagation that is needed for establishment of the desired metric. Hasselman has published a great deal in this area, including papers on structural dynamics model accuracy [2] and on UQ, focusing on quantifying and propagating structural dynamic model uncertainty using modal test [3, 4]. His UQ papers describe a rigorous methodology using the system frequency response functions as well as mass and stiffness matrices, and the use of a proprietary software code for implementation. Chen in 2004 laid out a step-by-step process for model validation using uncertainty propagation that does have elements considered useful for this research [5]. A metamodel, or Response Surface Model, is used as a surrogate for the original numerical model to enable large sample Monte Carlo simulation, and an assessment of model validity then is obtained by generating a probability density function (PDF) comparing the response and experiment, and identifying the “critical limit of confidence level where the physical experiment falls exactly at the boundary of the performance range obtained from the computer model.” This process is very similar to that eventually chosen by the authors for this work. Other valuable work in this field include a number of publications by Kammer that focus on quantifying the uncertainty propagation in substructures when they are coupled together into a system model [6].

33.3 Methodology

The methodology here somewhat follows the procedure laid down by Chen by creating a limit state of the ratio of the modal test and model primary natural frequency. Our interpretation of the GNC requirement is that the true frequency can be no less than a value that is 3% less than the pre-test prediction, which comes from the FEM. The performance limit-state ratio is applicable here, therefore, because we assume that the true value of the natural frequency lies within a statistical range defined by a mean equal to the test value obtained by the modal test and a distribution that is a function of sensor placement and other purely test-based errors.

The other critical concept is an assumption that the statistical distribution of the relationships between the natural frequencies of the modelled ground-modal test model and flight model are accurate, so therefore that same uncertainty can be used in propagating the uncertainties in the actual ground modal test to what we call here a “pseudo-test” flight configuration. This assumption requires that there is a clear shape equivalence between a ground-modal test mode and the critical flight mode upon which the requirement is levied. If this is the case, we assume that the distribution of the ratio between the modeled flight configuration critical frequency and modeled fixed configuration equivalent modal frequency can also be used to relate the tested ground fixed configuration to the “pseudo-modal-tested” flight configuration, i.e.

$$\{f_{ft}\} = \{f_{gt}\} * \left\{ \frac{f_{fm}}{f_{gm}} \right\} \quad (33.1)$$

where $\{f_{gm}\}$ = vector of frequencies of shape equivalent mode from FEM of ground-modal-test, created using Monte Carlo with assumed statistical distributions of parameters; $\{f_{fm}\}$ = vector of frequencies of critical mode from flight FEM, created using Monte Carlo with assumed statistical distributions of structural parameters; $\{f_{gt}\}$ = vector of frequencies of shape equivalent mode from ground-modal-test, created using Monte Carlo with assumed statistical distributions of measurements; and $\{f_{ft}\}$ = vector of frequencies of critical mode from flight configuration extrapolated from modal-test vector.

Using these values, we then formulate the performance limit state as the ratio of the flight “test” frequency (which is really only a “pseudo-test”, and which we have defined to be the distribution about the true value) to the flight model frequency, and subtract 1.0 to calibrate it about zero

$$g = \frac{f_{ft}}{f_{fm}} - 1. \quad (33.2)$$

The PDF of g can be generated directly from the random vectors, and can be integrated from -0.03 to $+\infty$ to obtain the probability of “success”, i.e., the probability that the model frequency is within the acceptable range of the critical true frequency. If this probability is higher than the value determined by the program authority, the model is “acceptable.” It should be noted that although this new metric is based on the physics of the problem, engineering judgment is still necessary to assess what level of success is adequate.

33.4 Examples

Two examples were created to flesh out the process and to more clearly identify the critical concepts and assumptions used. The first example is a multi degree of freedom (DOF) lumped spring mass system developed and analyzed in Mathematica[®], as shown in Fig. 33.2. The “flight” configuration, which has free-free boundary conditions, is represented by substructure A, which includes the spring $k1$ to the boundary DOF, while the “ground-modal-test” configuration is simulated with an additional substructure B which is grounded. It was initially thought that the ground test configuration could be represented by simple springs to ground, but it was then realized that since the ground-test fixture was the entire Mobile Launcher (ML, see Fig. 33.1), which possesses its own complex structural dynamics, representation by a mere stiffness (or even a number of springs) could not be used. We let all the springs in the system be random variables (rv’s) representing modeling, material, and other uncertainties, and assign distribution types, means and standard deviations to each rv. A 10,000 sample Monte Carlo analysis is then performed to obtain random vectors of the model fixed first frequency $f1gm$ and the model free-free second frequency $f2fm$ (first flexible mode), using the same sample sets for the shared rv’s in substructure A.

At this point a modal test is assumed to be performed on the entire “ground-test-configuration” and the fundamental frequency is obtained. As described previously, due to sensor placement, measurement and other testing errors, it is assumed that this value would be within the range of the true value of this frequency established by the distributions on these errors. For this MDOF system, we assume these errors follow a normal distribution about the mean, which will be the result from the modal test, and possess a 2% coefficient of variation. We now use the previous vector of ratios of the “flight” model to the “ground-modal-test” model to extrapolate the “tested” flight frequencies from the tested ground frequencies, i.e., a “pseudo flight-test configuration”.

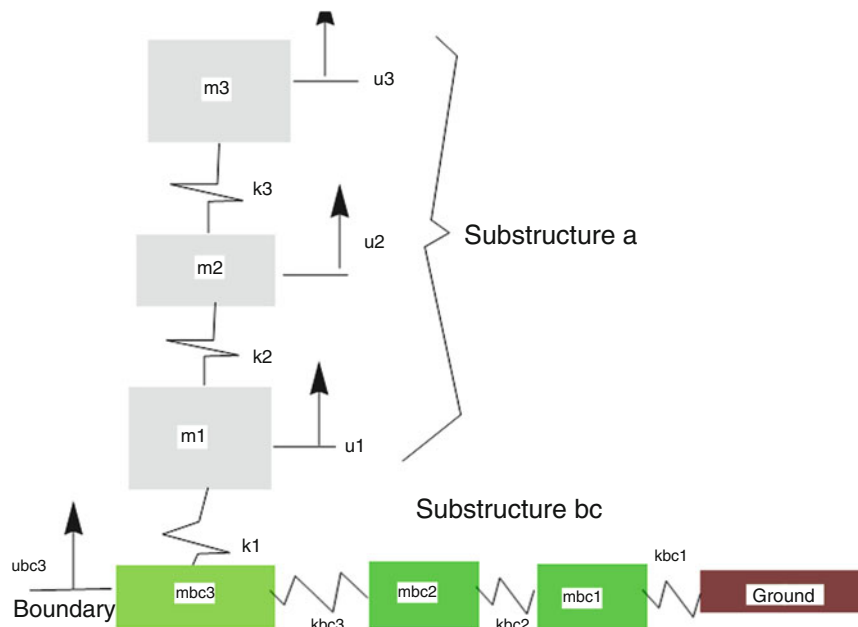


Fig. 33.2 Discrete MDOF system representing SLS vehicle and Mobile Launcher

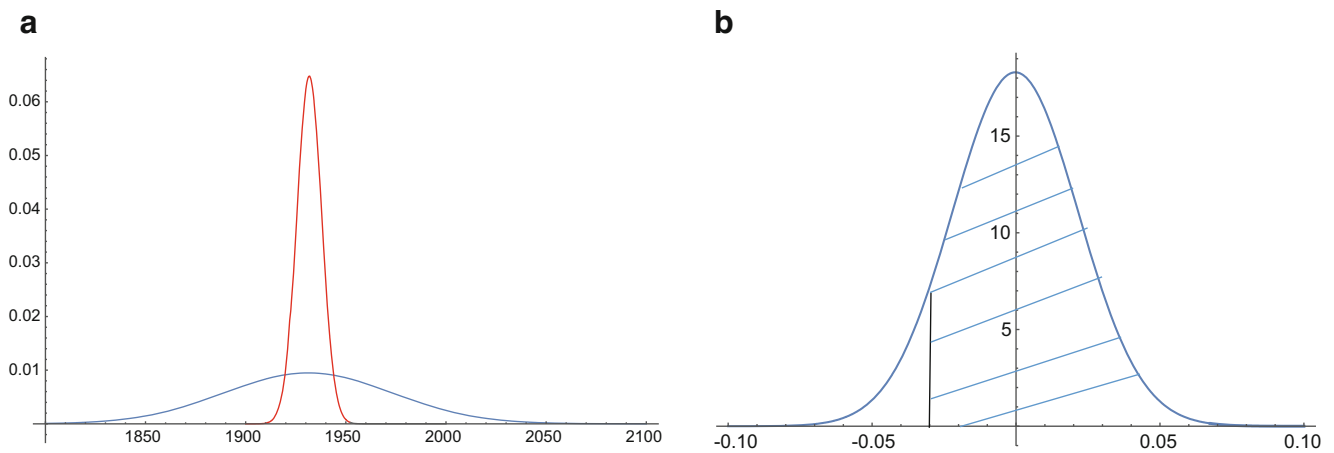


Fig. 33.3 Example 1 (a) PDF's of model frequency (red) and test frequency (blue); (b) PDF of Limit State g with success defined by hatched area

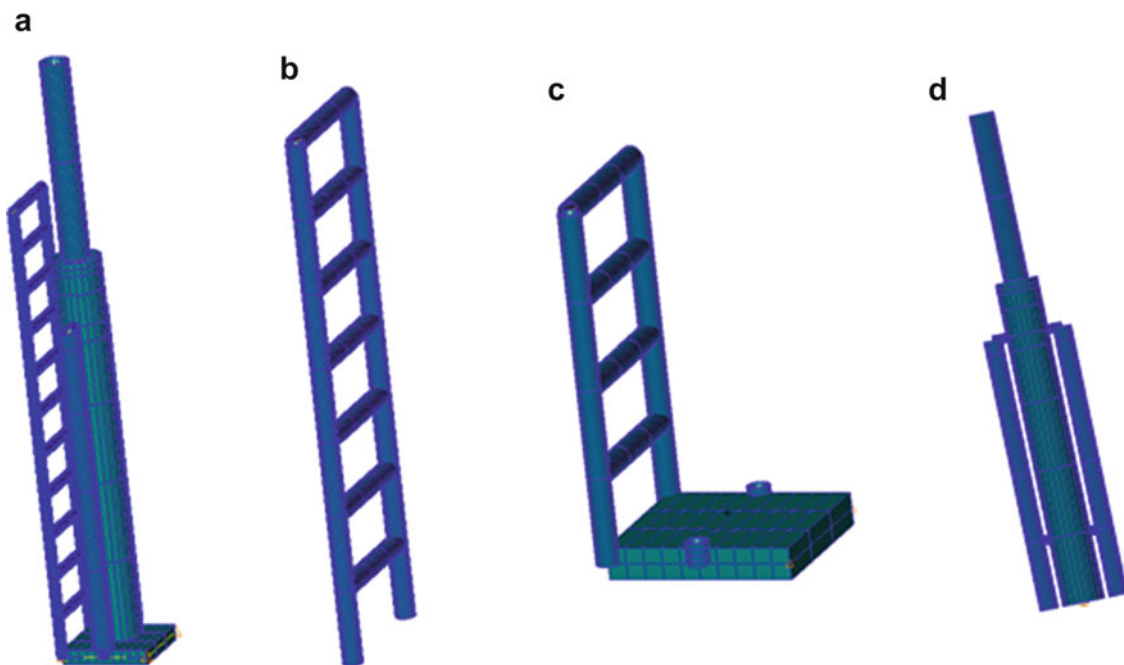


Fig. 33.4 (a) Entire simplified SLS model on Mobile Launcher; (b) Upper ML substructure; (c) Lower ML substructure; (d) SLS substructure (and flight configuration when propellant mass added)

We now create the limit state as the ratio of the flight “test” frequency (which is really only a “pseudo-test”) to the flight model frequency, and subtract 1.0 to calibrate it about zero. For the values assumed in this example, the PDF of this limit state is shown in Fig. 33.3. The probability of success is defined to be the integral under the PDF from -0.03 to $+\infty$, and is 91.3% for this set of parameters.

The second example is intended to be a simple but reasonable facsimile of the actual flight and ground-test configuration of the SLS (see Fig. 33.4). Approximate lengths and masses were used for the entire system, and the parameters were tweaked to approximately obtain a match with the primary frequency of interest in the actual SLS, which is the third flexible mode at 1.22 Hz (here we get 1.38 Hz). This example allows experimentation with the various deterministic and probabilistic software packages necessary for the analysis of the true vehicle. In addition, an additional non-structural mass was added to the “flight” configuration-only to represent the propellant mass. A distribution is assigned to this parameter, but it has to be assumed that this distribution is correct as testing in the flight configuration isn’t possible.

The same process as used for the MDOF lumped system was applied to this simplified SLS system model. For this model, the Young’s moduli of the SLS core stage, the SRB, the hold-down posts on the ML pad, the ML pad plates, and the upper

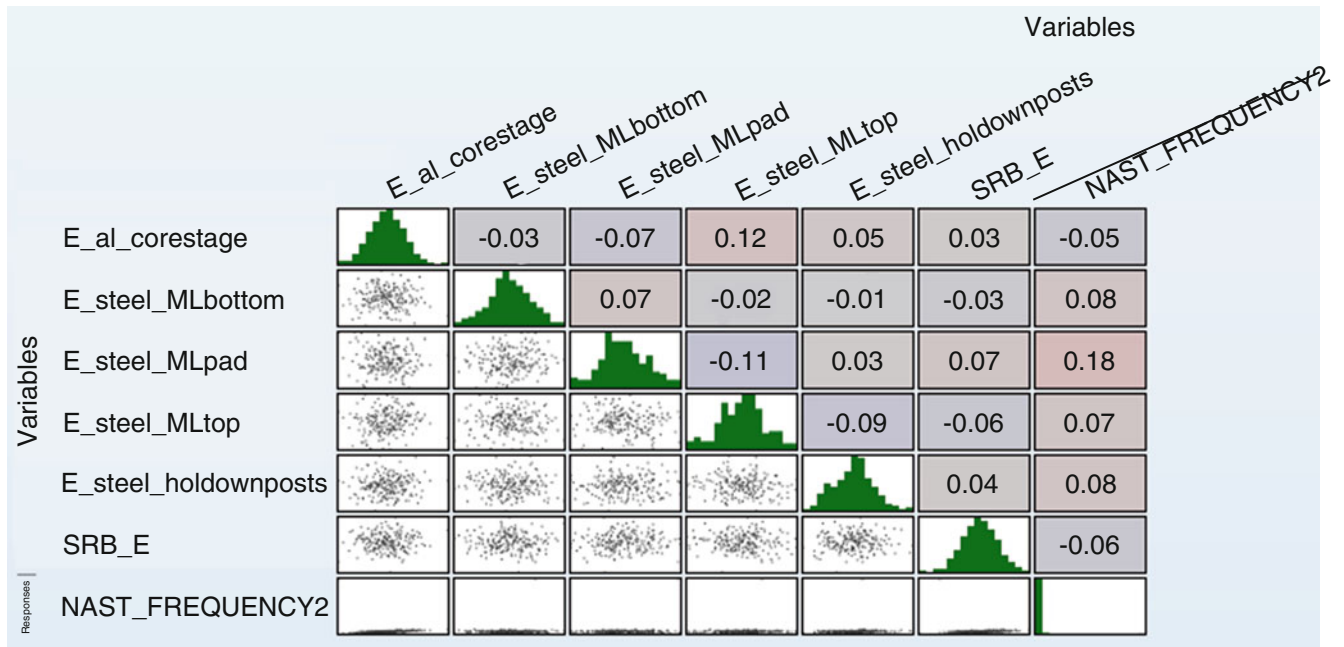


Fig. 33.5 Correlation matrix relating random variables with response variable, and showing distributions

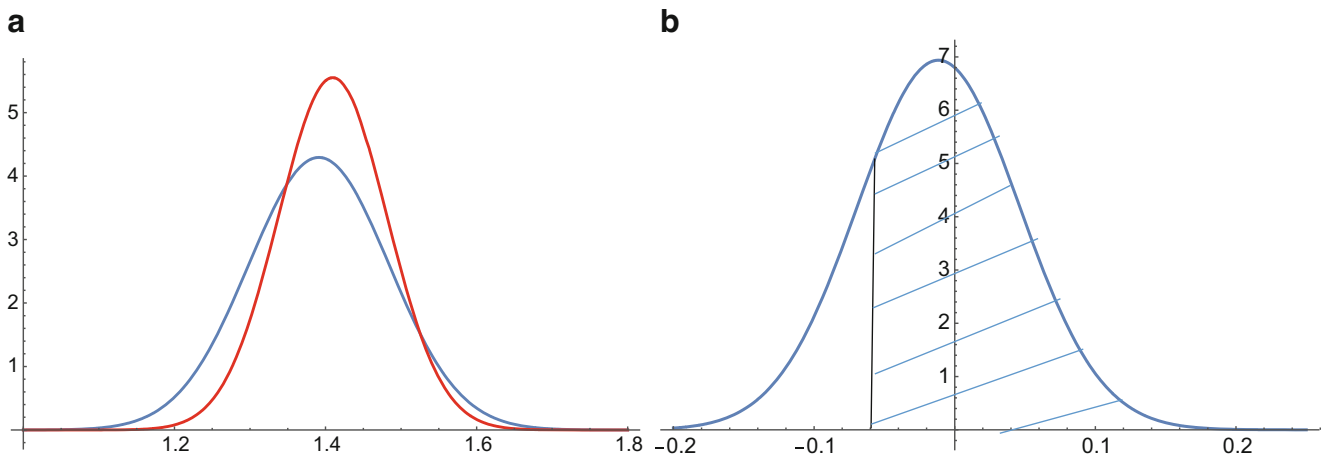


Fig. 33.6 Example 2 (a) PDF's of model frequency (red) and test frequency (blue); (b) PDF of Limit State g with success defined by hatched area

ML and lower ML main beams, and the propellant mass were established to be independent rv's. The probabilistic wrapper code LS-OPT[®] is used to define the distributions of the random variables and to run NX[™] Nastran[®] jobs varying each of the parameters in a Monte Carlo analysis. The analysis on the flight configuration is performed first, and the resulting vector of the primary bending mode natural frequencies saved. The Monte Carlo rv sample set is also saved and the random variables shared with the ground test configuration (all of the SLS substructure except for the propellant) were reused along with the ML substructure rv's in a Monte Carlo analysis of the ground-modal test configuration to obtain the appropriate bending mode closest to the flight mode of interest. A chart output from LS-OPT showing the correlation of the response natural frequency to each of the input random variables is shown in Fig. 33.5.

The ratio for each sample from the two MC analyses is then calculated and imported into Mathematica, where the limit state PDF generated and a probability of success is calculated, shown in Fig. 33.6. In this case, the probability of "success" is only 61%. Figures 33.5 and 33.6 introduce several questions which will need to be examined. First, the correlation is almost non-existent between most of the random variables and the response variable, and only weak for one of them; this result indicates that the particular mode of interest is more a function of some other parameter that has not been accounted for. Secondly, looking at a variety of choices for the statistics of the random parameters in these examples, which at this point

are completely arbitrary, various success rates point to the fact that the requirements will favor either an overestimation of the natural frequency rather than a more accurate estimation if there is substantial aleatory variability in the test or model, or a small variation in the model variability, which is expected. This is indicated by examining the individual PDF's of the "pseudo-test" versus "model" for the examples (Figs. 33.3a and 33.6a).

33.5 Forward Work and Conclusion

A major point of consideration identified is how to implement the random parameters. We presently believe that "primitive" random variables that attempt to approximate actual material and stiffness variations in the structure will be implemented for the vehicle, but that more gross variations on the entire mass and stiffness matrices of the ML will be applied to avoid unnecessary complication; there is no need to perform an excessive amount of analysis on the ML as the only quantity of interest is how it affects the fundamental mode at the boundary with the SLS at the hold-down posts. Another key avenue for investigation, as identified in the simplified SLS model case, is thoroughly understanding the sensitivity of the response variable to each of the random variables. Special attention must be paid to accurately identify the statistical parameters of those input rv's with the highest sensitivity. Finally, an examination is also being undertaken to use techniques developed by Allen [7] to replace the modes of the entire system with purely fixed modes of the vehicle, which would simplify the uncertainty model significantly.

After this decision is made, an attempt will be made to apply the process using the model and test results for the Ares I-X, a 2012 NASA test launch vehicle, to further identify adequacy of the technique. If this is successful, the technique will be applied to SLS as planned with a final deadline in mid-2018. Successful application of this technique would also be an important contribution to the development of metrics for dynamic models, and would mark one of the first attempts at using system requirements to develop these metrics.

References

1. Stewart, E., Hathcock, M.: Using dispersed modes during model correlation, AIAA SciTech Forum (2017)
2. Hasselman, T., Coppelino, R., Zimmerman, D.: Criteria for modeling accuracy: a state-of-the-practice survey. In: Proceedings of the 18th IMAC Conference, San Antonio, TX, February 2000
3. Hasselman, T.: Effect of modal test statistics on modeling uncertainty and model updating, AIAA structures, Structural Dynamics & Materials Conference 2000, Paper 2000-1443
4. Hasselman, T.: Quantification of uncertainty in structural dynamic models. *ASCE J. Aerosp. Eng.* **14**, 158-165 (2001)
5. Chen, W.: Model validation via uncertainty propagation and data transforms (2004)
6. Kammer, D.C., Krattiger, D.: Propagation of spacecraft free-Interface substructure uncertainty into system test-analysis correlation. *J. Vib. Acoust.* **134**(2), 051014 (2012)
7. Allen, M.S., Gindlin, A., Mayes, R.: Experimental modal substructuring to estimate fixed-base modes from tests on a flexible fixture. *J. Sound Vib.* **330**, 4413-4428 (2011)



Chapter 34

Natural Frequency Testing and Model Correlation of Rocket Engine Structures in Liquid Hydrogen: Phase I, Cantilever Beam

Andrew M. Brown, Jennifer L. DeLessio, and Preston W. Jacobs

Abstract Many structures in the launch vehicle industry operate in liquid hydrogen (LH2), from the hydrogen fuel tanks through the ducts and valves and into the pump sides of the turbopumps. Calculating the structural dynamic response of these structures is critical for successful qualification of this hardware, but accurate knowledge of the natural frequencies is based entirely on numerical or analytical predictions of frequency reduction due to the added-fluid-mass effect because testing in LH2 has always been considered too difficult and dangerous. This fluid effect is predicted to be approximately 4–5% using analytical formulations for simple cantilever beams. As part of a comprehensive test/analysis program to more accurately assess pump inducers operating in LH2, a series of frequency tests in LH2 are being performed at NASA/Marshall Space Flight Center’s unique cryogenic test facility. These frequency tests are coupled with modal tests in air and water to provide critical information not only on the mass effect of LH2, but also the cryogenic temperature effect on Young’s Modulus for which the data is not extensive. The authors are unaware of any other reported natural frequency testing in this media. In addition to the inducer, a simple cantilever beam was also tested in the tank to provide a more easily modeled geometry as well as one that has an analytical solution for the mass effect. This data will prove critical for accurate structural dynamic analysis of these structures, which operate in a highly-dynamic environment.

Keywords Structural Dynamics · Modal Test · Liquid Hydrogen · Model Correlation · Modulus temperature dependence

Nomenclature

A_{ml}	added mass for beam-type modes
a	cantilever beam length
b	beam width
{f}	Vector of Natural Frequencies
[Φ]	Modal Matrix
DOF	Degrees of Freedom
DOE	Design of Experiments
LH2	Liquid Hydrogen
LOX	Liquid Oxygen
LPFP	Low Pressure Fuel Pump
RT	Room Temperature
ρ_f	fluid mass density
SAVPE	Sum of Absolute Values of Percent Errors
SSME	Space Shuttle Main Engine
ω_f	natural frequency of the beam immersed in fluid
ω_v	natural frequency of the beam in vacuum

A. M. Brown (✉)

NASA/Marshall Space Flight Center, ER41/Propulsion Structural & Dynamic Analysis, Huntsville, AL, USA
e-mail: andy.brown@nasa.gov

J. L. DeLessio

Jacobs-ESSSA – NASA/Marshall Space Flight Center, ER41/Propulsion Structural & Dynamic Analysis, Huntsville, AL, USA

P. W. Jacobs

Jacobs-ESSSA – NASA/Marshall Space Flight Center, EM22/Materials Test, Chemistry, and Contamination Control Branch, Huntsville, AL, USA

34.1 Introduction

Liquid rocket engines are powered by the combustion of two propellants at very high pressure, a fuel and an oxidizer. Frequently, the fuel is liquid hydrogen (LH₂). While the pressure can be provided by a very high-strength storage tank, usually this would be weight-prohibitive, so a turbopump or series of turbopumps are required to provide these extremely high pressures. These rotating shafts of these turbopumps are usually driven by a hot gas in the turbine side, and the pumping side consists of either axial inducers, which increase the velocity by conically swept blades on the shaft, or centrifugal impellers, which force the fluid into spinning outward radiating channels; both these actions significantly increase the flow velocity, and high pressures are then obtain by diffusing the flow.

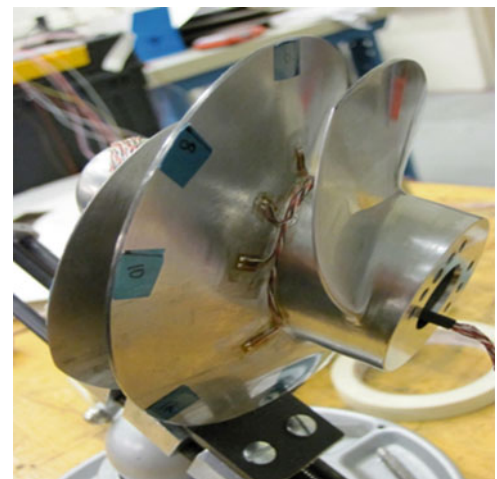
Because of a number of highly-energetic fluid excitation sources at both narrow-band frequency range or harmonic frequencies, a structural dynamic analysis is required for all the components in the flow path on both the turbine and pump sides in order to prevent high dynamic response. However, because of several complicating factors, this analysis is problematic. First, the components operate in a liquid, which not only provides the excitation forcing function but also affects both the damping and structural dynamic characteristics due to virtual mass loading (natural frequencies $\{f\}$ and modes $[\Phi]$). Second, for liquid hydrogen pumps, the operating temperature is $-253\text{ }^{\circ}\text{C}$ ($-423\text{ }^{\circ}\text{F}$), which has a substantial effect on the Young's Modulus E of the metallic materials used for the components, and therefore affects the natural frequencies substantially.

This issue has always been a problem for the design of liquid hydrogen turbopumps, but it became much more of a risk during the design phase of the J-2X engine, from 2006 to 2012. The frequency range of one of the excitation sources, higher order cavitation, was predicted to overlap with the oxidizer pump inducer natural frequencies. This motivated an extensive analytical examination, which was forced to incorporate the large variability in the structural dynamic characteristics due to the large uncertainties discussed above, and a test program to characterize the environment with high-frequency pressure taps and structural response via strain gages in a water (not liquid oxygen) rig (see Fig. 34.1). A great deal of important data was obtained including some information on damping and the mass loading effect of water on the inducer natural frequencies. The most challenging goal of fully anchoring the forcing function was not completed before the J-2X program was cancelled.

This same potential HOC issue existed during Space Shuttle Main Engine (SSME) and has arisen again during the implementation of the RS-25, which is an updated SSME engine for the core stage of NASA's new Space Launch System. The SSME had operated with some speed placards to avoid this resonant condition, but new operating requirements for the RS-25 meant the condition could not be avoided easily. An extensive analysis was performed, but due to the uncertainties discussed above, along with the uncertainties in the forcing function itself, the analysis predicted failure even for SSME operation, which testing and run-time in the millions of seconds had shown was not occurring. An empirically-based, non-physics-based damage-fraction analysis was therefore performed based upon one of the tested units, and an acceptance criteria stemming from this analysis were imposed upon the inducer and the operation of the turbopump. Some of the resulting restrictions are quite undesirable, though, and possibly could be severe if conditions show the levels of HOC are greater than expected.

A new integrated test/analysis program has been initiated, therefore, both to mitigate some of the restrictions of the criteria and to provide data for a physics-based analysis that would produce believable results. This integrated program includes an updated waterflow test, hydroelastic analysis and testing, acoustic modeling, and unique natural frequency testing of the sub-

Fig. 34.1 J-2X LOX turbopump inducer (not to scale)



scale stainless-steel inducer used in the water-flow test in LH2. Along with more complete modal testing in air and water, this LH2 test will provide data necessary to correlate the inducer natural frequencies and validate analytical predictions of the structural characteristics in this environment. The LH2 testing is enabled by the unique capabilities of the NASA/Marshall Space Flight Center Cryogenic Test Facility. The authors have not found documentation of modal testing in LH2 of any kind in the literature.

In addition to testing the inducer in LH2, an opportunity existed to perform a test of a much simpler “cantilever beam” structure. This test would allow very precise modeling of the exact physical structure, and allow comparison with purely analytical as well as numerical modal analyses. This test would also provide an opportunity to implement any lessons learned prior to testing the inducer. Here, we provide preliminary results and data on this LH2 “ping” test of the cantilever beam. Final documentation will be provided upon completion of both phases of the LH2 frequency test/analysis program and the entire inducer water-flow integrated test/analysis program.

34.2 Literature Survey

The first aspect examined by this test/analysis program is the effect on the Young’s Modulus of metals at cryogenic temperatures, in particular the Titanium alloy used for the RS-25 LPFP inducer. We examined a number of publically available sources, shown in Fig. 34.2, including the well-known MMPDS [1], a recent hybrid test/analysis study by Ghisi and Mariani [2], and a dynamic modulus test by Zhang et al. [3], using a modal test of a cantilever beam in a cryostat, similar to the one performed in this study. We also have access to several proprietary sources, which cannot be reported here. The variability in this data resulted in a non-trivial uncertainty in the operating natural frequency of the inducer blades. We will discuss how this data was used in the results section of this document.

The second aspect is the effect of the liquid mass of the LH2 on $\{f\}$ and $[\Phi]$ of the inducers. There has been a great deal of both analytical and numerical work in this field beginning with Lindholm in 1965 [4] and continuing until the present. Although Lindholm’s experiments were in water, as is the case for almost every other experimental study, he did generate an equation relating the density of the liquid to the natural frequencies, where the same equation is applicable for all cantilever beam-type modes, as derived below

$$A_{m1} = \frac{\pi}{4} \rho_f a b^2 \quad (34.1)$$

Where A_{m1} is the added mass for beam-type modes, ρ_f is fluid mass density, a is the beam length, and b is beam width. This added mass can then be used to calculate the ratio of the natural frequency of the beam immersed in fluid ω_f to the natural frequency of the beam in vacuum ω_v (or a low-density gas) using

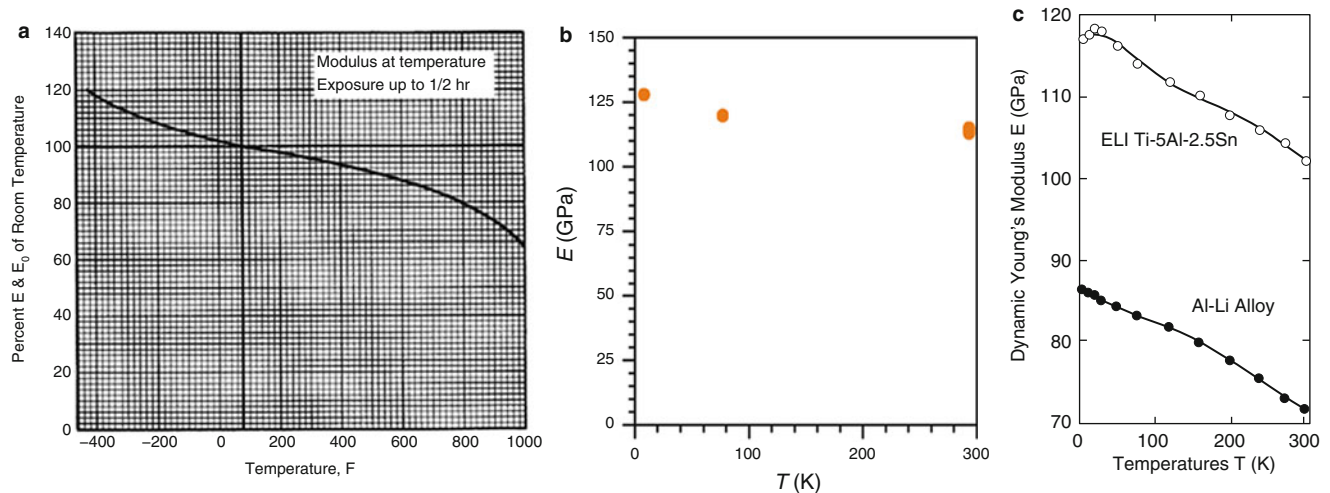


Fig. 34.2 Public data relating Young’s modulus of Ti 5–2.5 to temperature; (a) MMPDS, (b) Ghisi and Mariani, (c) Zhang

$$\frac{\omega_f}{\omega_v} = \frac{1}{\sqrt{1 + \frac{A_{m1}}{m_b}}}. \quad (34.2)$$

Much of the published work deals with rectangular plates with low aspect ratios, (e.g., Ergin and Ugurlu [5], Hosseini-Hashemi [6]) but some do examine longer beams which have aspect ratios on the order of 10 as used here, in particular Liang [7], who used previous experimental and analytical results to generate a correction factor for aspect ratio. Liang succinctly derives and identifies the important parameters as follows:

The added mass/unit span due to the fluid is

$$A_{m1} = 0.25C_f \frac{\pi\rho_f b}{\rho_p h_p}, \quad (34.3)$$

where ρ_f is fluid mass density, ρ_p is structural mass density, b is beam width, h_p is beam thickness, and

$$C_f = \frac{2 * aspect_ratio}{1 + 2 * aspect_ratio}. \quad (34.4)$$

These then can be directly used to calculate the natural frequency in the fluid using

$$\omega_f = \omega_v \sqrt{\frac{1}{1 + \frac{A_{m1}}{C_f}}}. \quad (34.5)$$

As far as other work published in the literature, many of these focus on numerical solutions to the problem (e.g. Kerboua [8]). As a high-fidelity multi-physics numerical code ANSYS® is already being used in this correlation effort, we do not believe it adds value to implement these solutions.

34.3 LH2 Ping Test Setup

The test environment for the ping test is a large cryostat, essentially a cylindrical canister that can be filled with cryogenic fluids. The cryostat is bolted to a top section (Dewar Head) that contains an actuator that can move axially. Upon examination by the analysis/testing team, a simple and reliable test design and process was conceived. First, since LH2 is a very low-density fluid, a previous study by Chiu and Brown [9] indicated that the mode shapes would not vary perceptibly from the in-vacuo case, so only a natural frequency test, rather than a full modal test, was necessary since the {f} of interest could be tied to the correct [Φ] using previous in-vacuo modal analysis and modal testing in air. Second, since access to the filled cryostat would be difficult, the availability of an existing actuating mechanism within the cryostat could be taken advantage of by fabricating a “pick” (similar to a guitar pick) that could be lowered at a rate fast enough to pluck the structure and still get out the way fast enough to prevent a repeated impact. A photo of the cryostat in operation and the ping-test assembly is shown in Fig. 34.3.

A titanium beam of aspect ratio 10 was then fabricated using a billet of material from the same batch as is used to construct the inducers. The closest producible reproduction of a theoretically fully-fixed end was to bolt the beam onto a stiff column, as shown in a subset of pre-test modal analysis results in Fig. 34.3. Although pre-test analysis showed that the targeted modes were almost pure “cantilever” modes, as intended, the mounting column as well as the four bolts connecting it to the beam, including their pre-load, were modelled to capture the natural frequencies as accurately as possible. The influence of the mounting column is clear in the second mode, which is not one of the four targeted modes. In addition, four thermocouples were installed inside the cryostat to provide temperature measurements, and two LH2-compatible strain gages were installed on the upper and lower surfaces of the beam near the fixed end (Fig. 34.4).

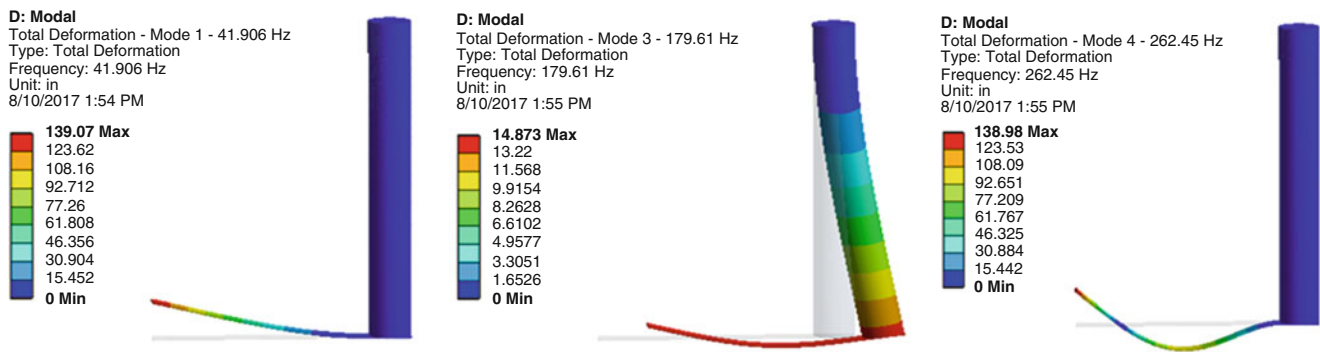


Fig. 34.3 Pre-test modal analysis results



Fig. 34.4 Cryostat and cantilever beam test setup

34.4 Correlation Procedure

Determining a well-defined correlation procedure a-priori is also critical for accurately assessing the validity of the models for predicting the effect of liquid mass and temperature on natural frequency. Of course, this procedure was adapted to the test results, and resulted in the following steps:

1. Using optimization procedure, vary the room temperature (RT) Young's Modulus to best match the four measured natural frequencies, with the result being four new calculated frequencies. The error-function for the optimization is to minimize the sum of the absolute values of the percent errors (SAVPE) for all four tested beam bending modes.
2. If the resulting RT Modulus is within the range given by estimates from the available sources, use this Modulus and apply ANSYS numerical methods to determine predictions for frequencies in water and compare to measured frequencies. The purpose of this step was to calibrate the fluid modeling techniques in ANSYS. Although the results in water were considered estimates, the calculated results provided confidence in these tested values.
3. If the optimized RT Modulus is within the range given by estimates from the available sources, repeat for the Boil-off case.
4. Evaluate whether the optimized Modulus at Boil-off conditions is within the spread of available data. If so, extrapolate this Modulus to LH2 temperature and calculate the natural frequencies using the same method as step (2) and compare to measured frequencies. In addition, apply each of previously-discussed purely analytical techniques developed by Lindholm and Liang to obtain frequency predictions, and compare with ANSYS results.

34.5 Measurement, Modeling and Numerical Analysis of Modal Test Configuration

Engineering drawings used to fabricate the beam and column provided a starting point for generating the solid model geometry (in ANSYS SpaceClaim). Post-test, the volume and weight of the beam were precisely measured. The beam weight was measured on a calibrated scale, which read to four decimal places. The volume of the beam was measured using a graduated cylinder. In addition, precise measurements of the beam dimensions were taken with digital calipers. The length and width were reported and the thickness of the beam was reported every half inch. These measurements provided the data to construct a more accurate solid model in SpaceClaim and to also calculate the density of the material and compare to published values. The calculated density calculated was 4462.0 kg/m^3 (0.1612 lb/in^3), which compares well to available data. In order to match the as-measured mass of the beam, the density in the ANSYS finite element model (FEM) was defined such that:

$$\rho_{\text{Meas}} = m_{\text{Meas}}/V_{\text{Meas}}$$

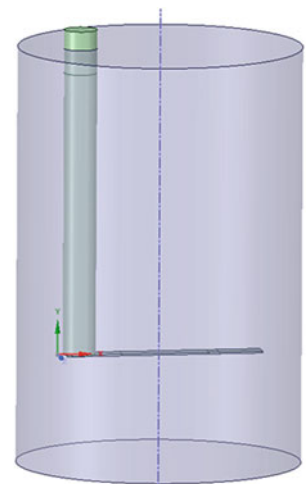
$$\rho_{\text{Model}} = [V_{\text{Meas}}/V_{\text{model}}]^* \rho_{\text{Meas}} = m_{\text{Meas}}/V_{\text{model}}$$

ANSYS version 18.0 was used for all analysis. ANSYS SpaceClaim was used to construct the geometry, Mechanical was used for the pre-stressed modal solutions, and DesignXplorer was used for the optimization procedure. The Acoustics Application Customization Toolkit (ACT) extension was used in ANSYS Mechanical for the simulations with modeled fluids.

For the FEM models used in steps (2) and (4) above, the fluid volume was also constructed in SpaceClaim, as shown in Fig. 34.5. An Enclosure was constructed around the beam and column using the dimensions of the cryostat and fluid level during test. Shared topology (merged nodes) were defined between the beam/fluid and the column/fluid interfaces, but the topology was not shared between the beam and the column. This is because nonlinear contact was used in the static pre-stress solution. Early modeling of the beam found that the inclusion of the column and the actual contact interface between the beam and the column were necessary to adequately model the stiffness of the structure. Initially the model included only the beam fixed at one end in all degrees of freedom (DOF). The column was then added and was initially fully bonded to the beam. The next and final configuration included the bolts at the beam/column interface with pretension, shown in Fig. 34.6. As the model fidelity increased the modal results converged and the optimized RT Modulus increased and converged as well (final shapes shown in Fig. 34.7).

The prestressed modal analysis was defined within ANSYS Mechanical. Beam Connections were created to define the bolts between the beam and the column. This connection type inserts beam elements which can have pretension applied. As the assembly torque was not measured, a reasonable preload force was defined for each bolt. The modal results were found to be relatively insensitive to the actual preload values (as long as a similar contact pattern was achieved.) The upper surface of the column (which attaches to the Dewar Head) was assumed fixed in all DOF. For the models with fluid elements, the acoustic body and fluid structure interfaces were defined in the static solution and the flag for “subsequent linear perturbation” analysis was defined. The water or LH2 density and speed of sound were defined for their respective temperatures.

Fig. 34.5 SpaceClaim model with fluid



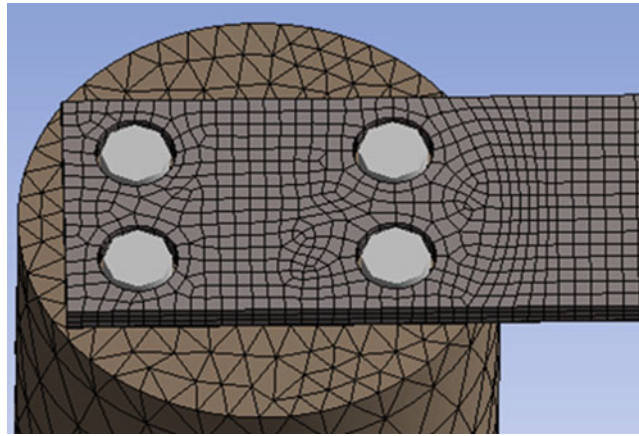


Fig. 34.6 View of ANSYS FEM mesh

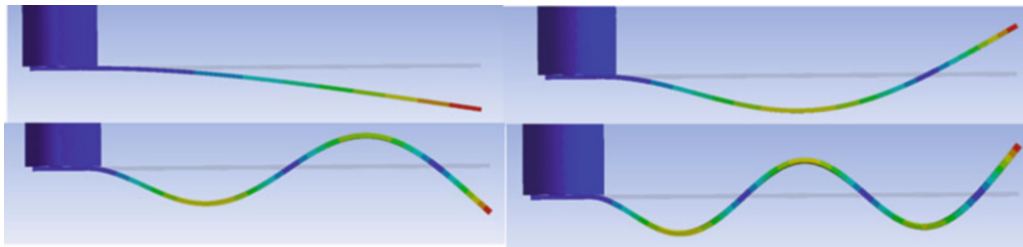


Fig. 34.7 Final analytical mode shapes used for correlation

The “True” contact status was used in the subsequent modal solution. The Unsymmetric solver was used for the modal analyses with fluid elements.

ANSYS DesignXplorer was used to determine optimal Modulus values in correlation steps (1) and (3). A Central Composite Design was completed with the Modulus as the single input parameter and the SAVPE as the single, custom-defined output parameter. A Genetic Aggregation response surface was developed and Screening Optimization was performed where SAVPE was minimized.

34.6 Testing

In order to isolate the effects of temperature and added liquid mass on natural frequency, as well as enabling recognition of existing sources of uncertainty, a well-defined testing procedure was necessary. The first step was a ping test of the beam setup under ambient conditions, where the air temperature was measured with thermocouples. There are four thermocouples in the cryostat, one at the surface of the fluid, one slightly above the beam, one slightly below, and one near the bottom of the cryostat. The beam temperature used for each test is the average of the thermocouples just above and just below. Three separate pings were performed for this (and every) step, and the time histories obtained and transformed into the frequency domain where the first four peaks could clearly be identified. Next, LH2 was slowly added to the cryostat, and when the entire apparatus was fully submerged with several inches of clearance from the top of the mounting cylinder, the next three ping tests were performed. The LH2 was then quickly removed by opening the liquid vent and filling with gaseous Helium, and three more pings were performed while the temperatures were still close to cryogenic (“Boil-off” configuration). Readings from the thermocouples were also taken. The data from this series of tests was also considered to be high quality. The next day, after the apparatus had completely warmed to ambient temperatures, a fourth series of ping tests was performed in water. Unfortunately, the strain gages never fully stabilized, perhaps due to a possible incompatibility with water, so the results from this water-test phase can only be considered “best estimates”.

34.7 Results

The complete results for the test and analysis series are shown in Table 34.1 to enable appropriate comparisons and error assessment. These should be considered preliminary, as they have not been through a quality control process yet, but the authors believe they will not be changed in any way. The first step in the modal correlation procedure involved optimizing the SAVPE error by adjusting the RT Modulus of the cantilever beam. The DOE bounds were reasonably defined based on the spread of available data at RT with some additional margin. The screening optimization produced three candidate points and the Modulus was selected based on the lowest SAVPE. This Modulus value aligned well with several of the propriety data sources. This same optimization approach was used for the Boil-off configuration. Each bending mode was matched to less than 0.5% with an SAVPE value of 1.04%. There was some concern in these results because the Modulus values obtained are significantly higher than those reported by Zhang, which had a very similar test setup. We believe that the discrepancies are most likely due to the fact that his team used analytical methodologies to predict the beam natural frequencies and assumed a fixed edge boundary condition. The fixed edge assumption over-predicts the frequencies, and analytical techniques frequently do so as well, so the calculated Young’s Modulus would be too low.

The measured temperature at the beam location in the cryostat for the air RT and water tests was only two degrees different. Thus this same optimized RT Modulus value was applied in the model with the added water fluid elements as discussed in the modeling section. The results are excellent, with less than 1% error for each of the four modes compared with test and an SAVPE value of 2.58%. In addition, the added mass frequency factor (ω_f/ω_v) are calculated and shown for the test cases, the ANSYS models, and applying the analytical techniques from Lindholm and Liang, and these all show excellent agreement of less than 1% error.

Moving to the last step of the correlation procedure, since all available data indicates that the Modulus does not change between temperatures at the Boil-off configuration and LH2, the ANSYS fluid elements were added and the analytical techniques were applied to the model using the Boil-off optimized Modulus and compared with the LH2 test results. Again, the results are excellent, with frequency errors and errors in added mass frequency factors all less than 1% and an SAVPE error of 2.36%.

34.8 Conclusions

The first natural frequency test of a cantilever beam in LH2 reported in the literature has been performed at NASA/MSFC to experimentally validate techniques for predicting the effect of the added mass of LH2. In addition, tests were performed at room temperature in air and in gas at close-to-cryogenic temperatures to enable an exhaustive correlation procedure that

Table 34.1 Modal test and analysis summary

Air RT				Boil-off and LH2 Temperature										
Mode (Test Order)	Test (Hz)	ANSYS FEM Opt-imized E	% Error	Boil-off				LH2						
				Test (Hz)	ANSYS FEM Optimized E (Hz)	% Error	Test (Hz)	ANSYS Acoustic FEM (Hz)	% Error	Test	ANSYS	Lindholm	Liang	
1	43.00	42.88	-0.28%	45.00	42.88	-2.28%	42.50	42.12	-0.89%	0.944	0.939			
2	270.00	270.00	-0.00%	283.00	282.33	-0.24%	267.50	265.37	-0.80%	0.945	0.940			
3	756.25	758.5	0.30%	792.25	793.08	0.10%	750.75	747.48	-0.44%	0.948	0.943			
4	1481.25	1488.10	0.46%	1553.00	1555.90	0.19%	1475.0	1471.50	-0.24%	0.950	0.946			
<i>Optimized E</i>		<i>1.7957E+07</i>		<i>Optimized E</i>		<i>1.96237E+07</i>								
Water RT				Added Mass Frequency Factors				LH2			Added Mass Frequency Factors			
Mode (Test Order)	Test (Hz)	ANSYS Acoustic FEM	% Error	Test	ANSYS	Lindholm	Liang	Test (Hz)	ANSYS Acoustic FEM (Hz)	% Error	Test	ANSYS	Lindholm	Liang
1	25.25	25.46	0.82%	0.587	0.594			42.50	42.12	-0.89%	0.944	0.939		
2	161.75	160.30	-0.90%	0.599	0.594			267.50	265.37	-0.80%	0.945	0.940		
3	459.75	459.49	-0.06%	0.608	0.606			750.75	747.48	-0.44%	0.948	0.943		
4	911.00	918.34	0.81%	0.615	0.617			1475.0	1471.50	-0.24%	0.950	0.946		
				0.602	0.603	0.622	0.597				0.947	0.942	0.948	0.941

precisely generated values for Young's Modulus as a function of temperature. A final test of the beam in room temperature water was also performed. Based on the results, ANSYS® acoustic modeling can be considered extremely accurate and can confidently be applied to more complex geometries. Our results for the Modulus of the Titanium alloy used in the test also fall well within the range predicted by proprietary sources. Both of these findings will prove extremely useful for the follow-on phase of this test-analysis program on the RS-25 inducer, and will be valuable for modeling of other structures in similar liquid cryogenic environments.

References

1. Metallic materials properties development and standardization-08. Battelle Memorial Institute (2013)
2. Ghisi, A., Mariani, S.J.: Mechanical characterization of Ti-5Al-2.5Sn ELI alloy at cryogenic and room temperatures. *Int J. Fracture*. **146**, 61–77 (2007). <https://doi.org/10.1007/s10704-007-9140-z>
3. Zhang, Z., Zhao, L.Z., Tu, Z.H., Zhang, P.Q.: Dynamic Young's moduli of space materials at low temperatures. *Cryogenics*. **34**(10), 839–842 (1994)
4. Lindholm, U., et al.: Elastic vibration characteristics of cantilever plates in water. *J. Ship Res.* **9**, 11–36 (1965)
5. Ergin, A., Urgulu, B.: Linear vibration analysis of cantilever plate partially submerged in fluid. *J. Fluids Struct.* **17**, 927–939 (2003)
6. Hosseini-Hashemi, S., Karimi, M., Rokni, H.: Natural frequencies of rectangular Mindlin plates coupled with stationary fluid. *Appl. Math. Model.* **36**, 764–778 (2012)
7. Liang, C.-C., Liao, C.-C., Tai, Y.-S., Li, W.-H.: The free vibration analysis of submerged cantilever plates. *Ocean Eng.* **28**, 1225–1245 (2001)
8. Kerboua, Y., et al.: Vibration analysis of rectangular plates coupled with fluid. *Appl. Math. Model.* **32**, 2570–2586 (2008)
9. Chiu, J., Brown, A.M.: Characterization of the modal characteristics of structures operating in dense liquid turbopumps, ASME Gas Turbo Expo 2017, Charlotte, North Carolina, June 26–30, 2017, paper GT2017–63633

Chapter 35

Optimal Maintenance of Naval Vessels Considering Service Life Uncertainty



Yan Liu and Dan M. Frangopol

Abstract Life-cycle analysis is increasingly being used to assess the structural performance and total cost incurred during the service life of naval vessels. Decision making on maintenance scheduling is based on minimizing life-cycle cost and risk metrics. However, existing life-cycle frameworks generally consider deterministic service life in the analysis process. Due to budgetary reasons, naval vessels are often required to extend their service life beyond the originally designed life. Management plans based on deterministic service life concepts do not consider the uncertainties associated with service life assessment and prediction. Structural aging can have significant effects on operational costs and risks during the service life extension. This paper presents the modeling of service life uncertainty and its impacts on the life-cycle management of naval vessels. The proposed framework is aimed to provide robust maintenance strategies addressing service life uncertainties. The presented approach is applied to fatigue of a high speed naval vessel.

Keywords Decision making · Life-cycle assessment · Service life uncertainty · Risk management · Fatigue

35.1 Introduction

Ship structures are inevitably subjected to deteriorations during their service life. Structural damage such as fatigue can affect ship safety and serviceability. Lifetime maintenance thus becomes important for risk management of structures during their service life. Due to budgetary constraints, structural systems are often required to continue service beyond their planned service life. Planning of lifetime structural maintenance should include the possibility of service life extension. This paper examines the planning of lifetime optimum maintenance schedule of naval vessels considering fatigue reliability and life-cycle cost under uncertain service life.

Under repeated loading, fatigue damage accumulates in fatigue-sensitive details of naval vessels. Prediction and modeling of the fatigue damage have to consider uncertainties from sea loads and fatigue growth model, among others. Structural health monitoring (SHM) information, if available, can provide accurate structural response and loading condition for fatigue prognosis [1, 2]. Most of the time probabilistic methods are adopted to model the fatigue damage accumulations based on $S-N$ (stress vs. number of cycles) approach. Time-dependent fatigue reliability is considered as a rational performance indicator that fully considers the uncertainties involved in the fatigue propagation process. The estimated fatigue reliability can be included into life-cycle analysis to drive decision making on maintenance scheduling [3]. Maintenance actions such as inspection and repair are scheduled to prevent the fatigue damage from reaching a critical state that endangers the structural safety. The effect of a maintenance action on improving fatigue reliability is qualitatively shown in Fig. 35.1. The optimal maintenance actions are scheduled such that the life-cycle cost is minimized. The formulation of life-cycle cost considers both the maintenance cost and failure cost for rational decision making.

Fatigue becomes more critical for aging structures that are operating beyond the designed service life [4]. If maintenance actions are not scheduled appropriately, fatigue may pose safety issues to ship structures during extended service life. This paper examines the impact of service life uncertainty on the lifetime maintenance planning of fatigue-sensitive structures. Fatigue damage and fatigue reliability are reviewed. The life-cycle cost formulation is used for probabilistic lifetime maintenance optimization. Subsequently, the drawback of optimal maintenance solutions based on deterministic service life is discussed. In the end, a robust maintenance decision process considering service life uncertainty is presented and illustrated using a high speed naval vessel under fatigue.

Y. Liu (✉) · D. M. Frangopol

Department of Civil and Environmental Engineering, ATLSS Engineering Research Center, Lehigh University, Bethlehem, PA, USA
e-mail: dan.frangopol@lehigh.edu

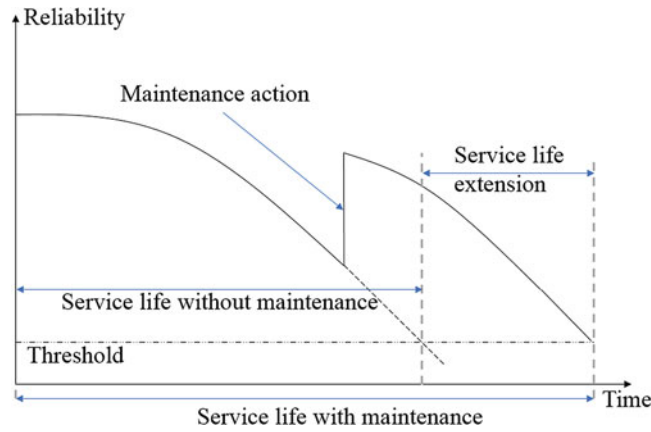


Fig. 35.1 Illustration of service life extension

35.2 Fatigue Reliability Assessment

Fatigue is a major stressor that causes damages in ship structures. In fatigue life evaluation of steel structures, the $S-N$ approach is widely used to describe the relationship between stress range and number of cycles to failure. The $S-N$ relationship is:

$$S = \left(\frac{A}{N} \right)^{\frac{1}{m}} \quad (35.1)$$

where S is the stress range, A and m are coefficients of $S-N$ curve, and N is number of cycles. In the assessment of fatigue damage accumulation, the damage caused by certain stress range level is assumed linearly related with its corresponding cycles. The total fatigue damage is expressed with the Miner's damage index D as [5]:

$$D = \sum_{i=1}^n \frac{n_i}{N_i} \quad (35.2)$$

where n_i is number of cycles at i^{th} stress range, and N_i is number of cycles to failure for i^{th} stress range. The damage index value of 1 implies fatigue failure. However, D is usually less than 1 [6]. To account for the variable stress ranges from sea loading, the equivalent constant stress range [5]:

$$S_{re} = \left(\sum \frac{n_i}{n_{total}} S_i^m \right)^{\frac{1}{m}} \quad (35.3)$$

is often used, where S_i is the stress range of the i^{th} bin in the stress range histogram, n_i is number of cycles in stress range S_i , and n_{total} is total number of cycles. Based on the $S-N$ approach and Miner's rule, the fatigue limit state can be defined with the performance function [3]:

$$g(t) = \Delta - D(t) = \Delta - (N/A) \cdot (e \cdot S_{re})^m \quad (35.4)$$

where Δ is Miner's critical damage accumulation index and $D(t)$ is the time-dependent fatigue damage accumulation index. $D(t)$ is a function of the $S-N$ parameters, equivalent stress range, and number of cycles. e is the modeling uncertainty associated with equivalent stress range [6]. The number of cycles N is estimated as $N(t) = N_{avg}t$, where N_{avg} is the estimated number of yearly cycles and t is the ship service life in years.

Based on the performance function and probabilistic information of the fatigue process, the failure probability of the fatigue detail, $P_f = P[g(t) < 0]$, and corresponding reliability index, β , can be obtained [7].

35.3 Life-Cycle Cost and Optimization

Inspection and repair are essential life-cycle maintenance actions to prevent the fatigue failure during the service life of ships. Fatigue reliability represents a performance indicator that can help to plan maintenance actions. Essential maintenances can be scheduled whenever the reliability level is closed to the predefined threshold. Life-cycle cost is a rational indicator in lifetime maintenance planning [8]. Life-cycle cost analysis includes the consideration of all inspection and repair costs during the lifetime horizon. Minimizing the life-cycle cost has proved to be an effective tool to schedule maintenance during the service life. In this paper, life-cycle cost is formulated to include inspection, repair, and expected failure costs during the service life. The expected total life cycle cost, C_{ET} , is calculated as [9]:

$$C_{ET} = C_{INS} + C_{REP} + C_F \quad (35.5)$$

where

$$C_{INS} = \sum_{i=1}^k \frac{C_{ins}}{(1+r)^{t_i}} \quad (35.6)$$

$$C_{REP} = \sum_{j=1}^n \frac{C_{rep}}{(1+r)^{t_j}} \quad (35.7)$$

$$C_F = C_f \cdot \max [P_f(t)] \quad (35.8)$$

and r is discount rate of money assumed 2%; C_{ins} and C_{rep} are undiscounted inspection and repair cost, respectively; k and n are numbers of inspections and repairs, respectively; t_i and t_j are times of inspection i and repair j , respectively; C_f is failure cost; P_f is time-dependent fatigue failure probability; and C_F is the expected failure cost. As indicated in Eq. (35.5), the expected total life-cycle cost includes expected failure cost, and discounted inspection and repair costs.

The formulation of maintenance optimization problem to minimize the expected total life-cycle cost is:

$$\begin{aligned} &\text{Minimize } C_{ET} \text{ with respect to inspection and repair times } t_i \text{ and } t_j \\ &\text{While satisfying inspection and repair time constraints :} \\ &0 < t_{i-1} < t_i < t_{life} \text{ and } 0 < t_{j-1} < t_j < t_{life} \end{aligned} \quad (35.9)$$

where t_i is i -th inspection time, and t_j is j -th repair time. t_{life} is designed service life. Inspection is assumed to be perfect when the accumulated fatigue damage $D(t)$ is at least 0.1. After repair, the number of cycles to failure is updated as [3]:

$$N_{new} = \frac{A}{(1.3 \cdot S)^m} = N_{avg} t_{new} \quad (35.10)$$

where t_{new} is the number of years to failure after repair.

The optimization is applied to fatigue in a Joint High Speed Sealift (JHSS) vessel [10]. The probabilistic properties of fatigue damage model are listed in Table 35.1. The critical damage index Δ is assumed lognormal with mean = 1.0 and coefficient of variation (COV) = 0.3 [11]; material parameter A is assumed lognormal with mean = 1×10^{12} and COV = 0.3;

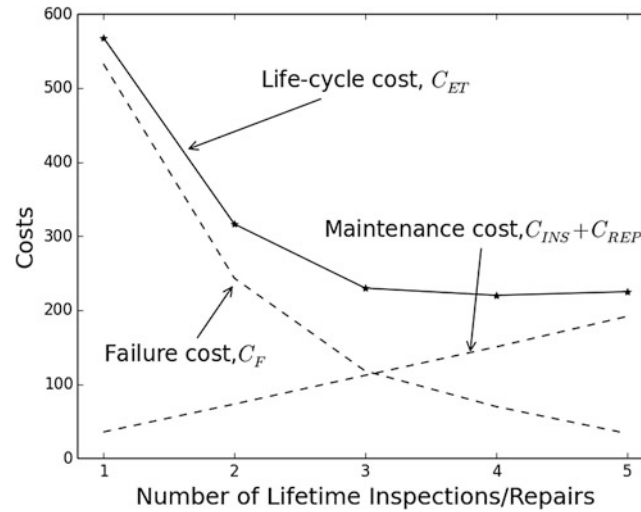
Table 35.1 Random variable description for fatigue reliability

Parameter	Distribution	Mean value	COV
A	Lognormal	1×10^{12}	0.3
m	Deterministic	4.0	–
e	Lognormal	1.0	0.1
S_{re}	Weibull	8.01 MPa	0.1
Δ	Lognormal	1.0	0.3

Adopted from [10]

Table 35.2 Lifetime maintenance optimization results

Number of lifetime inspections/repairs	Costs			
	C_{INS}	C_{REP}	C_F	C_{ET}
1	3.22	32.20	532.71	568.13
2	6.64	66.45	243.23	316.33
3	10.17	101.79	117.78	229.74
4	13.66	136.64	69.71	220.02
5	17.41	174.08	33.43	224.93

**Fig. 35.2** Life-cycle cost as function of specified number of lifetime inspections/repairs

measurement error factor e is assumed to be lognormal with mean = 1.0 and COV = 0.1; and m is assumed deterministic, $m = 4$. The equivalent stress range S_{re} is assumed to follow Weibull distribution. The designed service life is 30 years and is associated with 10^8 cycles [10].

The maintenance optimization is solved separately for one, two, three, four and five interventions. The ratio of undiscounted inspection cost C_{ins} , repair cost C_{rep} , and failure cost C_f is assumed to be 1:10:2000, with failure cost = 10,000. Nelder-Mead simplex method [12] is employed to solve the optimization problem. The optimal life-cycle cost results are shown in Table 35.2. It is seen that the life-cycle cost formulation include consideration for both maintenance cost and potential failure cost. As the intervention number increases, the failure probability decreases due to more frequent repairs on fatigue damage. Consequently, the failure cost decreases with the increasing number of lifetime maintenances. Intuitively the inspection and repair costs increase with number of lifetime maintenances. As shown in Fig. 35.2, life-cycle cost metric strikes a balance between failure cost and maintenance cost for decision makers. The optimized lifetime maintenance schedules are plotted in Fig. 35.3. Decision makers can choose the maintenance schedule based on their risk attitudes.

It should be noted that these optimal maintenance schedules are obtained for deterministic service life of 30 years. The structural performance may not be well maintained for potential service life extension. The optimized maintenance solution based on two interventions ($k = n = 2$) is used as an example to illustrate the critical problem faced under service life uncertainty.

Figure 35.4 shows the scenario of optimized lifetime maintenance facing service life extension. When naval ships are approaching the end of their designed service life, it is possible that they would be requested to continue service until replacements are available. Service life extension may bring undesirable consequences to aged structures. It can be seen in Fig. 35.4 that failure cost is well controlled with the optimized maintenances during the designed service life of 30 years. However, if service life extension becomes an urgent need, the failure cost can increase abruptly during prolonged service life. The fatigue failure probability increases dramatically after the designed service life. To prepare for the possible service life extension under uncertainty, it is recommended to adjust the maintenance schedule to avoid a large risk of fatigue failure during life extension.

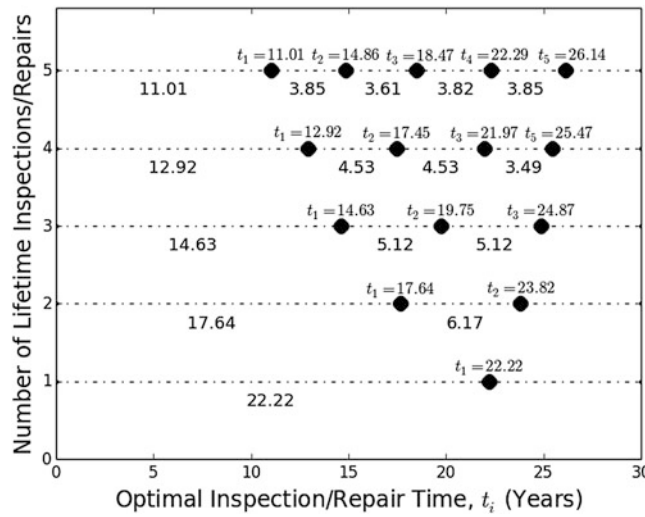


Fig. 35.3 Optimized maintenance schedule during designed service life of 30 years

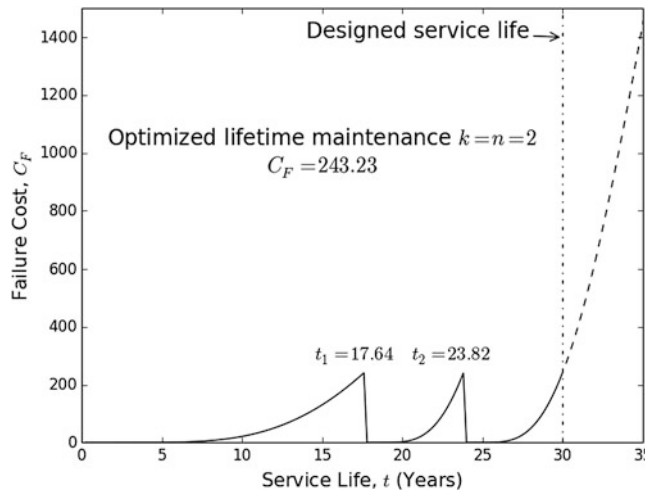


Fig. 35.4 Optimal maintenance schedule based on deterministic service life of 30 years

35.4 Addressing Service Life Uncertainty

As mentioned previously, the optimal maintenance schedules for a fixed service life are not optimal when facing service life extension. A robust maintenance considering the service life uncertainty is needed for rational life-cycle management. The consideration of failure cost during service life extension needs to be included in the life-cycle cost formulation. Assuming that the probability of extending service life with t_{ext} years is described with the probabilistic mass function $f_T(t_{ext}) = \Pr(T = t_{ext})$, the failure probability considering potential service life extension set $E : t_{ext} \in E$, can be expressed as:

$$P_f^{ext} = \sum_{t_{ext} \in E} f_T(t_{ext}) P_f(t_{ext} + t_{life}) \tag{35.11}$$

The failure cost during extended service life is defined as:

$$C_F^{ext} = C_f \cdot P_f^{ext} \tag{35.12}$$

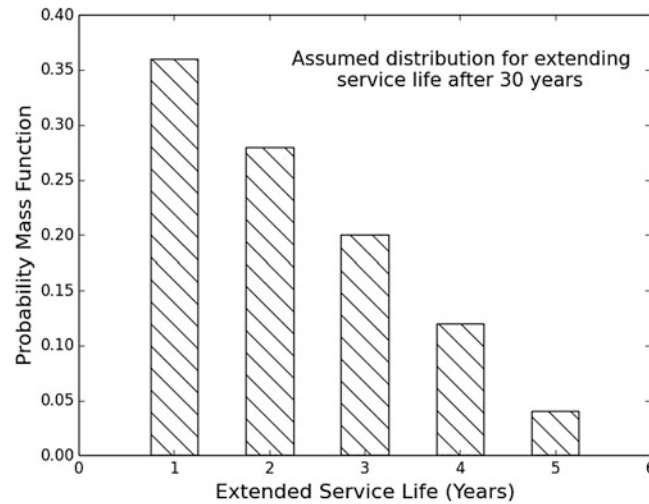


Fig. 35.5 Assumed probability for potential service life extension after designed service life of 30 years

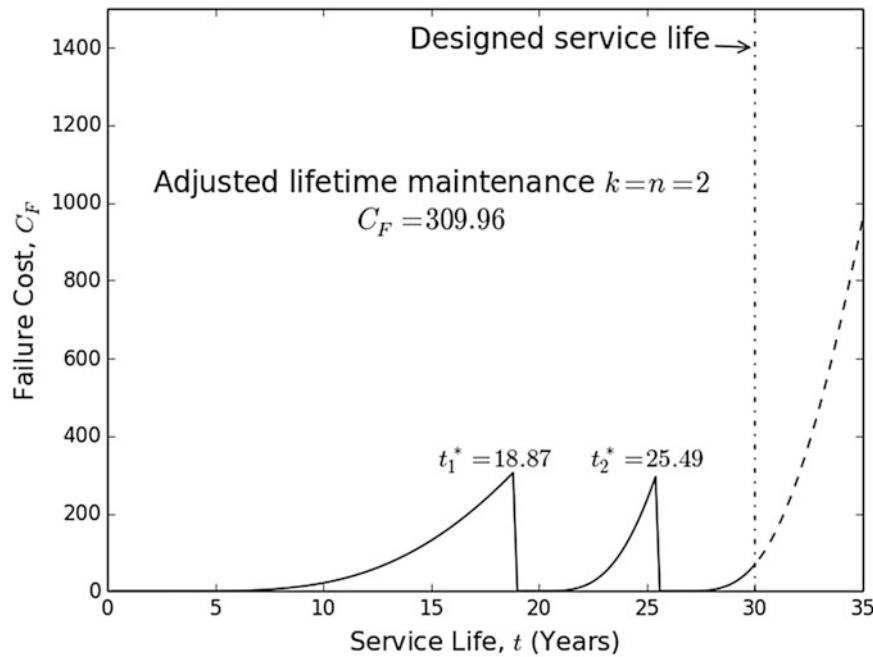


Fig. 35.6 Optimal maintenance schedule considering uncertainty in service life extension

The failure cost during designed service life C_F and failure cost during extended life C_F^{ext} are compared. $\max [C_F, C_F^{ext}]$ is adopted for the life-cycle cost formulation (see Eq. 35.5) for optimization. With this adjusted life-cycle cost formula, the optimized maintenance schedule addresses the concern for increasing failure cost during potential life extension.

The robust optimization scheme is tested in a hypothetical service life extension case, where the assumed probability mass function of life extension is shown in Fig. 35.5. The probability of extension time is assumed to linearly decrease during life extension assumed as 5 years. The robust maintenance optimization scheme is applied to address this uncertain service life scenario. With the number of maintenances specified as two, the optimized maintenance schedule is plotted in Fig. 35.6. Compared with the original maintenance plan in Fig. 35.4, the maintenance plan considering life extension shown in Fig. 35.6 delays the repair times and decreases the failure cost at the end of the extended life.

A detailed comparison of the two maintenance schedules is listed in Table 35.3. Deterministic service life optimization framework schedules the two maintenance times such that the failure cost and life-cycle cost are minimized during the designed service life of 30 years. The failure cost and life-cycle cost values considering life extension are more than twice the amount of those related with the initial designed life. In contrast, robust optimization framework controls the cost rise

Table 35.3 Comparison of optimization results

Strategy	Optimal solution		Costs considering 30 years designed life			Costs considering 5 years life extension (total life = 35 years)		
	t_1	t_2	$C_{INS} + C_{REP}$	C_F	C_{ET}	$C_{INS} + C_{REP}$	C_F^{ext}	C_{ET}
Deterministic method	17.64 yrs.	23.82 yrs.	73.09	243.23	316.32	73.09	649.35	722.44
Robust method	18.87 yrs.	25.49 yrs.	71.04	309.96	381.00	71.04	309.96	381.00

during life extension. Though the life-cycle cost of robust schedule (381.00) is larger than that of deterministic schedule (316.32) considering the 30 years design service life, the robust schedule provides a much smaller life-cycle cost (381.00) than that associated with the deterministic service life approach (722.44) considering service life extension.

35.5 Conclusions

Existing naval ships are often required to extend their service life. This can incur significant costs associated with maintaining aged structures in operation. The risk of structural failure rises during extended service life. The undesirable performance deterioration during service life extension is illustrated in this paper. Fatigue damage accumulation is used to represent the structural performance deterioration in the aging process. Life-cycle cost optimization is implemented to schedule lifetime inspections and repairs to ensure the sustained performance during a prescribed design service life. Fatigue failure probability will substantially increase when the structure is required to serve beyond the designed service life. Consequently, the life-cycle cost is subjected to large increase during service life extension. To address the uncertainty in service life, a robust approach is presented to optimize the lifetime maintenance scheduling. The robust optimization approach presented in the paper provides insights for maintaining aging structures beyond their design service life at minimum life-cycle cost.

Acknowledgements The support from the U.S. Office of Naval Research (contracts N00014-08-1-0188, N00014-12-1-0023, and N00014-16-1-2299, Structural Reliability Program), the NSF Award CMMI-1537926, and the Commonwealth of Pennsylvania, Department of Community and Economic Development, through the Pennsylvania Infrastructure Technology Alliance (PITA) is gratefully acknowledged. The opinions and conclusions presented in this paper are those of the authors and do not necessarily reflect the views of the sponsoring organizations.

References

- Soliman, M., Frangopol, D.M.: Reliability quantification of high-speed naval vessels based on SHM data. In: Model Validation and Uncertainty Quantification, vol. 3, pp. 99–106. Springer, Cham (2014)
- Kwon, K., Frangopol, D.M., Kim, S.: Fatigue performance assessment and service life prediction of high-speed ship structures based on probabilistic lifetime sea loads. *Struct. Infrastruct. Eng.* **9**(2), 102–115 (2013)
- Kwon, K., Frangopol, D.M.: Fatigue life assessment and lifetime management of aluminum ships using life-cycle optimization. *J. Ship Res.* **56**(2), 91–105 (2012)
- Temple, D.W., Collette, M.D.: Minimizing lifetime structural costs: optimizing for production and maintenance under service life uncertainty. *Mar. Struct.* **40**, 60–72 (Jan. 2015)
- Miner, M.A.: Cumulative damage in fatigue. *J. Appl. Mech.* **12**(3), A159–A164 (1945)
- Ayyub, B.M., Assakkaf, I.A., Kihl, D.P., Siev, M.W.: Reliability-based design guidelines for fatigue of ship structures. *Nav. Eng. J.* **114**(2), 113–138 (2002)
- Madsen, H.O.: *Methods of Structural Safety*. Dover Publications, Mineola (2006)
- Frangopol, D.M.: Life-cycle performance, management, and optimisation of structural systems under uncertainty: accomplishments and challenges. *Struct. Infrastruct. Eng.* **7**(6), 389–413 (2011)
- Frangopol, D.M., Lin, K.-Y., Estes, A.C.: Life-cycle cost design of deteriorating structures. *J. Struct. Eng.* **123**(10), 1390–1401 (1997)
- Zhu, J., Collette, M.: Lifecycle fatigue management for high-speed vessels using local approaches. In: 11th International Conference on Fast Sea Transportation, Honolulu, Hawaii, USA (2011)
- Wirsching, P.H.: Fatigue reliability for offshore structures. *J. Struct. Eng.* **110**(10), 2340–2356 (1984)
- Nelder, J.A., Mead, R.: A simplex method for function minimization. *Comput. J.* **7**(4), 308–313 (1965)

Chapter 36

On the Monitoring-Driven Assessment of Engineered Systems



Eleni N. Chatzi and Vasilis K. Dertimanis

Abstract The life-cycle management of structural systems operating under diverse loads involves the tasks of simulation (forward engineering), identification (inverse engineering) and maintenance/control actions. The efficient and successful implementation of these tasks is however non-trivial, due to the ever-changing nature of these systems, and the variability in their interactive environment. Two defining factors in understanding and interpreting such large-scale systems are nonlinear behavior and structural uncertainty. The former is related to the external dynamic loading that might shift the structural response from purely linear to nonlinear regimes, while the latter is related to erroneous modeling assumptions, imprecise sensory information, ageing effects, and lack of a priori knowledge of the system itself. This paper discusses implementation of methods and tools able to tackle the aforementioned challenges. Among other topics, the use of surrogate models and Bayesian-type filters for the reduced representation and identification of uncertain and nonlinear structural systems is discussed.

Keywords Structural Health Monitoring · AutoRegressive Models · Structural Metamodels · Polynomial Chaos Expansion · Kalman filtering

36.1 Uncertainties in Monitored Systems

Contrary to popular belief, structure and infrastructure systems comprise a dynamic ensemble; they experience motion, interact with their environments, are exposed to hazards, and undergo ageing and deterioration. At this point in time, a significant part of existing infrastructure is reaching, or has exceeded, the end of its life-expectancy, with catastrophic events revealing the necessity to undertake preventive measures and to come up with methodologies for assessing structural performance and safety. In response to this pressing need, Structural Health Monitoring (SHM) has in recent years risen to prominence as a tool for condition assessment and life-cycle management of engineered systems. SHM harvests information from sensors suitably deployed on structural systems. In recent years, technological advances have provided an abundance of low-cost and easily deployable sensors, delivering diverse information including strains, dynamic response quantities, loads and environmental condition data. When coupled with appropriate models, this information may guide engineers and operators in the effective management of these systems. However, the task of inferring adequate system models and indicators of performance, is hindered by the so-called polymorphic uncertainties [1], stemming from a mixture of modeling and measurement imprecisions. Due to lack of a priori knowledge, damage and deterioration processes, variability of environmental and operational influences, measurement errors, as well as simplified simulation assumptions, almost every structural system is characterized by uncertainty. The propagation of uncertainty through such a system comprises a non-trivial task, particularly when the system at hand is described by nonlinear [2] or time varying dynamics [3], thus furthering the complexity of the governing laws involved. For a number of tasks however, as for increasing the safety, robustness, resilience and capacity of engineered systems, it is necessary to develop models that are able to encompass the aforementioned uncertainties. In what follows, a step-wise deconstructive take is presented on dealing with the aforementioned diverse sources of uncertainty for different classes of structural identification problems of varying complexity.

E. N. Chatzi (✉) · V. K. Dertimanis

Institute of Structural Engineering, Department of Civil, Environmental and Geomatic Engineering, ETH Zurich, Zurich, Switzerland
e-mail: chatzi@ibk.baug.ethz.ch

36.2 Representation of Monitored Dynamical Systems Operating Under Uncertainty

Assume a linear time invariant structural system, of n degrees of freedom (DOFs), typically described by $\mathbf{M}\ddot{\mathbf{d}}(t) + \mathbf{C}_d\dot{\mathbf{d}}(t) + \mathbf{K}\mathbf{d}(t) = \mathbf{u}(t)$, where $\mathbf{M}, \mathbf{C}_d, \mathbf{K} \in \mathbb{R}^{n \times n}$ designate the system’s mass, damping and stiffness matrix respectively; $\mathbf{d}(t) \in \mathbb{R}^n$ denotes the vector of displacement; and $\mathbf{u}(t) \in \mathbb{R}^n$ denotes the exogenous input vector. Availability of a set of observations $\mathbf{y}(t) \in \mathbb{R}^n$, obtained through deployment of an appropriate sensor network, allows for rewriting the system using compact parametric representations, as in Table 36.1. The first is a state-space representation, where matrices $\mathbf{A}, \mathbf{B}, \mathbf{C}, \mathbf{D}$ are related to the system’s equation of motion, and may be determined either via a-priori knowledge of the system properties and corresponding matrices, or alternatively, inferred from the data via appropriate time-domain identification methods. Depending on the availability of information on the input, these algorithms may be deterministic (e.g. Subspace Identification) or stochastic (e.g. Stochastic Subspace Identification).

In an alternative parametric representation, a monitored DOF, $y(t)$, may be expressed in AutoRegressive form, specifically via an AutoRegressive model with exogenous input (ARX). In the ARX formula offered in Table 36.1, $[t]$ signifies discrete time notation, $y[t]$ is the monitored output, $u[t]$ is the exogenous input to the system, $v[t]$ corresponds to the unmodeled part of the disturbances acting on the input-output process, and the ARX parameters a_i, b_i are further defined as in [5]. Depending on availability of information on the input $u[t]$, variants of the above representations, such AutoRegressive Moving Average (ARMA) models may be employed. In the case of systems extending beyond linear response, generalized versions of the above representations may be utilized, as summarized in Table 36.2.

36.3 A Metamodeling Approach to Global System Models

Metamodeling refers to the process of identifying a reduced order, computationally efficient representation of a high-dimensional system. Different approaches may be adopted to such an end, including Proper Orthogonal Decomposition (POD), reduced-basis methods, or Gyan condensation. A metamodel may be constructed within two contexts. Firstly, to replace a refined but computationally costly numerical model [4], while maintaining an accurate prediction of its dynamic response. Secondly, a metamodel may be formulated purely on the basis of monitoring data, for inferring a relationship linking the inputs to the outputs of a system. Let us consider a structural system represented by a numerical model \mathbf{M} characterized by a number of input parameters relating to the properties of the modeled structure (mechanical and/or geometric). It is assumed that these parameters are subject to uncertainty, and may be described by independent random variables gathered in a random vector ξ . In order to approximate the numerical model dynamic response $y[t, \xi]$ for every

Table 36.1 Parametric representations for Linear Systems

Type	Equation	Remarks
State space	System Equation $\mathbf{x}_{k+1} = \mathbf{A}\mathbf{x}_k + \mathbf{B}\mathbf{u}_k + \mathbf{w}_k$	$\mathbf{x}_k = \begin{bmatrix} \mathbf{d}_k & \dot{\mathbf{d}}_k \end{bmatrix}$ $\mathbf{w}[t] \sim \text{NID}(0, \mathbf{Q}), \mathbf{v}[t] \sim \text{NID}(0, \mathbf{R})$
	Observation Equation $\mathbf{y}_k = \mathbf{C}\mathbf{x}_k + \mathbf{D}\mathbf{u}_k + \mathbf{v}_k$	
ARX model	$y[t] + \sum_{i=1}^{n_a} a_i y[t-i] = \sum_{i=1}^{n_b} b_i u[t-i] + v[t]$	$v[t] \sim \text{NID}(0, \sigma_v^2)$

Table 36.2 Parametric representations beyond Linear Systems

Type	Equation	Remarks
Nonlinear state space	System Equation $\mathbf{x}_{k+1} = \mathbf{f}(\mathbf{x}_k, \mathbf{u}_k, \boldsymbol{\theta}_k) + \mathbf{w}_k$ Observation Equation $\mathbf{y}_k = \mathbf{h}(\mathbf{x}_k, \mathbf{u}_k, \boldsymbol{\theta}_k) + \mathbf{v}_k$	\mathbf{f}, \mathbf{h} are the nonlinear system and observation functions respectively, $\boldsymbol{\theta}_k$: System parameters
Nonlinear AR model	$y[t] = \sum_{i=1}^{n_\theta} \theta_i \cdot g_i(\mathbf{z}[t]) + e[t]$	$\mathbf{z}[t] = \{y[t-1], \dots, y[t-n_a], u[t], \dots, y[t-n_b]\}$ $e[t] \sim \text{NID}(0, \sigma_e^2[t])$ $g_i(\mathbf{z}[t])$: nonlinear model terms
Time varying AR models	$y[t] + a_1[t]y[t-1] + \dots + a_n[t]y[t-n] = e[t] + c_1[t]e[t-1] + \dots + c_n[t]e[t-n]$	$(1-B)^k a_i[t] = w_{a_i}[t], w_{a_i}[t] \sim \text{NID}(0, \sigma_{w_a}^2[t])$ $(1-B)^k c_i[t] = w_{c_i}[t], w_{c_i}[t] \sim \text{NID}(0, \sigma_{w_c}^2[t])$

realization of ξ in an efficient way, we may exploit the AR model form described above and enhance it using a stochastic tool, namely a Polynomial Chaos Expansion (PCE). In [4], a Polynomial Chaos Nonlinear AutoRegressive with eXogenous input (PC-NARX) model is then introduced as $y[t] = \sum_{i=1}^{n_\theta} \theta_i(\xi) \cdot g_i(z[t]) + e[t]$, where it should be mentioned that the model terms $g_i(z[t])$ may be constructed from a variety of local or global basis functions including polynomials, splines, neural networks, wavelets and others. The important feature of PC-NARX models, in comparison with the conventional NARX models is that they are characterized by parameters, which are random variables themselves, admitting the following polynomial chaos expansion: $\theta_i(\xi) = \sum_{j=1}^{\infty} \theta_{i,j} \cdot \phi_{d(j)}(\xi)$, where $\theta_{i,j}$ are unknown deterministic coefficients of projection, $d(j)$ is the multi-index of the multivariate polynomial basis, and $\phi_{d(j)}$ are multivariate basis functions that are orthonormal with respect to the joint pdf of ξ . Linear ARX models with functionally dependent parameters have further been used in a number of studies for the purposes of structural identification and damage detection (see [6]). For monitored systems, PCE may also be directly employed for constructing a surrogate representation between monitored input and output features of a dynamic system. For instance, monitored response quantities (e.g. frequencies) of a structural system may be linked to influencing inputs (e.g. temperature and humidity), leading to robust condition indicators. The interested reader is referred to [3, 7] for further details on construction of such global system models.

36.4 Bayesian Filters for Identification of Monitored Systems

Availability of an adequate system model along with and sparse observations from dynamic systems, further allows to improve estimates of system response, in an online manner. The latter is often required in SHM implementations or control applications, where the real-time feedback is necessary. In serving such a purpose, time domain identification methods constitute a class of methods that are particularly well-suited for the online monitoring of dynamic systems.

Among other available tools, Bayesian approximation techniques in the form of Kalman-type filters (KF) may be exploited for (i) estimating system response in unmeasured locations, (ii) inference of the system parameters via appropriate joint parameter-state identification algorithms (e.g. Unscented KF, Particle Filters [2]), and (iii) joint input-state estimation (e.g. Dual KF [9], Augmented KF [10]), as well as for the challenge of (iv) joint input-state-parameter identification [11]. In recent works, output-only vibration measurements are coupled with substructuring approaches [10] and a system model, for feeding into a KF scheme to predict strains in critical (hotspot) structural locations [9] for the purpose of estimating fatigue accumulation. Shifting to the field of structural control, [12] demonstrates how the coupling of online joint state-parameter estimation algorithms with semi-active control schemes leads in effective structural vibration mitigation. The interested reader is referred to [8] for further details on the adoption of Bayesian filters for real-time identification.

References

1. Graf, W., Götz, M., Kaliske, M.: In: Deodatis, G., Ellingwood, B.R., Frangopol, D.M. (eds.) *Analysis of Dynamical Processes Under Consideration of Polymorphic Uncertainty, Safety, Reliability, Risk and Life-Cycle Performance of Structures and Infrastructures*, pp. 453–460. CRC Press, Boca Raton, FL (2014)
2. Chatzi, E., Smyth, A.W.: The unscented Kalman filter and particle filter methods for nonlinear structural system identification with non-collocated heterogeneous sensing. *Struct. Control. Health Monit.* **16**(1), 99–123 (2009)
3. Bogoevska, S., Spiridonakos, M., Chatzi, E., Dumova-Jovanoska, E., Höffer, R.: A data-driven diagnostic framework for wind turbine structures: a holistic approach. *Sensors.* **17**(4), 720 (2017)
4. DiazDelaO, F., Adhikari, S., Saavedra Flores, E., Friswell, M.: Stochastic structural dynamic analysis using Bayesian emulators. *Comput. Struct.* **120**, 24–32 (2013)
5. Spiridonakos, M., Chatzi, E.N.: Metamodeling of dynamic nonlinear structural systems through polynomial chaos NARX models. *Comput. Struct.* **157**, 99–113 (2015)
6. Kopsaftopoulos, F.P., Fassois, S.D.: A functional model based statistical time series method for vibration based damage detection, localization, and magnitude estimation. *Mech. Syst. Signal Process.* **39**(1–2), 143–161 (2013)
7. Spiridonakos, M., Chatzi, E., Sudret, B.: Polynomial chaos expansion models for the monitoring of structures under operational variability. *ASCE-ASME J. Risk Uncertainty Eng. Syst., Part A: Civ. Eng.* **2**, 3 (2016)
8. Chatzi, E.N., Smyth, A.W.: Nonlinear system identification: particle based methods. In: Beer, M., Patelli, E., Kougiumtzoglou, I., Au, I. (eds.) *Encyclopedia of Earthquake Engineering*: SpringerReference (www.springerreference.com). Springer, Berlin Heidelberg (2014)

9. Eftekhar Azam, S., Chatzi, E., Papadimitriou, C.: A dual Kalman filter approach for state estimation via output-only acceleration measurements. *Mech. Syst. Signal Process.* **60**, 866–886 (2015)
10. Lourens, E., Papadimitriou, C., Gillijns, S., Reynders, E., De Roeck, G., Lombaert, G.: Joint input-response estimation for structural systems based on reduced-order models and vibration data from a limited number of sensors. *Mech. Syst. Signal Process.* **29**, 310–327 (2012)
11. Dertimanis, V.K., Eftekhar Azam, S., Chatzi, E., Papadimitriou, C.: Output-only fatigue prediction of uncertain steel structures, 8th European Workshop On Structural Health Monitoring (EWSHM 2016), Spain, Bilbao, 5–8 2016
12. Miah, M.S., Chatzi, E., Dertimanis, V., Weber, F.: Real-time experimental validation of a novel semi-active control scheme for vibration mitigation. *Struct. Control. Health Monit.* **24**(3), e1878 (2016)